# Compositional Engineering of Solution-Processed Solar Cells: Aligning Computational and Experimental Screening Strategies



by

Matthew Thomas Klug

B.S.. Cornell University (2007)
M.Eng.. Cornell University (2008)

Submitted to the Department of Mechanical Engineering
in partial fulfillment of the requirements for the degree of

Doctor of Philosophy

at the

MASSACHUSETTS INSTITUTE OF TECHNOLOGY

September 2015



Author ..... Signature redacted ....
Department of Mechanical Engineering
August 25. 2015

Certified by ..... Signature redacted .....
Angela M. Belcher
Professor of Biological Engineering and Materials Science & Engineering
Thesis Supervisor

Certified by ..... Signature redacted
Nicholas X. Fang
Professor of Mechanical Engineering
Thesis Supervisor

Accepted by ..... Signature redacted ....
David E. Hardt
Chairman. Department Committee on Graduate Theses

# Compositional Engineering of Solution-Processed Solar Cells: Aligning Computational and Experimental Screening Strategies

by

Matthew Thomas Klug

Submitted to the Department of Mechanical Engineering
on August 25, 2015, in partial fulfillment of the
requirements for the degree of
Doctor of Philosophy

## Abstract

Unlike silicon, solution-processable solar materials are flexible, lightweight, easily processed at low temperatures, and display a wide variety of colors and degrees of transparency. These attributes open new opportunities to integrate solar power creatively and inexpensively into new markets such as electric vehicles and multifunctional architecture, as well as augment the performance of current solar technology in tandem cell configurations. One of the central challenges to realizing this vision is the high degree of disorder generally exhibited by solution-processed materials, which provides an abundance of trap sites that limit carrier transport. Hence, the performance of many solution-processed materials is governed by a trade-off between light harvesting and carrier collection, where complete absorption of sunlight requires active layer thicknesses greater than the diffusion lengths of the performance-limiting charge carrier. Overcoming this compromise requires either modifying the optical and electronic properties of solar materials themselves or designing device architectures that improve charge extraction or photon management. The work presented here pursues both of these strategies by leveraging a central feature of solution-processed solar cells - the ability to control the composition of the active layer by simply blending different ingredients in the precursor solutions. This simple concept provides the opportunity to tune the chemical composition of ionic solar materials, adjust the kinetics of film formation, add passivating agents that reduce trap densities, or introduce nanomaterials with specialized functionality into the active layers.

To explore this concept, two specific projects were undertaken. The first evaluates how the light harvesting ability of bulk-heterojunction systems is impacted by incorporating plasmonic nanoparticles into the material bulk. By performing a series of finite-difference time-domain (FDTD) calculations, many different active layer compositions were screened through to identify optimal optical configurations and predict performance trends. The results of this analysis informed the fabrication of actual solar cells, which generated photocurrent and external quantum efficiency en-

hancements consistent with the predicted trends. To fabricate several of these devices, biomolecules were used to mediate the assembly and growth of plasmonic metal-oxide nanocomposites.

The second project evaluates how replacing a portion of the metal content in metal-halide perovskite solar cells with alternative non-toxic metal species impacts the photovoltaic properties of the perovskite film. Relevant electronic properties such as the material band gap and carrier effective masses were theoretically evaluated using density functional theory (DFT). By computationally screening through a series of mixed-metal compositions that spans the periodic table, several promising candidates were identified that preserve the excellent electronic properties of the methylammonium lead triiodide perovskite, $MAPbI_3$, while simultaneously reducing material toxicity. The computational effort was paired with an exhaustive experimental screening study that systematically evaluated how replacing various amounts of lead with nine different metal species influence material properties and photovoltaic performance. By screening through a large set of active material compositions both computationally and experimentally, favorable embodiments were encountered and the experimental results were benchmarked against the theoretical predictions to help speculate on the mechanisms responsible for observed performance improvements.

Thesis Supervisor: Angela M. Belcher
Title: Professor of Biological Engineering and Materials Science & Engineering

Thesis Supervisor: Nicholas X. Fang
Title: Professor of Mechanical Engineering

Committee Member: Alexie M. Kolpak
Title: Professor of Mechanical Engineering

# Acknowledgments

First and foremost, I would like to thank God for granting me the strength and courage to pursue the research presented here over the past five years. I am not ashamed to say that I have been completely humbled by the graduate program at MIT and have often struggled against the onslaught of failure that seemed to accompany my scientific research. However, in the midst of disappointment, I have found renewal and wisdom in my faith. As Solomon once said:

*I have seen something else under the sun:*
*The race is not to the swift or the battle to the strong,*
*nor does food come to the wise or wealth to the brilliant or favor to the learned;*
*but time and chance happen to them all.*
*– Ecclesiastes 9:11*

I have drawn comfort from this verse, for despite my best efforts to control and predict outcomes, nature is often unpredictable. Hence, I have learned that the best way to find a favorable result in my work is to not despair, but rather press onwards and increase my chances of success by increasing the number of trials I attempt. By the grace of God, this approach has borne some fruit and it is with great pleasure that I am able to present this body of original work for my doctoral thesis.

I would like to express my deepest gratitude to Professor Angela Belcher for her continual support throughout my graduate work. Her research vision of using biology to assemble functional inorganic composites remains the most original and inspiring that I have ever seen. I have been continually impressed by her unending creativity and passion for scientific outreach, as well as her talent for translating technology out of the laboratory and building successful business ventures. I am exceedingly grateful for her patience and for her granting me the latitude to pursue the projects that have resulted in this dissertation. Without her support and mentorship, none of this would have been possible.

I am also profoundly indebted to Professor Nicholas Fang, my thesis committee chair and mentor in the mechanical engineering department. He is equal parts enthusiasm and brilliance, and has been a constant source of encouragement and knowledge

over the past five years. He was always willing to discuss the troublesome details of my research projects during our regular meetings, which was indispensable to making progress and promoting a productive frame of mind. He has pushed me to become a better scholar, researcher, teacher, and presenter by not only providing me resources but also opportunities to become a teaching assistant as well as engage in the greater academic community at conferences and focused gatherings. I am truly grateful not only for the guidance and kindness he has continually provided me, but also the chance to interact with such an inspiring leader and role model.

My thesis committee member, Professor Alexie Kolpak, has also been a continual source of support over the past few years. Not only did she teach me how to perform density functional theory calculations, but she generously provided all of the allocation necessary to run them at several different supercomputing clusters. She was always willing to find time to meet and discuss my projects even while on travel, and always offered valuable and insightful feedback. I am amazed at the depth of both her knowledge and kindness and am extremely thankful that she was willing to join my committee. Without her gracious support, I would never have embarked on one of the main projects presented in this dissertation.

I have been blessed with the opportunity to collaborate with some extraordinary researchers while at MIT, especially Dr. Sam Stranks and Dr. Anna Osherov. They are some of the brightest and most talented scientists with whom I have had the privilege of working. I am grateful for not only the scientific exploration of perovskites we have pursued together, but more importantly for the friendship we have developed in the process. Without their technical and moral assistance, I would not have been able to finish the work presented herein. The members of the Belcher, Fang, and Bulović groups helped me grow as a researcher by always being willing to chat about ideas, share their expertise, and help me troubleshoot when I was in need. I am also grateful for the financial support provided by the MIT Energy Initiative Eni-MIT Energy Fellowship, the Mechanical Engineering Department's SMA-2 Fellowship, and Eni, S.p.A (Italy) through the MIT Energy Initiative Program.

Aside from the research community at MIT, this work has been supported by my family, who always loved me even though I mostly talked to them about excitons, plasmons, and perovskites for five straight years. Words fall short of expressing how grateful I am for the encouragement that you have unceasingly provided through my countless failures and the celebration we shared at the moments of success. I am forever indebted to my parents who not only taught me the importance of hard work and how to persevere in times of adversity, but instilled in me the values that have shaped who I have become. My dad is not only an incredible man of faith and my personal role model, but has shown me that it is never too late to reinvent yourself and pursue your dreams. My mom has always been my greatest advocate and continually challenges me to become a better person. She has always been there to comfort me in my times of distress and provide much needed perspective when I couldn't see past my immediate concerns. I have also been blessed with the support of my indomitable twin sister, Katie, my brothers-in-law, Ben and Colin, and an amazing new set of parents, Mary and Gary.

Most importantly, I dedicate this work to my wonderful, beautiful, and loving wife, Summer. You never stopped believing in me, even when I lost faith in myself. I cannot imagine going through this process without your constant support, love, and counsel. I can't wait to see where life leads us and our fluffy goldendoodle next!

# Contents

# List of Figures

# List of Tables

# Chapter 1

# Introduction

The realm of solar research has historically been, and largely remains, claimed by physicists, chemists, materials scientists, and electrical engineers. The underlying principles and mechanisms that are responsible for solar cell operation, how light interacts with matter to produce useable electrical energy, fundamentally strikes at the very heart of physics. While chemists are needed to prepare ingredients and synthesize new photoactive materials, they also use computational approaches to examine known materials at the atomic level and extrapolate that knowledge to predict new ones with even improved properties. While the purer sciences generally fulfill the exploratory roles of identifying and characterizing new solar materials, it is the materials scientists and electrical engineers that translate the latest solar materials into prototype devices and scale the fabrication procedures for the eventual commercial manufacture of photovoltaic devices. This process of academic exploration in the pure sciences and practical implementation through applied engineering seems fairly complete, so where would a self-proclaimed mechanical engineer, such as myself, enter into this system? After all, quantum mechanics, electromagnetic wave theory, and solid state physics are eschewed by the core curricula of mechanical engineering programs in favor of topics such as solid and fluid mechanics, heat and mass transfer, system dynamics, and product design. While solar research is certainly unfamiliar territory for the traditional mechanical engineer, I believe that the field of mechanical engineering is poised to lay some claim to it for the following reasons:

1. Mechanical engineers are trained to become familiar with a very vast collection of disciplines in order to design, develop, and assemble products. As new technologies are prepared for manufacture, mechanical engineers are needed to develop the machines and equipment necessary to make the production process efficient and cost-effective. Therefore, mechanical engineers working for solar cell companies must obtain the required knowledge about solar science to inform this design process.

2. Some of the most interesting research in mechanical engineering occurs at the fringes of the field where the conventional boundaries of various disciplines begin to blur and overlap with one another. At these points of interdisciplinary convergence is perhaps the most fertile ground for mechanical engineers to develop breakthrough and disruptive technologies by "connecting-the-dots" in creative ways that were unforeseen by traditionalists in various related fields. This is a very attractive notion to mechanical engineers that aspire to invent and innovate alternative energy solutions.

3. Perhaps the broadest, yet correct, definition of mechanical engineering is *the study of using energy to generate movement, and vice versa.* While this has traditionally applied to macroscopic machines such as automotive engines and drive trains, steam turbines at power plants, or vehicles for powered flight, a new trend has emerged in the field to investigate the microscopic. Now it is no longer a question of discipline, but rather one of scale. This same concept of energy and movement can now be expanded to include topics of study such as how the lattice vibrations in materials relate to macroscopic heat conduction, how applied electric fields can move fluid through microchannels and manipulate biomolecules, and yes, even how photogenerated charge carriers in a material are transported through solar cells. At the micro- and nanoscale, the traditional domain of mechanical engineering bleeds into the territory of fundamental science, which provides the opportunity to not only *design*, but to also *discover*.

For all of these reasons, I decided to be an outlier among mechanical engineers while pursuing my coursework and research during my tenure as a graduate student. It has been challenging to meet the requirements of the mechanical engineering department and also learn about new and foreign topics, but I have relished the opportunity to explore the frontier of mechanical engineering by immersing myself in nanotechnology, biological engineering, computational chemistry, and photonics. I believe that the convergence of these disciplines will be invaluable in producing future innovations in energy, as well as healthcare.

Although I have attempted many different avenues of research, the topic of this thesis has been narrowed to focus specifically on my efforts in photovoltaic systems. The overarching goal of this research is:

*To identify new active layer compositions that are capable of improving the performance of solution-processable solar cells by screening through candidate embodiments both experimentally and computationally.*

At first glance, this might seem to be fairly broad and vague. However, it is the most precise, all-encompassing thread that has been woven through each of the topics that will be presented in this dissertation. Before discussing the specifics of these research topics, it is important to first set the stage by presenting the basic operating principles of photovoltaics and discussing how history has shaped the current state of the technology in the United States.

## 1.1 A Primer on Solar Cells

The solar cell, or photovoltaic cell, is an energy conversion device that generates electricity directly from sunlight. It must not be confused with electrochemical cells, which comprise the common battery. There are several primary distinctions between these two technologies that should be addressed upfront: [1]

1. The voltage generated in a battery arises from *permanent* electrochemical potential differences arising from the material properties of the phases comprising

its half-cells, whereas a solar cell derives its voltage from a *temporary* change in electrochemical potential caused by light.

2. The power supplied by a battery to a static load is constant, whereas the power delivered by a solar cell depends upon the intensity of light incident upon it. The amount of power generated by solar cells in the field can vary dramatically as cloud coverage and the orientation of the sun relative to the solar cell surface change.

3. The battery is a *voltage source*, whereas a solar cell is a *current source.*

4. A battery is completely discharged at the end of if its life, while a solar cell, in principle, is never depleted but can continually generate power whenever it is illuminated.

Now that the distinction has been drawn, it must be noted that if photovoltaic cells do indeed achieve widespread use as power sources they must be paired with a suitable energy storage technology, such as rechargable batteries, in order to make that power available on demand. If this is not done, then electricity will only be available when the sun is shining. For instance, the energy generated by solar cells could be stored electrochemically in high capacity rechargable batteries ( *e.g.* the Tesla Powerwall), thermally in reservoirs of molten salt, or chemically by using electrolysis to split water into hydrogen and oxygen. An energy storage mechanism is also needed so that the amount of current supplied to any given electrical load can be regulated, something that cannot be accomplished by directly connecting to a current source, such as a solar cell.

However the even greater question remains: why is generating and storing solar energy so important? Fundamentally, the answer is *energy availability.* The sun shines down a massive amount of energy. In fact, it provides the earth with enough energy in a single hour to meet the annual demand of the entire world. Stated differently, the approximate 20 TW of power required by the human population could be obtained by covering only about 0.16% of Earth's land with 10% efficient solar cells. This is

roughly equivalent to the surface area of the U.S. interstate system. As shown below in Table 1.1, the solar resource at Earth's surface vastly outweighs the combined estimated remaining availability of other renewable sources. [2]

Table 1.1: Availability of renewable energy sources [2]

| Source | Global Power Estimate (TW) |
|---|---|
| Hydroelectric | <0.5 |
| Tides & Currents | 2 |
| Geothermal | <2 |
| Wind | 2-4 |
| Solar | 120,000 |

Although insolation, the amount of solar energy radiating on a surface at a given place and time, depends upon latitude and varies with season and weather conditions, there is more than enough sunlight freely available to all. Accessibility to energy would no longer depend upon how large fossil fuel reserves are of a given country and possession of said resources would no longer be a motivation for conflict, or a tool for extortion. Secondly, any increase in the share of electricity generated by solar technologies would diminish the impact of fossil-fuel power plants upon the ecological state of the world.

The main challenge to deploying solar technologies isn't the merit of the idea, but rather the economics of development and implementation. Not only must solar modules reach a cost point that make it competitive with conventional energy sources, but the infrastructure necessary to store the intermittent electricity generated by the cells and deliver it to the consumer requires substantial changes to the electrical grid. [3] The current state of the solar industry and the economic advantages of next-generation solar technologies will be further discussed later in this chapter.

### 1.1.1 Basic Operation of Solar Cells

Although the principles of solar cell operation rely on quantum mechanics, the overall concept is fairly simple. First, the sun emits light of all different frequencies, or colors, which can be thought of as discretized packets of energy that act as particles, called

*photons*. The energy of a photon, $E$, depends only on its frequency, $\nu$, or inversely, its wavelength, $\lambda$:

$$E = h\nu = h\lambda/c \tag{1.1}$$

where $h$ is Planck's constant and $c$ is the speed of light in vacuum. Upon striking a solid surface, photons with sufficient energy are absorbed and excite electrons bound in the photoactive material to higher energy levels where they gain the ability to freely move. As shown in Figure 1-1a, the excited electron leaves behind an empty space in

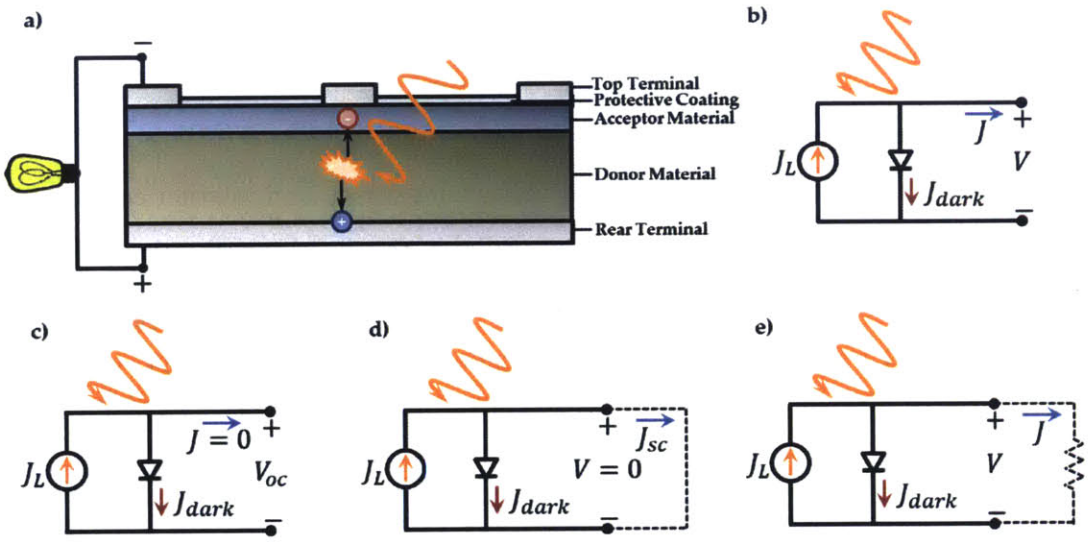


Figure 1-1: a) A simple solar cell consists of two layers of active material sandwiched between a rear electrode and a top transparent electrode. Upon light absorption, an electron-hole pair is generated and each charge migrates to different electrodes due to the asymmetry of the device structure. When an electrical load is attached to the terminals, a photovoltage develops across the terminals and a photocurrent flows, powering the load. b) The equivalent circuit of an ideal solar cell consists of a photocurrent generated upon illumination running in parallel with the diode characteristic of the material junction. c) When the solar cell terminals are isolated, the device is in the *open circuit* condition and a voltage is generated across the terminals. d) When the terminals are connected without an electrical load, the device is in the *short circuit* condition and a current flows between them. e) When the terminals are connected to an external load, the solar cell operates and both a photocurrent and photovoltage are generated.

the material, which is referred to as a hole. Because a hole is the absence of a negatively charged electron at a position where one could exist, it can be conceptualized as a positively charged particle, with an equal and opposite charge to the electron,

that is also free to move throughout the lattice. In order for a photovoltaic device to generate electrical energy, the device design must include some spatial asymmetry in the structure that allows for the electrons and holes to travel to separate electrodes. This spatial asymmetry usually takes the form of two materials with different electrical properties coming into physical contact to form a *heterojunction.* When the solar cell is not connected to an external circuit (Figure 1-1c), it is in a state referred to as the *open circuit* condition and a photovoltage is established by the charge separation mechanism that arises from the device asymmetry. Likewise, if the two terminals are connected without any electrical load (Figure 1-1d), it is in a state referred to as the *short circuit* condition and a photocurrent is established as electrons are extracted from their terminal, run through the electrical connection to the opposite terminal, and are injected back into the device at the opposite side where they can recombine with their awaiting counterpart holes. When an electrical load is added to the external circuit (Figure 1-1e) *both* photovoltage and photocurrent are generated and electrical work can be performed as electrons dissipate their energy in the load before being injected back into the solar cell.

### The Current-Voltage Characteristic in Ideal Solar Cells

The electrical behavior of solar cells are generally probed by measuring the *current-voltage characteristic*, usually referred to as the $JV$ curve. This is accomplished by applying a voltage bias, $V$, across the terminals of the solar cell and subsequently measuring the current, $I$, that flows through an external circuit connecting the two terminals. An ideal solar cell behaves like a diode in the dark, which allows current to flow under forward bias ($V > 0$) but an almost negligible amount under reverse bias ($V < 0$). Although current is the quantity that is actually measured during testing, the current density, $J = I/A$, where $A$ is the area of the solar cell, is generally preferred instead. Normalizing the measured current by the device area allows the current generated by two different solar cells to be compared regardless of size. The *dark current density*, $J_{dark}$ of a solar as a function of applied voltage bias is modeled

as a diode and is described mathematically by:

$$J_{dark}(V) = J_0(e^{qV/mk_BT} - 1) \tag{1.2}$$

where $J_0$ is a constant, $q$ is the charge on an electron, $T$ is temperature in Kelvin, $k_B$ is Boltzmann's constant, and $m$ is the ideality factor of the diode. For an ideal diode, $m = 1$.

When the solar cell is illuminated, light is absorbed and charge carriers are produced, which migrate to their respective terminals. Now if a voltage is applied across the terminals, the solar cell will produce a current in accordance with the diode behavior discussed in Equation 1.2 as well as generate its own photocurrent, $J_L$, in parallel. The equivalent circuit diagram shown in Figure 1-1b captures this concept schematically. The overall current density of the cell as a function of applied voltage can be approximated as the superposition of $J_{dark}$ and $J_L$. Therefore the current that flows between the device terminals when illuminated, $J(V)$ is:

$$J(V) = J_L - J_{dark} \tag{1.3}$$

When the solar cell is in the short circuit condition, there is no voltage across the terminals, and the measured current density is defined as the short circuit current density, $J_{sc} \equiv J(V = 0) = J_L$. Combining this with Equations 1.2 and 1.3 and yields the *ideal diode equation*:

$$J(V) = J_{sc} - J_0(e^{qV/mk_BT} - 1) \tag{1.4}$$

There is no light current, $J_L = 0$, when the solar cell is in the open circuit condition. Therefore, the open circuit voltage can be solved by rearranging Equation 1.4:

$$V_{oc} = \frac{mk_bT}{q} \ln\left(\frac{J_{sc}}{J_0} + 1\right) \tag{1.5}$$

Lastly, the power density, $P$, produced by the solar cell for a given bias is:

$$P = JV \tag{1.6}$$

The solar cell achieves its maximum power output at the maximum power point, which is denoted in Figure 1-2. In order to make use of all the power generated by the solar cell, the load in the external circuit must be appropriately sized to achieve the corresponding photovoltage, $V_m$, and photocurrent $J_m$. Therefore, the maximum power point is also referred to as the *operating point.*

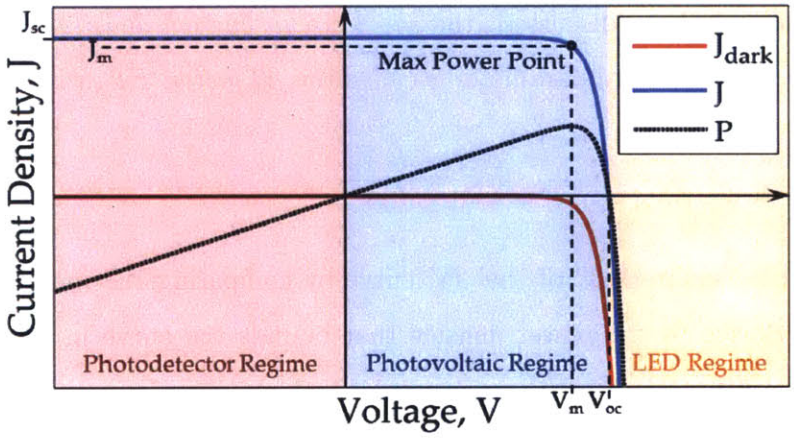


Figure 1-2: The $JV$ characteristic of an ideal solar cell when dark and illuminated and the three regimes of device operation.

Figure 1-2 shows the dark and light $JV$ curves for an ideal solar cell with the convention that the current density produced under forward bias is positive. It should be noted that this sign convention depends upon the solar cell type; for instance, the opposite convention is used for organic solar cells such that the current density is negative under forward bias. Although we are interested in using the device structure depicted in Figure 1-1a to generate electrical power, it can also be used for two other applications where electrical power is supplied to the device for different purposes. All three regimes of operation for this devices are:

**Photodetection Regime** ($V < 0$): Electrical power is *consumed* to produce a photocurrent upon illumination regardless of applied bias.

**Photovoltaic Regime** ($0 \leq V \leq V_{oc}$): Electrical power is *generated* upon illumination that is dependent upon applied bias.

**Light Emitting Regime** ($V > V_{oc}$): Electrical power is *consumed* to generate photons with energies equivalent to the material's band gap.

### Efficiency and Performance Metrics

Measuring the $JV$ characteristic of a solar cell is enough to provide several key performance metrics that are used to benchmark solar devices against one another. The first two have already been discussed: the *short circuit current density*, $J_{sc}$, and *open circuit voltage*, $V_{oc}$. The third parameter is called the *fill factor*, $FF$, which is unitless:

$$FF = \frac{J_m V_m}{J_{sc} V_{oc}} \tag{1.7}$$

and describes the "squareness" of the $JV$ curve by comparing the maximum power density of the device to the power density that bounds the curve in the regime of photovoltaic operation, $J_{sc}V_{oc}$.

The power conversion efficiency, $PCE$ or $\eta$, is the fourth and most important performance metric. It defines how much of the solar power shining on the solar cell is converted into electrical power. It is defined as:

$$PCE = \frac{P_m}{P_s} = \frac{J_m V_m}{P_s} = \frac{J_{sc} V_{oc} FF}{P_s} \tag{1.8}$$

where $P_s$ is the power density of light incident on the solar cell, which can be obtained by integrating the spectral irradiance, $M(\lambda)$, (*i.e.*, power density contained in each wavelength of the source) of the light source over all wavelengths:

$$P_s = \int_0^\infty M(\lambda) d\lambda \tag{1.9}$$

The standard solar spectrum used for testing solar cells is the AM1.5G spectrum, which when integrated over the visible and infrared wavelengths yields 1,000 W/m$^2$.

The certified record solar cell efficiencies achieved in research laboratories as of June 9, 2015 of several important solar technologies are summarized in Table 1.2. It must be noted that if solar cells of a given type are available commercially, they generally have lower performance due to additional inefficiencies that are incorporated upon building solar modules. Larger area panels also have a higher probability of detrimental defects arising in the active layers than the typically small areas used in research devices, which reduces performance.

Table 1.2: Certified record efficiencies of research solar cells [4]

| Solar Cell Type | $PCE$ (%) | Manufacturer |
|---|---|---|
| Multijunction w/Concentrator | 46.0 | Fraunhofer ISE/Soitec |
| Monocrystalline Si | 25.0 | SunPower |
| Thin-Film Crystalline Si | 20.8 | Trina Solar |
| Thin-Film Amorphous Si:H | 13.6 | AIST |
| Monocrystalline GaAs | 27.5 | LG Electronics |
| Thin-Film Crystalline GaAs | 28.8 | Alta Devices |
| Thin-Film CdTe | 21.5 | First Solar |
| Thin-Film $CuInGaSe_2$ (CIGS) | 21.7 | ZSW |
| Perovskite | 20.1 | KRICT |
| Organic | 11.5 | Hong-Kong UST |
| Dye-Sensitized | 11.9 | Sharp |
| Quantum Dot | 9.9 | U. Toronto |

### Non-Ideal Solar Cells

Although the highest performing solar cells often approach the ideal diode behavior previously discussed, most solar cells that use non-crystalline or lower quality materials demonstrate $JV$ characteristics that deviate in several important ways. There are nominally three detrimental situations that commonly occur in real devices:

**Diode Non-Ideality ($m$):** accounts for deviation from ideal diode behavior of the solar material. An ideal solar cell has a value of unity, however often non-ideal devices demonstrate values between 1 and 2, which can be attributed to second order effects such as various recombination mechanisms.

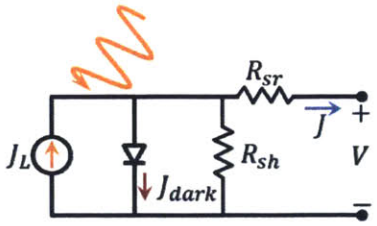


Figure 1-3: The standard equivalent circuit of a non-ideal solar cell contains additional parasitic resistances, one in series and the other in parallel with the ideal solar cell circuit shown in Figure 1-1b.

**Parasitic Series Resistance ($R_{sr}$):** accounts for current dissipation that arises when travelling through the layers of the solar cell. This includes both resistances in the materials layers themselves as well as interfacial contact resistances between them.

**Parasitic Shunt Resistance ($R_{sh}$):** accounts for power losses that occur when defects in the solar cell provide alternate pathways, or shunts, for current to travel through between the terminals besides the solar materials.

When these non-ideal behaviors are incorporated into the standard model of a solar cell, the equivalent circuit gains two additional resistors: one in parallel the other in series with the ideal device depictied in Figure 1-1b. Each act to reduce the overall efficiency of the solar cell by lowering the fill factor. A real solar cell will approach the ideal diode model when $R_{sr} \to 0$ and $R_{sh} \to \infty$. Understanding how each of these parasitic effects manifest in the $JV$ characteristic is crucial to diagnosing problems in the device structure without destructive examination. The standard equivalent circuit of the standard solar cell including these parasitic resistances is shown in Figure 1-3 and the diode equation becomes:

$$J(V) = J_{sc} - J_0(e^{q(V+JAR_{sr})/mk_BT} - 1) - \frac{V + JAR_{sr}}{R_{sh}} \tag{1.10}$$

Using this equation, $JV$ curves of a non-ideal solar cell with three different sets of parasitic resistances are shown in Figure 1-4. When compared against Figure 1-2, it is obvious that the slope of the curves near the short circuit condition increases in magnitude due to reducing shunt resistance and the slope near the open circuit condition decreases in magnitude due to increasing series resistance. The fill factor

of these curves are listed in the inset and are substantially lower than the 81% value demonstrated by the ideal diode curve in Figure 1-2.

The series and shunt resistances can also be extracted from a measured $JV$ characteristic by calculating the slope of the curve near the $x-$ and $y-$intercepts, respectively. From Ohm's Law, $V = IR = JAR$, resistance can be determined from the derivative of $V$ with respect to $J$:

$$\frac{1}{R} = A\left|\frac{dJ}{dV}\right| \tag{1.11}$$

Thus, the greater the magnitude of the $JV$ curve's slope near the intercepts, the lower the parasitic resistance.

The parasitic resistances can also be normalized against the characteristic resistance of the solar cell, $R_{ch} = V_m/J_m A$, which provides a non-dimensional way to compare resistances regardless of device size. The normalized series, $r_{sr}$, and shunt, $r_{sh}$, resistances and are defined as:

$$r_{sr} = \frac{R_{sr}}{R_{ch}} \qquad \text{and} \qquad r_{sh} = \frac{R_{sh}}{R_{ch}} \tag{1.12}$$

Unlike the parasitic resistances, which become most evident in the $JV$ curves when illuminated, the ideality factor can be diagnosed from the dark current by rearranging Equation 1.2:

$$m = \frac{qV}{k_b T} \ln\left(\frac{J_{dark}}{J_0} + 1\right) \tag{1.13}$$

In practice, it is easier to determine the ideality factor from a semilog plot of the dark current as a function of applied bias. This relationship is found by first dividing both sides of Equation 1.4 by $J_0$ and taking the natural logarithm of each side:

$$\ln\left(\frac{J_{dark}}{J_0}\right) = \frac{qV}{mk_b T} \tag{1.14}$$

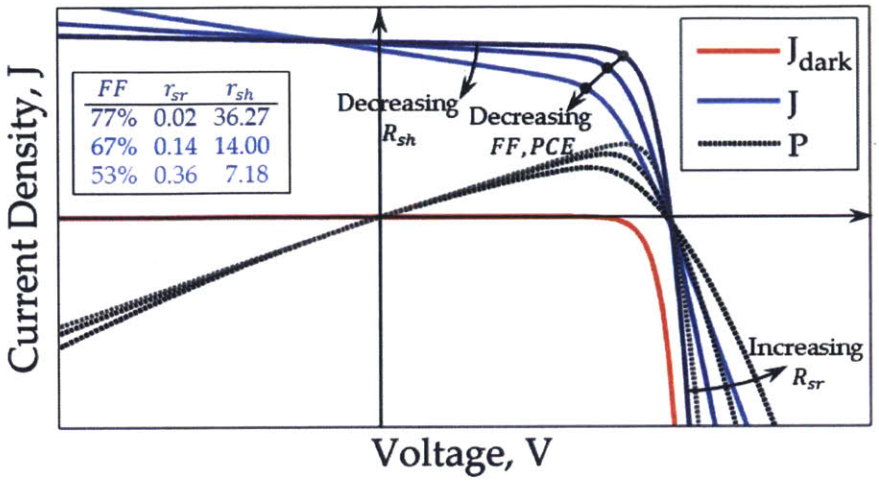


Figure 1-4: The $JV$ characteristic of a non-ideal solar cell when dark and illuminated show significantly lower fill-factors than ideal solar cells due to the presence of series and shunt parasitic resistances. As $r_{sr}$ increases and $r_{sh}$ decreases, the $FF$, $P_m$, and $PCE$ consequently decrease as well. A simple measurement of the $JV$ curve provides important insight into the behaviors that limit performance and an understanding of physical conditions that can generate parasitic resistances allows for troubleshooting to be target to specific device features.

Taking the derivative of both sides with respect to $V$:

$$\frac{d\Big(\ln(J_{dark}/J_0)\Big)}{dV} = \frac{d(\ln J_{dark})}{dV} - \frac{d(\ln J_0)}{dV} = \frac{q}{mk_bT} \tag{1.15}$$

and noting that the $d(\ln J_0)/dV = 0$ because $J_0$ is a constant, yields:

$$\frac{1}{m} = \frac{k_BT}{q}\left(\frac{d\ln J_{dark}}{dV}\right) \tag{1.16}$$

which demonstrates that the ideality factor is inversely proportional to the slope of the dark current-voltage characteristic plotted with a logarithmic scale for current density. This equation provides a simpler means to evaluate the rectifying behavior of the diode simply from the dark $JV$ curve. Therefore, it is always good practice to test devices under both dark and illuminated conditions.

The ideality factor can provide information about recombination mechanisms that are occurring in the device. In a $p-n$ junction solar cell, the ideality factor will depend upon the number of carriers involved in the dominant recombination mechanism and can change depending upon the applied voltage bias. The recombination of electrons and holes usually occurs radiatively across the band gap in direct band gap materials, such as GaAs, or at a deep-trap near the middle of the band gap for indirect band gap materials, such as Si. In these processes, recombination is limited by the minority carrier only and the ideality factor has a value of 1. However, if recombination occurs inside the depletion region of the junction, both carriers limit recombination and the ideality factor has a value of 2. Likewise, for the case of Auger recombination where energy is donated to a third carrier in a three-carrier process, the ideality factor becomes 2/3. By investigating how the ideality factor varies with applied bias, information about the physical mechanisms that dominate device operation can be easily inferred.

### 1.1.2 A Brief History of Solar Cells

The discovery of the photovoltaic effect is credited to the French physicist, Alexandre-Edmond Becquerel, who in 1839 discovered that an electric current could be generated by illuminating silver chloride when placed in an acidic solution and connected to platinum electrodes. Although this accomplishment led Becquerel into some interesting work using silver halides in the burgeoning field of photography, it wasn't until about forty years later that the first solar cells were constructed from the semiconductor selenium after the English electrical engineer, Willoughby Smith, discovered in 1873 that its conductivity significantly increases upon light exposure. [5] An American inventor named Charles Fritts was the first to construct a solid state solar cell from a slab of selenium in 1883 by coating it with a semi-transparent gold film. [6] His device only achieved a power conversion efficiency of about 1% due to the inherent limitations of selenium, which along with its high cost, precluded this technology from ever being deployed as a power source. However, selenium-based cells were widely used as light sensors for exposure timing mechanisms in cameras well into the 1960s since

they did not require an external power supply. Aside from being the first solid-state solar cell, Fritts' device was also the first incarnation of a device architecture that is now known as a Schottky barrier, which demonstrates rectifying behavior due to the establishment of a potential energy barrier for electrons at the metal-semiconductor junction. This is named after Walter Schottky who developed the theory for the phenomenon along with Neville Mott in the 1930s. Yet it wasn't until silicon wafers of sufficient purity became available in the 1950s that photovoltaic devices with the potential to generate useful amounts of power began to emerge.

The development of good quality crystalline silicon closely followed the initial demonstration of a silicon $p$-$n$ junction in 1941 by Russel Ohl, a scientist at Bell Laboratories. He showed that intrinsically $n$-type silicon, which has a larger electron concentration than hole concentration, could be treated with boron trichloride gas to develop a $p$-type, or hole rich, skin near the wafer surface. This process allowed two layers of silicon with dramatically different electrical properties to be synthesized from the same wafer without bringing two initially separate materials into physical contact. Not only was this advantageous from a processing perspective, but the resultant $p$-$n$ junctions demonstrated better rectifying behavior than the metal-semiconductor Schottky barriers, and thus better photovoltaic behavior. Ohl also proved that the behavior of $p$-$n$ junctions became more reliable with higher purity semiconductor materials, which launched a substantial effort in the 1950s to develop silicon for solid-state electronics. Soon after, Daryl Chapin, Calvin Fuller, and Gerald Pearson, also at Bell Laboratories, demonstrated the first embodiment of the modern solar cell in 1954 using the $p$-$n$ junction, which achieved a light to electrical power conversion efficiency of 6%. Over the next several decades, silicon solar cells saw gradual improvement, but the only significant market for the technology in the early years was aerospace with the Vanguard 1 satellite being the first launched with solar cell installations in 1958. Although the production cost of solar cells at this time are estimated to have been around $200 per watt, their high reliability and high power-to-weight ratio made them a judicious choice for integration into spacecraft designs regardless of expense. [1] In fact, for this reason there was little motivation for solar cell manufacturers to invest

in less efficient, less costly solutions.

In 1961, William Shockley and Hans Queisser developed the analytical model for the detailed balance limit, also known as the Shockley-Queisser limit, which refers to the maximum theoretical efficiency a single junction solar cell can achieve. [7] Within the assumption of their model, the maximum efficiency of a *p-n* junction device is a function only of *material band gap* and the *incident spectrum of light.* The band gap of a material corresponds to the minimum amount of energy needed to excite an electron to a higher energy level where it gains the freedom to move around. Therefore, only photons with an energy greater than or equal to the band gap can contribute to current generation; all others will simply pass through the cell. Shockley and Queisser demonstrated that there is a fundamental trade-off for solar cell efficiency: lower band gaps allow a solar cell to generate current from a greater portion of the solar spectrum (*i.e.*, there will be an increase in photocurrent), but the energy of these excited photons will be lower (*i.e.*, there will be a decrease in photovoltage). As shown in Equation 1.8, the overall device PCE depends upon both these quantities, and an optimum band gap will exist that maximizes performance. The detailed balance limit for the standard AM 1.5 solar spectrum has been plotted in Figure 1-5, which shows that the maximum achievable efficiency of 33% is possible with a material whose band gap is near 1.4 eV. Research stemming from this seminal work along with other theoretical studies began to identify other semiconductors such as gallium arsenide (GaAs), indium phospide (InP), and cadmium telluride (CdTe) as materials capable of achieving even higher performance. As shown in Table 1.3, the band gap of each of these materials is closer to the optimum value of 1.4 eV than traditional silicon.

Table 1.3: Band gaps of common semiconductors used in *p-n* junction solar cells [1]

| Material | Band Gap (eV) |
|---|---|
| Si | 1.124 |
| GaAs | 1.424 |
| InP | 1.344 |
| CdTe | 1.500 |

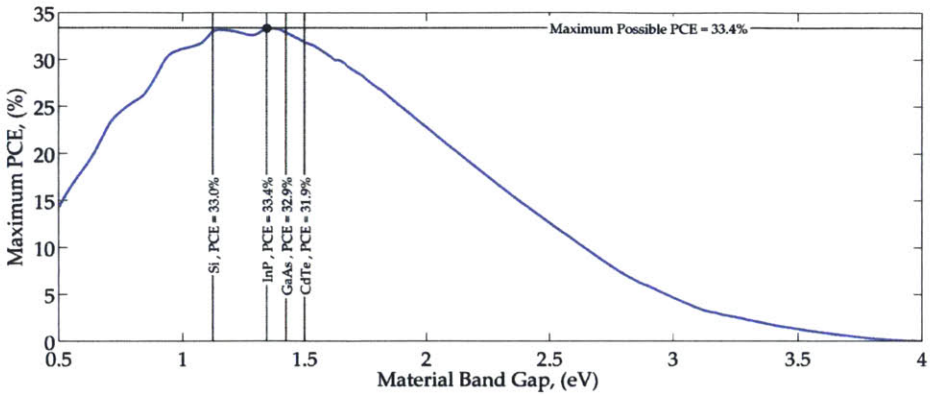


Figure 1-5: The Shockley-Quiesser Limit presents the maximum possible power conversion efficiency of an ideal single-junction $p-n$ solar cell is dependent upon the material band gap for the incident solar spectrum. This calculation was performed using the AM1.5G standard solar spectrum.

In fact, each of these identified materials are commonly used in current solar and optoelectronic technologies. Despite the existence of such higher efficiency photovoltaic materials, silicon has historically been, and remains to this day, the dominant solar material. This is largely due to it benefiting from continual advances in silicon processing technology for the microelectronics industry. By the early 1970s, the cost of solar cells had dropped to about $100 per watt due to the increasing availability of large boules of silicon intended to supply integrated circuit manufacturers.

The petroleum shortages of the late 1970s forced the western world to seek out alternative energy sources as major industrial centers struggled against escalating energy prices and widespread economic stagnation. This precipitated a renewed interest in solar energy and substantial funding became available for the research and development of less expensive solar cells. It was at this time that cheaper thin-film materials such as amorphous silicon, polycrystalline silicon, and copper sulfide/cadminum sulfide were first explored and concepts such as multijunction solar cells were developed to achieve theoretical efficiencies exceeding the Shockley-Quiesser limit. The 1970s and 1980s was also the first time that breakthroughs emerged in another class of solar cells, those based on organic photoactive ingredients rather than inorganic crystallline solids.

Ching Tang demonstrated the first organic-based solar cell with an efficiency ex-

ceeding 1% by evaporating an organic electron acceptor material on top of an organic electron donor material to form a bilayer planar heterojunction. As an employee at Kodak, this initial finding was first patented in 1979 and later published in 1986. [8] It was shortly after in the early 1990s that Alan Heeger's [9] and and Katsumi Yoshino's [10] research groups independently discovered that pairing a polymeric donor material with a fullerene derivative yielded extremely fast electron transfer times, which dominated over all other photophysical processes. Ever since, the conjugated polymer donor and fullerene-based acceptor materials have been the main ingredients in almost all polymer solar cells.

Likewise, in 1988 the first embodiment of the modern dye-sensitized solar cell (DSSC) was constructed by Michael Grätzel and Brian O'Regan while students at UC Berkeley. As opposed to the long macromolecules utilized in polymer solar cells, DSSCs use considerably smaller organic dye molecules as the main photoactive ingredient. In follow-up studies, Grätzel published the first high-efficiency DSSC in 1991, which achieved a power conversion efficiency of 7-8%, making it the highest performing organic-based solar cell technology at the time by a wide margin. [11]

As these organic systems were being developed at academic institutions, the worldwide production of crystalline solar cells doubled from 10 megawatts in 1982 to over 20 in 1983 alone. As the semiconductor industry continued to mature and produce ever-larger silicon boules, the production of monocrystalline solar cells continued to rise. By 1990 the module cost of solar photovoltaics had dropped to just under $10 per watt and significiant investment was being made in polycrystalline silicon in an effort to achieve lower operating costs, even though it was less efficient than its monocrystalline counterpart. Due to overproduction of crystalline silicon panels in China and Taiwan, coupled with a drop in European demand due to economic turmoil, the cost of crystalline modules dropped to $1.10 per watt in 2011 and continued to fall to $0.62 per watt in 2012. [12]

Although crystalline silicon panels continue to dominate the worldwide market, the American company, First Solar, has developed an alternative technology that maintains an economic advantage over silicon. First Solar uses cadmium telluride

instead of silicon, which not only has a more desirable band gap, as discussed previously, but it can achieve high efficiencies using significantly thinner cells than silicon. CdTe is a much better light absorber than Si, therefore thin-film CdTe solar cells require only about one micron thickness, whereas monocrystalline silicon devices are generally around 300 microns thick. By using less material and a fabrication process based on vapor-deposition, First Solar has been able to historically produce solar cells at a lower cost point than silicon. CdTe also offers a higher resistance to performance reductions than silicon at the operating higher temperatures experienced in the field due to lower temperature coefficients. On February 24, 2009, First Solar was the first technology to break the $1 per watt cost barrier, and has continued to drop in price. They currently hold the record for CdTe solar cells at a certified 21.5% [4] and achieved a record-breaking thin-film photovoltaics module in March 2014 with a certified 17.0% efficiency. [13] The module cost at this time was only $72 per square meter.

### 1.1.3 State of Solar Energy in the United States

Even though solar cell technology has consistently improved in performance and dropped in price over the past several decades, both energy consumption and electricity generation in the United States remains dominated by non-renewable sources. According to the U.S. Energy Information Administration, solar technologies supplied a slim 0.3% of the total energy consumed in the United States during 2013. Likewise, only 0.2% of electricity was generated at solar power plants. [14] Instead, the United States still consumes petroleum for the larger part of its overall energy needs and generates most of its electricity by burning coal. Why is the contribution from solar technologies so marginal? The answer is still *cost.*

Although significant concerns exist about the ecological impact of fossil-fuel energy sources as well as the economic and political ramifications of dependence on foreign petroleum, the fact remains that fossil-fuels are cheap and the U.S. has a lot them. The United States has the world's richest oil shale deposits, the world's largest proven coal reserves, and is the world's greatest producer of natural gas. [14] It is only

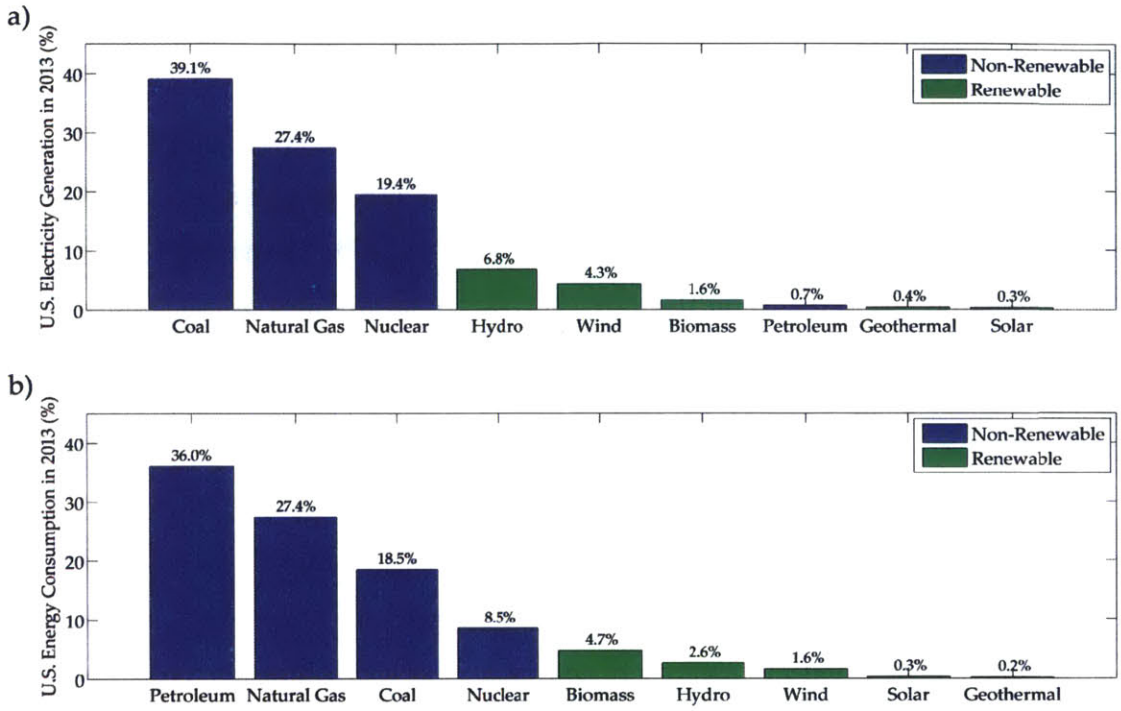


Figure 1-6: In 2013, the majority of energy consumption (a) and electricity generation (b) was derived from non-renewable energy sources. [14]

natural that these abundant energy reserves be used to power the country, especially when our energy infrastructure was originally built to make use of these traditional fuels. In a capitalistic country, transitioning from conventional fossil-fuels to alternative energy sources requires not only overcoming a century of historical inertia in power production, but also ensuring that it makes fiscal sense. The recent success of hydraulic fracturing and horizontal drilling techniques have increased the domestic production of oil and natural gas, which has caused net energy imports to decline by 58% between 2013 and the peak levels in 2005, making it increasingly hard for alternative energy sources to compete without significant subsidies and policy intervention from the government. [14]

### 1.1.4 Overcoming the Barriers

According to the Solar Energy Industry Association, 2014 was a record year for growth in the solar industry. During this year 195,000 solar panel installations were con-

structed bringing the total number of American homes and business that generate solar power to nearly 645,000. [15] The cumulative capacity of photovoltaics grew by 51% from 2013 and brought the total solar capacity to over 20 GW, enough to power over 4 million average American homes. Likewise, the U.S. solar industry provides nearly 174,000 jobs at over 8,000 businesses across all 50 states. Although the solar capacity is projected to double in the next two years, photovoltaics still face substantial challenges that must be overcome for solar power to become a core energy source. These include:

1. **Lowering Solar Module Cost:** It has been estimated that solar modules will become competitive with traditional energy source once they reach a cost point of \$0.40/W. [2] It must be stressed that although this is a target mark that is commonly quoted by researchers and even solar companies, the cost of photovoltaics extends significantly beyond just the module to include installation and maintenance fees, as well as account for fluctuations in the energy market. Regardless, solar cell manufacturers are quickly approaching this target mark. Chinese company, JinkoSolar, recently announcing in 2014 a silicon module cost of \$0.48/W. [16] However, there remains skepticism that such numbers are artificially deflated due to heavy subsidization by the Chinese Government. Prof. Michael McGehee at Stanford University suggests that the true cost of these silicon cells is closer to \$0.85/W and is skeptical that they will ever reach the desired target cost without subsidy. [16]

2. **Lowering Solar Power Plant Cost:** The cost of building a photovoltaic power plant (\$130/MWh) is twice the cost of a conventional combined cycle natural gas plant (\$66.30/MWh) and 1.4 times the cost of conventional coal (\$95.60/MWh, which accounts for the \$15/tonne of $CO_2$ penalty added by the federal government). [14] Furthermore, solar power plants are generally built in sunny, arid locations that are far from major population centers, which requires building costly transmission lines to distribute the electricity to consumers. For instance, the estimated cost of building the powerlines for the 120-mile Sunrise

Powerlink in Southern California is $1.88 billion. [14]

3. **Storing Solar Energy:** Solar power is diffuse and intermittent. Solar photovoltaic power plants only operate at peak efficiency about 25% of the time. [14] In order to make power available on demand, the electricity generated from photovoltaics must first be stored. For residential installations, an effective option would be to pair the solar cells with a large rechargeable battery such as Tesla's PowerWall. Although banks of massive batteries might also be an option for large photovoltaic power plants, other concepts have been proposed. One of these would be to use the photocurrent produced by solar cells to split water into hydrogen and oxygen gas via electrolysis, store the gases separately, and later recombine them to form water and heat, which in turn produces electricity via conventional steam generators. Although energy storage will always dilute the efficiency of solar power, it will be necessary as photovoltaic cells replace conventional sources. Concentrated solar power plants, which focus sunlight with parabolic mirrors to heat fluid, bypass the need for electrochemical storage system because the thermal energy can be more efficiently stored and used with steam generators to produce electricity on demand. Although concentrated solar power plants are currently twice as expensive to build than photovoltaic power plants, they would likely play a crucial role in a future energy economy that is heavily dependent on solar by generating base-load power for the electrical grid in sunny remote areas to help even out the variable production of solar cells.

4. **Acquiring Investors:** Although solar power is appealing, it is currently very challenging for solar photovoltaic startups to gain financing. Part of the problem is that venture capital firms are shying away from investing in early-stage clean energy startup technologies, making it difficult for new innovations to be launched. Venture capital funds generally invest no more than $30 million in a company and aim for a public offering or acquisition within ten years, [17] a criteria that is rarely met by energy startups. Instead, photovoltaic technologies

usually require massive initial capital investment largely because complex fabrication procedures are involved and there is rarely any intermediate product that can be sold for profit until a full-scale solar module is produced. Then to survive, that module must perform better and have a price competitive with those from established foreign manufacturers that are heavily-subsidized by their governments. This poses too much risk for traditional investors, who would rather finance software or social media companies that require little capital and either fail or succeed spectacularly in a short time. [18]

5. **Operating Without Subsidy:** Currently the U.S. federal government provides generous subsidies for electric production from solar technologies. The federal subsidies to solar power in 2010 totaled $775.64/MWh, which is substantially higher than the $56.29/MWh for wind, $3.14/MWh for nuclear, and $0.85 for hydroelectric power. [14] Over the past five years about $150 billion was spent by the U.S. Government on the solar industry to finance grants, subsidize tax credits, guarantee loans, and fund programs such as the Department of Energy's SunShot Initiative, which is focused on driving down the production, installation, and operation costs of solar power. [19] With all of this heavy investment in the solar industry, the question remains whether manufacturers, solar power installers, and power plants will remain solvent once they are forced to compete without assistance. Although many advocates of the solar industry are calling on policy makers to continue subsidization to accelerate growth and generate new jobs, lessons can be drawn from intensive government intervention in Europe. In 2008, Spain subsidized the solar industry by paying up to 575% above the average electricity price from solar photovoltaic plants. This resulted in 40% of the global solar cell installations to be built there that year. The financial burden forced the Spanish government to considerably reduce their subsidizes by 30% in 2010 and now face a deficit of $40 billion. [14] To address this debt, Spain threatens the owners of residential solar installations with unreasonably high fines for disconnecting from the electrical grid but no longer

compensate them for donating their excess power. When the subsidies were in place, solar-powered Spanish homeowners would have been able to pay-off the capital cost of their installations in five years, but estimates now project the current policy stretches the payback period to 17 years, which has stunted further growth. [14] Balance must be struck in policy to ensure that sustainable levels of subsidization can be achieved and a plan for withdrawal is in place that will allow solar solutions to become self-reliant in the energy market. This might occur in the near future as the 30% federal Investment Tax Credit (ITC) is set to expire on December 31, 2016, and drop subsidy to 10% for commercial projects and will be eliminated entirely for privately owned residential installations. [20]

Although these barriers remain challenging, the state of solar energy has changed dramatically in recent years. Technical improvements to photovoltaic technology continue to slowly raise performance and lower cost, but the main driving force behind the recent solar boom has been the emergence of new business models. The key innovation was developed by Jigar Shah, who interestingly enough is a *mechanical engineer*. He founded his company, SunEdison, on the idea of selling solar services instead of solar modules to commercial customers. The *modus operandi* of small-scale solar installers prior to this point was that the private customer would have to provide the initial capital to outright purchase panels for installation and wait several decades to slowly make up the cost in electricity savings. This was quite unattractive for all those but the most zealous since it didn't offer much immediate benefit. Shah's disruptive business offered a solar-power purchase agreement (PPA) to commercial customers, where panels were installed at no initial cost and SunEdison would sell the electricity generated by the panels to the customer at a fixed rate for 20 years. Because the rate was less than the utility companies would offer and wouldn't rise over time, major companies would see immediate savings. SunEdison raised capital from investors to fund the installations, who would in turn benefit not only from solar energy tax credits, but would receive a share of SunEdison's profits from selling electricity. Many current solar financing companies such as Sungevity and Sunnova Energy offer leases instead of PPAs, where the customer pays a fixed

fee every month to use the panels regardless of output instead of strictly purchasing the actual amount electricity produced. More than 50% of new residential solar capacity in California, Arizona, Colorado, and Massachusetts are owned by third-party companies. The net effect of these innovative solar cell financing strategies, federal subsidies, and ever-dropping solar cell prices has resulted in "grid-parity" to be reached as of 2014 in several states, including: Arizona, California, Connecticut, Hawaii, Nevada, New Hampshire, New Jersey, New Mexico, New York, and Vermont. [21] According to a report by Deutsche Bank Securities Inc., solar power could reach parity with conventional energy sources in an additional 37 states by 2017. [21]

A second exciting movement is emerging in the United States where federal funding is given to national laboratories to help develop innovative technologies that have the potential for disruption in clean energy but are inherently poor candidates for financing through the conventional venture capital pathway. Perhaps the first of its kind is the Cyclotron Road program developed at the Lawrence Berkeley National Laboratory in Berkeley, CA. The concept is to provide some seed money and laboratory space to candidates with innovative yet feasible visions for new energy technologies to develop prototypes to a late-stage maturity level that would be more attractive to outside investors. In a sense, they aim to stand in the gap between academic research and industry to assist in commercializing technology that could simultaneously create new jobs, help secure America's role in the cleantech economy, and reduce harmful emissions to the environment. This program is aimed to accelerate the advancement of next-generation technologies that might not otherwise have the opportunity to even enter the market.

## 1.2 Next-Generation Solar Technologies

Although it is undoubtedly an exciting time for solar energy and the challenges listed in Section 1.1.4 will likely be surmounted, there are several emerging next-generation technologies that provide new opportunities for solar energy that have not been achievable with the current technology.

### 1.2.1 Motivation for Solution-Processing

The silicon cells that dominate the photovoltaic market are capable of producing electricity from sunlight with efficiencies as high as 25%, [4] however they have several undesirable characteristics that limit their widespread adoption in both solar power installations as well as their deployment in more creative environments. Some of these are:

1. **High Cost:** silicon solar cells are expensive to manufacture because the wafers must not only be of exceptional purity, but they must also be very thick ($\sim$150 microns) in order to absorb sufficient sunlight.

2. **Rigidity:** current solar cells are generally rigid and can only be installed easily on planar surfaces. This is generally not too much of an issue as most solar panels are installed on the roofs of residential and commercial buildings, however installation is generally avoided on curved surfaces such as grain silos and dams, or continuous, yet variable surfaces such as paved roads or hillsides.

3. **Unattractive:** although attractiveness is certainly subject to individual taste, silicon solar cells offer only one look to designers: opaque bluish-black panels plaided with metallic lines. The integration of solar cells into new and existing structures is becoming appealing from a practical standpoint, however it is often dismissed due to unpleasing aesthetics.

4. **Environmentally-Unfriendly Manufacturing Techniques:** the Czochralski process is used to synthesize single-crystal silicon ingots up to 2 meters in length that are virtually free of defects. However growing the ingots requires incredibly high temperatures near 1400°C and the purification process of the poly-silicon reagents produce large quantities of a very toxic byproduct: liquid silicon tetrachloride ($SiCl_4$). Although most of the $SiCl_4$ can be recycled in the fabrication process, there have been reports of high-profile Chinese manufacturers dumping the toxic waste in the fields surrounding the plants. [22] Even if properly regulated to halt this unscrupulous practice, the manufacturing pro-

cess is currently both energy-intensive and potentially hazardous, both of which are detrimental to the environment.

In contrast, next-generation solar materials are almost foils to silicon. They are generally inexpensive, flexible, come in many different colors and degrees of transparency, and can often be processed using inexpensive techniques at significantly lower temperatures. Although the power conversion efficiencies of next-generation materials often are not yet competitive with high-end silicon and CdTe modules, their attributes make them attractive candidates for generating power in markets that are currently not accessible to mainstream solar panels. Imagine artistic stained glass windows that illuminate the lobbies of museums, the reading rooms of libraries, and even homes with brilliant colors while also generating electricity. The blue tint coloring each skyscraper window could be a 10% efficient solar cell that provides power to the building while simultaneously tempering the intensity of incident sunlight to make a more pleasant working environment. Or perhaps dark-colored lenses in sunglasses might be thin film solar panels capable of charging cell phones or small electronic devices while on the move, making such devices completely mobile and portable. As most next-generation technology is solution processable, it might be possible to develop "photovoltaic paints" that could be applied to many surfaces. In the near future it might be possible to coat solar cells on electric vehicles so they would actively recharge when they're sitting in a parking lot or speeding down the open road. Photovoltaics could cover the surfaces of buildings, billboards, monuments, airplanes, or even the pavement or shoulders of roads... the possibilities are endless. Even grander yet, sufficiently light and flexible photovoltaic materials might enable future solar power plants to be large balloons that rise above the clouds and transmit power down through their tethers. As these examples illustrate, inexpensive, flexible, and aesthetically pleasing photovoltaic films could revolutionize the realization of solar power by becoming integrated in convenient and creative ways that access new markets that are currently impossible or impractical.

One of the key advantageous attributes of next-generation photovoltaic technologies is that they are *solution-processable.* This means that the active ingredient of the

solar cells and many corresponding hole transport and electron transport materials can be dissolved in solvents and deposited using various techniques to build devices. Generally devices in the laboratory are synthesized by spin-coating where the solution is dropped onto a substrate that is spinning in order generate a continuous and uniform coating. Although this is an easy and reliable method, it is only suitable for prototypes and large scale production would require using other techniques. The most likely candidate is roll-to-roll processing where flexible substrates are routed through rolls where material is transferred onto the surface and treated in different ways. This technique would allow spools of flexible solar cells to be manufactured that could be draped over surfaces. However, other opportunities exist to build solar cells directly on surfaces using techniques such as inkjet printing, slit casting, and spray coating. For instance inkjet printing would allow solar cells to be precisely patterned on objects themselves, whereas slit casting and spray coating could cover larger areas.

A second advantage of next-generation technology is that they could be deployed in some of the aforementioned markets where efficiency and cost aren't the only important driving factors. Flexible and semitransparent photovoltaic films could be easily integrated into consumer electronics markets initially as niche products. While this doesn't immediately provide lasting energy solutions, it could provide an intermediate product that would allow next-generation solar companies to make a profit from low volume product without significant investment from venture capital firms. This would enable companies to grow organically and scale production gradually to meet demand in these niche markets until the point is reached where mass-production could be achieved to enter into architectural photovoltaics or utility-level markets. An additional option would be to combine the solution-processed film with existing solar modules to make tandem solar cells that could achieve higher efficiencies without significant effort. This pathway would allow startup companies to partner with established manufacturers to make an improved product capable of boosting efficiency in residential and utility-scale installations. Such strategies provide a means for development that has not been traditionally available to solar cell manufacturers.

### 1.2.2 Types of Solution-Processed Solar Cells

There are a number of next-generation solar technologies that are solution-processable and have experienced significant advances in the last decade. These include:

1. **Semiconducting Polymers:** conjugated organic macromolecules that have a band gap between their highest occupied molecular orbital (HOMO) and lowest unoccupied molecular orbital (LUMO) energy levels. They generally contain sulfur heterocycles and can conduct electrons along the conjugated backbones through overlapping $\pi$-orbitals. They can become either $n$-type or $p$-type by adding or removing electrons in the $\pi$-system, respectively. Most often, $p$-type conjugated polymers are paired with $n$-type fullerene derivatives to build organic heterojunctions. Currently the most popular polymers are P3HT and PTB7. [23]

2. **Quantum Dots:** semiconducting nanocrystals that have electrical properties between those of bulk materials and single molecules. They exhibit quantum mechanical properties when the nanoparticle radius is smaller than its exciton Bohr radius (generally less than 10 nm) due to its excitons being confined in all three spatial directions (*i.e.* a 3D quantum well). In photovoltaic systems, quantum dots are packed into layers that act as bulk semiconductors in $p-n$ junctions with the added benefit that the electronic properties are highly tunable. [24] The band gap varies inversely with particle size, the band edge locations depend upon the ligand molecules capping the particle surfaces, [25] and the material can be either $n$- or $p$-type by controlling material composition. [26, 27] Photovoltaic quantum dots are generally synthesized from IV-VI (e.g. PbS, PbSe, PbTe, SnS, SnSe, SnTe) or from II-VI (e.g. CdS, CdSe, CdTe) semiconductor materials with PbS and PbSe being the most popular.

3. **Organometal Halide Perovskites:** ionic semiconducting materials that are crystallized from organic halide and metal halide salts to form an $ABX_3$ crystal structure where A is an organic cation, B is a metal cation, and X is a halide

anion. In five years, the performance of perovskite solar cells has risen dramatically in the laboratory from an initial 3.5% [28] to a recent 20.1% [29]. The band gap of perovskite materials can be easily tuned by adjusting the composition of the perovskite material and films are generally formed at low temperatures, around 100°C. The most efficient perovskite materials are methylammonium lead triiodide ($CH_3NH_3PbI_3$ or $MAPbI_3$) [30, 31] and formamidinium lead triiodide ($CH(NH_2)_2PbI_3$ or $FAPbI_3$) [32].

4. **Chalcogenide Inks:** polycrystalline semiconductors comprised of copper-indium-gallium-selenide (CIGS) or its less-expensive analogue, copper-zinc-tin-sulfide (CZTS), which exhibit a chalcopyrite crystal structure. CIGS is a thin-film material that is being commercialized by several solar cell companies (*e.g.* Nanosolar) using vapor deposition, however new solution-based methods have recently emerged that are approaching the 21.7% efficiency listed in Table 1.2. Solution-processing with these materials takes many forms including completely dissolving the materials in hydrazine, using colloids of chalcogenide nanoparticles, or an intermediate approach where films of nanoparticle precursor materials are chemically transformed to form the final material. [33] As with the previous two technologies, the band gap of the material can be tuned by tailoring the stoichiometry of the metals comprising the material or by replacing some of the sulfur content with selenium.

5. **Dye-Sensitized Solar Cells (DSSCs):** unlike the previously discussed solid-state technologies, DSSCs are traditionally liquid-based devices. Instead of using a semiconductor solid that is capable of both light absorption and carrier transport, it delegates each process to a separate material. A monolayer of sensitizing single-molecule organic dyes are absorbed onto the surface of a mesoporous scaffold of an electron-accepting wide-band gap semiconductor such as titanium dioxide ($TiO_2$) or zinc oxide (ZnO), which is then filled with a liquid electrolyte. Upon absorbing a photon, the dye molecule immediately injects an electron into the metal oxide scaffold and the electrolyte molecule is oxidized to

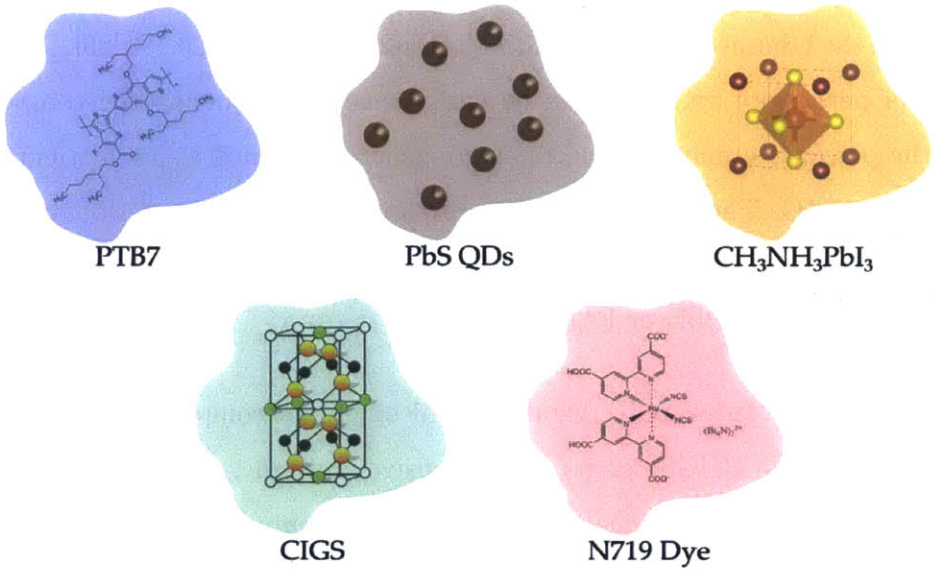


Figure 1-7: Five different classes of emerging solar materials can be processed using solution-based techniques. The most popular material from each class is presented.

act like a hole. Each carrier then migrates to their respective electrodes for collection. [34] Historically, DSSCs have been the highest performing photovoltaic technology based on organic materials, however new semiconducting polymers are poised to challenge their position in the near future.

Each of these five classes of solution-processed solar technologies have reached or surpassed the 10% efficiency mark in research environments and the most popular material from each is shown in Figure 1-7. The current challenge is to continue progress in material design and processing technique to achieve efficiencies capable of competing with the dominant silicon and CdTe technologies. One of the common issues with solution-processed solar materials is that there exists a trade-off between light absorption and carrier collection. The typical diffusion lengths for the the minority carrier, which limits the performance, is generally between 5-500 nm for solution-processed materials but often the film thicknesses must be greater than this to achieve complete absorption. [33] Although some of the inorganic (*e.g.* CIGS and CZTS) and organic-inorganic hybrid materials (*e.g.* $MAPbI_3$ and $FAPbI_3$) can achieve excellent performance with planar heterojunctions, most of them require

highly nanostructured interfaces to efficiently collect charges in thicker films. Likewise, solution-processing generates disorder in the final materials with either crystalline domains oriented in random directions or the existence of amorphous regions. It is more likely that charges will be lost due to non-radiative recombination when traversing through grain-boundaries and defective regions, which dilutes performance. Therefore, improved processing techniques and a greater understanding of the mechanisms responsible for non-idealities are required to reduce the density of detrimental defects in the films. Developing techniques that are capable of improving the performance of these technologies without sacrificing the attributes that make them desirable is the focus of much ongoing research in the field.

## 1.3 Research Focus

As mentioned in the previous sections, the unique attributes of solution-processed solar cells offer new opportunities to integrate solar power creatively and inexpensively into new markets as well as augment the performance of current silicon technology. Although the research performed in this dissertation uses the standard spin-coating method to construct solar cells, I envision these emerging materials being adopted by different large-scale deposition technologies [33] such as spray coating, slot casting, and inkjet printing, which would allow the mass-production of products as well as customized solar cells at low cost.

### 1.3.1 Vision

Imagine a future where colorful, light-weight solar modules coat the exterior of electric cars and skyscrapers converting them into self-sufficient power systems. Vehicles and portable electronics will no longer rely on outlets to recharge power reserves and cities will be able to contribute to energy generation instead of solely relying on their umbilical connections to remote utility power plants. What if it were possible to make large balloons out of flexible photovoltaics that would rise about the clouds and transmit electricity down their tethers? Concerns over cloud coverage and land usage

would no longer be major issues to building PV power plants.

Furthermore, I envision a future where emerging solar materials are rapidly developed for commercialization using automated platforms that combine inkjet technology with high-throughput screening to optimize the printing of efficient, low-cost solar cells. New solar materials will no longer be discovered through serendipity, but identified through exhaustive screening procedures that work around the clock. This approach has proven successful with identifying catalysts and discovering pharamceuticals, why shouldn't it be applied to generating energy solutions? Let us consider some potential impacts of this technology. First, the risk to our nation's solar industry would be minimized if material-specific fabrication equipment were replaced with adaptable printing platforms capable of quickly manufacturing the latest technology to emerge from our research institutions. Second, the integration of solar power into daily life would occur at an extraordinary pace if building and installing a solar panel were as simple as loading an inkjet printer with a special cartridge, printing a sheet of photovoltaic devices, and affixing it to any illuminated surface. Grander yet, imagine how much pollution and greenhouse gas emissions could be avoided if low-cost, high-efficiency printed solar cells could accommodate demand increases in developing nations. This is a sample of the possibilities that solution-processed solar cells promise and although this dissertation will not present any printed solar cells, it aims to improve the materials that would be compatible with this technology.

### 1.3.2 Strategies to Improve Next-Generation Photovoltaics

As stated in the introduction of this chapter, the fundamental goal of the work presented in this dissertation is to develop nanoscale solutions to improve next-generation, solution-processable solar technologies. Although much of the current body of literature in pioneering solar cell research could be filed under this broad category, I pursued two different avenues: one that uses *optics* to improve the ability of *existing* solar materials to harvest light and another that aims to modify the active *materials* themselves to generate *new* active layers. Specifically:

1. **Improve Light Harvesting:** By synthesizing plasmonic nanostructures and incorporating them into solar-cells, light that would otherwise not be fully absorbed by the device can be concentrated in the active layers of solution-processed solar cells via the phenomenon of localized surface plasmon resonance (LSPR).

2. **Solar Material Modification:** By replacing lead content of organolead halide perovskite with different elements, the toxicity of the material can be reduced while additionally improving performance in certain cases.

The first of these strategies provides a means to circumvent the aforementioned trade-off between light absorption and carrier collection in most solution-processed technologies by simply blending nanoparticles of various shapes, sizes, and materials in with the photovoltaic inks. Although this strategy can help squeeze additional performance out of current materials, it is a stop-gap solution. It can be argued that larger leaps in improvement result from modifications to processing procedures and the active materials themselves in order to make the necessary physical processes more efficient such as light absorption, charge generation, and charge collection — all of which depend strongly on the *electrical* properties of materials. Hence, the second stragey was developed in order to simultaneously address some of the weak points of current perovskite materials such as toxicity and stability, by means of modifying the material composition, and study the resulting effect on device performance and electrical characteristics.

### 1.3.3 Approach

There are several common threads that have been woven throughout this dissertation, which result from the approaches I have taken to pursue these strategies for improving solution-processed solar cells. These approaches are:

**Compositional Engineering:**

One of the main features of solution-processable solar materials is that the composition of the final active layer can be simply modified by blending additional ingredients into the precursor solution. This provides the opportunity to tune the chemical composition of ionic solar materials such as perovskites, adjust the kinetics of film formation, add passivating agents that reduce trap densities, and introduce nanomaterials with specialized functionality into the active layers.

**Computational and Experimental Screening:**

Finding modifications that improve the performance of solar cells is a challenging process. Attempting a few improvements here and there is generally an ineffective strategy to finding solutions that have favorable outcomes, mainly because it is simply easier to make changes that are detrimental to performance than beneficial. Rather an approach that systematically screens over many conditions is much more likely to identify new conditions or compositions that improve solar performance. This approach also provides information about the sensitivity of the performance to these conditions and supplies enough data to potentially illuminate and characterize the underlying mechanism responsible for improvement. In order to increase the likelihood of success, the following process was used to search for favorable active layer compositions:

1. An undesirable feature of a solar material must be first identified.

2. A strategy needs to be devised that proposes a solution that has the potential to address this need.

3. Computational screening is performed over wide range of different active layer compositions to ensure that the concept is valid and identify the most favorable embodiments.

4. The results of the computational screening are used to guide the fabrication of actual solar cells. By screening through a candidate pool to investigate how

the compositional changes to the active layer influence the solar performance, optimum embodiments can be identified. Furthermore, by comparing the experimental and computational findings, mechanisms that are responsible for improvement can be confirmed or speculated upon.

The computational methods used throughout this work are:

1. **Analytical Theory:** some simple problems have analytical solutions, but often numerical techniques are required to solve specific systems. Such calculations were generally performed using MATLAB scripts.

2. **Finite-Difference Time-Domain (FDTD):** this is a computational technique that takes an optical system, discretizes the space into a mesh, and numerically solves Maxwell's equations at each node. It is very useful for evaluating how light interacts with systems that do not have analytical solutions, or in systems that are too complicated to practically evaluate. The commercial software package Lumerical FDTD Solutions was utilized for these calculations.

3. **Density Function Theory (DFT):** is a computational quantum mechanical modeling method that is used to investigate the electronic structure of many-body systems comprised of atoms and molecules by calculating the spatially dependent electron density throughout the system. For these calculations, the open-source software, Quantum Espresso, was utilized in conjunction with resources at computing facilities such as the Texas Advanced Computing Center (TACC).

**Biological Self-Assembly:**

The bottom-up approach of using biomolecules to assemble nanocomposite structures was used whenever it was advantageous to do so. This process is generally inexpensive and environmentally-friendly as biomolecules are native to aqueous environments at low temperatures. Therefore, existing mechanisms were utilized when possible and new ones were developed to synthesize photoactive structures that could be useful in solar cells.

**Low-Cost Processing:**

Since the key driving factor behind solar cells is the cost per watt of generated power, it only makes sense that emerging photovoltaics should aim to be constructed using the least expensive materials and least energy-intensive processes available. For this reason, device architectures were adopted that use less expensive metals such as aluminum for the electrodes instead of silver or gold. Likewise, fabrication process were chosen that require lower processing temperatures.

As will become evident in the following chapters, these approaches acted as guidelines from which I sought creative solutions to synthesize materials and build solar devices by integrating aspects of photonics, biological engineering, and materials science together.

It should also be mentioned that of the five families of solution-processed solar cells presented in Section 1.2.2, most of my computational and experimental work was focused on the first three technologies. I did not pursue work with chalcogenide solar cells because the required solvent, hydrazine, raises very serious safety concerns due to its high toxicity and reactivity. Although I performed some computational work for DSSCs constructed by colleagues, I chose to personally fabricate only solid-state devices. Thus, most of the original research presented in this dissertation will focus on polymer, quantum dot, and perovskite solar cells.

## 1.4 A Note on Organization

This chapter was intended to present both the immense potential that solar energy offers as well as the challenges that must be overcome for emerging photovoltaic technologies to become competitive. By providing brief summaries of both the basic operation of solar cells and the history of the field, it is hoped that the reader would have sufficient perspective to appreciate how various technical, economic, and political factors are shaping the future of photovoltaics whilst it grasps for purchase in a complicated energy landscape. The particular goals of my research have been motivated and presented to utilize various facets of engineering to address some of

the technical issues solution-processed solar cells face, particularly the needed for improved light harvesting techniques and improved materials.

The following chapters will explore each of these avenues in turn, with the first half focused on how plasmonic structures can improve light harvesting and the latter half focused on modifying the materials of perovskite solar cells. However, not every chapter will be specifically focused on solar cells. Rather some will build the theoretical foundation of these strategies and explore aspects that are important for solar cells, while later chapters will discuss performance trends in actual devices. The remaining chapters will discuss the following topics:

**Chapter 2:** presents the concept of localized surface plasmon resonance (LSPR) as well as the underlying theory behind the phenomenon. The use of the M13 bacteriophage to assemble and organize plasmonic nanostructures will also be presented and compared against theoretical measurements.

**Chapter 3:** presents a new synthesis procedure that uses amino acids to mediate the growth of zincous shells on gold nanoparticles. A synthesis pathway is proposed and the materials are characterized using various imaging and spectroscopy techniques. By comparing the location of the plasmon resonance peaks in measured extinction spectra to theoretical predictions, the complex index of refraction for the shell material was determined.

**Chapter 4:** presents how plasmonic strutures are able to enhance performance in solution-processed solar cells. This is accomplished by presenting both the computational and experimental efforts that investigate how the structures discussed in Chapters 2 and 3 impact solar cell performance. The specific technology discussed is a lead sulfide quantum dot bulk heterojunction devices.

**Chapter 5:** presents the theoretical effort to computationally identify new perovskite materials with reduced toxicity. The crystal and electronic structure of mixed metal perovskite materials based on Pb, Sn, and Bi are presented and discussed.

**Chapter 6:** presents the experimental effort to reduce the toxicity of lead-based per-

ovskite solar cells. The influence of elemental substitution of less-toxic metals into the film is explored from both a performance and a materials characterization perspective. Based on the collected data, speculations are made upon mechanisms that might be responsible for observed performance improvements.

**Chapter 7:** presents a summary of the findings of this dissertation as well as thoughts about the future of the technologies discussed herein.

# Chapter 2

# Analytical Modeling and Biological Assembly of Plasmonic Composites

A *plasmon* is a quantum of plasma oscillation that arises from the excitation of free electrons in conductors by electromagnetic fields. It is much akin to the more familiar quasiparticle, the phonon; however instead of describing collective mechanical vibrations in condensed matter, a plasmon describes collective oscillations of free electron gas density with respect to the fixed positive ions of a metal. Although this definition of a plasmon relies on the quantum mechanical concept of quantization and was first proposed by David Pines and David Bohm in 1952 to describe long-range electron-electron interactions, the physics can be accurately described within the classical framework of electromagnetic theory. [35]

Plasmons are generally classified into three different categories, one which occurs in the material bulk and two which occur at the surface of conductors:

1. **Bulk or Volume Plasmons:** are longitudinal plasma oscillations generated within the volume of conductive materials. These modes cannot be excited by plane waves, which are transverse in nature, and instead are generated only by particle impact. [36]

2. **Surface Plasmon Polaritons (SPPs):** are electromagnetic surface waves that *propagate* along a conductor-dielectric interface and are evanescently con-

fined in the perpendicular direction on both sides of the interface. SPPs can be excited by incident plane waves, but special phase-matching techniques are required such as prism or grating coupling.

3. **Localized Surface Plasmons (LSPs):** are *non-propagating* oscillations of conduction electrons in closed metallic nanostructures that are driven by an electromagnetic wave whose wavelength is larger than the nanostructure size. Unlike SPPs, LSPs are excited directly by incident light without any need for coupling geometries.

Although all of these situations are very interesting from an electromagnetic perspective, only the two types of surface plasmons constitute active area of photonics research because they provide the opportunity to break the diffraction limit and squeeze light into structures that are significantly smaller than the wavelength of light. In the case of SPPs, light is confined to an interface that is essentially infinitesimally thin. However, when it comes to using plasmons for energy applications the most useful type is the localized surface plasmon for the following reasons:

1. Unlike SPPs that arise at infinite planar interfaces between a metal and a dielectric, LSPs can be excited in nanoparticles directly by sunlight without fancy coupling geometries.

2. LSPs generate a secondary electric field near the particle surface that is greatly enhanced locally. This allows light to be concentrated in the regions directly surrounding the metal nanoparticles.

3. The spectral response of a nanoparticle depends strongly upon geometry and material, which allows the excitation frequency of LSP modes to be tuned to the needs of a particular system.

Therefore, this chapter will focus almost wholly on the background theory necessary to understand how localized surface plasmons arise and how nanoscale systems can be designed to make use of this phenomenon for interesting applications such as sensing and light concentration. No solar cells will be specifically discussed here, but

this chapter is intended to lay the groundwork for the plasmon-enhanced solar cells presented in Chapter 4.

## 2.1 Optical Properties of Metals

As will be shown in the next section, the ability of conducting nanoparticles to support localized surface plasmons arises directly from the unique optical properties of metals. Although mathematics will be used in the next section to present the plasmon, analytical solutions can only be found for a few very simple geometries. Therefore, what is more important is to build a foundation based on physical pictures that can explain observable macroscopic behavior. Discussions that start from established material models will provide a framework from which physical intuition can be developed, which will be critical to explaining more complicated systems when analytical mathematical solutions are not available. Therefore, this section aims to briefly present the necessary background to understand the basic optical behavior of metals, which is captured almost wholly by the complex dielectric function, $\varepsilon(\omega)$.

The optical properties of metals can be classically explained with a *plasma model*, where free electrons are treated as a charged gas that can move with respect to the fixed ionized nuclei of the crystal lattice. The model is valid for frequencies through the ultraviolet for alkali metals, however deviates in noble metals at frequencies where interband transitions cause significant light absorption. [36] Gold and copper metals appear reddish because higher energy photons are exciting electrons in filled bands just below the Fermi surface to higher energy levels, and therefore bluer colored light is not reflected as efficiently as redder wavelengths. Conversely, silver and most other metals appear whitish-grey because interband transitions require higher energies that are outside the visible range and all colors are reflected fairly efficiently. The plasma model avoids quantum mechanical considerations by lumping band structure effects into an effective electron mass, $m$. Therefore, a classical model aptly captures the behavior of metals by presenting electrons as negatively charged particles that are constantly bouncing off the immobile positive ions of the metal lattice. Using

Newton's second law, the force acting on an electron can be modeled simply as a mass-damper oscillator system that is driven by an external electric field, $\mathbf{E}(t)$, which allows for its motion to be determined:

$$m\ddot{\mathbf{x}}(t) + m\gamma\dot{\mathbf{x}}(t) = -e\mathbf{E}(t) \tag{2.1}$$

where $m$ is the effective optical electron mass, $\gamma$ is the damping constant due to collisions of electrons with fixed metal ions, $e$ is the electron charge, and $\mathbf{x}$ is the displacement vector of the electron from its equilibrium position and is a function of time. In this equation, the first term on the left is the inertial term, the second term accounts for dissipation of electron motion by collisions with ions, and the term on the right is the electrostatic excitation force. The damping coefficient can be defined as $\gamma = 1/\tau \approx 100$ THz, where $\tau$ is the characteristic relaxation time.

By assuming the external electric field drives the system with a harmonic time dependence $\mathbf{E}(t) = \mathbf{E}_0 e^{-i\omega t}$ Equation 2.1 becomes:

$$\mathbf{x}(t) = \frac{e}{m(\omega^2 + i\gamma\omega)}\mathbf{E}(t) \tag{2.2}$$

A polarization, $\mathbf{P}$, is produced by the displacement of the electrons relative to the atomic cores, $\mathbf{P} = -ne\mathbf{x}$, which yields:

$$\mathbf{P} = -\frac{ne^2}{m(\omega^2 + i\gamma\omega)}\mathbf{E} \tag{2.3}$$

The dielectric displacement, $\mathbf{D}$ is related to $\mathbf{P}$ by:

$$\mathbf{D} = \varepsilon_0\mathbf{E} + \mathbf{P} = \varepsilon_0\left(1 - \frac{{\omega_p}^2}{\omega^2 + i\gamma\omega}\right)\mathbf{E} \tag{2.4}$$

where $\omega_p$ is the *plasma frequency* of the free electron gas:

$$\omega_p = \sqrt{ne^2/m\varepsilon_0} \tag{2.5}$$

Since $\mathbf{D} = \varepsilon_0 \varepsilon \mathbf{E}$, the dielectric function of the free electron gas is:

$$\varepsilon = 1 - \frac{{\omega_p}^2}{\omega^2 + i\gamma\omega} \tag{2.6}$$

Equation 2.6 is known as the *Drude model* and describes the complex dielectric function of an ideal metal. This can be broken down into the real, $\varepsilon_1$, and imaginary, $\varepsilon_2$, components such that $\varepsilon = \varepsilon_1 + i\varepsilon_2$:

$$\varepsilon_1(\omega) = 1 - \frac{{\omega_p}^2\tau^2}{1+\omega^2\tau^2} \qquad \text{and} \qquad \varepsilon_2(\omega) = \frac{\tau{\omega_p}^2}{\omega(1+\omega^2\tau^2)} \tag{2.7}$$

where $\tau = 1/\gamma$ is used because $\omega\tau$ is a convenient dimensionless parameter to use for investigating the behavior of metals in different frequency regimes. Consider the following limits:

**Low Frequencies** ($\omega\tau \ll 1$)**:** in this limit, $\varepsilon_1 = 1 - {\omega_p}^2\tau^2$ and $\varepsilon_2 = \tau^2{\omega_p}^2/\omega\tau$. Hence, $\varepsilon_1 < 0$ and the imaginary component dominates the dielectric function since $\varepsilon_2 \gg \varepsilon_1$. This indicates that the metal is strongly absorbing at low frequencies. This occurs because free electrons screen out the incident electric field by oscillating out-of-phase with the excitation source, which produces a secondary electric field that cancels the incident light and thereby quickly attenuates light incident on the metal.

The dielectric constant is related to the extinction coefficient, $\kappa$, by:

$$\kappa = \sqrt{\frac{|\varepsilon_2| - \varepsilon_1}{2}} \tag{2.8}$$

therefore in this regime,

$$\kappa \approx \sqrt{\frac{|\varepsilon_2|}{2}} = \sqrt{\frac{{\omega_p}^2\tau}{2\omega}} \tag{2.9}$$

The absorption coefficient, $\alpha$, of the metal can be determined by introducing the DC conductivity, $\sigma_0 = {\omega_p}^2\tau\epsilon_0$ into the above equation, and noting that the skin depth, $\alpha = 2\kappa\omega/c$, and the speed of light, $c = 1/\sqrt{\epsilon_0\mu_0}$, where $\epsilon_0$ and $\mu_0$

are the permittivity and permeability of free space, respectively:

$$\alpha = \sqrt{2\omega\sigma_0\mu_0} \tag{2.10}$$

At low frequencies, $\alpha$ is large and electric fields are quickly attenuated upon striking a metal surface as the sea of free electrons are able to easily screen out the electric field.

**High Frequencies** ($\omega\tau \gg 1$)**:** in this limit, $\varepsilon_1 \approx 1 - {\omega_p}^2/\omega^2$ and $\varepsilon_2 \approx 0$. Therefore, the dielectric function of the metal is predominantly real and obtains the form of a classical plasma:

$$\varepsilon(\omega) = 1 - \frac{{\omega_p}^2}{\omega^2} \tag{2.11}$$

which allows waves to propagate when $\omega > \omega_p$ but forbids passage if $\omega < \omega_p$. When the wave is allowed to propagate, $\varepsilon_1 > 0$ while $\varepsilon_2 \approx 0$ and the metal adopts dielectric character. Physically, the excitation is above the resonance frequency of the plasma and the free electrons cannot react quickly enough to counteract the incident electric field. Therefore, the free electrons are unable to screen the electric field and the metal transmits the wave like an insulator.

According to Equation 2.6, when $\omega \gg \omega_p$ then $\varepsilon \to 1$. However, real noble metals deviate from this behavior because filled electrons in the $d$-band cause a highly polarized background of positive ions in the lattice to contribute a residual polarization. The Drude model can be modified to account for this with a dielectric constant $\varepsilon_\infty$:

$$\varepsilon = \varepsilon_\infty - \frac{{\omega_p}^2}{\omega^2 + i\gamma\omega} \tag{2.12}$$

which can be broken down into real and imaginary components:

$$\varepsilon_1(\omega) = \varepsilon_\infty - \frac{{\omega_p}^2}{\omega^2 + \gamma^2} \qquad \text{and} \qquad \varepsilon_2(\omega) = \frac{\gamma{\omega_p}^2}{\omega(\omega^2 + \gamma^2)} \tag{2.13}$$

Experimental data for gold (Au), silver (Ag), and copper (Cu) by Johnson and Christy are presented in Figure 2-1 along with the Drude model fits. [37] As can be

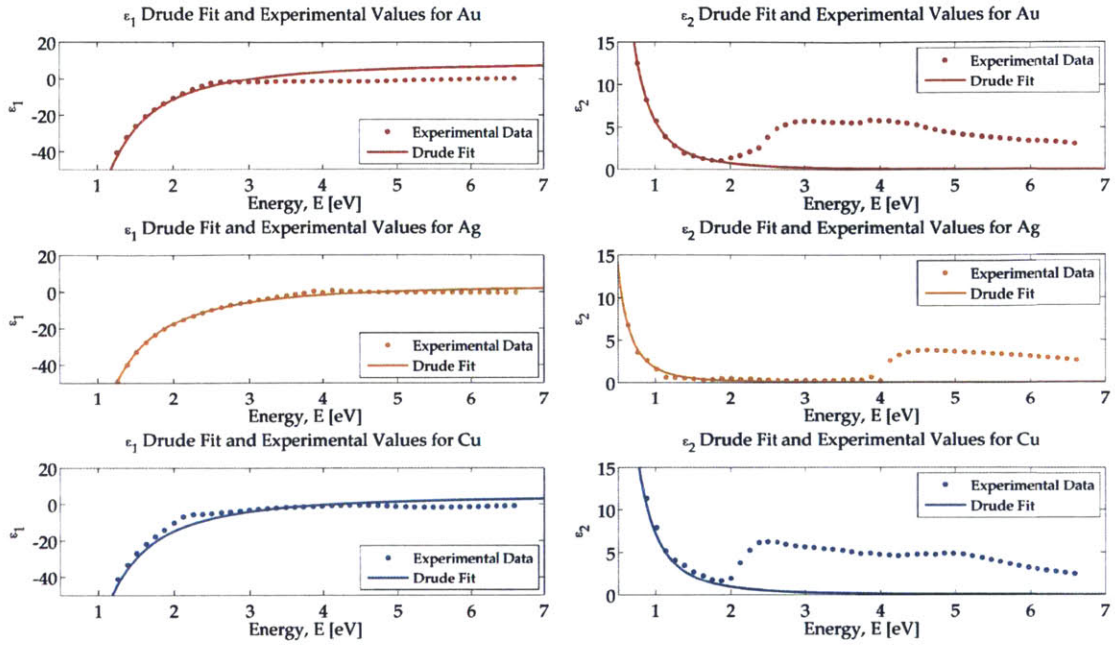


Figure 2-1: The real and imaginary part of the dielectric constants for the noble metals gold, silver, and copper as measured by Johnson and Christy along with the fits to the Drude model. [37]

seen, the fits are in good agreement at low photon energies for $E < 2$ eV, which are below the threshold for band transitions with these metals. However, at higher photon energies, significant deviation arises when the interband transitions occur and excite electrons below the Fermi surface to higher bands. Also notice that the interband transitions occur at much higher energies for silver compared with gold and copper, which accounts for their different characteristic hues, as discussed previously. Therefore, although the Drude model provides the opportunity to understand how the behavior of electrons in metals influence their complex dielectric constants, it is best to use the actual measured values for calculations whenever possible to predict accurate behavior. In FDTD simulations, a high order polynomial is usually fit to experimental values in order to sample the material parameters at any appropriate wavelength.

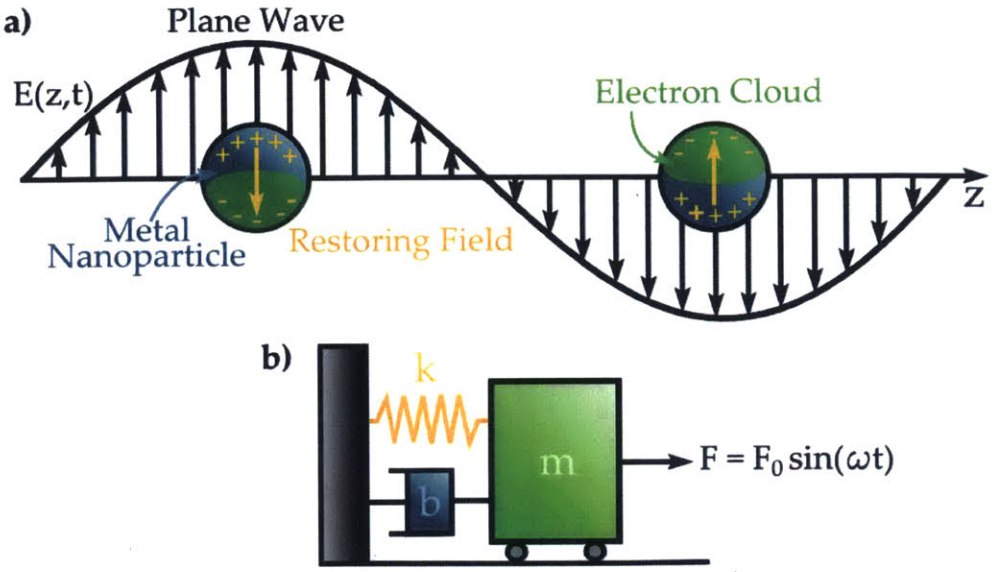


Figure 2-2: The electric field of a traveling plane wave causes the cloud of free electrons in a metal nanoparticle to distort, which uncovers the positive ions of the metal lattice. This gradient in charge density produces an electric field in the direction opposite the excitation source that acts to restore the electrons to their equilibrium position. This system is analogous to the classical driven mass-spring-damper harmonic oscillator where the restoring force is akin to the spring, the dissipation of electron momentum by collision with the metal ions is the damper, the electron itself is the block of mass, and light is a harmonic driving force.

## 2.2 Localized Surface Plasmon Resonance

Localized surface plasmons arise in metal nanoparticles when light of a particular frequency incites free electrons into collective resonance. Noble metals are of particular interest because the resonance frequencies fall into the visible range of the electromagnetic spectrum, making them useful for many optical applications. The simplest problem that has an analytical solution is the electromagnetic response of a spherical nanoparticle that is much smaller than the wavelength of light, which is classically known as Rayleigh scattering theory and holds true regardless of whether the nanoparticle is a metal or a dielectric because the physical difference of each material is captured wholly by the dielectric function.

The concept of plasmon resonance in metal particles can be intuited with a simple thought experiment that is illustrated in Figure 2-2. Imagine that a plane wave is

propagating through space and encounters a metal nanoparticle that is much smaller than its wavelength. At one moment in time, the nanoparticle will be fully immersed in an electric field that is oriented upwards and the free electron cloud in the metal will feel an electric force that causes the cloud to distort towards the bottom of the particle. As the electrons migrate, they will leave the fixed positive ions of the metal lattice unscreened and an electric back-field will develop to pull the free electrons back to their original positions. Therefore the free electrons experience an applied force from the electric field of the incident plane wave, a restoring force that arises from the distortion of the cloud, and a damping force due to the collision of electrons with positive ions immobilized in the metal lattice. At another moment slightly later in time, the plane wave will travel through space and immerse the nanoparticle in an electric field that is oriented in the opposite direction. The electrons will now experience the same forces, but the directions will all be reversed. Hence the electrons will be oscillating in time as the incident plane wave passes by. This situation is directly analogous to a classical mechanical system: the *harmonically driven mass-spring-damper oscillator*. Here, the electrical back-field generates a restoring force akin to that produced by a spring, light is the driving force, the dissipation of momentum upon collisions is a damper, and an electron is the proverbial block of mass. It is well known that a resonance frequency exists for this particular oscillator system in the under-damped condition (*i.e.* when the dissipation of electron momentum is not the dominant contribution to electron motion):

$$\omega_r = \sqrt{\frac{k}{m}\left(1 - \frac{b^2}{4mk}\right)} \tag{2.14}$$

where $k$ is the spring constant, $m$ is the mass, and $b$ is the damping coefficient. Driving the mechanical mass-spring-damper system at the resonance frequency causes the mass to achieve very large displacements that do not occur at any other frequency. By extension, it is natural to conclude that a particular frequency of light would drive the electrons of the metal nanoparticle into resonance as well. In fact, the exact same concept holds true for free electrons in the metal nanoparticle with one

additional consequence, the constant collective acceleration and deceleration of electrons in driven harmonic motion produces a secondary electric field with an intensity that is very high close to the particle surface (*i.e.* the near-field) and quickly decays spatially until it disappears far away from the particle (*i.e.* the far-field). This concentrated field arises directly from the oscillation of the free electrons and is the physical manifestation of a localized surface plasmon.

### 2.2.1 Rayleigh Scattering Theory

In order to fully grasp how different system parameters influence the electromagnetic response of a metal nanoparticle and thus the generation of plasmons, it is instructive to analytically solve for the electromagnetic field in the near-field and investigate behavior that is observable in the far-field. The starting point for all electromagnetics problems is Maxwell's Equations, which consist of four coupled phenomenological equations that capture the interactions of fields and charges inside media:

$$\nabla \times \mathbf{E} = -\frac{\partial \mathbf{B}}{\partial t} \tag{2.15}$$

$$\nabla \times \mathbf{H} = \frac{\partial \mathbf{D}}{\partial t} + \mathbf{J}_f \tag{2.16}$$

$$\nabla \cdot \mathbf{D} = \rho_f \tag{2.17}$$

$$\nabla \cdot \mathbf{B} = 0 \tag{2.18}$$

where $\mathbf{D}$ is the electric displacement field, $\mathbf{E}$ is the electric field, $\mathbf{H}$ is the magnetic field, $\mathbf{B}$ is the magnetic induction, $\mathbf{J}_f$ is the free current density, and $\rho_f$ is the free charge density. If the material is linear, isotropic, and nonmagnctic, the following constitutive relations can be written that relate the fields:

$$\mathbf{D} = \varepsilon_0 \varepsilon \, \mathbf{E} \tag{2.19}$$

$$\mathbf{B} = \mu_0 \mu \, \mathbf{H} \tag{2.20}$$

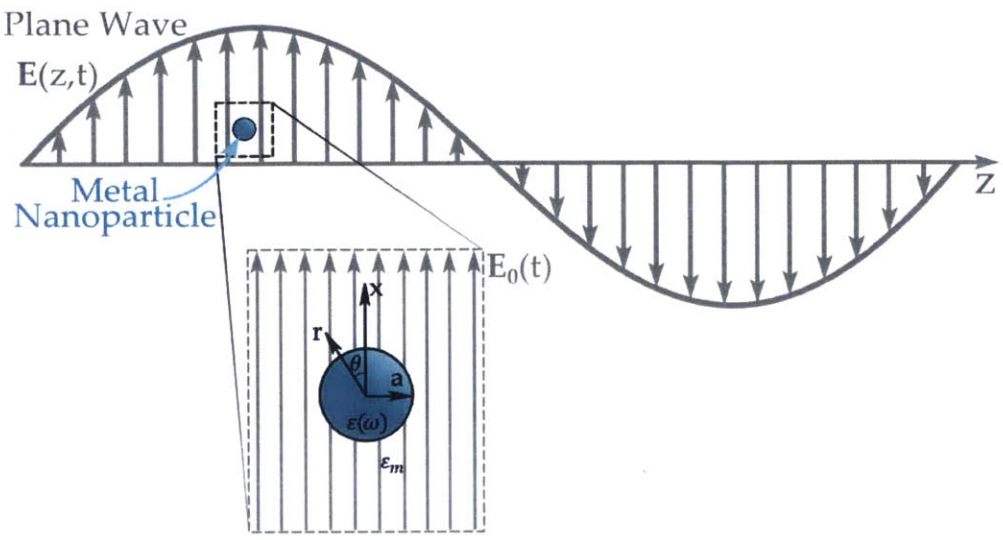


Figure 2-3: When a plane wave with wavelength, $\lambda$, illuminates a small nanoparticle with a radius, $a \ll \lambda$, the particle feels an electric field that is approximately uniform in magnitude across its spatial extend at any given moment in time. Therefore, the quasi-static approximation can be used which allows the problem to be treated as if a sphere were placed between parallel plates.

where $\varepsilon_0$ and $\mu_0$ are the permittivity and permeability of free space, $\varepsilon$ is the dielectric constant, and $\mu = 1$ is the relative permeability of nonmagnetic media.

As discussed above, the simplest analysis that can be performed for the electromagnetic response of metal nanoparticles is to consider the situation when a plane wave travels through a space that is occupied by a small nanoparticle. As illustrated by Figure 2-3, if the diameter of the particle is significantly smaller than the wavelength of incident light (*i.e* $a \ll \lambda$), the quasi-static approximation can be used, which substantially simplifies the analysis by removing any time dependence. The idea is that since the particle is so small, it experiences an essentially uniform electric field across its entire spatial extent. Therefore, at any given moment the particle can be thought of as being inserted between two parallel plates. Although the electric field magnitude will vary slowly in time, the analysis can be performed by simply considering a single snapshot. If all time dependence is removed, then $\partial/\partial t \rightarrow 0$ and if there are no external sources then $\rho_f = 0$ and $\mathbf{J}_f = 0$, then Equations 2.15-2.18

simplify to:

$$\nabla \times \mathbf{E} = 0 \tag{2.21}$$

$$\nabla \times \mathbf{H} = 0 \tag{2.22}$$

$$\nabla \cdot \mathbf{D} = 0 \tag{2.23}$$

$$\nabla \cdot \mathbf{B} = 0 \tag{2.24}$$

The electric and magnetic fields are now completely decoupled and the analysis can proceed by considering only the electric field. Since $\nabla \times \mathbf{E} = 0$, a scalar electric potential, $\Phi$ can be defined since the curl of the gradient of any scalar quantity is always zero:

$$\mathbf{E} = -\nabla\Phi \tag{2.25}$$

Which can be combined with Equatons 2.23 and 2.19 to produce Laplace's Equation:

$$\nabla \cdot \varepsilon\varepsilon_0\mathbf{E} = \nabla \cdot (-\varepsilon\varepsilon_0\nabla\Phi) = 0 \rightarrow \nabla^2\Phi = 0 \tag{2.26}$$

Laplace's equation takes the following form in spherical coordinates ($r$, $\theta$, $\phi$):

$$\frac{1}{r}\frac{\partial^2}{\partial r^2}(r\Phi) + \frac{1}{r^2\sin\theta}\frac{\partial}{\partial\theta}\left(\sin\theta\frac{\partial\Phi}{\partial\theta}\right) + \frac{1}{r^2\sin^2\theta}\frac{\partial^2\Phi}{\partial\phi^2} = 0 \tag{2.27}$$

Since the system has azimuthal symmetry, that is the incident and scattered electric fields are expected to be axisymmetric about the $x$-axis pictured in Figure 2-3. Thus, $\partial/\partial\phi \rightarrow 0$ and the solution to Equation 2.27 has the general form: [36]

$$\Phi(r,\theta) = \sum_{l=0}^{\infty}\left[A_l r^l + B_l r^{-(l+1)}\right]P_l(\cos\theta) \tag{2.28}$$

where $P_l(\cos\theta)$ are the Legendre Polynomials of order $l$ and $\theta$ is defined in accordance with Figure 2-3. At this point it is easiest to separately solve for the electrical potential

inside, $\Phi_{in}$, and outside, $\Phi_{out}$, the sphere:

$$\Phi_{in}(r,\theta) = \sum_{l=0}^{\infty} \left[ A_l r^l + B_l r^{-(l+1)} \right] P_l(\cos\theta) \tag{2.29}$$

$$\Phi_{out}(r,\theta) = \sum_{l=0}^{\infty} \left[ C_l r^l + D_l r^{-(l+1)} \right] P_l(\cos\theta) \tag{2.30}$$

The coefficients $A_l$, $B_l$, $C_l$, and $D_l$ must be determined by applying appropriate boundary conditions.

**$\Phi$ is Finite at $r = 0$ :** In order to ensure that the potential doesn't become infinite at the center of the sphere, $B_l = 0$ for all values of $l$.

**$\Phi_{out}(r \to \infty) = E_0 x$ :** The electromagnetic response of the sphere should fully decay away far from the sphere such that the potential that exists only results from the excitation plane wave. As $r \to \infty$, only $B_l$ remain and in order for $\Phi_{out} = -E_0 x = -E_0 r\cos\theta$ these coefficients must be $B_1 = -E_0$ and $B_{l\neq 0} = 0$.

**Gauss's Law at $r = a$, $\hat{r} \cdot (\varepsilon_0 \varepsilon_m \mathbf{E}_{out} - \varepsilon_0 \varepsilon \mathbf{E}_{in}) = \rho_s$ :** Applying Gauss's law at the surface of the sphere ensures that the radial component of the $\mathbf{D}$ is conserved across the interface. At the surface of the sphere for $\rho_s = 0$, the boundary condition becomes:

$$\varepsilon_m \left. \frac{\partial \Phi_{out}}{\partial r} \right|_{r=a} = \varepsilon \left. \frac{\partial \Phi_{in}}{\partial r} \right|_{r=a} \tag{2.31}$$

**Faraday's Law at $r = a$, $\hat{r} \times (\mathbf{E}_{out} - \mathbf{E}_{in}) = 0$ :** Similarly, applying Faraday's law to the interface ensures that the transverse component, $E_\theta$, of the electric field is matched across the interface. When converted into electric potential this becomes:

$$\left. \frac{\partial \Phi_{out}}{\partial \theta} \right|_{r=a} = \left. \frac{\partial \Phi_{in}}{\partial \theta} \right|_{r=a} \tag{2.32}$$

Although the details of the solution can be found elsewhere, [36,38] when both Gauss's Law and Faraday's Law are applied across the interface between the nanoparticle and the surrounding medium, it is found that all of the Legendre polynomial coefficients

vanish except for:

$$A_1 = -3E_0\Big(\frac{\varepsilon_m}{\varepsilon + 2\varepsilon}\Big) \tag{2.33}$$

$$D_1 = a^3E_0\Big(\frac{\varepsilon - \varepsilon_m}{\varepsilon + 2\varepsilon_m}\Big) \tag{2.34}$$

Which yields a final solution for the electric potential both inside and outside of the sub-wavelength sphere:

$$\Phi_{in}(r,\theta) = -\Big(\frac{3\varepsilon_m}{\varepsilon + 2\varepsilon_m}\Big)E_0 r\cos\theta \tag{2.35}$$

$$\Phi_{out}(r,\theta) = -E_0 r\cos\theta + E_0\Big(\frac{a}{r}\Big)^3\Big(\frac{\varepsilon - \varepsilon_m}{\varepsilon + 2\varepsilon_m}\Big)r\cos\theta \tag{2.36}$$

The electric field inside and outside the particle can be found by combining these expressions for the respective electric potentials with its definition, $\mathbf{E} = -\nabla\Phi$:

$$\mathbf{E}_{in}(r,\theta) = \Big(\frac{3\varepsilon_m}{\varepsilon + 2\varepsilon_m}\Big)E_0\underbrace{\big(\hat{r}\cos\theta - \hat{\theta}\sin\theta\big)}_{\mathbf{E_0}} = \Big(\frac{3\varepsilon_m}{\varepsilon + 2\varepsilon_m}\Big)\mathbf{E}_0 \tag{2.37}$$

$$\mathbf{E}_{out}(r,\theta) = \underbrace{E_0\big(\hat{r}\cos\theta - \hat{\theta}\sin\theta\big)}_{\text{Incident Field}} - \underbrace{E_0\Big(\frac{a}{r}\Big)^3\Big(\frac{\varepsilon - \varepsilon_m}{\varepsilon + 2\varepsilon_m}\Big)\big(\hat{r}2\cos\theta + \hat{\theta}\sin\theta\big)}_{\text{Scattered Field by NP}} \tag{2.38}$$

The scalar potential field, $\Phi(r,\theta)$, and the total electric field, $\mathbf{E}(r,\theta)$ through the center of a silver nanoparticle with a 5 nm radius for several different excitation wavelengths are shown in Figure 2-4 along with the maximum normalized electric field magnitude $E_{max}/E_0$ as a function of $\lambda$.

There are several very important observations that can be drawn from these equations that provide some useful insight about localized surface plasmon resonance:

1. The electric field inside the sphere is aligned along the direction of excitation and has a constant magnitude that depends solely on the dielectric function of the sphere and the surrounding medium.

2. The electric field outside the nanoparticles is the superposition of the incident field, $\mathbf{E}_0$, and the scattered field that is generated by the nanoparticle in response

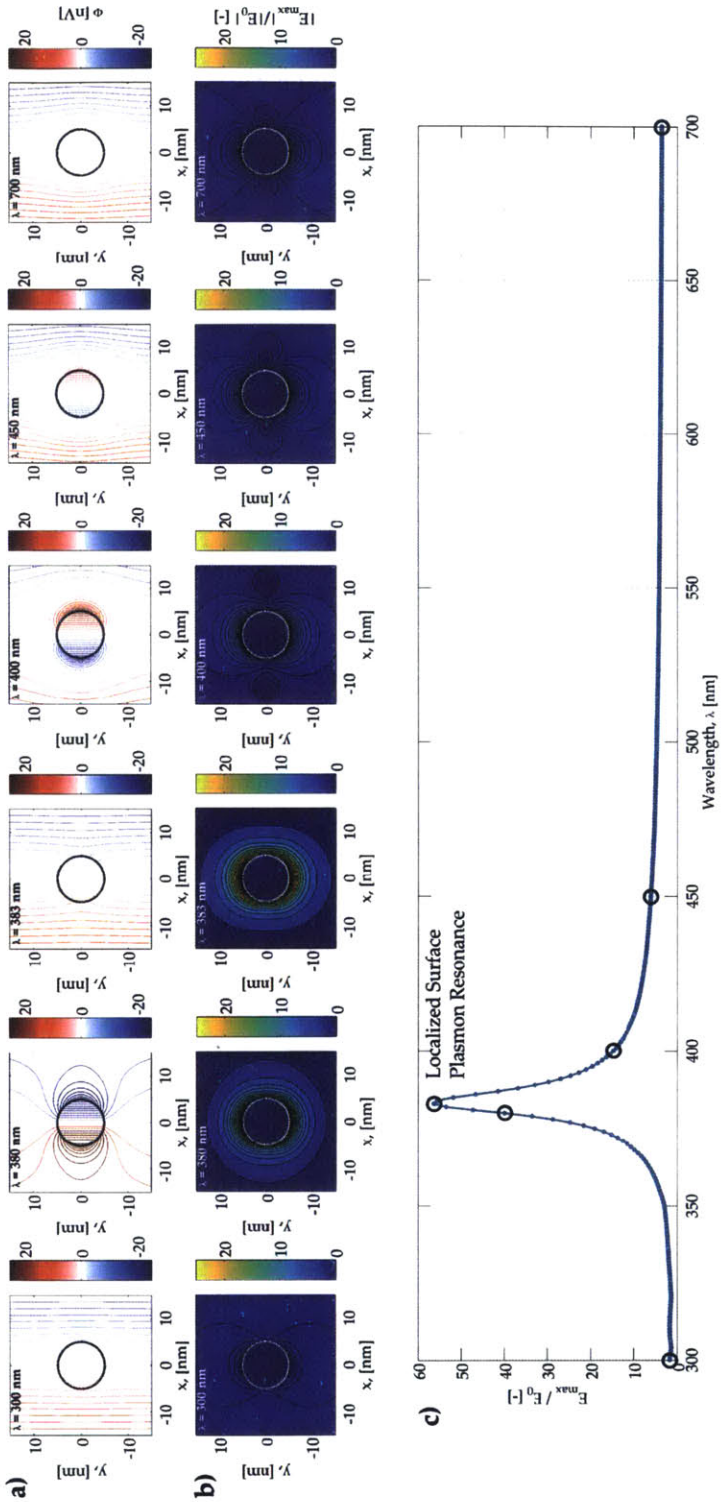


Figure 2-4: Contour maps of the a) potential field $\Phi(\lambda)$, and b) normalized electric field magnitude $|E_{max}(\lambda)|/|E_0|$ for a plane through the center of a silver nanoparticle with $a = 5$ nm that is immersed in water ($\varepsilon_m = 1.777$). c) The spectral response of the normalized electric field magnitude shows that $|E_{max}(\lambda)|/|E_0|$ is largest when $\lambda = 383$ nm.

to the incident field. The nanoparticle's electromagnetic response takes the form of a Hertzian dipole. For this reason, nanoparticles can be considered as electric dipole nano-antennas that resonantly absorb and scatter incident light.

3. The scattered electric field outside the nanoparticle decays with $1/r^3$ from the surface of the sphere and relaxes to zero far away. Hence light is concentrated more strongly closer to the nanoparticle surface, but the field intensity drops to about 1.5% of its original value only one radius away from the particle surface.

4. From the scattering term in Equation 2.38, it is clearly seen that the amplitude of the electric field would be maximized when the $\varepsilon + 2\varepsilon_m \rightarrow 0$. If both the nanosphere and the surrounding medium are dielectric, then this quantity is always positive. However, as previously discussed in Section 2.1, metals can achieve negative values for $\varepsilon_1$ when $\omega < \omega_p$ as is demonstrated in Figure 2-1 for both ideal metals that obey the Drude model as well as real noble metals. When the metal nanoparticle is embedded in a dielectric medium, there will exist a particular frequency called the localized surface plasmon resonance frequency, $\omega_{LSPR}$, where the denominator will approach zero. If $\varepsilon_2$ is small, then the resonance frequency will depend only on the real part of dielectric functions for the sphere. This is known as the Fröhlich condition:

$$\varepsilon_1(\omega_{LSPR}) = -2\varepsilon_m(\omega_{LSPR}) \tag{2.39}$$

Near the resonant frequency, the free electrons in the metal nanoparticle will collectively oscillate to form a localized surface plasmon. This in turn generates a very strong electric field in its immediate vicinity, which is referred to as the *dipole surface plasmon mode.* Although the scattered field can be very large near the surface of a sub-wavelength metal nanoparticle, it is not infinite because there is also an imaginary component, $\varepsilon_2$, that limits the amplitude to a finite value. If interband transitions occur near the LSPR frequency, then $\varepsilon_2$ will be increased and the enhancement of the electric field intensity in the near-

field will be dramatically reduced. For this reason, silver nanoparticles typically demonstrate significantly higher field enhancements than gold and copper.

5. The resonance frequency of the nanoparticle depends not only on the complex dielectric function of the metal nanoparticle, $\varepsilon(\omega) = \varepsilon_1 + i\varepsilon_2$, but also on the dielectric function of the surrounding medium, $\varepsilon_m(\omega)$. For standard dielectric materials such as air, water, and glass the dielectric function has little variation throughout the visible spectrum, therefore $\varepsilon_m$ is usually taken to be constant and is always positive for simple insulators. Although the the Frölich Condition is only strictly valid for nearly ideal metals where the imaginary component of $\varepsilon$ is small, it provides an easy way to identify how the plasmon resonance frequency is influenced by different media. As shown in Figure 2-5, when a sub-wavelength metal nanoparticle is immersed in a dielectric media, the resonance wavelength ($\lambda_{LSPR} = 2\pi c/\omega_{LSPR}$) will red-shift as $\varepsilon_m$ increases. Therefore, the optical response of metal nanoparticles is sensitive to changes in the dielectric constant of the surrounding media. As will be discussed in the next section, this features has allow metal nanoparticles to be used as probes for sensing environmental changes or binding events with biomolecules.

### 2.2.2 Extinction of Small Particles

All of the theory so far has focused on the electromagnetic response of sub-wavelength metal nanoparticles in the near-field. However, it is very difficult in practice to experimentally measure the light that is contained within the few nanometers of space directly surrounding small particles. The simplest way to understanding what is happening locally is to perform a calculation for both the near-field and the far-field and compare it to a simple macroscopic measurement. Fortunately, $\lambda_{LSPR}$ can be easily determined by measuring the *extinction* spectrum of a colloidal suspension with a spectrophotometer. This provides a measure of how much light is extinguished by the particles, provided the surrounding medium is non-absorbing. Extinction is the sum of the scattering and absorbing by the nanoparticles, which is directly

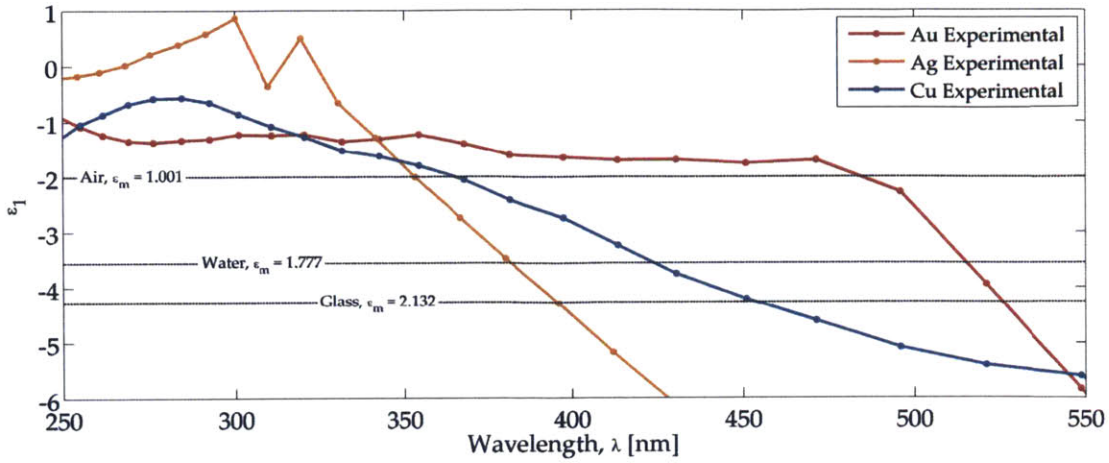


Figure 2-5: According to the Fröhlich Condition given by Equation 2.39, when a sub-wavelength metal sphere is immersed in a dielectric media, the plasmon resonance wavelength will red-shift with increasing $\varepsilon_m$. Experimental values from Johnson and Christy, [37] for $\varepsilon_1$ of Au, Ag, and Cu are shown by the circles and the dotted lines correspond to $-2\varepsilon_m$. Therefore, the graphical solution of the Fröhlich Condition corresponds to the intersection of the dotted lines with the circles.

proportional to the corresponding cross-sections, $C_{scat}$, $C_{abs}$, and $C_{ext} = C_{scat} + C_{abs}$. Although the derivation of these quantities can be found elsewhere, [36] [39] these cross-sections are calculated by determining the power that is absorbed or scattered by the particle and comparing that to the incident power density:

$$C_{scat} = \frac{8\pi}{3} k^4 a^6 \left| \frac{\varepsilon - \varepsilon_m}{\varepsilon + 2\varepsilon_m} \right|^2 \tag{2.40}$$

$$C_{abs} = 4\pi k a^3 \mathrm{Im}\left\{ \frac{\varepsilon - \varepsilon_m}{\varepsilon + 2\varepsilon_m} \right\} \tag{2.41}$$

$$C_{ext} = \frac{24\pi^2 a^3 \varepsilon_m^{3/2}}{\lambda} \left( \frac{\varepsilon_2}{(\varepsilon_1 + 2\varepsilon_m)^2 + \varepsilon_2} \right) \tag{2.42}$$

Thus, the extinction spectra measured by a spectrophotometer for a suspension of monodisperse sub-wavelength nanoparticles is expected to be directly proportional to $C_{ext}$ as provided by Equation 2.42. According to Equations 2.40 and 2.41, when the Fröhlich condition is met, both $C_{scat}$ and $C_{abs}$ (and hence $C_{ext}$) will increase dramatically as well. Hence, not only will the particle's local electric field be enhanced at resonance but also its ability to both absorb and scatter light. Since $C_{scat}$ scales

with $a^6$ whereas $C_{abs}$ only scales with $a^3$, scattering will become more significant with increasing particle size and will eventually dominate absorption. This is part of the reason why suspensions of larger nanoparticles look hazier than those with smaller diameters. Likewise, the color of light scattered from larger metal nanoparticles will corresponds to $\lambda_{LSPR}$.

### 2.2.3 Dependence of LSPR on Size, Shape, and Material

Now that the optical properties of the simplest particle geometry, the small sphere, has been presented. It is worth quickly exploring how nanoparticle material, size, and shape tend to influence the strength and resonance frequency of LSPs in metal nanoparticles.

#### Size Dependence

Rigorous mathematical treatment was applied for the response of small nanoparticles in the quasi-electrostatic limit, $a \ll \lambda$. However. it is worth discussing how nanoparticles that are even smaller or larger than this regime behave. Metal nanoparticles can be classified into three different size regimes:

1. **Nanoclusters ($a \lesssim \lambda_f$):** if the size of a metallic nanoparticle is less than Fermi wavelength, $\lambda_f$, ($\approx$ 0.5 nm in metals) the continuous bandstructure characteristic of metals begins to breaks into discrete energy levels. [40] In this regime, no plasmon modes are supported because the particle has too few atoms to achieve metallic behavior. Rather, nanoclusters exhibit strong fluorescence in the manner characteristics of molecular materials such as dyes.

2. **Small Nanoparticles ($\lambda_f \lesssim a \lesssim \Lambda$):** if the nanoparticle is smaller than the mean free path of the free electrons in the metal, $\Lambda$, ($\approx$ 30-50 nm) then the electromagnetic behavior is well described by the electrostatic treatment presented in Section 2.2.1. If the particle is spherical in shape, it will produce only the dipole plasmon mode under excitation. The behavior of small particles is generally dominated by absorption. Thus, dilute colloidal solutions will look

transparent and vividly colored depending upon which wavelengths are strongly absorbed.

3. **Large Nanoparticles** ($a \gtrsim \Lambda$): for nanoparticles that are even larger, the quasi-electrostatic approximation is no longer valid and a more rigorous electrodynamic treatment is required to capture how different regions of the particle volume experience different phases of the driving electromagnetic field. [36]. This is done by expanding the internal and scattered fields into a set of normal modes described by vector harmonics, a process which is known as *Mie theory* after Gustav Mie published the method in 1908. [41] The results of the quasi-electrostatic approximation form the first term of the expanded set, whereas other higher-order modes arise due to retardation effects in the larger nanoparticle interior. The behavior of large particles is dominated by scattering and solutions will look increasingly turbid with particle size.

Mie theory is applicable for any spherically symmetric nanoparticle that supports plasmons and can be generalized to predict the electrodynamic response of core-shell nanoparticles with multiple concentric shell layers.

### Material Dependence

As discussed previously, the resonance wavelength depends strongly on the dielectric function of the nanoparticle, $\varepsilon(\lambda)$, and the dielectric constant of the surrounding medium, $\varepsilon_m$. This is illustrated in Figure 2-6 for a 10 nm diameter nanoparticles of several different metals (Au, Ag, Cu, Ni) immersed in either water ($\varepsilon_m = 1.777$) or chlorobenzene ($\varepsilon_m = 2.323$ ). First notice that $C_{ext}^{Ag} > C_{ext}^{Au} > C_{ext}^{Cu}$, which is due to interband transisions arising at the resonance wavelength for gold and copper but not for silver. Secondly, the resonance wavelength, which corresponds to the peak position, shifts dramatically to longer wavelengths with the dielectric constant of the surrounding media increases.

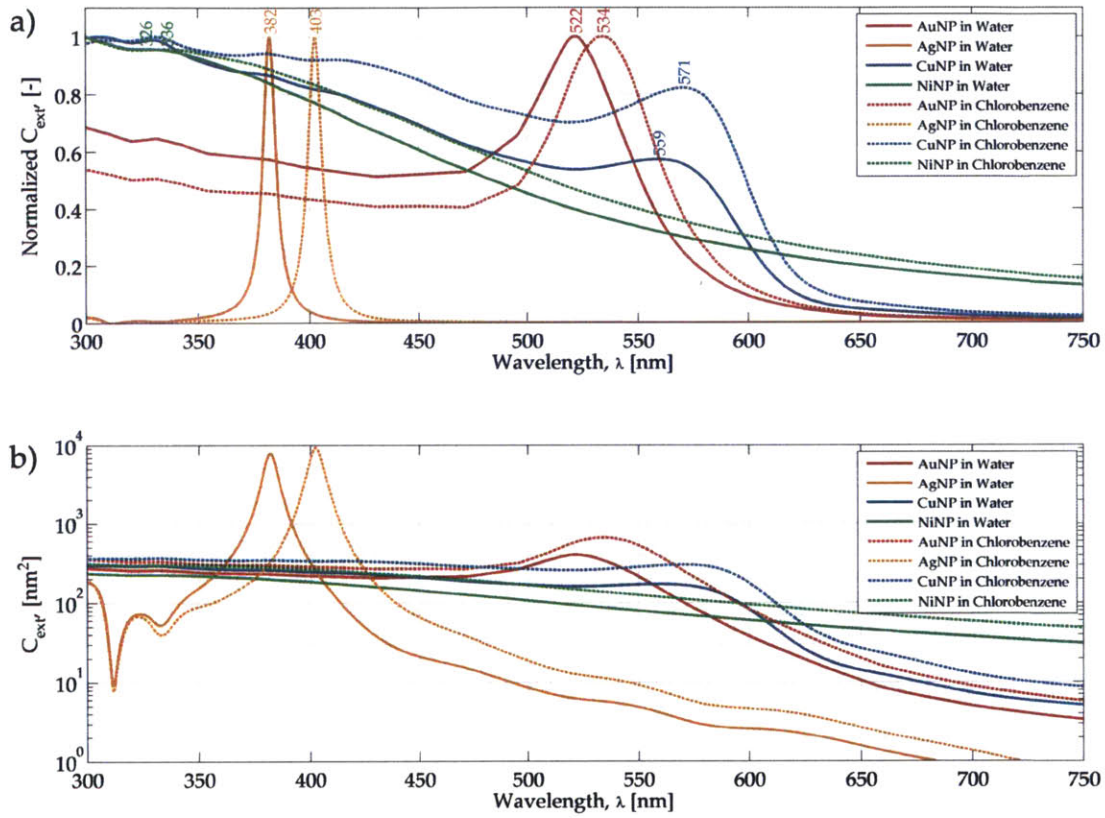


Figure 2-6: The a) absolute magnitude and b) peak-normalized extinction cross-section for a 10 nm metal nanoparticle depends on the dielectric function of both the metal and the surrounding medium. The wavelength at which localized surface plasmon resonance arises corresponds to the peak position of the extinction cross-section spectrum. The resonance wavelength red-shifts when immersed in media with higher dielectric constants. The peak extinction cross-section of silver is quite high because unlike, gold and copper, interband transitions do not arise at the resonance wavelength. The extinction spectra of nickel does not have an obvious peak like the noble metals and only exhibits a fairly even extinction over the entire visible range. For this reason, colloids of nickel nanoparticles appear black whereas silver appears yellow and both gold and copper appear red. Nickel is a more complicated material anyways owing to its ferromagnetism.

### Shape Dependence

When the shape of a metal nanoparticle deviates from that of a solid sphere, new plasmon modes arise. The number of modes that arise increases as the symmetry of the particle is reduced. For instance, there are two modes for metal nanorods, which correspond to electrons oscillating in parallel with or transverse to the central axis of the rod. Which of these modes is excited is determined by the polarization of the incident light. When the electrons are oscillating in resonance, charge density will accumulate on the metal surfaces and a restoring force will develop between the accumulated electrons and the unscreened ions of the metal. As discussed previously, this restoring force acts like a spring to return the electrons to their equilibrium positions. The longer the distance between the opposite surfaces of a particle, the weaker the restoring force will be, which means the spring constant will be reduced. According to our mechanical analogue, the resonant frequency from Equation 2.14 will decrease with reduced values for $k$. Hence, the greater the distance between surfaces for a given polarization of light, the longer the expected resonance wavelength. Thus, the longitudinal mode of the nanorod will have a resonance position red-shifted from the transverse mode.

In geometries such as triangular nanoprisms, further reductions in symmetry lead to more modes that can arise. Because many different lines can be drawn across the triangle, several different dipole modes can arise each with a slightly different resonant frequency. Hence the ensemble average over all of these modes will lead to a broadened dipole peak.

## 2.2.4 Applications

There are two main features of the optical response of metal nanoparticles to visible light that make them useful in practical applications:

**Sensing:** as demonstrated in Figure 2-6, the peak position (i.e. $\lambda_{LSPR}$) of the extinction spectrum of a system with well-dispersed metal nanoparticle is very sensitive to the dielectric constant of the surrounding medium. If the dielectric

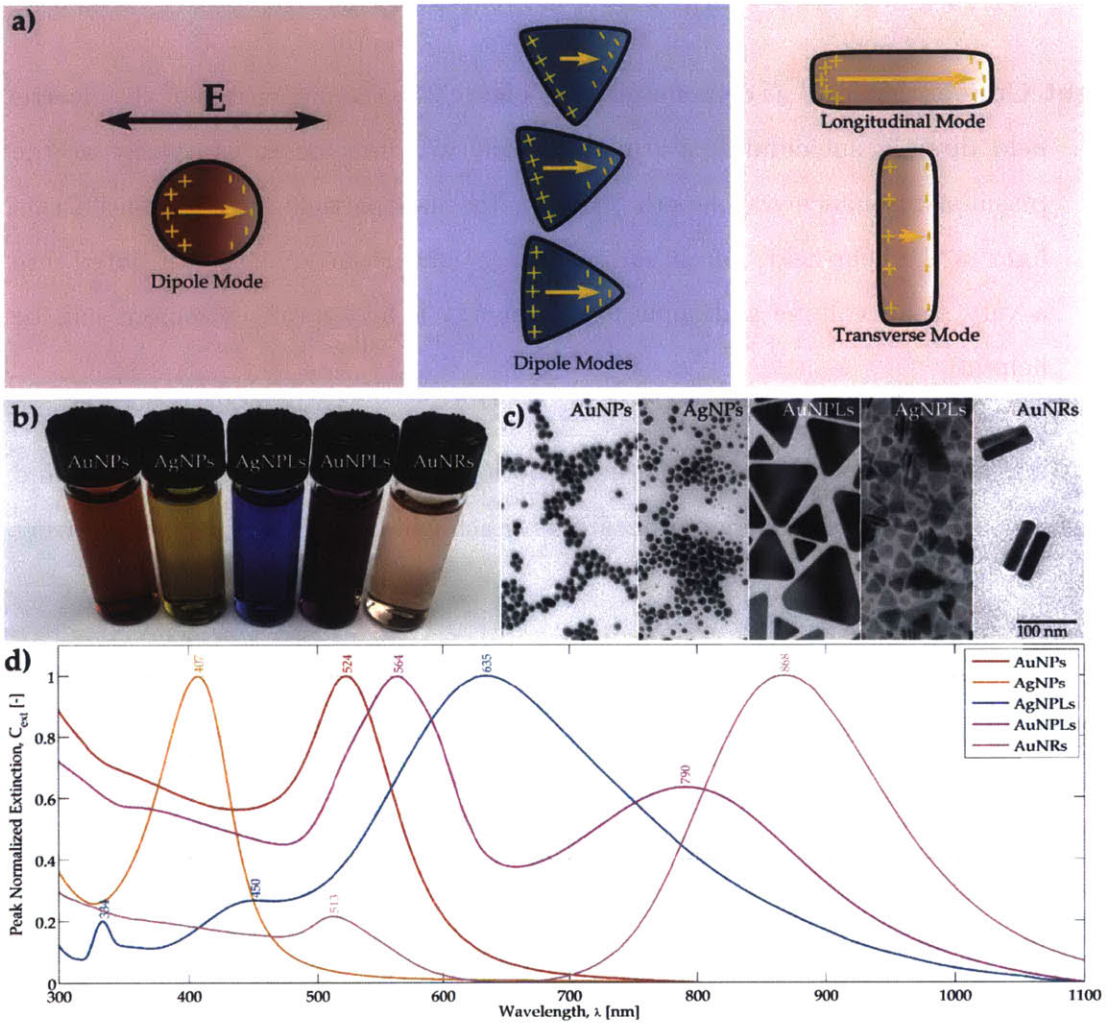


Figure 2-7: a) As symmetry is reduced, various plasmon modes arise that are dependent on the polarization of the incident light. b) The color of metal nanoparticle colloids in water depends strongly on shape and material. The color of each solution is determined by the wavelengths where light is efficiently transmitted, that is where the extinction spectra is low. c) TEM images of each gold nanoparticles (AuNPs), silver nanoparticles (AgNPs), gold nanoplates (AuNPLs), silver nanoplates (AgNPLs), gold nanorods (AuNRs), and d) the peak normalized extinction spectra measured for each of these solutions.

constant of the environment changes, then the peak will shift accordingly. This finds practical use in biological applications where the event of a biomolecule binding to the nanoparticle will cause the local dielectric constant to change.

**Light Concentration:** as demonstrated in Figure 2-4, the magnitude of the electric field directly surrounding the nanoparticle will increase substantially at the plasmon resonance wavelength. Hence, the nanoparticle acts to concentrate light in the near-field. For situations where light needs to be redistributed into a very small volume and some loss of energy is acceptable, plasmons can be helpful.

Noble metal nanoparticles were used as both probes for sensing applications and as light-concentrators for energy applications. Each will be discussed in the following sections.

## 2.3 Biological Interactions with Metal Nanoparticles

There are many situations where it is desirable to interface biomolecules with metal nanoparticles. For instance, localized surface plasmons have enabled the use of metal nanoparticles as dark-field imaging agents in biological tissue [42] [43], photoactive biomolecule release systems [44], as probes for biomolecular sensing [45], and as photothermal agents for proposed site-selective cancer therapy [42]. Finding methods that enable biomolecular materials to bind with noble metal nanoparticles is key to accomplishing any of these tasks. Typical methods for attaching biomolecules to the surface of noble metals involve thiolated antibodies or oligonucleotides due to the strong affinity of sulfur atoms for noble metals. However, a more elegant approach is to build peptides into antibodies or other biomolecules that have affinity for gold or silver. In the remaining sections of this chapter, this concept will be discussed in detail where the M13 bacteriophage is used as a platform to bind and disperse noble metal nanoparticles.

### 2.3.1 M13 Bacteriophage

The M13 bacteriophage is a filamentous-type virus that replicates by infecting the bacteria *Escherichia coli* with its genome. As shown in Figure 2-8a, it consists of a protein capsid that enshrouds a single-stranded loop of DNA. The virus is about 880 nm in length and 6 nm in diameter with ~2,700 identical copies of the pVIII protein comprising the coat along the major axis. At the outer surface of either end of the virus, there are about 5 copies of the pIII and pIX proteins. Due to the simple structure and well-studied genome of the virus, these outer-coat proteins can be genetically engineered to display peptides that enable the virus to interact with materials in its environment. To illustrate this, virus variants were amplified that have gold-binding peptides incorporated into either the pIII or pVIII proteins. Figure 2-8b sketches how gold nanoparticles (AuNPs) dispersed in aqueous media would bind to the virus. Binding events are clearly demonstrated in the actual system by the TEM images shown in Figure 2-8d where AuNPs are clearly bound to the virus and outline the filamentous morphology of the virus.[1] Likewise, Figure 2-8c illustrates the concept of the pIII protein binding to AuNPs that have been patterned on a substrate. It is clearly seen in Figure 2-8e that the end of each of the virus particles is attached to a AuNP. Thus, both the pIII and pVIII proteins can be modified so that a particular region of the virus demonstrates an affinity for inorganic materials.

### 2.3.2 Self-Assembly of Nanoparticle-Virus Complexes

When a protein of the virus has been programmed to display affinity for a noble metal, structures such as the decorated virion in Figure 2-8d can be easily assembled by simply combining an aqueous colloid of appropriately-capped nanoparticles with an aqueous solution of the virus. In the solution, the peptide at the outermost end of the capsid protein will be able to bind with the nanoparticle in the event that they

[1] When many nanoparticles are packed along the virus, it becomes nearly impossible to directly image the bacteriophage with transmission electron microscopy (TEM) due to the high contrast between the metal nanoparticles and the organic virion. When less particles are attached to a virion, the bare proteins become easier to image directly.

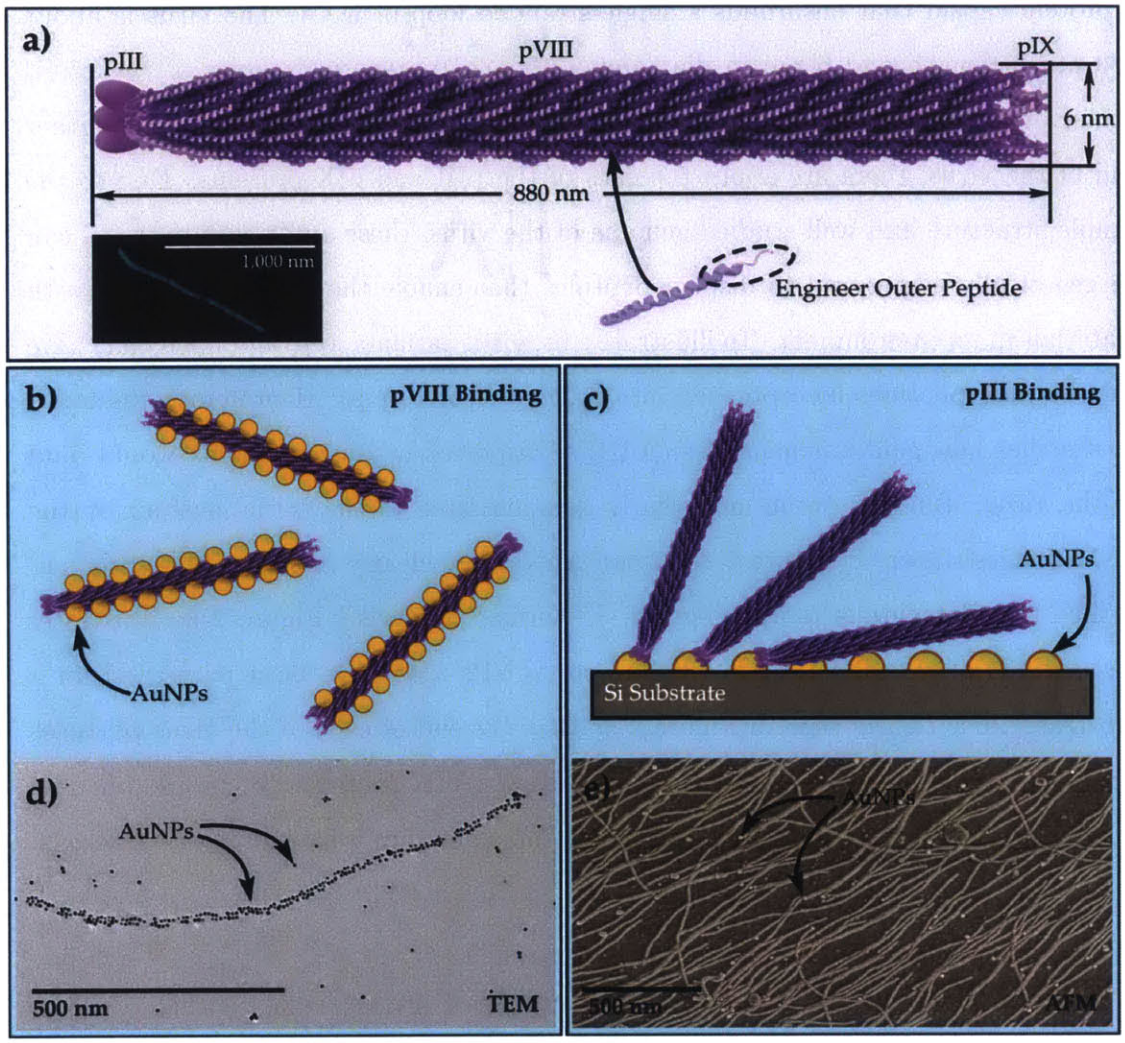


Figure 2-8: a) The M13 bacteriophage is a filamentous-type virus whose outer coat proteins, pIII, pVIII, and pIX can be engineered to display peptides with affinity for inorganic materials (virus sketch is not to scale). The inset shows an AFM image of a single virus. Viruses that have been designed to bind gold nanoparticles with the pVIII and pIII proteins are shown schematically in (b-c) and using microscopy techniques (d-e).

come into contact.

There are several established sequences that are capable of binding either gold, silver, or both. These are listed in Table 2.1.

Table 2.1: Virus Variants with Affinity for Au or Ag

| Variant | Binds Au? | Binds Ag? | Sequence | Functional Group |
|---|---|---|---|---|
| p8#9 (pVIII) | Y | Y | VSGSSPDS | Hydroxyl |
| DSPH (pVIII) | Y | N | DSPHTELP | Imidazole |
| E3 or EEAE (pVIII) | N | Y | EEE or EEAE | Carboxylic Acid |
| C7C (pIII) | Y | Y | CSHLHSPLC | Thiol |

Each of the virus variants listed uses a different functional group to bind directly to the metal nanoparticle surface. The pIII peptide, C7C, contains two cysteine residues that tend to form a disulfide bridge, which must be reduced prior to use with tris(2-carboxyethyl)phosphine (TCEP) in order to liberate the thiol groups for interaction with the metal. Conversely, all of the pVIII peptides do not require any mild reducing agents for use and can each be used in its native state. For the purposes of this thesis, the variant called p8#9 is used almost exclusively because it has the ability to bind with both gold and silver and does so in a gentle manner that does not damage the particles. [46] This should be contrasted against the E3 variant, which tends to have a significant enough catalytic interaction with Ag that it will decompose large nanoparticles and redistribute the material along the virus major coat.

There are two types of interactions that can bind a nanoparticle to the virus:

1. **Protein Affinity:** this occurs when the sequence of amino acids comprising the peptide on the outermost end of either the pIII, pVIII, or pIX proteins demonstrates affinity for the material itself.

2. **Electrostatic:** if the virus major coat proteins and the nanoparticles are oppositely charged, then they will become bound based purely on electrostatic attraction.

Electrostatic interactions are generally difficult between nanoparticles and the virus because usually both the capping agent that stabilizes the nanoparticle and

the virus are negatively charged at neutral pH. Adding buffer to a solution of colloidal nanoparticles can cause them to precipitate irreversibly from solution if the salt concentration is high enough to screen the charges on the capping-agent molecules. Therefore, protein-metal affinity is a simpler mechanism for binding and can usually be performed in deionized (DI) water regardless of the surface charges of the nanoparticles and virions.

### 2.3.3 Role of Capping Agent in Metal-Protein Interactions

Although the virus variants listed in Table 2.1 are capable of binding with Au and Ag, allowing the virus proteins to recognize and bind to a metal *nanoparticle* requires that: (1) the affinity of the virus binding peptide for the metal be significantly stronger than that of the capping-agent, and (2) that the capping-agent molecules be easily displaceable by the protein itself. Although many different types of nanoparticles have been grown or bound to the virus, there has not yet been much discussion of the surface chemistry that is required to promote the bonding of two materials that have already been formed, as opposed to the act of nucleating new materials directly on the phage. In order to explore the limitations of the p8#9 virus to bind to AuNPs and AgNPs, a study was performed to identify which capping-agents would allow for direct protein-metal binding.

There are several main findings that have resulted from this effort:

1. **Citrate is an ideal capping agent for enabling the binding of the virus to both AuNPs and AgNPs**. It is compact, highly charged, and only weakly bound to the metal surface. Furthermore, the most common methods for synthesizing gold and silver nanoparticles in aqueous solution are derived from the Turkevich method, which uses citrate as both a reducing agent and capping agent. [47] The three carboxylic acid groups present on each citrate polyanion are all deprotonated near neutral pH, which allows the nanoparticles to be negatively charged and electrostatically stabilized in aqueous solution. Even though the surface of both the citrate-capped metal nanoparticles and the virus are neg-

atively charged, as is clearly demonstrated by Figure 2-9a and d-f, binding still occurs, which indicates that mechanism must be based on protein recognition of the metal surface.

2. **Any metal nanoparticle capped with a thiolated ligand will prevent interaction between the capsid proteins and the metal surface, regardless of the size of the ligand molecule.** All evidence from TEM images suggests that even in the case of mercaptosuccinic acid (MSA), the closest thiol analogue to citrate, the nanoparticles do not bind to the virus. This is believed to happen for two reasons: (a) the thiol functional group is so much more hydrophobic than the the pVIII binding peptides on the virus variants that the peptide is denied access to the metal surface, and (b) the affinity of thiols for noble metals is so much stronger than the pVIII binding peptides that it will never be sufficiently displaced. As is shown in Figure 2-9c, AuNPs capped with MSA do not have specific affinity for the virus to the same degree as citrate and the few observable NPs are believe to be simply sitting on the bundle of viruses. Should the thiolated capping agent be positively charged, then electrostatic interaction could occur between a nanoparticle and the virus, however in this situation the only role that the proteins on the virus have in binding is displaying negatively charged functional groups.

3. Besides citrate, the only other type of capping molecule that is both compact enough to produce a highly charged nanoparticle and has a weaker affinity for the metal surface than the pVIII binding peptides is based on aminated pyridine compounds, specifically 4-(dimethylamino)pyridine (4DMAP) [48] and 4-(methylamino)pyridine (4MAP). The only difference between them is that 4DMAP has an extra methyl group on the amine, hence both molecules act similarly as capping agent. However, 4DMAP is extremely toxic upon skin contact whereas 4MAP is significantly less hazardous. The planar structure of these molecules sufficiently stabilize AuNPs by packing tightly onto the surface and the dipole moment between the amine and the nitrogen atom in the pyridine

ring provides the partial positive charge to appear on the surface of the capped particle. As is evidenced by the TEM image in Figure 2-9b, AuNPs capped with 4MAP are able to bind to the virus in the same fashion as the citrate capped particles.

### 2.3.4 Optical Properties of Nanoparticle-Virus Complexes

Upon binding to a virus molecule, the overall optical properties of the noble metal nanoparticle largely remain the same. The virus proteins and the capping agents on the nanoparticles generally prevent the individual particles from losing their surface charge and aggregating. Hence, only the dipole resonance mode characteristic of individual particles that are well-dispersed in a medium are generally observed. However, in accordance with the Fröhlich condition presented in Figure 2-5 the measured extinction spectra will shift slightly as the virus has a higher index of refraction than DI water. Figure 2-10 demonstrates that upon binding both gold and silver nanoparticles in solution, the resonance peak position of the extinction spectra will shift to slightly redder wavelengths.

## 2.4 Plasmonic Sensing of Porosity in Nanoporous Virus Films

Now that the fundamentals of plasmon resonance and biological assembly of noble metal nanoparticles have been presented, this section will present an interesting application where gold nanoparticles are used as probes to quantify the porosity of nanoporous organic and inorganic films. As discussed in Section 2.2.3, this utilizes the sensitivity of the LSPR resonance peak position to the dielectric function of the surrounding medium. Although this thesis is focuses on solar cells, this project is a worthwhile detour into the field of sensing because it not only reveals how useful simple gold nanoparticles can be in providing information about their surroundings, but the theoretical framework used to describe the optical properties of nanostruc-

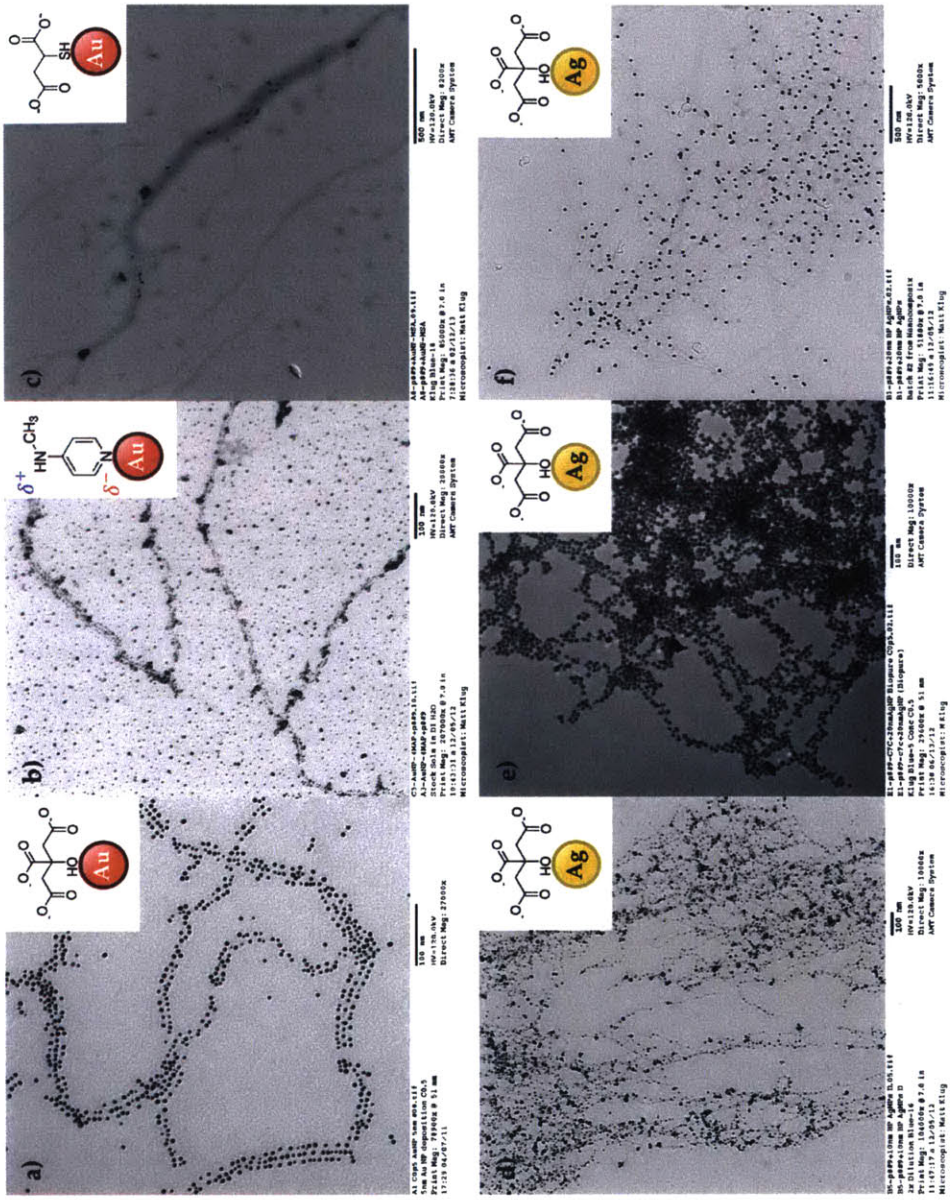


Figure 2-9: Both AuNPs and AgNPs are able to bind the virus variant p8#9 when the capping agent on the metal nanoparticle is easily displaced by the virus. a) Negatively charged 5nm citrate-capped AuNPs and b) positively charged 4MAP-capped AuNPs are capable of binding to the virus. c) However, thiolated capping agents prevent interactions with the proteins as is evidence by the lack of uniform binding when MSA-capped AuNPs are mixed with p8#9. d) 10nm and e) 20nm citrate-capped AgNPs are able to densely coat p8#9 virions, whereas f) lower ratios of NP to virus allow the 20nm AgNPs to become more separate and underfocusing the microscope allows both the bare virions and the AgNPs to be imaged simultaneously.

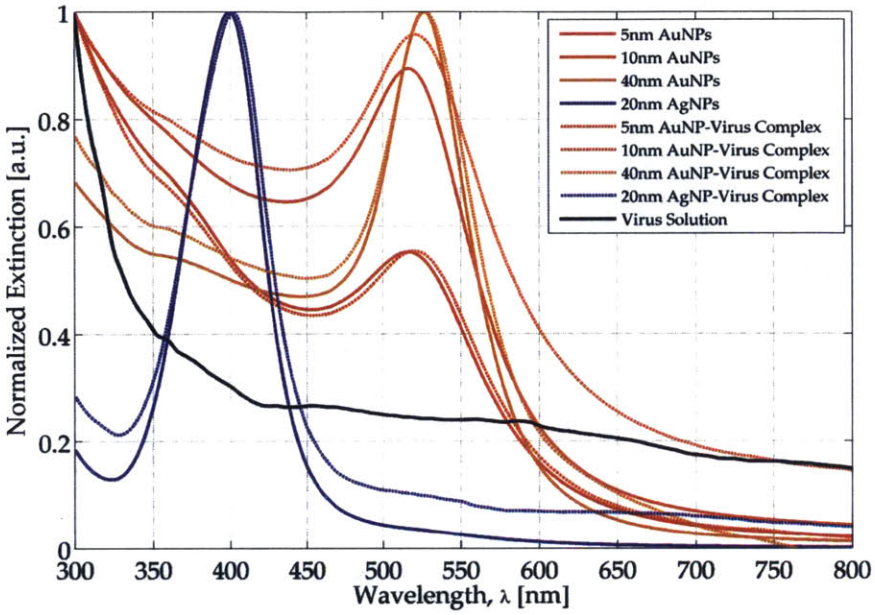


Figure 2-10: Measured extinction spectra of gold and silver colloids of different sizes as well as observed red-shifts in spectra upon complexation of metal nanoparticles with the p8#9 virus variant.

tured materials is used for modeling the active layer of bulk-heterojunction solar cells in Chapter 4. This work was originally published in *Advanced Materials* and is expounded upon in this section. [49]

### 2.4.1 Synthesis of Nanoporous Films

Although the details can be found elsewhere, nanoporous virus-based films were assembled using a covalent layer-by-layer (LbL) assembly process developed and performed by Noémie-Manuelle Dorval Courchesne. [49] In brief, gold nanoparticles were first complexed to the p8#9 virus in solution. A glass or silicon substrate was then sequentially dipped into the solution containing the virus-AuNP complexes, a solution of the zero-length cross-linker 1-Ethyl-3-(3-dimethylaminopropyl)-carbodiimide (EDC), and a rinse bath. The EDC molecules activate the available carboxylic acid groups on the virus outer coat proteins, which then covalently bond with the terminal amines of other virions when the substrate is dipped back into the solution containing

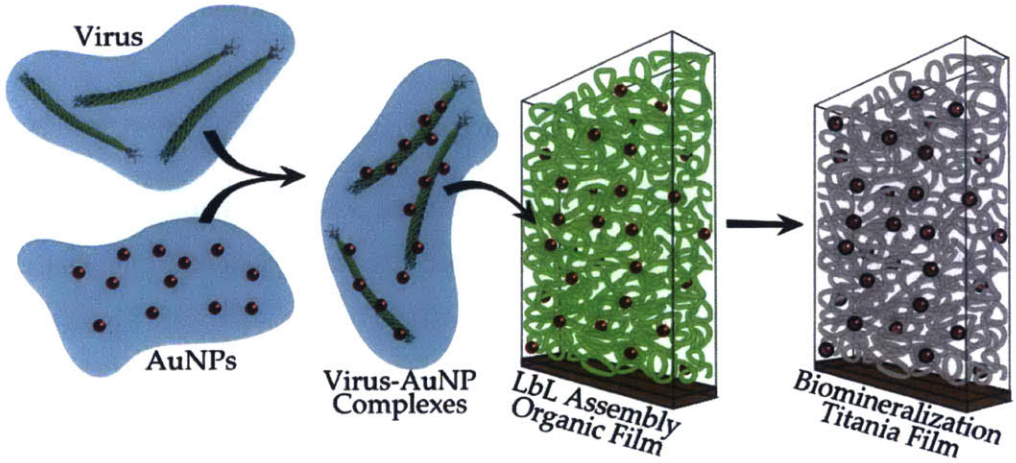


Figure 2-11: The M13 bacteriophage is first complexed with gold nanoparticles (AuNPs) in aqueous solution. The complexes are then cross-linked using EDC chemistry by covalently forming amide bonds from the carboxylic acid and primary amine groups available on the complexes. By controlling the cross-linking process with layer-by-layer (LbL) assembly, a nanoporous organic film can be built that has AuNPs evenly dispersed throughout the film thickness. The organic film can be mineralized with $TiO_2$ and converted into a nanoporous inorganic anatase film with heat treatment.

the viruses. As sketched in Figure 2-11, repeating this process allows a nanoporous virus-based film to be generated with any desired thickness that has gold nanoparticles uniformly dispersed throughout the film. This nanoporous film can further act as a scaffold upon which amorphous titanium dioxide can be nucleated and coated from a solution of titanium tetrachloride ($TiCl_4$). Through heat treatment, amorphous titania will transform into crystalline anatase titania and the virus will burn out of the film through combustion.

As evidenced by the TEM cross-sections presented in Figure 2-12a-b, the LbL process produces nanowire meshes with even porosity and morphology throughout the film thickness both before and after mineralization by titania. Figure 2-12c-d show that gold nanoparticles can be evenly distributed throughout the film as evidenced directly by the SEM image and indirectly by the uniform red hue of the assembled film, which is characteristic of well-dispersed gold nanoparticles due to LSPR. Since this assembly process is capable of dispersing AuNPs without aggregation, the location of LSPR peak can provide useful information about the effective index of the phage

film when the optical properties of the system are properly modeled.

### 2.4.2 Dielectric Function of Nanoporous Media

In order to develop an optical model that describes the behavior of gold nanoparticles embedded in the nanoporous films, we first need accurate values of the dielectric function for both the virus and anatase titania. Although measurements are available for anatase films [50], the M13 bacteriophage is a less common material and its optical properties have not been previously reported. Therefore, ellipsometry measurements were performed by J.A. Woollam Co., Inc. to calculate the complex refractive index of a 59% porous virus film as a function of wavelength between 500 and 1700 nm. As is discussed in the following paragraphs, this measurement provided the information from which the dielectric function of pure bacteriophage was estimated using effective medium theory.

Because the pores of the bacteriophage are significantly smaller than the wavelength of incident light, light cannot distinguish between the individual domains of bacteriophage and air in the film, rather it perceives an effective dielectric medium that is a blending of the material properties of the two components. The Bruggeman model for an effective dielectric function was chosen because it is valid for a two-component inhomogeneous medium and does not assume the presence of particulate inclusions like the Maxwell Garnett model does. [39] The expression for the complex effective dielectric function $\varepsilon_{eff}$, according to the Bruggeman model is: [39]

$$f\left(\frac{\varepsilon_{pp}-\varepsilon_{eff}}{\varepsilon_{pp}+2\varepsilon_{eff}}\right)+(1-f)\left(\frac{\varepsilon_{m}-\varepsilon_{eff}}{\varepsilon_{m}+2\varepsilon_{eff}}\right)=0 \tag{2.43}$$

where $\varepsilon_{pp}$ is the complex dielectric function of pure bacteriophage, $\varepsilon_m$ is the dielectric function of the other medium (either air, $\varepsilon_{air} = 1.000$, or water, $\varepsilon_{water} = 1.777$), and $f$ is the volumetric fill fraction of the bacteriophage in the two-component material. The effective dielectric function, $\varepsilon_{eff}$, must be solved for numerically using Equation 2.43, however, since the effective dielectric constant of a 59% porous bacteriophage film (i.e. 41% volumetric bacteriophage fill fraction) is known from ellipsometry, this

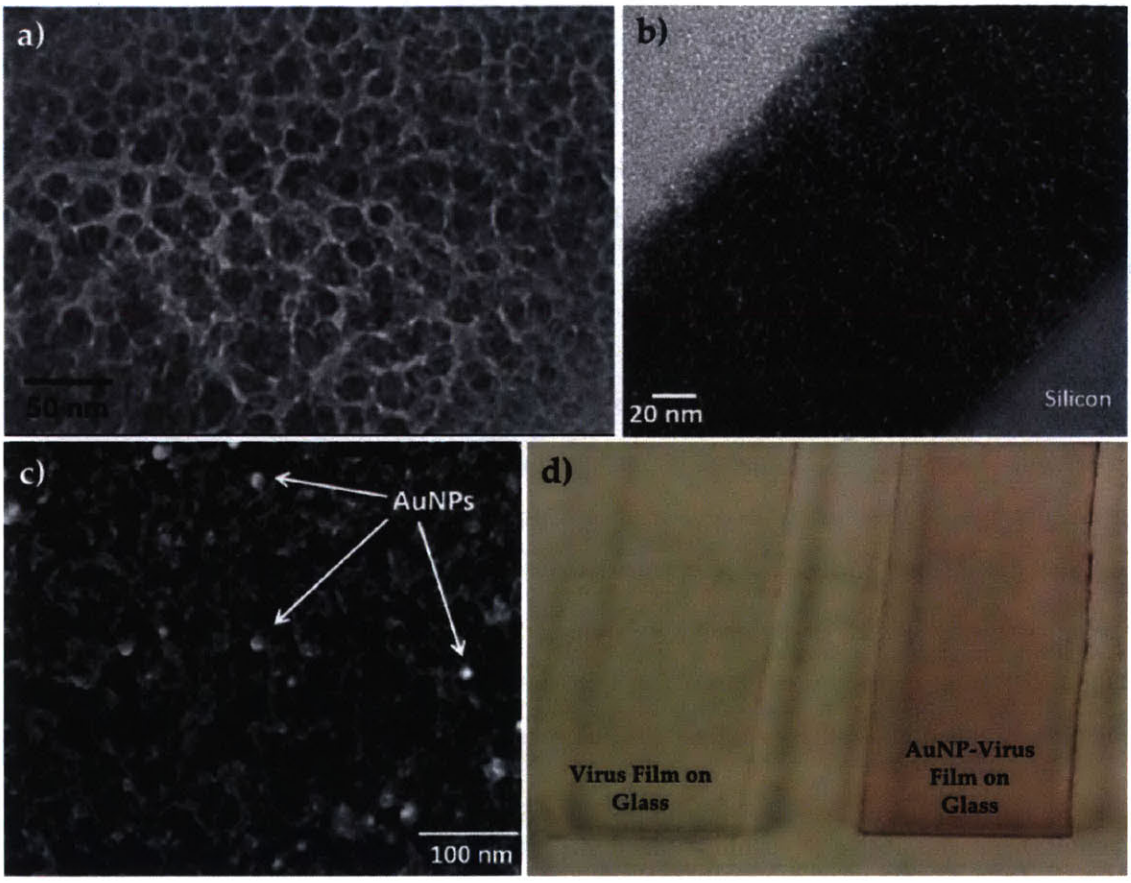


Figure 2-12: Cross-sectional transmission electron micrographs of the nanoporous (a) virus film and (b) titania network resulting from mineralization of the virus film both nanowire networks are linked to form pores that are uniformly distributed through the thickness as a result of the layer-by-layer assembly process. c) A top-down SEM images shows that gold nanoparticles are distributed throughout the film when the process uses AuNP-virus complexes instead of bare virions. d) Optical images of virus films coated on glass with (right) and without (left) gold nanoparticles complexed to the virus during LbL assembly.

data allows the dielectric function for pure phage, $\varepsilon_{pp}$, (i.e. 0% porous phage film) to be estimated. Rearranging Equation 2.43 and solving for $\varepsilon_{pp}$ provides:

$$\varepsilon_{pp} = \varepsilon_{film} \frac{2\left(\frac{f_{film}-1}{f_{film}}\right)\left(\frac{\varepsilon_{air}-\varepsilon_{film}}{\varepsilon_{air}+2\varepsilon_{film}}\right)+1}{\left(\frac{1-f_{film}}{f_{film}}\right)\left(\frac{\varepsilon_{air}-\varepsilon_{film}}{\varepsilon_{air}+2\varepsilon_{film}}\right)+1} \tag{2.44}$$

where $f_{film}$ is the bacteriophage fill fraction (41% for measured sample) and $\varepsilon_{film}$ is the dielectric function for the bacteriophage film obtained from ellipsometry measurements. Also, note that the complex index of refraction for a non-magnetic material is simply:

$$n + i\kappa = \sqrt{\varepsilon_1 + i\varepsilon_2} \tag{2.45}$$

where $n$ is the real part of the refractive index, and $\kappa$ is the imaginary part. Figure 2-13 shows both $n$ and $\kappa$ for the 59% porous phage film as determined by ellipsometry measurements and the estimated values for a pure bacteriophage film from Equations 2.44 and 2.45. This analysis was extended to show how the complex refractive index of a virus-film would change as a function of virus fill fraction. Both the real and imaginary component are displayed as contour plots in Figure 2-14. The complex dielectric function of pure, voidless anatase titania was calculated from the values reported by Kim *et al.* for a 16% porous anatase titania thin film using the same method discussed above to estimate the complex index of pure, voidless bacteriophage films. [50] In short, the reported dielectric function for the 16% porous film was substituted for $\varepsilon_{film}$ in Equation 2.44 and a titania volumetric fill fraction of 84% (i.e. 100-16 = 84) was used for $f_{film}$ to extrapolate the dielectric function of pure, voidless anatase titania (i.e. $f_{film} = 100\%$), $\varepsilon_{pp}$. The complex index of refraction was produced using Equation 2.45 and the result presented in Figure 2-15.

Once the complex dielectric function of pure anatase titania was calculated, Bruggeman effective medium theory was again used to calculate the effective complex dielectric function, $\varepsilon_{eff}$, of a nanoporous anatase film with an arbitrary volumetric fill fraction of titania, $f$, by numerically solving Equation 2.43. However this time, the calculated complex function of pure titania was substituted into $\varepsilon_{pp}$. By calculating

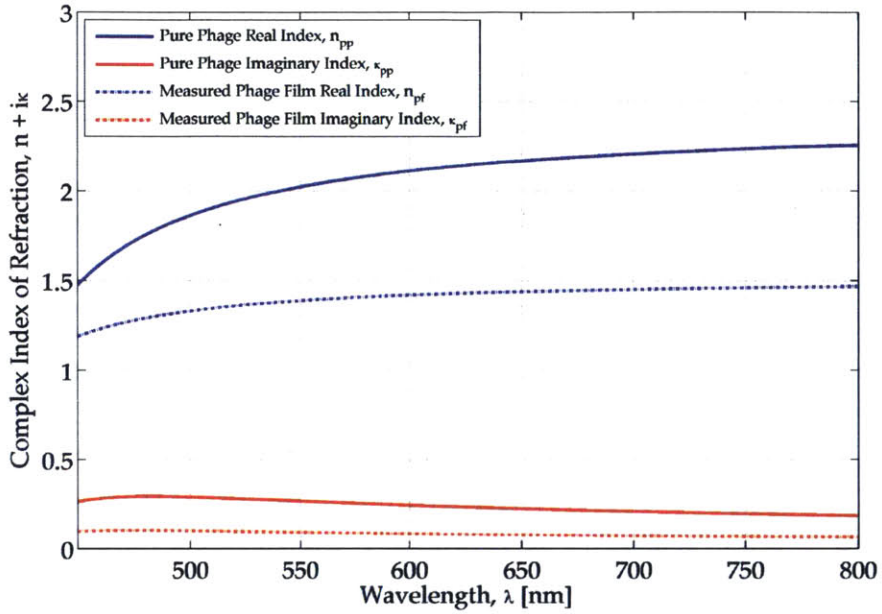


Figure 2-13: Real (blue) and imaginary (red) components of the index of refraction for the 59% porous bacteriophage films (dotted lines) as determined through ellipsometry measurements and the estimated function for pure bacteriophage films (i.e. 0% porous films, solid lines) as predicted by Bruggeman effective medium theory.

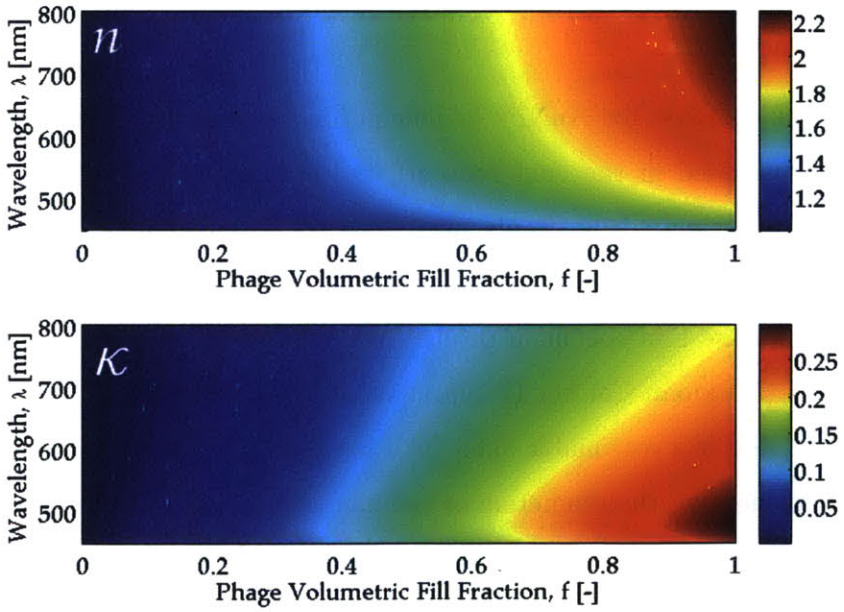


Figure 2-14: Real (top) and imaginary (lower) components of the index of refraction for bacteriophage films as a function of virus fill fraction

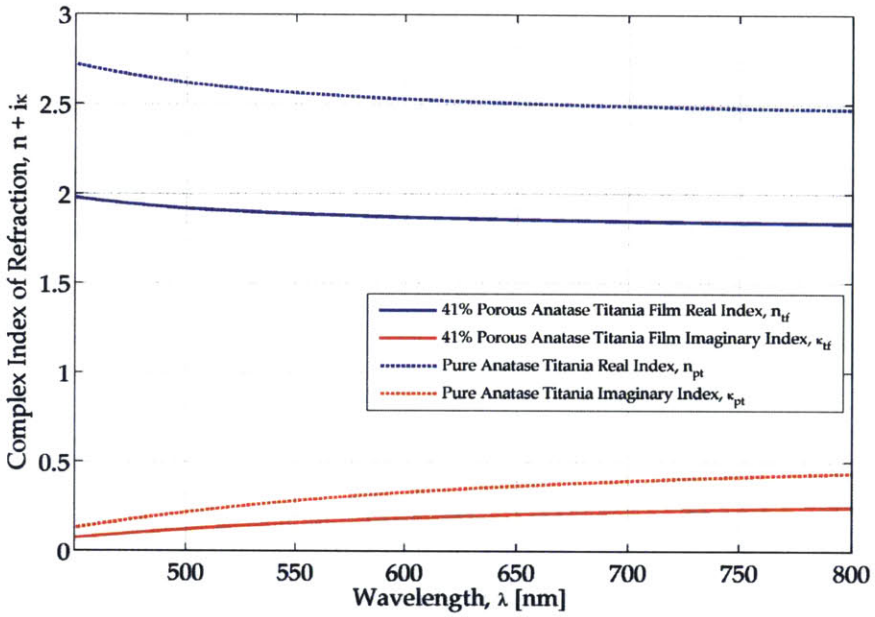


Figure 2-15: Real (blue) and imaginary (red) components of the index of refraction for pure (i.e. 0% porous films, dotted lines) and 53% porous anatase titania films.

the extinction peak location for AuNPs in nanoporous anatase films as a function of film porosity (discussed in the next section), the porosity of actual nanoporous anatase films can be estimated by simply measuring the absorption peak of AuNPs dispersed in the film and comparing it to Figure 2-21. Absorption measurements performed on an anatase film specimen produced a peak at 567 nm using a UV-vis spectrophotometer (Beckman-Coulter DU800), which is predicted using this method to be 41% porous. This is a reasonable value as it is expected that the biomineralization process would increase the diameters of the nanowire mesh and thereby reduce pore volume. It should be noted that quartz crystal microbalance measurements of the anatase sample could not be obtained as the substrate does not survive the annealing temperatures during the crystallization process. The estimated complex effective index of this sample is reported in Figure 2-15.

### 2.4.3 Predicted and Measured Extinction Spectra

Due to the phenomenon of localized surface plasmon resonance, the location and width of the absorption peak for spherical AuNPs is very sensitive to two factors: (1) the dielectric function of the medium surrounding the nanoparticle and (2) the distance between neighboring nanoparticles in the system. By comparing the absorption measurements of AuNPs in different environments to theoretical predictions, inferences can be made about the degree of particle aggregation present in virus-based composites. Thus far, the complex dielectric function has been developed for nanoporous virus and titania films, however the calculated dielectric function for the pure bacteriophage should be tested against another system to ensure validity. To do so, a model was developed to predict how AuNPs complexed onto the virus in solution would affect the extinction spectra.

The developed model uses Rayleigh scattering theory to investigate how 8 nm diameter gold nanoparticles interact with light in both the near- and far-fields. The electric-field intensity profile in the region immediately outside of the nanoparticle reveals how much light is being concentrated in the near-field. In the preceding section, the dielectric function of the 59% porous bacteriophage film was found experimentally. However, in order to predict the extinction spectra for a AuNP complexed onto a bacteriophage that is suspended in aqueous solution, an effective dielectric function must also be obtained for the water-bacteriophage medium. This is not straightforward because Bruggeman theory requires that a volumetric phage fill-fraction be known. The method chosen for computation here is to choose a domain size that is representative of the volume over which the near-field extends. By making this the domain volume over which to calculate the volumetric fill-fraction of bacteriophage, we are considering how the electric field produced by the AuNP will perceive the media directly surrounding it. The near-field electric field profile is calculated using Equation 2.38 for a AuNP with a diameter if 8 nm. The dielectric function for gold nanoparticles used for all the calculations is the experimental values reported by Johnson and Christy. [37]. Figure 2-16 shows the electric field intensity, $|E|^2$, profile

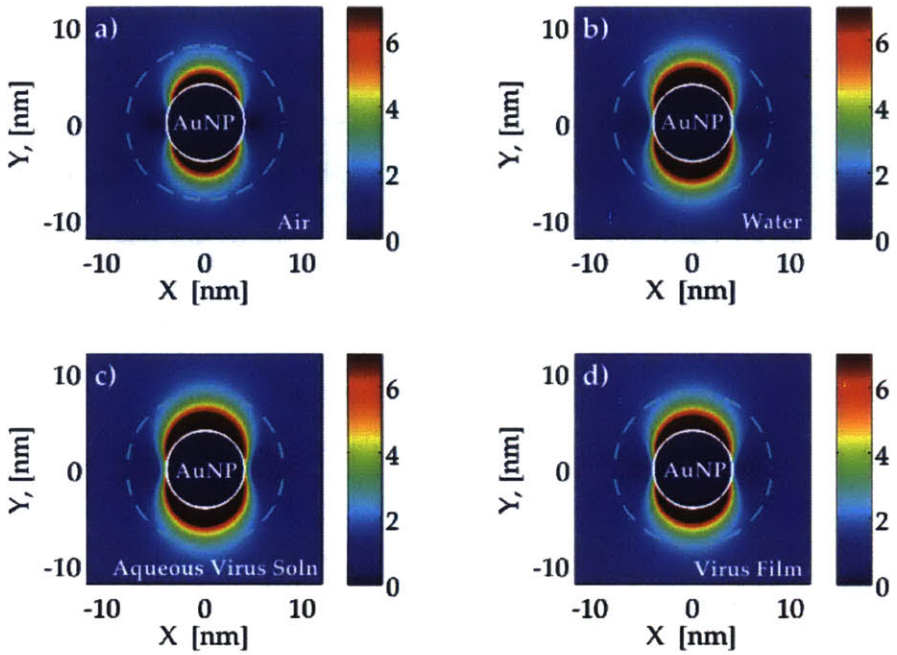


Figure 2-16: Contour plots of the normalized electric field intensity profile when illuminated at the resonance wavelength of the system through the center of a gold nanoparticle (a) embedded in air, (b) embedded in water, (c) complexed to a bacteriophage in aqueous solution, or (d) embedded in a 59% porous dried-bacteriophage film. The white circle represents the AuNP surface and the dashed cyan circle is drawn two AuNP radii from the nanoparticle center.

produced at the LSPR resonance wavelength of the system on a plane through the center of a AuNP embedded in each of the four media, which has been normalized to the intensity of the incident plane wave, $|E_0|^2$. The white circle represents the boundary of the AuNP and the dashed cyan circle is located two NP radii from the center of the AuNP. As can be seen in Figure 2-16, most of the electric field enhancement is contained within the dashed cyan circle. Therefore, it is argued that a sphere located two radii from the AuNP center is the outer extent to which the nanoparticle will feel the surrounding media, and the fill-fraction of phage contained within this sphere will be the value for $f$ used to calculate the effective dielectric function felt by a AuNP complexed onto a bacteriophage suspended in water.

By approximating the filamentous bacteriophage as a cylinder with a radius, $r_{virus}$

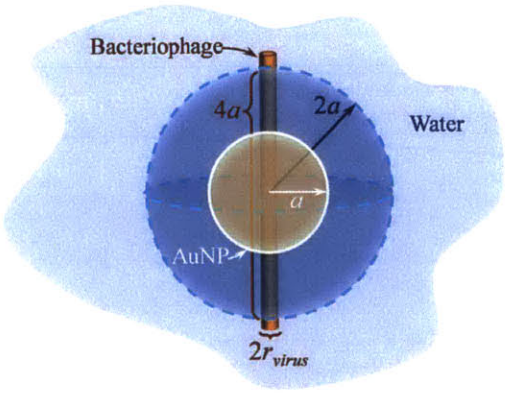


Figure 2-17: Schematic of geometry for gold nanoparticle complexed onto a bacteriophage used to calculate the fill-fraction occupied by the bacteriophage.

= 3.5 nm and a length of 880 nm, the volume fraction that the virus-cylinder occupies in a sphere with radius $2a = 8$ nm is (see Figure 2-17):

$$f_{complex} = \frac{V_{virus}}{V_{sphere}} \approx \frac{\pi r_{virus}^2 (4a)}{\frac{4}{3}\pi(2a)^3} = \frac{\pi(3.5\text{nm})^2(4 \cdot 4\text{nm})}{\frac{4}{3}\pi(2 \cdot 4\text{nm})^3} = 0.287 \tag{2.46}$$

By plugging $f_{complex}$ for $f$, the estimated dielectric function for pure phage obtained from Equation 2.44 for $\varepsilon_{pp}$, and the dielectric constant of water, $\varepsilon_{water} = 1.777$, for $\varepsilon_m$ into the Bruggeman effective medium equation provided in Equation 2.43, the effective dielectric function for the bacteriophage-water complexes can be found by numerically solving for $\varepsilon_{eff}$. The resulting complex effective index of a bacteriophage complex in water as perceived by a gold nanoparticle is presented in Figure 2-17.

The extinction spectra of spherical nanoparticles can be calculated using Mie theory, which provides an exact solution for the electromagnetic field of an isolated, homogeneous sphere interacting with an incident plane wave. Since the AuNPs used in this study are significantly smaller than the wavelength of light, only the dipole mode contributes to the extinction cross-section and higher order terms can be neglected. Therefore, the simplified form for the extinction cross-section, $C_{ext}$, of gold nanoparticles presented in Equation 2.42 can be used to predict the absorption spectrum of different AuNP systems. The predicted extinction spectra for AuNPs suspended in air, suspended in water, complexed onto a bacteriophage in aqueous solution, dispersed in a 59% porous dried bacteriophage film, and dispersed in a 41% porous

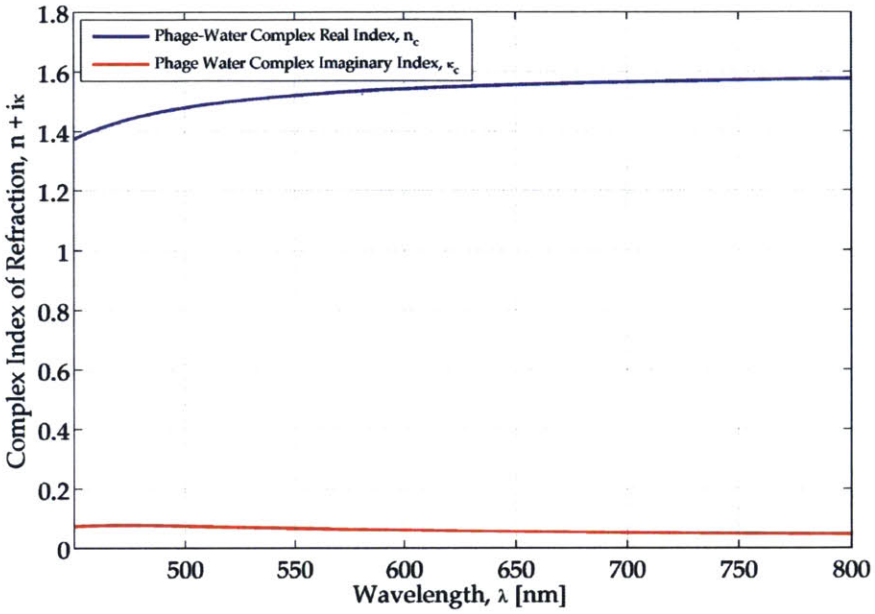


Figure 2-18: Real (blue) and imaginary (red) components of the effective index of refraction calculated for bacteriophage-water complexes with a bacteriophage fill-fraction of $f_{complex} = 0.287$, as predicted by Bruggeman effective medium theory.

anatase titania film are presented in Figure 2-19. As the effective dielectric constant of the medium surrounding the AuNP is increased, the location of the extinction peak is expected to red-shift, which matches the trend observed in Figure 2-19.

It is well known that the formation of AuNP aggregates drastically changes the observed absorption spectra because higher order modes arise with resonance at lower energies, which collectively act to generate a broadened and red-shifted absorption peak. [51] As shown in Table 2.2 and Figure 2-20, the predicted peak positions are in excellent agreement with experimental observations and additional peaks or shoulders are not observed in any of the absorption measurements. Together these two observations indicate that aggregates do not occur in significant enough abundance to be detected in the samples.

In contrast, when AuNPs are dropcast onto the bacteriophage film after it has been formed, they tend to fill the pores and form larger aggregates because the citrate capping agent loses its negative charge once the solvent is evaporated and an attractive van der Waals force causes neighboring nanoparticles to cluster. As shown by the red

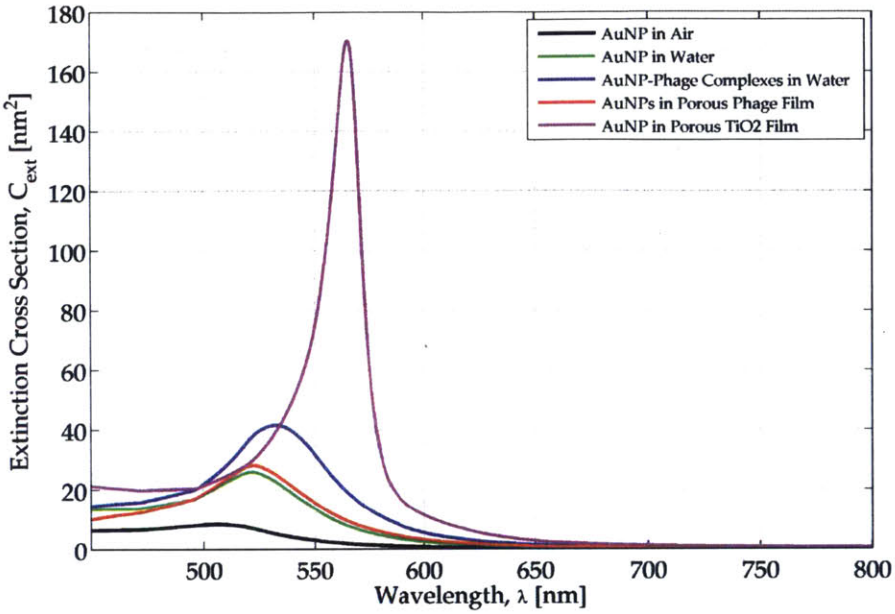


Figure 2-19: Extinction spectra predicted by Mie theory for AuNPs in different dielectric media: air, water, complexed onto bacteriophage in aqueous solution, a 59% porous dried bacteriophage film, and a 41% porous anatase titania film.

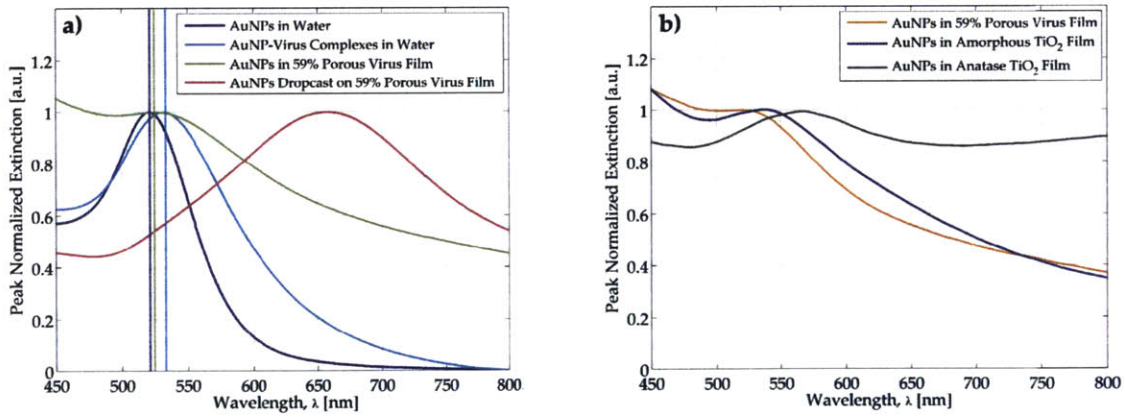


Figure 2-20: a) Comparison of optical properties of AuNPs under different conditions: freely suspended in water, complexed to bacteriophages in solution, and incorporated into 59% porous dried bacteriophage films during LbL , or dropcast onto a film post-assembly. The theoretical prediction for each peak is shown with a dotted vertical line corresponding to the color of the experimental data. b) Measured extinction spectra of AuNPs embedded in organic virus-based film and amorphous and crystalline nanoporous titania films.

Table 2.2: Predicted and measured extinction peak positions, $\lambda_{LSPR}$, for 8 nm gold nanoparticles in different media. [49]

| Sample | Measured $\lambda_{LSPR}$ (nm) | Predicted $\lambda_{LSPR}$ (nm) |
|---|---|---|
| AuNPs in Water | 521.5 | 521.5 |
| AuNP-Virus Complexes in Water | 533.5 | 533.5 |
| AuNPs in 59% Porous Virus Film | 525.0 | 523.5 |

curve in Figure 2-20, the measured absorption peak of such films is significantly broadened and red-shifted from the LbL film peak, because, as opposed to isolated sub-wavelength AuNPs that only support the dipole resonance mode, AuNP clusters are able to support multiple higher-order resonance modes. The effect is the same as that observed when citrate-capped gold nanoparticles lose stability in the presence of salt and ethanol [52] or are aggregated via ligand exchange [53].

### 2.4.4 Optical Sensing of Film Porosity

The extinction peak location of AuNPs dispersed in a nanoporous phage or anatase titania of arbitrate porosity was determined using the methods previously described. That is, the complex effective dielectric function was first solved using Equation 2.43 and those values were entered into Equation 2.42 to calculate the extinction spectra of the AuNP system. Figure 2-21 shows the calculated extinction peak location for nanoporous phage and anatase films (solid lines) as a function of porosity, $p = 1 - f$. The extinction peak position curves decrease monotonically with increasing porosity, which is expected because as the volume fraction of air increases relative to phage or titania, the effective dielectric function is lowered and the resonance wavelength of AuNPs dispersed in the media is expected to blue-shift. This figure also shows the measured absorption peak position for a porous phage film and a porous anatase titania film (dotted lines). Where the dotted and solid lines intersect is the graphical solution for the porosity of the nanoporous virus-based films as determined by the LSPR wavelength of the AuNPs dispersed in each film. Hence the AuNP probes indicate a film porosity of 55%, which is in good agreement of the microbalance mea-

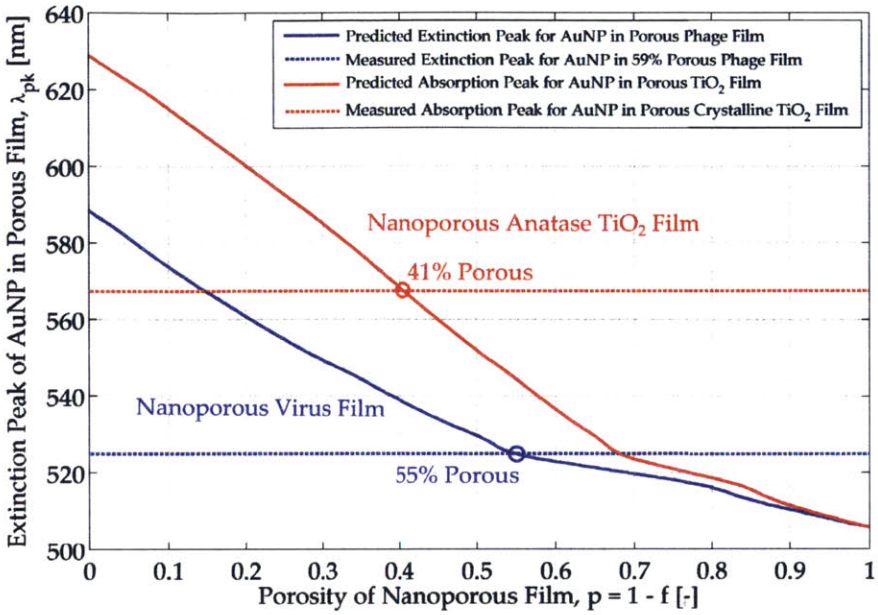


Figure 2-21: Real (blue) and imaginary (red) components of the index of refraction for the 59% porous bacteriophage films (dotted lines) as determined through ellipsometry measurements and the estimated function for pure bacteriophage films (i.e. 0% porous films, solid lines) as predicted by Bruggeman effective medium theory.

surement of 59%. Likewise, the AuNP probes suggest that the nanoporous anatase titania films are 41% porous. This result is very useful because it is difficult to measure the porosity otherwise, since the quartz crystals used for microbalance measurements would not survive the annealing conditions to convert virus-films that were minearlized with amorphous titania into a wholly inorganic nanocrystalline nanowire mesh.

## 2.5 Conclusion

By laying the theoretical groundwork for the optical properties of metals and the interaction of sub-wavelength metal nanospheres with incident light, the phenomenon of localized surface plasmon resonance has been explored from both mathematical and conceptual perspectives. This foundation has been used to provide some physical intuition that is able to explain the optical response of more complicated particle ge-

ometries such as nanorods and triangular nanoplates, where analytical solutions are much more challenging to develop. At the nanoscale, plasmon resonance produces a very strong electromagnetic response in the near-field directly surrounding the particle, which provides a mechanism through which light can be concentrated at the nanoscale. The effects of plasmon resonance can also be observed at the macroscale as a peak in the particle's extinction spectra, which is shown to be dependent on the refractive index of the surroundings as well as the dielectric function of the metal particle itself. As a result, the wavelength at which plasmon resonance is excited is sensitive to the refractive index of the particle's environment, which we leveraged to derive some information about the properties of nanoscale systems. Specifically, both gold and silver nanoparticles experience slight, yet measurable red-shifts in their extinction peak positions in the event of binding to the M13 bacteriophage in solution. Such a shift can be used to verify binding events to biomolecules without the need of continual evaluation with electron or atomic force microscopy. Likewise, by matching the measured extinction peak locations with predictions made using effective medium theory and Mie scattering theory, the porosity of nanoporous virus and virus-templated titania films was determined in a simple, but innovative manner. This concept will be used once more in Chapter 3 to allow the refractive index to be quantified for shell materials that coat gold nanoparticles. Furthermore, the physical intuition developed here for plasmonic particles will be valuable for understanding why light-harvesting is enhanced in the experimental and simulated solar cells presented in Chapter 4.

# Chapter 3

# Mediated Growth of Zincous Shells on Gold Nanoparticles by Free-Base Amino Acids

The preceding chapter presented a theoretical framework for localized surface plasmon resonance in noble metal particles and introduced how the M13 bacteriophage can be engineered to express capsid proteins capable of assembling and organizing them into photoactive nanostructures. This chapter aims to further study metal-biomolecule interactions by considering what is arguably the simplest two-component system of this type: metal nanoparticles and free-base amino acids. Here we present a powerful synthesis strategy that screens through several candidate amino acids to identify those capable of mediating the growth of stably suspended core-shell particles in aqueous solutions. From this effort, histidine was identified as a biomolecule that directs the formation of amorphous zinc oxide shells on gold nanoparticles with remarkable precision and quality in an elegant and simple manner. Although no solar cells are fabricated in this chapter, these nanoparticles are suitable for enhancing the performance of solution-processed solar cells through localized surface plasmon resonance.

## 3.1 Motivation

Due to the phenomenon of localized surface plasmon resonance (LSPR), noble metal nanoparticles demonstrate unique optical and electronic properties that are useful for biological and energy applications. They are commonly employed as optical dark-field imaging agents [42, 43] and nanoscale sensors [45, 54] due to their large extinction cross-sections and the high sensitivity of the extinction peak to the refractive index of the surrounding environment. Likewise, their ability to concentrate light and heat in the near-field is often utilized to improve the light-harvesting ability of solar energy technologies and serve as agents for triggered drug delivery [44, 55, 56] or photothermal therapy [42, 57]. However, the practical implementation of noble metal nanoparticles in such applications generally requires that the metal surface be coated with a dielectric shell. For instance, metal oxides such as silica improve the stability and biocompatibility of metal nanoparticles, [58] can prevent photoluminescence quenching by separating fluorophores from the metal surface, [54, 58] and are functionalizable with silane linkers. [59] Likewise, the performance of solution-processed dye-sensitized, [60–62] quantum dot, [63] polymer, [64] and perovskite [65] solar cells has been enhanced by incorporating into the active layers metal nanoparticles with thin dielectric shells, which prevent charge trapping and exciton quenching from occurring at the bare metal surface. [66] This role requires that the shell be as thin as possible, yet continuous, to maximize field-enhancement in the near-field and prevent photocurrent loss. Similarly, metal-semiconductor core-shell particles have also been used to enhance performance in many different types of catalytic systems. [67–69] Although many shell materials have been synthesized on gold nanoparticles (AuNPs) including $SiO_2$ [70–75], $TiO_2$ [61], $MnO_2$ [76], $Cu_2O$ [77–79], $Fe_2O_3$ [80], ZnO [81, 82], CdS [63, 83], CdSe [83], ZnS [83, 84], and PbS [83] it is generally difficult to find procedures that are simple, reliable, and provide precise control over the shell geometry. The most common shell materials, amorphous silica and titania, are synthesized in ethanolic solutions, which tend to induce particle agglomeration. [73] Although procedures have been developed to stabilize the particles by priming the gold surface

with aminopropyltrimethoxysilane [70] or polyvinylpyrrolidone [75], an excess of such molecules will nucleate free particles in solution, while a deficiency will allow some degree of particle aggregation to occur during shell growth. Cuprous oxide can be easily grown on AuNPs in aqueous solution, however the resultant polycrystalline shells tend to be rough and cannot form continuous shells thinner than ~10 nm. [78] Conversely, non-epitaxial growth through solid-state cation exchange provides a means to form metal chalcogenide shells of precise thickness on AuNPs, but the procedure is a multi-step process that requires exchanging particles between organic and aqueous solvents. [83] In contrast to these methods, we present an aqueous, one-step process that uses free-base amino acids to mediate the growth of continuous and uniform shells of either amorphous zinc oxide (a-ZnO) or polycrystalline zinc sulfide (c-ZnS) on AuNPs. When L-histidine is used, the resulting core-shell colloids are monodisperse, unaggregated, directly functionalizable with peptides, and can be tuned to have shell thicknesses between 2 and 25 nm, thereby meeting the needs of plasmonic core-shells for many biological and energy applications. Our approach is inspired by the ability of nature to:

1. Fold proteins at the active sites of enzymes such as carbonic anhydrases by coordinating with transition metal ions.

2. Use proteins to direct the assembly of inorganic materials such as calcium carbonate in seashells and calcium phosphate in bones.

Such *in vivo* interactions between biological and inorganic materials arise in part from the inherent functionality of amino acids, which we aim to leverage for the *in vitro* synthesis of core-shell particles. In an analogous nature to protein-directed inorganic growth, successfully synthesizing shells on individual nanoparticles requires finding capping agents capable of:

1. Stabilizing the particles by coordinating with both the core and shell materials.

2. Mediating the deposition of shell material throughout the growth process.

As a class of compact molecules, free-base amino acids meet these general requirements by:

1. Naturally displaying a wide-array of functional groups, some of which might have affinity for both the core and shell materials.

2. Displaying a carboxylic acid on the end opposite the functional group that can be deprotonated to provide the required negative charge for stabilizing the nanoparticles via electrostatic repulsion.

3. Potentially retaining their ability to promote the growth of inorganic materials.

Zincous materials were targeted for shell growth in this study because several amino acids have been previously identified as possessing affinity for both zinc chalcogenides and gold. [85] Additionally, zinc sulfide has been successfully nucleated and grown on biomolecules such as the M13 bacteriophage in aqueous conditions at room temperature. [86] By screening over a set of 13 candidates, four free-base amino-acids were identified as capable of stabilizing and mediating the growth of zincous shells on gold nanoparticles. Of the four, three mediated the growth of amorphous zinc oxide shells (Au@a-ZnO) and one mediated the growth of polycrystalline zinc sulfide (Au@c-ZnS). Although the optical and material properties of all four of these amino-acid mediated core-shells were characterized, this chapter focuses mostly on Au@a-ZnO core-shell particles that were mediated by histidine as it is capable of growing colloids of remarkable quality.

## 3.2 Experimental Methods

### 3.2.1 Chemicals

DL-Alanine (ALA, 99%), L-Arginine (ARG, 98+%) L-Cysteine (CYS, 98+%), L-Glutamine (GLN, 98+%), L-Histidine (HIS), L-Phenylalanine (PHE, 99%), L-Proline (PRO, 99%), L-Tryptophan (TRP, 99%), L-Tyrosine (TYR, 99%), zinc chloride ($ZnCl_2$, anhydrous 98+%), and tetrachloroaurate(III) hydrate ($HAuCl_4 \cdot 3H_2O$) were

purchased from Alfa Aesar. L-Lysine (LYS, >98%), L-Methionine (MET, >98%), and L-Serine (SER, >99%) were purchased from Sigma-Aldrich. Sodium citrate dihydrate (ACS Grade, 99% min) and Glycine (GLY, Genar) were purchased from Mallinckrodt Chemicals. Ammonium hydroxide ($NH_4OH$ 30 wt% in $H_2O$) was purchased from VWR International, Inc. All water was deionized by an EMD Millipore Milli-Q system (18.2 MΩ).

### 3.2.2 Synthesis of AuNPs

The Turkevich method [87] is modified to produce 16 nm citrate-capped gold nanoparticles (~3e12 NPs/mL). In brief, a solution of $HAuCl_4 \cdot 3H_2O$ (20 mM, 6.2 mL) is combined with 188 mL of deionized water in a round-bottom flask and brought to a boil while stirring and refluxing. A solution of sodium citrate (34 mM, 12.5 mL) is quickly added under vigorous stirring and boiling was continued for another 20 minutes before the flask was cooled to room temperature. Within a minute after injection, the solution turns black and gradually ripens into a deep ruby color. The AuNP solution is used without further purification.

### 3.2.3 Synthesis of Zincous Shells on AuNPs

The total volume of the aqueous reaction solution is fixed at 20 mL. Before beginning, the threads of a clean 20 mL glass vial are wrapped with Teflon tape in order to better seal the vial during hydrothermal growth. In a typical reaction, following items are sequentially combined in the vial: citrate-capped AuNPs (2 mL of the prepared solution), an appropriate amount of deionized water (17.08 to 16.10 mL), an aqueous solution of freshly prepared free base amino-acid (100 mM, 0.75 mL), and $NH_4OH$ (30 wt% in water, 0.15 mL). An aqueous stock solution of 50 mM $ZnCl_2$ was freshly prepared and an aliquot (50 to 1000 $\mu$L) is added to the vial, which is then immediately capped and shaken. The cap is sealed with electrical tape and placed inside an oven at 80°C for 9 days in the dark without stirring. The as synthesized colloidal core-shell solutions are purified by centrifuging the particles down at 15,000

rcf for 5 minutes, discarding as much of the supernatant as possible without disturbing the particles, resuspending the pellet in DI water, and repeating the cycle. Purified particle solutions were used for the imaging, materials characterization, and optical measurements.

### 3.2.4 Characterization Methods

The powder X-ray diffraction (XRD) patterns were recorded using a Panalytical X'Pert Pro X-ray diffractometer (Cu K$\alpha$ radiation, $\lambda$ = 0.154056 nm, operated at 45 kV 40 mA), with a continuous $2\theta$ scan from 20° to 80° at step size 0.0169° . The optical extinction measurements were performed using a Beckman Coulter DU800 UV-vis spectrophotometer with a step size of 0.2 nm. Transmission electron microscopy (TEM) was performed using a FEI Technai (G2 Spirit TWIN) with 120 kV accelerating voltage. Energy dispersive x-ray spectroscopy (EDS) was performed on the FEI Technai TEM with an EDAX octane silicon drift detector. X-ray photoelectron spectroscopy (XPS) was performed to characterize the surface composition of the samples using a PHI Versa-Probe II X-ray photoelectron spectrometer with a scanning monochromated Al source (1,486.6 eV; 50 W; spot size, 200 $\mu$m).

High-resolution transmission electron microscopy (HRTEM) was performed with a JEOL 2100 FEG microscope using the largest area size of parallel illumination beam and 100 $\mu$m diameter condenser aperture. The microscope was operated at 200 kV with magnifications between 20k and 800k. All images were recorded on a Gatan 2k×2k UltraScan CCD camera. Scanning tunneling electron microscopy (STEM) imaging was performed with a high-angle annular dark field (HAADF) detector with 0.5 nm probe size and 12 cm camera length.

## 3.3 Amino Acid Screening Study

The first task was to identify amino acids that can cap both the AuNP core and the zincous shell surfaces, as well as promote the growth of the shell over the course of the reaction. To do so, simple visual screening tests were performed to assess the ability

of several candidate free-base amino acids (Figure 3-1a) to stabilize the particles via electrostatic repulsion before and throughout the growth process.

### 3.3.1 Stabilizing Gold Colloids

An aqueous solution of each amino acid candidate was first added to a colloid of citrate-capped AuNPs (AuNPs-Cit) to provide it the opportunity to displace the citrate capping agent (Figure 3-1b), and ammonium hydroxide and zinc chloride were added thereafter. At this point, the ability of each amino acid to stabilize the AuNPs in the presence of salt is simply assessed by color. Solutions that retain the red color characteristic of well-dispersed AuNP colloids indicate that the amino acid has sufficient affinity to displace citrate from the gold surface and stabilize the particles even in the presence of the precursor ions. Conversely, solutions that turn purple indicate that the AuNPs are aggregating and the associated amino acid is unable to stabilize the particle surface. As is shown in Figure 3-2 and summarized in Table 3.1, only CYS, HIS, LYS, MET, TRP, and TYR sufficiently stabilize AuNPs in the presence of the shell precursor materials, whereas all others behaved like AuNPs-Cit in the absence of any amino acid and begin to flocculate prior to heating.

These observations are in excellent agreement with previously reported molecular dynamic computations that predicted the interaction strengths of amino acids with a bare (111) gold surface, which identified TYR, PHE, HIS, TRP, MET, CYS, ARG, and LYS as having the strongest affinities for the gold surface in decreasing order. [88] The strong interaction between aromatic amino acids and the gold surface has been attributed to $\pi$-electrons whereas the sulfur atoms are known to form covalent bonds with gold. [89] Unlike the computations, our assay does not identify ARG and PHE as capable of stabilizing the gold colloid under the synthesis conditions. Although ARG has been used to stabilize [73] and even reduce [90] gold nanoparticles, it is speculated that the ionic strength of our solution is too high for successful stabilization to occur during ligand exchange. While PHE is indeed aromatic like HIS, TRP and TYR, it may have difficulty displacing the citrate capping agent on the AuNPs due to the hydrophobic nature of the benzyl side chain. Hence PHE might be unable to reach

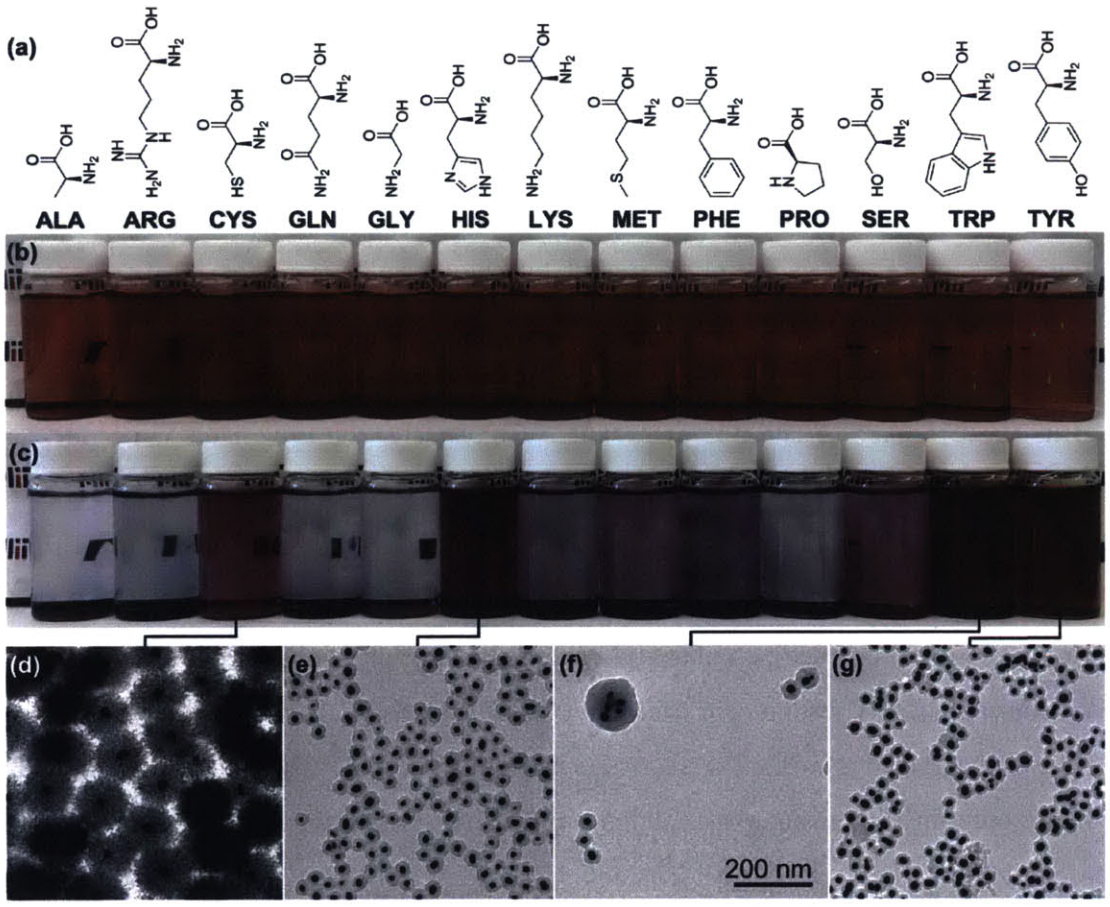


Figure 3-1: Visual screening of reaction solutions identified four amino acids as capable of stabilizing and mediating the growth of zincous shells on AuNPs from a (a) candidate pool of 13 free-base amino acids. b) The initial solutions of AuNPs and amino acids prior to the addition of $ZnCl_2$ are visually identical. c) After heating the reaction volume at 80°C for 9 days, only CYS, HIS, TRP, and TYR yields stable colloidal solutions, whereas significant particle flocculation occurs with the other candidates. TEM images of the core-shell particles generated by d) CYS, e) HIS, f) TRP, and g) TYR mediation reveal the presence of a shell material coating the AuNPs in each case.

the gold surface, whereas the respective imidazole, indole, and phenol groups of HIS, TRP, and TYR are sufficiently polar to do so.

### 3.3.2 Stabilizing and Mediating Growth of Core-Shells

The ability of each amino acid to mediate the growth of a shell and stabilize the shell material was assessed by visual examination after sealing the reaction solution in a vial and heating it at 80°C for over a week. Stabilization of the particles during the shell growth reaction requires that the excess amino acid molecules cap the surface of the freshly formed shell material, otherwise the particles will lose their surface charge and irreversibly aggregate with neighboring particles due to van der Waals attraction. The candidate solutions that remain suspended after several days at 80 °C are the sought amino acids capable of stabilizing both the gold and shell materials while mediating shell growth, or simply candidates that stabilize the AuNPs but prevent shell formation altogether. As is shown in Figure 3-1c and summarized in Table 3.1, stable solutions were obtained at the end of the screening test with cysteine (CYS), histidine (HIS), tryptophan (TRP), and tyrosine (TYR). As confirmed with transmission electron microscopy in Figures 3-1d-g and 3-3b-e, each of these molecules does indeed mediate the growth of a zincous shell around the AuNPs, however those synthesized from HIS and CYS are remarkably monodisperse and unaggregated.

The identification of CYS and HIS from the screening study is not surprising as their respective thiol and imidazole functional groups are known to interact strongly with both gold and zincous materials. Both free-base histidine [91] and cysteine [92] have been used to cap quantum dots coated with a ZnS shell and a similar procedure has been reported to form Au-ZnS nanocomposites using cysteine as a sulfur source. [93] Our findings are consistent with previous yeast display studies, which demonstrated that CYS, HIS, and TRP each have a strong affinity for Au, ZnS, and ZnSe. [85] Similarly, a previous peptide display study with *e. coli* identified ARG, TRP, and GLY as residues that enriched binder proteins for ZnO. [94] Our results are able to confirm the affinity of TRP for ZnO but are unable to do so for ARG and GLY since neither molecule was able to stabilize the AuNPs in the reaction

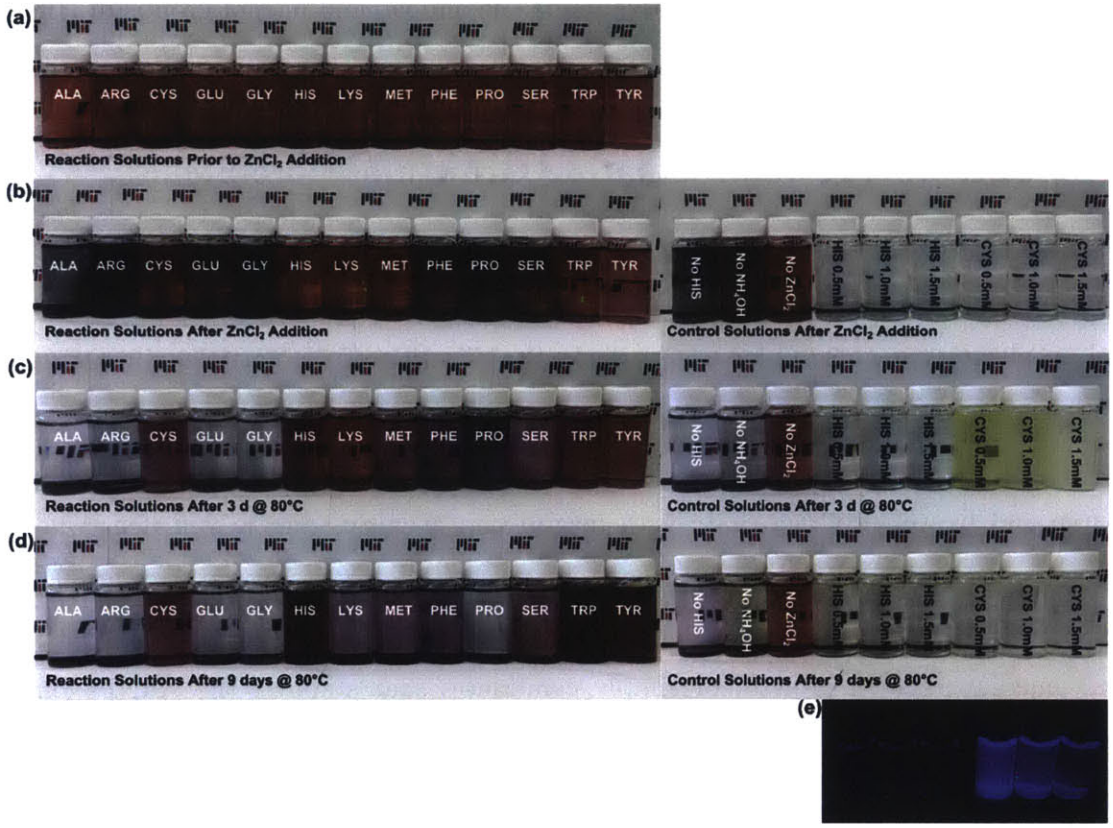


Figure 3-2: Visual screening tests identify amino acids capable of stabilizing the particles throughout the shell growth process. Photographs of reaction (left) and control (right) solutions for the mediated growth of zincous shells on gold nanoparticles (AuNPs) by 13 different candidate amino acids (a) before adding $ZnCl_2$, (b) several minutes after adding $ZnCl_2$, (c) after 3 days at 80°C, and (d) after 9 days at 80°C. The six control solutions on the right did not contain AuNPs. The concentration of $ZnCl_2$ is 0.5 mM unless otherwise indicated. (e) The control solutions without AuNPs are fluorescent upon excitation with an ultraviolet lamp.

solution prior to shell growth.

## 3.4 Materials Characterization of Core-Shells

### 3.4.1 Determination of Shell Materials

As is shown in the TEM images of Figure 3-3b-c, two very different types of shells can be synthesized with the same process depending upon whether HIS or CYS is used in the reaction. In each case, individual and monodisperse core-shell nanoparticles are

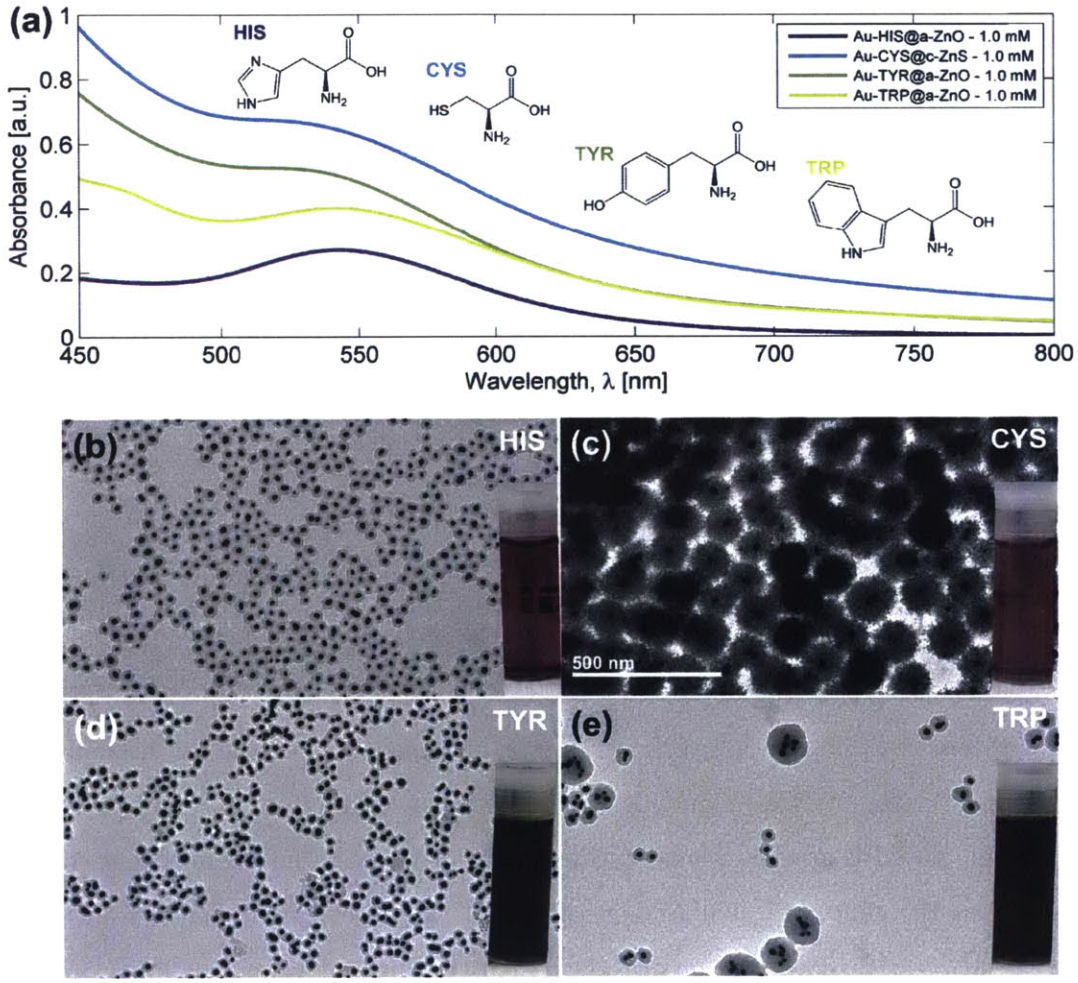


Figure 3-3: Optical and morphological characterization of zincous shells mediated by each of the amino acids identified from the screening study: histidine (HIS), cysteine (CYS), tyrosine (TYR), and tryptophan (TRP). (a) Measured extinction spectra of core-shell solutions synthesized with 1.0 mM $ZnCl_2$. (b-e) Representative TEM images of each core-shell type and an image of the unpurified reaction solutions.

Table 3.1: Results of stability screening test for growing zincous shells on AuNPs with candidate amino acids

| | ALA | ARG | CYS | GLN | GLY | HIS | LYS | MET | PHE | PRO | SER | TRP | TYR |
|---|---|---|---|---|---|---|---|---|---|---|---|---|---|
| Colloid Stability Prior to Heating | − | − | + | − | − | + | + | + | − | − | − | + | + |
| Colloid Stability after 3 h at 80°C | − | − | + | − | − | + | + | + | − | − | − | + | + |
| Colloid Stability after 9 d at 80°C | − | − | + | − | − | + | − | − | − | − | − | + | + |

Table 3.2: Results of stability screening test for growing zincous shells in controls

| | No $ZnCl_2$ | No HIS | No $NH_4OH$ |
|---|---|---|---|
| Colloid Stability Prior to Heating | + | − | − |
| Colloid Stability after 3 h at 80°C | + | − | − |
| Colloid Stability after 9 d at 80°C | + | − | − |

clearly formed with only a single gold nanoparticle comprising the cores. The striking difference between the particles is the shell morphology; the HIS-mediated shells are smooth and uniform, whereas the CYS-mediated shells are rough and polycrystalline.

A series of characterization techniques were performed to identify each shell material. In the case of HIS-mediated shells, the x-ray diffraction (XRD) spectra of Figure 3-4a reveal that even for thick shells, the only crystalline component of the core-shells is the gold core. The high-resolution TEM (HRTEM) image presented in Figure 3-4d clearly shows the lattice of the AuNP core but no crystallinity in the shell, which directly confirms that the shell is indeed amorphous. Elemental analysis of the these core-shells through both energy dispersive x-ray spectroscopy (EDS) and x-ray photoelectron spectroscopy (XPS), respectively shown in Figure 3-4b and 3-4c, reveal the presence of Zn, O, and Au atoms in the samples, thereby confirming that the amorphous shells are indeed zincous. The binding energy of the O1s peak is closer to the reported value for ZnO rather than $Zn(OH)_2$. [95] This in concert with the fact that the hydrothermal growth of zinc oxide nanoparticles and nanorods commonly occurs under similar conditions indicate that the shell material is indeed amorphous

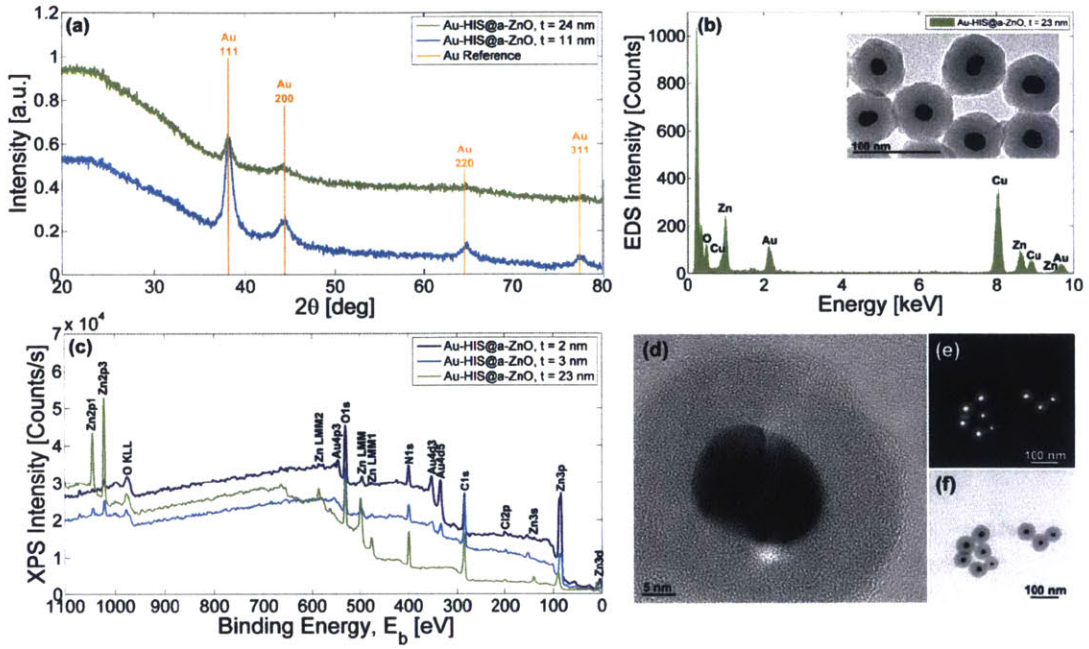


Figure 3-4: Materials characterization of histidine-mediated Au@a-ZnO core-shell particles. (a) XRD spectra of particles with shell thicknesses of 11 and 24 nm along with standard reference for Au. (b) EDS spectra obtained from the TEM sample shown in the inset of particles with 23 nm thick shells. (c) XPS spectra for samples with 2, 3, and 23 nm thick shells. (d) High-resolution, (e) dark-field, and (f) bright-field TEM images of core-shell particles.

zinc oxide (a-ZnO). [96, 97] The XPS spectra for samples with very thin (~2 nm) and very thick shells (~24 nm) both indicate a nitrogen peak consistent with amines, which is evidence that histidine molecules cap the shell surface. The EDS signal for Cu arises from the TEM grid and not the core-shell sample.

Conversely, the XRD spectrum plotted in Figure 3-5a and HRTEM images of the CYS-mediated shells in Figure 3-5c-d clearly show that both the gold core and shell material are polycrystalline. The measured lattice spacings of 0.31 nm in the HRTEM micrographs are consistent with the (002) planes of wurtzite ZnS, which is confirmed by the good agreement of the XRD spectra peaks with its reference spectra. The XPS survey scans shown in Figure 3-5b identify the presence of Zn, S, and Au atoms in the samples. However, the spectrum also identifies the presence of oxygen, which could either result from oxygen atoms in the carboxyl group of the capping cysteine molecules or from impurities in the ZnS crystallites. The incorporation of oxygen into

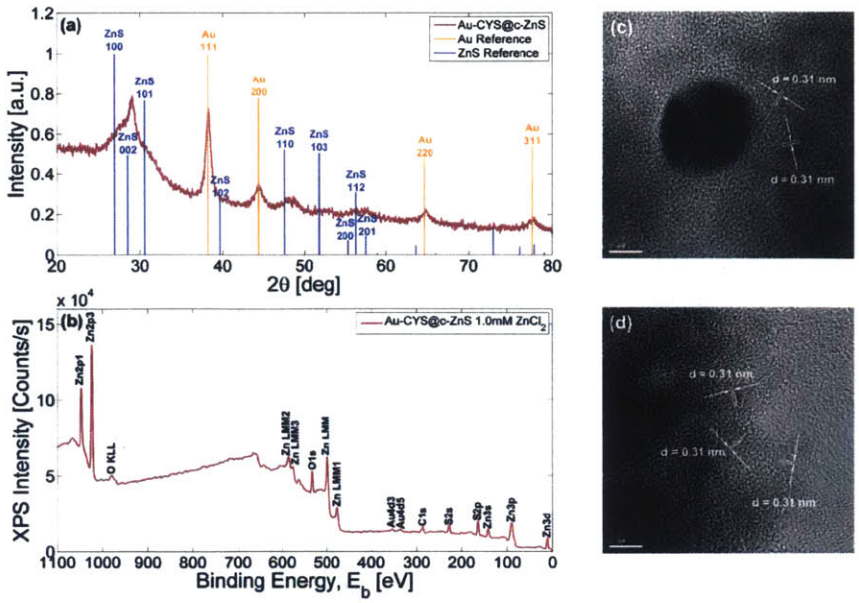


Figure 3-5: Materials characterization of cysteine-mediated Au@c-ZnS core-shells. (a) XRD spectra and standard references for Au and hexagonal ZnS (wurtzite). (b) XPS spectra. HRTEM images of the ZnS shell material (c) in the vicinity of the AuNP core and (d) at the particle surface.

the ZnS lattice could explain the observed shift of the (110) and (103) XRD peaks from the reference for pure wurtzite ZnS.

Both the XRD spectrum and HRTEM images presented for TRP-mediated core-shells in Figure 3-6a,e-f clearly reveal that the shell is amorphous. Similarly, the corresponding XPS spectrum in Figure 3-6b is nearly identical to that obtained for HIS-mediated shells where Zn, O, and N are all present near the surface of the shells. The presence of nitrogen is once again attributed to the TRP molecules that are likely capping the surface of the shells.

The HRTEM images of TYR-mediated core-shells presented in Figure 3-6c-d clearly show that the shells are amorphous in nature, however the XRD spectrum shows peaks that are consistent with crystalline hexagonal ZnO. Although the shell material is indeed amorphous, it is postulated that free-crystalline nanoparticles are nucleated elsewhere in the solution. The XPS spectrum presented in Figure 3-6b is also nearly identical to those measured for both TRP- and HIS-mediated a-ZnO shells.

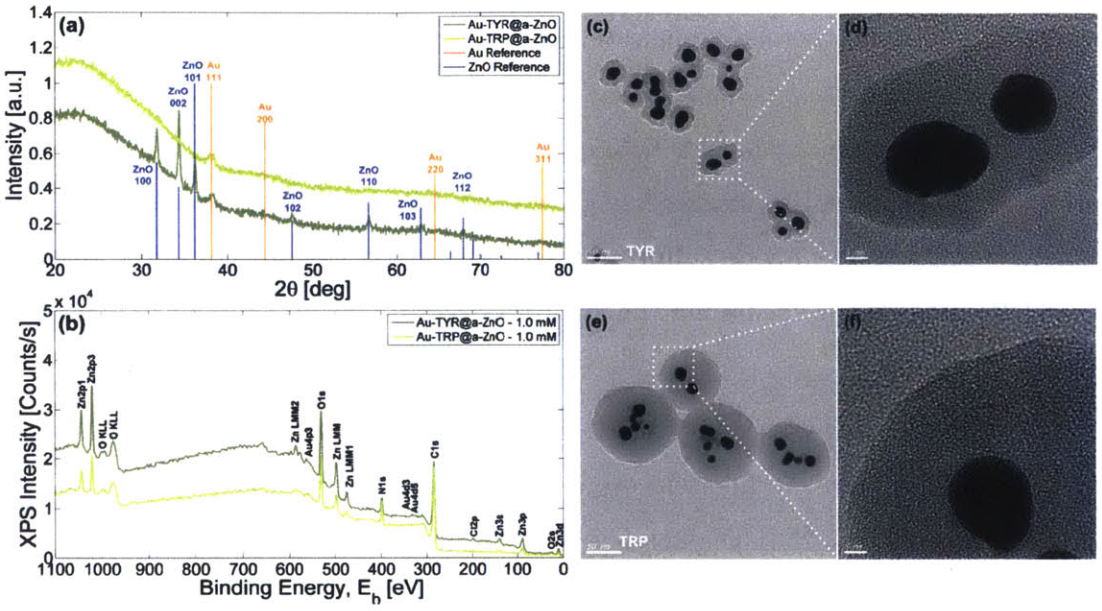


Figure 3-6: Materials characterization of Au@a-ZnO core-shells mediated by tyrosine and tryptophan. (a) XRD spectra and standard references for Au and hexagonal ZnO. (b) XPS spectra. (c,e) TEM images of TYR- and TRP-mediated core-shells for 1.0 mM ZnCl2 reaction conditions and (d,f) HRTEM images of the indicated regions.

### 3.4.2 Proposed Synthesis Pathway

A proposed synthesis pathway for the formation of zincous shells on AuNPs via amino-acid mediation is illustrated in Figure 3-7. First, the functional group on the amino acid displaces the citrate capping agent on the AuNP and binds to the gold surface. Adding ammonia raises the pH and ensures the particle is electrostatically stabilized by deprotonating the outer carboxylic acid group. Upon addition of aqueous $ZnCl_2$, $Zn^{2+}$ ions are coordinated by ammonium ions to form tetramminezinc(II) complexes $[Zn(NH_3)_4]^{2+}$:

$$Zn^{2+}_{(aq)} + 4\ NH_{3(aq)} \rightarrow [Zn(NH_3)_4]^{2+}_{(aq)} \tag{3.1}$$

This is evidenced by the initial formation of a white precipitate upon dispensing $ZnCl_2$ into the reaction solution, which quickly redissolves upon mixing. The positively charged complexes are attracted to the negatively charged AuNPs, however the bulky size of the complex prevents them from packing densely enough around the nanoparticles to screen out their surface charge. Upon heating, the complexes

decompose and hydrothermally nucleate a-ZnO or c-ZnS on the AuNPs. When the new material is formed, it is immediately capped by the excess amino acid molecules in solution. Thus, the amino acids help mediate the growth process by allowing new material to be deposited while stabilizing the particles in solution. Whereas cysteine clearly decomposes to provide sulfur atoms for the formation of c-ZnS, any role of HIS, TRP, and TYR in mediating the growth of a-ZnO beyond capping the surface cannot be inferred.

This proposed pathway is supported by control experiments where each of the ingredients in the reaction fluid was systematically omitted; the results of these are summarized in Table 3.2. In the absence of histidine, AuNPs-Cit flocculate immediately upon the addition of $ZnCl_2$, even in the presence of ammonia, as shown by the purple color of the solution in Figure 3-2. The ionic strength is too high for citrate ions to stabilize the surface of the AuNPs. The histidine-capped AuNPs (AuNPs-HIS) also flocculate immediately upon $ZnCl_2$ addition in the absence of ammonium hydroxide. This is likely because $Zn^{2+}$ ions are more compact than the $[Zn(NH_3)_4]^{2+}$ complexes and are able to pack densely enough around AuNPs-HIS to screen the charge on the surface. In the absence of $ZnCl_2$, the AuNPs remain stable and unchanged throughout the growth process, which indicates that histidine and cysteine remains strongly bound to the AuNP surface even at elevated temperatures. During the 9 days of heating at 80°C, the flocculated AuNPs-Cit nucleated the growth of ZnO nanorods (Figure 3-8), although no shell is formed around the particles. Likewise, in the absence of ammonia, AuNP-HIS formed chained aggregates with only a very thin shell observable on the surface (Figure 3-9). These findings reveal that both the amino acid and $NH_4OH$ are necessary to grow shells and preserve colloidal stability.

Finally, in the absence of AuNPs in the HIS-based reaction fluid, no free-particles form in the solution. Interestingly, this suggests that gold itself has a catalytic role in the formation of a-ZnO shells. In the absence of AuNPs in the CYS-based reaction fluid, a polydisperse population of very large c-ZnS particles is produced as shown by the TEM images in Figure 3-10. This demonstrates that free cysteine can nucleate particles in solution, however the fact that the particle size is controlled with AuNPs

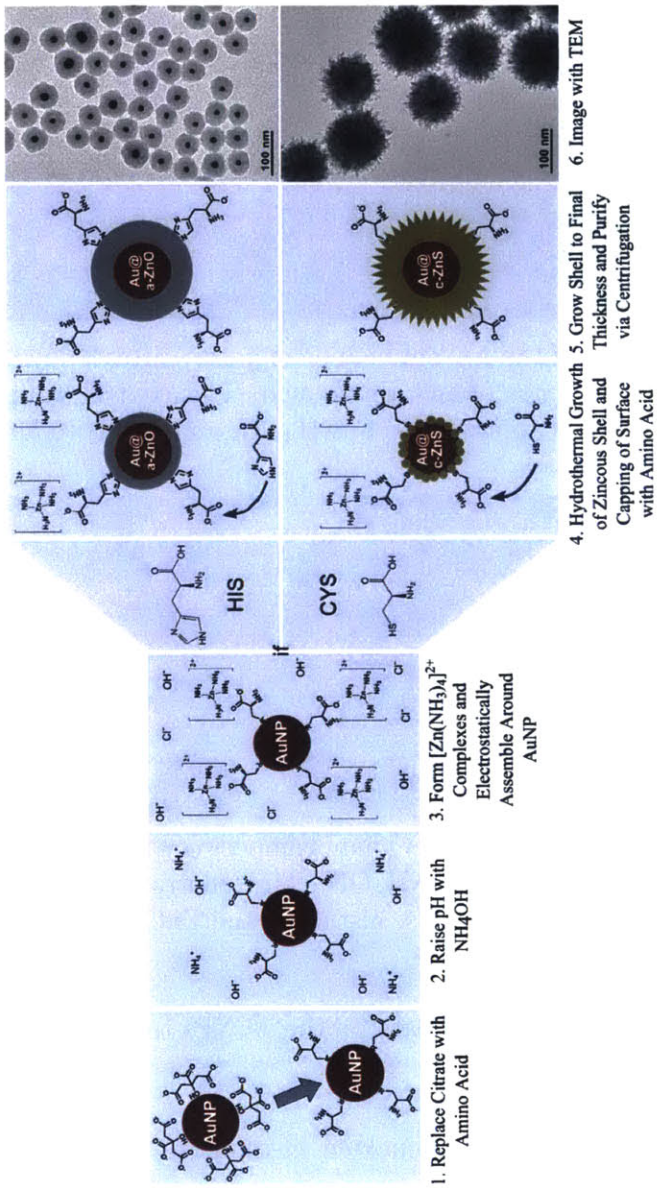


Figure 3-7: A synthetic pathway is proposed where amino acids mediate the hydrothermal growth of zincous shells on gold nanoparticles (AuNPs) in aqueous solution. First, the functional group on the amino acids has a stronger affinity for the gold surface and displaces the original citrate capping agent. The addition of $NH_4OH$ ensures the carboxylic acid groups on the amino acid are deprotonated and coordinates $Zn^{2+}$ into tetrammine complexes, which are electrostatically attracted to the negatively charged AuNPs. Upon heating at 80°C, the amino acids mediate the hydrothermal growth of the zincous shell material on the AuNP surface. The amino acids cap the shell surface and keep the core-shell particles electrostatically stabilized throughout the growth process. Histidine (HIS) promotes the growth of smooth amorphous ZnO shells, whereas cysteine (CYS) participates in the growth of rougher polycrystalline ZnS shells.

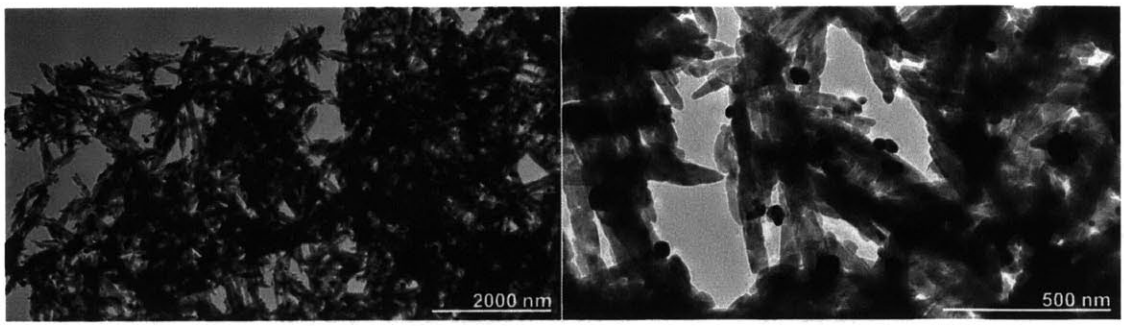


Figure 3-8: TEM images of the Au-ZnO nanocomposites after 9 days of hydrothermal growth at 80°C in the absence of any amino acid. This control sample was obtained by combining only citrate-capped AuNPs, $NH_4OH$, and $ZnCl_2$ (0.5mM).

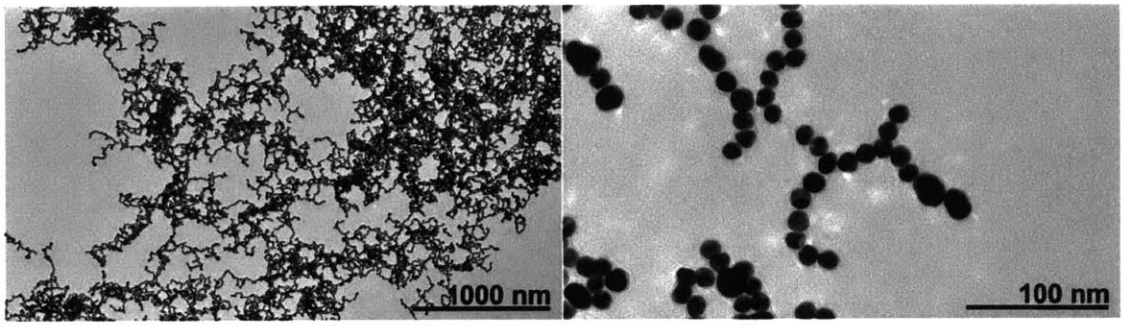


Figure 3-9: TEM images of the Au-ZnO nanocomposites after 9 days of hydrothermal growth at 80°C in the absence of $NH_4OH$. This control sample was obtained by combining only citrate-capped AuNPs, histidine, and $ZnCl_2$ (0.5mM).

suggests that ZnS would rather nucleate on the AuNPs to grow shells than generate free particles.

Although previous studies have reported methods to synthesize a-ZnO [81] and c-ZnS [84] shells on gold nanoparticles in aqueous solutions, our screening method provides a flexible approach through which core-shells comprised of different materials could be synthesized aside from the Au@a-ZnO and Au@c-ZnS particles presented. Furthermore, our approach has several advantages over these other methods. The previously reported method for generating a-ZnO shells relies on using cetyltrimethylammonium bromide (CTAB) as a capping agent for the core particle, hexamethylenetetramine (HMT) as a growth mediator and base for shell formation, and ascorbic acid as a complexing agent for $Zn^{2+}$. [81] This process constructs highly porous, loosely-formed shells that condense with aging and is capable of producing

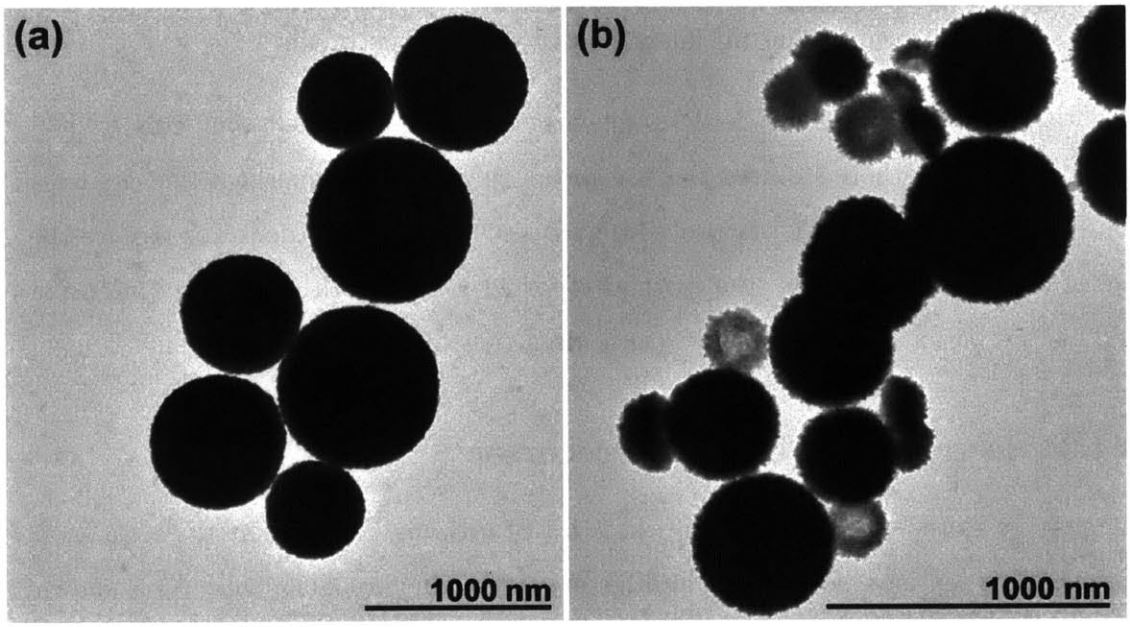


Figure 3-10: TEM images of control reaction for ZnS particles grown from free CYS molecules without AuNPs after 9 days at 80°C for initial $ZnCl_2$ concentrations of (a) 0.5 mM and (b) 1.0 mM.

free a-ZnO particles in the absence of AuNPs. In contrast, our method:

1. Uses less ingredients since the amino-acid serves the dual role of both capping agent and growth mediator while ammonia is both a base and a complexing agent.

2. Produces shells that are not porous but rather appear solid and continuous, although small voids may occasionally form. TEM imaging suggests that our shells are generally solid and continuous (Figure 3-4d-f), which likely results from the histidine gradually mediating the growth of the shells over several days rather than a few hours.

3. Minimizes the synthesis of free a-ZnO particles in solution, whereas the cooperative effect of CTAB, HMT, and ascorbic acid is capable of generating free particles in the absence of AuNPs.

4. Provides a means to create shells of controllable thickness, whereas it is unclear from the previous report whether the previously reported method is able to do

so with precision as no thickness control was demonstrated.

Likewise, cysteine has been used to generate similar c-ZnS shells on AuNPs. [84] However, this method requires the use of an autoclave to superheat the aqueous solution to 130°C, whereas our procedure proceeds at 80°C and does not require the use of an autoclave. Hence, the method reported here is both less energy-intensive and can be performed simply with sealed glass vials in a conventional oven.

### 3.4.3 Dependence on Zinc Precursor

It must be noted that the reaction kinetics of growing HIS-mediated Au@a-ZnO core-shells is sensitive to the type and history of the zinc precursor salt. As is shown in Figure 3-11, a-ZnO shells have been successfully synthesized on AuNPs from both $Zn(NO_3)_2 \cdot 6H_2O$ and several different lots of $ZnCl_2$ under the same reaction conditions, however in each case the resultant shell thickness was different. The chemistry of $ZnCl_2$ is notoriously complex as the salt is both hygroscopic and capable of forming several different hydration states and hydroxychloride ions in alkali solutions. [98] Hence, the reaction kinetics of the formation of a-ZnO appears to depend strongly on the exact history of each $ZnCl_2$ salt, with salts aged in air being capable of producing thicker shells in shorter amounts of time.

### 3.4.4 Shell Thickness Tuning

An advantage of the HIS-mediated growth process is that the thickness of the a-ZnO shells can be precisely tuned by adjusting the concentration of $ZnCl_2$ in the reaction solution. Figure 3-12b presents the average shell thickness for each reaction condition, as determined by processing TEM images, as well as an image of an individual representative core-shell particle. This series of TEM images in Figure 3-12a clearly demonstrates that uniform and continuous shells with thicknesses between 2 and 40 nm can be grown on individual AuNPs. The measured thickness for each $ZnCl_2$ concentration is compared against a predicted thickness, which assumes complete conversion of $ZnCl_2$ to a-ZnO shell material and the shell density is 4.6 $g/cm^3$

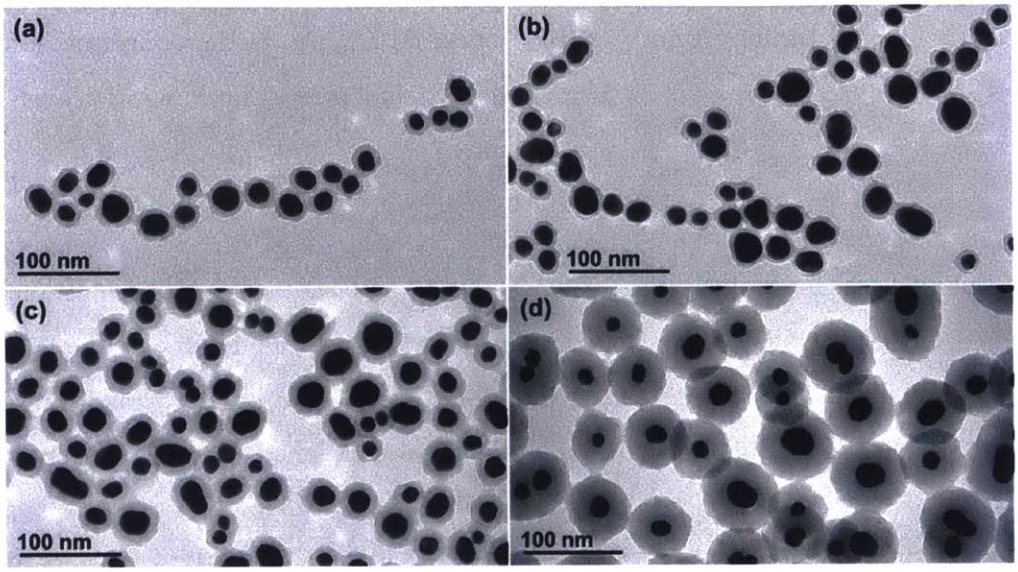


Figure 3-11: Effect of zinc salt and precursor condition on shell thickness. Histidine-mediated Au@a-ZnO core-shells grown after 9 days at 80°C from 2.0 mM $Zn^{2+}$ solutions using a) $Zn(NO_3)_2{\cdot}6H_2O$, b) 0.1M $ZnCl_2$ stock solution purchased from Sigma-Aldrich, c) new lot of anhydrous $ZnCl_2$ from Alfa Aesar, and d) lot of anhydrous $ZnCl_2$ from Alfa Aesar that was aged in air.

in accordance with experimental values from a-ZnO thin films. [99] The a-ZnO shell thicknesses were predicted by assuming that all of the $ZnCl_2$ was converted into ZnO over the course of the hydrothermal growth period. The total volume of ZnO expected from the complete conversion is:

$$V_{ZnO} = \frac{V_{rxn} \cdot C_{ZnCl_2} \cdot MW_{ZnO}}{\rho_{ZnO}} \eta_{conv} \tag{3.2}$$

where $V_{ZnO}$ is the total volume of ZnO in the solution in $cm^3$, $V_{rxn}$ is the reaction volume (0.02 L), $C_{ZnCl_2}$ is the concentration of $ZnCl_2$ in the reaction volume [M], $MW_{ZnO}$ is the molecular weight of ZnO (81.408 g/mol), $\rho_{ZnO}$ is the density of amorphous ZnO (assumed to be 4.6 $g/cm^3$), and $\eta_{conv}$ is the conversion efficiency, which represents the fraction of $ZnCl_2$ in the reaction volume that is converted to ZnO (for full conversion, $\eta_{conv} = 1$). The shell thickness, $t_{shell}$, can be estimated from:

$$t_{shell} = \left( \frac{3}{4\pi} \frac{V_{ZnO}}{V_{rxn}} \frac{1}{C_{AuNPs}} + R^3 \right)^{1/3} - R \tag{3.3}$$

where $R$ is the NP radius (8 nm = $8{\cdot}10^{-7}$ cm) and $C_{AuNPs}$ is the concentration of AuNPs in the reaction volume ($3{\cdot}10^{14}$ NPs/L). Combining Equations 3.2 and 3.3 provides:

$$t_{shell} = \left( \frac{3}{4\pi} \frac{MW_{ZnO}}{\rho_{ZnO}} \frac{c_{ZnCl_2}}{c_{AuNPs}} \eta_{conv} + R^3 \right)^{1/3} - R \tag{3.4}$$

where the shell thickness has units of cm. In the event that not all of the $ZnCl_2$ is consumed during the shell formation (i.e. $\eta_{conv} < 1$), then the density of the a-ZnO shell must be lower than the assumed value of 4.6 g/cm$^3$ in order to maintain the same profile plotted in Figure 3-12b. This can be seen by rearranging Equation 3.4:

$$\rho_{ZnO} = \eta_{conv} \frac{C_{ZnCl_2}}{C_{AuNPs}} MW_{ZnO} \left[ \frac{4}{3}\pi \left( (t_{shell} + R)^3 - R^3 \right) \right]^{-1} \tag{3.5}$$

This situation could arise if the amino acid molecules become trapped in the shell, which could result in a reduced shell density as well as a reduced index of refraction for the shell material.

The measured shell thicknesses are in good agreement with the predicted values for intermediate shell thicknesses but deviate at both high and low $ZnCl_2$ concentrations. Figure 3-13 reveal that for concentrations below 2.0 mM the core-shell particles are remarkably monodisperse with a single AuNP nearly always comprising the core. However for $ZnCl_2$ concentration above 2.0 mM, populations of core-shells emerge with multiple AuNPs in the core and hence the shells become thicker since the material is not distributed between individual AuNPs but rather across small AuNP aggregates. This observation suggests that 2.0 mM $ZnCl_2$ is the threshold for instability where at some point during the growth of the shells, the surface charge is sufficiently screened by the ions to destabilize a significant population of the individual particles and promote the formation of clusters. Both the population of multiple-core core-shells and the average number of AuNPs comprising the core increase with increasing $ZnCl_2$ concentration. The observation that the a-ZnO shell is thinner than expected at $ZnCl_2$ concentrations below 0.75 mM suggests that the zinc precursor was not fully consumed. A simple explanation is that concentration of $[Zn(NH_3)_4]^{2+}$ is simply too low to drive the reaction to completion through mass

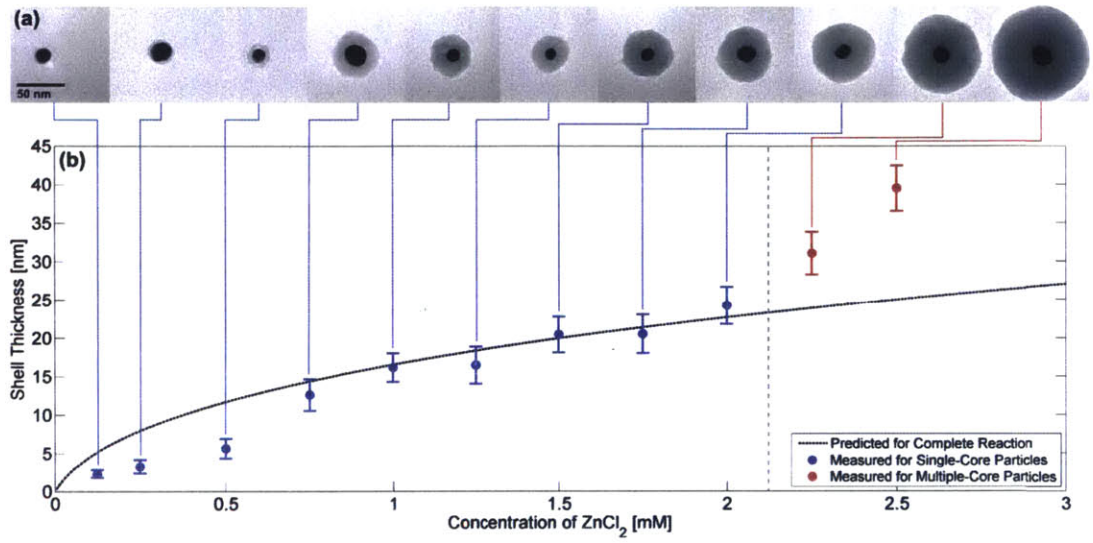


Figure 3-12: Synthesis conditions of histidine-mediated Au@a-ZnO core-shell particles. (a) Representative TEM images of individual core-shell particles and (b) the corresponding $ZnCl_2$ concentration required to synthesize them. The average shell thickness for each reaction condition (circles), as obtained by processing TEM images of each sample, is compared against the predicted shell thickness (dotted line) in the event of complete consumption of the $ZnCl_2$ reagent. The blue circles correspond to samples where the nearly all of the particles contain a single AuNP in the core, whereas the red circles indicate that a significant portion of the population has multiple AuNPs in the core. The error bars correspond to the standard deviation.

action, thereby leaving some unreacted complexes in equilibrium with the core-shells.

The appearance of the histidine reaction solutions before and after hydrothermal shell growth is shown in Figure 3-14b-d and the corresponding extinction spectra for each is shown in Figure 3-14a. Upon combining all of the ingredients together, each solution was identical in color and appearance, as is evident from Figure 3-14b. After 9 days of heating at 80°C in the sealed vials, the appearance changed with the solutions becoming increasingly violet (Figure 3-14c) and hazy (Figure 3-14d) with increasing $ZnCl_2$ concentration. As the shells increase in thickness, scattering becomes increasingly pronounced and the solutions appear increasingly translucent. The measured extinction spectra of each solution reflect this quantitatively by revealing amplitudes that increase with shell thickness. For solutions with $ZnCl_2$ concentrations below 2.0 mM the solution is dominated by single-core particles and the amount of absorp-

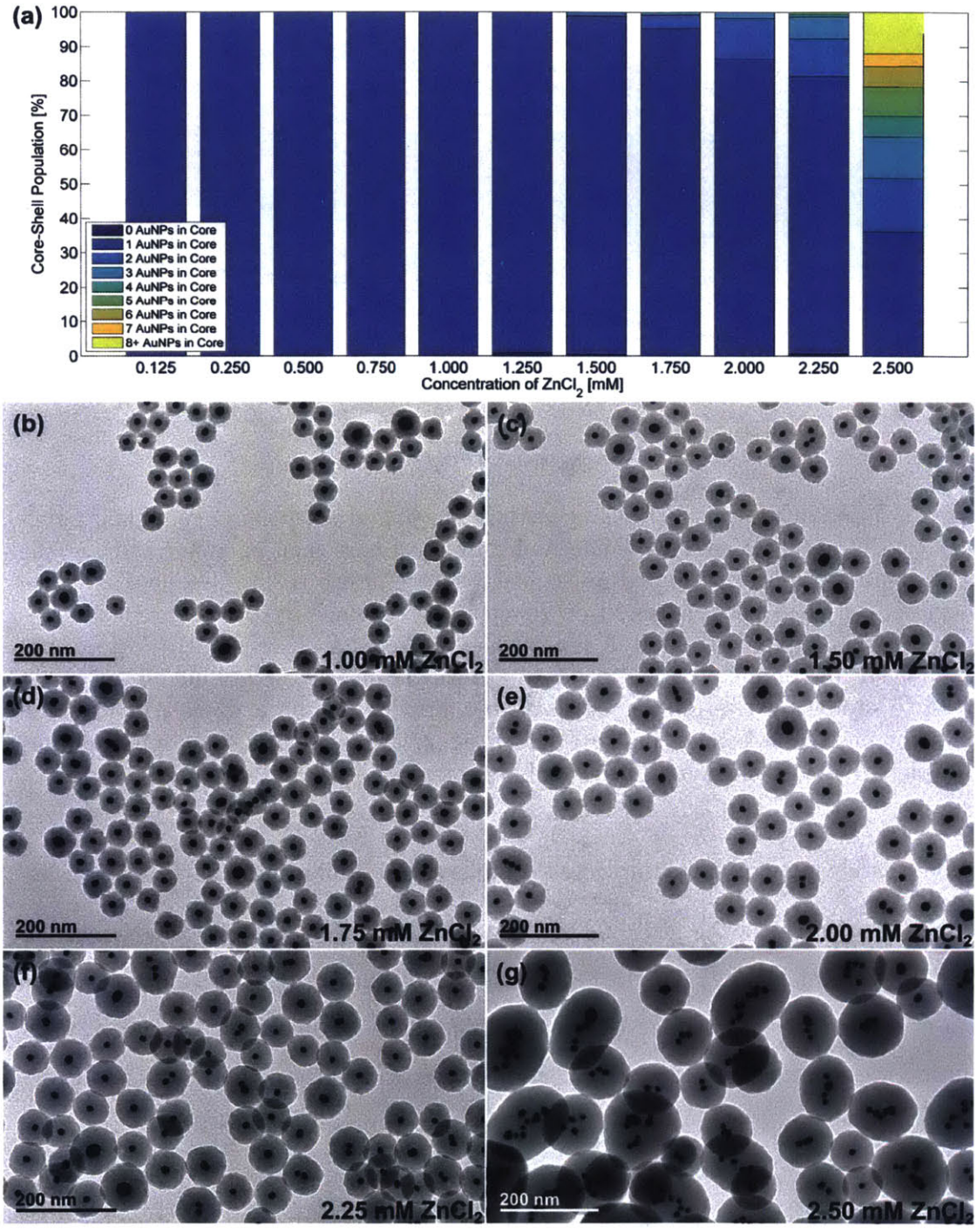


Figure 3-13: Influence of $ZnCl_2$ concentration on the number of AuNPs in the core of histidine-mediate Au@a-ZnO particles. (a) The occurrence of core-shells with different numbers of AuNPs in the core as a function of $ZnCl_2$ concentration, as determined by sampling over 100 particles from TEM images. (b-g) Representative TEM images of core-shell particles obtained from reaction solutions with $ZnCl_2$ concentrations between 1.0 and 2.5 mM.

tion in each case should be approximately equal. Hence, the incremental increase in amplitude is largely the result of an increase in scattering. The incremental increases become greater between samples with $ZnCl_2$ concentrations in excess of 2.0 mM, which is the result of multi-core particles having larger overall sizes and an even higher scattering efficiency.

## 3.5 Optical Characterization of Core-Shells

### 3.5.1 Optical Analysis and Calculation of Shell Complex Refractive Index

As discussed in Section 2.2.2, the peak observed in the extinction spectra of the Au@a-ZnO core-shells arises from the phenomenon of localized surface plasmon resonance and its position is very sensitive to the refractive indices of the media surround the AuNP core. As the shells grow in size, the fraction of the medium directly surrounding the AuNP core will become increasingly occupied by a-ZnO and the resonance frequency of the localized surface plasmons will shift, which is manifested by a change in the extinction peak position. According to Mie scattering theory, the extinction peak of a noble metal nanosphere is expected to continually red-shift as the refractive index of the surrounding dielectric environment increases. [36] As is shown in Figure 3-14, the position of the measured extinction peaks for the Au@a-ZnO core-shells indeed initially red-shift with increasing shell thickness. However, the peak reaches a maximum position of 541.7 nm and surprisingly begins to blue-shift with further increases in shell thickness. In order to explain this anomalous behavior, computations using generalized Mie theory were performed to predict the extinction spectra of the synthesized core-shell structures.

### 3.5.2 Calculation of Shell Complex Refractive Index

The sensitivity of the LSPR extinction peak to refractive index changes provides an interesting opportunity to use the gold core of the Au@a-ZnO core-shells as a probe

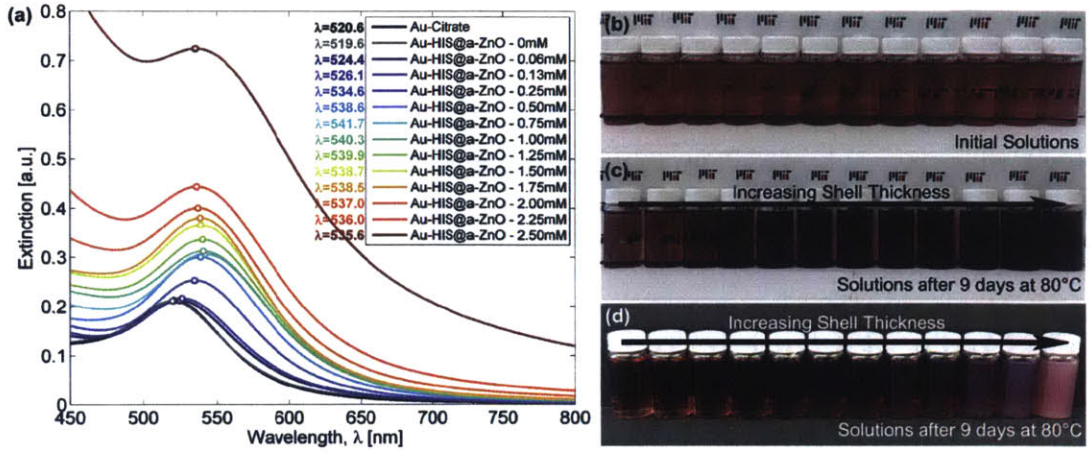


Figure 3-14: Optical properties of the histidine-mediated Au@a-ZnO core-shell particles. (a) Extinction spectra measured for the original citrate-capped AuNPs and purified solutions of core-shells from each of the specified reaction conditions. The position of the extinction peak for each curve is listed next to each legend entry and denote in each curve by an open circle. Photographs of the reaction solutions (b) before and (c-d) after heating at 80°C for 9 days.

to determine the refractive index of the amorphous ZnO shell material. This quantity can be extracted from the measured extinction spectra of core-shells with various shell thicknesses by comparing the measurements against a series of generalized Mie theory calculations performed for the corresponding geometries. The HIS-mediated Au@a-ZnO core-shells are excellent candidates for these calculations because the populations for $ZnCl_2$ concentrations below 2.0 mM are monodisperse, unaggregated, contain a single AuNP in the core, and have shells of uniform thickness. Hence, measured extinction spectra for these core-shell solutions are expected to find good agreement with the calculated spectra for idealized core-shell geometries.

Generalized Mie theory provides a solution to Maxwell's equations that describes how stratified spherical particles scatter light. [39] The extinction spectrum for each Au@a-ZnO core-shell embodiment was simulated using the Generalized Multiparticle Mie (GMM) method. GMM is a semi-analytical computation method based on Mie theory, [41] which provides the analytical solution for a single spherical scatterer by expanding the incident, scattered, and internal fields using vector spherical harmonics. The rigorous multiple scattering solution of Bruning and Lo [100] is used

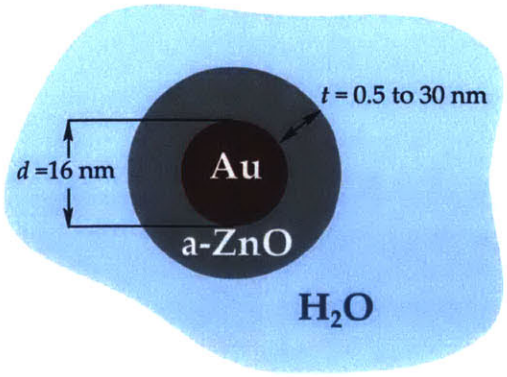


Figure 3-15: Geometry of core-shells for GMM calculations consists of a uniformly coated AuNP immersed in water.

to numerically extend the Mie theory for multiple, non-overlapping spherical boundaries. We use the open-source Fortran implementation of GMM by Xu *et al.*, [101] modified to run for a range of wavelengths ($\lambda$ = 350 to 1200 nm) rather than a single wavelength.

Calculations were specifically performed for individual gold spheres coated with a uniform shell thickness between 0.5 and 35 nm and surrounded by water (refractive index, $n$ = 1.333) as is shown in Figure 3-15. The diameter of the gold core was fixed at 16 nm in accordance with the measured core diameter of 15.9 $\pm$ 4.0 nm, as determined by image processing over 200 individual core-shells observed with TEM, and the dielectric function used for gold was sampled from the experimental values provided by Palik. [102] For each core-shell geometry a set of calculations was performed that systematically varied the real, $n$, and imaginary, $\kappa$, parts of the complex refractive index from 1.4 to 1.7 and 0.0 to 0.1, respectively. The scattering, absorption, and extinction spectra were calculated for each embodiment of shell thickness and refractive index and the position of the extinction peak was extracted. The contour plots shown in Figure 3-16 present the calculated extinction peak wavelengths as a function of shell thickness and $n$ for several fixed values of $\kappa$. Overlaid on each plot is the measured extinction peak position for a given shell thickness. The position of each data point on the contour plots was determined by matching the measured LSPR peak to the range of predictions (where $n$ is varied between 1.4 and 1.7) for the corresponding shell thickness. If it is reasonable to assume that the refractive index

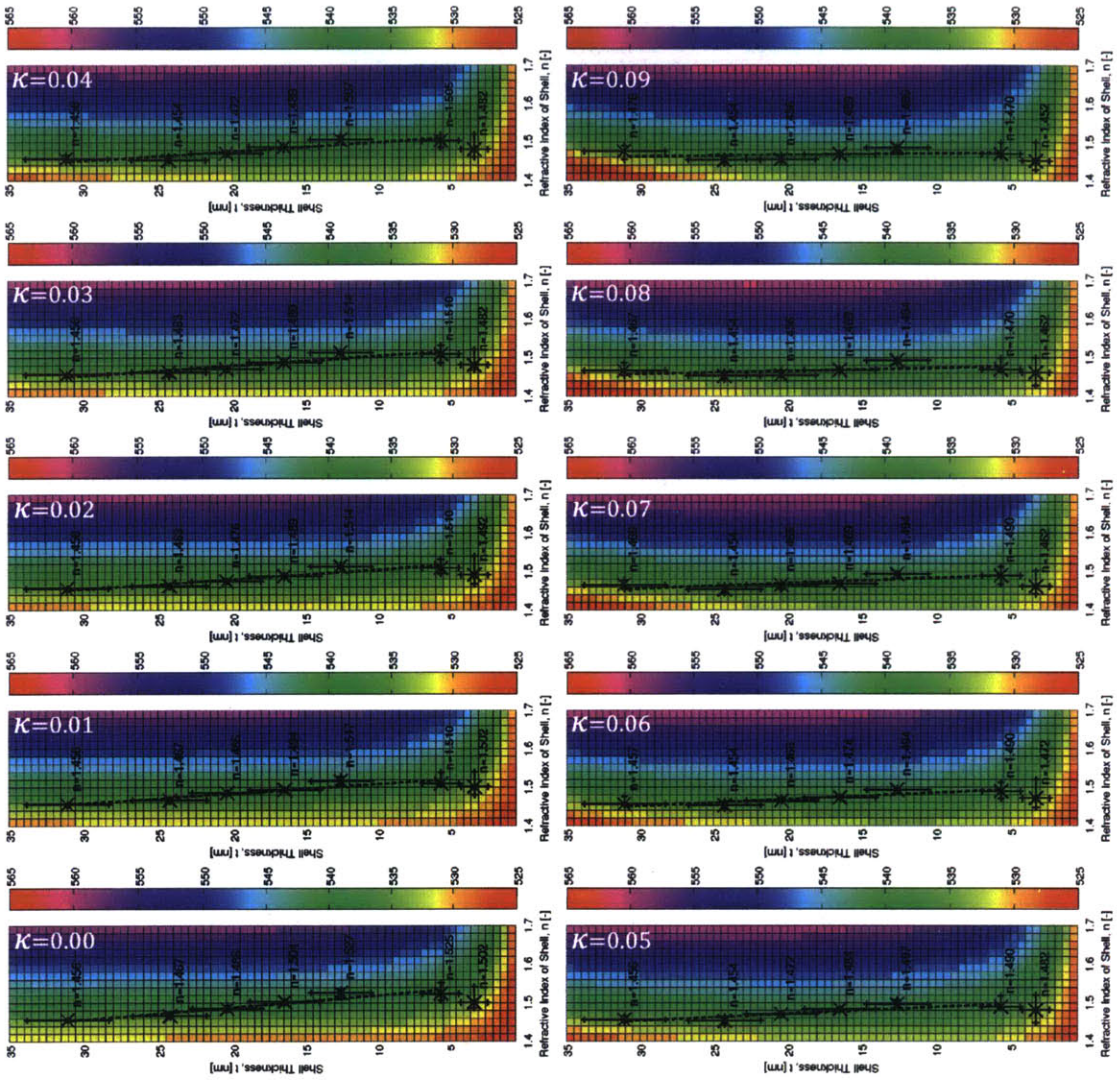


Figure 3-16: Comparison of the experimental (black $\times$'s) extinction peaks positions (units of nm) with calculated values as a function of shell thickness and complex refractive index, $n + i\kappa$. When $\kappa = 0$, the predicted extinction peaks monotonically increase with increasing shell thickness for any value of n. However, when the shell becomes somewhat absorbing ($\kappa > 0$), the predicted extinction peaks initially red-shift but begin to blue-shift with increasing shell thickness. The experimental values collapse to a single value of $n$ when $\kappa = 0.09$.

of a-ZnO is constant over the spectral range of measured extinction peak positions (*i.e.* $\lambda$ = 520 to 540 nm) and is independent of shell thickness, then it is expected that the experimental data points will indicate the complex refractive index of the shell by collapsing to a single value of $n$ for the proper value of $\kappa$.

The first panel in Figure 3-16 confirms that when the shell material is *purely dielectric* (*i.e.* $\kappa = 0$), the extinction peak location monotonically red-shifts with increasing shell thickness. This is in accordance with the intuition built from the Fröhlich condition discussion in Section 2.2.1. However, this behavior was not observed in the measured extinction spectrum, which causes the experimental data points plotted in this panel to be misaligned as is indicated by a sloping linear fit. Only when the shell material is somewhat absorbing (*i.e.* $\kappa > 0$) will the peak positions begin to blue-shift at sufficiently large shell thicknesses. Figure 3-16 shows that as the shell becomes more absorbing with increasing values of $\kappa$, the extinction predictions begin to display the blue-shifting behavior observed in the experimental data and increasingly align. Full alignment occurs within the error bars of most of the data points when $\kappa = 0.09$ and the experimental values collapse to a single value of $n = 1.47$. The calculations also suggest that shells thinner than 5 nm have a lower refractive index. One possible explanation is that the histidine amino acids never release from the AuNP surface upon nucleating the shell, but rather become incorporated into the shell and occupy a significant enough volume fraction to reduce the effective index of the material. This value is also lower than previous measurements of $n$ and $\kappa$ for a-ZnO films around wavelengths near 530 nm [103], which suggests that our HIS-mediation method likely produces shells with a lower material density.

The calculated extinction spectra for core-shells with several shell thicknesses a shell complex refractive index of $n = 1.47$ and $\kappa = 0.09$ is shown in Figure 3-17a and the calculated and measured extinction peak positions are compared against one another in Figure 3-17b. As expected, the predicted spectra and peak positions reproduce the behavior that is observed in the experimental measurements.

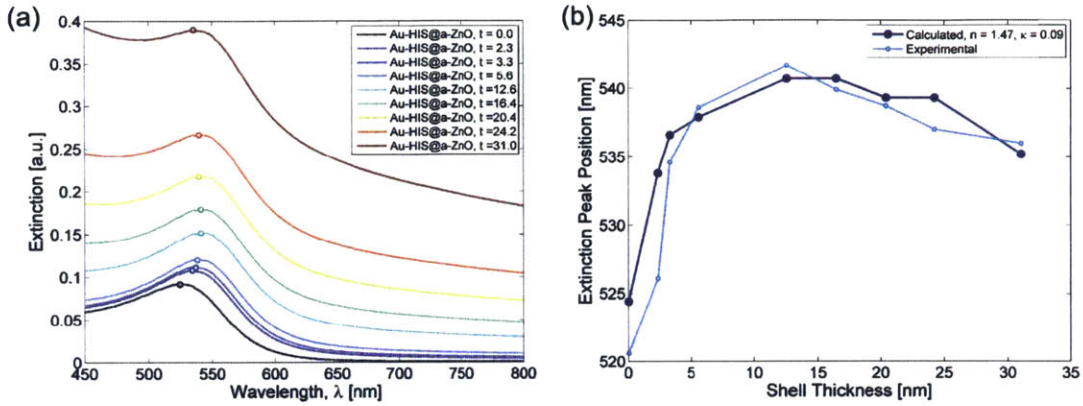


Figure 3-17: (a) Calculated extinction spectra for core-shells with shell refractive index of $1.47 + i0.09$. The extinction peak position is indicated by an open circle for each geometry. (b) Comparison of calculated and experimental extinction peak positions as a function of shell thickness.

## 3.6 Binding of Core-Shells to Biomolecules

As a result of the amino acid screening study, we have identified several amino acids that are capable of stabilizing the core-shell particles by capping the shell surface. This is advantageous because any biomolecule that displays these amino acids on its surface will also be able to interact directly with the shell material and bind the core-shell particles. To demonstrate this, we use a variant of the filamentous-type M13 bacteriophage that displays approximately ~2,700 identical copies of a peptide with several histidine residues along its major axis. This particular virus clone has a pVIII outer capsid protein sequence of DDAHVHWE and was developed as an artificial enzyme for catalyzing carboxylic esters. [104] By simply blending either Au-HIS@a-ZnO particles with an aqueous solution of the virus, we observe through TEM imaging (Figure 3-18) that the particles become bound to the virus. Hence, residues displayed on the exterior peptides of biomolecules are able to displace their free-base counterparts that cap the core-shell surface and bind directly to the shell material without any further modification. This opens the opportunity for the facile biological assembly of plasmonic nanostructures by naturally occurring proteins rich in HIS, TRP, or TYR-residues or through the use of polyhistidine-tags, which are commonly engineered into proteins to assist in purification. This is a significant advantage over

silica shells which generally are functionalized using silane linkers and EDC chemistry to achieve affinity for biomolecules.

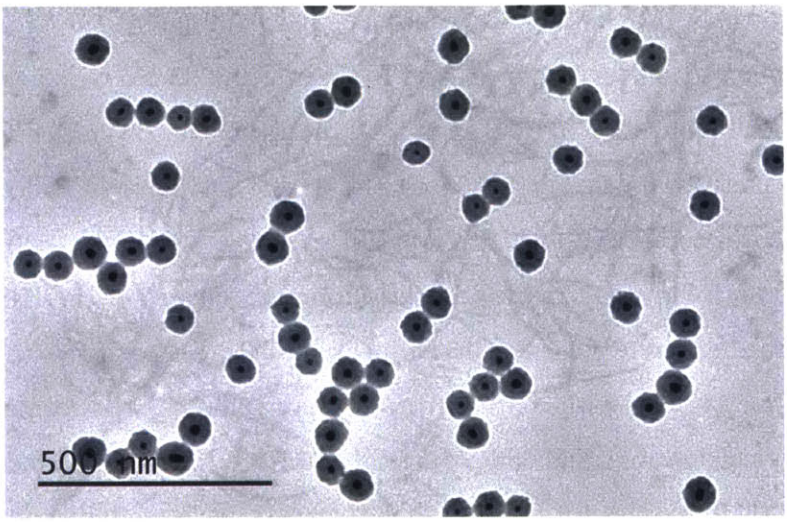


Figure 3-18: TEM microscopy reveals that histidine-capped Au@a-ZnO bind to filamentous M13 bacteriophages that display peptides rich in histidine residues on the surface of the major capsid protein. The image is intentionally under-focused to better image the individual filamentous virions.

## 3.7 Conclusion

Inspired by the ability of proteins to interact with inorganic materials to perform critical biological functions, it was postulated that free-base amino acid molecules would retain some degree of this inherent functionality and enable the synthesis of stable core-shell particles in a simple, streamlined process. By using a visual screening test of colloidal stability, four amino acids were identified out of an initial pool of thirteen candidates as being capable of growing zincous shells on AuNPs and stabilizing the particle surface through electrostatic repulsion. Amorphous zinc oxide shells (a-ZnO) were produced by histidine, tryptophan, and tyrosine, whereas polycrystalline zinc sulfide shells (c-ZnS) were grown using the exact same process but with cysteine. The shell materials were identified and characterized using standard XRD, XPS, EDS, and HRTEM methods. To our knowledge, this is the first report of growing a-ZnO shells on metal nanoparticle with amino acids and the approach presented here could be

easily extended to screen for amino-acids that enable the synthesis of nanocomposites with other core and shell materials. Histidine demonstrated stronger affinity for the a-ZnO material than TRP and TYR, which allowed it to enable the growth of uniform and continuous shells with thicknesses between 2 and 25 nm on cores comprised of single AuNPs. Above a $ZnCl_2$ reaction concentration of 2.0 mM, histidine was unable to sufficiently stabilize all of the particles during shell growth and populations emerged with cores comprised of multiple AuNPs.

An anomalous trend was observed in the extinction spectra of the HIS-mediated Au@a-ZnO core-shells where the extinction peak position blue-shifts with increasing shell thickness for samples with coatings greater than 15 nm. By performing generalized Mie theory calculations and comparing the results with the measured extinction spectra of core-shell samples with known shell thickness, it was found that these blue-shifts can arise if the shell material is not purely dielectric, but rather has a small but significant extinction coefficient. From this analysis, it has been inferred that the complex refractive index of the shell material is $1.47 + i0.09$ at wavelengths near 530 nm. Lastly, by virtue of using amino acids to grow and stabilize the core-shells in aqueous solution, it has been shown that biomolecules that express peptides rich in this amino acid are able to displace the free molecules capping the particle surface and bind directly to the shell material.

It is expected that Au@a-ZnO core-shells grown with histidine-mediation will find use in both energy and biological applications owing to our unique ability to precisely and reliably produce uniform and continuous shells as thin as 2 nm, and our ability to directly functionalize the surface with polyhistidine-tags or peptides rich in HIS, TRP, or TYR residues. Our process of identifying amino-acids that promote the growth of inorganic shells on nanoparticles could be extended to synthesizing nanocomposites of other materials and geometries for use in any application where it is necessary to interface biological and inorganic materials. It is anticipated that the thin-shelled Au@a-ZnO particles will be useful in enhancing the light-harvesting ability of solution-processed solar cells by concentrating light through localized surface plasmon resonance.

# Chapter 4

# Plasmon-Enhancement of Solution-Processed Solar Cells

The aim of the chapter is to apply the concepts and nanoscale materials presented in the previous two chapters to improving the performance of solution-processed solar cells by using plasmonic nanoparticles to enhance the ability of an active material to absorb light. This is done by developing simulations that analyze how light is absorbed throughout solar cells and comparing the results against experimental trials where actual plasmonic solar cells were fabricated. The system presented uses the nanoporous virus-films presented in Section 2.4 to organize the construction of depleted bulk-heterojunction quantum dot solar cells, where the composition of the active layer has been modified by incorporating several types of plasmonic nanoparticles during the solution-based assembly process. By matching simulated parameters to experimental results, the observed improvements in performance accompanying the incorporation of metal nanoparticles into the architecture can be confidently attributed to localized surface plasmon resonance.

## 4.1 Balancing Spectral Light Harvesting

Next-generation photovoltaic technologies are appealing because they offer the promise of fabricating colorful, flexible, and inexpensive solar cells using solution-processing

techniques such as slot-casting, roll-to-roll processing, and even inkjet printing. [33] These attributes meet all of the criteria for deploying solar cells in markets that are currently inaccessible to conventional silicon solar modules, such as photovoltaics integration into consumer electronics or architectural and infrastructural installations. However, most solution-processable solar technologies are still topics of academic research mainly because the one feature these technologies generally lack is high power conversion efficiencies. Hence, of paramount importance to the future commercialization of these solar materials is developing strategies that can compensate for the inherent weaknesses each material possesses.

### 4.1.1 Central Concept

One of the central limitations to solution-processed solar cells is that there exists a fundamental trade-off between light absorption and carrier collection. The typical minority diffusion length in solution-processed materials is generally between 5-500 nm, but often the film thicknesses must be greater than this to achieve complete light absorption. Different solar materials are limited by different physical processes. For instance polymer-based devices have poor exciton transport, charge transport in quantum devices can be hindered by defects in surface chemistry, and dye-sensitized solar cells suffer from interfacial recombination. [3] However, the effect of each of these situations is the same in that they each reduce the carrier collection efficiencies of the solar material.

Semiconducting materials are capable of absorbing light that has energy greater than the band gap. However, the ability of a given material to absorb light will vary with wavelength. For a photon to be absorbed, it must interact with an electron that is capable of accepting that energy and become excited to a higher energy state. Photons with energies close the band gap are relatively poorly absorbed because only the electrons that are close to the valence band edge would be excited across the band gap. while the energy is insufficient to excite an electron from a lower energy state. As the photon energy increases, there are more electrons available at lower energy levels that are capable of absorbing the photon and becoming excited. As a result of

this process, higher energy photons are generally quickly absorbed by solar materials, whereas lower energy photons must travel deeper into the material to encounter an electron capable of being excited to the conduction band with its energy. In other words, the probability of interacting with an excitable electron decreases with photon energy, and thus longer wavelengths penetrate deeper into the active material of solar cells. This concept is illustrated in Figure 4-1 by showing that a thick active layer is capable of absorbing all photons with energy above the band gap, while some low energy photons will pass through a thinner film without being collected. The issue with solution processed solar cells is that there are generally plenty of defects that can cause charge carriers to recombine non-radiatively and the energy is lost as heat. Although thick films are able to absorb all the wavelengths of useable light, the generated charge carriers will need to travel a greater distance to reach the electrodes, which means it is more likely they will encounter a defect and be lost. Conversely, very thin films are capable of efficiently collecting charges if they don't need to travel far to be collected, however less charges will be generated in the first place because a significant amount of useable light is passing through the device without being absorbed. Hence, there exists an optimum thickness that maximizes performance by balancing light harvesting with carrier collection.

Therefore, some solar materials, such as polymers, can only be about a hundred nanometers thick before the losses from poor carrier collection efficiencies overcome any gain in light absorption. Hence, these films are colorful and semitransparent, but struggle to achieve efficiencies comparable with silicon.

### 4.1.2 Strategies to Improve Light Harvesting

There are two options about how to proceed in order improve the performance of such materials. The first is to improve charge collection efficiency so that charges from thicker films can be collected. The second is to develop methods that improve the ability of these films to absorb light. The first generally requires the development of new fabrication procedures the reduce defect densities in films or the development of nanostructured architectures that assist in extracting carriers from the material bulk.

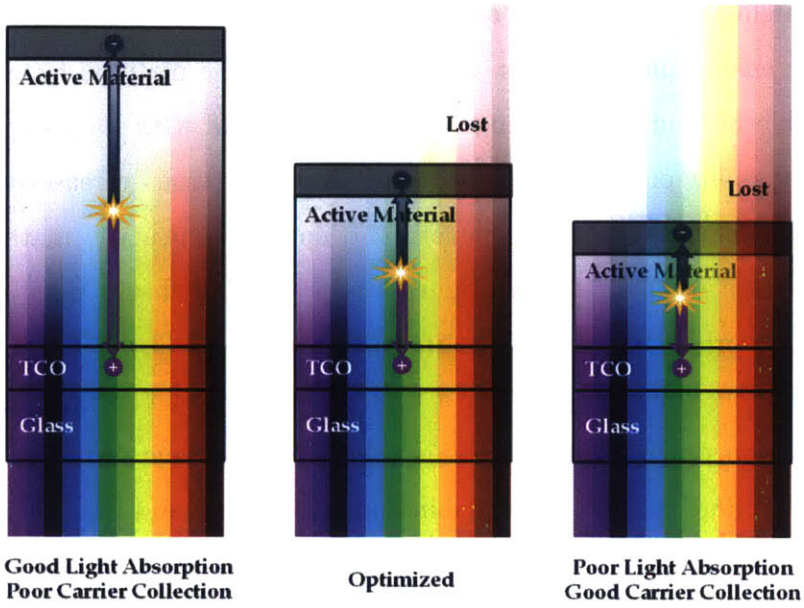


Figure 4-1: The performance of solution-processed solar cells is governed by a fundamental trade-off between light harvesting and carrier collection. a) Devices with thick active layers are able to absorb most of the light but the charge carriers are more likely to recombine at defects before collection. b) Devices with an optimized thickness are able to maximize performance by balancing light harvesting with carrier collection, however some longer wavelengths pass through the device uncollected. c) Devices with thin active layers can efficiently collect charges from the bulk but longer wavelength light will pass right through the device.

While this can be an effective route to improving performance, each specific solar material requires tailoring in different ways. In contrast, there are several strategies that allow photons to be managed more efficiently that are independent of solar material. The most common strategies are:

1. **Tandem Solar Cells:** multiple solar materials are stacked and the thickness of each layer is optimized for a separate spectral range of the visible spectrum. [105–107]

2. **Stacked Multilayers:** one-dimensional photonic crystals can either act as anti-reflective coatings or can focus light through interference in a specific spatial region. [108]

3. **Light-Trapping Arrays:** periodic arrays of holes or posts are often used to

enhance light absorption by redirecting or focusing light. [109]

4. **Plasmonic Nanoparticles:** plasmonic nanoparticles can act to concentrate light in the near-field. [61, 64]

Although any of these techniques can be applied to any solar material, generally there are particular wavelengths of light that are more poorly absorbed than others. An ideal solar material would have a completely flat absorption spectrum for photon energies above the material band gap. Such a material would allow an active layer thickness to be found that is optimal for every wavelength throughout the useable solar spectrum. However, generally many solar materials do not have flat absorption spectra, and therefore for any given thickness there will be particular wavelengths of light that are lost more than others. Therefore, any photon management strategy should be designed to ensure that the light that is otherwise lost can be redirected back into the active layer of the solar cell. Figure 4-2 displays the peak-normalized absorption spectra for several common solar materials such as the N719 dye used in DSSCs, two common polymer-fullerene blends, and lead sulfide (PbS) quantum dots (QDs). The first two sets of materials have dips in the middle of the spectrum which is fairly common for organic materials such as these, which could contribute to loss if the device thicknesses are too thin. Likewise, the PbS QDs have an absorption peak at high energies but is followed by a slowly sloping absorption tail where there can be substantial loss of long wavelengths for thin films.

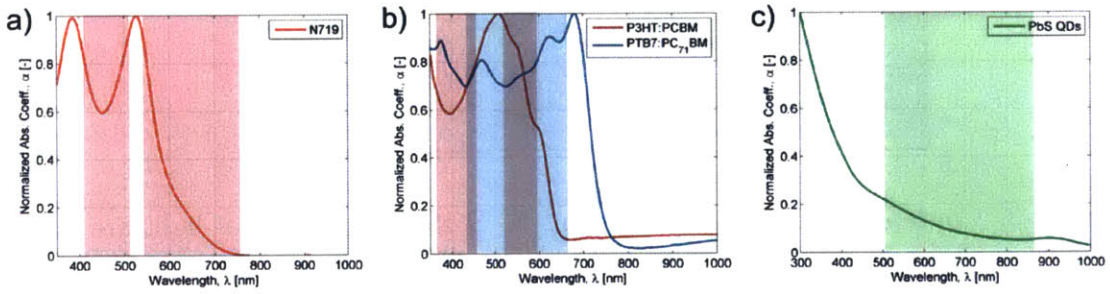


Figure 4-2: The absorption spectra for several solution-processed solar materials: a) N719 dye for DSSCs, b) P3HT:PCBM and PTB7:$PC_{71}BM$ polymer-fullerene blends, and c) PbS quantum dot film

Out of the listed options for managing photons, the first three options require precisely controlled layer thicknesses or patterned structures to tune the light to match a desired spectral range. In contrast, plasmonic nanoparticles can be easily incorporated into any solution-processed active layer by simply mixing the nanoparticles into the precursor solutions. As discussed previously in Chapter 2, plasmons can be excited with direct sunlight and the resonance wavelengths can be tuned by choice of material and geometry. By tuning the nanoparticles to exhibit resonances at wavelengths that are poorly absorbed, plasmonic nanoparticles can absorb light that is otherwise lost and concentrate it inside the active material, as is illustrated by Figure 4-3. In this scenario, the nanoparticle essentially captures the lost light and concentrates it into a thin space that is substantially below the diffraction limit. This is particularly useful in solution-processed materials that generally have nanoscale features and film thicknesses on the order of 100 nm.

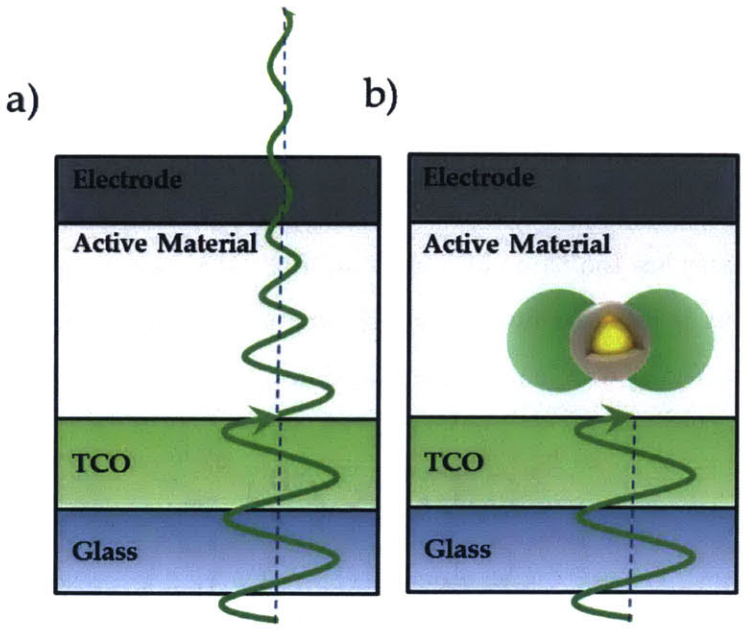


Figure 4-3: Concept of plasmon enhancment. a) Some wavelengths of light are not fully absorbed for an optimized solar cell. b) If a plasmonic nanoparticle is in the active layer, this light would excite plasmon resonance and become concentrated in the near-field surrounding the nanoparticle.

### 4.1.3 Tuning the Resonance Wavelength

As discussed in Section 2.2.3, the resonance position of plasmonic nanoparticles is determined by the shape of the nanoparticle, the material of the nanoparticle, and the material of the medium directly surrounding it. Figure 2-7 presents the extinction spectra for aqueous colloids of several different nanoparticle types, which shows that enhancing a particular range of wavelengths can be achieved through making a judicious choice of geometry and metal material. While measuring the resonance position of colloidal particles in aqueous solution provides an indication of the shape of the plasmon response, the peak positions will shift when incorporated into solid-state solar cells where the medium surrounding the nanoparticles is no longer water. If the complex refractive index of the media surrounding the particles are known, then the peak shifts can be predicted through computational means for any arbitrary particle shape or material.

## 4.2 Plasmon-Enhanced Depleted Bulk-Heterojunction Quantum Dot Solar Cells

In a joint effort with Noémie-Manuelle Dorval Courchesne, plasmon-enhanced depleted bulk-heterojunction solar cells were constructed using the virus-templated nanoporous titania networks previously discussed in Section 2.4. By building upon the optical model established for the effective medium of the nanoporous films, the ability of plasmonic nanoparticles to enhance light harvesting in quantum dot solar cells was computationally modeled and validated experimentally by fabricating devices that displayed improved performance and light harvesting ability in the spectral regions of expected plasmon-enhancement. That work presented here was published in the *Journal of Physical Chemistry C* in 2015. [110]

### 4.2.1 Introduction to the System

The aim of this work is to use the M13 bacteriophage to construct solution-processable thin film solar cells that are light weight, solid-state alternatives to the thicker, liquid-based dye-sensitized solar cells (DSSCs) previously constructed through biotemplation procedures by colleagues in the Biomolecular Materials Group at MIT. [111, 112]. Solid-state solution-processed solar cells are generally substantially thinner than DSSCs, which requires photoanodes that are tens of microns thick due to the low absorption coefficient of the organic dye molecules when adsorbed on a mesoporous titania scaffold. The nanoporous bacteriophage-based anatase titania films discussed in Section 2.4 offer the ability to precisely control both film thickness and porosity, making it a desirable platform for assembling solar cells that require thin thicknesses and can benefit from organization at the nanoscale to improve performance. As discussed in Section 2.4 gold nanoparticles were incorporated into the nanoporous networks and employed as probes to sense the porosity of the film. Here we aim to apply this same multifunctional plasmonic composite to concentrate light into thin-film solar cells in order to improve photocurrent generation. As shown by Figure 4-4, the approach is two-fold:

1. The nanoporous virus-based titania nanowire network provides directed pathways that efficiently collect and transport charges from the bulk material.

2. Solution-processing enables the network to be easily loaded with plasmonic metal nanoparticles, which increase light harvesting by concentrating light in the active layer that would otherwise pass through the film.

Colloidal quantum dots were chosen as the active material for the solar cell because they are efficient charge transporters, their band gaps can be tuned throughout the infrared spectrum by changing the particle size, their band edges can be modified with various ligand molecules, [113] and they are often paired with anatase titania to form a heterojunction. Furthermore, colloidal quantum dot solar cells are solution-processable, low-cost, and have achieved efficiencies as high as 9.2% [25] and 9.9% [4].

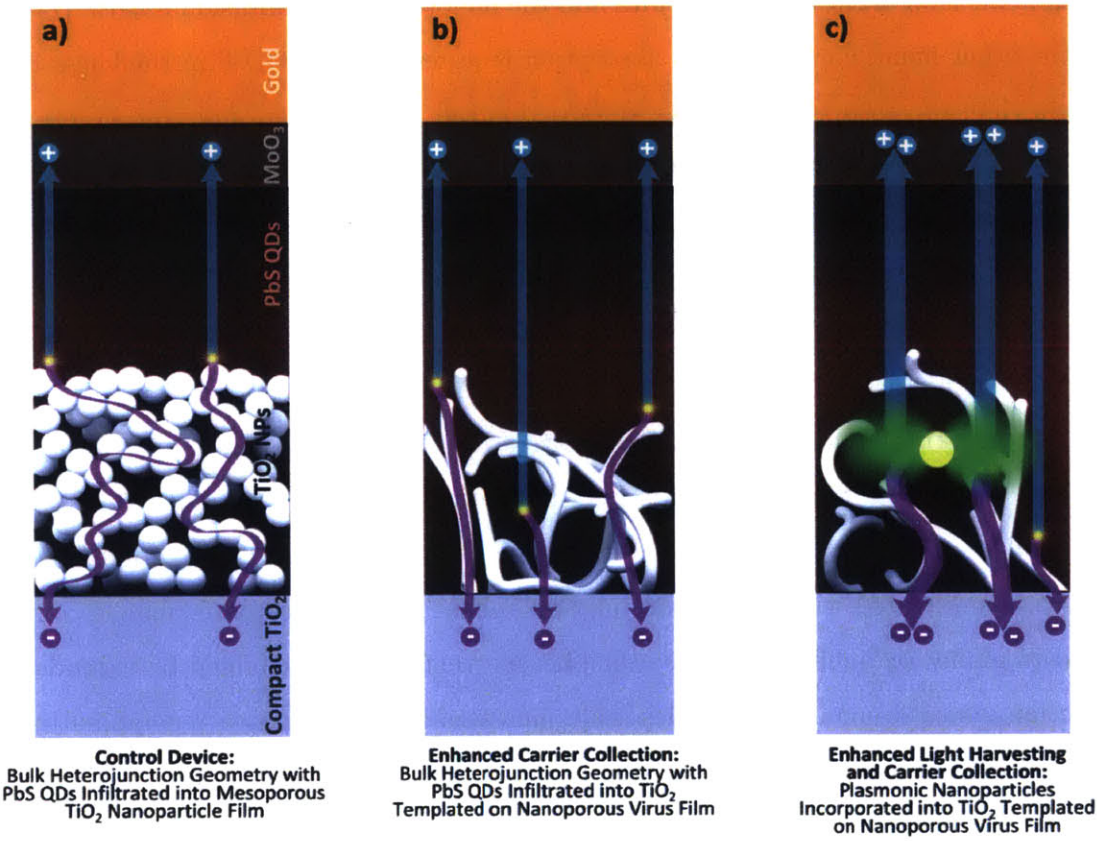


Figure 4-4: Illustration of two fold-strategy employed in building a virus-based nanoscale device architecture to enhance the photocurrent generation in PbS QD solar cell over a randomly-organized geometry. a) The control device has a disorganized geometry that consists of a layer of PbS QDs infiltrated into a porous layer of titania nanoparticles. The percolation pathways for electrons can be circuitous depending on how the $TiO_2$ NPs sinter together. b) Virus-templated titania network provides a blended heterojunction morphology that allows photogenerated charges to be collected from QDs that have infiltrated into the network and provides more direct pathways to conduct electrons. c) Metal nanoparticles act as nano-antennas to concentrate light in their near-field region, thereby producing a higher photon flux on nearby QDs and an increased rate of carrier generation.

Traditionally, PbS QDs are stacked on top of a nonporous titania film to form a depleted heterojunction. In order to extract carriers efficiently in this planar device, the QD film thickness must be thinner than the carrier collection length ( 200 to 250 nm), which is the sum of the depletion width and the minority carrier diffusion length. [114] On the other hand, complete light absorption requires that the QD film thickness be greater than the absorption length (>1 $\mu$m). Instead, a bulk heterojunction structure can be constructed by infiltrating QDs into nanostructured titania, which can extend the width of the depletion region and allow for more light to be absorbed with thicker QD films. However, these structures are more prone to trap-assisted recombination at defects if the conduction pathways are tortuous and if the interfacial surface area is high. For this reason, nanowire-based titania morphologies that provide continuous and direct pathways for charge transport are advantageous over disorganized mesoporous nanoparticle films commonly used in solution-processed solar cells. [115,116] It has been shown that using an array of titania [24] or zinc oxide [96] nanopillars or nanowires infiltrated with PbS quantum dots enhances the device performance compared to planar oxide layers because the photocurrent increases enabled by extended depletion zones overcome any undesirable increases in non-radiative recombination that result from a larger interfacial area between the active material and the titania nanostructures.

Our plasmonic virus-templated porous composite is rationally designed to generally compensate for the weaknesses of photoactive materials with relatively short lifetimes. Specifically for titania-PbS QD depleted bulk heterojunctions, our system offers the following advantages:

1. The highly porous film allows for substantial infiltration of QDs into the titania networks, thereby extending the depletion region of the device.

2. Compared to a porous film made using a titania nanoparticle paste, the interconnected network of titania nanowires formed by the high aspect ratio viruses provides direct pathways for transporting charges from the bulk of the device to the electrodes. Likewise, forming titania along a high aspect ratio template

like the M13 bacteriophage produces a smaller overall surface area compared to a porous film comprised of spherical particles, and is therefore expected to have less surface defects to promote non-radiative recombination.

3. PbS QDs suffer from an absorption spectrum that preferentially absorbs high energy photons. Therefore, it is susceptible to the classic tradeoff in solar cells between light harvesting and carrier collection, where thick active layers are required to absorb light throughout the visible and infrared ranges, but carrier generated in the quasi-neutral region are less likely to diffuse to the depletion region before recombining. By using the M13 bacteriophage to carry and assemble metal nanoparticles with plasmon resonances in the visible range within nanoporous films, photons at poorly absorbed wavelengths can be concentrated in the near-field surrounding the NPs and light harvesting is improved without further increasing the QD film thickness.

4. The uniformity and sub-wavelength pore size combined with the ability of the virus to evenly disperse metal nanoparticles throughout the film offers an ideal environment where effective medium theory can be paired with finite-difference time-domain (FDTD) simulations to theoretically evaluate how several metal nanoparticle types can enhance light absorption in the devices.

### 4.2.2 Device Architecture

The device assembly process is schematized in Figure 4-5. In brief, a dense compact layer of anatase $TiO_2$ was assembled on patterned fluorine-doped tin oxide (FTO) substrates by spincoating a titania paste, followed by subsequent annealing at 500 °C. The plasmonic nanoporous scaffold is assembled through a layer-by-layer process that covalently cross-links viruses that have formed complexes with either gold nanospheres (AuNPs), silver nanospheres (AgNPs), or silver nanoplates (AgNPLs) through protein interactions. As previously discussed in Chapter 2, this assembly process allows the metal nanoparticles to be evenly dispersed throughout the nanoporous film without forming aggregates. In these device, the virus variant p8#9 was utilized because it

exhibits affinity for both gold and silver, as was previously indicated in Table 2.1. The nanoporous film is then mineralized with amorphous titania which coats both the virus and the nanoparticles complexed to them. The films are further annealed to crystallize the $TiO_2$ and remove the virus from the film. PbS QDs with an average diameter of 2.9 nm and a first excitonic absorption peak at 905 nm ($E_g$= 1.37 eV) were then infiltrated into the pores of the film via dropcasting or spin-coating to create the $TiO_2$-PbS blend layer with an overlayer of PbS QDs capping the device. Finally, a 25 nm thick hole transporting layer of $MoO_3$ was thermally evaporated, followed by a 100 nm thick gold electrode. The device area of the resulting solar cells was 0.0547 $cm^2$.

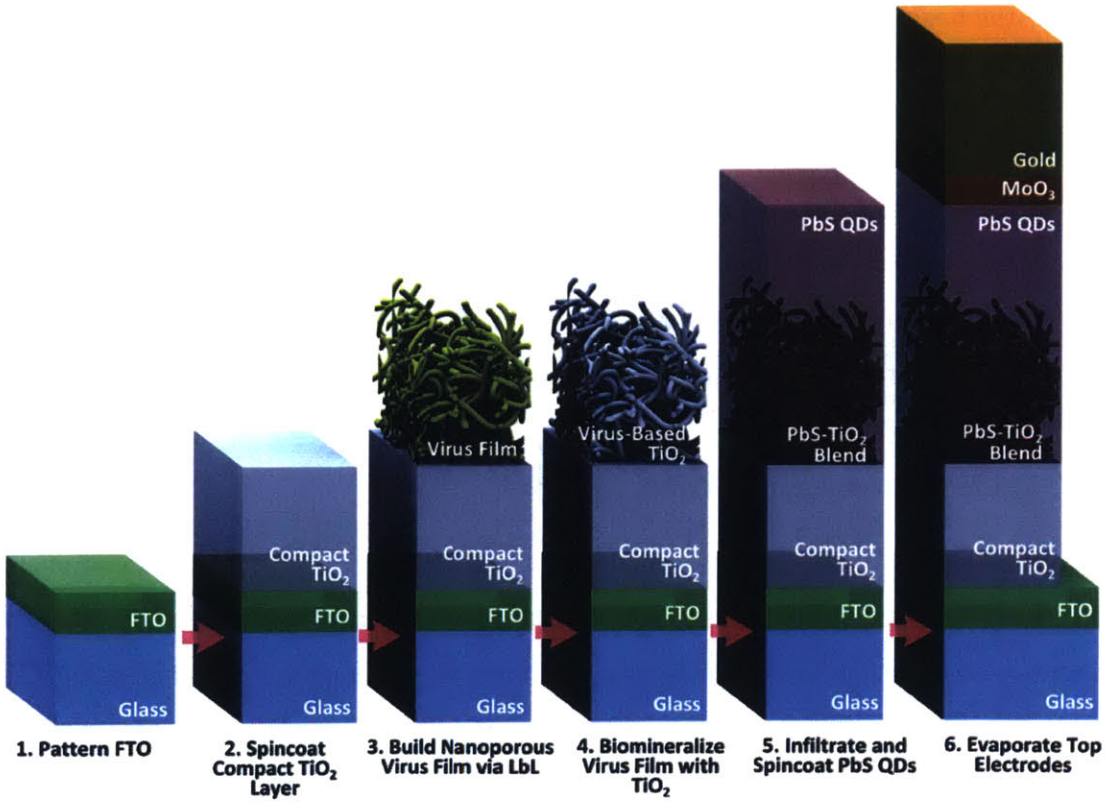


Figure 4-5: Virus-based titania-PbS QD composites are assembled via sequential solution-processing to result in the final solar cells.

Any additional details about the device fabrication can be found in the published

manuscript. [110] This work was a collaboration with Noémie, who developed the process for assembling the nanoporous films and was responsible for fabricating the solar cells. My role was to synthesize the metal nanoparticles, assist in developing the complexation procedure to bind them to the virus, and model the plasmon enhancement theoretically in order to establish when observed improvement is indeed produced by localized surface plasmon resonance (LSPR).

### 4.2.3 Synthesis Procedures

#### Materials

Gold(III) chloride ($\geq$ 99.99% trace metal basis), silver nitrate, coumalic acid, hydrogen peroxide (Perdrogen, 30% solution), sodium borohydride, and glycerol were purchased from Sigma-Aldrich (St-Louis, MO). Sodium citrate dihydrate was purchased from Alfa Aesar (Ward Hill, MA).

#### Gold Nanoparticle (AuNP) Synthesis

Gold nanoparticles with ~20 nm diameters were synthesized following the Turkevich method. [47] In summary, 95 mL of deionized water and 2.6 mL of 50 mM gold(III) chloride were combined in a 250 mL round-bottom flask and brought to a boil while stirring in a silicone oil bath. While boiling, 10 mL of 1% wt sodium citrate dihydrate was quickly added while vigorously stirring. The color of the solution quickly turned black and then ripened into a deep ruby red. The solution was kept boiling and stirring for an additional 20 minutes. The solution was cooled to room temperature and stored without further purification.

#### Silver Nanoparticle (AgNP) Synthesis

Silver nanoparticles were synthesized following a modified Turkevich method. [47] In summary, 95 mL of deionized water and 4 mL of 30 mM silver nitrate were combined in a 250 mL round-bottom flask and brought to a boil while stirring in a silicone oil bath. While boiling, 10 mL of 5% wt sodium citrate dihydrate was quickly added

while vigorously stirring. After stirring for a minute, 6 mL of 100 mM coumalic acid was quickly added. The color of the solution slowly ripened into a deep yellow-brown color. The solution was kept boiling and stirring for an additional 20 minutes. The solution was cooled to room temperature and stored without further purification.

#### Silver Triangular Nanoplate (AgNPL) Synthesis

Silver nanoparticles were synthesized by modifying the method previously reported by Zhang *et al.* [117] In a 1 L Erlenmeyer flask, 240 mL of deionized water was combined with 5 mL of 50 mM silver nitrate and 5 mL of 750 mM sodium citrate dihydrate while stirring at room-temperature, followed by 6 mL of 30% hydrogen peroxide stock solution. While stirring at room-temperature, 10 mL of freshly prepared 100 mM sodium borohydride was added dropwise to the solution. The color of the solution changed from yellow to brown to amber-red within about fifteen minutes. Once the color has stabilized, an additional mL of 30% hydrogen peroxide solution was added. The addition of hydrogen peroxide was repeated until the solution changed color and stabilized to a deep blue. Then 1 mL of glycerol was added to stabilize the solution for long-term storage.

### 4.2.4 Assembling NP-Virus Complexes

Each of the metal nanoparticle types was bound to the virus by mixing the p8#9 virus with each metal nanoparticle with a ratio of approximately 0.1 NPs per virion. As confirmed by the transmission electron microscopy (TEM) images shown in Figure 4-6, the complexation process spaces the nanoparticles fairly evenly along the bacteriophages, which avoids aggregation and allows the characteristic absorption peaks of plasmonic particles to be preserved.

### 4.2.5 Plasmon-Enhanced Device Performance

Each of the three types of nanoparticles improved the overall power conversion efficiency of the titania-PbS devices with the AgNPLs producing the largest photocurrent

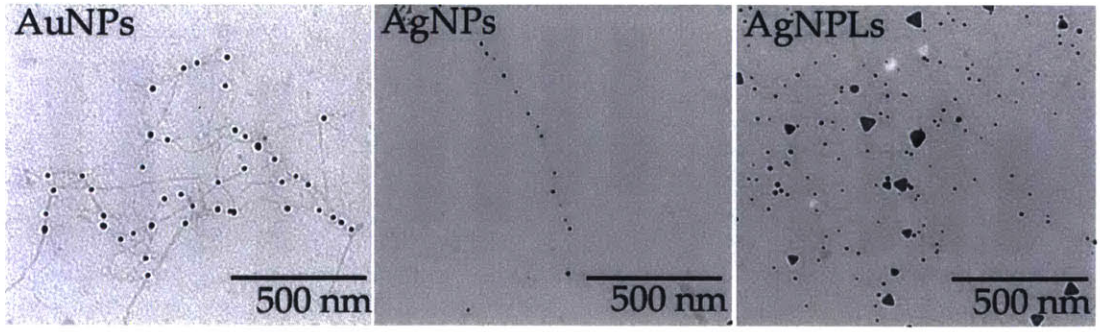


Figure 4-6: TEM images of a) AuNPs, b) AgNPs, and c) AgNPLs complexed to the p8#9 virus

enhancement (Figure 4-7a). The short-circuit current was enhanced in the presence of each nanoparticle type, with statistically significant improvement occurring with AgNPs and AgNPLs. In addition, the open circuit voltage, $V_{oc}$ increased by approximately 50 mV and the parasitic resistances improved when adding any type of metal nanoparticle to the devices. The improvement in $V_{oc}$ is attributed to a natural increase that results from the plasmonic NPs generating a higher photocurrent through LSPR. Likewise, the slight improvement in resistances could be attributed to either local changes in morphology or titania crystallite quality around the nanoparticles that improve charge transport. The improvement in power conversion efficiency, PCE, caused by the metal nanoparticles in the virus-templated devices was calculated to be 22.2% for AuNPs, 25.1% for AgNPs, and 36.5% for AgNPLs on average (Figure 4-7b and Table 4.1). The top performing Ag NPL device reached a PCE close to 4%, and its JV curve is compared to a virus-templated device without plasmonic nanoparticles in Figure 4-7c.

## 4.3 Modeling Plasmon-Enhancement in Virus-Templated Bulk-Heterojunction PbS QD Solar Cells

The effect of each nanoparticle type on the ability of the devices to harvest light was computationally predicted prior to device fabrication by combining effective medium

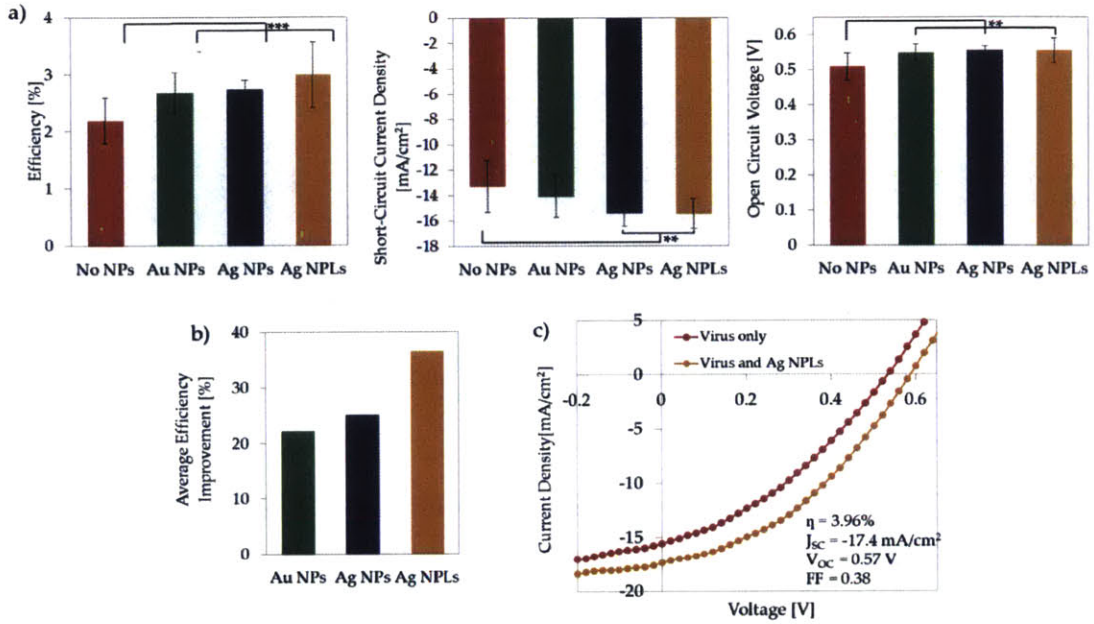


Figure 4-7: a) Comparison of power conversion efficiency, short-circuit current density and open circuit voltage for devices with naked virus, or for viruses complexed with AuNPs, AgNPs or AgNPLs. Paired t-tests were performed and the statistically significant differences between pairs of results are shown by ** for a p-value $< 0.005$ and *** for a p-value $< 0.0005$. b) Average percentage improvement in efficiency with addition of metal nanoparticles. c) Comparison of the JV curves for the best device with and without metal nanoparticles. Overall, the nanoparticle device with the highest efficiency contained Ag NPLs.

theory with finite-difference time-domain (FDTD) calculations. Before performing the numerical simulations, the material properties of the various media were established.

### 4.3.1 Effective Dielectric Function Calculations using Effective Medium Theory

Modeling the power absorption throughout the solar cells requires the development of effective complex dielectric functions for the nanostructured active layers of the devices (i.e. the virus-templated network infiltrated with PbS QDs, and the PbS QD film layers). Properly modeling the optical material properties is critical for accurately predicting how light propagates and is absorbed throughout the solar cell

Table 4.1: Solar cell performance parameters for plasmon-enhanced virus-based PbS QD solar devices. Average values and standard deviations are presented for each parameter, as well as the maximum power conversion efficiency (PCE) for each type of device. The averages presented are based on at least 10 to 20 devices of each type.

| Device | $J_{sc}$ [mA/cm$^2$] | $V_{oc}$ [V] | FF [%] | PCE [%] | Max PCE [%] |
|---|---|---|---|---|---|
| Virus Only | -13.2 ± 2.0 | 0.51 ± 0.04 | 32 ± 3 | 2.18 ± 0.40 | 2.93 |
| Virus-AuNPs | -14.1 ± 1.6 | 0.55 ± 0.02 | 35 ± 3 | 2.67 ± 0.36 | 3.15 |
| Virus-AgNPs | -15.5 ± 1.0 | 0.56 ± 0.01 | 32 ± 2 | 2.73 ± 0.16 | 3.04 |
| Virus-AgNPLs | -15.5 ± 1.2 | 0.55 ± 0.04 | 35 ± 4 | 2.98 ± 0.58 | 3.96 |

volume. This section describes the methods used to perform this task.

### Pure Anatase Titania

The complex dielectric function for pure anatase titania, $\varepsilon_{TiO_2}$, was calculated from the values reported by Kim et al. [50] for a 16% porous thin film (84% anatase volume fraction) using Bruggeman effective medium theory established in Section 2.4.2: [39]

$$\varepsilon_{TiO_2} = \varepsilon_{film} \frac{2\left(\frac{f_{film}-1}{f_{film}}\right)\left(\frac{\varepsilon_{air}-\varepsilon_{film}}{\varepsilon_{air}+2\varepsilon_{film}}\right)+1}{\left(\frac{1-f_{film}}{f_{film}}\right)\left(\frac{\varepsilon_{air}-\varepsilon_{film}}{\varepsilon_{air}+2\varepsilon_{film}}\right)+1} \tag{4.1}$$

where $\varepsilon_{TiO_2}$ is the complex dielectric function of the 16% porous anatase film reported by Kim *et al.*, [50] $f_{film}$ is the volume fraction of anatase titania in this film (84%), and $\varepsilon_{air}$ is the dielectric function of air (taken to be 1.000). The complex index of refraction can be calculated from the dielectric function with Equation 2.45. The complex index of refraction for pure anatase used for the computations is plotted in Figure 4-8.

### Blend Layer (58% Anatase $TiO_2$, 15% PbS QDs, 27% Air)

The complex dielectric function of pure PbS QDs was adjusted from the values reported by Moreels *et al.* [118] to have an absorption peak that matches the measurement of 904 nm for the PbS QDs used in the devices (see Figure 4-10).

In reality, a *pure* PbS QD film can never be achieved because void space will always exist between the QDs when the spheres pack into a film. Therefore, effective

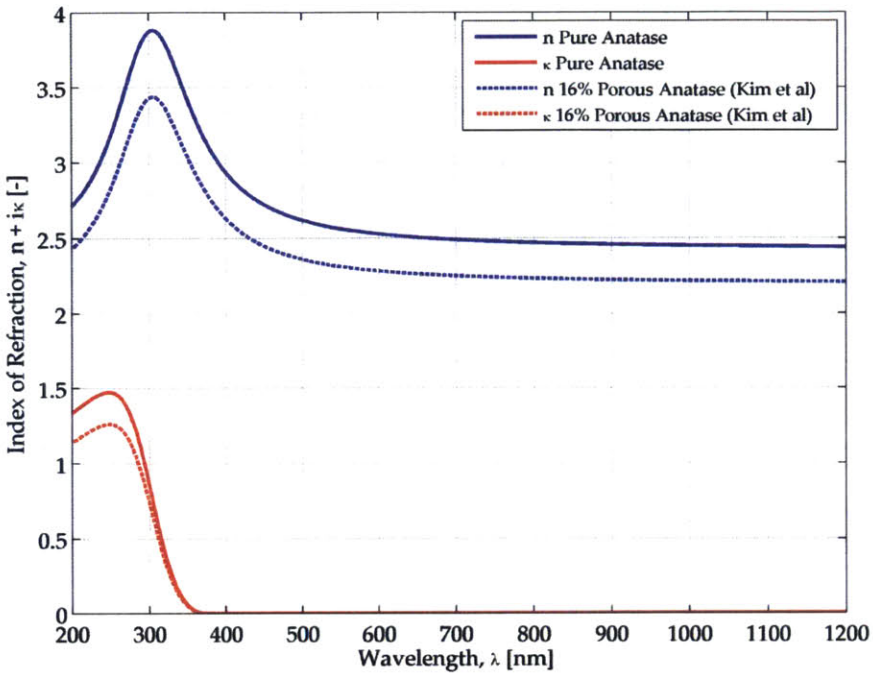


Figure 4-8: Real (blue) and imaginary (red) components of the index of refraction for the 16% porous anatase $TiO_2$ film reported by Kim *et al.* (dotted lines) and the estimated function for pure anatase films (i.e. 0% porous films, solid lines) as predicted by Bruggeman effective medium theory.

medium theory must be used to estimate the effective index of the virus-templated titania network when PbS QDs are infiltrated into its pores (referred to as the *blend layer*) and for the packed QD film that was spin-coated to form an overlayer on top of the blend layer (referred to as *random-packed PbS QD layer*). For simplicity the blend layer was modeled as a homogeneous planar slab with an effective index resulting from a blending of anatase titania (corresponding to virus-templated titania nanowires, comprising 58.1% of the film volume) with the PbS QDs and air occupying the pore space of the virus-templated network. The volume fraction of PbS in the blend layer was determined to be 15% by averaging the PbS concentration profile reported in Figure 1D of the manuscript [110] over the 50 nm thickness of that film. Although assuming a homogeneous distribution of PbS is a simplification of the system, by using the average PbS concentration measured for the actual films, the total amount of light absorbed by the PbS QDs in the idealized slab will be equal to that absorbed in the actual film. This can be proven using the Beer-Lambert

law for light absorption, where light with intensity, $I_0$, is incident on a slab with a 1-D concentration gradient, $c(z)$, of PbS QDs with a molar absorptivity of $\varepsilon$. The intensity at any position within the slab, $I(z)$, is:

$$I(z) = I_0 \exp\left(\varepsilon \int_0^z c(z)dz\right) \tag{4.2}$$

For a slab of thickness $L$, the intensity of light after passing through the entire film is:

$$I(L) = I_0 \exp\left(\varepsilon \int_0^L c(z)dz\right) = I_0 \exp(\varepsilon \bar{c} L) \tag{4.3}$$

where $\bar{c}$ is the average PbS QD concentration and is equal to:

$$\bar{c} = \frac{1}{L} \int_0^L c(z)dz \tag{4.4}$$

A volume fraction of 15% PbS in the blend layer corresponds to a 35% fill fraction of the pore volume. Therefore, the effective index of the overall blend layer was calculated in two steps. First, the Maxwell Garnett effective medium theory [39] was used to determine the effective dielectric function of the material in the pores, $\varepsilon_{eff}^{pores}$, which is taken to be a 35% fill fraction of PbS QDs with the balance being air:

$$\varepsilon_{eff}^{pores} = \varepsilon_{air}\left[1 + \frac{3f_{PbS}^{pores}\left(\frac{\varepsilon_{PbS}-\varepsilon_{air}}{\varepsilon_{PbS}+2\varepsilon_{air}}\right)}{1 - f_{PbS}^{pores}\left(\frac{\varepsilon_{PbS}-\varepsilon_{air}}{\varepsilon_{PbS}+2\varepsilon_{air}}\right)}\right] \tag{4.5}$$

where $\varepsilon_{PbS}$ is the dielectric function of pure PbS QDs and $f_{PbS}^{pores}$ is the volumetric fill fraction of PbS QDs in the pore material (35%).

The second step once again uses effective medium theory to blend the anatase titania with the effective medium developed for the pores, $\varepsilon_{eff}^{pores}$. The Maxwell Garnett model was not used for this blending because it is only strictly valid for spherical inclusions. Thus, the Bruggeman model was chosen because it applies to a completely randomly inhomogeneous medium. The effective dielectric function of the blend layer,

$\varepsilon_{eff}^{blend}$, can be found by numerically solving the following transcendental equation: [39]

$$f_{TiO_2}\left(\frac{\varepsilon_{TiO_2}-\varepsilon_{eff}^{blend}}{\varepsilon_{TiO_2}+2\varepsilon_{eff}^{blend}}\right)+(1-f_{TiO_2})\left(\frac{\varepsilon_{eff}^{pores}-\varepsilon_{eff}^{blend}}{\varepsilon_{eff}^{pores}+2\varepsilon_{eff}^{blend}}\right)=0 \tag{4.6}$$

where $f_{TiO_2}$ is the volumetric fill fraction of anatase titania in the blend layer (58.1%) and $\varepsilon_{TiO_2}$ is the dielectric function of pure anatase titania calculated earlier with Equation 4.1. Figure 4-9 plots the real and imaginary parts of the complex refractive indexes calculated for pure anatase, the effective medium in the pores, and the final blend layer comprised of anatase titania, PbS QDs, and air.

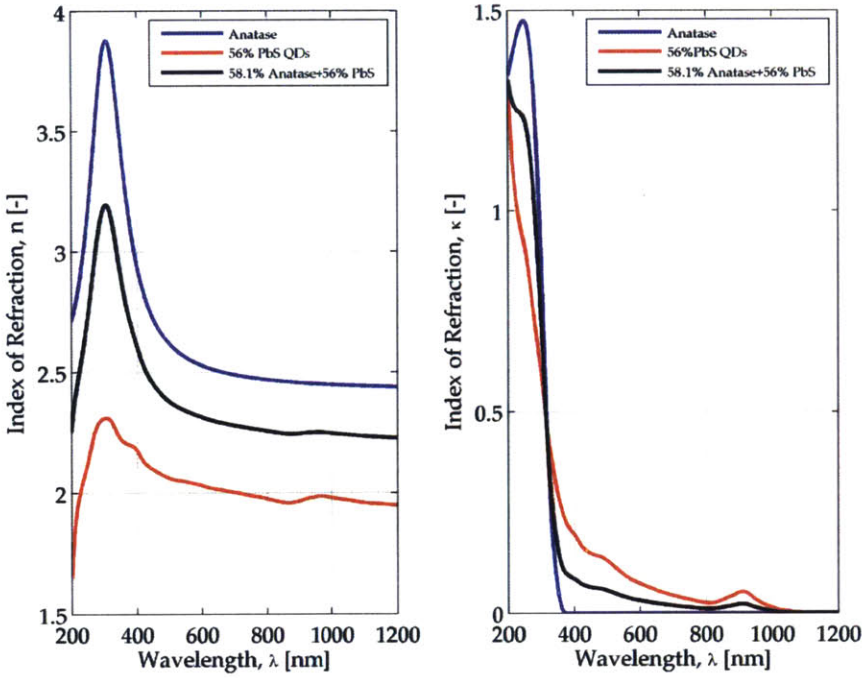


Figure 4-9: Real (Left) and imaginary (Right) parts of the complex refractive index computed for pure anatase titania (blue lines), the 35% PbS QD 75% air mixture in the pores of the blend layer (red lines), and the final blend layer (black lines) consisting of a 58% volume fraction of anatase titania, 15% PbS QDs, and 27% air.

### PbS QD Layer (56% PbS QDs, 44% Air)

When the PbS QD solution is spin-coated on top of the blend layer, the nanospheres will pack into a film that consists only of PbS and air. The densest possible packing

density for a bed of equal size spheres is 74%, which corresponds to perfect close-packing. In practice, this upper limit is not achieved, rather studies of QD films assembled by spin-coating colloidal solutions indicate that packing densities are closer to 50%. [119] Therefore a PbS volume fraction of 56% was chosen for modeling the spincoated PbS QD film, which corresponds to a typical value used for a loose random-packing of equal spheres. [120] The effective dielectric function, $\varepsilon_{eff}^{film}$, of this layer can be calculated by using the Maxwell Garnett effective medium model presented in Equation 4.5, but substituting $f_{PbS}^{pores}$ with $f_{PbS}^{film}$ (56%):

$$\varepsilon_{eff}^{film} = \varepsilon_{air}\left[1 + \frac{3f_{PbS}^{film}\left(\frac{\varepsilon_{PbS}-\varepsilon_{air}}{\varepsilon_{PbS}+2\varepsilon_{air}}\right)}{1 - f_{PbS}^{film}\left(\frac{\varepsilon_{PbS}-\varepsilon_{air}}{\varepsilon_{PbS}+2\varepsilon_{air}}\right)}\right] \tag{4.7}$$

The effective dielectric function resulting from this calculation is plotted in Figure 4-10.

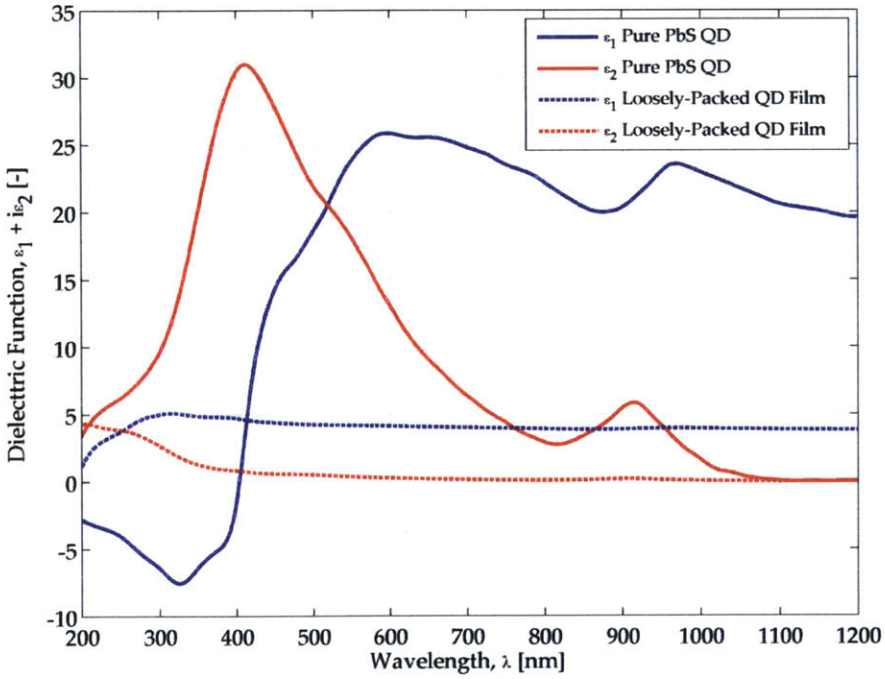


Figure 4-10: Real (blue) and imaginary (red) components of the complex dielectric function for the pure PbS QDs modified from Moreels *et al.* [118] for 904 nm QDs (solid lines) and the estimated effective dielectric function for a spincast film of loosely random-packed PbS QDs (56% volume fraction of PbS QD and 44% air) as predicted by Maxwell Garnett effective medium theory.

### 4.3.2 Finite-Difference Time-Domain Simulations

In order to computationally predict how a PbS QD solar cell would perform with and without plasmonic metal nanoparticles, the finite-difference time-domain (FDTD) method was used to determine how light would propagate and become absorbed throughout an idealized device. The simulations were carried out with the software Lumerical FDTD Solutions, Version 8.9.163.

#### Model Geometry and Materials

The model geometry follows the approximate dimensions of an actual device cross-section, which consists of stacked planar slabs of material starting with 50 nm of FTO at the bottom followed by 100 nm of pure anatase titania, 100 nm of the virus-templated blend layer that has been infiltrated with PbS QDs (58% volume fraction of $TiO_2$, 15% PbS, 27% Air), 100 nm of PbS QD film (56% PbS, 44% Air), and 25 nm of $MoO_3$ on top. The complex dielectric functions developed for pure anatase titania, the virus-built titania-PbS QD blend layer, and the random-packed QD film layers using effective medium theory in the previous section were assigned to the corresponding slabs of the model geometry. The lateral extent of the slabs in the $x$- and $y$-directions was fixed to be 60 nm, which is the estimated approximate distance between NPs in the solar cells. Three different types of nanoparticles were considered in the plasmon-enhanced solar cells: gold nanosphere (AuNP), silver nanosphere (AgNP), and silver nanoplate (AgNPL). The radius of the nanospheres was taken to be 10 nm whereas the cylindrical silver nanoplates had a radius of 10 nm and a thickness of 6 nm. (Although the silver nanoplates were originally synthesized as triangles. It was observed that upon binding to the virus, the interaction caused the corners of the plates to round until the triangular plates changed into cylindrical discs.) The complex dielectric function reported by Johnson and Christy [37] was used for gold, whereas the function reported by Palik [102] was used for silver. Periodic boundary conditions were placed on each of the lateral $x-$ and $y-$faces of the model in order to simulate an infinite slab with periodically spaced NPs. Likewise, this allows any light that is scattered

obliquely from a NP through the lateral faces to re-enter the simulation volume. Six different configurations were performed for each nanoparticle type, each with the nanoparticle positioned at a different location throughout the thickness of the active materials. Because the nanoparticles were built into the blend layer using the layer-by-layer assembly method with the M13 virus, the NPs can be located anywhere within this layer. Five configurations consider a nanoparticle located within the blend layer (10, 30, 50, 70, or 90 nm from the bottom of the blend layer slab). However, in an actual device, the interfaces between the blend and random-packed QD layers is not expected to be smooth, rather the virus-templated titania nanowire film is expected to be rough. Therefore, a NP that exists near the top of the film could almost be considered to be embedded within the random-packed QD film layer. Thus, a sixth configuration was considered where the metal NP was located 10 nm into the random-packed QD film layer. Because the AgNPL is not spherically symmetric, its orientation to the incident light will impact the nature of its plasmon resonance; thus, for each vertical position, three separate orientations were considered with the NPL located at 0°, 45°, and 90°to the incident field (*i.e.* 18 total cases were considered for the AgNPL geometry and 6 cases for the AuNPs and AgNPs.).

The model geometry was illuminated from the FTO side with a plane-wave source at 400 different wavelengths between 200 and 1200 nm to fully capture the incident solar spectrum of interest. All simulations were performed with a refined mesh size of 1 nm in the region around the metal NP and used conformal meshing option "Conformal Variant 1" to provide greater accuracy in elements where multiple materials are present. A three-dimensional power absorption monitor was placed throughout the active regions of the solar cell to capture how much power was absorbed at each point in the solar cell. A cross-section of the mesh through the NP center is shown in Figure 4-11a for the nanosphere case and Figure 4-11b shows the mesh configuration for all three orientations of the nanoplate cases.

The silver nanoplates are believed to transform into a polydisperse population of silver nanospheres during the annealing process the virus-templated titania film undergoes to convert the nanowires from amorphous to crystalline titania. The sim-

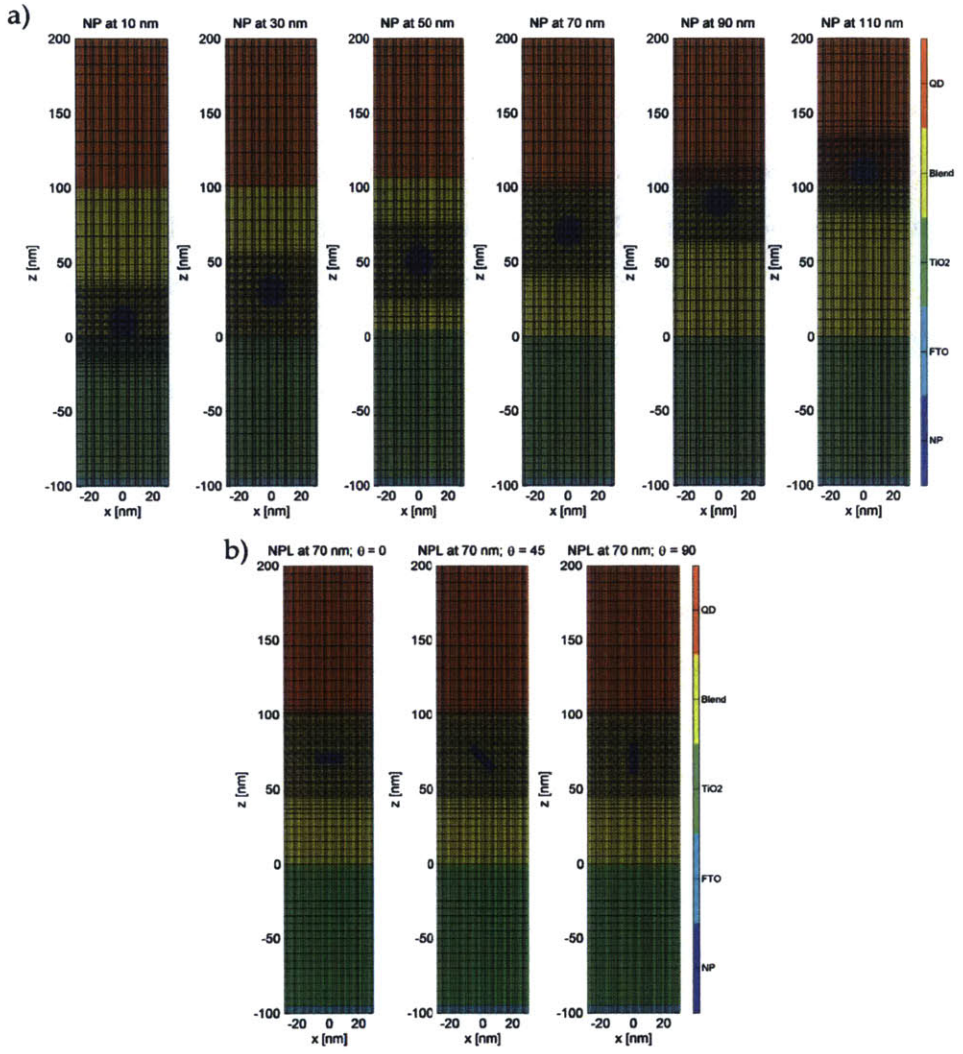


Figure 4-11: The mesh, materials, and geometry of each simulated configuration performed with the FDTD method. a) All six of the different positional configurations of metal NPs. Five configurations exist for a NP within the blend layer and 1 in the random-packed PbS QD film layer. b) Because silver nanoplates are not spherically symmetric, their orientation within the blend layer will change the way light is concentrated in the near-field surrounding them. Therefore, at each of the six positional configurations shown in A, three orientational configurations were considered with the NPL positioned at 0°, 45°, and 90°with respect to the faces of the material slabs (18 total cases performed for the NPL device).

ulations performed to test this hypothesis are exactly the same as those done for the AgNPs except that nanospheres of radius 8.2, 10.4, and 11.9 nm were considered, which conserve the volume of a stack of 1, 2, and 3 NPLs.

### Calculating Power Absorption, External Quantum Efficiency, and Photocurrent Enhancement

Upon completion of the simulation, the power absorption monitor provides the source-normalized power density that has been absorbed at each node throughout the mesh for each illumination wavelength. This can be thought of as a measure of *absorption efficiency density*, $p_{abs}$, which is how efficiently a given element can absorb photons of a particular wavelength that are incident upon the solar cell per unit volume (units of $m^{-3}$). By integrating this measure over the spatial extent of active regions in the solar cell, the total absorption efficiency of the solar cell can be determined as a function of wavelength. It must be noted that when metal NPs are incorporated into the model, any light that is absorbed in the NP interior cannot contribute to enhancing solar cell performance because the power it absorbs either goes into producing the near-field or is lost as heat. As discussed in Chapter 2, this lossiness is considered by the imaginary component of the dielectric function for the metal particle and is thereby considered in the FDTD calculations. Only the light that is concentrated by the LSPR of the NP in the active material directly surrounding it can contribute to photocurrent enhancement. Therefore, when determining the total amount of power absorbed by the solar cell with the goal being to estimate the photocurrent the device can produce, only the power absorbed in the active media should be considered. This raises an important point. The act of adding a metal nanoparticle into a system essentially removes active material from the solar cell and replaces it with metal, which cannot produce photogenerated charges. Hence, in order for plasmon-enhancement to occur, the nanoparticle must concentrate enough light in the near-field so that the generated photocurrent overcome the current loss incurred by occupying volume in the active layer. For this reason, the particle must be tuned to focus wavelengths of light that are otherwise lost by the system, not wavelengths that are currently fully absorbed by the active layer. In this particular QD system, the total thickness of the active layer is only 200 nm, whereas most systems of this type are closer to 300 nm. The film thickness is limited by the fabrication procedure used to create the nanoporous virus-

mesh. Hence, the devices need the plasmonic particles to absorb light not only at long wavelengths, but also shorter ones, which would otherwise pass through uncollected.

The external quantum efficiency, $EQE$, of the solar cell, which quantifies how many photons of a given wavelength incident on the solar cell are converted into collected charges, can be estimated by:

$$EQE(\lambda) = \eta_c \eta_a(\lambda)(1 - R(\lambda)) \tag{4.8}$$

where $\eta_a$ is the absorption efficiency, $\eta_c$ is the charge collection efficiency, and $R$ is the reflectance of the solar cell. For simplicity the following assumptions are made in the solar cell.

1. It is assumed that none of the incident light is reflected: $R = 0$. In reality this is not the case, but the reflectance of the actual device will be similar among all of the solar cells since the same materials are used for each embodiment. Hence, reflectance is taken to be zero for pure convenience.

2. It is assumed that the PbS QDs in the blend layer are fully depleted by the nanoporous virus-templated titania film. Therefore, any carriers generated within the blend layers will be efficiently transported by drift due to the built-in field in this region. Thus, it is assumed $\eta_c = 1$ within the blend layer.

3. For simplicity, it is assumed that the depletion region only encompasses the blend layer and does not extend into the random-packed QD layer above. The basis of this assumption is that there are less quantum dots and titania present in this layer than in a bilayer geometry, which causes the depletion width to be shorter than the typical value of ~150 nm. Therefore, the random-packed QD layer is assumed to be within the quasi-neutral region of the heterojunction where diffusion governs charge extraction. Hence, electrons that are generated deeper in the PbS QD film above the blend layer are less likely to diffuse to the depletion region for efficient collection. To capture this effect, an exponential decay envelop with a decay length of 30 nm, [121] corresponding to the diffusion

length of electrons in the PbS QD film, is used for the charge collection efficiency in the random-packed PbS QD film layer. Therefore:

$$\eta_c = \begin{cases} 1, & 0 \leq z \leq L_b \\ e^{-(z-L_b)/L_d}, & L_b < z \leq L_b + L_{QD} \end{cases} \tag{4.9}$$

where $L_b$ is the thickness of the titania-PbS QD blend layer, $L_{QD}$ is the thickness of the close-packed QD layer, and $L_d$ is the decay length (*i.e.* 30 nm).

The absorption efficiency, $\eta_a$, is determined by integrating the absorption efficiency density, $p_{abs}$, over the volume of the active layers, $V$:

$$\eta_a(\lambda) = \int_V p_{abs}(x, y, z, \lambda) dx^3 \tag{4.10}$$

The EQE can be estimated from the FDTD simulations by multiplying the normalized power absorption density provided by the 3D power monitor, *i.e.* $p_{abs}$, by the $\eta_c$ given in Equation 4.9, and integrating over the volume, $V$, of the active layer that contains the blend material or the random-packed PbS QD layer active materials (we exclude the power absorbed in the metal NP volume from consideration):

$$EQE(\lambda) = \int_V \eta_c(z) p_{abs}(x, y, z, \lambda) dx^3 \tag{4.11}$$

To account for the different geometrical configurations that the NP and NPL can have in the actual devices, the simulated EQE reported in Figure 4-12 is the ensemble average over all of the cases considered for that device type (i.e. 6 cases for No NPs, AuNPs, and AgNPs; 18 cases for AgNPLs). For the corrected AgNPL predictions, which instead simulate three differently sized nanospheres, a total of 18 cases are considered and the ensemble average is taken over this set.

Figure 4-12b and c, respectively, show the computed and measured EQE spectra for devices loaded with each type of silver plasmonic particle. The overall shape of the simulated and measured EQE spectra for the devices without nanoparticles are

remarkably similar, with a main peak arising around 375 nm followed by a slowly decaying profile at higher wavelengths. The simulations predict a clear plasmon-induced performance enhancement starting around 400 nm for AgNPs and 525 nm for AuNPs, which is in good agreement with the observed regions of power enhancement in the actual devices.

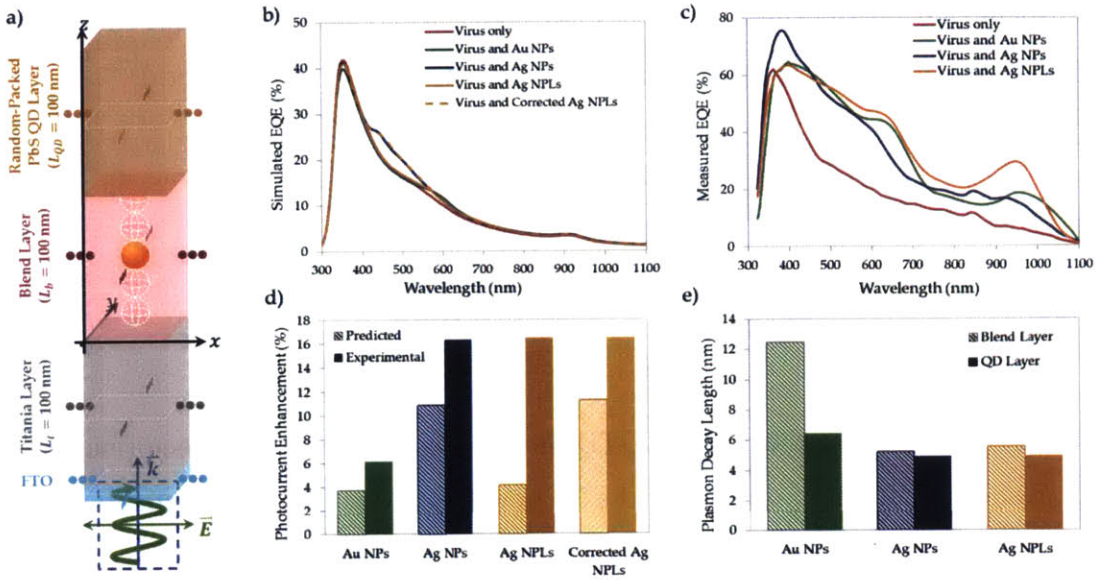


Figure 4-12: FDTD simulations we used to rationally design and predict the plasmon enhancement in devices containing metal nanoparticles. a) Geometry of simulations. b) Predicted and c) Measured EQE spectra for devices containing AuNPs, AgNPs or AgNPLs, compared to virus-only devices. Experimental EQE curves with metal nanoparticles were adjusted based on measured average short-circuit current values for each type of device. d) Predicted and measured photocurrent enhancement compared to virus-templated devices without nanoparticles. e) Predicted plasmon decay length for different nanoparticles embedded in the blend and random-packed QD layers.

The presented model clearly demonstrates for the Ag nanosphere case that the wavelengths between 400 and 600 nm where significant EQE enhancement occurs can be explained by LSPR acting to concentrate light in the near-field region surrounding the noble metal nanoparticles. This increases the photon flux incident on QDs located within the near-field, thereby increasing their rates of charge carrier generation.

Once the ensemble average quantum efficiency has been determined, the photocurrent enhancement for a given device type (i.e. no NPs, AuNPs, AgNPs, AgNPLs)

can be calculated by comparing the estimated short circuit photocurrent densities of the devices with metal NPs to that without. The short circuit current density can be predicted by:

$$J_{sc} = q\int_{\lambda_{min}}^{\lambda_{max}} EQE(\lambda)b_s(\lambda)d\lambda = \frac{q}{hc}\int_{\lambda_{min}}^{\lambda_{max}} EQE(\lambda)M(\lambda)\lambda d\lambda \tag{4.12}$$

where $q$ is the charge on an electron, $b_s$ is the photon flux of the AM 1.5 solar spectrum, $M$ is the spectral irradiance of the solar spectrum (which can be related to $b_s$ by: $M(\lambda) = b_s(\lambda)/E(\lambda) = \lambda b_s(\lambda)/hc$), $h$ is Planck's constant, $c$ is the speed of light, and $\lambda_{min}$ = 200 nm and $\lambda_{max}$ = 1200 nm for the simulations.

Therefore, the photocurrent enhancement factor, $EF$, is defined to compare the photocurrent produced in the plasmonic devices to that generated in the same device without metal NPs:

$$EF = \frac{J_{sc}^{NP}}{J_{sc}^{NoNP}} = \frac{\int_{\lambda_{min}}^{\lambda_{max}} EQE_{NP}(\lambda)M(\lambda)\lambda d\lambda}{\int_{\lambda_{min}}^{\lambda_{max}} EQE_{NoNP}(\lambda)M(\lambda)\lambda d\lambda} \tag{4.13}$$

The enhancement factor can be directly compared to the ratio of the short circuit current density, $J_{sc}$, for a unit cell with NPs to that without, $J_{sc}^{NP}/J_{sc}^{NoNP}$, which is presented in Figure 4-12d. The measured devices demonstrate higher photocurrent enhancement than the simulations predicted with the measured enhancement being 6.2%, 16.3%, and 16.5% for solar cells with AuNPs, AgNPs, and AgNPLs respectively, whereas simulations predicted 3.8%, 10.9%, and 4.2%. When the photocurrent is calculated for a polydisperse population of AgNPs that have been transformed from AgNPLs, the predicted enhancement rises to 11.3%. Although the predictions were lower than observed photocurrent enhancement, the trend is clearly captured. It is worth noting that devices with AgNPs in both the simulated and measured devices produce a photocurrent enhancement roughly three times larger than devices with AuNPs. As discussed in Section 2.1, gold experiences interband transitions in the visible range which increase the optical losses as a fraction of the incident photons are exciting electronic transitions rather than electron oscillations (*i.e.* plasmons). Although the

predicted and measured EQE profiles show that the shorter wavelengths are the most efficiently absorbed and converted into useable current, the silver nanoparticles are still able to produce a substantial amount of current in this range due to the improved ability of silver to concentrate light even though the resonance frequency is blue-shifted relative to gold.

### Calculating Plasmon Decay Length

Some information about why the plasmons are able to substantially improve the performance of the solar cells can be garnered by looking at how far the near-field penetrates into the surrounding active material. The distance over which the near-field generated by the metal nanoparticles via LSPR can penetrate into the surrounding active media was determined by analyzing line profiles of the absorbed power density taken through the center of the NP while at resonance. The resonance wavelength was determined as the simulated illumination wavelength that produced the largest absorbed power value outside the metal NP core. Figure 4-13 shows a contour plot of the absorbed power density of each NP device case at resonance taken through the center plane of the metal NP.

The influence of illumination wavelength on the penetration length of the near-field generated by the metal NP into the active media was investigated by sampling the absorbed power density along a line through the center of the metal NP (indicated by the yellow dotted line in Figure 4-13). Figure 4-14 plots this line profile for every simulated wavelength for all three NP types. It can be observed that although plasmon resonance increases the absorbed power most strongly at the LSPR wavelength, enhancement occurs over a spectral range of about 100 nm for the nanospheres and 200 nm for the nanoplate cases. It should also be noted that the spatially flat absorption line around wavelength 350 nm corresponds to the main absorption peak of the PbS QD rather than plasmon resonance of the metal NPs.

In addition to performing simulations with the metal NPs located within the blend layer, simulations were also performed with the metal NPs located within the random-packed PbS QD film layer in the absence of the blend layer (device structure: FTO

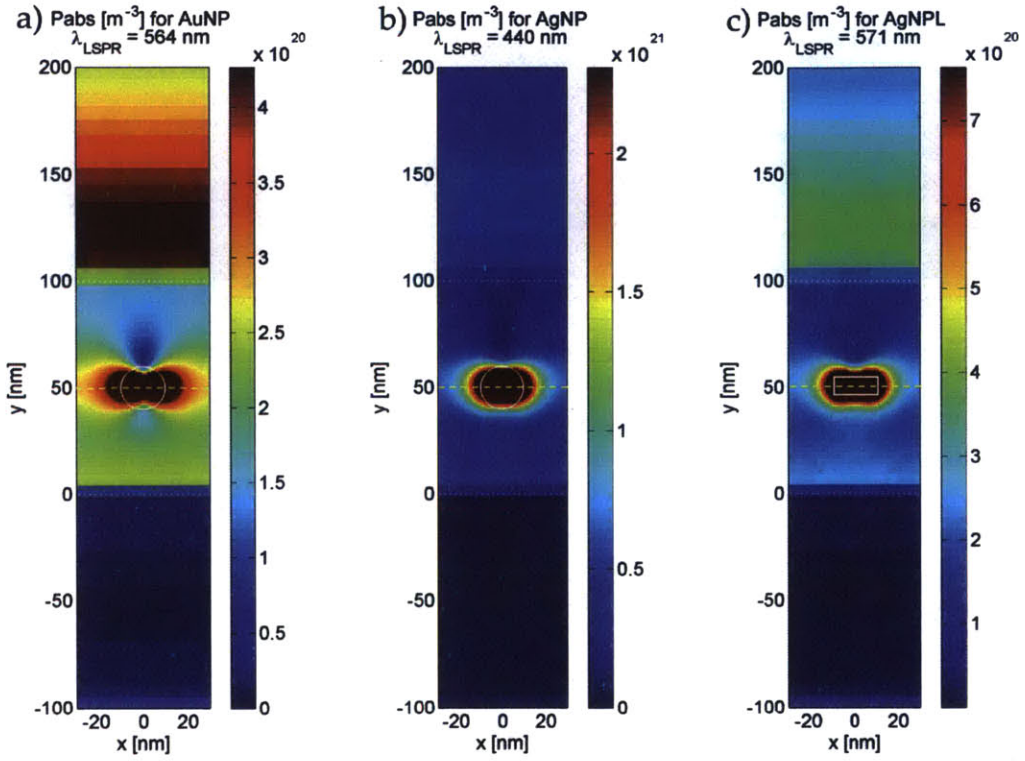


Figure 4-13: Contour plots of source-normalized absorbed power density, $p_{abs}$ [$m^{-3}$], throughout the simulated solar cell cross-section at a plane through the center of the a) AuNP at $\lambda$=564 nm, b) AgNP at $\lambda$=440 nm, and c) AgNPL at $\lambda$=571 nm. The dotted yellow line indicates the position where the line profiles are taken to determine the plasmon decay length.

(50nm)/Random-Packed PbS QD Layer (100 nm)/$MoO_3$). Figure 4-15 shows the power absorption density line profiles through the NP centers at the LSPR resonance peak and normalized to the maximum value within the active medium for each NP type embedded in both the blend (Figure 4-15a) and random-packed PbS QD layer (Figure 4-15b). The dotted line indicates that location where the normalized value reaches 1/e, which corresponds to the decay length. The plasmon decay lengths are tabulated in Table 4.2.

As demonstrated in Figure 4-12e, blending the PbS QDs with the titania nanoporous network provides an effective medium that allows the near-field surrounding the metal NPs to propagate further into the blend layer than they would if incorporated into

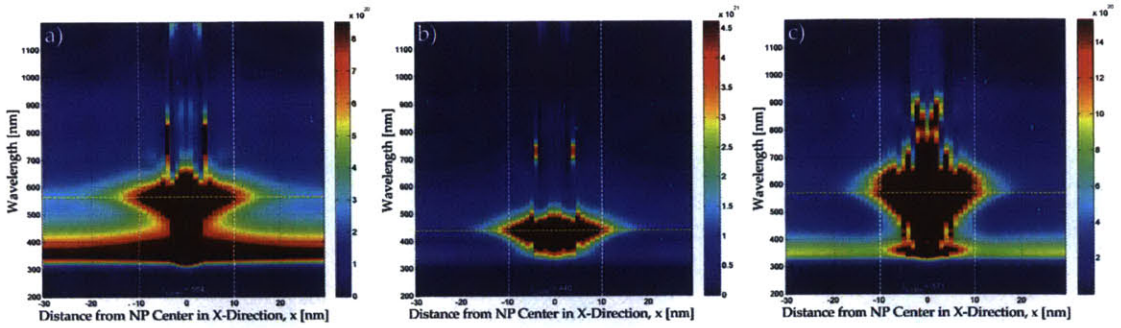


Figure 4-14: Line profile plots of source-normalized power density, $p_{abs}$, as a function illumination wavelength for a) AuNP, b) AgNP, and c) AgNPL (horizontal configuration). The dotted horizontal yellow line indicates the LSPR wavelength and the dotted vertical white lines indicate the edges of the metal NP. The area between the dotted white lines represents the power absorbed in the interior of the metal NP, whereas the area outside represents the power absorbed in the blend layer of the solar cell.

Table 4.2: The plasmon decay length is presented for each type of nanoparticle while embedded in either the blend or the random-packed QD layer.

| NP Type | Plasmon Decay Length, $L_D$ [nm] | |
|---|---|---|
| | Blend Layer | Random-Packed QD Layer |
| AuNPs | 12.46 | 6.43 |
| AgNPs | 5.23 | 4.92 |
| AgNPLs | 5.53 | 4.92 |

the random-packed QD layer. This is a direct result of the effective complex index of the blend layer being lower than the random-packed QD film by virtue of its lower volume fraction of PbS. This is useful from a practical standpoint because the larger the extent of the near-field, the greater the chance a PbS QD can experience a higher photon-flux and exist in a defect-free region that can efficiently generate and transport charge carriers. This illustrates that the effective optical properties of the bulk-heterojunction architecture are beneficial to further boosting plasmon-enhancement in practical devices.

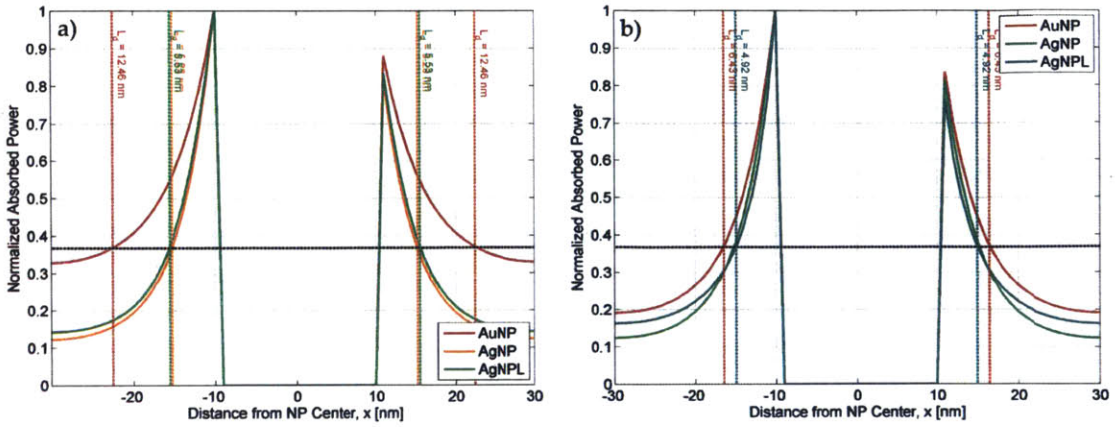


Figure 4-15: Line profile plots of absorbed power density normalized to the maximum value outside of the metal NP core for each of the NP types at the LSPR wavelength. The decay profile for the metal NPs embedded in (a) the blend layer and (b) the random-packed PbS QD layer of a device without the blend layer (a simple bilayer). The horizontal dotted black line represents the value 1/e, which corresponds to the decay length, indicated by the vertical dotted lines. The printed value $L_d$ is the decay length, *i.e.* the distance from the NP surface when a normalized value of 1/e is reached. Note that profiles appear slightly asymmetric due to the way the simulation domain was meshed.

### 4.3.3 Modeling Voltage Increase in Plasmon-Enhanced Solar Cells

The optical model presented in the previous sections can only explicitly account for enhancement of the device photocurrent and cannot account for any differences in parasitic resistances and the fill factor between devices, which fortunately do not change significantly between virus-based solar cells with and without plasmonics NPs. However, an increase in both $V_{oc}$ is observed for each of the plasmonic devices, which suggests that the incorporation of metal nanoparticles into the active layer is responsible for this improvement.

It is possible that the increased open-circuit voltage, $V_{oc}$, is simply a natural result of the plasmonic solar cells producing a higher photocurrent. The intuition behind this notion is that the standard diode model of solar cells couples together the bias voltage and the photocurrent according to Equation 1.10. Therefore, it would be expected that if the same device would somehow generate a higher current (for

instance due to improved light harvesting by LSPR), then the open-circuit voltage would also increase accordingly. Figure 4-7e shows that the measured JV curves of the virus-based solar cell without NPs has a similar shape to that of the virus-based solar cell that has been assembled with AgNPLs, and one could imagine that the curve for the AgNPL device might be almost reproduced if the virus-only curve was translated along the $y-$axis to match the short-circuit current values. This hypothesis was tested by fitting the measured JV data to the standard diode equation for solar cells that includes parasitic resistances given in Equation 1.10.

The series and shunt resistances were determined by calculating the inverse of the slope of the measured $JV$ curves near the $x-$intercept and $y-$intercept, respectively. Likewise, the dark and light short-circuit current densities were determined from the measured light and dark $JV$ curves for each of the devices by finding the current density when the applied bias voltage is equal to zero. The ideality factor, $m$, characterizes how far the actual solar cell behavior deviates from an ideal diode ($m = 1$) while under illumination. This factor was determined for each applied bias by rearranging Equation 1.10:

$$m = \frac{q(V + JAR_{sr})}{k_b T}\left[\ln\left(\frac{J_{sc} - J_0 - \frac{V+JAR_{sr}}{R_{sh}}}{J_0}\right)\right]^{-1} \tag{4.14}$$

The calculated ideality factor for illuminated devices are plotted in Figure 4-16 for the devices made from $TiO_2$ paste (no virus), the virus-film device without metal NPs, and the virus-film device with AgNPLs.

The advantage of the standard model described by Equation 1.10 is that every term represents a physical characteristic of the solar cell. Thus, changes in solar cell performance can be predicted by adjusting some of these terms and solving the equation. Now that the parasitic resistances and the ideality factor have been determined from the measured light JV curves, it can be predicted how a given device would perform if it were able to somehow generate a different photocurrent. By taking the values for $R_{sr}$, $R_{sh}$, and $m(V)$ determined for the *virus-film solar cell without plasmonic nanoparticles* and plugging them into the standard model, but now substi-

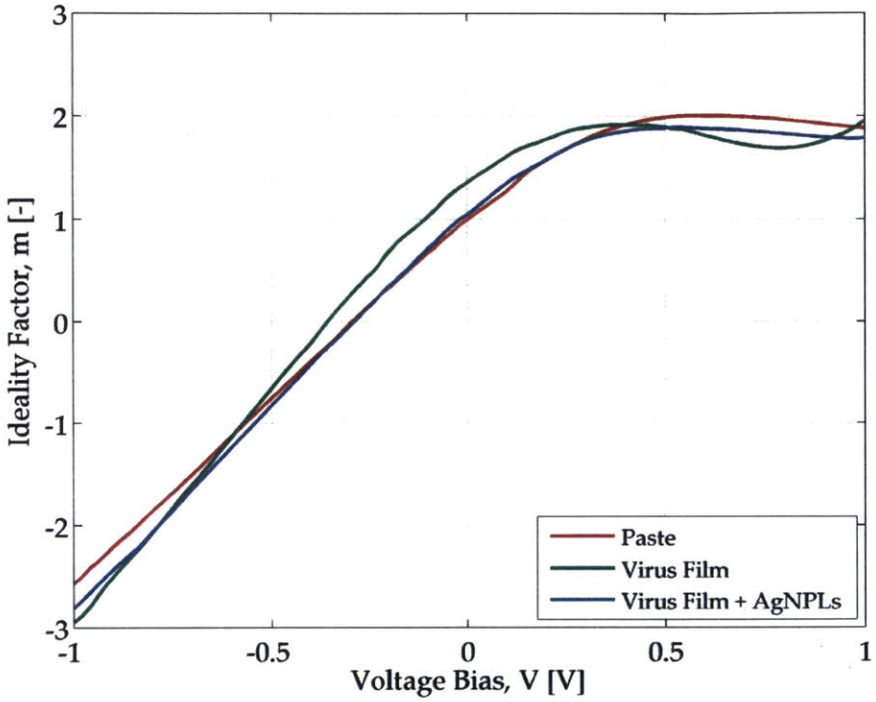


Figure 4-16: The ideality factor as a function of applied voltage bias, as determined from the measured JV curves while illuminated (*i.e.* the light ideality factor)

tuting the $J_{sc}$ and $J_0$ values measured for the *virus-film solar cell with AgNPLs*, the $JV$ curve can be predicted for how the non-plasmonic virus-based solar cell would perform if it could suddenly generate the current measured in the virus-based device with AgNPLs. This was accomplished by numerically solving the transcendental diode equation with these values; the result is plotted in Figure 4-17. The fact that the predicted $V_{oc}$ is so close to that measured for the virus-based device with AgNPLs strongly indicates that the increase in open-circuit voltage shown by the plasmonic solar cells is a natural result of the increase in photocurrent that results from the improved light harvesting in the device via LSPR by the metal NPs. It could be argued that any difference in fill-factor between the measured curve for the virus-based device with AgNPLs and the curve predicted from the non-plasmonic virus solar cell is due to slight variations in the device morphologies that produce slightly different series and shunt resistances.

Therefore, the effect of LSPR conveniently causes both the $J_{sc}$ and $V_{oc}$ to rise in the plasmonic devices, causing the observed overall enhancement in PCE to be even

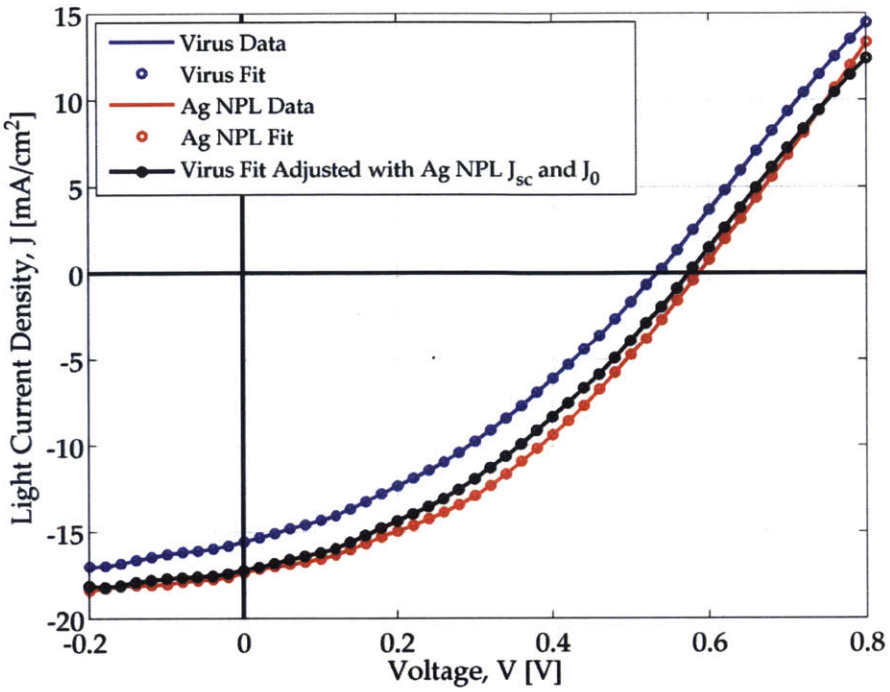


Figure 4-17: The measured light $JV$ curves for the virus-film solar cell without plasmonic NPs (solid blue line) and the virus-film solar cell with Ag NPLs (solid red line), with the open circles indicating the predicted curve that has been fit to the standard solar cell equation given in Equation 1.10. The black line represents the predicted $JV$ curve from standard diode equation of the non-plasmonic virus-film solar cell (solid blue line) if it generated the short-circuit photocurrent produced by the virus-based device with Ag NPLs.

higher.

## 4.4 Conclusion

Significant care was taken in this study to model the optical behavior of this nanoscale composite solar cell architecture in order to definitively demonstrate that the improvement observed in the devies with metal nanoparticles was caused by localized surface plasmon resonance. This was accomplished by being able to predict the observed trend in photocurrent enhancement as well as the spectral regions of observed EQE enhancement. Unfortunately, the solution-processed solar cell community at large generally abuses the term "plasmon-enhancement" by claiming that any difference in performance between a device with and without nanoparticles must be attributed to

LSPR without substantial modeling to support the claim. The issue in part is due to the fact that synthesizing metal nanoparticles and blending them into devices is fairly straightforward, that it is commonly attempted without sufficient understanding of how performance should be affected from an optics point of view. It is often the case that experimental EQE curves are presented in articles that do not show any boost in efficiency specifically at the expected wavelengths of LSPR enhancement, but instead show a uniform EQE improvement across the entire spectrum. This occurrence is evidence that the increases in photocurrent are in fact *not* due to plasmon resonance, since the phenomenon of LSPR is strongly wavelength dependent. Rather, uniform increases across the spectrum suggest there is an improvement in charge collection, which might be the result of serendipity or changes in processing conditions, which might somehow reduce material defects, change interfacial contacts, or alter material crystallization, for instance. Furthermore, often device improvements are not proven to be statistically significant by repeating experimental conditions over multiple batches of nominally identical devices. Especially in polymer-fullerene solar cells where the active thicknesses are often less than 100 nm, small variations in thickness between nominally identical devices could have a profound impact upon efficiency. Hence, simply comparing a single $JV$ curve without nanoparticles against one with them included is not sufficient to make any serious claims and the community at large needs to ensure that publications provide sufficient statistical evidence that trends are repeatable.

Lastly, although plasmon enhancement can take a material that is limited by carrier collection and often improve its ability to reclaim some light that is lost. However, in the grander picture of photovoltaics, this approach is not a practical way forward to translate solution-processed materials to commercialization. The reason is two-fold:

1. The driving force behind photovoltaics is inherently cost. Hence, adding gold and silver even in small quantities is unlikely to generate cost savings. Commercializing a polymer solar cell, for instance, would be more likely if new polymers were developed that were simply better solar materials.

2. Plasmon-enhancement is only significant for devices that are already poor solar performers. Devices that already achieve high-efficiency do not garner a large boost in performance upon adding metal nanoparticles because they generally already do a good job of absorbing light and transporting charges to begin with. That is, they have already overcome the trade-off between light harvesting and current collection.

Although the physics is very interesting, the approach of plasmon-enhancement is ultimately only a stop-gap solution to squeeze some additional performance out of materials that are not competitive with conventional photovoltaic semiconductors, like Si and GaAs. Plasmonic solar cells are interesting to researchers in nanophotonics because it offers a trendy application for nanoscale phenomena, however the solar cell community at large does not view this approach as being valuable to solving the greater issues facing current solar technologies. On the other hand, other strategies for managing photons such as generating anti-reflective layers and tandem devices are incredibly important for allowing high performance solar cells to maximize the use of every photon that is incident on the solar cell. An excellent example of this is the champion single-junction GaAs solar cells developed by Alta Devices that achieved record performance by controlling the optics of interfaces to promote photon recycling through simple, yet effective light trapping strategies.

Therefore, the remaining two chapters of this dissertation will leave the realm of nanophotonics and focus on alternate approaches to improving photovoltaic performance at the nanoscale by modifying *material* properties of solution-processed solar materials, specifically organic-inorganic hybrid perovskites.

# Chapter 5

# Computational Screening of Mixed-Metal Perovskite Materials for Photovoltaic Applications

Inorganic-organic hybrid perovskites are an exciting new class of solar materials that have become the leading field of research in emerging photovoltaic technology. Having risen from an initial efficiency of 3% [28] to over 20% [122] in less than five years, perovskites promise to be the long-sought material class capable of producing efficient, thin, and inexpensive solar cells that are synthesized from earth abundant materials. If the current pace of development holds steady, it is likely that perovskites will not only swiftly translate out of the research laboratory and into the energy marketplace but overtake crystalline silicon as the leading solar material. One of the main issues that threaten this outcome is that all of the highest performing perovskite materials are based on Pb and are inherently toxic. The safety concern regarding this material is compounded by the fact that these ionic perovskite crystals are soluble in several solvents, including water.

The goal of this chapter is to theoretically screen through a postulated set of perovskites with mixed-metal compositions to identify new materials that retain the desirable photovoltaic characteristics of the standard methylammonium lead triiodide, $MAPbI_3$, perovskite material but are substantially less toxic. This effort is intended

to establish the feasibility of these materials and provide insight that will guide experimental attempts to synthesize those that are the most promising. To accomplish this task, density functional theory (DFT) was used to predict the crystallographic and electronic properties of several candidate materials comprised of multiple metal species. As introduced in Chapter 1, DFT is a computational quantum mechanical modeling method that calculates the spatially dependent electron density and total energy for a given arrangements of atoms or molecules. From this information, the DFT code can calculate additional output quantities such as atomic forces, stresses, and positions within the system. A self-consistent loop can be performed on a simulated system where:

1. The total energy, electron density, and atomic forces acting on each atom is calculated for an initial configurations of atoms.

2. The atomic positions are allowed to relax to a more favorable position by displacing each according to the net force acting on it.

3. The process repeats until the lowest total energy state is found for the system within a specified tolerance limit (estimated energy error is less than 1e-9 Ry).

4. The lattice constants and electronic bandstructure are then calculated for the lowest energy configuration.

Since perovskite materials are crystalline bulk semiconductors, the calculations were performed for only the unit cell of the material and periodic boundary conditions were applied in all three spatial directions to reduce the computation time. The technique is generally computationally intensive and requires the use of supercomputing clusters to calculate relevant material parameters. Therefore, calculations were performed judiciously to obtain the most important metrics and some parameters that are usually calculated with DFT were omitted, such as density of states (DOS) and projected density of states (pDOS) quantifications.

## 5.1 Motivation

The rapid paradigm shift of the emerging photovoltaics field from liquid-state to solid-state devices was catalyzed by the discovery that the solution-processable organic-inorganic hybrid $ABX_3$ perovskite, $CH_3NH_3PbI_3$ (methylammonium (MA) lead triiodide), could produce solar cells that were stable at ambient conditions and displayed power conversion efficiencies exceeding 8%. [123] This finding challenged the long-held reign of dye-sensitized solar cells as the premiere solution-processed solar technology by matching their power conversion efficiencies while replacing the liquid-based electrolyte with a solid-state hole transporter. As illustrated by Figure 5-1, perovskite materials have a characteristic $ABX_3$ crystal structure. Solar materials generally use an organic cation (methylammonium, $MA^+$, or formamidinium, $FA^+$) as the A-site cation, $Pb^{2+}$ or $Sn^{2+}$ as the B-site cation, and a halide anion ($Cl^-$, $Br^-$, or $I^-$) at the X-site with $MAPbI_3$ and $FAPbI_3$ being the most well-studied, high-performing solar materials of this type. Perovskite solar cells generally adopt a *p-i-n* device architecture, illustrated by Figure 5-2a where the active material is used intrinsically (*i.e.* without external doping) and is sandwiched between an *n*-type and a *p*-type material. When the perovskite is stacked between *n*-type anatase $TiO_2$ and the *p*-type solid-state hole transporter 2,2',7,7'-tetrakis-(N,N,-di-p-methoxyphenyl-amine)9,9'-spirobifluorene (spiro-OMeTAD), devices have achieved efficiencies exceeding 15% [29,124,125] with open-circuit voltages up to 1.07 V using scalable solution processing or vapor phase deposition methods. The high photovoltaic efficiency of these lead-based devices has been attributed to the material's near-optimum band gap of ~1.6 eV and high carrier mobilities, which allow a significant portion of sunlight to be absorbed and the efficient extraction of charges from the sites of photogeneration. Experimental measurements have shown that lead perovskites can display carrier diffusion lengths greater than 1 $\mu$m, [126,127] which is a remarkable achievement for multi-crystalline, solution-processed materials.

Although lead-based hybrid perovskites are the most commonly studied, there are serious concerns about their practical incorporation into next generation photovoltaics

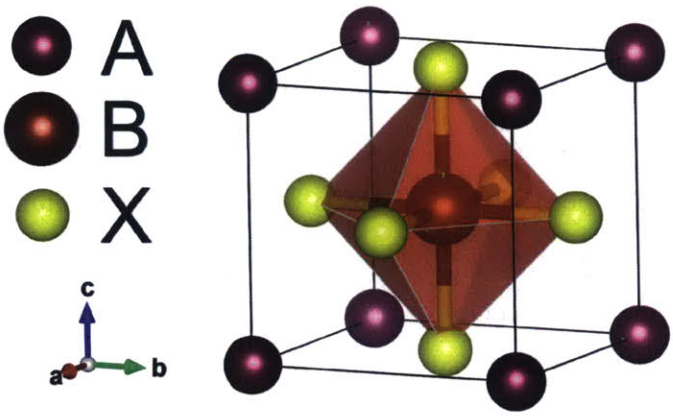


Figure 5-1: Schematic of the simplified $ABX_3$ perovskite crystal structure. The A-sites are generally occupied by an organic cation, the B-sites by a metal cation, and the X-sites by halide anions.

due to the toxicity of lead compounds. Only recently has the field begun to branch out in search of environmentally-friendly analogues that could display comparably high photovoltaic performance and the main focus has centered around tin. Also a group 14 metal, tin demonstrates similar chemical behavior to lead, which enables the formation of $ABX_3$ perovskites that are analogous to the traditional Pb-based solar materials using the same reaction pathway and fabrication procedures. [128,129] Similarly, perovskite materials have been synthesized from germanium, another group 14 element, but have not yet been incorporated into working devices. [130]

In order to maintain bulk neutrality of the $ABX_3$ crystal, the A-site cation must have a $+2$ oxidation state since the valency of the halide is fixed at $-1$ and the methylammonium at $+1$. However, the stability of the $+2$ oxidation state decrease as one travels up the group 14 elements. [131] While $MAPbX_3$ compounds are stable under ambient conditions, the photovoltaic performance of pure $MASnX_3$ tends to quickly degrade once removed from an inert atmosphere as the $Sn^{2+}$ ions oxidize to $Sn^{4+}$, which disrupts the charge neutrality of the perovskite compound and induces phase separation into tin oxides or hydroxides and methylammonium iodide. [128] Nonetheless, $MASnI_3$ devices with efficiencies over 6% have been achieved by performing the materials synthesis, device fabrication, and sealing procedures in an inert atmosphere

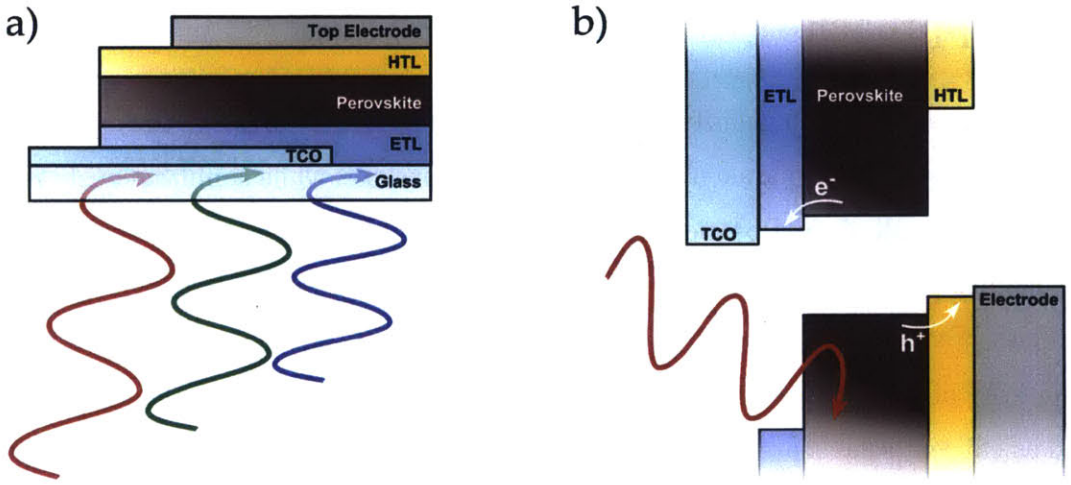


Figure 5-2: Schematic of conventional perovskite solar cells. (a) The conventional device architecture used for perovskite solar cells forms a *p-i-n* heterojunction stack where the hole transport layer (HTL) functions as the *p*-type material, the perovskite is the intrinsic active material, and the electron transport layer (ETL) is *n*-type. (b) The simplified flat-band energy diagram for the conventional architecture allows for electrons to be extracted at the transparent conductive oxide (TCO) and holes to collect at the top electrode and await electron injection back into the device.

before performing device characterization. [128] Although the crystal structures between $MAPbI_3$ and $MASnI_3$ are nearly identical, studies demonstrate that the band gap and band edge locations are different, with $MASnI_3$ exhibiting a narrower band gap around 1.2 eV and open-circuit voltages up to 880 mV in actual devices. [128, 132]

Mixed Pb:Sn perovskites can also be generated by mixing the $PbI_2$ and $SnI_2$ precursors in the proper molar ratios during the synthesis of perovskite films. While investigating such materials, Ogomi *et al.* reported that these mixed metal perovskite films can remain stable under ambient conditions when a critical amount of $Pb^{2+}$ is incorporated into the lattice and that the band gap and band edges locations can be tuned by varying the ratio of $Pb^{2+}$ to $Sn^{2+}$ content in the crystal. [129] Therefore, combining various metals ions into mixed-metal hybrid pervoskite materials provides an opportunity to rationally design non-toxic next generation solar cell materials that might be stable without encapsulation and have electronic properties that are tunable with compositional changes.

## 5.2 Approach

The goal of this work is to identify less-toxic solar materials that preserve the excellent photovoltaic properties characteristic of pure Pb perovskites while simultaneously replacing some or all of the $Pb^{2+}$ ions. To accomplish this, criteria was first established that qualifies a theoretical crystal as a promising solar material. Second, a pool of candidate mixed-metal perovskite materials was designed that are rationally based on the $MAPbI_3$ and $MASnI_3$ materials that have been previously experimentally validated as efficient solar materials. Third, computations were performed to numerically predict important metrics that are necessary for any material to exhibit reasonable photovoltaic behavior. Finally, the predicted properties of mixed-metal materials were compared against those calculated for the pure Pb and Sn perovskites to look for trends in behavior upon B-site substitution. Those candidates that met all the criteria for a theoretical solar material were identified as final candidates that should be attempted experimentally to validate the numerical predictions of electronic and crystallographic properties.

### 5.2.1 Defining Criteria for Efficient Solar Materials

In order for a computational screening approach to identify new solar material compositions, criteria must first be established that quantify the qualities of a "good theoretical photovoltaic material". The simplest way forward is to recount the basic physical mechanisms involved in producing electricity from solar cells and identify the material parameters that promote efficient operation. A good solar material must be a semiconductor that is capable of absorbing light over much of the visible spectrum and producing photogenerated charge carriers. As discussed in Section 1.1.2, the detailed balance limit presents an inherent trade-off in device performance between photocurrent and photovoltage that is a function of the material band gap. As depicted graphically in Figure 1-5, the theoretical efficiency of solar materials is maximized when the band gap is near 1.4 eV. Band gaps higher than this are capable of generating higher photovoltages, but will have a reduced photocurrent since less

infrared light will be absorbed. Similarly, materials with lower band gaps will produce additional current from longer infrared wavelengths, however the photovoltage will be reduced as excited charge carriers will thermalize to the band edges, which are now closer together. *Therefore, we are interested in solar materials that display band gaps that are as close to 1.4 eV as possible.*

Upon generating electron-hole pairs, good solar materials must be capable of separating those charges and transporting each species to its respective electrode. The *p-i-n* device architecture commonly used in perovskite solar cells establishes a built-in electric-field across the thickness of the perovskite allowing charges to be collected by drift during operation. In most thin film solar cells, the thickness of the intrinsic layer must be smaller than the depletion width and limits the thickness of the active layer. However, solar materials with sufficiently high carrier diffusion lengths allow useable charges to be collected from the quasi-neutral region where the electric field has been completely screened by residual background charges from impurities. *Therefore, a good theoretical perovskite solar material is expected to have high mobilities, or equivalently, low effective masses for both free electrons in the conduction band edge (CBE), $m_e^*$, and free holes in the valence band edge (VBE), $m_h^*$.*

When the photogenerated charges are transported out of the bulk perovskite crystal through drift and diffusion mechanisms, they must be efficiently collected by the flanking *n*- and *p*-type charge transport layers as shown by the flat band diagram in Figure 5-2b. *To do so, the conduction and valence band edges of all three materials in the* p-i-n *structure must favorably align to promote electron extraction at the* i-n *heterojunction and electron injection at the* p-i *heterojunction.* If the edges are misaligned when all three materials are in physical contact, electronic barriers will form at the interfaces that impede current collection. It is highly desirable that the band edges of new solar materials be compatible with known electron (ETL) and hole transport layers (HTL), such as $TiO_2$ or phenyl-C61-butyric acid methyl ester (PCBM) and spiro-MeOTAD or poly(3,4-ethylenedioxythiophene) polystyrene sulfonate (PEDOT:PSS), respectively.

In order for any solar material to attain practical use in devices, it must be not

only thermodynamically stable at rest but also stable during device operation. This is a point of concern for perovskite materials. As a result of its ionic nature, there is the possibility that ions could migrate throughout the crystal or that the bulk material will phase separate back into its precursor materials in various environments. In fact, it is well-known that the traditional $MAPbI_3$ material phase separates into MAI and $PbI_2$ when humidity is high. Likewise, the crystal destabilizes at elevated temperatures near 150°C and methylammonium iodide evaporates out of the bulk crystal. The perovskite can be stabilized by replacing the organic $MA^+$ cations at the A-site with $FA^+$, [32] however the long-term stability required for sustained operation in the field remains to be proven with this material. Before such affects are even a concern, it must first be established that a mixed-metal perovskite material is more stable in the $ABX_3$ crystal than as its separate constituent precursors. *Hence, it must be ensured that any promising theoretical mixed-metal perovskite would theoretically form and remain stable at the calculated conditions.*

Each of these four qualities of desirable solar materials are summarized in Table 5.1. It must be mentioned that there are always many other factors that affect device performance that are difficult to predict theoretically, such as grain size, defect formation in the film, or the presence and character of sub-gap states that provide non-radiative recombination pathways. Therefore, even though certain materials might demonstrate theoretically desirable properties, it might be difficult to synthesize a postulated material in sufficient purity to make practical use of it in solar cells. The results from any calculations must only be viewed as *guidelines* that suggest solar performance is possible and predictions must be confirmed with experimentation.

### 5.2.2 Selecting Initial Candidates

The governing premise behind this work is that by replacing only a portion of the metal content in $MAPbI_3$ and $MASnI_3$ perovskite crystals with a second metal species, it might be possible to develop less-toxic or wholly non-toxic perovskites with tunable material properties that retain the excellent overall photovoltaic behavior of the pure materials. In other words, the goal is to *perturb* the electronic structure of the

Table 5.1: Summary of Criteria for Classifying a Hypothetical Perovskite Material as a Good Theoretical Photovoltaic Material

| | Characteristic | Metric | Criterion |
|---|---|---|---|
| 1 | Absorb over Visible Spectrum | Band Gap, $E_g$ | $E_g \approx 1.4eV$ |
| 2 | Efficient Carrier Transport | Effective Mass, $m_e^*$ and $m_h^*$ | Minimize($m_e^*$, $m_h^*$) |
| 3 | Thermodynamically Stable | Total Energy, $E$ | $E_{ABX_3} < \sum_{precursors} E$<br>$E_{ABX_3} < \sum_{phases} E$ |
| 4 | Charge Extraction | Band Edge Locations, $CBE$ and $VBE$ | $CBE_{ABX_3} < CBE_{ETL}$<br>$VBE_{ABX_3} > VBE_{HTL}$ |

perovskite in an effort to reduce toxicity and potentially improve the stability of the crystals.

The pool of candidate mixed-metal perovskite materials was constrained by the following conditions:

1. The A-site cation and X-site anion are fixed as $MA^+$ and $I^-$, respectively.

2. No more than two different B-site species should exist in the same compound.

3. Mixed B-site systems must result in a neutral crystal.

4. All secondary B-site cations, B′, must be relatively non-toxic.

5. All B-site cations must form a stable iodide salt with the proper oxidation state.

Constraints 1 and 2 were imposed for simplicity and Constraint 3 out of physical necessity. Constraint 4 is a requirement if the mixed-metal perovksites are to be less toxic than the pure Pb materials. Constraint 5 was imposed so that the simplest chemical reaction pathway used to synthesize triiodide perovskites, written in Equation 5.1, with either solution-processing or thermal evaporation might be maintained to make the mixed-metal analogs.

$$PbI_2 + MAI \rightarrow MAPbI_3 \quad \text{and} \quad SnI_2 + MAI \rightarrow MASnI_3 \tag{5.1}$$

Therefore, potential replacement metal species, B′, were restricted to those that form stable iodide salts of the proper valency.

Three sets of candidate materials were developed based on mixtures of Pb, Sn, or Bi. Although lead-mixtures, $MA(Pb:B')I_3$, are still inherently toxic, these have the greatest chance of successful implementation into devices as Pb-based perovskites are the most well-studied and generate the highest performing devices. However, it would be desirable to narrow the band gap slightly from 1.6 eV to a value closer to 1.4 eV in the mixed-metal systems. Tin-mixtures, $MA(Sn:B')I_3$, are structurally analogous to the lead-mixtures but offer the potential of being wholly non-toxic. The band gap of $MASnI_3$ is around 1.2 eV [128, 133], thus it is hoped that replacing a portion of Sn atoms with a second species will widen the band gap slightly to bring it closer to the ideal value. Bismuth was chosen to be the basis for the third set since it is only one column removed from lead and is the least toxic of all the heavy metals. Evaluating bismuth-mixtures, $MA(Bi:B')I_3$, provides the interesting opportunity to see how choosing an element outside of the Group 14 elements would impact the electronic character of the perovskite material. While $B'^{2+}$ ions can be mixed with $Pb^{2+}$ or $Sn^{2+}$ in any ratio, the candidate materials chosen focus mostly on blends where 25% of the Pb or Sn ions are replaced with B′, denoted throughout the study as $MA(3Pb:1B')I_3$ and $MA(3Sn:1B')I_3$, in an effort to investigate how substituting a second metal species at some of the B-sites would perturb the $MAPbI_3$ and $MASnI_3$ systems. However, some of the most promising 3Sn:1B′ mixtures were further studied with 1:1 ratios, $MA(2Sn:2B')I_3$, to assess the impact of further B-site substitution. On the other hand, bismuth ions most commonly have an oxidation state of +3 and exist in a precursor form as $BiI_3$. In order to meet bulk neutrality with the $ABX_3$ lattice, all bismuth-based perovskites must be blended with a monovalent metal species (*i.e.* $B'^{+}$) in equal molar proportions to form $MA(2Bi:2B')I_3$ materials.

Figure 5-3 presents the iodide compounds that are available across the periodic table and those that were chosen for investigation in this study. Of the available divalent iodide salts that could be mixed with $PbI_2$ and $SnI_2$, the salt for Be, Ba, Cd, Hg, and Tl were excluded from consideration due to their toxicity. Although AuI

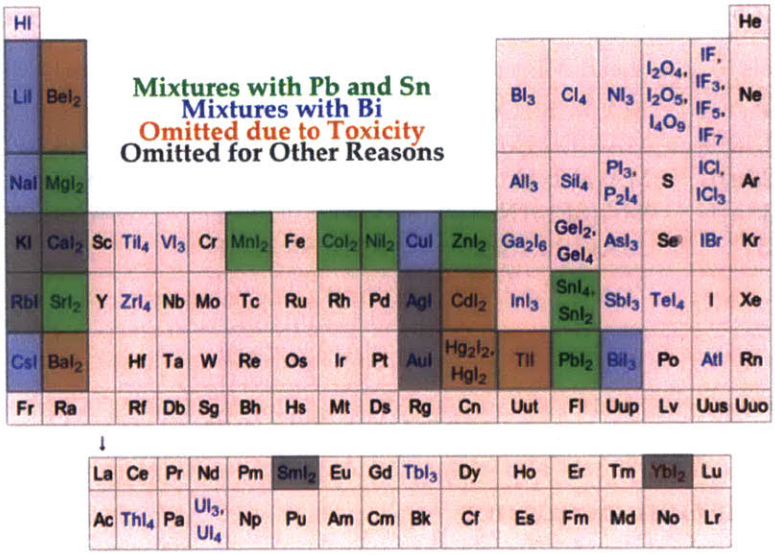


Figure 5-3: Iodide compounds that are available across the entire periodic table. Divalent metal species blended with Pb and Sn are highlighted in green. Monovalent metal species blended with Bi are highlighted in blue. Elements omitted from the study for reasons of toxicity or otherwise are highlighted in red and orange, respectively.

and AgI are non-toxic and could be blended with $BiI_3$, they were excluded due to their high cost. Likewise, the divalent lanthanide salts, $SmI_2$ and $YbI_2$, were excluded because of the difficulty in properly capturing the behavior of $f$-shell electrons with a pseudopotential. To further reduce the number of computations that need performing, the largest and smallest non-toxic alkali and alkali earth metals were used, whereas some of the intermediate sized ions were omitted. It was assumed that the characteristics of the intermediate ions would be bounded by the extremes since the chemical behavior of the ions in each column is expected to be very similar. Hence, KI, RbI, and $CaI_2$ were omitted from the study.

In order to ensure that the DFT calculations produce reasonable results, a set of control devices comprised of pure Pb and Sn as well as several Pb:Sn mixtures were included in the candidate pool so that predictions of lattice parameters, band gap, and effective carrier masses could be benchmarked against published experimental values. The full set of perovskite compositions considered in this computational study is listed in Table 5.2.

Table 5.2: Pool of Mixed-Metal Perovskite Candidates by Series

| Controls | Lead-Mixtures | Tin-Mixtures | Bismuth-Mixtures |
|---|---|---|---|
| $MAPbI_3$ | $MA(3Pb:1Co)I_3$ | $MA(3Sn:1Co)I_3$ | $MA(2Bi:2Cs)I_3$ |
| $MA(3Pb:1Sn)I_3$ | $MA(3Pb:1Mg)I_3$ | $MA(3Sn:1Mg)I_3$ | $MA(2Bi:2Cu)I_3$ |
| $MA(2Pb:2Sn)I_3$ | $MA(3Pb:1Mn)I_3$ | $MA(3Sn:1Mn)I_3$ | $MA(2Bi:2Li)I_3$ |
| $MA(1Pb:3Sn)I_3$ | $MA(3Pb:1Ni)I_3$ | $MA(3Sn:1Ni)I_3$ | $MA(2Bi:2Na)I_3$ |
| $MASnI_3$ | $MA(3Pb:1Sr)I_3$ | $MA(3Sn:1Sr)I_3$ | |
| | $MA(3Pb:1Zn)I_3$ | $MA(3Sn:1Zn)I_3$ | |
| | | $MA(2Sn:2Mg)I_3$ | |
| | | $MA(2Sn:2Ni)I_3$ | |
| | | $MA(2Sn:2Sr)I_3$ | |
| | | $MA(2Sn:2Zn)I_3$ | |

### 5.2.3 Calculation Sequence

Although the details of the computations are discussed in the Section 5.3, a particular sequence of calculations was performed to predict the relevant crystallographic and electronic properties of each candidate material listed in Table 5.2. In order to calculate the band gap, effective carrier masses, total energy, and band edge locations required to evaluate each material against the criteria for future consideration listed in Table 5.1, the following calculations were performed:

1. Postulate an initial crystal structure based on available literature or prior calculations for the given material composition.

2. Relax the crystal structure in all three dimensions to find the lowest energy atomic configuration. This provides the lattice constants for the crystal.

3. Repeat Step 2 for all possible atomic arrangements that exist for the material (*i.e.* for a material with 1 B′ and 3 B atoms, there exist four possible arrangements, one where the B′ atom occupies a different B-site in the postulated lattice). Use the relaxed crystal structure from the first arrangement evaluated as the starting point for the others. The arrangement with the lowest total energy is the most probable one and is used for the following calculations.

4. Calculate the band structure. This provides the band gap, Fermi level energy, and band edge locations relative to the Fermi level.

5. Recalculate the band structure for all major crystallographic directions and estimate the effective carrier masses from curvature of the band edges.

6. Relax the crystal structure for each of the precursor compounds and compare the ensemble energy of the reactants to the total energy of the perovskite product. Likewise, compare the energy of a mixed-metal perovskite to a corresponding system that has formed multiple material phases. This indicates whether a material is thermodynamically favorable.

7. Perform slab calculations to estimate the workfunctions and absolute band edge locations.

This calculation sequence allows the lattice parameters, band gap, effective carrier masses, and thermodynamic stability of each candidate material to be quantitatively assessed. Slab calculations were performed to estimate the workfunctions for different terminations of the (001) surface of the perovskite lattice. This scheme allows the "flat band" energy levels to be roughly estimated for a material that is physically isolated from other materials, which can be compared with some accuracy against measurements of the absolute position of the VBE and Fermi level with respect to the vacuum energy level obtained with ultraviolet photoelectron spectroscopy (UPS). However, this approach is not entirely accurate because other crystal facets besides the (001) surface will be displayed in the grains of actual perovskite films and workfunction measurements will be a weighted ensemble average of the set of these surfaces. Furthermore, complete understanding of the energetics that arise when a perovskite material is in physical contact with the HTL and ETL materials in actual solar cells, requires performing slab where the perovskite crystal is in contact with a reference material such as anatase titania in order to capture the influence of dipoles at these interfaces. Simulating stacked superlattices of both materials would involve hundreds of atoms, which is too many for the DFT software to handle. Even if calculations were possible, the result would still be specific for the particular termination of the perovskite and anatase $TiO_2$ crystals comprising the interface. Since, the perovskite films are not epitaxially grown on the titania layers, the nature of the interface is

not controlled. Hence, trying to predict interface energetics for the material stacks commonly used in perovskite solar cells was considered to be too costly given the expected uncertainty in the results.

## 5.3 Computational Methods

The relaxed crystal structure and electronic properties of each candidate material were calculated using density functional theory with the generalized gradient approximations (DFT-GGA). Specifically, DFT-GGA calculations used the PBE exchange-correlation functional [134] and were performed on the Stampede cluster at the Texas Advanced Computing Center (TACC) or the Hopper Cluster at the National Energy Research Scientific Computing Center (NERSC) with the PWSCF code of Quantum Espresso v5.0.1. [135]

All bulk material calculations were performed on the orthorhombic phase of the hybrid pervoskite with the unit cell comprised of four repeated units of $MABI_3$. Periodic boundary conditions were placed on the calculation volume in all three directions to simulate the bulk crystal material. The lattice unit cell contains 48 total atoms, four of which are B-sites. Therefore mixed-metal perovskites can be calculated for compositions of 3B:1B′ and 2B:2B′. This larger cell is need to allow the methylammonium ions and the octahedral iodide cage to obtain different orientations at different locations in the unit cell. Scalar relativistic ultrasoft pseudopotentials [136] were employed to describe electron-ion interactions and electrons in the shells listed for each element in Table 5.3 were explicitly included in the calculations. A $3 \times 3 \times 3$ $k$-point mesh was chosen to sample the Brillouin zone and a kinetic energy cutoff of 70 Ry was used for all calculations based on convergence testing of $MASnI_3$ and $MAPbI_3$. The crystal structure of each candidate material was allowed to relax in all directions in order to obtain the lowest energy crystal configuration.

It must be noted that scalar relativistic calculations were performed in this study and the choice was made to not include spin-orbit coupling (SOC). Several computational chemistry groups that are investigating perovskites with DFT calculations

Table 5.3: Shells Explicitly Considered in the Ultrasoft Pseudopotential (USPP) for Each Element

| Element | Shells Included in USPP |
|---|---|
| H | 1s |
| Li | 1s, 2s, 2p |
| C | 2s |
| N | 2s |
| Na | 2s, 2p, 3s |
| Mg | 2s, 2p, 3s |
| Mn | 3s, 3p, 3d, 4s, 4p |
| Co | 3s, 3p, 3d, 4s, 4p |
| Ni | 3s, 3p, 3d, 4s, 4p |
| Cu | 3s, 3p, 3d, 4s, 4p |
| Zn | 3s, 3p, 3d, 4s, 4p |
| Sr | 4s, 4p, 4d, 5s, 5p |
| Sn | 4d, 5s, 5p |
| Cs | 5s, 5p, 5d, 6s, 6p |
| I | 5s, 5p |
| Pb | 5d, 6s, 6p |
| Bi | 5d, 6s, 6p |

stress that SOC is necessary to accurately capture the density of states in the conduction band. Failure to include SOC generally results in an overestimation of the density of states near the CBE of perovskites, which causes the effective electron masses and optical absorption to be overestimated. [137] However, spin-orbit coupling generally substantially underestimates the band gap of the perovskite materials. A computational study demonstrated that the band gaps were underestimated by almost 1 eV for both $MAPbI_3$ and $MASnI_3$ materials compared with the experimental values. [138] The best way to compensate for this is to include many-body effects using GW self-energy corrections, which has been shown to accurately predict both the effective masses and band gaps. GW-SOC studies predicted band gaps for both the Pb- and Sn-based perovskites within 0.1 eV of experimental values. [138] The main issue is that including SOC in DFT calculations increases the computation time and GW calculations are at least an order of magnitude more costly. It is impractical to screen through multiple postulated compositions with GW calculations that include SOC since resources are not available to do so. Hence, the decision was between per-

forming more costly calculations that more accurately predict the electron effective mass but dramatically underestimate the band gap (DFT calculations with SOC) and performing the most cost-effective calculations possible that yield decent band gap estimates but overpredict $m_e^*$ (scalar-relativistic, *i.e.* DFT calculations without SOC). The primary goal is not to predict the absolute material propeties with the highest degree of accuracy, especially since most of these materials are purely hypothetical. Rather, this is a *feasibility study* that is meant to investigate how replacing a portion of Pb, Sn, and Bi atoms with a second metal species changes the crystallographic and electronic properties relative to the pure perovskite materials. In other words we are interested in investigating *trends* and *relative changes* as a function of material composition and not in absolute accuracy. Hence, the choice was made to pursue the most cost-effective option that would allow the largest number of compositions to be computed within the amount of available computer time at the supercomputing clusters, which is *scalar relativistic calculations without SOC.*

The crystal structure for both the $MAPbI_3$ control material was found by allowing the atoms to relax from the initial configuration reported by Mosconi et al. [131] The crystal structure of $MASnI_3$ was found by replacing all of the $Pb^{2+}$ atoms with $Sn^{2+}$ and relaxing the lattice from the positions found for $MAPbI_3$. The relaxed crystal structure for both the pure Pb and Sn perovskites are shown in Figure 5-4 and the unit cell is outlined for each view. Clearly, the structure is substantially more complicated than the schematic depicted in Figure 5-1 due to the $MA^+$ ions not being spherically symmetric like the other ions. The crystal structures are nearly identical for $MAPbI_3$ and $MASnI_3$, with the main difference being that the octahedral iodide cage distorts more dramatically between layers for the Pb-based lattice.

As mentioned in Section 5.2.3, there are multiple possible atomic arrangements that mixed-metal species can adopt in the unit cell of the perovskite lattice. Since there are a total of four B-sites in the unit cell, there are four locations that a second species could occupy for the 3B:1B′ blends. Finding the most likely crystal structure for $MA(3B{:}1B')I_3$ candidates requires relaxing all four possible combinations of 3 $B^{2+}$ ions and 1 $B'^{2+}$ ions. Likewise, testing all six combinations of 2 $Bi^{3+}$ and 2

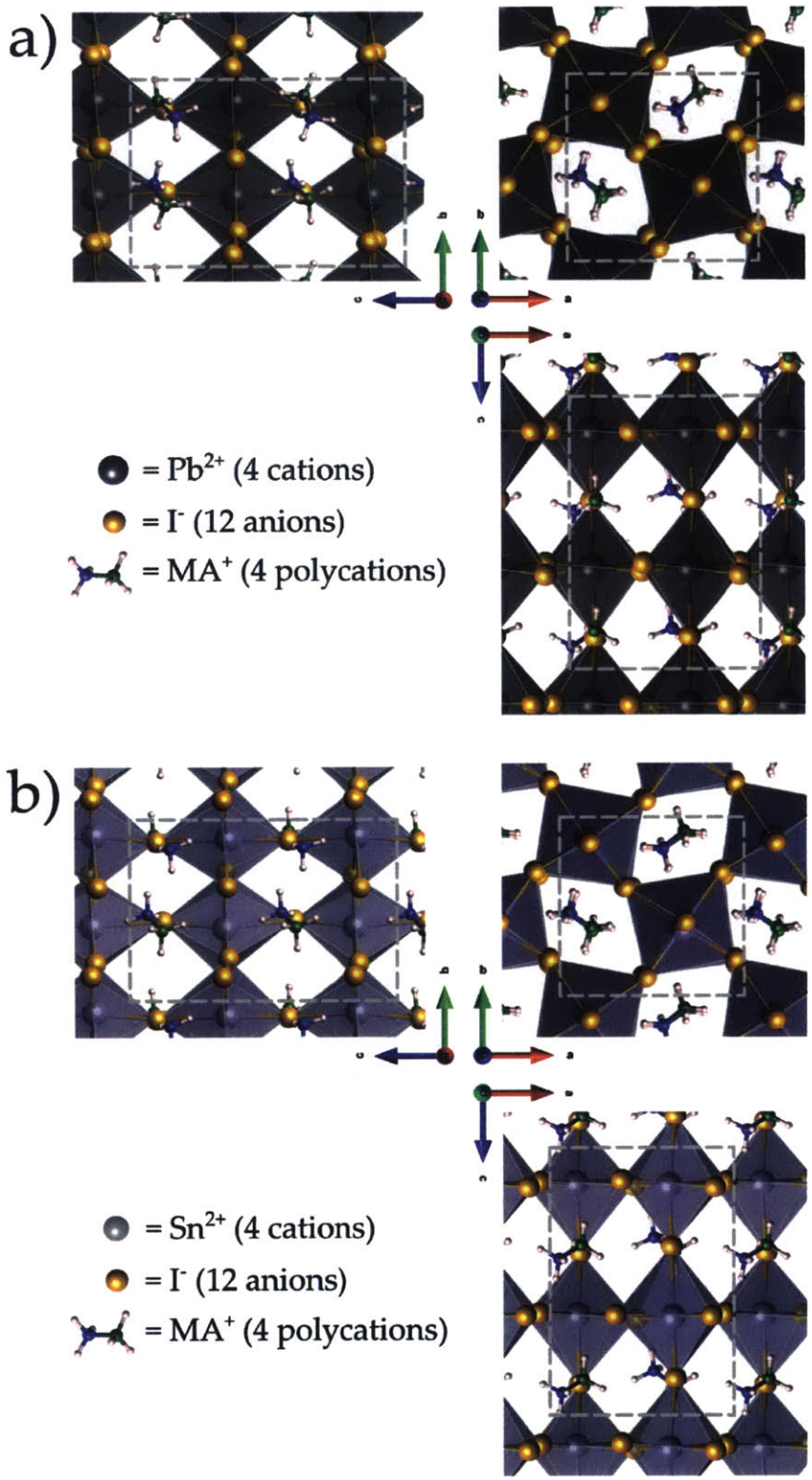


Figure 5-4: Calculated crystal structure of (a) $MAPbI_3$ and (b) $MASnI_3$

$B'^{+}$ ions is required for analyzing the MA(2Bi:2B)$I_3$ candidates. All of the possible arrangements were tested for two different materials in the Sn-mixture set and two materials in the Bi-mixture set. Both Sn-mixtures yielded the same lowest energy configuration and both Bi-mixtures yielded the same configuration as well. Similarly, all four arrangements were considered for a single composition of the Pb-mixtures. Since the B′ ion is always divalent in the Pb-mixtures and Sn-mixtures and monovalent in the Bi-mixtures, it is assumed that the electrostatic ion-ion interactions will always cause this lowest energy configuration to be consistent within each material set.

### 5.3.1 Convergence Tests

Before performing the full series of calculations, convergence tests were performed to ensure that the number of $k$-points used to sample the Brillouin zone and the kinetic energy cutoff are sufficient. Therefore, a series of self-consistent calculations were performed on the relaxed crystal structures of both the $MAPbI_3$ and $MASnI_3$ materials where $k$ was ranged between 2 and 6 and the energy cutoff, $E_{cut}$, was ranged between 30 and 130 Ry. The convergence test results for $MAPbI_3$ and $MASnI_3$ are shown in Figure 5-5 and Figure 5-6, respectively. In both cases, an energy cutoff of 70 Ry was deemed sufficient as the total energy varied by less than 2 meV from the converged value. Likewise, 3 points were determined to be sufficient for the $k$-point mesh as it varied by less than 0.3 meV from the converged value in each case. Hence, all calculations for mixed-metal systems employed these values in the DFT input files.

## 5.4 Crystal Structure Predictions

Density functional theory is generally very accurate at predicting the crystal structure and lattice parameters of most materials. This is especially true in ionic crystals such as the perovskite, where the interaction between ions is primarily electrostatic in nature. By default, DFT calculations are performed for crystals held at absolute-zero (*i.e.* T = 0 K), hence when comparing predicted crystal structures to experimental measurements using x-ray diffraction or a similar technique, it is possible there will

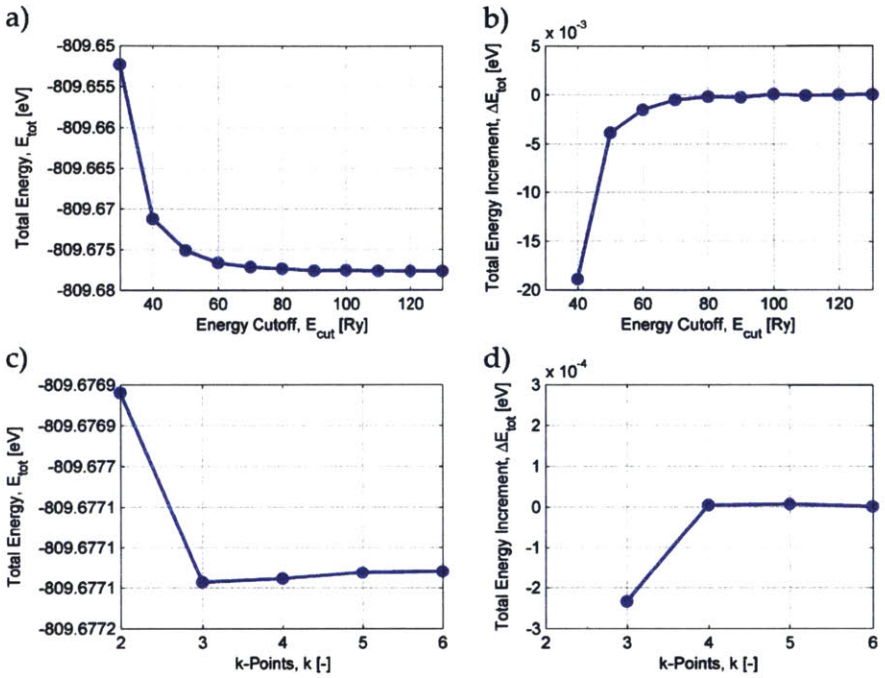


Figure 5-5: Convergence tests of (a-b) energy cutoff and (c-d) number of $k$-points for the $MAPbI_3$ lattice.

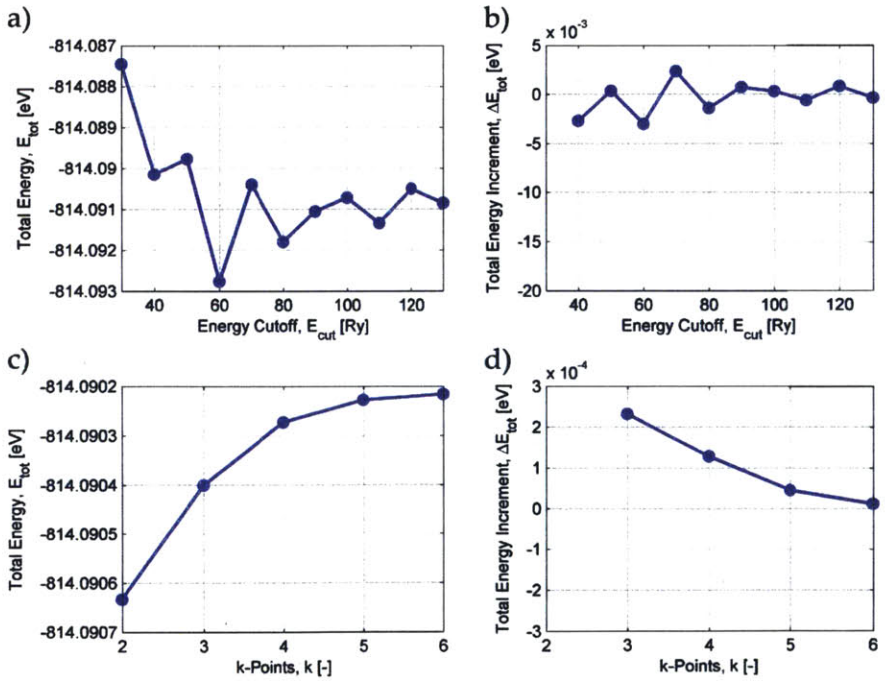


Figure 5-6: Convergence tests of (a-b) energy cutoff and (c-d) number of $k$-points for the $MASnI_3$ lattice.

be some discrepancies. The perovskite system is known to adopt an orthorhombic geometry at low-temperatures and undergoes a phase transition to a tetragonal lattice near T = 150 K. [139] When the temperature is further increased, the distortions of the octahedral cage disappear and the crystal becomes cubic at temperatures above T = 330 K. [133] The difference between the $a$ and $b$ lattice parameters of the orthorhombic perovskite phases are minimal, which means they can be compared against reported measurements of the tetragonal phase that arises at room temperature.

### 5.4.1 Benchmarking with Mixed Pb:Sn System

In order to validate that the pseudopotentials are properly capturing the behavior of the perovskite systems, the calculated lattice parameters of the $MAPbI_3$ and $MASnI_3$ and the mixed $MA(Pb:Sn)I_3$ systems are compared against the experimental values reported by Stoumpos *et al* in Reference [140].

As seen in Table 5.4, the relaxed structures of the single metal perovskites, $MASnI_3$ and $MAPbI_3$, and the mixed-metals are in excellent agreement with the experimental values available in literature even though the predicted crystal structure is orthorhombic and the experimental values are tetragonal. In each case, the difference between the lattice parameters is around a few percent. Each of the lattice parameters is plotted as a function of composition for the spectrum of mixed Pb:Sn systems in Figure 5-7. While the experimental values show that the transverse lattice constants, $a$ and $b$, increase as more of the Pb content is replaced with Sn, the predictions show

Table 5.4: Comparison of Calculated and Experimental Lattice Parameters for Mixed-Metal Pb:Sn Perovskites

| | Predicted | | | Experimental | | | % Difference | | |
|---|---|---|---|---|---|---|---|---|---|
| Material | $a$ [Å] | $b$ [Å] | $c$ [Å] | $a$ [Å] | $b$ [Å] | $c$ [Å] | $a$ [Å] | $b$ [Å] | $c$ [Å] |
| $MAPbI_3$[a] | 9.10 | 8.95 | 13.06 | 8.75 | 8.75 | 12.47 | 4.0% | 2.3% | 4.7% |
| $MA(3Pb:1Sn)I_3$ | 9.01 | 8.86 | 13.09 | 8.86 | 8.86 | 12.65 | 1.7% | 0.0% | 3.4% |
| $MA(2Pb:2Sn)I_3$ | 9.10 | 8.84 | 12.98 | 8.96 | 8.96 | 12.65 | 1.6% | 1.3% | 2.6% |
| $MA(1Pb:3Sn)I_3$ | 9.11 | 8.84 | 12.98 | 8.98 | 8.98 | 12.60 | 1.4% | 1.6% | 3.0% |
| $MASnI_3$[b] | 9.10 | 8.82 | 13.10 | 8.91 | 8.91 | 12.56 | 2.1% | 1.0% | 4.3% |

[a]Experimental values for pure Pb and Pb:Sn systems taken from Reference [140]
[b]Experimental values for pure Sn taken from Reference [141]

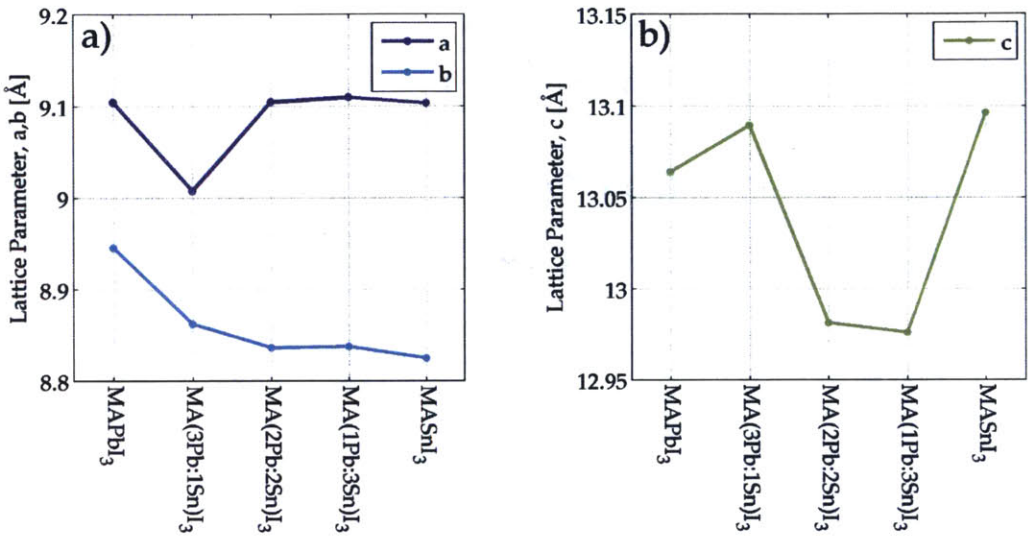


Figure 5-7: Calculated (a) transverse and (b) longitudinal lattice parameters for $MA(Pb:Sn)I_3$ mixed-metal perovskites.

that $a$ remains nearly constant whereas $b$ decreases slightly. Likewise, there is some discrepancy in the trend for the $c$ lattice parameter as well. However, these slight differences are likely an outcome of the simulations investigating an orthorhombic structure rather than a tetragonal one.

The crystal structures for each mixed-metal Pb:Sn system is shown in Figure 5-8. Although $Pb^{2+}$ is a larger ion (119 pm ionic radius) than $Sn^{2+}$ (93 pm ionic radius), both of the metal atoms sit squarely in the octahedral iodide cage of the lattice. [142] Hence, the overall structure of the mixed-metal lattices look almost identical.

### 5.4.2 Lead Mixtures

Aside from mixtures with tin, six other mixed-metal perovskite compositions were investigated computationally by replacing a quarter of the $Pb^{2+}$ ions with either $Co^{2+}$, $Mg^{2+}$, $Mn^{2+}$, $Ni^{2+}$, $Sr^{2+}$, or $Zn^{2+}$. Of this set of metals, $Sr^{2+}$ is the largest with an ionic radius that is nearly identical to $Pb^{2+}$, and $Ni^{2+}$ is the smallest. For reference, the ionic radius of each divalent atom used for Pb and Sn-mixtures is listed in Table 5.5. [142] The relaxed crystal structure for each Pb-based mixed-metal perovskite

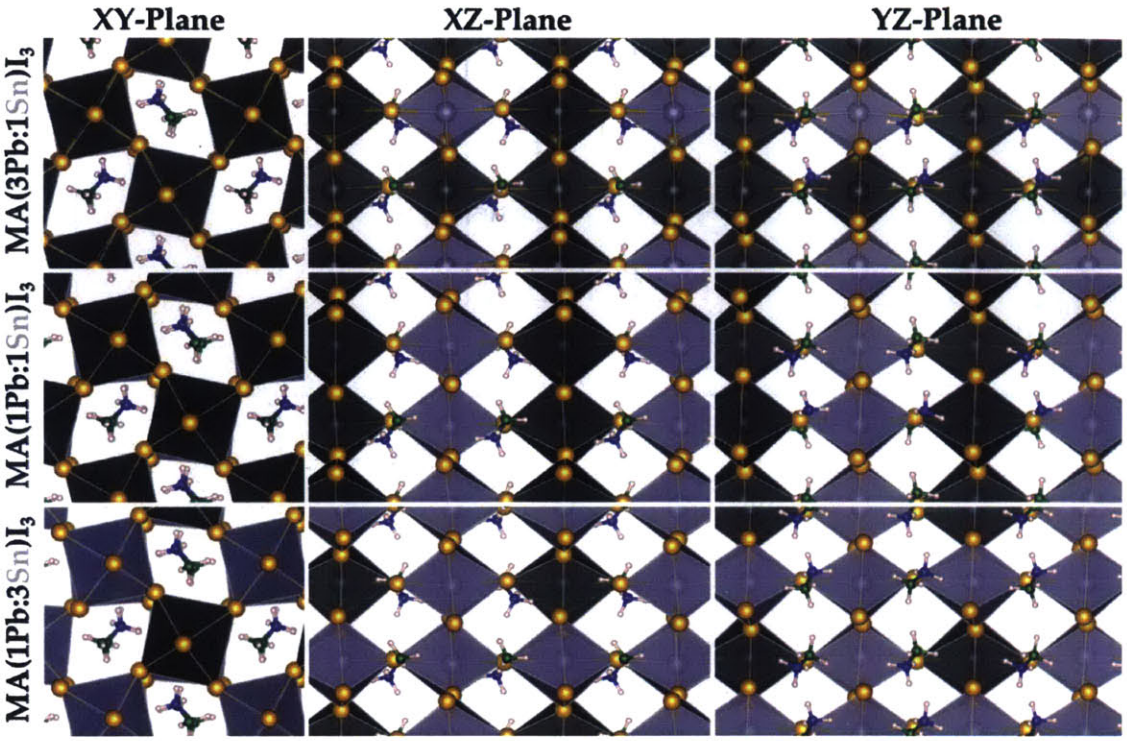


Figure 5-8: Crystal structure for mixed-metal MA(Pb:Sn)$I_3$ perovskites compositions.

composition is shown in Figure 5-10. The MA(3Pb:1Sr)$I_3$ and MA(3Pb:1Sn)$I_3$ lattices are remarkably well-behaved. In each case, the $Sr^{2+}$ and $Sn^{2+}$ ions sit squarely in the center of the octahedral iodide cage. As the ionic radius of the secondary metal species decreases, distortions in the crystal lattice begin to arise. Both the $Co^{2+}$, $Mn^{2+}$, and $Mg^{2+}$ ions are centered in the $x$ and $y$-directions, however each is slightly displaced in the $z$-direction. Both $Zn^{2+}$ and $Ni^{2+}$ distort more dramatically by displacing laterally and vertically in an effort to reach one of the faces of the iodide cage. The direction of displacement is towards the nearest $MA^+$ ion that has the positively charged nitrogen atom oriented furthest away. It appears in these situations that the overall crystal structure is still determined by the interactions between the $MA^+$, $Pb^{2+}$, and $I^-$ ions. As such, the second metal species is not as strongly secured in position and finds a lower total energy by shifting its position upwards slightly. Since this is a bulk crystal calculation, it is likely that the ions would distort downwards if the $MA^+$ ions rotated accordingly to accommodate electrostatic interactions between the small metal cation and the positive charge on the nitrogen atom of $MA^+$. Therefore, it is

quite possible that these materials will display some sort of ferroelectric behavior (*i.e.* the polarization of the material will switch directions with an applied electric field) during device operation if the displacement of these ions can switch directions when an applied field changes polarity.

Table 5.5: Ionic radii of divalent metal species. [142]

| Ion | Ionic Radius[a] [pm] |
|---|---|
| $Pb^{2+}$ | 119 |
| $Sr^{2+}$ | 118 |
| $Sn^{2+}$ | 93 |
| $Co^{2+}$ | 88.5 |
| $Mn^{2+}$ | 83 |
| $Zn^{2+}$ | 74 |
| $Mg^{2+}$ | 72 |
| $Ni^{2+}$ | 69 |

[a]The values listed for ionic radii are specific for a coordination number of 6, which is the number of iodide atoms that would surround each of these divalent metal species while at the B-site of the perovskite lattice.

Table 5.6: Calculated lattice parameters for mixed-metal Pb-based perovskites in order of decreasing ionic radius of secondary metal species

| Material | $a$ [Å] | $b$ [Å] | $c$ [Å] |
|---|---|---|---|
| $MAPbI_3$ | 9.10 | 8.95 | 13.06 |
| $MA(3Pb:1Sr)I_3$ | 9.02 | 8.89 | 13.26 |
| $MA(3Pb:1Sn)I_3$ | 9.01 | 8.86 | 13.09 |
| $MA(3Pb:1Co)I_3$ | 8.71 | 8.64 | 13.19 |
| $MA(3Pb:1Mn)I_3$ | 8.77 | 8.67 | 13.18 |
| $MA(3Pb:1Zn)I_3$ | 9.14 | 8.78 | 13.26 |
| $MA(3Pb:1Mg)I_3$ | 8.84 | 8.74 | 13.18 |
| $MA(3Pb:1Ni)I_3$ | 8.98 | 8.84 | 13.03 |

The crystal lattice parameters reported in Table 5.6 and plotted in Figure 5-9 suggest that even though replacing a quarter of the Pb-atoms with a second species is a significant amount, the overall crystal structure changes very little. Using $Co^{2+}$ as the replacement induces the largest shift in the transverse parameters with $a$ and $b$ each shrinking by 4.3% and 3.4%, respectively. Likewise, the largest change in the normal direction occurred with $Zn^{2+}$ stretching the lattice by 1.5%. Hence, the crystal structure is indeed only perturbed by replacing this portion of Pb atoms.

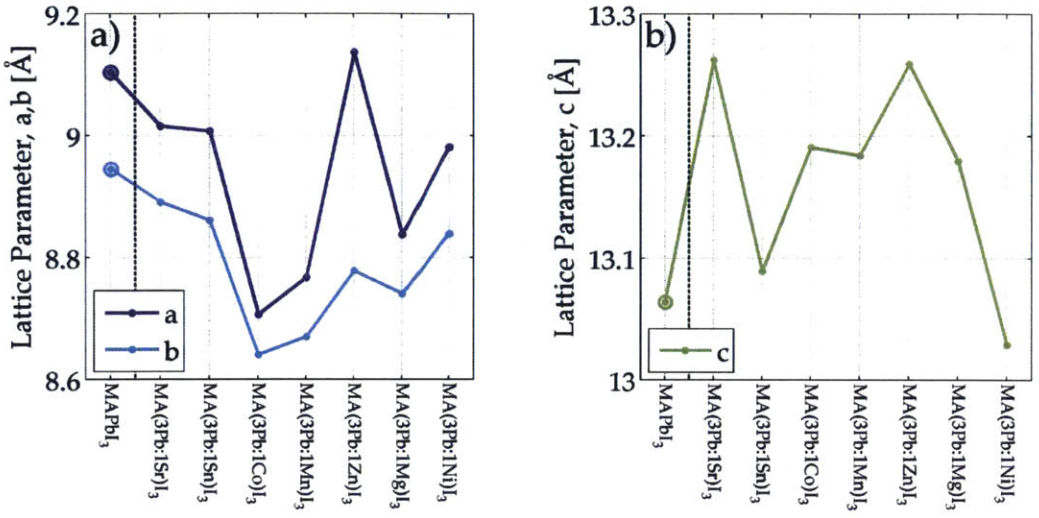


Figure 5-9: Calculated (a) transverse and (b) longitudinal lattice parameters for mixed-metal Pb-based perovskites in order of decreasing ionic radius of secondary metal species.

Figure 5-9 shows that as the transverse dimensions decrease, generally the longitudinal parameter increases in order to conserve volume. The figure also shows that the transverse lattice parameters, $a$ and $b$, tend to initially decrease with decreasing ionic radius but then rise slightly thereafter. It is likely that the similarly sized $Sr^{2+}$ and $Sn^{2+}$ ions can generally maintain the same electrostatic interactions with all of the neighboring atoms. Due to their slightly smaller size, they pull all of the surrounding iodide ions inwards, thereby causing the crystal lattice to distort locally. $Co^{2+}$ and $Mn^{2+}$ behave similarly, however they are can only strain the bonds with the iodides so much before they are forced to displace slightly from the center of the halide cage. Even smaller ions, have weaker electrostatic interactions with their neighbors and resort to more dramatic displacements to reduce the total energy. The more the B-site ions displaces, the less the lattice needs to distort, and the $a$ and $b$ lattice parameters start to relax back towards the original value for pure $MAPbI_3$. From this perspective, $Co^{2+}$ ions are very interesting since they induce the largest change in the lattice parameters but do not significantly displace from the center of the iodide octahedron.

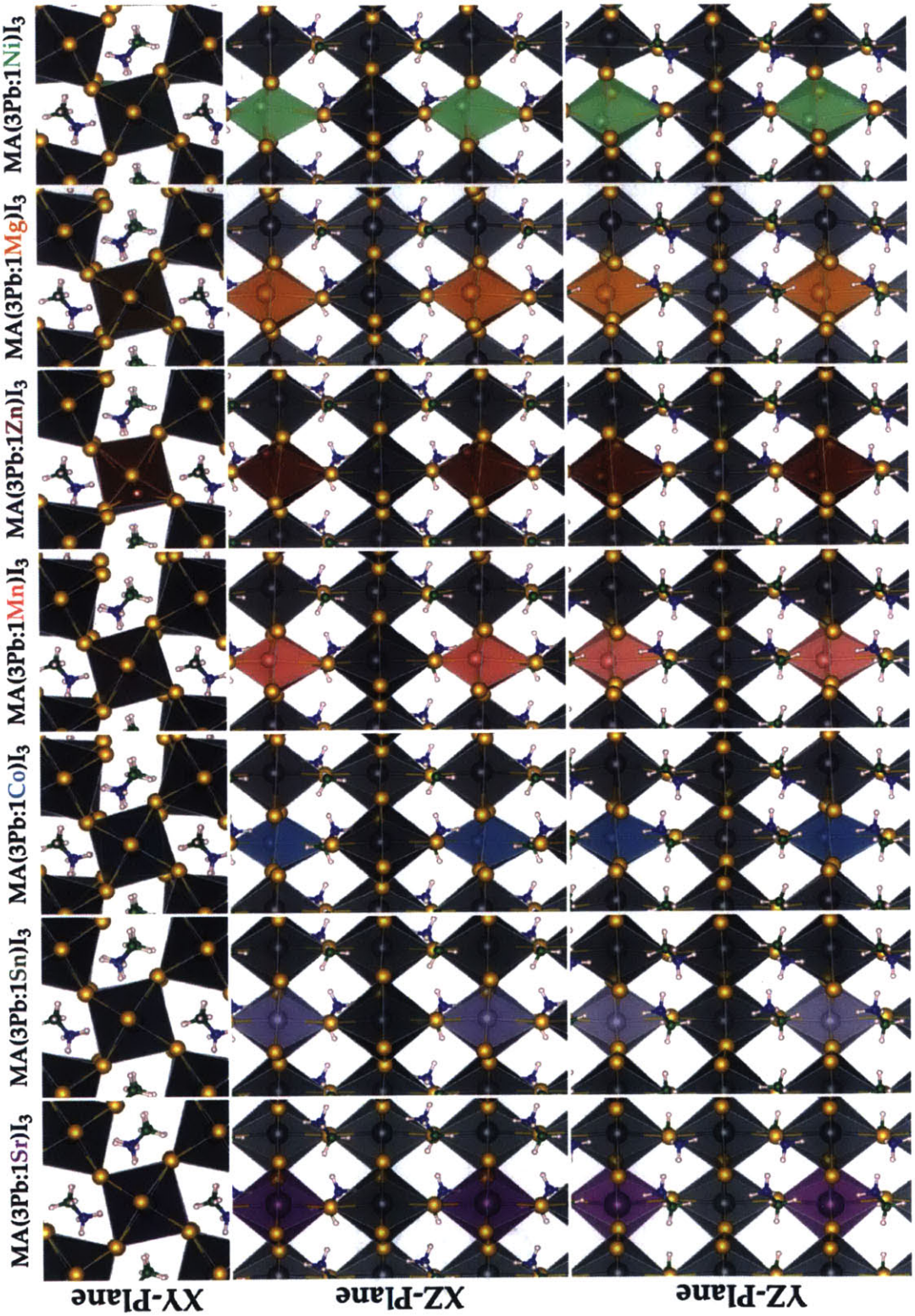


Figure 5-10: Relaxed crystal structures for Pb-based mixed-metal perovskites with 25% replacement of Pb with a second metal species, MA(3Pb:1B′)$I_3$. Ionic radius of second metal species decreases in size from $Sr^{2+}$ to $Ni^{2+}$.

### 5.4.3 Tin Mixtures

The crystal structure for each of the Sn-based mixed-metal perovskites was determined in the exact same manner used for the Pb-based analogs by allowing each atom in the postulated initial crystal configuration to relax its position until the lowest energy state was found. This set contains seven different compositions where a quarter of the $Sn^{2+}$ ions are replaced with a second metal species and four compositions where half of the Sn content is replaced. Figure 5-12 shows that the predicted crystal structures for the MA(3Sn:1B′)$I_3$ compositions are very similar to those observed for Pb-mixtures in Figure 5-10. The largest replacement species, $Sr^{2+}$ and $Sn^{2+}$, remain centered in the octahedral iodide cage, whereas smaller ions become increasingly displaced from the center. When substituted into the Pb-mixtures, $Co^{2+}$, $Mn^{2+}$, and $Mg^{2+}$ only displaced in the $z$-direction, however when incorporated into the Sn-mixtures they displace both laterally and vertically in all three principal directions. Similar to the Pb-based analogs, $Zn^{2+}$ and $Ni^{2+}$ demonstrate the largest displacements. One of the most notable differences in the Sn-based systems is that the octahedral cage around the $B'^{2+}$ ions does not shrink biaxially, rather it becomes squeezed in one direction and elongated in the other to form a diamond shape as is clearly observed in the XY-plane diagrams of Figure 5-12.

Table 5.7: Calculated lattice parameters for mixed-metal Sn-based perovskites in order of decreasing ionic radius of secondary metal species

| Material | $a$ [Å] | $b$ [Å] | $c$ [Å] |
|---|---|---|---|
| $MASnI_3$ | 9.10 | 8.82 | 13.10 |
| MA(3Sn:1Pb)$I_3$ | 9.11 | 8.84 | 12.98 |
| MA(3Sn:1Sr)$I_3$ | 9.12 | 8.85 | 13.07 |
| MA(3Sn:1Co)$I_3$ | 8.98 | 8.92 | 12.84 |
| MA(3Sn:1Mn)$I_3$ | 9.00 | 8.93 | 12.85 |
| MA(3Sn:1Zn)$I_3$ | 9.11 | 8.89 | 13.87 |
| MA(3Sn:1Mg)$I_3$ | 9.04 | 8.88 | 13.79 |
| MA(3Sn:1Ni)$I_3$ | 9.22 | 8.82 | 12.95 |
| MA(2Sn:2Pb)$I_3$ | 9.10 | 8.84 | 12.98 |
| MA(2Sn:2Sr)$I_3$ | 9.16 | 8.89 | 13.10 |
| MA(2Sn:2Zn)$I_3$ | 8.96 | 8.80 | 14.32 |
| MA(2Sn:2Mg)$I_3$ | 8.59 | 8.99 | 14.80 |
| MA(2Sn:2Ni)$I_3$ | 9.20 | 8.42 | 12.69 |

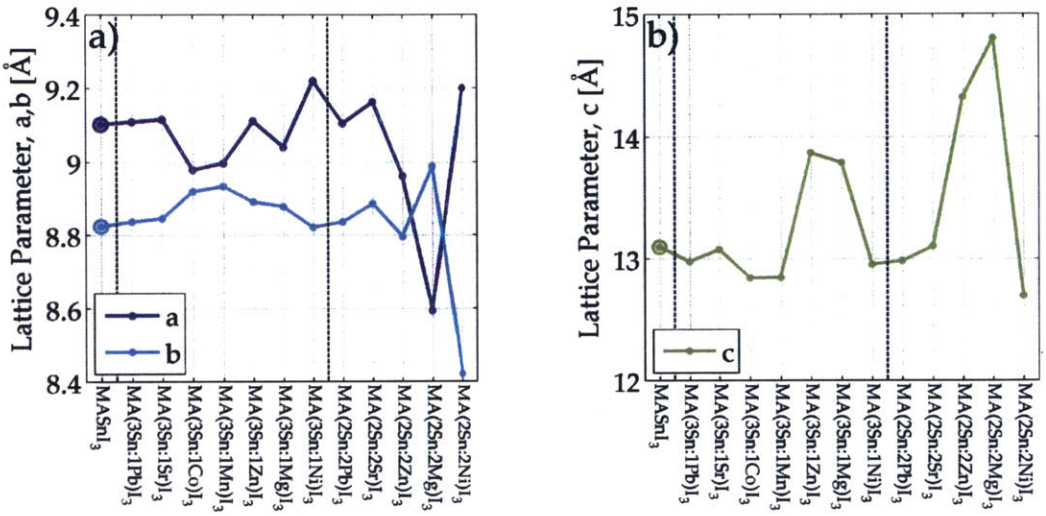


Figure 5-11: Calculated (a) transverse and (b) longitudinal lattice parameters for mixed-metal Sn-based perovskites in order of decreasing ionic radius of secondary metal species.

The relaxed lattice parameters for each configuration are tabulated in Table 5.7 in order of decreasing ionic radius of the $B'^{2+}$ ion. Likewise, the lattice parameters are plotted in Figure 5-11. Interestingly, the trends in lattice parameters differ slightly from those observed for the Pb-mixtures. Since $Pb^{2+}$ and $Sr^{2+}$ are larger than $Sn^{2+}$, they cause the lattice to locally dilate, which is observed by slight increases in both $a$ and $b$ with little change in $c$. However, $a$ and $b$ become inversely correlated for smaller ions. As shown in the crystal structure diagrams, the octahedral cages around $Co^{2+}$ and $Mn^{2+}$ become laterally squeezed and forms a trapezoidal cross-section in the XY-plane, which causes $a$ to decrease while $b$ increases for the full lattice. For even smaller ions, the octahedral cages experience further distortions and adopt diamond cross-sections for $Zn^{2+}$ and $Mg^{2+}$. This distortion generates an internal torsion that causes the overall lattice to expand back towards the pure $MASnI_3$ lattice parameters.

Although the crystal structures are not explicitly shown for the $MA(2Sn:2B')I_3$ samples, the lattice parameter trends for $Pb^{2+}$ and $Sr^{2+}$ are similar to that for the $MA(3Sn:1B')I_3$ compositions, which indicates that these lattices are well-behaved since their ionic sizes are comparable to $Sn^{2+}$. However, the predictions for $Zn^{2+}$,

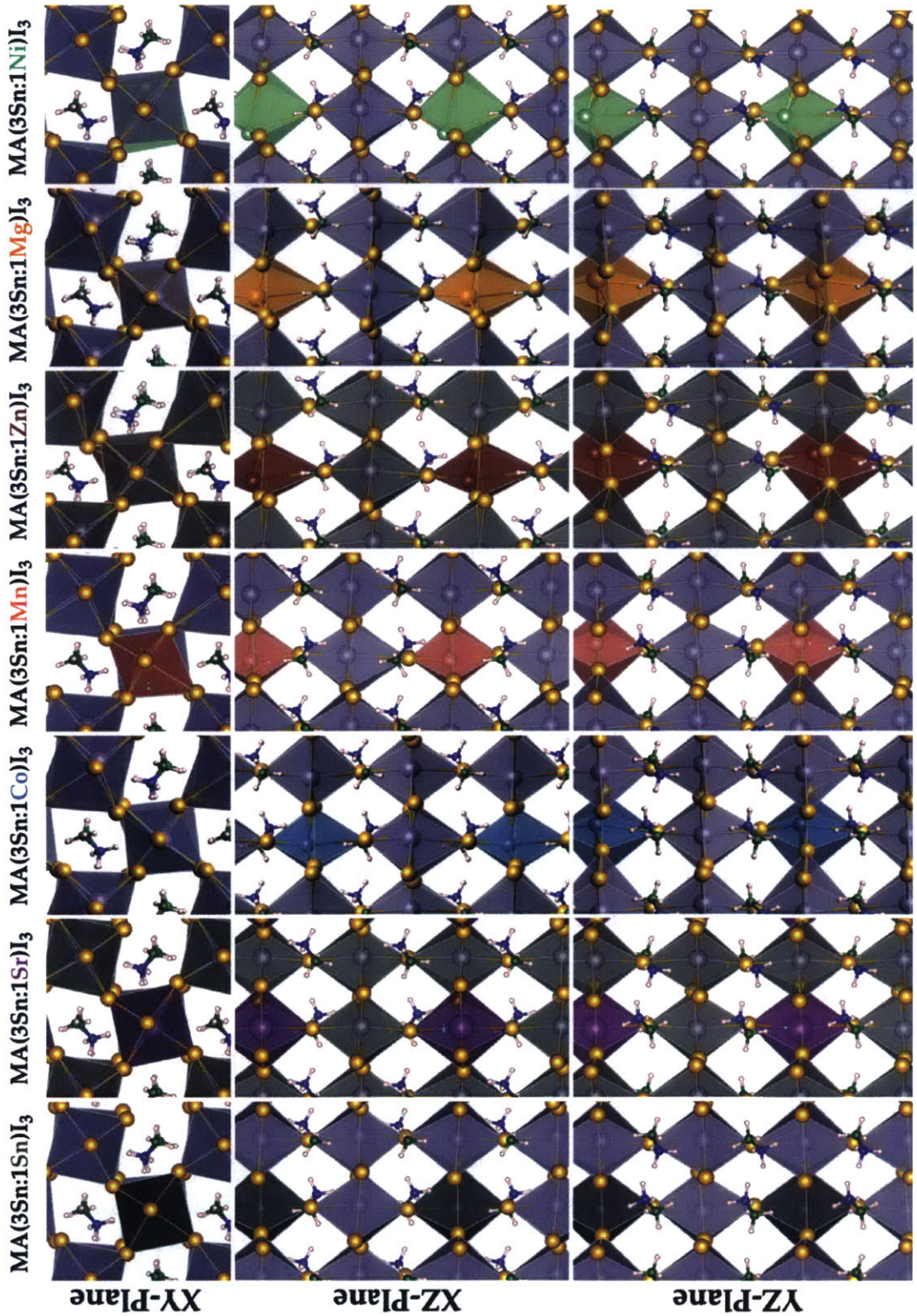


Figure 5-12: Relaxed crystal structures for Sn-based mixed-metal perovskites with 25% replacement of Sn with a second metal species, $MA(3Sn:1B')I_3$. Ionic radius of second metal species decreases in size from $Sr^{2+}$ to $Ni^{2+}$.

$Mg^{2+}$, and $Ni^{2+}$ show dramatic changes in the lattice parameters, which suggest that the crystal structure becomes increasingly distorted and that these ions occupy too large of a fraction of B-sites to preserve the desired 3D perovskite lattice. Hence, the substituting a portion of $Sn^{2+}$ atoms with a second species only *perturbs* the crystal structure when less than about a quarter of the ions are replaced unless the ions are very similar in size.

### 5.4.4 Bismuth Mixtures

As with the other sets of mixed-metal perovskites, the crystal structure of Bi-based materials was predicted for compositions with half of the B-sites occupied by $Bi^{3+}$ ions and the other half occupied by either $Cs^+$, $Na^+$, $Cu^+$, or $Li^+$. For reference, the ionic radius of each of these ions is listed in Table 5.8. [142] The relaxed crystal structures of these materials are shown in Figure 5-14. It is not surprising that the lowest energy configuration of these systems adopt a simple cubic pattern for the B-site where $Bi^{3+}$ and $B'^{+}$ alternate. This atomic arrangement is needed in order for simple electrostatic interactions to bring all the atoms close together while minimizing the total energy.

Table 5.8: Ionic radii of metal species comprising the Bi-based perovskites. [142]

| Ion | Ionic Radius[a] [pm] |
|---|---|
| $Cs^+$ | 181 |
| $Bi^{2+}$ | 103 |
| $Na^{2+}$ | 102 |
| $Cu^{2+}$ | 91 |
| $Li^{2+}$ | 90 |

[a]The values listed for ionic radii are specific for a coordination number of 6, which is the number of iodide atoms that would surround each of these divalent metal species while at the B-site of the perovskite lattice.

As with the Pb and Sn-based mixed metals, the crystal structure is the least perturbed when the ion size of B′ is closely matched to $Bi^{3+}$. For this system, $MA(2Bi{:}2Na)I_3$ produced the least distorted crystal structure due to the excellent match in size between the ions. On the other hand, $Cu^+$ and $Li^+$ become substan-

Table 5.9: Calculated lattice parameters for mixed-metal Bi-based perovskites in order of decreasing ionic radius of secondary metal species

| Material | $a$ [Å] | $b$ [Å] | $c$ [Å] |
|---|---|---|---|
| $MA(2Bi:2Cs)I_3$ | 9.32 | 9.27 | 13.91 |
| $MA(2Bi:2Na)I_3$ | 8.89 | 8.82 | 12.99 |
| $MA(2Bi:2Cu)I_3$ | 8.88 | 8.68 | 13.14 |
| $MA(2Bi:2Li)I_3$ | 8.80 | 8.71 | 13.50 |

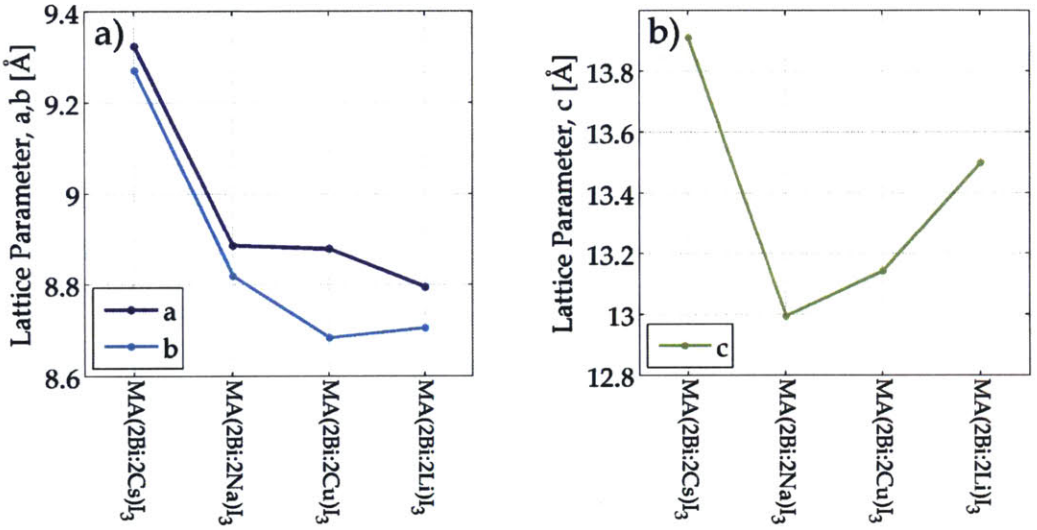


Figure 5-13: Calculated (a) transverse and (b) longitudinal lattice parameters for mixed-metal Bi-based perovskites in order of decreasing ionic radius of secondary metal species.

tially displaced at certain sites in the same manner that $Zn^{2+}$ and $Ni^{2+}$ demonstrated in the Pb-based systems. When $Bi^{3+}$ was partially replaced with $Cs^{+}$ neither ion experienced displacement in the $z$-direction. However, $Cs^{+}$ ions became displaced laterally from $Bi^{3+}$. Cesium was chosen for investigation because it provides an upper bound on available ion size for perovskite systems, however, the ion is so massive that it has been used to replace $MA^{+}$ ions at the A-sites in the lattice to make $CsSnI_3$ and $CsPbI_3$ materials. Although the ions are forced to sit at the B-sites by design, there is a good chance it might attempt to swap places with $MA^{+}$ if the crystal would form at all.

The predicted lattice parameters are reported in Table 5.9 and plotted graphi-

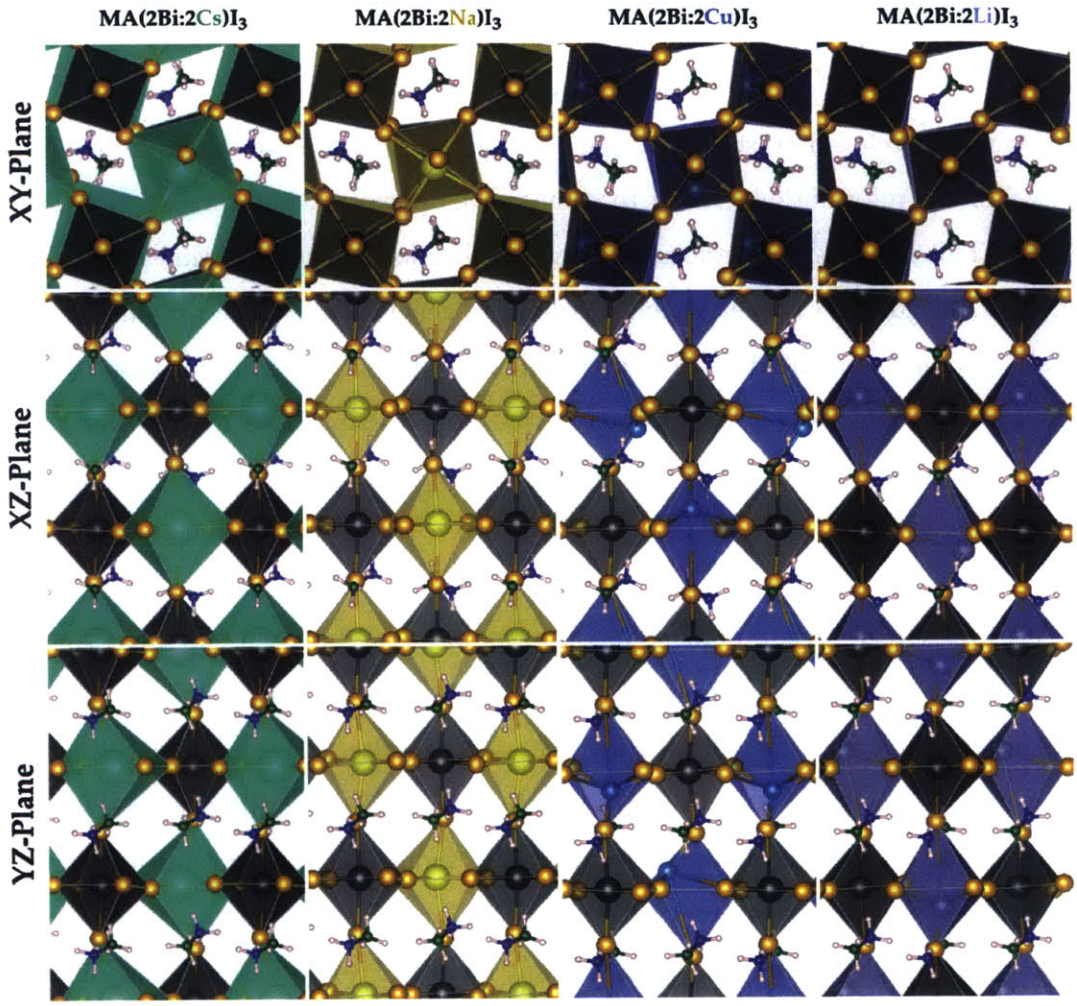


Figure 5-14: Relaxed crystal structures for Bi-based mixed-metal perovskites with 50% replacement of Bi with a second metal species, MA(2Bi:2B′)$I_3$. Ionic radius of second metal species decreases in size from $Cs^+$ to $Li^+$.

cally in Figure 5-13. Although a pure bismuth perovskite was not simulated here for comparison against the mixtures, the MA(2Bi:2Na)$I_3$ composition yields predicted lattice parameters closest to that of $MAPbI_3$. As expected, $Cs^+$ addition produces the largest lattice parameters for all three directions and the crystal relaxes to smaller values with smaller $B'^+$ ions. The small sizes of $Cu^+$ and $Li^+$ attempt to further compress the lattice, but like the Sn-based analogs, are unable to do so and translate relative to the iodide octahedron to lower the energy. By relaxing through ion translation, the lattice is allowed to also relax slightly and the lattice constants assume larger values.

### 5.4.5 Simulated X-Ray Diffraction Spectra

Calculating the relaxed crystal structure of the mixed-metal perovskite systems provides all of the information needed to simulate the powder x-ray diffraction (XRD) patterns. This analysis was performed using the PowderPlot package that is included in the distribution of VESTA, which was used to generate all of the graphics of the crystal structures presented in this section. [143] Copper K$\alpha$ radiation was used as the light source and the powder diffraction pattern was simulated for angles $2\theta$ between 10° and 80°. As shown in Figure 5-15, there are many peaks for each Pb-based sample owing to the asymmetry of the orthorhombic Bravais lattice and the fact that the simulation does not have any preferred orientation. The most notable feature is that there is very little difference in the peak locations between the mixed-metal samples. This is not surprising as the lattice parameters and crystal structure diagrams indicate that replacing 25% of the $Pb^{2+}$ with an alternative metal species does not generally influence the overall crystal structure. Likewise, the similar size and bonding behavior between Sn and Pb cause their simulated spectra to also be quite similar. The slight changes observed between $2\theta = 20°$ to 30° might disappear in actual crystal lattices where it is expected that the $MA^+$ would produce a significant amount of disorder throughout the crystal.

Similarly, the simulated XRD spectra for MA(Sn:B′)$I_3$ mixed-metal perovskites do not change dramatically with composition either, as is shown in Figure 5-16. The mixed-metal Bi-based perovskites generate XRD patterns with the largest differences. As shown in Figure 5-17, the Bi-mixtures produce an additional peak around $2\theta = 12°$ compared to $MAPbI_3$ and $MASnI_3$ and the peaks between 20° and 30° are more pronounced.

However, regardless of whether the particular lattice is based on Pb, Sn, or Bi, the overall XRD patterns are very similar due to the fact that all of these crystals have the $ABX_3$ perovskite crystal structure. These findings suggest that it might be very difficult to observe differences in peak locations in actual mixed-metal perovskite films when compared against the pure $MAPbI_3$ or $MASnI_3$ materials. For instance,

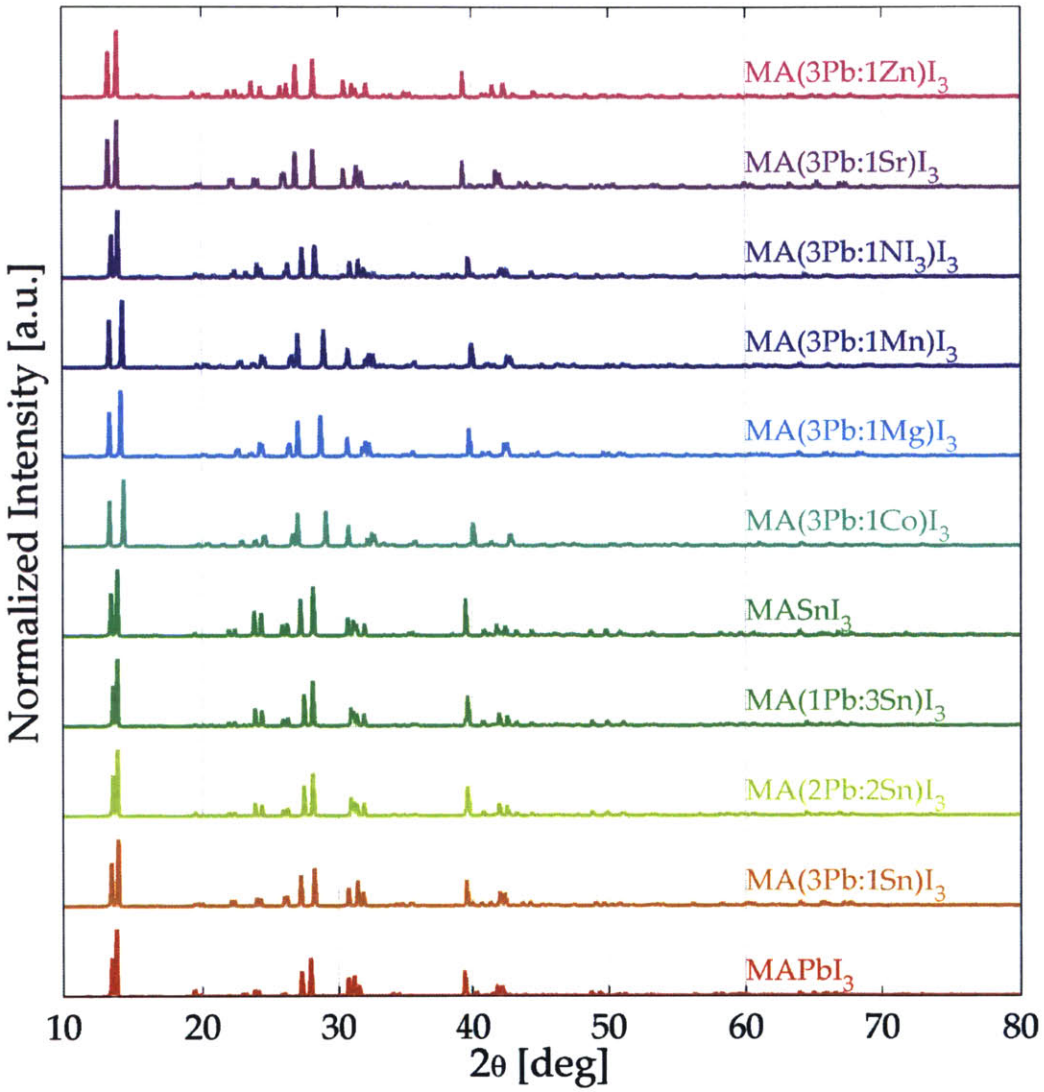


Figure 5-15: The simulated powder XRD spectra for the mixed-metal Pb-based perovskite materials.

the tetragonal structure of room-temperature perovskites will cause measured XRD patterns to exhibit less peaks and the disorder in actual materials might obscure slight peak shifts that are distinguishable in these simulations. Hence, it might be difficult to know whether a mixed-metal material is actually experiencing B-site substitution, or if the atoms are precipitating from the pure $MAPbI_3$ or $MASnI_3$ and forming a second phase that is amorphous.

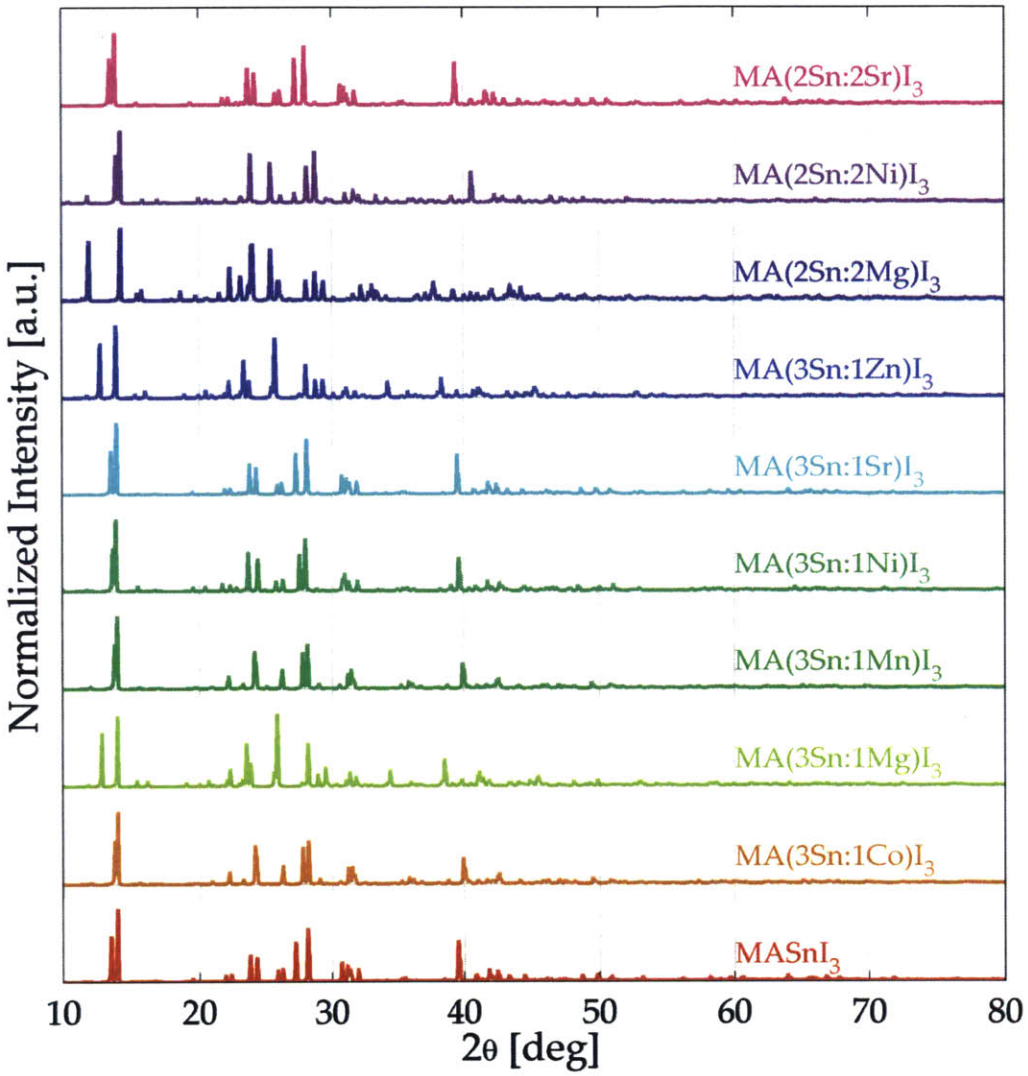


Figure 5-16: The simulated powder XRD spectra for the mixed-metal Sn-based perovskite materials.

## 5.5 Band Structure and Band Gap Predictions

The band structure was calculated from the converged wavefunctions previously determined for the relaxed crystal structure of each mixed-metal embodiment using the pw.x and bands.x programs in Quantum Espresso. [135] The band structure was generated by first defining a path along the high-symmetry points of the orthorhombic Bravais lattice and sampling the Brillouin zone at those specific $k$-points for 110 different energy bands. The band gap was determined from the band structure by

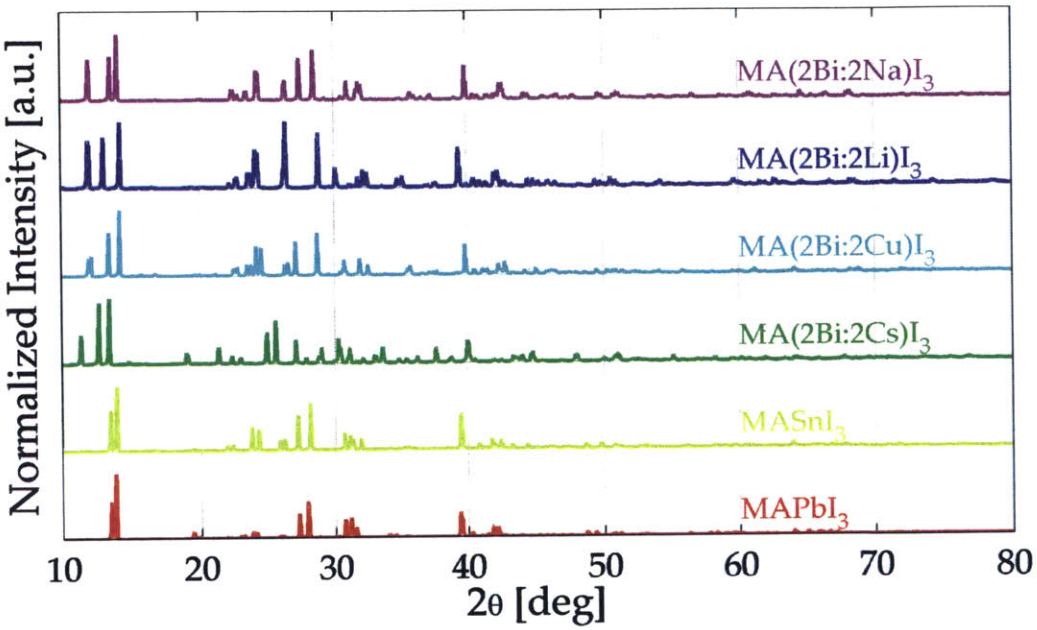


Figure 5-17: The simulated powder XRD spectra for the mixed-metal Bi-based perovskite materials.

taking the difference between the lowest energy in the conduction band edge (CBE) and the highest energy in the valence band edge (VBE). Whereas DFT-GGA calculations accurately predict crystal structure, they tend to typically *underestimate* band gaps because the PBE exchange-correlation does not always fully capture the interaction between electrons. Hence, different results are usually obtained with different exchange-correlations and experimental values are required to identify which functionals provide the best fit for any given material.

### 5.5.1 Benchmarking with Mixed Pb:Sn System

To assess our ability to predict the band gaps of the perovskite materials, the calculated values for the pure and mixed Pb:Sn perovskites are compared against experimental values reported in literature [129] in Table 5.10 and Figure 5-19. Each of the predicted values for the bandgap was determined from the band structures shown in Figure 5-18. All of these compositions have very similar bandstructures due to the fact that Sn and Pb are from the same group of the periodic table. Although the density of states were not explicitly calculated or projected onto orbitals, other

studies have shown that the VBE is composed mainly of I $p$-orbitals mixed with Pb or Sn $s$-orbitals, whereas the CBE is mainly comprised by the Pb or Sn $p$-orbitals. [144] Hence, it is not surprising that the character of the band edges is preserved as the Sn content increases. In each Pb:Sn mixture, the band gap is always direct and located at the Γ-point of the band diagram.

Good agreement arises between the predicted value of 1.67 eV for $MAPbI_3$ and the experimental values of 1.6 eV [14], which is likely due to fortuitous error cancellation since DFT-GGA calculations generally underestimate band gap values. Likewise, the predicted band gap of 1.04 eV for $MASnI_3$ is within only 0.2 eV of the measured value, which is substantially better than 0.6eV value previously reported for similar scalar relativistic DFT calculations. [138] Better agreement has been obtained for $MASnI_3$ in other studies using post-processing algorithms such as GW with spin-orbit coupling [138] or hybrid functionals such as HSE06 [145]. However, the aim of this study is to see how Pb-, Sn-, and Bi-based perovskites are perturbed by the addition of a second B-site cation species to produce new materials that have not been previously attempted. Regardless of the absolute accuracy of a particular exchange-correlation or hybrid functional, the overall error might be somewhat consistent between candidates within a given material set, which allows more confidence to be placed in *trends* rather than in absolute values. Therefore, the PBE exchange-correlations were used for all calculations without any corrections for van der Waals interactions or post-processing routines. This notion is validated by the ability of the DFT-GGA calculations to accurately predict the trend exhibited by actual mixed Pb:Sn perovskites, where the band gap narrows with increasing Sn content, as is shown in Figure 5-19.

### 5.5.2 Lead Mixtures

The calculated band structure for each Pb-based mixed-metal perovskite composition, $MA(3Pb{:}1B')I_3$, is shown in Figure 5-20. Interestingly, there are some striking differences between the different samples. First, $MA(3Pb{:}1Sr)I_3$ has a character that is very similar to $MA(3Pb{:}1Sn)I_3$ (shown in Figure 5-18c). There is a single direct energy gap between the CBE and VBE at the Γ-point in the crystal, however sub-

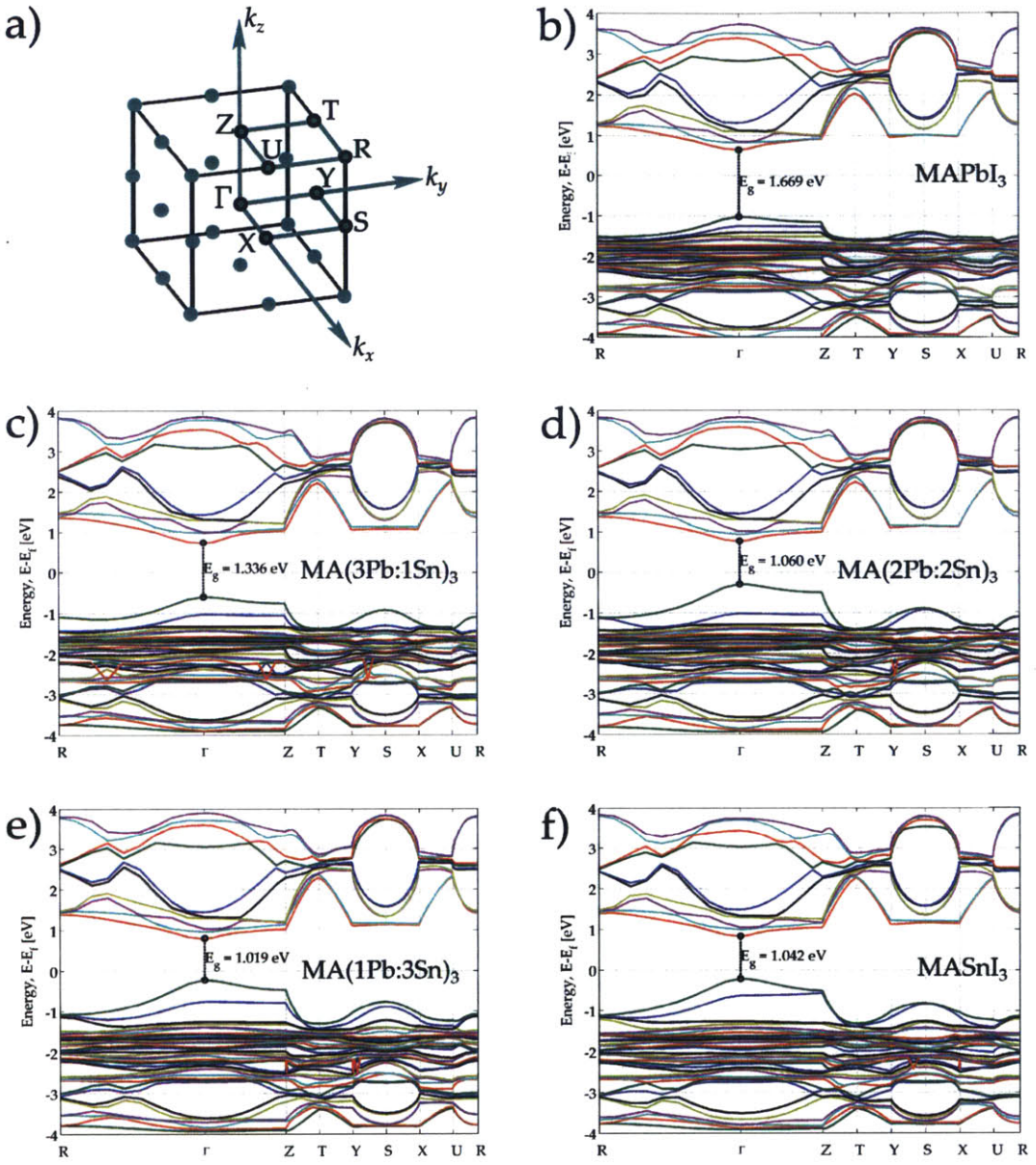


Figure 5-18: (a) The symmetry points in the orthorhombic crystal lattice and the calculated band structure for Pb:Sn blends: (b) $MAPbI_3$, (c) $MA(3Pb:1Sn)I_3$, (d) $MA(2Pb:2Sn)I_3$, (e) $MA(1Pb:3Sn)I_3$, (f) $MASnI_3$,

stituting Sr into a quarter of the B-sites widens the gap, whereas Sn narrows it. Furthermore, the character of the band edges is largely preserved. Interestingly, this situation is also true for $MA(3Pb:1Zn)I_3$ even though the crystal structure displayed in Figure 5-10 shows the $Zn^{2+}$ ion is substantially displaced from the center of the

Table 5.10: Comparison of Calculated and Experimental Band Gaps for Mixed-Metal Pb:Sn Perovskites

| Material | Predicted $E_g$ [eV] | Experimental $E_g$[a] [eV] | % Difference |
|---|---|---|---|
| $MAPbI_3$ | 1.67 | 1.57 | 6.3% |
| $MA(3Pb:1Sn)I_3$ | 1.34 | 1.31 | 2.0% |
| $MA(1Pb:1Sn)I_3$ | 1.06 | 1.28 | 17.2% |
| $MA(1Pb:3Sn)I_3$ | 1.02 | 1.23 | 17.2% |
| $MASnI_3$ | 1.04 | 1.20 | 13.2% |

[a]Experimental band gaps referenced here are the values reported by Ogomi *et al* in reference [129].

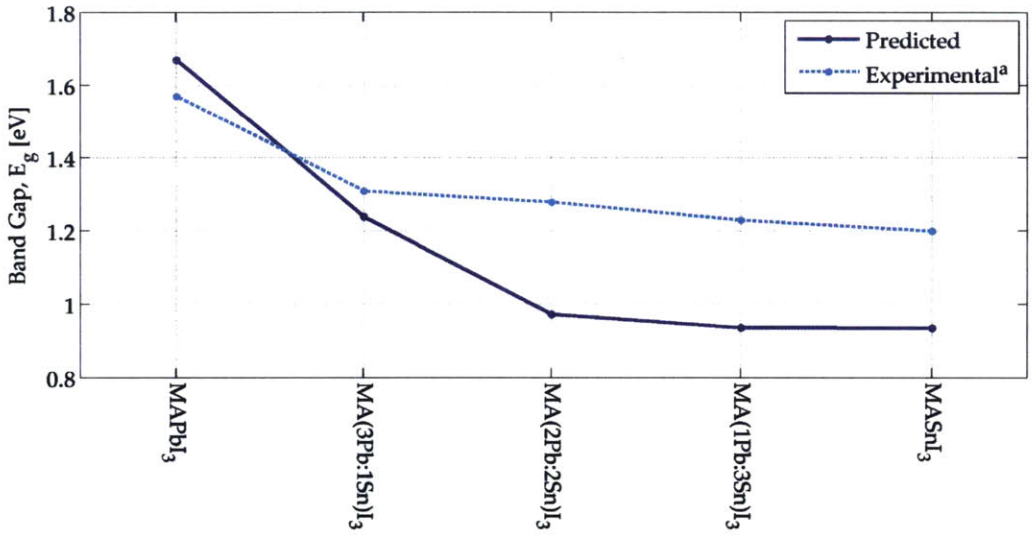


Figure 5-19: Comparison of calculated and experimental band gaps for mixed-metal Pb:Sn perovskites. [a]The experimental band gaps referenced here are the values reported by Ogomi *et al* in reference [129].

octahedral iodide cage. It has a direct band gap that has similarly widened and the character of the band edges remains preserved.

The character of the CBE for $MA(3Pb:1Mg)I_3$ is different compared to that for the previous cases. As a result the lowest energy location shifts from the Γ-point to the U-point in the CBE causing this perovskite material to have an indirect band gap. However, the magnitude of the band gap is almost identical to that of the pure $MAPbI_3$ material.

The remaining Pb-based mixtures with Co, Mn, and Ni demonstrate the most

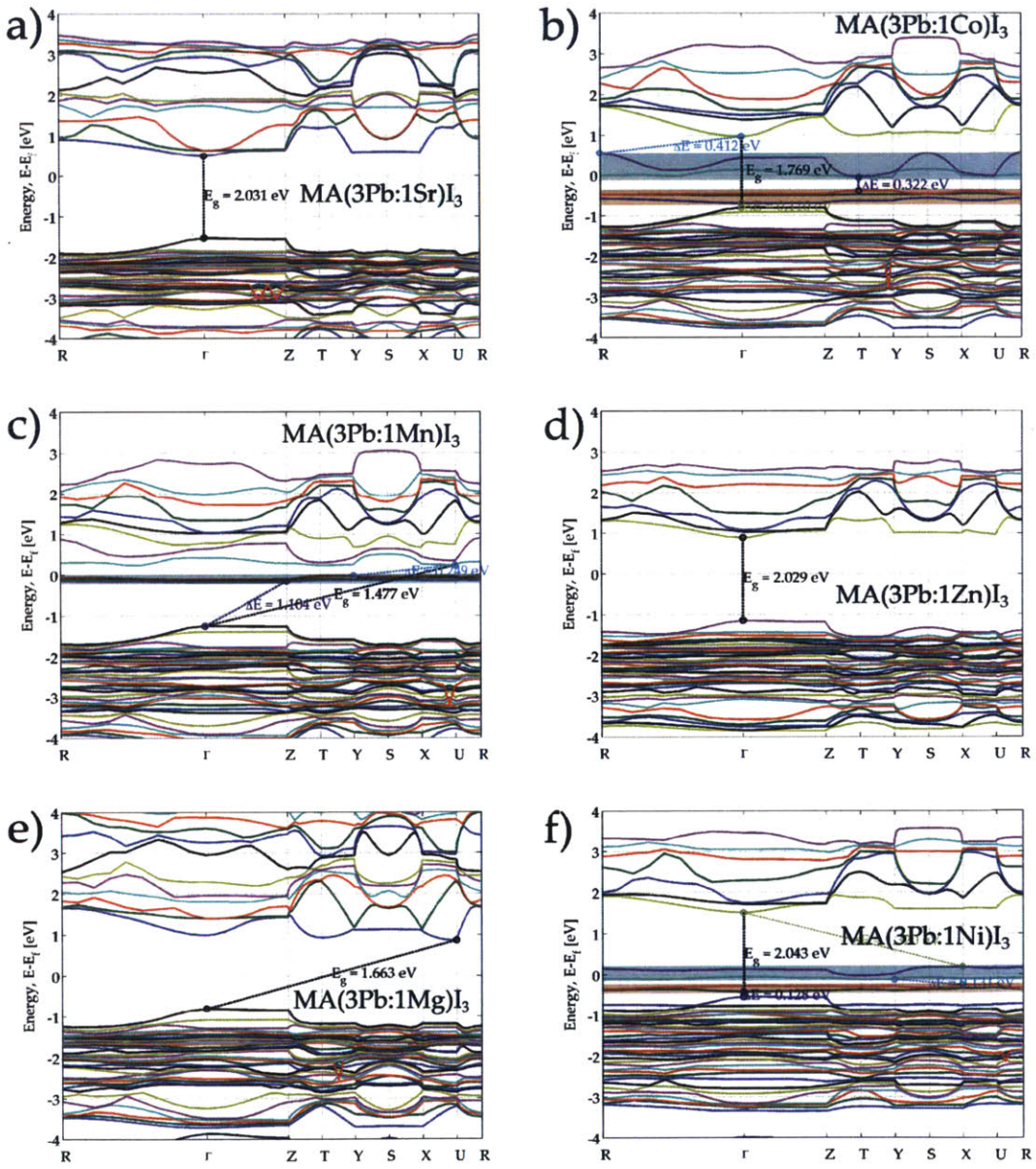


Figure 5-20: The calculated band structures for Pb-based mixed-metal perovskites (a) MA(3Pb:1Sr)$I_3$, (b) MA(3Pb:1Co)$I_3$, (c) MA(3Pb:1Mn)$I_3$, (d) MA(3Pb:1Zn)$I_3$, (e) MA(3Pb:1Mg)$I_3$, and (f) MA(3Pb:1Ni)$I_3$

interesting behavior of this set by generating intermediate bands inside the band gap. These states likely arise from the *d*-orbitals of the transition metals which have a lower energy than the *p*-orbitals and are hence more likely to generate states in the band gap. In each case a band arises at the predicted Fermi level and is isolated from the band edges of the material by small energy gaps, denoted in the figures as $\Delta E$. In the case of MA(3Pb:1Co)$I_3$, it appears that two thin bands arise. The one highlighted in blue is clearly in the center of the gap whereas the one highlighted in brown is only isolated from the VBE by a 0.1 eV gap, which would likely disappear at elevated temperatures. The VBE and CBE retain the same character as the $MAPbI_3$ system and the overall energy gap between them widens to a value of 1.77 eV while remaining at the Γ-point.

Table 5.11: Calculated band gap, $E_g$, and energy gaps, $\Delta E$, for mixed-metal Pb-based perovskites in order of decreasing ionic radius of secondary metal species

| Material | $E_g$ [eV][a] | $\Delta E_1$ [eV] | $\Delta E_2$ [eV] | $\Delta E_3$ [eV] |
|---|---|---|---|---|
| $MAPbI_3$ | 1.67 | - | - | - |
| MA(3Pb:1Sr)$I_3$ | 2.03 | - | - | - |
| MA(3Pb:1Sn)$I_3$ | 1.34 | - | - | - |
| MA(3Pb:1Co)$I_3$ | 1.77 | 0.41 | 0.32 | 0.11 |
| MA(3Pb:1Mn)$I_3$ | 1.48 | 1.10 | 0.25 | - |
| MA(3Pb:1Zn)$I_3$ | 2.03 | - | - | - |
| MA(3Pb:1Mg)$I_3$ | 1.66 | - | - | - |
| MA(3Pb:1Ni)$I_3$ | 2.04 | 1.32 | 0.13 | 0.13 |

[a]In the cases of Co, Mn, and Ni there exists one or more intermediate bands in the band structure. For these cases, the band gap value reported is the energy difference between the valence band and conduction band edges (*i.e.*, the usual band gap in the event the intermediate bands did not form). The energy for each gap is clearly labelled in Figure 5-20.

The case of MA(3Pb:1Ni)$I_3$ is similar to the Co composition, however both bands are small and are hardly isolated from one another. It is likely that these bands would essentially blend into the valence band and cause the material to behave as an indirect semiconductor with a band gap of 1.32 eV. As with Co, the character of the CBE and VBE retain the overall character of the $MAPbI_3$ system.

Finally, MA(3Pb:1Mn)$I_3$ also demonstrates a narrow intermediate band but it is closer to the CBE and is separated from it by a gap of 0.25 eV, which is about twice

the energy separating the lower energy intermediate bands in the Co and Ni systems from the VBE. However, unlike those systems, the character of the CBE has changed and causes the lowest energy to arise at the U-point and the band gap to become indirect, like the case for MA(3Pb:1Mg)$I_3$.

The introduction of these states into the band gap could either act as deep traps that promote non-radiative recombination, or they could potentially have a beneficial role for performance. From a theoretical perspective, a system with an intermediate conduction band in the band gap provides the opportunity to break the detailed-balance limit. When an electron-hole pair is generated, the electron can be excited either into the intermediate or upper conduction band depending upon the energy of the incident photon. Upon absorption of a second photon, the electron in the intermediate band could be excited to the upper conduction band and contribute to the photocurrent of the device. Hence, the intermediate band provides mid-gap states for electrons to be generated from photons with energy below the overall band gap in a two photon process. An intermediate band solar cell must meet the following conditions for proper operation: [1]

1. The gaps in the band structure must be large compared to the maximum phonon energy. If the energy separation is too small, electrons excited into the conduction or intermediate bands are likely to scatter into a lower band by means of colliding with phonons.

2. The CBE of the electron transport layer should selectively contact only the upper conduction band and remain isolated from the intermediate band. Otherwise, the electrons populating the intermediate band will achieve thermal equilibrium with the contact and the CBE of the intermediate band will act as the CBE for the entire device, thereby dramatically reducing the attainable photovoltage.

3. The physical feature that generates the intermediate levels must be periodic in space. Periodicity allows for electrons to become delocalized, which aids transport through the semiconductor. If this condition is not met, such as in

the case of randomly distributed impurities, the carriers will become localized and carrier transport will become impeded.

The idealized mixed-metal perovskite systems inherently meet the third condition as the substituted atoms are periodically distributed throughout the bulk crystal. The second condition can be easily met through judicious choice of the electron transport layer. However, the first condition is the one that is problematic for these systems. The ambient thermal energy, $k_bT$, under operating conditions near 50°C is already around 0.03 eV. Hence, the 0.1 eV gaps are likely too small to prevent interband scattering from occurring. However, perhaps if different A-site or X-site ions are chosen instead of $MA^+$ and $I^-$ the intermediate band might be more securely separated from the band edges for these mixed-metal systems.

The band gap and energy gaps for the compositions that produce intermediate bands are tabulated in Table 5.11 and plotted in Figure 5-21. Upon comparing this figure against Figure 5-9, it is clear there is a correlation between the material band gap and the $c$ lattice parameter. Metal ions that elongate the crystal in the $z$-direction, such as $Sr^{2+}$ and $Zn^{2+}$, also widen the bandgap. Whereas, the compositions with smaller $c$ parameters, such as $Sn^{2+}$ and $Mn^{2+}$ also tend to have reduced band gaps. This suggests that the interaction between the B-site cations and the apical iodides in the octahedral cage strongly influence the character and location of the conduction and valence band edges. Figure 5-22 plots the CBE and VBE with respect to the Fermi level for each of the Pb-based perovskites with the composition of $MA(3Pb{:}1B')I_3$. This simplified flat band representation clearly shows that each material is indeed semiconducting since the Fermi level always runs through the band gap. It also suggests that replacing $Pb^{2+}$ can shift the location of the Fermi level within the band gap closer towards one of the band edges, thereby indicating that the material demonstrates a shift in electronic character. For instance, the cases of $MAPbI_3$, $MA(3Pb{:}1Sr)I_3$, and $MA(3Pb{:}1S)I_3$ have the Fermi level closer to the conduction band edge, which suggests these materials are slightly more $n$-type than the other compositions. Likewise, the case of Ni shifts the Fermi level closer to the valence band edge providing it with a character that is slightly more $p$-type. The cases of

Sn, Co, and Mg have a Fermi level positioned close to the center of the band gap indicating that these materials are closer to being intrinsic semiconductors. Generally, the perovskite materials are considered to be intrinsic semiconductors since there is usually no extinsic doping that would change the charge carrier densities, however the introduction of these secondary species could have an impact on carrier densities. For metal impurities in silicon, it has been observed that elements in Group 8 or below tend to act as electron donors, whereas those in Group 9 or as acceptors. [146] It is interesting that these simulations seem to generally support that observation in the perovskite material.

### 5.5.3 Tin Mixtures

The band structure was calculated for Sn-based perovskites compositions using the exact same method employed previously for the Pb-based perovskites. The band diagram for the $MA(3Sn:1B')I_3$ and $MA(2Sn:2B')I_3$ compositions are shown in Figure 5-23 and Figure 5-24, respectively. It is not surprising that the band structures for the $MA(3Sn:1B')I_3$ materials are very similar to the Pb-based analogs reported in Figure 5-20. The overall shape of the bands are very similar due to the fact that $Sn^{2+}$ and $Pb^{2+}$ have the same bonding behavior. Furthermore, the compositions with $Co^{2+}$, $Mn^{2+}$, and $Ni^{2+}$ once again produce intermediate bands, however the bands for Co and Ni are located even closer to the VBE. In fact, the lower energy band in Co and the band in Ni are so thinly separated from the VBE, that they hardly qualify as a band in the first place. The intermediate band for the Mn case is the first definitive band that does not have the Fermi level running through it. It is offset from the Fermi level by 0.23 eV and is thus the first identified intermediate band that could be accurately described as a second conduction band since it would be unpopulated at $T = 0$ K. This case is even more interesting since all of the gaps are indirect between the bands, which indicates that photogenerated electrons might be longer lived in the intermediate band since radiative recombination requires interactiong with a phonon to match momentum. The only other change between the Pb- and Sn-based analogs is that the embodiment with Sr now has an indirect band gap although the new lowest

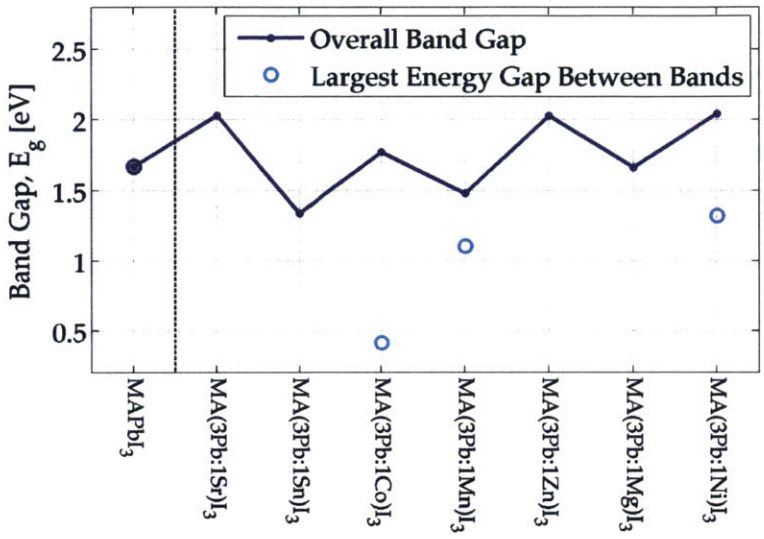


Figure 5-21: Calculated band gaps for mixed-metal Pb-based perovskites in order of decreasing ionic radius of secondary metal species.

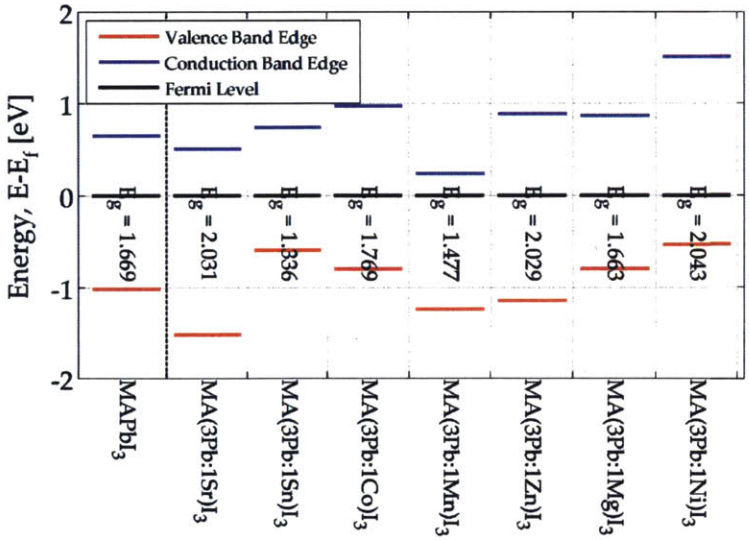


Figure 5-22: Calculated band edges with respect to the Fermi level for mixed-metal Pb-based perovskites in order of decreasing ionic radius of secondary metal species.

energy location is hardly removed from the Γ-point and the Mg case now has a direct band gap and retains the CBE character of the $MASnI_3$ material.

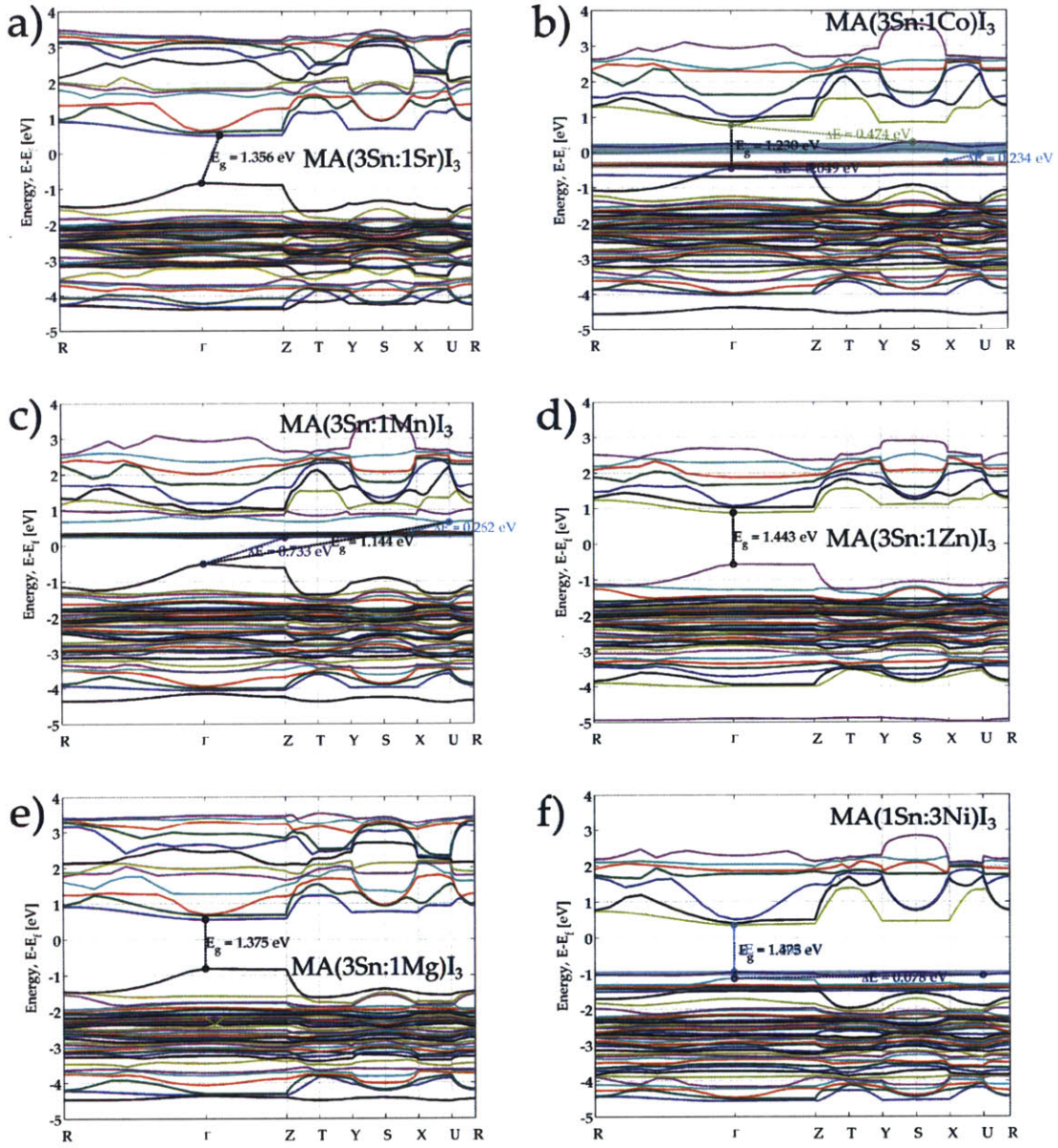


Figure 5-23: The calculated band structures for (a) $MA(3Sn:1Sr)I_3$, (b) $MA(3Sn:1Co)I_3$, (c) $MA(3Sn:1Mn)I_3$, (d) $MA(3Sn:1Zn)I_3$, (e) $MA(3Sn:1Mg)I_3$, and (f) $MA(3Sn:1Ni)I_3$

Increasing the content of the B′ species in the Sn-based materials to 50% generally changes the shape of the bands around the $X$-point. The only other major difference is

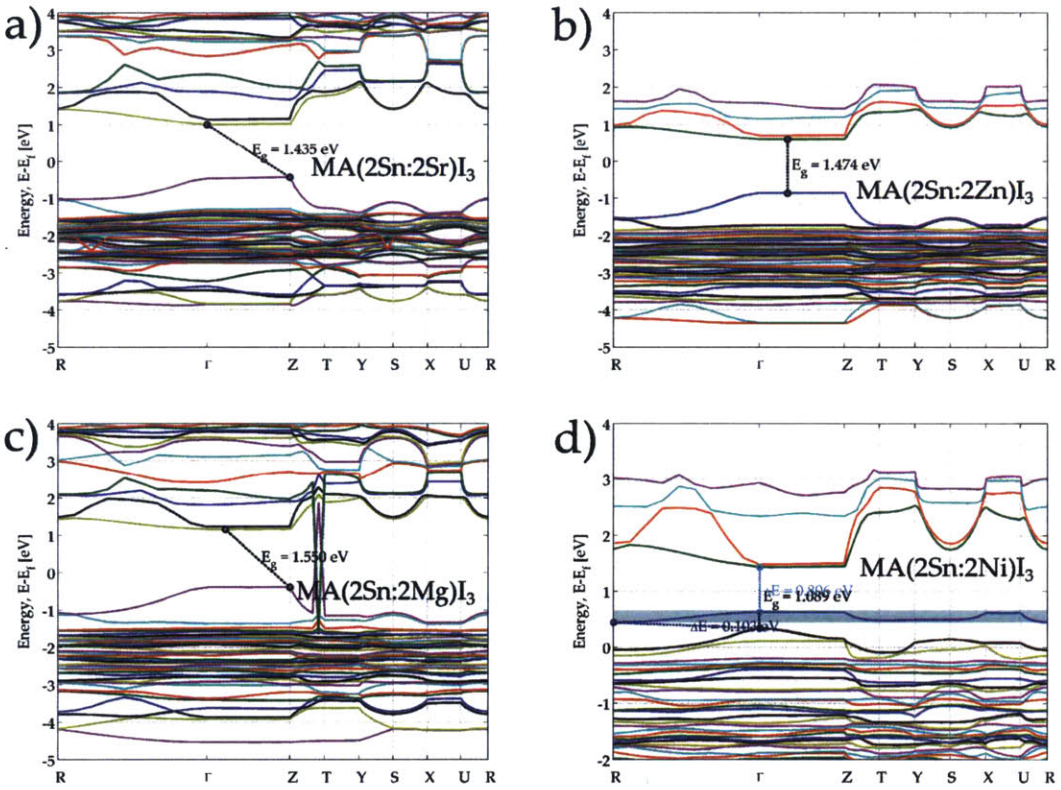


Figure 5-24: The calculated band structures for Sn-based mixed-metal perovskites (a) $MA(2Sn:2Sr)I_3$, (b) $MA(2Sn:2Zn)I_3$, (c) $MA(2Sn:2Mg)I_3$, (d) $MA(2Sn:2Ni)I_3$

that a strange cross-over point arises for the $MA(2Sn:2Mg)I_3$ material which appears to be reminescent of a topological insulator. It is unclear whether this is a physical effect or a result of some numerical error in the computation.

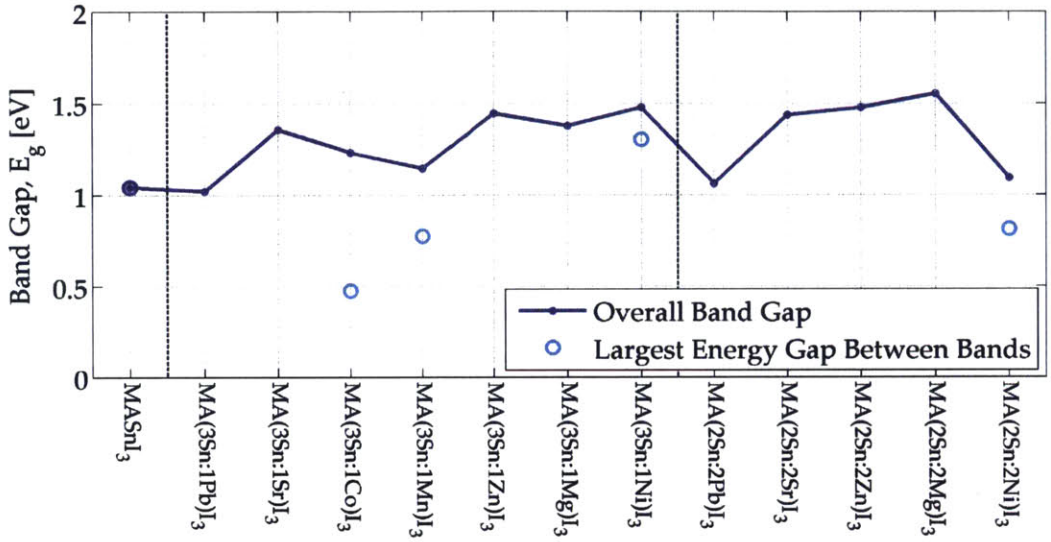


Figure 5-25: Calculated band gaps for mixed-metal Sn-based perovskites in order of decreasing ionic radius of secondary metal species.

The calculated band gaps are reported for each composition in Table 5.12 and Figure 5-25. For the 3Sn:1B′ compositions, the bandgap widens with decreasing ionic radius. These predictions suggest that the $MASnI_3$ is the smallest bandgap material that can be generated at absolute zero. However, as the temperature is increased, electrons will likely scatter into the valence band from the intermediate band in the Ni and Co systems, causing the effective band gap of these materials to decrease to even smaller values.

The band edges for each Sn-based composition are plotted in Figure 5-26. Of this set all of the compositions are semiconducting except for the case of $MA(2Sn:2Ni)I_3$, which is technically metallic since the Fermi level runs through the valence band rather that the gap. As seen with the Pb-mixtures, the Fermi level can shift to different positions within the band providing each composition with behavior that is intrinsic, $n$-type, or $p$-type. Most notably, pure Sn and the mixtures with Pb are the

Table 5.12: Calculated band gap, $E_g$, and energy gaps, $\Delta E$, for mixed-metal Sn-based perovskites in order of decreasing ionic radius of secondary metal species

| Material | $E_g$ [eV][a] | $\Delta E_1$ [eV] | $\Delta E_2$ [eV] | $\Delta E_3$ [eV] |
|---|---|---|---|---|
| $MASnI_3$ | 1.04 | - | - | - |
| $MA(3Sn:1Pb)I_3$ | 1.02 | - | - | - |
| $MA(3Sn:1Sr)I_3$ | 1.36 | - | - | - |
| $MA(3Sn:1Co)I_3$ | 1.23 | 0.47 | 0.23 | 0.05 |
| $MA(3Sn:1Mn)I_3$ | 1.14 | 0.73 | 0.26 | - |
| $MA(3Sn:1Zn)I_3$ | 1.44 | - | - | - |
| $MA(3Sn:1Mg)I_3$ | 1.38 | - | - | - |
| $MA(3Sn:1Ni)I_3$ | 1.47 | 1.30 | 0.08 | - |
| $MA(2Sn:2Pb)I_3$ | 1.06 | - | - | - |
| $MA(2Sn:2Sr)I_3$ | 1.44 | - | - | - |
| $MA(2Sn:2Zn)I_3$ | 1.47 | - | - | - |
| $MA(2Sn:2Mg)I_3$ | 1.55 | - | - | - |
| $MA(2Sn:2Ni)I_3$ | 1.09 | 0.81 | 0.10 | - |

[a]In the cases of Co, Mn, and Ni there exists one or more intermediate bands in the band structure. For these cases, the band gap value reported is the energy difference between the valence band and conduction band edges (*i.e.*, the usual band gap in the event the intermediate bands did not form). The energy for each gap is clearly labeled in Figure 5-23.

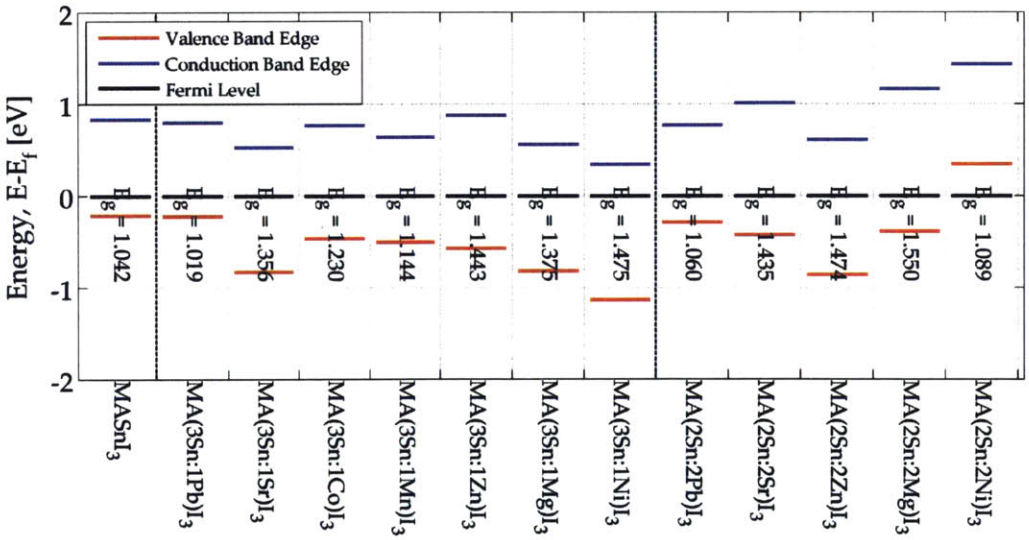


Figure 5-26: Calculated band edges with respect to the Fermi level for mixed-metal Sn-based perovskites in order of decreasing ionic radius of secondary metal species.

most $p$-type with the band edges closest to the VBE, whereas 3Sn:1Ni and 3Sn:1Mg materials are the most $n$-type with the band edges closest to the CBE.

### 5.5.4 Bismuth Mixtures

The calculated band structure for the MA(2Bi:2B′)$I_3$ mixed-metal perovskites are plotted in Figure 5-28. Compared with the Pb- and Sn-based systems, the Bi-based systems are relatively uninteresting. Each of the four compositions demonstrate relatively flat bands, especially at the VBE, and relatively wide bandgaps. The predicted values for this series of materials are tabulated in Table 5.13 and plotted in Figure 5-27. Only the composition with Cu is able to produce a band gap below 2 eV.

Table 5.13: Calculated band gap for mixed-metal Bi-based perovskites in order of decreasing ionic radius of secondary metal species

| Material | $E_g$ [eV] |
|---|---|
| MA(2Bi:2Cs)$I_3$ | 2.61 |
| MA(2Bi:2Na)$I_3$ | 2.17 |
| MA(2Bi:2Cu)$I_3$ | 1.49 |
| MA(2Bi:2Li)$I_3$ | 2.34 |

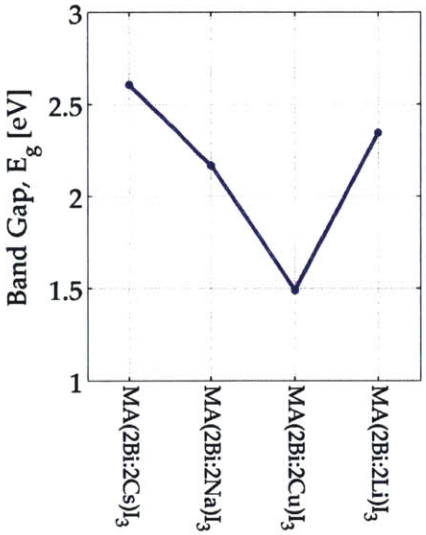


Figure 5-27: Calculated band gaps for mixed-metal Bi-based perovskites in order of decreasing ionic radius of secondary metal species.

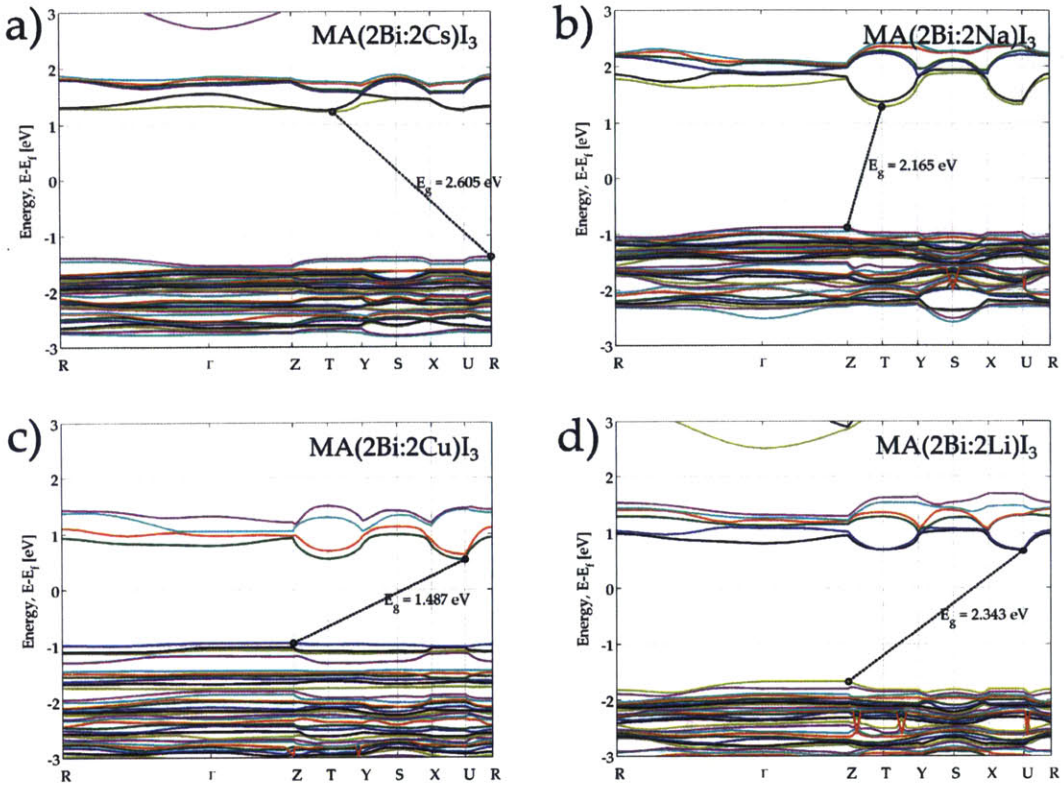


Figure 5-28: The calculated band structures for Bi-based mixed-metal perovskites (a) $MA(2Bi:2Cs)I_3$, (b) $MA(2Bi:2Na)I_3$, (c) $MA(2Bi:2Cu)I_3$, and (d) $MA(2Bi:2Li)I_3$

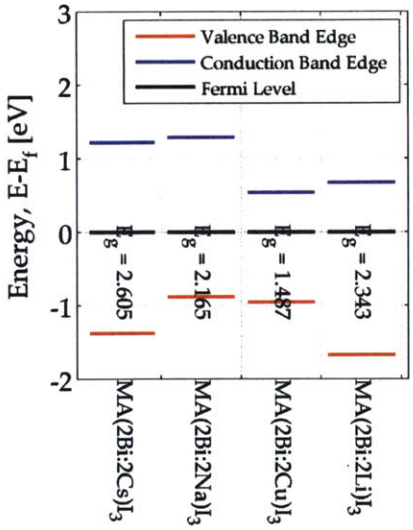


Figure 5-29: Calculated band edges with respect to the Fermi level for mixed-metal Bi-based perovskites in order of decreasing ionic radius of secondary metal species.

As can be easily seen from the band edges plotted with respect to the Fermi level for each Bi-based perovskite in Figure 5-29, the electronic structure is indeed semiconducting. The compositions with Cu and Li are more noticeably $n$-type while Na is $p$-type.

## 5.6 Carrier Effective Mass Calculations

Efficient solar materials must be able to quickly transport electrons and holes away from the site of photogeneration inside the crystal and inject them into their respective transport layers to minimize non-radiative charge recombination and maximize charge collection at the device electrodes. The material metric that gauges this is the respective carrier mobility of the holes and electrons. Carrier mobility, $\mu$, is defined as:

$$\mu = q\tau/m^* \tag{5.2}$$

where $q$ is the charge on an electron, $\tau$ is the average carrier scattering time, and $m^*$ is the effective mass of the carrier. Although it is generally very challenging to theoretically estimate $\tau$, the effective mass can be estimated directly from the calculated band structure. It is a measure of how easily electrons in a medium respond to applied forces, such as those exerted by the electric fields associated with solar cell operation. Equation 5.2 shows that the mobility of free charges in a semiconductor will be higher when the effective mass is low and charges are more likely to be efficiently transported through the solid material. The band structure $E(\mathbf{k})$ for classical semiconductors can often be locally approximated as having a simple parabolic form:

$$E(\mathbf{k}) = E_0 + \frac{\hbar^2 k^2}{2m^*} \tag{5.3}$$

where $E(\mathbf{k})$ is the energy of an electron at wavevector $\mathbf{k}$ in the band of interest and $E_0$ is a constant corresponding to the energy of the band edge. Equation 5.3 therefore provides the means to calculating the effective mass of carriers from the curvature of the bands if the parabolic approximation is valid.

In solar cells, a photoexcited electron will quickly thermalize down to the conduction band edge (CBE) and the corresponding hole will relax to the valence band edge (VBE). Since the free carriers will exist almost exclusively at the band edge, only the curvature of the VBE and CBE need be considered in the calculation. The effective mass of an electron, $m_e^*$, traveling along a particular crystallographic direction can be estimated by taking the second derivative of Equation 5.3: [1]

$$\frac{1}{m_e^*} = \frac{1}{\hbar^2}\frac{\partial^2 E}{\partial k^2}\bigg|_{CBE} \tag{5.4}$$

The effective mass of a hole, $m_h^*$, is analogously:

$$\frac{1}{m_h^*} = -\frac{1}{\hbar^2}\frac{\partial^2 E}{\partial k^2}\bigg|_{VBE} \tag{5.5}$$

Photogenerated carriers could be generated at any point inside the crystal and could travel along various crystallographic directions, some of which are easier to travel through than others. The effective masses were estimated for each candidate material by evaluating the band structure along a series of $k$-points between the Γ-point and every other major orthorhombic symmetry point, fitting a parabola to the local region around the Γ-point, and then evaluating the effective masses according to Equations 5.4 and 5.5. The band structures for the control MA(Pb:Sn)$I_3$ mixtures and the MA(3Pb:1B′)$I_3$, MA(3Sn:1B′)$I_3$, MA(2Sn:2B′)$I_3$, and MA(2Bi:2B′)$I_3$ mixed-metal perovskites are shown in Figures 5-30 through 5-34.

The crystallographic directions that have the largest curvature are the preferred pathways since they will result in the lowest effective mass of the carriers. Perovskite films can adopt several different preferred orientations of its grains depending upon the procedure used for synthesizing the films as well as the exact perovskite composition. For instance, reports suggest that grains of $FAPbI_3$ films have preferred orientation with the (110) [147] or (111) [29] planes, whereas $MAPbI_3$ films generally display preferred orientation with the (100) and (001) planes [148]. Therefore, although ideal perovskites will display low effective masses in each of the high-symmetry directions, the most-important are from $\Gamma \rightarrow X$ (*i.e.* [100]), $\Gamma \rightarrow Y$ (*i.e.* [010]), $\Gamma \rightarrow S$ (*i.e.*

[110]), and $\Gamma \rightarrow R$ (*i.e.* [111]).

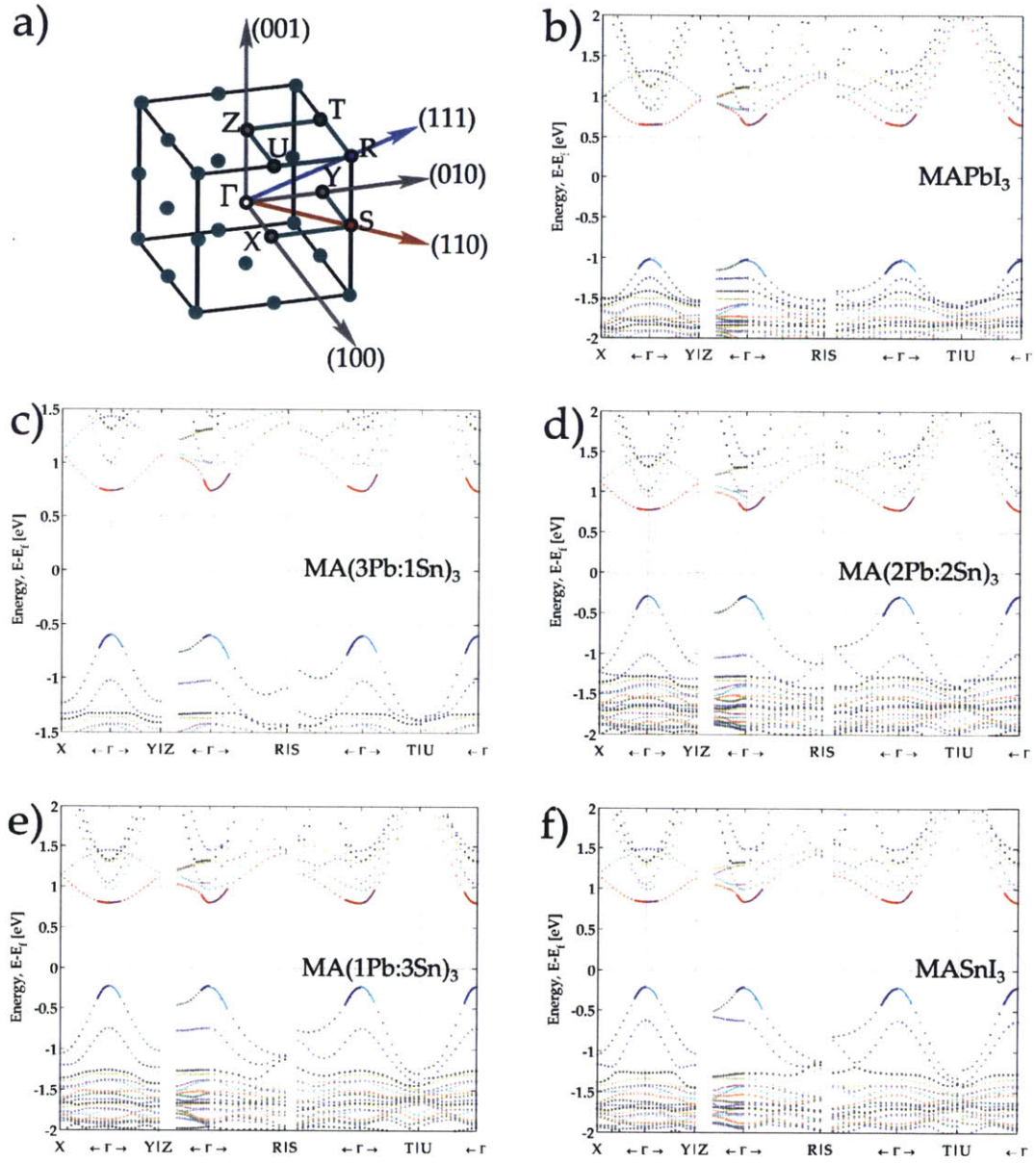


Figure 5-30: (a) The main crystallographic directions in the orthorhombic crystal lattice. The calculated band structure for each of the main crystallographic directions are shown as open-circles and the quadratic curvature fits near the Γ-point for each are outlined for the Pb:Sn blends: (b) $MAPbI_3$, (c) $MA(3Pb:1Sn)I_3$, (d) $MA(2Pb:2Sn)I_3$, (e) $MA(1Pb:3Sn)I_3$, and (f) $MASnI_3$.

The calculated values for the effective mass of electrons in the CBE and holes in the VBE for each of the perovskite systems are tabulated in Table 5.14 through

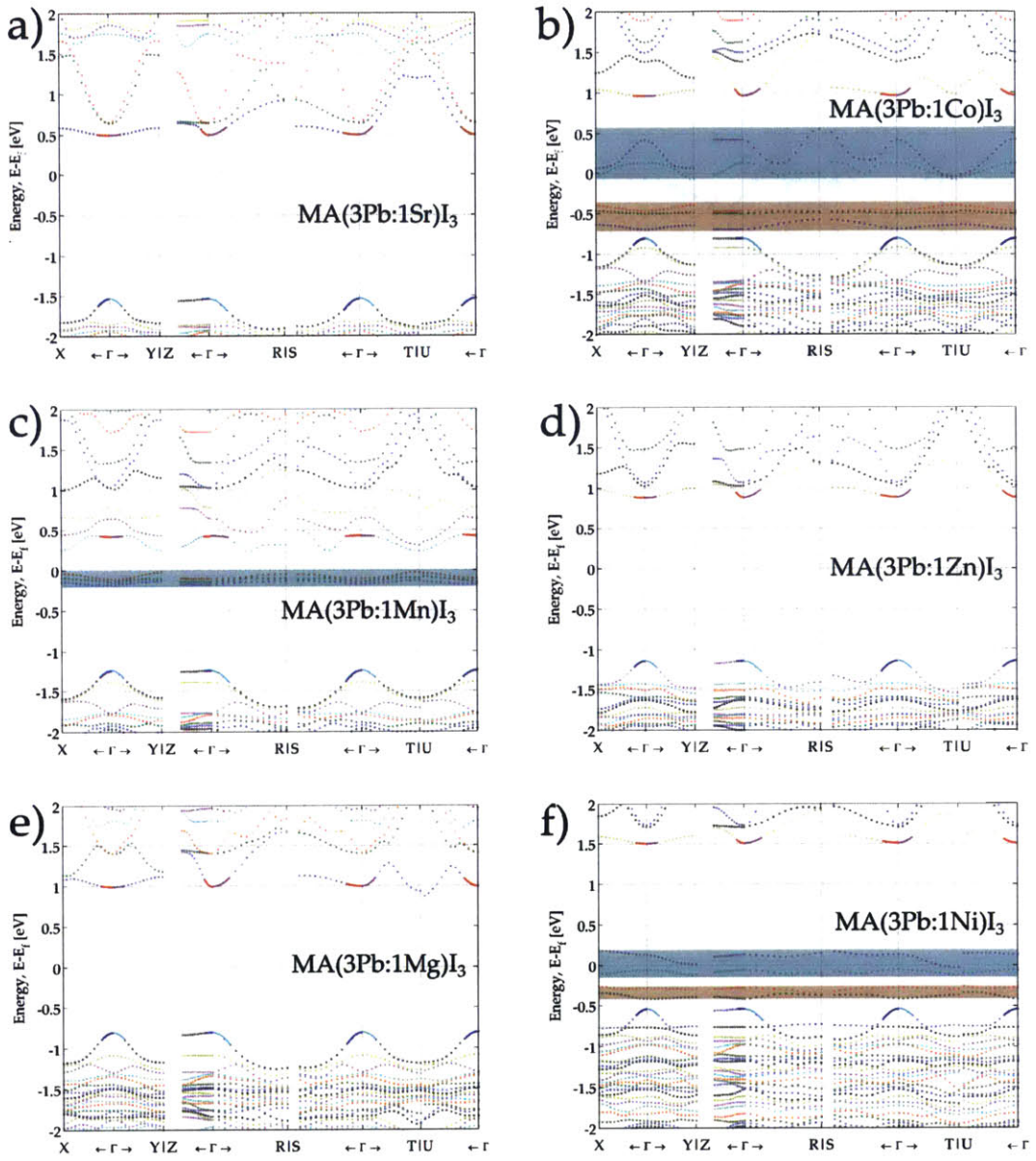


Figure 5-31: The calculated band structure for each of the main crystallographic directions are shown as open-circles and the quadratic curvature fits near the Γ-point for each are outlined for the Pb-based mixed-metal perovskites (a) MA(3Pb:1Sr)$I_3$, (b) MA(3Pb:1Co)$I_3$, (c) MA(3Pb:1Mn)$I_3$, (d) MA(3Pb:1Zn)$I_3$, (e) MA(3Pb:1Mg)$I_3$, and (f) MA(3Pb:1Ni)$I_3$.

5.16. The effective mass that has been averaged over all of the considered crystallographic directions is represented by the bar graphs in Figures 5-35 through 5-37 and the error bars span from the minimum to the maximum calculated value. For

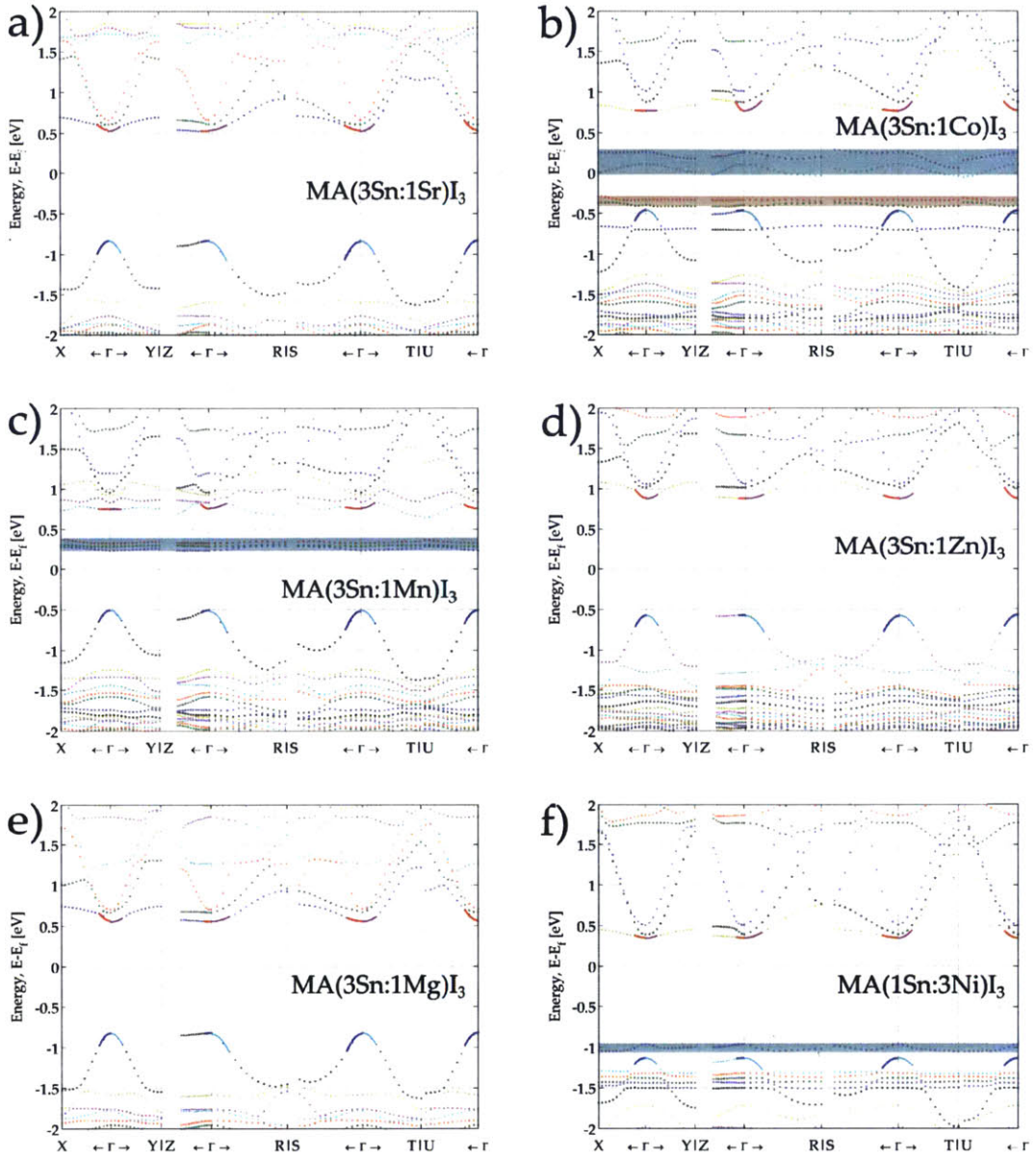


Figure 5-32: The calculated band structure for each of the main crystallographic directions are shown as open-circles and the quadratic curvature fits near the Γ-point for each are outlined for the Sn-based mixed-metal perovskites (a) MA(3Sn:1Sr)$I_3$, (b) MA(3Sn:1Co)$I_3$, (c) MA(3Sn:1Mn)$I_3$, (d) MA(3Sn:1Zn)$I_3$, (e) MA(3Sn:1Mg)$I_3$, and (f) MA(3Sn:1Ni)$I_3$.

the case of $MAPbI_3$, the reduced effective masses for holes are both low and vary little with direction, whereas the reduced effective masses for electrons are generally slightly higher and are worse for directions in the XY-plane than any vector with a

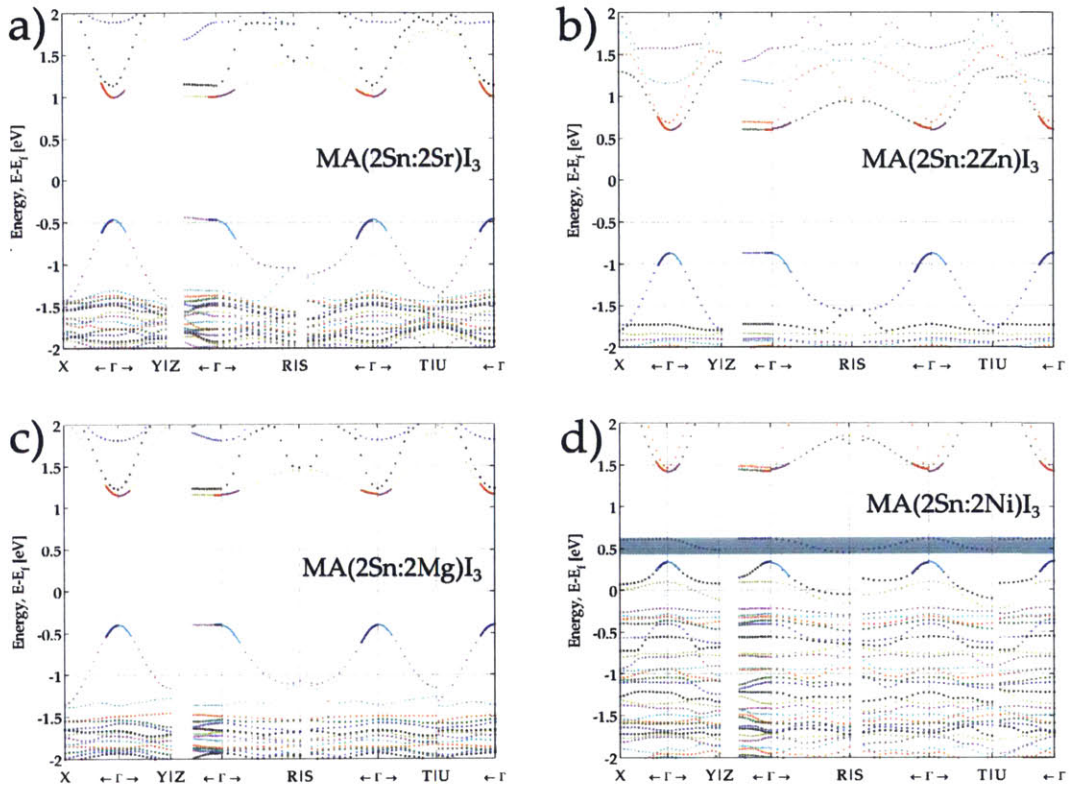


Figure 5-33: The calculated band structure for each of the main crystallographic directions are shown as open-circles and the quadratic curvature fits near the Γ-point for each are outlined for the Sn-based mixed-metal perovskites (a) MA(2Sn:2Sr)$I_3$, (b) MA(2Sn:2Zn)$I_3$, (c) MA(2Sn:2Mg)$I_3$, and (d) MA(2Sn:2Ni)$I_3$.

component along the $z$-direction. These values for electrons are much higher that the recently measured value of $m_e^*/m_0 = 0.104$ in $MAPbI_3$, which was achieved through spectroscopic methods that use very high magnetic fields. [149] As discussed previously, the effective masses of the electrons are expected to be overestimated in our DFT calculations as a result of not using spin-orbit coupling. However, the trends between compositions is still expected to be informative as the error is likely to be systematic for the entire set of mixed-metal perovskites. Most of the Pb-based blends exhibit comparable effective masses to the values for pure Pb with two notable deviations: Co and Mn. As discussed previously, both of these compositions produce intermediate bands and hence the character of the band edges change. The curvature is flattest for the $\Gamma \rightarrow X$ and $\Gamma \rightarrow Y$ directions in the pure Pb case and become

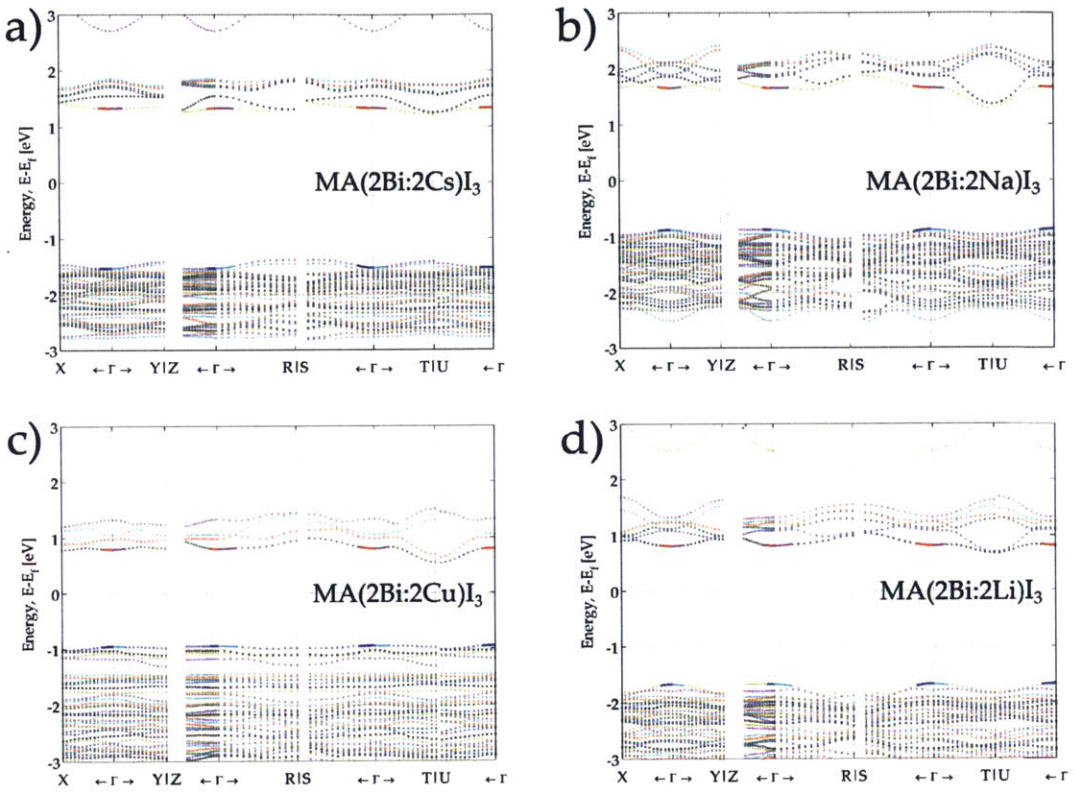


Figure 5-34: The calculated band structure for each of the main crystallographic directions are shown as open-circles and the quadratic curvature fits near the Γ-point for each are outlined for the Bi-based mixed-metal perovskites (a) MA(2Bi:2Cs)$I_3$, (b) MA(2Bi:2Na)$I_3$, (c) MA(2Bi:2Cu)$I_3$, and (d) MA(2Bi:2Li)$I_3$.

even flatter upon substitution with $Co^{2+}$. Also the $\Gamma \rightarrow Z$ case is remarkably flat for both the valence and intermediate bands. However, the effective masses in all other directions are similar to the $MAPbI_3$. The case of Mn is unique among this set because the character of the CBE is remarkably different. It is similar to the VBE in that the local curvature is slightly concave-down rather than concave-up. As a result, the effective mass of electrons in several directions is negative, which indicates that the electrons will act as if they have a positive charge with positive mass. Otherwise, the calculations suggest that the effective masses of the electrons generally decrease when a second species is substituted at some of the B-sites, whereas the effective mass of the holes generally increase slightly. It is quite possible that this behavior would be rectified if spin-orbit coupling was included. Regardless, these calculations

still demonstrate that the carrier transport properties of Pb-based perovskites is generally preserved upon replacing a quarter of the $Pb^{2+}$ ions with a non-toxic metal species.

The pure Sn perovskite, $MASnI_3$ is predicted to have slightly lower effective masses than lead-based counterpart. As with the Pb-based materials, the 3Sn:1Co composition displays higher $m_e^*$ in the $\Gamma \rightarrow X$ and $\Gamma \rightarrow Y$ principal directions and the 3Sn:1Mn composition displays some oddly shaped bands in the same locations that are not accurately captured with a parabolic fit. The effective masses of the holes are nominally the same as the pure Sn case since the VBE is not strongly perturbed in either case. The local curvature for $\Gamma \rightarrow Z$ for the case of 3Sn:1Sr also is not quite parabolic and hence a negative effective mass is calculated here for electrons in the CBE. Otherwise, substantial changes to the effective masses only arise at higher dopings, where both the CBE and VBE almost completely flatten with $\Gamma \rightarrow Z$ generating exorbitantly high reduced effective masses, that exceed $1 \cdot 10^{13}$ (hence these values are reported as $\infty$ in the Table 5.15.) Overall, these calculations suggest that replacing a quarter of the $Pb^{2+}$ or $Sn^{2+}$ ions with a second metal species is indeed only *perturbing* their respective pure $MABI_3$ systems, as evidenced by the similarity in calculated effective masses between the mixed and pure materials. However, the $MA(2Sn:2B')I_3$ systems reveal that transport can become substantially impeded in the $\Gamma \rightarrow Z$ direction when the replacement level is increased to half of the metal atoms.

Compared to Pb- and Sn-based perovskites, Bi-based blends have considerably worse transport properties. The reduced effective masses of both carriers are always greater than unity regardless of the crystallographic direction and the average values of $m_e^*/m_0$ for 2Bi:2Cs and $m_h^*/m_0$ for 2Bi:2Na only appear low because some directions produce positive values while others are negative. Hence, even though $MA(2Bi:2Cu)I_3$ demonstrates a reasonably good band gap, its effective masses are so high that the material would not be able to efficiently extract photogenerated carriers from the material bulk.

Table 5.14: Calculated effective masses for electrons in CBE, $m_e^*$, and holes in the VBE, $m_h^*$, for major crystallographic directions in the Pb-based mixed-metal perovskites.

| | $m_e^*/m_0$ [-] | | | | | | | |
|---|---|---|---|---|---|---|---|---|
| Material | Avg | Γ →X | Γ →Y | Γ →Z | Γ →R | Γ →S | Γ →T | Γ →U |
| $MAPbI_3$ | 1.90 | 4.89 | 5.83 | 0.14 | 0.44 | 1.33 | 0.27 | 0.37 |
| $MA(3Pb:1Sr)I_3$ | 1.30 | 2.44 | 2.51 | 0.17 | 0.67 | 2.48 | 0.39 | 0.41 |
| $MA(3Pb:1Sn)I_3$ | 0.63 | 1.20 | 1.18 | 0.12 | 0.39 | 1.03 | 0.24 | 0.29 |
| $MA(3Pb:1Co)I_3$ | 3.09 | 8.20 | 8.33 | 0.15 | 0.76 | 3.22 | 0.44 | 0.54 |
| $MA(3Pb:1Mn)I_3$ | -0.92 | 3.79 | 4.60 | -4.13 | -3.29 | -4.81 | -7.73 | 5.15 |
| $MA(3Pb:1Zn)I_3$ | 1.22 | 2.66 | 2.12 | 0.18 | 0.62 | 2.10 | 0.41 | 0.44 |
| $MA(3Pb:1Mg)I_3$ | 1.05 | 2.02 | 2.07 | 0.13 | 0.56 | 1.82 | 0.36 | 0.40 |
| $MA(3Pb:1Ni)I_3$ | 1.44 | 2.46 | 2.54 | 0.28 | 0.95 | 2.58 | 0.55 | 0.74 |

| | $m_h^*/m_0$ [-] | | | | | | | |
|---|---|---|---|---|---|---|---|---|
| Material | Avg | Γ →X | Γ →Y | Γ →Z | Γ →R | Γ →S | Γ →T | Γ →U |
| $MAPbI_3$ | 0.30 | 0.22 | 0.26 | 0.43 | 0.32 | 0.32 | 0.28 | 0.25 |
| $MA(3Pb:1Sr)I_3$ | 0.56 | 0.28 | 0.29 | 1.77 | 0.42 | 0.36 | 0.40 | 0.38 |
| $MA(3Pb:1Sn)I_3$ | 0.27 | 0.20 | 0.23 | 0.36 | 0.30 | 0.29 | 0.25 | 0.23 |
| $MA(3Pb:1Co)I_3$ | 1.88 | 0.34 | 0.32 | 10.72 | 0.46 | 0.39 | 0.45 | 0.48 |
| $MA(3Pb:1Mn)I_3$ | 0.86 | 0.34 | 0.32 | 3.58 | 0.45 | 0.38 | 0.44 | 0.47 |
| $MA(3Pb:1Zn)I_3$ | 0.62 | 0.34 | 0.31 | 1.97 | 0.46 | 0.40 | 0.42 | 0.46 |
| $MA(3Pb:1Mg)I_3$ | 0.55 | 0.30 | 0.30 | 1.68 | 0.42 | 0.36 | 0.40 | 0.41 |
| $MA(3Pb:1Ni)I_3$ | 0.87 | 0.34 | 0.32 | 3.66 | 0.47 | 0.39 | 0.44 | 0.47 |

Table 5.15: Calculated effective masses for electrons in CBE, $m_e^*$, and holes in the VBE, $m_h^*$, for major crystallographic directions in the Sn-based mixed-metal perovskites.

| | $m_e^*/m_0$ [-] | | | | | | | |
|---|---|---|---|---|---|---|---|---|
| Material | Avg | Γ →X | Γ →Y | Γ →Z | Γ →R | Γ →S | Γ →T | Γ →U |
| $MASnI_3$ | 0.82 | 1.37 | 2.10 | 0.13 | 0.40 | 1.19 | 0.27 | 0.29 |
| $MA(3Sn:1Pb)I_3$ | 0.71 | 1.29 | 1.55 | 0.12 | 0.37 | 1.11 | 0.24 | 0.26 |
| $MA(3Sn:1Sr)I_3$ | -1.08 | 0.35 | 0.50 | -10.92 | 0.95 | 0.78 | 0.46 | 0.30 |
| $MA(3Sn:1Co)I_3$ | 2.44 | 4.63 | 7.82 | 0.12 | 0.49 | 3.33 | 0.33 | 0.33 |
| $MA(3Sn:1Mn)I_3$ | -0.18 | 6.40 | -12.99 | 0.21 | 1.01 | 2.76 | 0.57 | 0.79 |
| $MA(3Sn:1Zn)I_3$ | 0.99 | 0.22 | 0.48 | 2.85 | 1.23 | 1.33 | 0.56 | 0.26 |
| $MA(3Sn:1Mg)I_3$ | 0.99 | 0.26 | 0.59 | 2.89 | 1.10 | 1.18 | 0.63 | 0.26 |
| $MA(3Sn:1Ni)I_3$ | 0.88 | 0.76 | 0.88 | 1.21 | 0.88 | 1.65 | 0.38 | 0.40 |
| $MA(2Sn:2Pb)I_3$ | 0.69 | 1.34 | 1.42 | 0.13 | 0.38 | 1.05 | 0.23 | 0.29 |
| $MA(2Sn:2Sr)I_3$ | 1.46 | 0.14 | 0.28 | 7.77 | 0.77 | 0.64 | 0.40 | 0.20 |
| $MA(2Sn:2Zn)I_3$ | $-\infty$ | 0.16 | 0.33 | $-\infty$ | 0.89 | 0.76 | 0.45 | 0.23 |
| $MA(2Sn:2Mg)I_3$ | $-\infty$ | 0.22 | 0.38 | $-\infty$ | 1.30 | 1.14 | 0.53 | 0.30 |
| $MA(2Sn:2Ni)I_3$ | 1.25 | 0.21 | 0.31 | 5.79 | 0.90 | 0.76 | 0.43 | 0.32 |

| | $m_h^*/m_0$ [-] | | | | | | | |
|---|---|---|---|---|---|---|---|---|
| Material | Avg | Γ →X | Γ →Y | Γ →Z | Γ →R | Γ →S | Γ →T | Γ →U |
| $MASnI_3$ | 0.21 | 0.17 | 0.20 | 0.22 | 0.24 | 0.24 | 0.20 | 0.19 |
| $MA(3Sn:1Pb)I_3$ | 0.20 | 0.15 | 0.18 | 0.23 | 0.22 | 0.22 | 0.19 | 0.17 |
| $MA(3Sn:1Sr)I_3$ | 0.30 | 0.16 | 0.18 | 0.85 | 0.26 | 0.22 | 0.24 | 0.21 |
| $MA(3Sn:1Co)I_3$ | 0.40 | 0.20 | 0.22 | 1.29 | 0.29 | 0.27 | 0.28 | 0.25 |
| $MA(3Sn:1Mn)I_3$ | 0.25 | 0.18 | 0.20 | 0.44 | 0.24 | 0.22 | 0.23 | 0.22 |
| $MA(3Sn:1Zn)I_3$ | 0.90 | 0.17 | 0.20 | 4.85 | 0.30 | 0.25 | 0.28 | 0.24 |
| $MA(3Sn:1Mg)I_3$ | 0.54 | 0.16 | 0.18 | 2.45 | 0.27 | 0.23 | 0.25 | 0.22 |
| $MA(3Sn:1Ni)I_3$ | 0.51 | 0.31 | 0.33 | 1.32 | 0.43 | 0.40 | 0.42 | 0.38 |
| $MA(2Sn:2Pb)I_3$ | 0.20 | 0.15 | 0.18 | 0.26 | 0.23 | 0.22 | 0.19 | 0.18 |
| $MA(2Sn:2Sr)I_3$ | -0.32 | 0.16 | 0.18 | -3.62 | 0.29 | 0.23 | 0.28 | 0.24 |
| $MA(2Sn:2Zn)I_3$ | $-\infty$ | 0.18 | 0.19 | $-\infty$ | 0.27 | 0.23 | 0.26 | 0.24 |
| $MA(2Sn:2Mg)I_3$ | $-\infty$ | 0.20 | 0.20 | $-\infty$ | 0.28 | 0.24 | 0.27 | 0.26 |
| $MA(2Sn:2Ni)I_3$ | 0.35 | 0.24 | 0.32 | 0.47 | 0.39 | 0.39 | 0.33 | 0.29 |

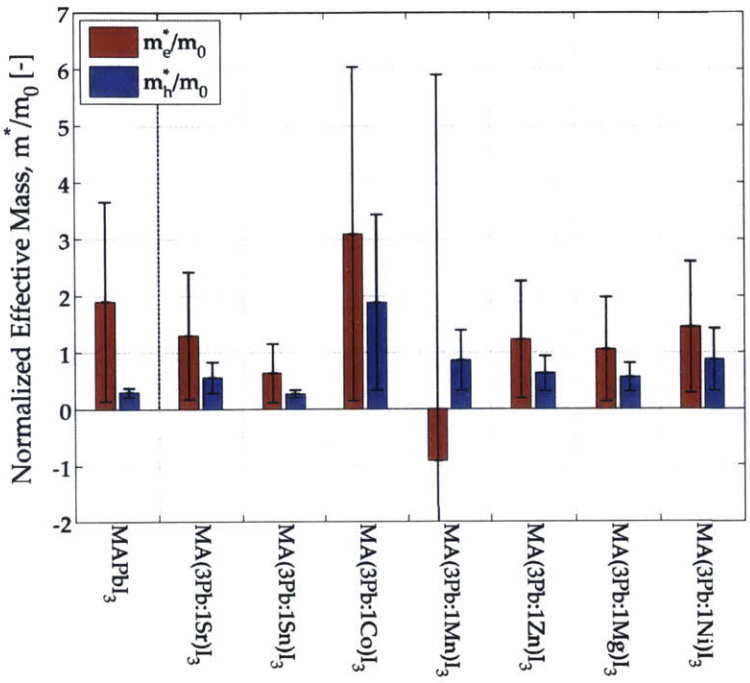


Figure 5-35: The mean effective mass of electrons in CBE (red), $m_e^*$, and holes in the VBE (blue), $m_h^*$, of each Pb-based perovskite normalized to rest mass of an electron, $m_0$. Error bars represent the full range of calculated values for the crystallographic directions.

## 5.7 Thermodynamic Stability

Although several of the mixed-metal perovskites have demonstrated favorable bandgaps and charge transport properties from the previous band structure calculations, the questions remains whether it would be thermodynamically favorable for these mixed-metal structures to even form. Basic thermodynamics states that a favorable reaction will proceed if the total energy of the products is less than that of the reactants. Therefore, the glaring question of whether these mixed-metal compounds are even theoretically stable was addressed by calculating the total energies of a handful of iodide precursor materials and comparing the total energies of the collection of precursor materials against that of the corresponding mixed-metal perovskite for stoichiometrically equivalent systems. Specifically, the Sn-based systems of $MA(3Sn{:}1B')I_3$ and $MA(2Sn{:}2B')I_3$ for $B' = \{Mg, Ni, Sr\}$ were computationally evaluated in the following manner:

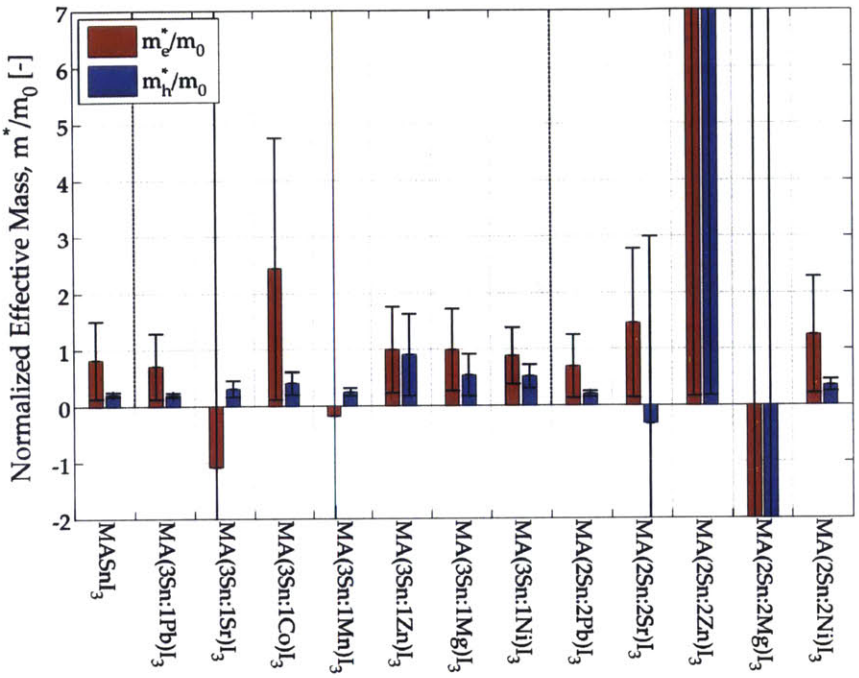


Figure 5-36: The mean effective mass of electrons in CBE (red), $m_e^*$, and holes in the VBE (blue), $m_h^*$, of each Sn-based perovskite normalized to rest mass of an electron, $m_0$. Error bars represent the full range of calculated values for the crystallographic directions.

1. The crystal structure of MAI, $SnI_2$, $MgI_2$, $NiI_2$, and $SrI_2$ were individually relaxed to the lowest energy configuration with the same pseudopotentials used for the mixed-metal perovskite calculations. The crystal structures for each of these are shown in Figure 5-38.

2. The total energy of each precursor material was adjusted to ensure that the stoichiometry of the chemical pathway for the perovskite formation reaction is balanced.

3. The total energy of the relaxed mixed-metal perovskite is compared against the sum of the total energies for the related precursor materials, with each adjusted to the proper molar amount.

4. If the energy of the final mixed-metal perovskite is less than that sum of the precursors, then it is thermodynamically favorable to form the perovskite.

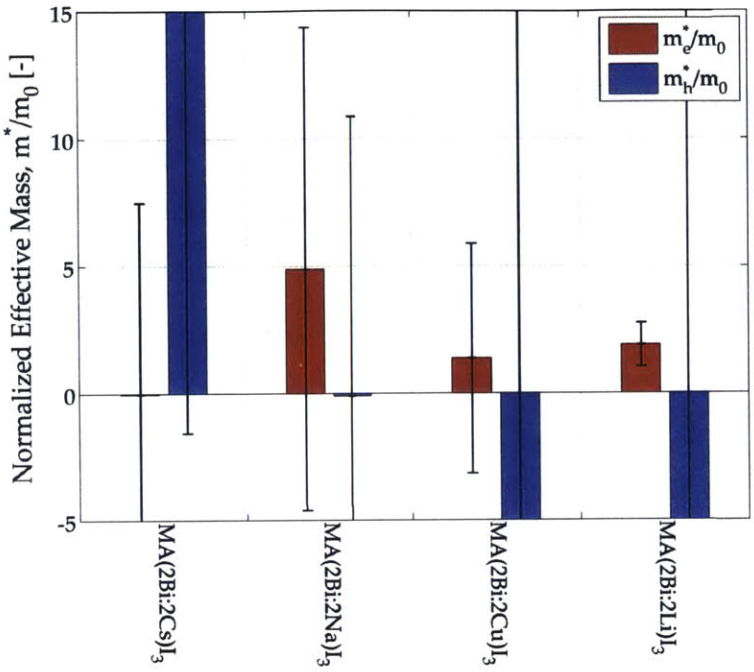


Figure 5-37: The mean effective mass of electrons in CBE (red), $m_e^*$, and holes in the VBE (blue), $m_h^*$, of each Bi-based perovskite normalized to rest mass of an electron, $m_0$. Error bars represent the full range of calculated values for the considered crystallographic directions.

For instance, the chemical reaction to form $MA(3Sn:1Sr)I_3$ is:

$$4\ MAI + 3\ SnI_2 + SrI_2 \rightarrow 4\ MASn_{0.75}Sr_{0.25}I_3 \tag{5.6}$$

The unit cell for MAI has 4 $MA^+$ ions and 4 I atoms; $SnI_2$ has 6 Sn and 12 I atoms; and $SrI_2$ has 4 Sr and 8 I atoms while the mixed metal perovskite unit cell is comprised of 4 $MA^+$ ions and 3 Sn, 1 Sr, and 12 I atoms. Therefore, the total energy calculated for each crystal must be adjusted so the stoichiometry of the reaction is correct:

$$E_{Precursors} = E_{MAI} + \frac{3}{6}E_{SnI_2} + \frac{1}{4}E_{SrI_2} \tag{5.7}$$

where $E$ is the calculated total energy for the relaxed crystal structure for each simulated material.

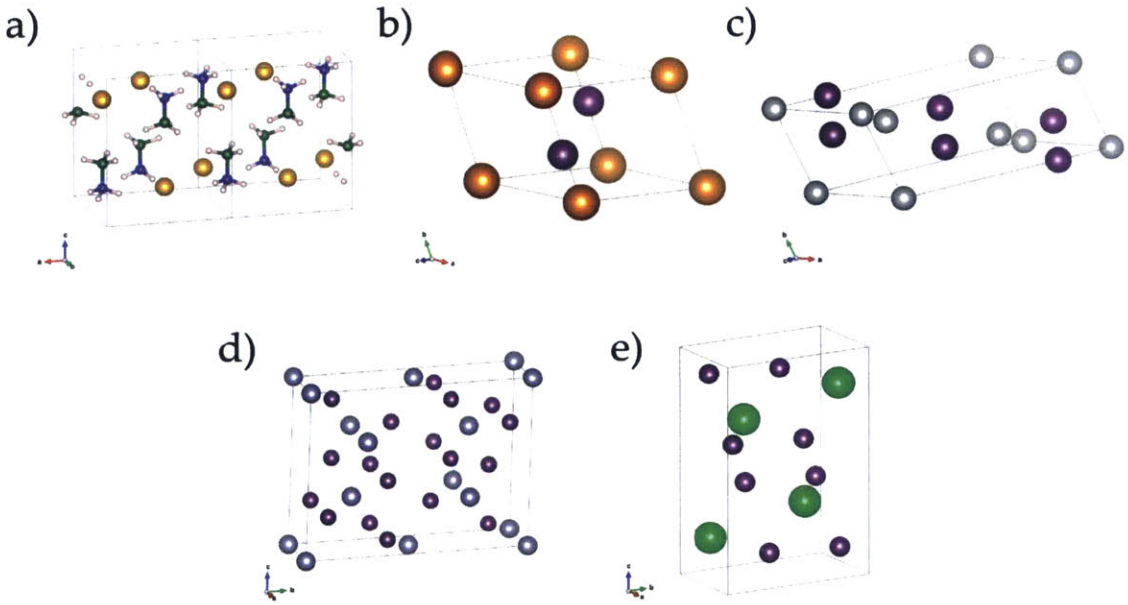


Figure 5-38: The crystal structures of the iodide precursor materials are very diverse as evidenced by the different structures of a) MAI, b) $MgI_2$, c) $NiI_2$, d) $SnI_2$, and e) $SrI_2$.

In each of the six cases investigated, it was always more energetically favorable for the precursors to form the mixed-metal material than for them to remain unreacted. The total energies of the collection of precursors is compared against that of the corresponding perovskite for each composition investigated in both Table 5.17 and Figure 5-39. The energy difference between the collection of reactants and the candidate perovskite is generally around 0.5 eV. This reveals that it is likely that the mixed-metal materials would form, or more accurately that if the material was synthesized, it would not phase separate back into its original precursors at absolute zero. The calculations do not provide any insight into the kinetics of the reaction, so although the perovskite is expected to form, it is not known how quickly the reaction would proceed. It also does not provide any information about whether the mixed-metal materials would remain stable at elevated temperatures. However, the calculated energy differential between the reactant and products is substantially above the 0.03 eV due to ambient thermal energy at room temperature, which provides some encouragement that the mixed-metal perovskites might be stable from this standpoint.

Table 5.16: Calculated effective masses for electrons in CBE, $m_e^*$, and holes in the VBE, $m_h^*$, for major crystallographic directions in the Bi-based mixed-metal perovskites.

| | $m_e^*/m_0$ [-] | | | | | | | |
|---|---|---|---|---|---|---|---|---|
| Material | Avg | $\Gamma \rightarrow$X | $\Gamma \rightarrow$Y | $\Gamma \rightarrow$Z | $\Gamma \rightarrow$R | $\Gamma \rightarrow$S | $\Gamma \rightarrow$T | $\Gamma \rightarrow$U |
| $MA(2Bi:2Cs)I_3$ | -0.02 | 3.35 | 9.05 | -0.85 | -7.55 | 4.59 | -2.53 | -6.22 |
| $MA(2Bi:2Na)I_3$ | 4.87 | 1.50 | 1.74 | 1.49 | 26.67 | 1.73 | -4.61 | 5.59 |
| $MA(2Bi:2Cu)I_3$ | 1.37 | 2.52 | 1.79 | 1.04 | 4.17 | 1.64 | 1.57 | -3.13 |
| $MA(2Bi:2Li)I_3$ | 1.90 | 1.75 | 1.78 | 1.04 | 2.46 | 1.83 | 2.64 | 1.79 |

| | $m_h^*/m_0$ [-] | | | | | | | |
|---|---|---|---|---|---|---|---|---|
| Material | Avg | $\Gamma \rightarrow$X | $\Gamma \rightarrow$Y | $\Gamma \rightarrow$Z | $\Gamma \rightarrow$R | $\Gamma \rightarrow$S | $\Gamma \rightarrow$T | $\Gamma \rightarrow$U |
| $MA(2Bi:2Cs)I_3$ | $\sim \infty$ | 21.46 | -1.07 | 9.64 | -1.37 | -1.12 | -1.55 | $\sim \infty$ |
| $MA(2Bi:2Na)I_3$ | -0.10 | 1.53 | 1.43 | -11.05 | 1.70 | 1.34 | 2.09 | 2.25 |
| $MA(2Bi:2Cu)I_3$ | $-\infty$ | 2.82 | 8.25 | $-\infty$ | 8.46 | 6.05 | 17.78 | 4.31 |
| $MA(2Bi:2Li)I_3$ | $-\infty$ | 1.36 | 1.60 | $-\infty$ | 1.83 | 1.47 | 2.26 | 2.05 |

Table 5.17: The thermodynamic stability of several Sn-based perovskites is established by comparing the total energy of the mixed-metal perovskite system to the sum of the individual precursors.

| Material | $\sum_{Precursors} E_T$ [Ry] | $E_{Perovskite}$ [Ry] | $E_{Perovskite} - \sum_{Precursors} E_T$ [Ry] | $E_{Perovskite} - \sum_{Precursors} E_T$ [eV] |
|---|---|---|---|---|
| $MASnI_3$ | -1537.961 | -1538.004 | -0.043 | -0.59 |
| $MA(3Sn:1Sr)I_3$ | -1459.411 | -1459.436 | -0.026 | -0.35 |
| $MA(3Sn:1Mg)I_3$ | -1514.155 | -1514.185 | -0.030 | -0.40 |
| $MA(3Sn:1Ni)I_3$ | -1732.819 | -1732.851 | -0.032 | -0.43 |
| $MA(2Sn:2Sr)I_3$ | -1380.860 | -1380.882 | -0.032 | -0.43 |
| $MA(2Sn:2Mg)I_3$ | -1490.349 | -1490.403 | -0.054 | -0.73 |
| $MA(2Sn:2Ni)I_3$ | -1927.677 | -1927.728 | -0.051 | -0.70 |

Table 5.18: The thermodynamic stability of several mixed-metal perovskites as determined by comparing the total energy of the mixed-metal material $MA(B:B')I_3$, $E_M$, against the case of phase separation, $E_{PS}$, where the pure $MABI_3$ forms and keeps the excess MAI and $B'I_2$ as separate phases.

| Material | Unit Cell | $E_T$ [Ry] | $E_{PS} = xE_{MAPbI_3} + yE_{MASnI_3}$ x | y | $E_{PS}$[Ry] | $E_{PS} = xE_{MABI_3} + yE_{B'I_2} + zE_{MAI}$ x | y | z | $E_{PS}$ [Ry] | $E_M - E_{PS}$ [Ry] | [eV] | Stable |
|---|---|---|---|---|---|---|---|---|---|---|---|---|
| $SnI_2$ | 6 Sn; 12 I | -1682.2598 | - | - | - | - | - | - | - | - | - | - |
| $SrI_2$ | 4 Sr; 8 I | -807.3055 | - | - | - | - | - | - | - | - | - | - |
| $MgI_2$ | 1 Mg; 2I | -256.5709 | - | - | - | - | - | - | - | - | - | - |
| $NiI_2$ | 3 Ni; 6I | -1425.7040 | - | - | - | - | - | - | - | - | - | - |
| MAI | 4 MA; 4 I | -416.4543 | - | - | - | - | - | - | - | - | - | - |
| $MAPbI_3$ | 4 MA; 4 Pb; 12 I | -1529.6611 | - | - | - | - | - | - | - | - | - | - |
| $MASnI_3$ | 4 MA; 4 Sn; 12 I | -1538.0039 | - | - | - | - | - | - | - | - | - | - |
| $MA(3Pb:1Sn)I_3$ | 4 MA; 3 Pb; 1 Sn; 12 I | -1531.7485 | $\frac{3}{4}$ | $\frac{1}{4}$ | -1531.7468 | - | - | - | - | -0.0017 | -0.023 | T |
| $MA(2Pb:2Sn)I_3$ | 4 MA; 2 Pb; 2 Sn; 12 I | -1533.8334 | $\frac{1}{2}$ | $\frac{1}{2}$ | -1533.8325 | - | - | - | - | -0.0009 | -0.012 | T |
| $MA(1Pb:3Sn)I_3$ | 4 MA; 1 Pb; 3 Sn; 12 I | -1535.9171 | $\frac{1}{4}$ | $\frac{3}{4}$ | -1535.9182 | - | - | - | - | 0.0011 | 0.015 | F |
| $MA(3Pb:1Mg)I_3$ | 4 MA; 3 Pb; 1 Mg; 12 I | -1507.9337 | - | - | - | $\frac{3}{4}$ | 1 | 1 | -1507.9303 | -0.0033 | -0.046 | T |
| $MA(3Pb:1Ni)I_3$ | 4 MA; 3 Pb; 1 Ni; 12 I | -1726.5919 | - | - | - | $\frac{3}{4}$ | $\frac{1}{2}$ | $\frac{1}{4}$ | -1726.5940 | 0.0022 | 0.029 | F |
| $MA(3Pb:1Sr)I_3$ | 4 MA; 3 Pb; 1 Sr; 12 I | -1453.1885 | - | - | - | $\frac{3}{4}$ | $\frac{3}{4}$ | $\frac{1}{4}$ | -1453.1858 | -0.0027 | -0.037 | T |
| $MA(3Sn:1Mg)I_3$ | 4 MA; 3 Sn; 1 Mg; 12 I | -1514.1851 | - | - | - | $\frac{3}{4}$ | 1 | $\frac{1}{4}$ | -1514.1875 | 0.0024 | 0.033 | F |
| $MA(3Sn:1Ni)I_3$ | 4 MA; 3 Sn; 1 Ni; 12 I | -1732.8506 | - | - | - | $\frac{3}{4}$ | $\frac{1}{2}$ | $\frac{1}{4}$ | -1732.8512 | 0.0006 | 0.008 | F |
| $MA(3Sn:1Sr)I_3$ | 4 MA; 3 Sn; 1 Sr; 12 I | -1459.4364 | - | - | - | $\frac{3}{4}$ | $\frac{3}{4}$ | $\frac{1}{4}$ | -1459.4429 | 0.0065 | 0.088 | F |
| $MA(2Sn:2Mg)I_3$ | 4 MA; 2 Sn; 2 Mg; 12 I | -1490.4032 | - | - | - | $\frac{1}{2}$ | 2 | $\frac{1}{2}$ | -1490.3710 | -0.0322 | -0.438 | T |
| $MA(2Sn:2Ni)I_3$ | 4 MA; 2 Sn; 2 Ni; 12 I | -1927.7280 | - | - | - | $\frac{1}{2}$ | $\frac{2}{2}$ | $\frac{1}{2}$ | -1927.6985 | -0.0295 | -0.402 | T |
| $MA(2Sn:2Sr)I_3$ | 4 MA; 2 Sn; 2 Sr; 12 I | -1380.8825 | - | - | - | $\frac{1}{2}$ | $\frac{1}{2}$ | $\frac{1}{2}$ | -1380.8819 | -0.0006 | -0.008 | T |

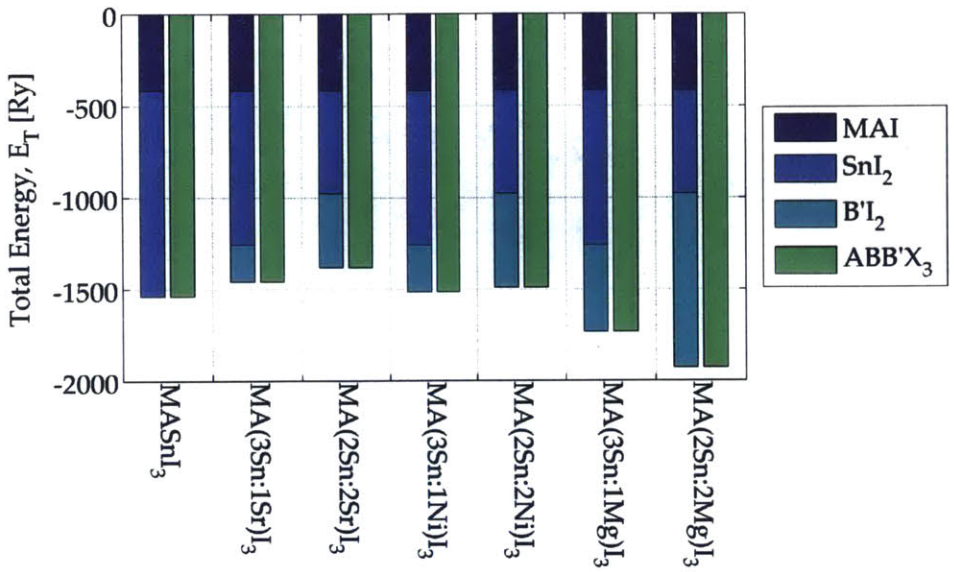


Figure 5-39: The thermodynamic stability of several Sn-based perovskites is established by comparing the total energy of the mixed-metal perovskite system to the sum of the individual precursors.

Perhaps a more accurate assessment of thermodynamic stability is to consider whether MAI, $BI_2$, and $B'I_2$ will form a single phase of $MA(B:B')I_3$ or will only form the pure metal perovskite $MABI_3$ and keep the excess MAI and $B'I_2$ in separate phases, as is sketched in Figure 5-40a. For instance, the corresponding chemical reaction for this situation when attempting to form $MA(3B:1B')I_3$ is:

$$4\ MAI + 3\ BI_2 + B'I_2 \rightarrow 3\ MABI_3 + B'I_2 + MAI \tag{5.8}$$

Likewise, when MAI, $PbI_2$, and $SnI_2$ are mixed is it more favorable to form the mixed-metal perovskite or two separate phases of pure perovskites, as shown in Figure 5-40b? An example chemical reaction is:

$$4\ MAI + 2\ PbI_2 + 2\ SnI_2 \rightarrow 2\ MAPbI_3 + 2\ MASnI_3 \tag{5.9}$$

Both of these situations can be analyzed in the same manner as the previous analysis where now the total energy of the mixed-metal perovskite is compared against the

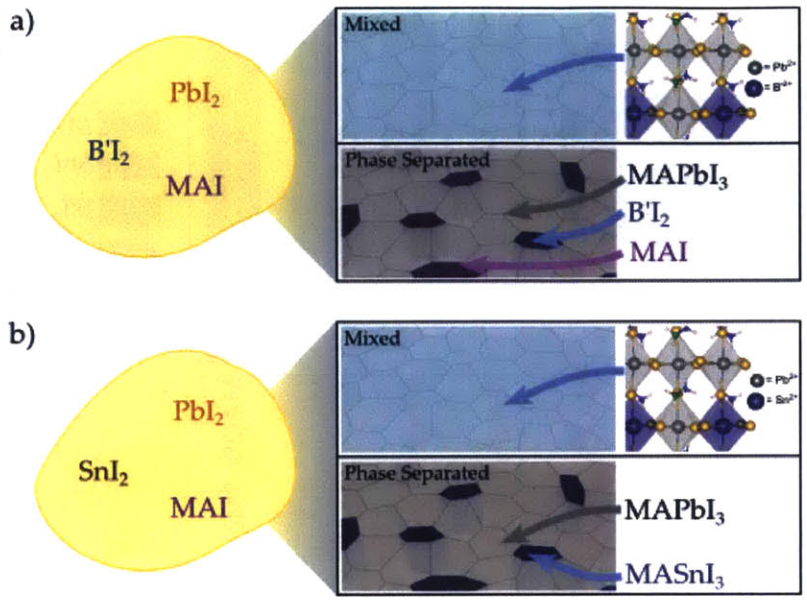


Figure 5-40: When (a) $PbI_2$, $B'I_2$, and MAI are mixed together, the active layer could crystallize into a single homogeneous mixed-metal perovskite phase or the pure $MAPbI_3$ could form in some grains and exclude the residual $B'I_2$ and MAI into separate phases. (b) Similarly, when $PbI_2$, $SnI_2$, and MAI are mixed together, the active layer could crystallize into a single homogeneous mixed-metal perovskite phase or two separate phases of pure $MAPbI_3$ and pure $MASnI_3$ could form.

combined total energies of the materials on the right side of Equations 5.8 or 5.9. The analysis and the findings are shown in Table 5.18. Interestingly, this analysis indicates that it is thermodynamically favorable for MA(3Pb:1Sn)$I_3$ and MA(2Pb:1Sn)$I_3$ to form. However when the Sn content is increased to 75% of the metal atoms, it is more likely that separate pure Pb and Sn phases will form rather than MA(1Pb:3Sn)$I_3$. Similarly, the formation of MA(3Pb:1Mg)$I_3$ and MA(3Pb:Sr)$I_3$ are favorable but not MA(3Pb:1Ni)$I_3$. The Sn-mixtures behave similarly as the Pb:Sn blends where all of the MA(2Sn:2B′)$I_3$ blends are favored and none of the MA(3Sn:1B′)$I_3$ are expected to form.

This result is actually quite interesting since previous studies have experimentally attempted Pb:Sn materials and devices. [129,140,150] It is very difficult to experimentally distinguish a film of MA(1Pb:3Sn)$I_3$ from a mixture of two separate pure metal perovskite phases. The DFT calculations indicate that neither the lattice parameters

(see Table 5.4) nor the band gap (see Table 5.10) are expected to appreciably change between MA(1Pb:3Sn)$I_3$ and $MASnI_3$. Similarly, the experimental values are nearly identical. Therefore, the only way to truly identify whether the material phase separates is to attempt to build a film of MA(1Pb:3Sn)$I_3$, mill out a TEM cross-section with a focused-ion beam, and perform high-resolution elemental mapping with energy dispersive x-ray spectroscopy (EDS) or electron energy loss spectroscopy (EELS) to see if different grains have different compositions or if the Sn and Pb are uniformly distributed throughout the film.

It must also be mentioned that the energy difference between the mixed-metal perovskite and phase separated cases for each of the Pb:Sn and 3B:1B′ mixtures is *very small.* The largest energy difference is only 46 meV which is hardly above the 25 meV value for thermal energy at room temperature. Hence, although these predictions are interesting, the question of thermal stability has not been definitively resolved with these calculations.

Furthermore, often the iodide precursors can be hydrated or adopt different crystal phases. Therefore, it is difficult to have too much confidence about whether phase separation would occur when attempted experimentally as the materials are above absolute zero and the precursor materials might either be different from those analyzed here or be impure or hydrated. In any of these cases, the total energy for the precursor and perovskite materials might be different from the ideal cases considered in this study.

## 5.8 Workfunction Estimates from Slab Calculations

When designing the device architecture of solar cells, it is common practice to compare the band edge locations (with respect to vacuum) of each material to one another to ensure electronic asymmetry exists that promotes the migration of electrons and holes in opposite directions and towards the desired collecting electrode. High performing perovskite solar cells generally place the hole transporter spiro-OMeTAD between the hybrid perovskite and a gold top electode and an electron transporter

such as titania in between it and a transparent conductive oxide, such as fluorine-doped tin oxide (FTO) or indium tin oxide (ITO). Thus, even if a material has a favorable band gap, it cannot produce working solar cells without having its conduction band edge align with a good electron transporter and the valence band edge align with a good hole transporter. The workfunction of each candidate material was estimated by performing a slab calculation that was periodic in the $z$-direction with a methylammonium-iodide terminated (001) surface at the top interface, a metal-iodide terminated (001) surface at the bottom interface, and vacuum in between. The (001) surface was selected because in some $MAPbI_3$ perovskite films it has been identified as having a preferred orientation normal to the substrate. [148] By using a dipole correction to account for the extra charge density at the interface, the electrical potential profile in the $z$-direction was found, enabling the workfunction of each interface to be calculated for the (001) plane. Figure 5-41 overlays the electrostatic potential line-trace on the the crystal structure of the $MA(3Sn{:}1Sr)I_3$ perovskite. The workfunction for each surface termination and the average value are reported for each perovskite material in Table 5.19. Because the perovskite materials are either solution-processed or vapor deposited instead of being epitaxially grown, other crystal faces besides the (001) planes will exist at surfaces, therefore this calculation is intended purely as a rough estimate and more rigorous analysis that explicitly considers a heterojunction is required to predict the energetics of the interfaces when multiple materials are in physical contact.

The absolute band edges with respect to the vacuum level are estimated by using the average workfunctions to position the Fermi level of each material with respect to the vacuum level. These predictions provide the edges of the "flat bands" for an isolated material that is not in physical contact with other layers. As shown in Figure 5-42, the predicted values for $MA(Pb{:}Sn)I_3$ mixtures are in surprisingly good agreement with the measured flat band CBE and VBE locations reported by Ogomi et al. [129] The DFT calculations predict values that are around 0.2 to 0.5 eV closer to the vacuum level. The fact that the offset is consistent between samples suggests that the workfunction predictions are somewhat erroneous, which is to be expected

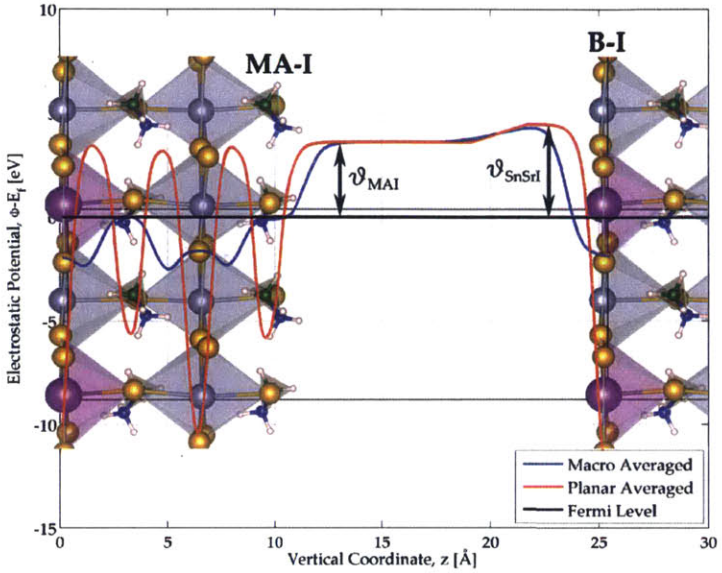


Figure 5-41: The workfunctions are determined from the electrostatic potential plots in the [001] direction for a MA(3Sn:1Sr)$I_3$ slab terminated with either Methlyammonium/Iodide (MA-I) ions or B-site/Iodide (B-I) ions at the (001) surfaces.

since the (001) surfaces are not the only facets that will comprise the surfaces of the grains in the polycrystalline perovskite film. However, the error seems systematic between the predicted and measured values, therefore the predictions for mixed-metal Sn and Bi-based perovskites are expected to demonstrate fairly accurate trends when compared against the $MASnI_3$ material.

The absolute location of the VBE provides some hints about the susceptibility of the perovskite material to oxidation. [138]. The closer the VBE is to the vacuum level, the more difficult it will be to remove electrons from the Pb or Sn atoms and oxidize from the +2 to +4 state. This notion is supported by the experimental and measured band edges shown in Figure 5-42, where the VBE edge is deepest for $MAPbI_3$ and becomes increasingly shallow with increasing Sn content. Comparing the mixed-metal Sn-based band edges to the $MASnI_3$ case suggests that Co, Mg, and Sr will not help prevent oxidation. However, the band edges of MA(3Sn:1Ni)$I_3$ are dramatically deeper and the VBE edge matches that of $MAPbI_3$. This encouraging result suggests that including Ni in the Sn-based perovskite might help stabilize the

material against oxidation.

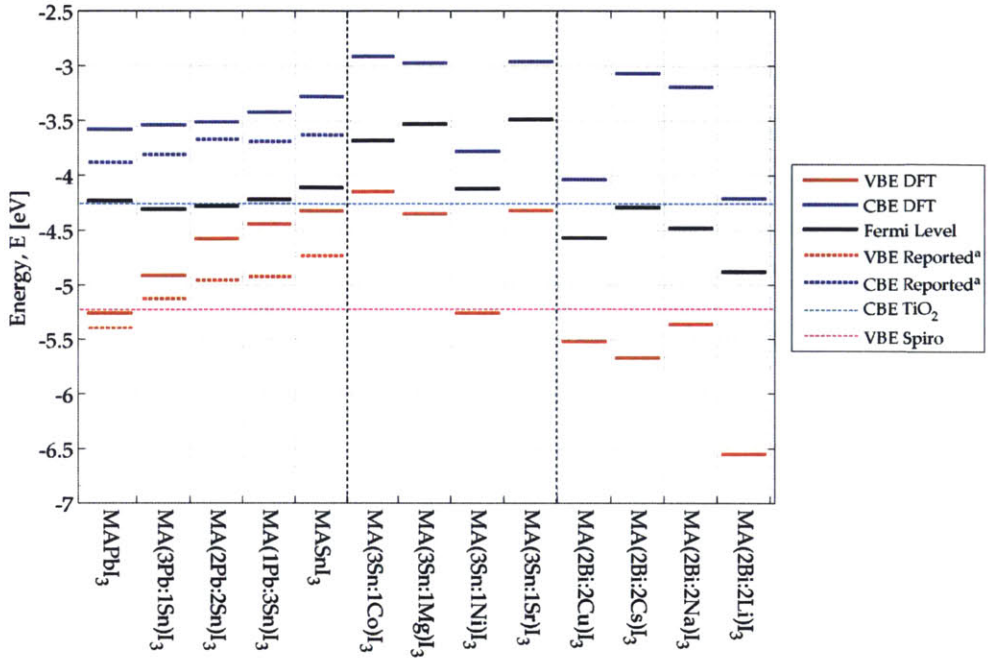


Figure 5-42: The predicted absolute band edges locations with respect to vacuum level for selected mixed-metal perovskites. [a]MA(Pb:Sn)$I_3$ blends are compared against experimental values reported by Ogomi *et al.* [129]

Table 5.19: Workfunction of select perovskite materials with the (001) surface terminated by either $MA^+$ and $I^-$ ions or with B-site and $I^-$ ions as determined by a slab calculation

| | Workfunction, $\phi$ [eV] | | |
|---|---|---|---|
| Material | MA-I | B-I | Average |
| $MAPbI_3$ | 3.33 | 5.13 | 4.23 |
| MA(3Pb:1Sn)$I_3$ | 3.31 | 5.30 | 4.31 |
| MA(2Pb:2Sn)$I_3$ | 3.37 | 5.20 | 4.28 |
| MA(1Pb:3Sn)$I_3$ | 3.47 | 4.98 | 4.22 |
| $MASnI_3$ | 3.17 | 5.06 | 4.11 |
| MA(3Sn:1Co)$I_3$ | 2.33 | 5.03 | 3.68 |
| MA(3Sn:1Mg)$I_3$ | 2.34 | 4.72 | 3.53 |
| MA(3Sn:1Ni)$I_3$ | 2.42 | 5.81 | 4.12 |
| MA(3Sn:1Sr)$I_3$ | 3.62 | 3.36 | 3.49 |
| MA(2Bi:2Cu)$I_3$ | 3.75 | 5.40 | 4.57 |
| MA(2Bi:2Cs)$I_3$ | 3.61 | 4.96 | 4.29 |
| MA(2Bi:2Na)$I_3$ | 3.72 | 5.23 | 4.48 |
| MA(2Bi:2Li)$I_3$ | 4.24 | 5.53 | 4.88 |

## 5.9 Identification of Final Candidates

In the preceding sections we first validated the use of DFT-GGA calculations to predict the crystal and electronic structure of organic-inorganic hybrid perovskite materials by accurately reproducing the experimental lattice constants reported for $MAPbI_3$, $MASnI_3$, and mixed $MA(Pb:Sn)I_3$ systems and predicting band gaps for these materials that reproduce the experimental trend reported in literature. These benchmarking efforts indicate that we can have good faith in the ability of this computational method to make reasonable predictions of similar yet wholly hypothetical materials that have reduced toxicity or are wholly non-toxic.

Now that the crystallographic and electronic properties have been presented in detail and discussed for each of the twenty hypothetical mixed-metal perovskite materials listed in Table 5.2, we are in a position to apply the criteria established in Table 5.1 and screen through the candidate pool to identify the most theoretically desirable materials for further experimental investigation. Table 5.20 summarizes the results of the computational screening study of mixed-metal perovskite materials by applying the established criteria to the predictions made for each material.

To identify new theoretical solar materials, cutoff values need to be defined for each quantified solar cell metric, which determined the range of acceptable predicted values for each criteria:

1. **Band Gap:** it is desirable that the solar materials have band gaps as close as possible to 1.4 eV, which according to the Shockley-Queisser limit will maximize the theoretical performance of an ideal single-junction semiconductor solar cell illuminated by the AM 1.5 solar spectrum. Calculated band gaps were considered acceptable if they were within 0.4 eV of 1.4 eV. Hence, any material with a band gap between 1.0 and 1.8 eV meets this criterion. This is considered appropriate in this situation because this range encompasses the predictions for $MAPbI_3$, $MASnI_3$, and the $MA(Pb:Sn)I_3$ mixtures, all of which are known to produce working devices - although the device performance generally drops off significantly as the Sn content is increased in actual devices. [129, 150] It

is also well-known that DFT-GGA calculations generally underestimate band gap predictions as a result of the exchange-correlation not fully capturing the behavior of electron-electron interactions. Hence, materials with low band gaps could be even more desirable in reality, whereas predictions with 1.8 eV could be even wider. Although the upper bound of 1.8 eV was arbitrarily established, Table 5.20 shows that the final candidate with the largest band gap is actually the $MAPbI_3$ control material, which encouragingly leaves the possibility open that some of the other final candidates might produce a value closer to 1.4 eV, if synthesized. The band gap reported here for solar cells with intermediate bands is the largest gap, which corresponds to the difference between the band edge of the valence band and the edge of the uppermost conduction band. As discussed previously, it is possible that a low energy intermediate band might effectively become an extension of the VBE in the cases of $MA(3B{:}B')I_3$ where $B' = \{Co, Ni\}$ and act to lower the band gap of the device.

2. **Carrier Effective Masses:** ensuring that the photogenerated charges in the perovskite materials can be easily transported through an ideal crystal requires that the effective masses of an electron in the CBE and a hole in VBE be as low as possible. Since the charges will have different effective masses as they migrate through different crystallographic planes, the mean value calculated over all the considered paths through $k$-space was used as the actual metric. The upper bound for acceptance for this criterion was set at the electron rest mass, $m_0$ for holes (*i.e.* $\overline{m_h^*}/m_0 < 1$) and twice this value for electrons (*i.e.* $\overline{m_e^*}/m_0 < 2$). These bounds were established to ensure that each of the control materials, $MAPbI_3$, $MASnI_3$, and the $MA(Pb{:}Sn)I_3$ mixtures, do not fail this criterion. It must be noted that the predicted effective masses were generally the highest and most troublesome along the principle directions of the orthorhombic crystal, <100>, whereas oblique directions such as [111] generally produce very favorable values.

3. **Band Edge Alignment:** although the electron and hole transport layers that

contact the upper and lower faces of a planar perovskite material must have the proper electronic structure to efficiently extract or inject charges, the estimates for material workfunctions are not accurate enough to make any theoretical assessments. For instance, the calculated average workfunction of $MAPbI_3$ for both terminations of (001) planes is 4.23 eV, and the CBE and VBE relative to the Fermi level are predicted to be 0.65 and -1.02 eV. This puts the estimated CBE and VBE edge at -3.58 eV and -5.25 eV, whereas most literature places the CBE around -3.9 eV and the VBE at -5.4 eV for $MAPbI_3$. [129,148] In this particular case, the predicted band edge locations are reasonable. However given that there is almost a 2 eV difference between the workfunctions of the same crystallographic plane but with different ions terminating the surface, as shown by Table 5.19 for $MAPbI_3$, the error in these rough predictions are considered too high to be of any realistic use in predicting the band edge locations. Hence, this physical requirement for creating practical solar cells is not adequately addressed in this computational study. Rather, the band edge locations should be measured experimentally using ultraviolet photoelectron spectroscopy or Kelvin probe in combination with measured optical band gaps.

4. **Thermodynamic Stability:** this is perhaps the most straightforward criterion since the total energy of the final perovskite must be less than the combined total energy of the precursor materials in order for the material to form according to basic thermodynamic principles. Each of the six evaluated cases indicated that the mixed-metal perovskites have a lower energy configuration than the unreacted precursors. However, a separate set of calculations indicate that it would be *slightly* more favorable in several compositons for a pure $MABI_3$ phase to form with the second species remaining as the iodide salt along with any excess MAI. However, in practice the temperature of these materials will never be below room temperature and it is unclear whether the materials would form or destabilize at elevated temperatures or when the perovskites undergo phase transitions. Although the materials are evaluated here based on the strict

finding of the computations, only experimental verification can firmly answer this question.

The final candidates of mixed-metal perovskites that are of the highest priority for experimental validation are highlighted in bold in Table 5.20, all of the control devices by design pass the screening test with the exception of $MA(1Pb:3Sn)I_3$, which is slightly more stable when it forms separate pure Sn and pure Pb perovskite phases. The promising materials of the Pb-based mixtures are $MA(3Pb:1Mg)I_3$ and $MA(3Pb:1Mn)I_3$, however the thermodynamic stability of the Mn composition was not evaluated. Although $MA(3Pb:1Co)I_3$ has the potential to create an intermediate band solar cell, it demonstrates relatively high carrier effective masses and has been screened out from the initial candidate pool for this reason. The thermodynamic stability analysis indicates that none of the $MA(3Sn:1B')I_3$ materials examined are expected to form, rather a pure $MASnI_3$ phase would exclude the secondary metal species and keep the original iodide precursor and the excess MAI as separate phases. Otherwise, these hypothetical Sn-based mixtures demonstrate desirable band gaps and low effective masses. Since the thermodynamic stability test did not specifically evaluate either the Mn or Zn materials, these are still included as final candidate solar materials. However, again the difference in energy between the mixed-metal and phase separated cases is only marginal and the question of stability cannot be confidently concluded. In contrast, the $MA(2Sn:2Mg)I_3$ and $MA(2Sn:2Ni)I_3$ compositions were thermodynamically stable by a much wider margin of 0.4 eV. Of this set, only $MA(2Sn:2Sr)I_3$ demonstrated reasonable electronic properties and was included as a final candidate although its stability margin is much lower. The mixed-materials based on bismuth display prohibitively high effective masses and wide band gaps, which excluded all of them from becoming final candidates. From this set, $MA(2Bi:2Cu)I_3$ displays the best electronic properties, however the crystal structure predictions suggest that the $Cu^+$ atom displaces significantly from the center of the octahedral cage, which might make the material unstable at operating conditions when the temperature is elevated to room temperature or above and a voltage bias is applied across the material.

## 5.10 Conclusion

In conclusion, this screening study used the computational technique of density functional theory to investigate the possibility of generating mixed-metal perovskite materials and has successfully identified several Pb-based and Sn-based candidates as promising materials that could potentially perturb the pure perovskite materials into similar or even more favorable solar materials. The thermodynamic stability test suggest that it might be difficult to form mixed-metal Sn-based perovskites when only a quarter of the $Sn^{2+}$ ions are replaced by a second metal species, including $Pb^{2+}$. However, it must be emphasized that these predictions are for *ideal* materials and generally the electronic predictions from DFT calculations are substantially less accurate than crystallographic predictions. Furthermore, these calculations are largely for *bulk* materials and generally perovskite films are multi-crystalline with grain sizes between 20 and 2,000 nm and the impact of those grain boundaries on the photovoltaic properties is not captured by the computations. Therefore, experimental validation is required to investigate the properties of these materials, assuming they even form and remain stable under testing conditions. However, it is believed that regardless of the accuracy of the absolute values made for the predictions, the observed trends between the samples is valuable and provides useful information about the mechanisms that might be responsible for good solar operation. These values provide a basis against which experimental measurements can be compared to look for indications that secondary metal species are actually taken up into the perovskite lattice and replace $Pb^{2+}$ ions at the B-site.

Table 5.20: Screening the pool of mixed-metal perovskite candidates against criteria established for good photovoltaic behavior.

| Material | Type[a] | 1.0 eV< $E_g$ <1.8 eV | $\overline{m_e^*}/m_0 < 2$ | $\overline{m_h^*}/m_0 < 1$ | Stable | Final Candidate[b] | $E_g$ [eV] | $\overline{m_e^*}/m_0$ [-] | $\overline{m_h^*}/m_0$ [-] |
|---|---|---|---|---|---|---|---|---|---|
| **$MAPbI_3$** | S | T | T | T | T | **T** | 1.67 | 1.90 | 0.30 |
| **MA(3Pb:1Sn)$I_3$** | S | T | T | T | T | **T** | 1.34 | 0.63 | 0.27 |
| **MA(2Pb:2Sn)$I_3$** | S | T | T | T | T | **T** | 1.06 | 0.69 | 0.20 |
| MA(1Pb:3Sn)$I_3$ | S | T | T | T | F | F | 1.03 | 0.71 | 0.20 |
| **$MASnI_3$** | S | T | T | T | T | **T** | 1.04 | 0.82 | 0.21 |
| MA(3Pb:1Co)$I_3$ | N | T | F | F | ? | F | 1.77 | 3.09 | 1.88 |
| **MA(3Pb:1Mg)$I_3$** | S | T | T | T | T | **T** | 1.66 | 1.05 | 0.55 |
| **MA(3Pb:1Mn)$I_3$** | N | T | T | T | ? | **T?** | 1.48 | -0.92 | 0.86 |
| MA(3Pb:1Ni)$I_3$ | N | F | T | T | F | F | 2.04 | 1.44 | 0.87 |
| MA(3Pb:1Sr)$I_3$ | S | F | T | T | T | F | 2.03 | 1.30 | 0.56 |
| MA(3Pb:1Zn)$I_3$ | S | F | T | T | ? | F | 2.03 | 1.22 | 0.62 |
| MA(3Sn:1Co)$I_3$ | N | T | F | T | ? | F | 1.23 | 2.44 | 0.40 |
| MA(3Sn:1Mg)$I_3$ | S | T | T | T | F | F | 1.38 | 0.99 | 0.54 |
| **MA(3Sn:1Mn)$I_3$** | N | T | T | T | ? | **T?** | 1.14 | -0.18 | 0.25 |
| MA(3Sn:1Ni)$I_3$ | N | T | T | T | F | F | 1.48 | 0.88 | 0.51 |
| MA(3Sn:1Sr)$I_3$ | S | T | T | T | F | F | 1.36 | -1.08 | 0.30 |
| **MA(3Sn:1Zn)$I_3$** | S | T | T | T | ? | **T** | 1.44 | 0.99 | 0.90 |
| MA(2Sn:2Mg)$I_3$ | S | T | F | F | T | F | 1.55 | $\infty$ | $\infty$ |
| MA(2Sn:2Ni)$I_3$ | M | T | T | T | T | F | 1.09 | 1.25 | 0.35 |
| **MA(2Sn:2Sr)$I_3$** | S | T | T | T | T | **T?** | 1.44 | 1.46 | -0.32 |
| MA(2Sn:2Zn)$I_3$ | S | T | F | F | ? | F | 1.47 | $\infty$ | $\infty$ |
| MA(2Bi:2Cs)$I_3$ | S | F | T | F | ? | F | 2.61 | -0.02 | $\infty$ |
| MA(2Bi:2Cu)$I_3$ | S | T | T | F | ? | F | 1.49 | 1.37 | $\infty$ |
| MA(2Bi:2Li)$I_3$ | S | F | T | F | ? | F | 2.34 | 1.90 | $\infty$ |
| MA(2Bi:2Na)$I_3$ | S | F | F | T | ? | F | 2.17 | 4.87 | -0.10 |

[a]Legend for type of materials as determined by the band structure: S = Semiconducting, M = Metallic, N = Intermediate Band

[b]T = True, F = False, T? = True but thermodynamic stability has not been computed

# Chapter 6

# Experimental Screening and Evaluation of Lead-Based Mixed-Metal Perovskite Solar Cells

The preceding chapter presented a computational screening effort to identify perovskite materials that maintain desirable photovoltaic characteristics such as band gaps reasonably close to 1.4 eV and low effective carrier masses while reducing the Pb content in the crystal. The aim of this chapter is to expand upon this theoretical foundation by experimentally incorporating a second divalent metal species into Pb-based perovskite films and evaluating the impact this action has on the material properties and photovoltaic performance of actual solar cells. The approach for this experimental compositional screening effort is similar to that used for the density functional theory calculations, where lead content is systematically replaced with nine different secondary metal species in an attempt to identify candidates that can preserve or improve photovoltaic performance while potentially reducing toxicity.

## 6.1 Motivation

The rapid rise in performance of lead-based organic-inorganic trihalide perovskite solar cells over the past five years from an initial 3% [28] efficiency to a value recently

exceeding 20% [29] places this nascent class of materials on par with other mature thin-film solar materials such as silicon (Si), cadmium telluride (CdTe), and copper indium gallium selenide (CIGS). This achievement coupled with initial reports demonstrating little to no performance degradation over extended outdoor testing [151] indicates that perovskite devices are quickly approaching a maturity level ripe for commercialization. The ability of the bandgap of perovskite materials to be tuned throughout a significant portion of the visible and near-infrared spectrum with mixed halide systems [32, 132, 152, 153] affords the opportunity to develop even higher efficiency multi-junction solar cells based on stacks of multiple perovskite materials or the pairing of perovskites with current thin-film technologies such as crystalline Si or CIGS. [154–156] Despite offering the promise of low-cost and high-efficiency, lead-based perovskites pose inherent toxicological issues that are compounded by the solubility of ionic perovskite materials in water. Although encapsulation techniques could minimize environmental impact, full life-cycle analyses of perovskite solar cells remain to be performed that comprehensively assess health and safety risks. Therefore, the identification of less toxic perovskite materials that can retain the excellent photovoltaic properties of their pure lead counterparts has become an increasingly attractive pursuit.

The construction of direct alternative analogues to lead-based organic-inorganic trihalide perovskite materials requires that the B-site cation of the $ABX_3$ crystal lattice be divalent. Therefore, the search for lead-free perovskites has presently focused almost exclusively on divalent ions found within the same column of the periodic table as Pb, mainly $Sn^{2+}$ and $Ge^{2+}$. Wholly tin-based perovskite solar cells built on mesoporous titania scaffolds have recently been reported with $MASnI_3$ and $MASnI_{3-x}Br_x$ devices reaching power conversion efficiencies (PCE) of 5-6%. [128, 132] Likewise the synthesis of many germanium-based perovskite materials has been reported [130], although a working device remains to be realized. One of the major drawbacks of both Sn and Ge-based perovskites is that $Sn^{2+}$ and $Ge^{2+}$ are prone to oxidize to $Sn^{4+}$ and $Ge^{4+}$ upon exposure to air, which causes the perovskite to destabilize into multiple phases, thereby destroying the device. Thus, Sn and Ge-based solar cells will require

encapsulation to avoid rapid degradation when installed outdoors. Terahertz spectroscopy has revealed that the carrier diffusion lengths in $MASnI_3$ is only 30 nm [128], compared to micrometer lengths measured for lead-based materials, [126, 127] which suggests that mesoporous or bulk-heterojunction architectures, rather than planar heterojunctions, are required for efficient charge collection in these devices. This poses an additional challenge to device operation as mesoporous $TiO_2$ scaffolds in sealed devices can experience substantial photocurrent drops upon ultraviolet light exposure, which has been attributed to the creation of deep trap sites at the $TiO_2$ interface. [157]. While it is encouraging that this effect does not appear in unencapsulated lead-based perovskite solar cells employing a double layer of mesoporous $TiO_2$ and $ZrO_2$ with a thick hydrophobic carbon top electrode [151, 158], this approach is not expected to be compatible with Sn- and Ge-based materials.

While completely removing lead content from perovskite solar cells remains challenging, a more practical step forward in mitigating toxicity is to replace only a portion of the $Pb^{2+}$ ions with a less-toxic divalent species. To date, only $Sn^{2+}$ has been successfully blended with $Pb^{2+}$ to make mixed-metal perovskite devices, which has achieved efficiencies up to 9.8% [150] in an inverted device architecture and 7.4% [159] in a conventional device architecture, by respectively replacing 15% and 25% of the Pb content with Sn. Many of the transition metals are substantially less-toxic than Pb and can achieve a divalent oxidation state. Although some of these ions such as $Cu^{2+}$ [160] and $Fe^{2+}$ [161], have been used in two-dimensional (2D) layered perovskite structures, to our knowledge, this is the first report that replaces a fraction of the Pb content in three-dimensional (3D) perovskite films with any element other than Sn and constructs functioning solar cells with the mixed-metal materials. Herein, we present several embodiments of mixed-metal perovskite devices, where between 1.56% and 25% of the Pb-content has been replaced with a second less-toxic divalent metal species to form methylammonium mixed-metal triiodide films, denoted here as $MA(Pb{:}B')I_3$ where $B' = \{Co, Cu, Fe, Mg, Mn, Ni, Sn, Sr, and Zn\}$. By experimentally screening through this set of transition and alkaline earth metals, we aim to:

1. Investigate how tolerant the photovoltaic performance of $MAPbI_3$ devices is to the introduction of a second metal species.

2. Identify new perovskite compositions that might significantly reduce the toxicity of perovskite films without sacrificing efficiency.

3. Characterize the material and electronic properties of the mixed-metal perovskite films to speculate on the mechanisms responsible for performance improvements.

By replacing small, but not insignificant, amounts of the lead content with a second metal species, it was hypothesized that the $MAPbI_3$ lattice might be tolerant of the extrinsic species and that the excellent electronic properties of the lead-based perovskite might be perturbed but not completely disrupted, allowing for efficient or even improved photovoltaic performance. This concept was theoretically validated by the computational effort presented in Chapter 5, where DFT calculations predicted Pb-based mixtures of Mg, Mn, and Sn as promising solar materials. By systematically replacing a portion of Pb atoms with a wide range of less-toxic metals in an exhaustive experimental screening study, it has been found that:

1. Device performance can often be improved upon modest levels of replacement, with a 63Pb:1Co molar ratio yielding a champion PCE of 11.4%. Note that this is a significant improvement over the average baseline efficiency of 7.3% for pure $MAPbI_3$ devices.

2. Devices with power conversion efficiency exceeding 8% can be achieved by replacing 25% of the Pb content with either Sn or Cu and 12.5% with Zn.

3. Different wavelength ranges of the EQE spectra of the films can be improved by incorporating certain elements into the perovskite film.

4. Introducing Co into the $MAPbI_3$ material shifts the band edge locations to a more favorable alignment with the transport layers.

These findings suggest that mixing metals provides a new dimension for tuning the electronic properties of perovskite materials while simultaneously preserving the excellent photovoltaic behavior characteristic of the material class and reducing material toxicity.

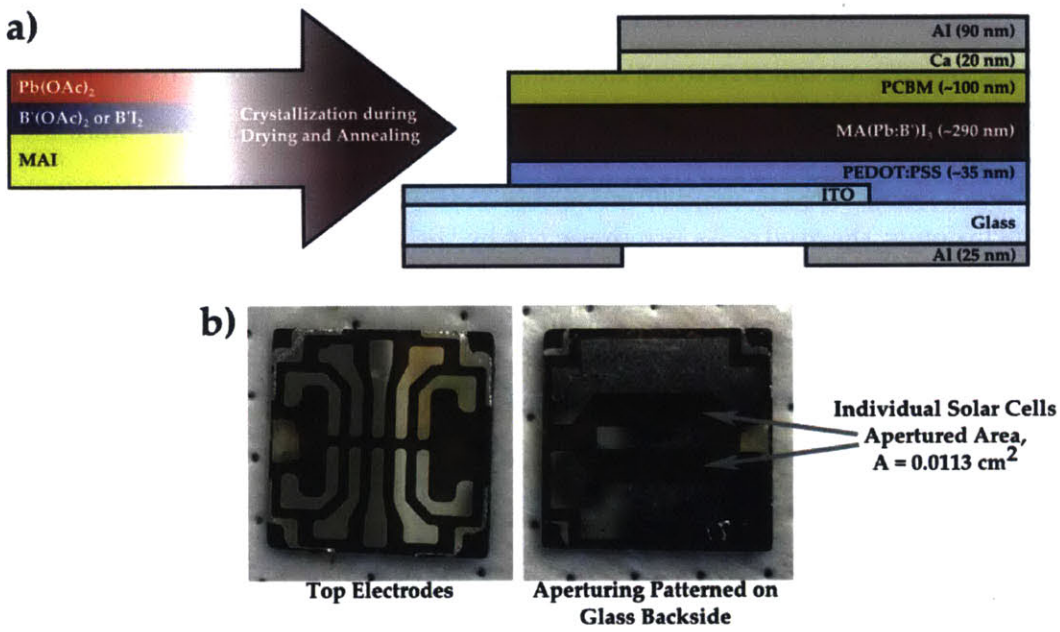


Figure 6-1: a) Polycrystalline planar mixed-metal perovskite films are formed by spincoating a solution of acetate and iodide precursors, which are then dried and annealed. b) Photograph of a typical perovskite device, which contains ten individual solar cells. Patterned aluminum is deposited on the glass backside to aperture each individual solar cells.

The perovskite solar cells were fabricated with the inverted device architecture and used acetate salts as the metal precursors. Although conventional architecture devices that build the perovskite film on a titanium dioxide electron transport layer have achieved the highest reported efficiencies, [29, 122, 162] this architecture commonly suffers from hysteresis, which is generally attributed to either insufficient carrier concentration in the $TiO_2$ layer or poor electrical contact with perovskite at its interface. [163] In contrast, hysteresis effects are minimal in perovskite devices with the inverted architecture, where the active layer is deposited on a $p$-type hole transport layer and utilizes an $n$-type fullerene derivative as the electron transport

layer. [164,165] However, devices that utilize this architecture generally exhibit lower device performance. In order to study the impact of adding a second metal species to the perovskite film, it was prudent to eliminate the device architecture itself as a source of hysteresis in the event mixed-metal devices displayed such behavior in the current-voltage characteristics. Divalent metal acetates, $B'(OAc)_2$, were chosen as the metal precursor material strictly on the basis that most acetate salts with the exception of calcium and strontium are soluble in DMF. In contrast, out of the more traditional metal iodide salts, only $CaI_2$, $MgI_2$, $PbI_2$, $SnI_2$, $SrI_2$, and $ZnI_2$ were found to be sufficiently soluble, thereby precluding nearly all of the divalent transition metals from inclusion in the study. As is represented by the schematic in Figure 6-1a, mixed perovskite films were synthesized in a one-step process by spin-coating a solution of MAI, $Pb(OAc)_2$, and $B'(OAc)_2$ in DMF with a 3:1 molar ratio of MAI to total metal acetate content. The one exception to this rule was the case of strontium, where a 3:1 molar ratio of MAI:$Pb(OAc)_2$ was blended with a 1:1 ratio of MAI:$SrI_2$ due to the insolubility of $Sr(OAc)_2$ in DMF. As previously reported, the acetate ions are spectators and their intrinsic volatility allows them to pair with the excess $MA^+$ cations and sublime out of the film during perovskite crystallization. [166, 167] To build the inverted device architecture, the perovskite solution was spin-coated on a PEDOT:PSS layer and crystallized by drying and annealing the film. This was followed by spin-coating and heat-treating a layer of the *n*-type fullerene-derivative, PCBM, and the sequential deposition of Ca and Al as the top electrode materials through thermal evaporation. In order to improve the quality of the perovskite film, the PEDOT:PSS surface was treated with 1,8-diiodooctane (DIO) prior to spin-coating the perovskite solution. The illumination area on each of the individual solar cells on the wafer was controlled by evaporating a 25 nm thick layer of patterned aluminum on the glass backside of each device to aperture the incident light, as is shown in Figure 6-1b.

## 6.2 Experimental Methods

### 6.2.1 Materials

Lead(II) acetate trihydrate (99.999% , $Pb(OAc)_2$), iron(II) acetate (>99.99% , $Fe(OAc)_2$), hydroiodic acid (57 wt% in water), chlorobenzene (anhydrous 99.8%, CB), and N,N-dimethylformamide (anhydrous 99.8%, DMF) were sourced from Sigma-Aldrich. Cobalt(II) acetate tetrahydrate (99.999%, $Co(OAc)_2$), copper(II) acetate (99.999%, $Cu(OAc)_2$), magnesium acetate tetrahydrate (99.997% Puratronic, $Mg(OAc)_2$), manganese(II) acetate tetrahydrate (99.999% Puratronic, $Mn(OAc)_2$), nickel(II) acetate tetrahydrate (99.999% Puratronic, $Ni(OAc)_2$), zinc acetate (99.98% anhydrous, $Zn(OAc)_2$), strontium iodide (99.99% anhydrous, $SrI_2$), 1,8-diiodooctane (>97%, DIO), calcium shot (99.5%), and aluminum shot (99.999% Puratronic) were sourced from Alfa Aesar. Methylamine solution (57 wt% in water) was sourced from TCI. Phenyl-C61-butyric acid methyl ester (99.5%, PCBM) was sourced from Nano-C, Inc. Poly(3,4-ethylenedioxythiophene)-poly(styrenesulfonate) (Clevios P VP AI 4083, PEDOT:PSS) was sourced from Heraeus.

### 6.2.2 Mixed-Metal Perovskite Solution

Methylammonium iodide (MAI) was synthesized according to a previously reported procedure. [30] Mixed metal perovskite solutions were freshly prepared before use by fully dissolving the MAI and divalent metal acetate ($B'(OAc)_2$) precursors in DMF to achieve final solutions containing 2.4 M MAI and 0.8 M total metal acetate content. The metal acetate content in the perovskite solutions was varied from a 1Pb:1B′ ratio (i.e. 0.4 M $Pb(OAc)_2$ and 0.4 M $B'(OAc)_2$ final solution) to 63Pb:1B′ (i.e. 787.5 mM $Pb(OAc)_2$ and 12.5 mM $B'(OAc)_2$ final solution) where B′ = {Co, Cu, Fe, Mg, Mn, Ni, Sn, Zn}. Due to the low solubility of $Sr(OAc)_2$ in DMF, the iodide precursor was used instead and mixed Pb:Sr perovskite solutions were prepared by making separate stocks of (2.4 M MAI):(0.8 M $Pb(OAc)_2$) and (0.8 M MAI):(0.8 M $SrI_2$), respectively, in DMF. These two stock solutions were mixed immediately before use to achieve the

desired ratios of Pb:Sr.

### 6.2.3 Solar Cell Fabrication

Patterned ITO-coated glass substrates (Thin Film Devices Inc.) were cleaned by scrubbing and sonication in a detergent solution (Alconox) followed by thorough rinsing with Milli-Q water (Millipore). The substrates were then sequentially sonicated for around 10 minutes in Milli-Q water, acetone, and isopropanol solvents, dried under flowing nitrogen, and exposed to air plasma for 10 minutes to remove any remaining organic contaminants and render the surface hydrophilic. The as-received PEDOT:PSS solution was initially filtered through 0.45 $\mu$m syringe filter (Pall Corp Acrodisc Supor membrane filters) and warmed to room temperature. Several drops of the PEDOT:PSS solution were dispensed through a second syringe filter directly onto the plasma-treated substrate and then spun at 3,000 rpm for 50 s. The substrates were immediately transferred to an oven and annealed in air at 125 °C for at least 15 minutes, after which, they were transferred to a nitrogen glove box for the remainder of the device processing. Onto each substrate was statically dispensed 45 $\mu$L of a solution of DIO (2 vol% in CB), and subsequently spin-coated at 2,250 rpm for 40 s. Immediately afterwards, 45 $\mu$L of a freshly prepared mixed-metal perovskite solution was statically dispensed onto the substrate and spin-coated at 2,250 rpm for 40 s. After spinning, the substrate was immediately removed from the spin-coater chuck and let rest at room temperature for 10 minutes, during which the film color slowly changed from colorless to a light brown hue. Each device was then annealed on a hot plate at 100°C for 30 minutes and the perovskite film darkened to achieve its final color within minutes.

A solution of PCBM (35 mg/mL in CB) was prepared the day before use and kept at 80°C overnight to ensure full dissolution. The warm solution was filtered through both a 100 nm and 200 nm PTFE (Whatman) filter an hour before use and kept at 80°C until spinning. The perovskite substrates were warmed at 80 °C for 10 minutes and 45 $\mu$L of the warm PCBM solution was statically dispensed and spin-coated at 1,200 rpm for 35 s ($\sim$100 nm film thickness). Each substrate was immediately

transferred to a hotplate and annealed at 90°C for 45 minutes. Afterwards, top electrodes consisting of 20 nm Ca and 90 nm of Al were thermally evaporated on top of the fullerene layer to complete the device. Finally, an aluminum film (25 nm thick) was patterned directly onto the glass backside of each device to act as an aperture mask during performance testing. As shown in Figure 6-1b, the final patterned device substrate (0.5 × 0.5 inches) contained 10 individual solar cells, each with an apertured active area of 0.0113 $cm^2$.

The approximate thicknesses of each solution-processed layer in the solar cell, as determined by a profilometer (Veeco Dektak 6M), are: PEDOT:PSS (35 nm), perovskite (290 nm), and PCBM (100 nm), as indicated in Figure 6-1a.

### 6.2.4 Device Characterization Methods

Current-voltage (JV) characteristics were recorded using a Keithley 2636A source meter under simulated solar light (1-Sun, 100 $mW/cm^2$) generated by a Newport 96000 solar simulator equipped with an AM1.5G filter. After warming the solar simulator, the light intensity was calibrated with a Newport 91150V reference cell prior to testing each batch of device. Each device was soaked under the AM 1.5G illumination for 5 minutes prior to measurement and the delay between data points was 20 ms. The external quantum efficiency (EQE) measurements were conducted under chopped monochromatic light from an optical fiber in an underfilled geometry without bias. Illumination was provided by coupling the white light from a xenon lamp (Thermo Oriel 66921) through a monochromator (Acton) into the optical fiber and the photocurrent was recorded using a lock-in amplifier (Stanford Research System SR830). Devices were continuously kept in a nitrogen atmosphere after electrode evaporation, including during both JV and EQE measurements. Devices were tested immediately after the top electrodes were evaporated.

### 6.2.5 Materials Characterization Methods

X-ray photoelectron spectroscopy (XPS) was conducted using a Thermo Scientific K-Alpha XPS with a monochromatic Al X-ray source (excitation energy 1486.6 eV). Data was collected under a base pressure of $8 \cdot 10^{-8}$ mbar at a photoelectron take-off angle of 90°. Energy calibration was performed using the position of the primary C 1s peak at 284.80 eV. Relative atomic ratios were calculated using the ratio of integrated spectral areas for each element from high resolution scans and the relative sensitivity factors inherent to the instrument. X-ray diffraction (XRD) patterns were collected using a Bruker D8 X-ray diffractometer with Cu K$\alpha$ radiation in order to verify the phase and orientation of the deposited films. Scanning electron microscopy (SEM, Zeiss FESEM Ultra Plus) was used to characterize film morphology.

### 6.2.6 Optical Characterization Methods

Steady-state photoluminescence emission spectra were obtained by exciting perovskite films with a 532 nm laser and measuring the emission spectra using a visible wavelength detector with a Horiba Jobin Yvon Fluorimeter with an integration time of 1 s and wavelength step size of 1 nm. Optical absorption measurements were made using a Beckman-Coulter DU800 UV-vis spectrophotometer with a wavelength step size of 0.5 nm.

## 6.3 Materials Characterization of Perovskites

Each of the 45 different compositions (*i.e.* 9 secondary divalent metal species, 5 different ratios of Pb:B′ atoms) of planar mixed-metal perovskite films was evaluated with several different materials characterization techniques in order to investigate how replacing $Pb^{2+}$ ions with several different less-toxic metal species impacts the material properties as a function of metal mole fraction. These techniques include standard diffraction, imaging, and optical techniques for gathering basic information about crystal structure, film morphology, and absorption.

### 6.3.1 X-ray Diffraction

Standard powder x-ray diffraction (XRD) measurements were performed on mixed-metal perovskite films that were synthesized using the exact same method taken to build the solar cells, with the exception that a bare glass substrate was used instead of indium tin oxide (ITO) (*i.e.* the perovskite film was produced by spin-coating the precursor solution on a DIO-treated PEDOT:PSS layer, which had previously been deposited on a glass substrate). The perovskite layers were capped with an amorphous film of poly(methyl methacrylate) (PMMA) to provide the films with some protection against air exposure during measurement. The XRD spectra for mixed-metal blends of Pb:Co, Pb:Cu, Pb:Fe, and Pb:Mg are shown in Figure 6-2(a-d), respectively, and blends of Pb:Mn, Pb:Sn, Pb:Sr, and Pb:Zn are found in Figure 6-3(a-d), respectively. A companion pure Pb perovskite, $MAPbI_3$, film was synthesized along with each material set in order to be used as a reference for that particular batch.

As is shown by these figures, the diffraction patterns are nearly identical regardless of the specific material composition. There are three possibilities that would explain this result:

1. The $B'^{2+}$ atoms are substituting the $Pb^{2+}$ ions at the B-site in the $ABX_3$ perovskite lattice, however the lattice constants and crystal structure are not sufficiently perturbed enough to noticeably change the XRD patterns.

2. The films are simply pure $MAPbI_3$. Even though various fractions of the $Pb^{2+}$ ions are replaced with a second species, $B'^{2+}$, in the perovskite precursor solution, these ions might be excluded from the crystal lattice and exist in a second phase that is amorphous and cannot be detected.

3. The $B'^{2+}$ ions phase separate into a secondary phase that is crystalline, but exists in quantities below the threshold of detection.

The first possibility is supported by the DFT crystal structure calculations presented in the preceding chapter, which show that even in the event of ion substitution at the B-site, the overall crystal structure is still maintained when less than a quarter

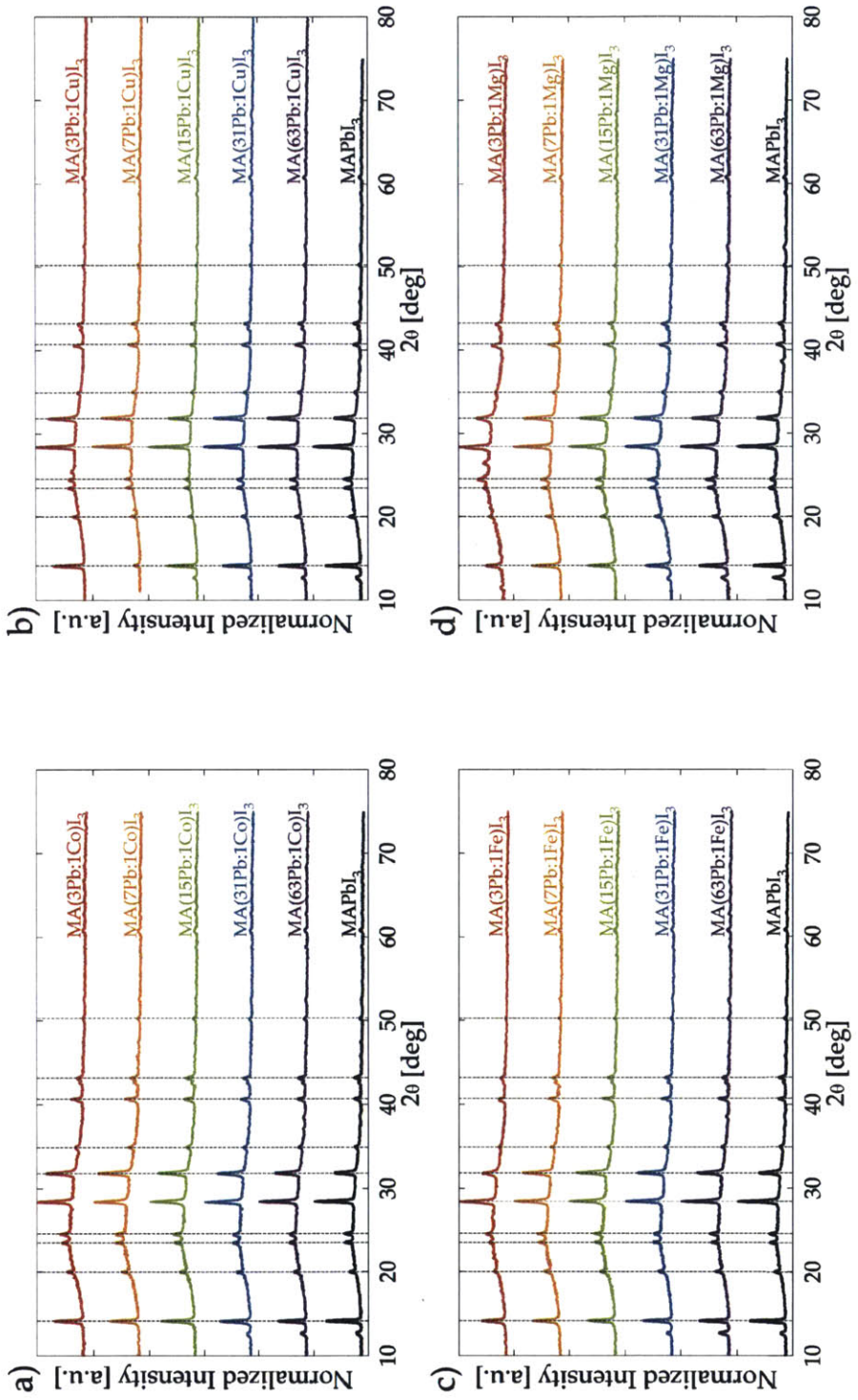


Figure 6-2: X-ray diffraction (XRD) spectra for films of mixed-metal perovskite blends of: a) Pb:Co, b) Pb:Cu, c) Pb:Fe, and d) Pb:Mg.

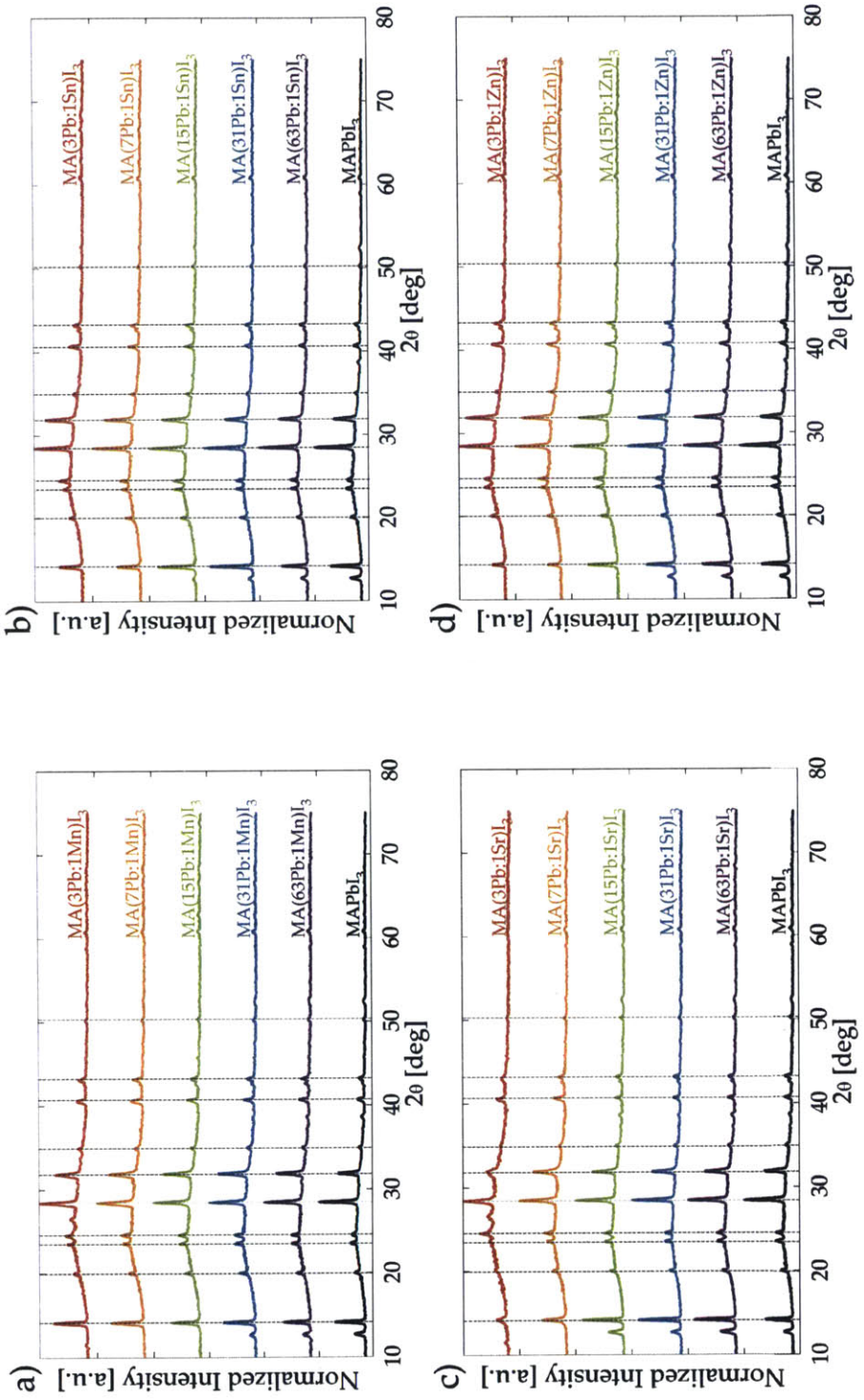


Figure 6-3: X-ray diffraction (XRD) spectra for films of mixed-metal perovskite blends of: a) Pb:Mn b) Pb:Sn, c) Pb:Sr, and d) Pb:Zn.

of the Pb atoms are replaced with a second metal species. Perovskite materials are known to have a large degree of disorder, which has been attributed to the asymmetry of the methylammonium cations and their ability to rotate. Hence, the crystalline peaks are broad enough that small changes to the lattice parameters might not be detected. The second and third possibilities are also supported by the thermodynamic stability calculations with density functional theory. These findings suggested that in some cases it is slightly more energetically favorable for a pure $MAPbI_3$ phase to form alongside the excess MAI and $B'^{2+}$ precursors. Although these calculations were performed exclusively for iodide precursors and acetate salts were used in the experimental study, it is likely that the residual B′ atoms would form an iodide phase. The acetate ions are spectators and evaporate out of the film, leaving the less-volatile iodide ions behind to form an iodide phase. The measured XRD spectra also provide some evidence that this is occuring with some of the B′ species in the samples with the highest levels of Pb replacement, $MA(3Pb:1B')I_3$. As shown in Figure 6-2b, an extra peak arises for the $MA(3Pb:1Cu)I_3$ and $MA(7Pb:1Cu)I_3$ samples near $2\theta = 25.5°$, which corresponds to the (111) planes of CuI. Similarly, extra peaks arises at both 11.6° and 26.4° for the $MA(3Pb:1Fe)I_3$, $MA(3Pb:1Mg)I_3$, $MA(3Pb:1Mn)I_3$, and $MA(3Pb:1Sr)I_3$ compositions in Figure 6-2c-d and 6-3a,c, respectively. It is unclear whether these peaks are simply additional perovskite peaks, or if they are indicative of iodide phases that each display a peak at these locations. Interestingly, the simulated XRD spectra for the orthorhombic mixed-metal materials shown in Fig 5-15 for $MA(3Pb:1Mg)I_3$, $MA(3Pb:1Mn)I_3$, and $MA(3Pb:1Sr)I_3$ all display a peak between 26.1° and 26.5°, which do not arise for either $MAPbI_3$ or $MA(3Pb:1Co)I_3$. It is possible that these additional peaks result from the secondary metal species substituting the $Pb'^{2+}$ ions at the B-site. Conversely, the spectra for Pb:Co, Pb:Sn, and Pb:Zn, however, do not show any additional peaks for any level of Pb replacement.

The other trend that is common for each set of mixed-metal materials is that two small peaks for $PbI_2$ are present at $2\theta = 12.6°$ and 38.6° for every $MAPbI_3$ and decrease in intensity as the Pb is replaced with more B′ content, until the peaks disappear completely by $MA(7Pb:B')I_3$ if not before. The presence of excess $PbI_2$

is common in many other reported systems [166, 168] even when device fabrication conditions are optimized. What is more interesting is that the quantity of $PbI_2$ reduces as more $Pb^{2+}$ is replaced with $B'^{2+}$. Perhaps the MAI that was intended to remove the the acetate ions from the $B'(OAc)_2$ salt is instead reacting with the excess $PbI_2$ and the $B'(OAc)_2$ remains partially intact, however there is no indication of acetate compounds being present in the material. It is possible that excess $MA^+$ could leave the crystal by pairing with excess $I^-$ ions leaving behind $MAPbI_3$ and crystalline iodide compound with B′, however it is clear that this not a possibility for several secondary metal species, as is evidenced by the lack of additional peaks for the Co, Sn, and Zn mixtures.

### 6.3.2 Film Morphology

The film morphology of each of the XRD samples was investigated by imaging the top surface of the film with scanning electron microscopy (SEM). The images for the 50 kx magnification is shown for the mixed-metal material sets in Figures 6-4 through 6-12.

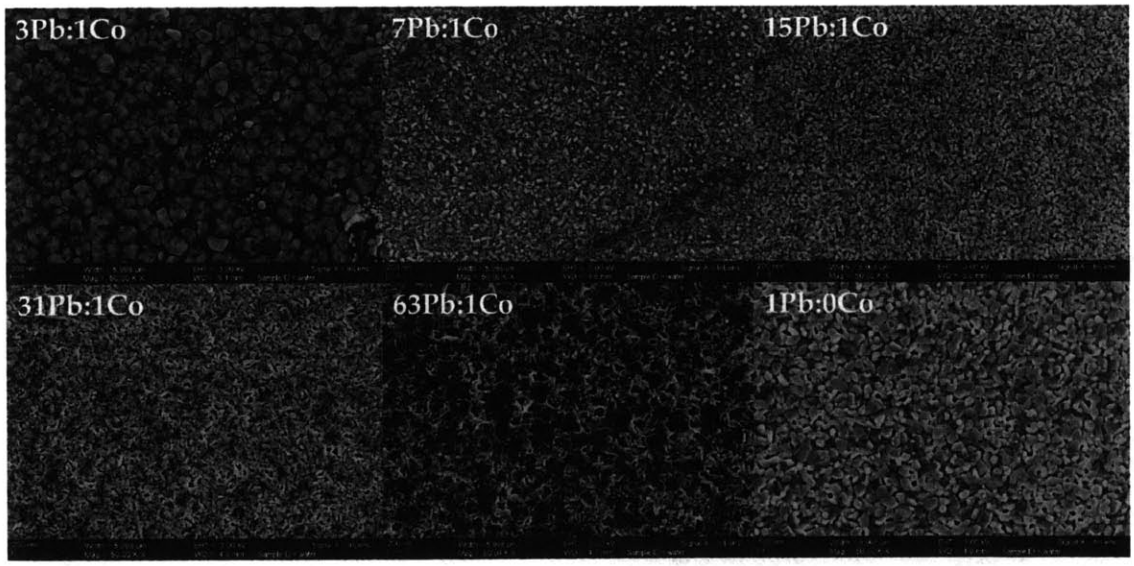


Figure 6-4: Scanning electron micrographs of $MA(Pb:Co)I_3$ perovskite films with different metal replacement fractions.

The morphology of the pure Pb perovskite sample, labeled as the 1Pb:0Co sam-

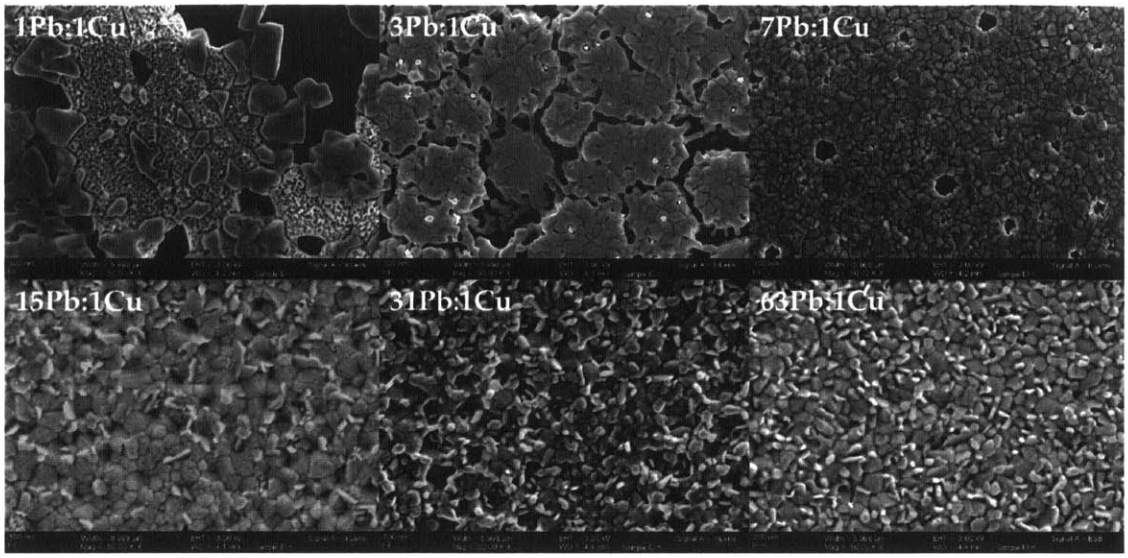


Figure 6-5: Scanning electron micrographs of MA(Pb:Cu)$I_3$ perovskite films with different metal replacement fractions.

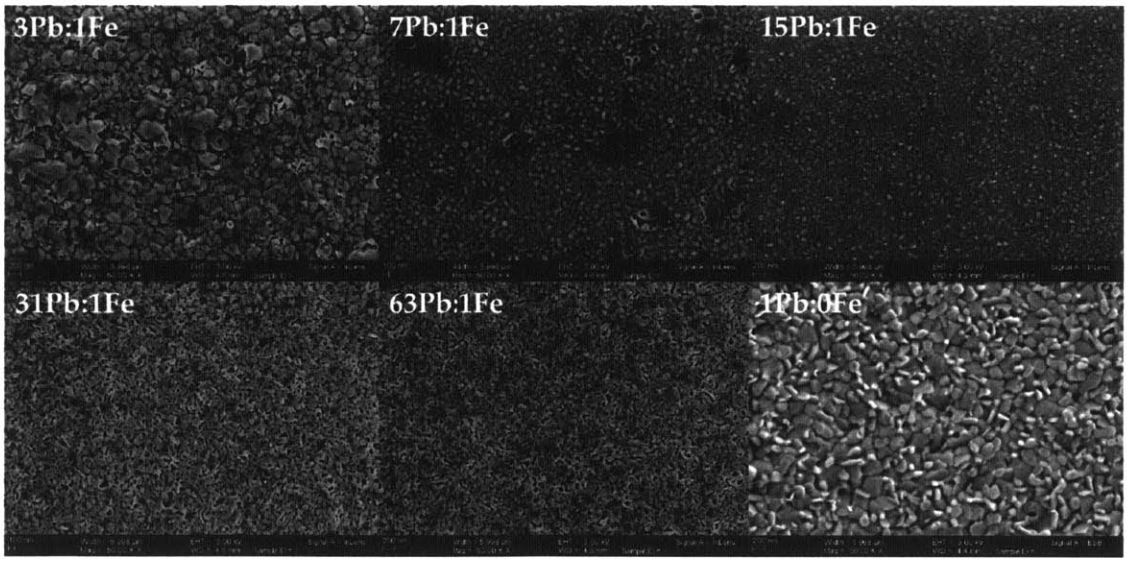


Figure 6-6: Scanning electron micrographs of MA(Pb:Fe)$I_3$ perovskite films with different metal replacement fractions.

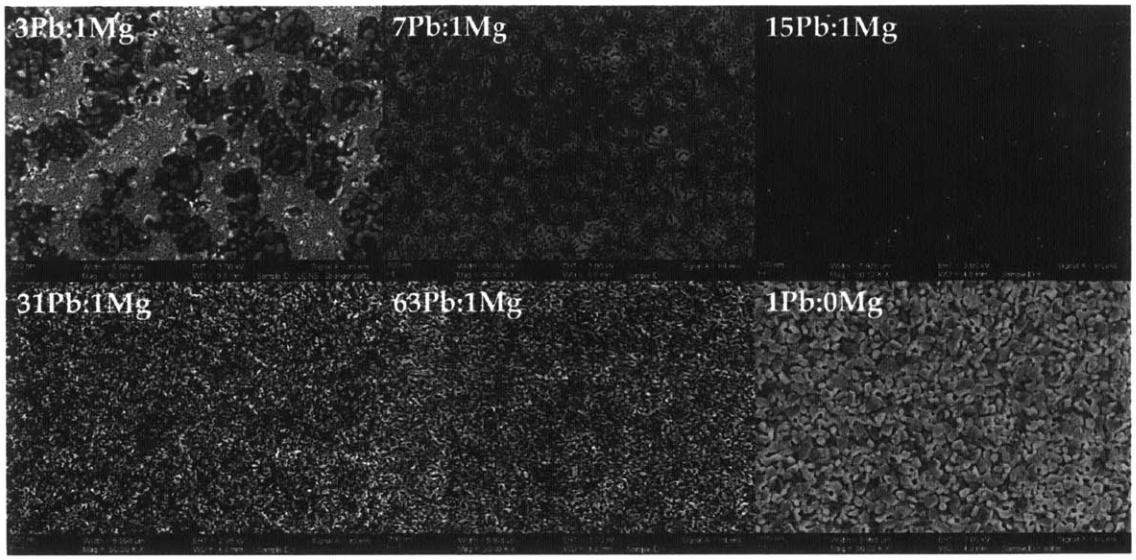


Figure 6-7: Scanning electron micrographs of MA(Pb:Mg)$I_3$ perovskite films with different metal replacement fractions.

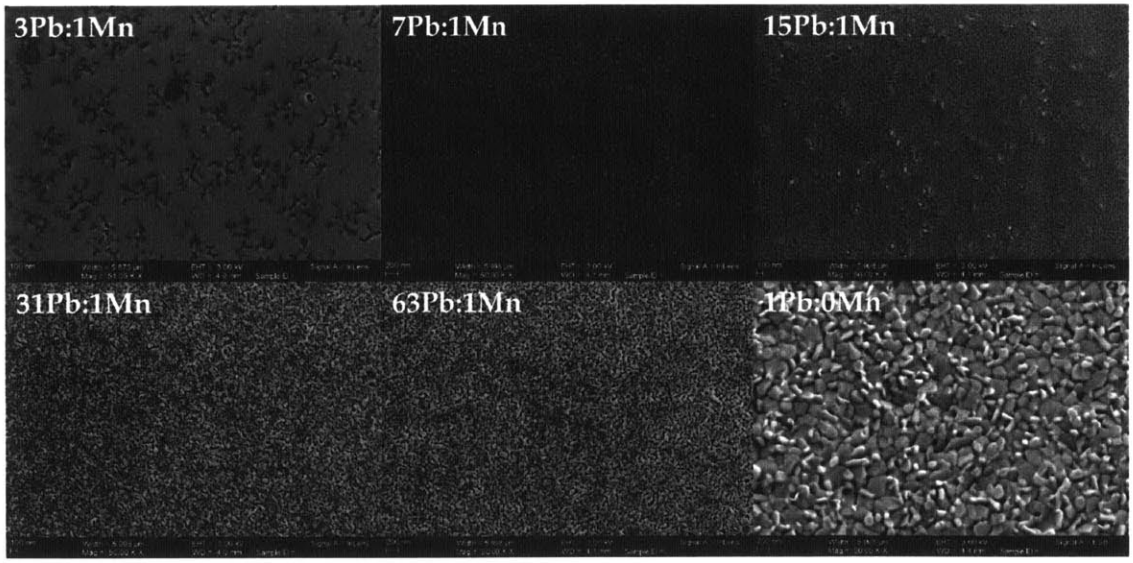


Figure 6-8: Scanning electron micrographs of MA(Pb:Mn)$I_3$ perovskite films with different metal replacement fractions.

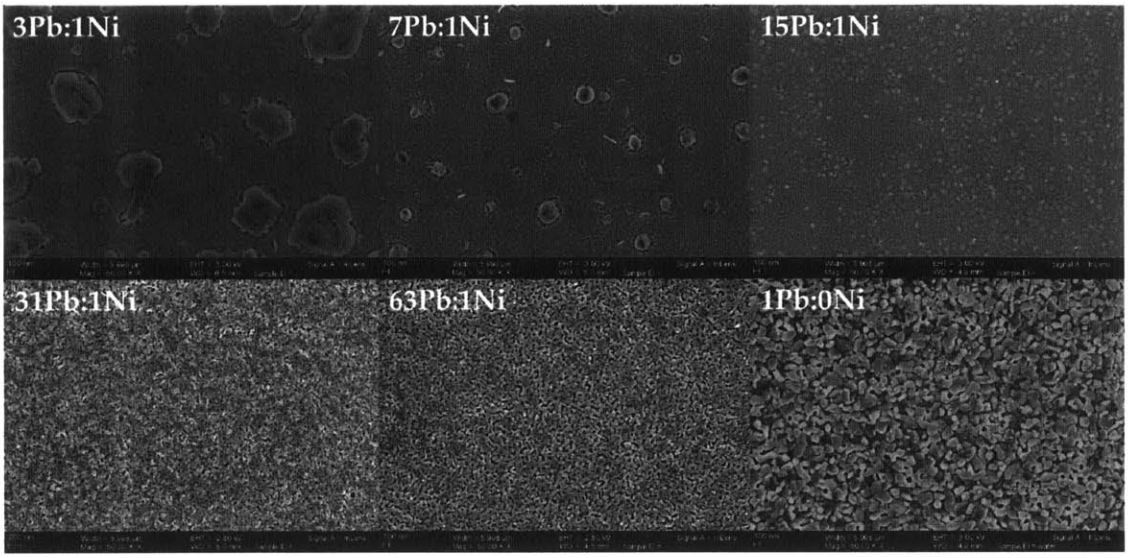


Figure 6-9: Scanning electron micrographs of MA(Pb:Ni)$I_3$ perovskite films with different metal replacement fractions.

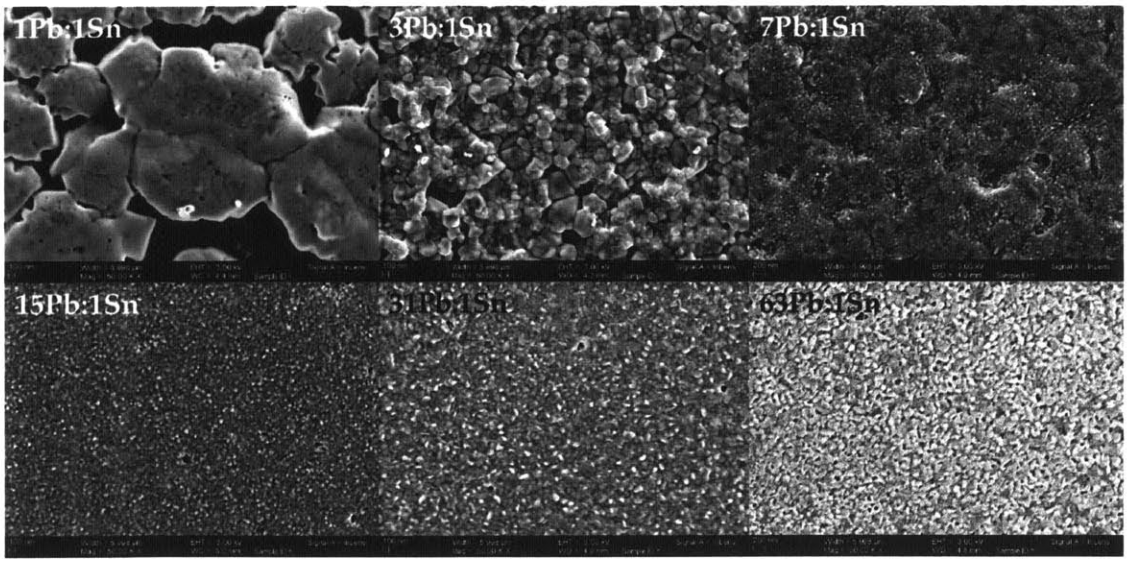


Figure 6-10: Scanning electron micrographs of MA(Pb:Sn)$I_3$ perovskite films with different metal replacement fractions.

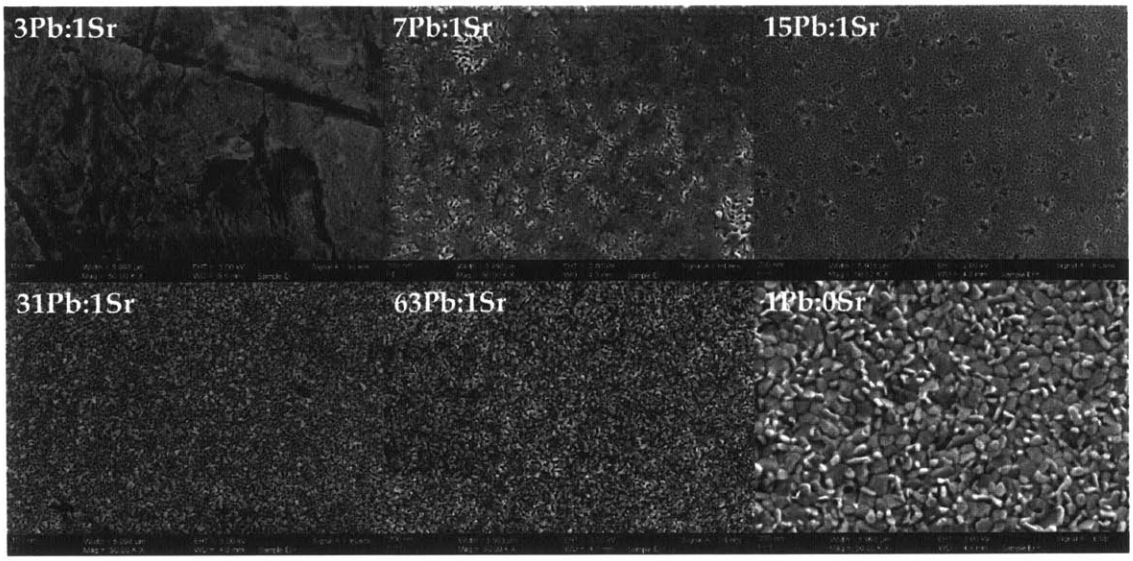


Figure 6-11: Scanning electron micrographs of MA(Pb:Sr)$I_3$ perovskite films with different metal replacement fractions.

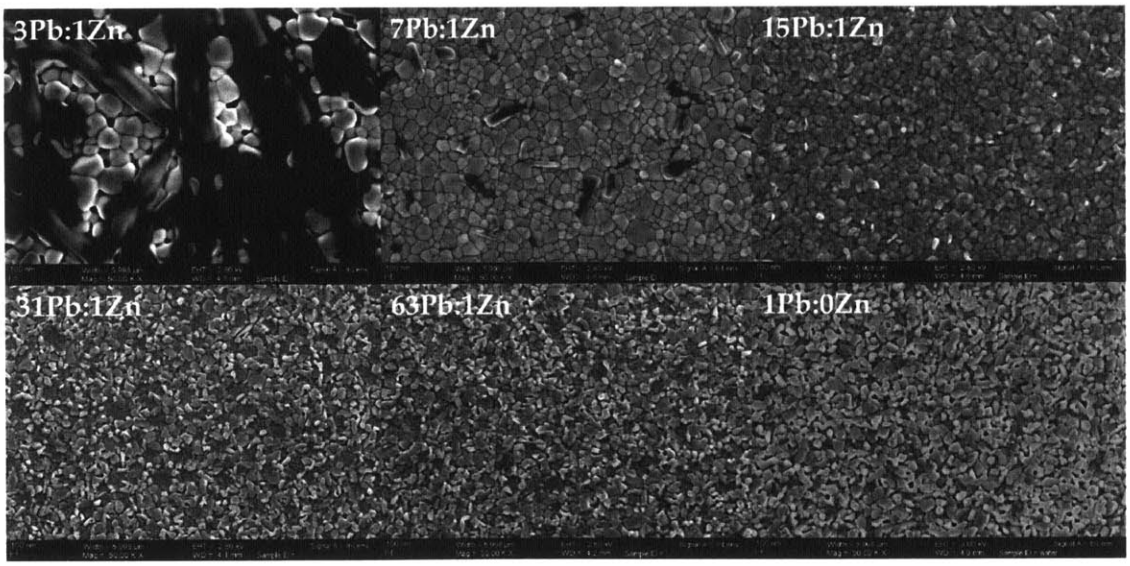


Figure 6-12: Scanning electron micrographs of MA(Pb:Zn)$I_3$ perovskite films with different metal replacement fractions.

ple in the bottom-right panel of Figure 6-4, reveals that the perovskite films on PEDOT:PSS consists of randomly oriented plate-like grains that are roughly 100 nm in size. These features are homogeneous across the film, which is evidenced by how smooth and reflective the actual devices appear in Figure 6-1b. The acetate precursor tends to produce perovskite films with smaller grains than those synthesized using chloride precursors, due in part to the quicker crystallization times of the acetate-based films. [166] It is also apparent from the micrograph that films contain pinholes, which will contribute to some current and voltage loss if the PCBM layer comes into direct contact with the PEDOT:PSS hole-transport layer.

The general trend across all compositions is that the morphology remains similarly small-grained with increasing B′ content until a molar ratio of 7Pb:1B′. At this point the films transition to often dramatically different morphologies as more Pb atoms are further replaced. The cases of 3Pb:1Co, 3Pb:1Cu, 3Pb:Sn, and 7Pb:1Zn (Figures 6-4, 6-5, 6-10), and 6-12 are instances where the grains are substantially larger than samples with lower B′ content. The films for both 1Pb:1Cu and 3Pb:1Mg (Figures 6-5 and 6-7) clearly show two different material phases, one consisting of large grains with a finer material filling in the space between them.

The second noticeable trend is that grain sizes in each material set almost always seem slightly smaller and often more porous at low levels of Pb replacement, which is particular evident in blends with Co (Figure 6-4), Fe (Figure 6-6), Mg (Figure 6-8), Mn (Figure 6-8), and Sr (Figure 6-11). The exceptions to this trend are copper and zinc. The series of Pb:Cu and Pb:Zn blends presented in Figures 6-5 and 6-12 show that the grain size of the pure Pb film is preserved at low replacement levels and that the film seems to be have less pinholes with the grains packed tightly in the film. Furthermore, the frequency of platelet-like grains seems to reduce with increasing Cu content until the 7Pb:1Cu and 7Pb:1Zn films, where they disappear altogether. In the case of Pb:Zn, at 7Pb:1Zn a second population of dark grains arise that more frequently appear in the 3Pb:1Zn samples (Figure 6-12).

### 6.3.3 Absorption and Photoluminescence Emission Spectra

In order to investigate the optical properties of each mixed-metal perovskite material, films were built directly on plasma-treated glass substrates without PEDOT:PSS in order to avoid photoluminescence quenching from occurring at the interface between the perovskite and PEDOT:PSS. In order to protect the films from ambient conditions during measurement, they were coated with a layer of poly(methyl methacrylate) (PMMA), which is hydrophobic and locks out moisture from accessing the perovskite.

The optical band gap of each material was determined from the position of the photoluminescence emission peak measured with a fluorimeter. The trends in PL peak shifts can be confirmed by corresponding shifts in the absorption edge of the material. Hence, the normalized absorption and PL emission spectra for each mixed-metal composition are presented together in Figures 6-13 and 6-14. In each case, the PL emission peak was locally fit to a parabola in order to compensate for any noise in the spectrum and identify the position of the emission peak. The PL emission peak positions and the shift from the pure Pb $MAPbI_3$ control films synthesized for each material set are tabulated in Table 6.1. The PL spectra and absorption spectra are not reported for Pb:Sn blends because the films were not emissive enough to generate reasonable PL peaks.

As expected, any observed shift in the PL emission spectrum is always confirmed by a corresponding shift in the absorption edge. Blends of Pb:Cu, Pb:Sr, and Pb:Zn blends do not exhibit any appreciable shifts in the PL spectra. Whereas, blends of Pb:Co, Pb:Fe, Pb:Mg, Pb:Mn, and Pb:Ni generally blue-shift with increasing B′ content. This shift could either result from electronic changes to the crystal lattice upon B-site substitution (as DFT calculations predict widened band gaps upon replacing a quarter of the $Pb^{2+}$ ions) or be a result of grain size change. It has been observed in previous reports [166] that PL peak position blue-shifts with decreasing grain size. As discussed in Section 6.3.2, all of these films appear to decrease in size with low levels of Pb replacement. Therefore, the blue-shifts could be attributed to either of the potential scenarios. It is intriguing however, that the peak continues to blue-shift

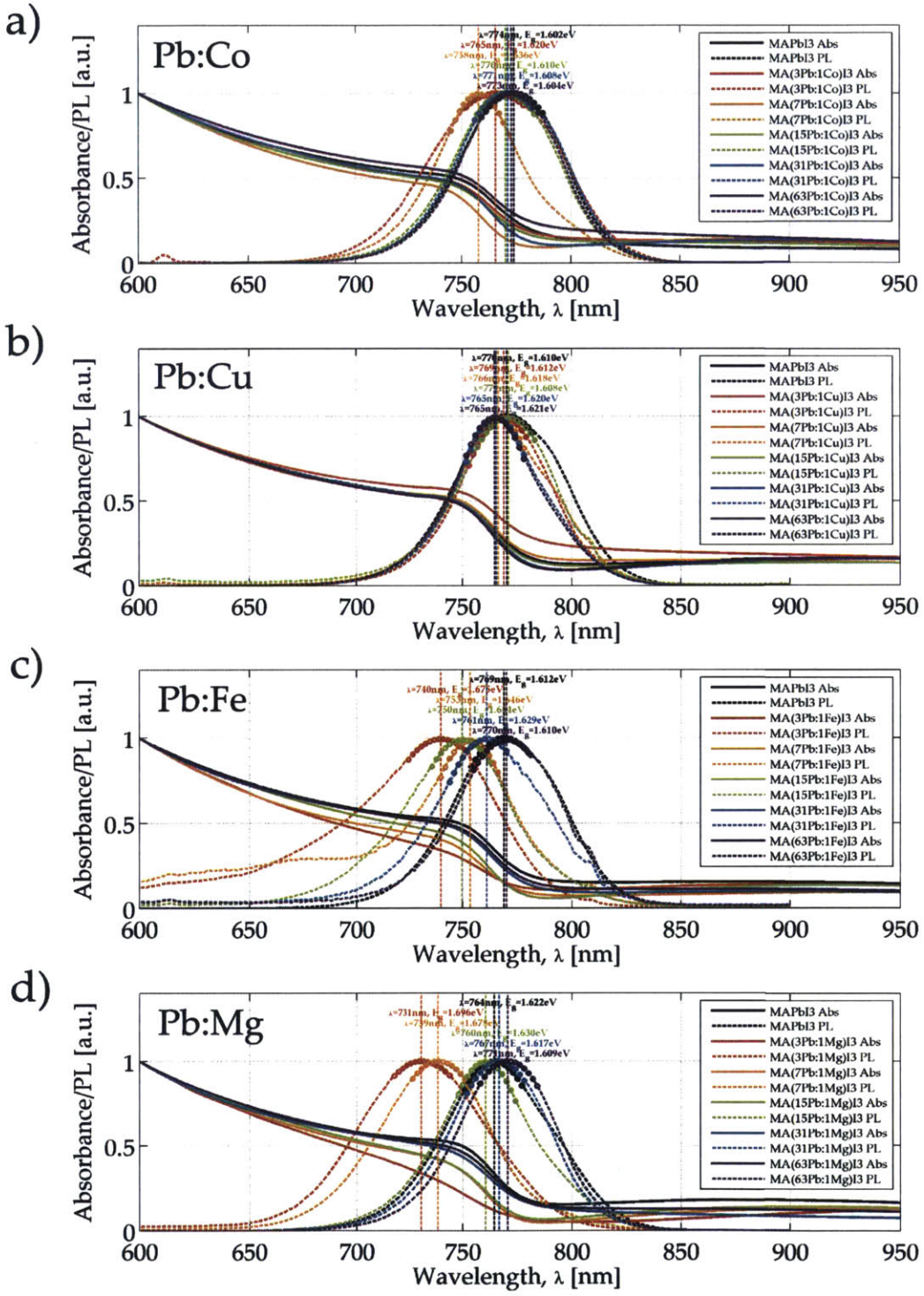


Figure 6-13: The normalized absorption (solid lines) and photoluminescence emission (dotted lines) spectra for the compositions in each mixed-metal material set (a) Pb:Co, (b) Pb:Cu, (c) Pb:Fe, and (d) Pb:Mg.

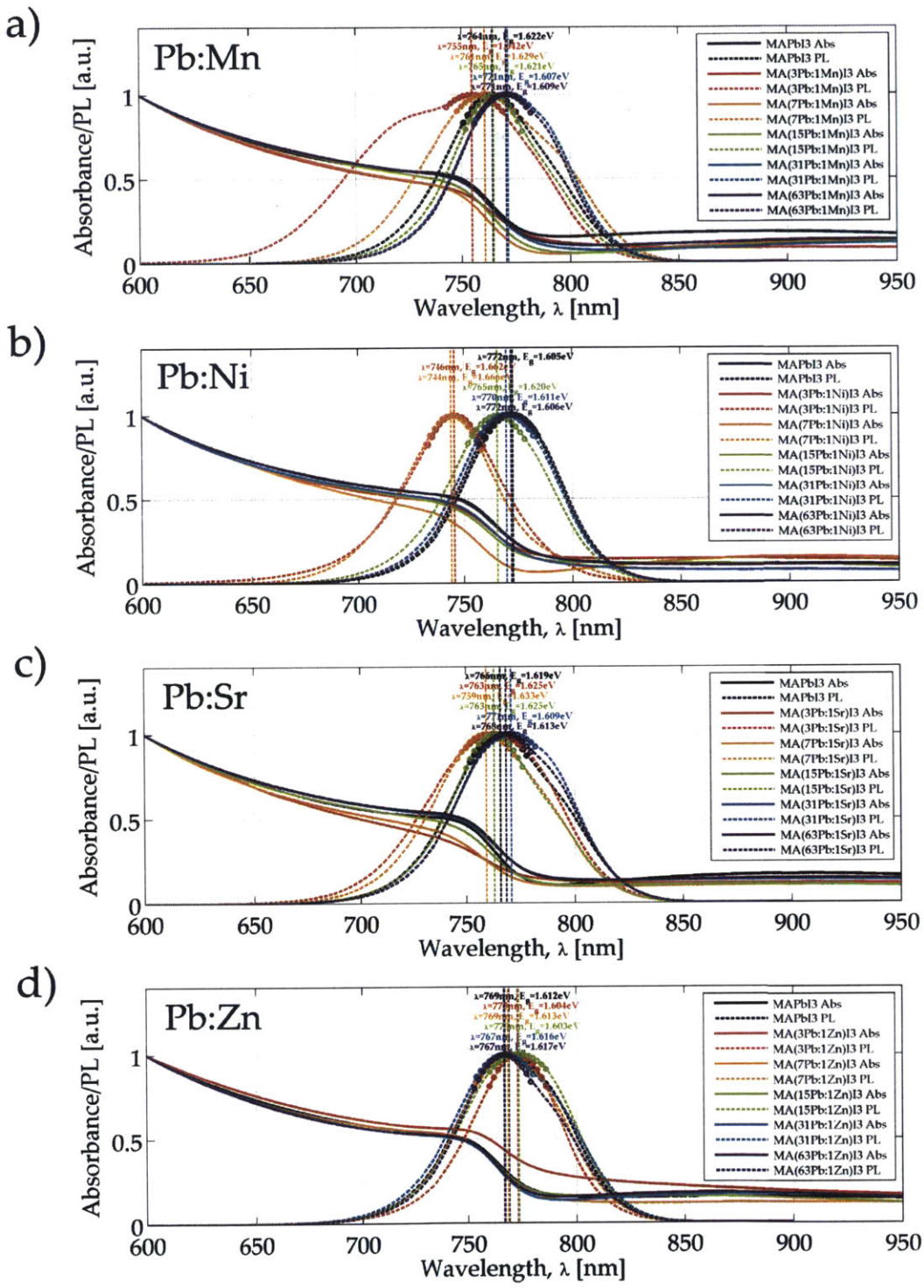


Figure 6-14: The normalized absorption (solid lines) and photoluminescence emission (dotted lines) spectra for the compositions in each mixed-metal material set (a) Pb:Mn, (b) Pb:Ni, (c) Pb:Sr, and (d) Pb:Zn.

Table 6.1: Optical band gap as determined from location of photoluminescence emission peak of mixed-metal perovskite films and the shift from peak position of pure $MAPbI_3$ control sample.

| Material | PL Peak Position $\lambda_{PL}$ [nm] | PL Peak Position $E_{PL}$ [eV] | Peak Shift from $MAPbI_3$ $\Delta\lambda_{PL}$ [nm] | Peak Shift from $MAPbI_3$ $\Delta E_{PL}$ [eV] |
|---|---|---|---|---|
| $MAPbI_3$ | 774 | 1.602 | - | - |
| $MA(63Pb{:}1Co)I_3$ | 773 | 1.604 | 1 | -0.002 |
| $MA(31Pb{:}1Co)I_3$ | 771 | 1.608 | 3 | -0.006 |
| $MA(15Pb{:}1Co)I_3$ | 770 | 1.610 | 4 | -0.008 |
| $MA(7Pb{:}1Co)I_3$ | 758 | 1.636 | 16 | -0.034 |
| $MA(3Pb{:}1Co)I_3$ | 765 | 1.620 | 9 | -0.018 |
| $MAPbI_3$ | 770 | 1.610 | - | - |
| $MA(63Pb{:}1Cu)I_3$ | 765 | 1.621 | 5 | -0.011 |
| $MA(31Pb{:}1Cu)I_3$ | 765 | 1.620 | 5 | -0.01 |
| $MA(15Pb{:}1Cu)I_3$ | 771 | 1.608 | -1 | 0.002 |
| $MA(7Pb{:}1Cu)I_3$ | 766 | 1.618 | 4 | -0.008 |
| $MA(3Pb{:}1Cu)I_3$ | 769 | 1.612 | 1 | -0.002 |
| $MAPbI_3$ | 769 | 1.612 | - | - |
| $MA(63Pb{:}1Fe)I_3$ | 770 | 1.610 | -1 | 0.002 |
| $MA(31Pb{:}1Fe)I_3$ | 761 | 1.629 | 8 | -0.017 |
| $MA(15Pb{:}1Fe)I_3$ | 750 | 1.654 | 19 | -0.042 |
| $MA(7Pb{:}1Fe)I_3$ | 753 | 1.646 | 16 | -0.034 |
| $MA(3Pb{:}1Fe)I_3$ | 740 | 1.675 | 29 | -0.063 |
| $MAPbI_3$ | 764 | 1.622 | - | - |
| $MA(63Pb{:}1Mg)I_3$ | 771 | 1.609 | -7 | 0.013 |
| $MA(31Pb{:}1Mg)I_3$ | 767 | 1.617 | -3 | 0.005 |
| $MA(15Pb{:}1Mg)I_3$ | 760 | 1.630 | 4 | -0.008 |
| $MA(7Pb{:}1Mg)I_3$ | 739 | 1.678 | 25 | -0.056 |
| $MA(3Pb{:}1Mg)I_3$ | 731 | 1.696 | 33 | -0.074 |
| $MAPbI_3$ | 764 | 1.622 | - | - |
| $MA(63Pb{:}1Mn)I_3$ | 771 | 1.609 | -7 | 0.013 |
| $MA(31Pb{:}1Mn)I_3$ | 771 | 1.607 | -7 | 0.015 |
| $MA(15Pb{:}1Mn)I_3$ | 765 | 1.621 | -1 | 0.001 |
| $MA(7Pb{:}1Mn)I_3$ | 761 | 1.629 | 3 | -0.007 |
| $MA(3Pb{:}1Mn)I_3$ | 755 | 1.642 | 9 | -0.02 |
| $MAPbI_3$ | 772 | 1.605 | - | - |
| $MA(63Pb{:}1Ni)I_3$ | 772 | 1.606 | 0 | -0.001 |
| $MA(31Pb{:}1Ni)I_3$ | 770 | 1.611 | 2 | -0.006 |
| $MA(15Pb{:}1Ni)I_3$ | 765 | 1.620 | 7 | -0.015 |
| $MA(7Pb{:}1Ni)I_3$ | 744 | 1.666 | 28 | -0.061 |
| $MA(3Pb{:}1Ni)I_3$ | 746 | 1.662 | 26 | -0.057 |
| $MAPbI_3$ | 766 | 1.619 | - | - |
| $MA(63Pb{:}1Sr)I_3$ | 768 | 1.613 | -2 | 0.006 |
| $MA(31Pb{:}1Sr)I_3$ | 771 | 1.609 | -5 | 0.01 |
| $MA(15Pb{:}1Sr)I_3$ | 763 | 1.625 | 3 | -0.006 |
| $MA(7Pb{:}1Sr)I_3$ | 759 | 1.633 | 7 | -0.014 |
| $MA(3Pb{:}1Sr)I_3$ | 763 | 1.625 | 3 | -0.006 |
| $MAPbI_3$ | 769 | 1.612 | - | - |
| $MA(63Pb{:}1Zn)I_3$ | 767 | 1.617 | 2 | -0.005 |
| $MA(31Pb{:}1Zn)I_3$ | 767 | 1.616 | 2 | -0.004 |
| $MA(15Pb{:}1Zn)I_3$ | 773 | 1.603 | -4 | 0.009 |
| $MA(7Pb{:}1Zn)I_3$ | 769 | 1.613 | 0 | -0.001 |
| $MA(3Pb{:}1Zn)I_3$ | 773 | 1.604 | -4 | 0.008 |

even when the grains are larger in the 3Pb:1B′ films.

### 6.3.4 Photoluminescence Lifetimes

Time-resolved photoluminescence (TRPL) is a material characterization method where a material is excited with a short laser pulse, creating photogenerated carriers which then move within the film and eventually recombine. Higher quality materials allow the light to persist longer as charge carriers recombine radiatively, produce a new photon which is then absorbed elsewhere and produces new charge carriers, which repeat the process. This cycle continues until the carriers either recombine non-radiatively and the light is lost as heat, or the emitted photon escapes from the film and is monitored by the detector. By monitoring how the pulse emitted by the material decays, information can be extracted about the kinetics and some light can be shed on the recombination processes that could be limiting performance.

Since the films must be emissive, the Pb:Fe and Pb:Sn composition sets were excluded from study since sufficient signal could not be detected. The normalized decay profiles for each composition are plotted in Figure 6-15 and the lifetime extracted from each profile is reported in Table 6.2. In this situation, the decay profiles largely do not follow the typical profiles observed in other perovskite films, which are generally either mono-exponential or bimolecular decays. This suggests that there are additional non-radiative decay pathways present that are not accounted for in traditional recombination kinetics models. In the absence of sufficient physical models to describe this trap-assisted recombination regime, it is difficult to accurately extract additional information from the decay profiles, hence the lifetimes defined here are simply taken to be the exponential decay time. The additional non-radiative pathways are likely due in part to the small grain size of the perovskite films, which produce an abundance of trap states in the grain boundaries.

The general trend here is that the PL lifetimes increase with increasing B′ content. This could be in part due to increases in the grain sizes observed for several samples in the images of the film morphologies shown in Figures 6-4 through Figure 6-12. For instance, the 3Pb:1Co, 1Pb:Mg, 7Pb:1Sr, and 7Pb:1Zn compositions have both

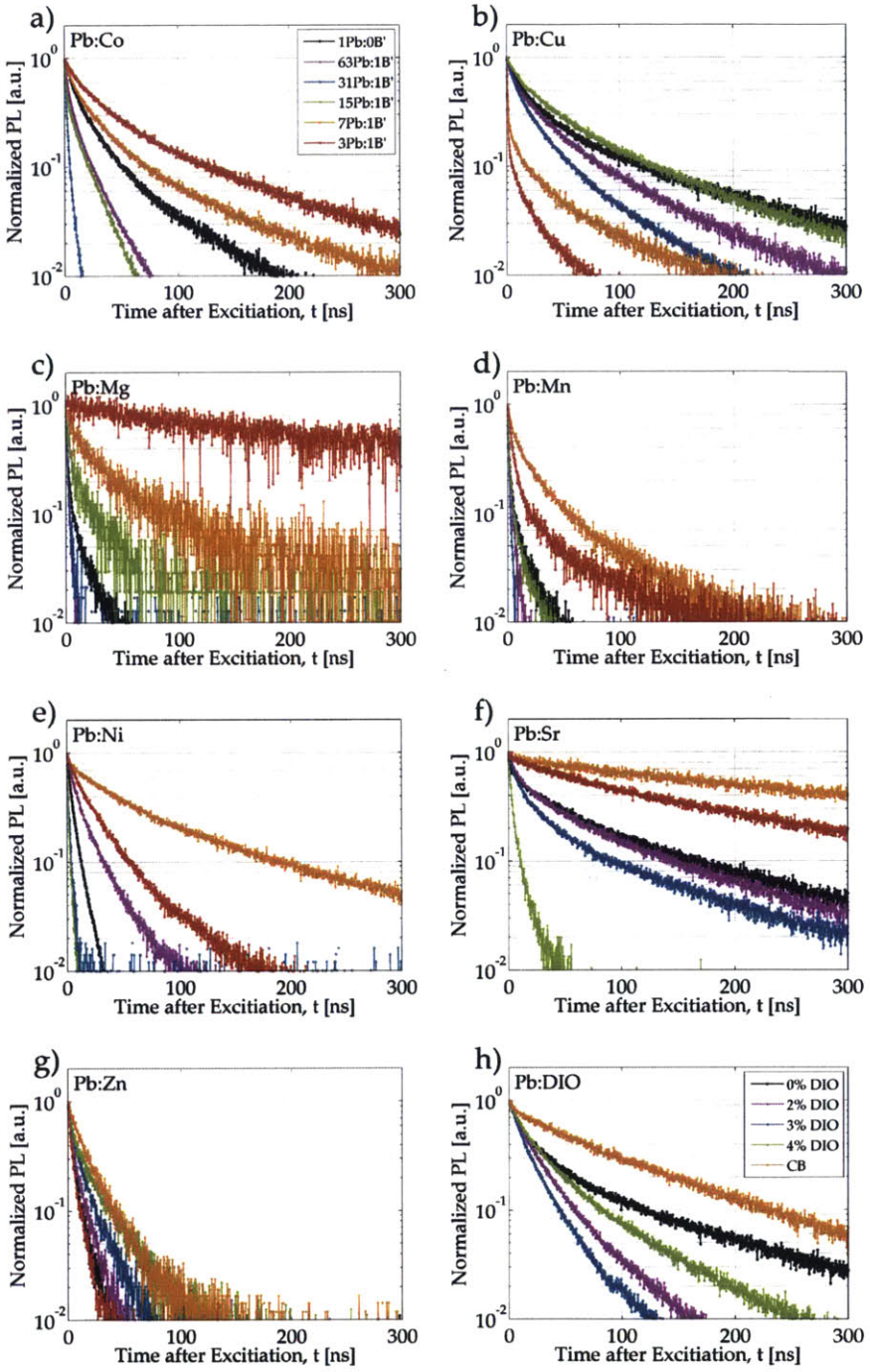


Figure 6-15: Time-resolved photoluminescence decay profiles for emissive mixed-metal perovskite films (a) Pb:Co, (b) Pb:Cu, (c) Pb:Mg, (d) Pb:Mn. (e) Pb:Ni. (f) Pb:Sr, (g) Pb:Zn, and (h) Pure Pb built on PEDOT:PSS that has been treated with DIO or chlorobenzene. Note that the $MAPbI_3$ curve in each plot corresponds to the control device that was fabricated in the same device set as the presented mixed-metal devices.

Table 6.2: Photoluminescence decay times for emissive perovskite films for each mixed-metal composition.

| | PL Lifetime, $\tau_{PL}$ [ns] | | | | | |
|---|---|---|---|---|---|---|
| Material | 3Pb:1B′ | 7Pb:1B′ | 15Pb:1B′ | 31Pb:1B′ | 63Pb:1B′ | 1Pb:0B′ |
| Pb:Co | 33.10 | 18.20 | 3.97 | 1.523 | 5.98 | 13.60 |
| Pb:Cu | 0.67 | 1.19 | 36.37 | 16.80 | 23.20 | 26.22 |
| Pb:Mg | 334.67 | 19.89 | 3.90 | 1.15 | 0.93 | 1.37 |
| Pb:Mn | 4.63 | 12.11 | 1.35 | 0.87 | 1.40 | 1.50 |
| Pb:Ni | 17.20 | 48.10 | 0.78 | 1.37 | 10.37 | 4.50 |
| Pb:Sr | 137.60 | 331.70 | 2.79 | 17.03 | 30.84 | 32.30 |
| Pb:Zn | 3.40 | 13.89 | 8.78 | 7.44 | 5.02 | 3.67 |

the largest well-defined grains in their respective material sets as well as the longest lifetimes. Conversely, Figure 6-5 clearly reveals that 1Pb:1Cu and 3Pb:1Cu demonstrate the largest grains, however these samples have significantly shorter lifetimes than the films with lower Cu content, which have smaller grains. An explanation for this observation is that a phase of CuI is present that quenches emission by removing holes from the perovskite grains. The presence of CuI has been confirmed for both the 3Pb:1Cu and 7Pb:1Cu films by an additional peak in the XRD spectrum. It is interesting, however that the lifetime of 7Pb:1Cu is the longest of its set even low it also has CuI, albeit a lower amount. The SEM image reveals that the grains in this sample are very compact, therefore it is possible that the CuI is either existing elsewhere in the crystal and is removed from most of the perovskite grains, or that the CuI exists at the grain boundaries and allows the holes to be transported to another grain where it can radiatively recombine.

## 6.4 Impact of Secondary Metal Substitution on Solar Cell Performance

This section aims to evaluate how replacing various quantities of Pb atoms with alternative non-toxic metal species impacts the photovoltaic performance of the perovskite solar cells. This empirical screening process allows trends to be identified and reveals how tolerant the perovskite material is to additional elements.

### 6.4.1 Trends in Performance Metrics

Figure 6-16 and Table 6.3 summarize the average photovoltaic performance metrics for each mixed-metal solar cell embodiment, where five different mole fractions of $Pb^{2+}$ were replaced systematically with nine different non-toxic divalent metal species. For each condition, at least 36 individual solar cells were tested from two different device batches in order to ensure that observed trends in photovoltaic performance were repeatable and not simply serendipitous. By comparing the performance metrics of the mixed-metal devices to the baselines obtained from pure Pb devices, several interesting observations can be made about the tolerance of perovskite solar cells to other metal species:

1. Performance improvements are generally seen upon replacing a small fraction of the Pb atoms with a second metal species.

2. Further reductions in the Pb content is generally accompanied by decreases in the photocurrent, which correspondingly decrease the PCE.

3. Iron is the only metal species whose inclusion in the perovskite is always detrimental to performance, regardless of Fe content.

4. Blends of Pb:Sn demonstrate the opposite behavior to most other mixed-metal materials. The performance is highest at 3Pb:1Sn but decreases with decreasing amounts of Sn. However, the performance generally improves substantially with longer light-soaking times.

The most notable efficiency enhancements arise when only $1/64^{\text{th}}$ of the Pb atoms, denoted as 63Pb:1B′, are replaced with Co, Cu, Sr, or Zn, which improves both the short-circuit current, $J_{sc}$, and open circuit voltage, $V_{oc}$. Modest PCE improvements are also observed for 63Pb:1B′ samples of Mg, Mn, and Ni, which clearly demonstrate that the $MAPbI_3$ perovskite material is not only quite tolerant of several metal species at relatively low concentrations, but that these atoms are generally beneficial to device performance.

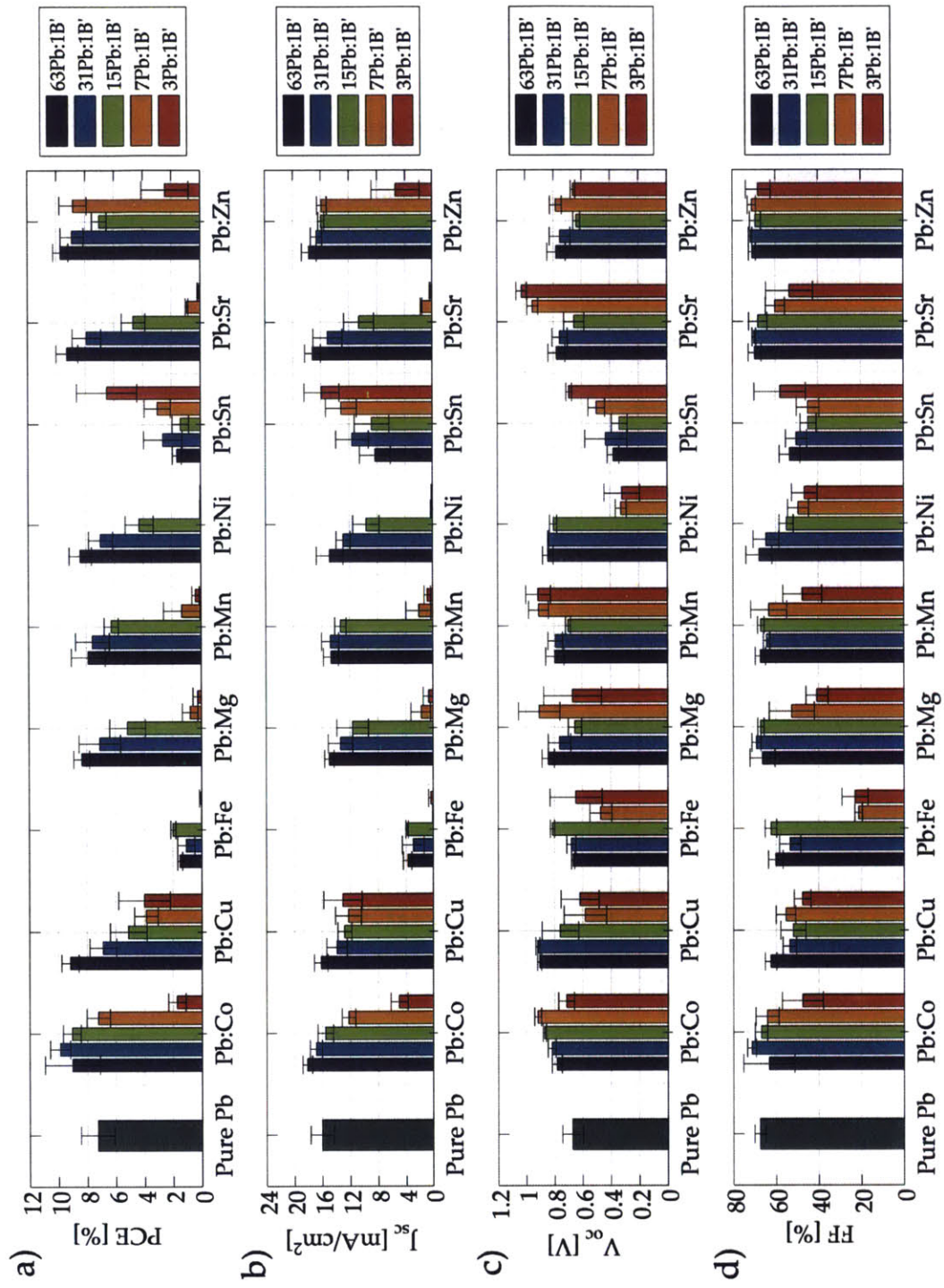


Figure 6-16: The compiled average performance metrics of planar mixed-metal perovskites for each of the embodiments considered in this study demonstrate that replacing small amounts of lead content with a second metal species can improve either (a) the power conversion efficiency (PCE), (b) the short-circuit current density ( $J_{sc}$), (c) the open-circuit voltage ($V_{oc}$), (d) the fill-factor (FF), or any combination of these.

Table 6.3: The compiled average performance metrics of planar mixed-metals for each composition. Error corresponds to the standard deviation.

| Material | Mean Short-Circuit Current Density, $J_{sc}$ [mA/cm$^2$] 63Pb:1B′ | 31Pb:1B′ | 15Pb:1B′ | 7Pb:1B′ | 3Pb:1B′ |
|---|---|---|---|---|---|
| Pb Only | | | 16.02 ± 1.62 | | |
| Pb:Co | 18.15 ± 0.71 | 16.89 ± 0.86 | 15.54 ± 1.12 | 12.25 ± 0.96 | 5.00 ± 1.20 |
| Pb:Cu | 16.18 ± 0.96 | 13.91 ± 1.46 | 12.81 ± 0.99 | 12.28 ± 1.84 | 13.07 ± 2.72 |
| Pb:Fe | 3.79 ± 0.64 | 2.95 ± 1.61 | 3.88 ± 0.19 | 0.02 ± 0.01 | 0.28 ± 0.34 |
| Pb:Mg | 14.94 ± 0.67 | 13.36 ± 1.73 | 11.64 ± 2.22 | 1.78 ± 1.47 | 0.60 ± 0.84 |
| Pb:Mn | 14.68 ± 1.07 | 14.78 ± 1.20 | 13.33 ± 0.81 | 2.11 ± 1.87 | 0.75 ± 0.48 |
| Pb:Ni | 14.82 ± 1.90 | 12.90 ± 0.99 | 9.63 ± 1.90 | 0.14 ± 0.10 | 0.06 ± 0.04 |
| Pb:Sn | 8.33 ± 2.22 | 11.59 ± 2.29 | 8.80 ± 2.47 | 13.16 ± 2.20 | 15.92 ± 2.49 |
| Pb:Sr | 17.16 ± 1.12 | 15.03 ± 2.06 | 10.60 ± 2.13 | 1.62 ± 0.14 | 0.25 ± 0.08 |
| Pb:Zn | 17.66 ± 1.06 | 16.60 ± 0.80 | 15.94 ± 0.44 | 15.86 ± 0.69 | 5.35 ± 3.44 |

| Material | Mean Open-Circuit Voltage, $V_{oc}$ [V] 63Pb:1B′ | 31Pb:1B′ | 15Pb:1B′ | 7Pb:1B′ | 3Pb:1B′ |
|---|---|---|---|---|---|
| Pb Only | | | 0.67 ± 0.07 | | |
| Pb:Co | 0.78 ± 0.04 | 0.82 ± 0.03 | 0.87 ± 0.01 | 0.92 ± 0.02 | 0.72 ± 0.06 |
| Pb:Cu | 0.91 ± 0.01 | 0.92 ± 0.01 | 0.76 ± 0.13 | 0.58 ± 0.15 | 0.62 ± 0.13 |
| Pb:Fe | 0.67 ± 0.01 | 0.68 ± 0.03 | 0.82 ± 0.01 | 0.47 ± 0.08 | 0.65 ± 0.19 |
| Pb:Mg | 0.84 ± 0.04 | 0.76 ± 0.08 | 0.65 ± 0.05 | 0.91 ± 0.15 | 0.67 ± 0.21 |
| Pb:Mn | 0.79 ± 0.07 | 0.79 ± 0.05 | 0.70 ± 0.02 | 0.91 ± 0.07 | 0.91 ± 0.09 |
| Pb:Ni | 0.84 ± 0.04 | 0.84 ± 0.00 | 0.80 ± 0.03 | 0.32 ± 0.04 | 0.32 ± 0.12 |
| Pb:Sn | 0.38 ± 0.04 | 0.43 ± 0.15 | 0.33 ± 0.06 | 0.49 ± 0.06 | 0.69 ± 0.02 |
| Pb:Sr | 0.78 ± 0.06 | 0.75 ± 0.05 | 0.65 ± 0.07 | 0.95 ± 0.04 | 1.03 ± 0.04 |
| Pb:Zn | 0.78 ± 0.07 | 0.75 ± 0.07 | 0.63 ± 0.02 | 0.78 ± 0.04 | 0.66 ± 0.02 |

| Material | Mean Fill Factor, FF [%] 63Pb:1B′ | 31Pb:1B′ | 15Pb:1B′ | 7Pb:1B′ | 3Pb:1B′ |
|---|---|---|---|---|---|
| Pb Only | | | 67.53 ± 2.54 | | |
| Pb:Co | 63.33 ± 11.91 | 71.43 ± 2.04 | 66.99 ± 2.91 | 64.19 ± 5.42 | 47.61 ± 9.65 |
| Pb:Cu | 62.49 ± 2.61 | 53.72 ± 3.17 | 52.03 ± 5.95 | 55.51 ± 4.55 | 47.70 ± 3.99 |
| Pb:Fe | 60.25 ± 3.43 | 53.47 ± 4.94 | 62.44 ± 2.70 | 21.39 ± 1.75 | 23.06 ± 6.10 |
| Pb:Mg | 66.41 ± 5.78 | 69.20 ± 2.14 | 67.12 ± 1.43 | 52.63 ± 10.61 | 40.80 ± 5.11 |
| Pb:Mn | 67.24 ± 2.45 | 64.35 ± 1.56 | 67.04 ± 1.59 | 63.32 ± 8.40 | 47.58 ± 9.12 |
| Pb:Ni | 67.83 ± 6.01 | 64.52 ± 6.03 | 55.04 ± 3.33 | 49.46 ± 4.97 | 46.45 ± 6.01 |
| Pb:Sn | 53.39 ± 4.89 | 50.29 ± 5.06 | 44.63 ± 3.81 | 44.81 ± 5.29 | 57.87 ± 12.05 |
| Pb:Sr | 69.60 ± 2.99 | 69.97 ± 0.83 | 68.12 ± 4.27 | 60.05 ± 4.48 | 53.38 ± 10.95 |
| Pb:Zn | 70.73 ± 1.62 | 71.49 ± 0.82 | 69.32 ± 2.56 | 70.94 ± 1.93 | 67.95 ± 5.75 |

| Material | Mean Power Conversion Efficiency, PCE [%] 63Pb:1B′ | 31Pb:1B′ | 15Pb:1B′ | 7Pb:1B′ | 3Pb:1B′ |
|---|---|---|---|---|---|
| Pb Only | | | 7.27 ± 1.18 | | |
| Pb:Co | 9.03 ± 1.91 | 9.88 ± 0.69 | 9.06 ± 0.61 | 7.23 ± 0.82 | 1.73 ± 0.61 |
| Pb:Cu | 9.18 ± 0.60 | 6.89 ± 0.93 | 5.12 ± 1.28 | 3.87 ± 0.82 | 4.00 ± 1.81 |
| Pb:Fe | 1.51 ± 0.17 | 1.08 ± 0.60 | 1.98 ± 0.17 | 0.00 ± 0.00 | 0.06 ± 0.08 |
| Pb:Mg | 8.35 ± 0.56 | 7.09 ± 1.45 | 5.15 ± 1.25 | 0.77 ± 0.54 | 0.24 ± 0.34 |
| Pb:Mn | 7.87 ± 1.19 | 7.57 ± 1.18 | 6.26 ± 0.49 | 1.33 ± 1.28 | 0.37 ± 0.25 |
| Pb:Ni | 8.40 ± 0.78 | 6.98 ± 0.84 | 4.28 ± 0.97 | 0.02 ± 0.02 | 0.01 ± 0.01 |
| Pb:Sn | 1.63 ± 0.32 | 2.61 ± 1.34 | 1.38 ± 0.58 | 2.99 ± 0.91 | 6.51 ± 2.10 |
| Pb:Sr | 9.26 ± 0.74 | 7.91 ± 1.00 | 4.66 ± 0.82 | 0.92 ± 0.10 | 0.13 ± 0.04 |
| Pb:Zn | 9.69 ± 0.51 | 8.92 ± 0.79 | 7.02 ± 0.50 | 8.83 ± 0.94 | 2.43 ± 1.65 |

Table 6.4: The best measured performance metric for each mixed-metal composition. $J_{sc}$, $V_{oc}$, and FF do not necessarily correspond to the device with the champion PCE.

| Material | Best Short-Circuit Current Density, $J_{sc}$ [mA/cm$^2$] 63Pb:1B′ | 31Pb:1B′ | 15Pb:1B′ | 7Pb:1B′ | 3Pb:1B′ |
|---|---|---|---|---|---|
| Pb Only | | | 18.97 | | |
| Pb:Co | 19.82 | 19.06 | 17.00 | 14.35 | 9.57 |
| Pb:Cu | 18.19 | 16.26 | 14.57 | 15.24 | 19.10 |
| Pb:Fe | 4.94 | 4.97 | 4.29 | 0.04 | 0.91 |
| Pb:Mg | 15.76 | 16.39 | 14.91 | 4.06 | 1.86 |
| Pb:Mn | 17.25 | 17.31 | 15.01 | 6.18 | 1.39 |
| Pb:Ni | 18.40 | 15.31 | 13.24 | 0.33 | 0.13 |
| Pb:Sn | 11.62 | 14.14 | 12.22 | 15.69 | 20.40 |
| Pb:Sr | 19.17 | 17.71 | 12.89 | 1.96 | 0.38 |
| Pb:Zn | 19.71 | 18.18 | 16.61 | 16.99 | 13.19 |

| Material | Best Open-Circuit Voltage, $V_{oc}$ [V] 63Pb:1B′ | 31Pb:1B′ | 15Pb:1B′ | 7Pb:1B′ | 3Pb:1B′ |
|---|---|---|---|---|---|
| Pb Only | | | 0.82 | | |
| Pb:Co | 0.85 | 0.87 | 0.89 | 0.94 | 0.84 |
| Pb:Cu | 0.93 | 0.94 | 0.87 | 0.80 | 0.86 |
| Pb:Fe | 0.68 | 0.73 | 0.84 | 0.57 | 0.77 |
| Pb:Mg | 0.92 | 0.91 | 0.73 | 0.96 | 0.94 |
| Pb:Mn | 0.91 | 0.88 | 0.74 | 0.96 | 1.01 |
| Pb:Ni | 0.91 | 0.85 | 0.85 | 0.40 | 0.52 |
| Pb:Sn | 0.46 | 0.71 | 0.50 | 0.68 | 0.73 |
| Pb:Sr | 0.88 | 0.84 | 0.84 | 1.02 | 1.11 |
| Pb:Zn | 0.89 | 0.88 | 0.65 | 0.82 | 0.70 |

| Material | Best Fill Factor FF [%] 63Pb:1B′ | 31Pb:1B′ | 15Pb:1B′ | 7Pb:1B′ | 3Pb:1B′ |
|---|---|---|---|---|---|
| Pb Only | | | 72.14 | | |
| Pb:Co | 74.10 | 76.11 | 71.04 | 68.82 | 54.34 |
| Pb:Cu | 66.55 | 61.29 | 61.01 | 62.88 | 66.16 |
| Pb:Fe | 64.67 | 63.03 | 66.59 | 26.21 | 36.90 |
| Pb:Mg | 75.10 | 72.61 | 70.36 | 68.95 | 48.63 |
| Pb:Mn | 70.65 | 67.50 | 70.19 | 73.58 | 59.52 |
| Pb:Ni | 76.62 | 71.94 | 59.38 | 56.51 | 54.77 |
| Pb:Sn | 63.25 | 57.44 | 51.14 | 60.36 | 70.94 |
| Pb:Sr | 75.37 | 71.69 | 70.90 | 66.82 | 65.90 |
| Pb:Zn | 73.19 | 73.02 | 72.98 | 73.78 | 73.03 |

| Material | Best Power Conversion Efficiency, PCE [%] 63Pb:1B′ | 31Pb:1B′ | 15Pb:1B′ | 7Pb:1B′ | 3Pb:1B′ |
|---|---|---|---|---|---|
| Pb Only | | | 10.27 | | |
| Pb:Co | 11.37 | 11.11 | 10.21 | 8.66 | 4.14 |
| Pb:Cu | 10.14 | 8.37 | 6.57 | 5.46 | 8.29 |
| Pb:Fe | 1.78 | 1.75 | 2.29 | 0.01 | 0.22 |
| Pb:Mg | 9.37 | 9.71 | 7.11 | 1.74 | 0.76 |
| Pb:Mn | 10.38 | 10.02 | 7.17 | 4.30 | 0.68 |
| Pb:Ni | 9.95 | 8.53 | 6.01 | 0.06 | 0.04 |
| Pb:Sn | 2.32 | 5.30 | 2.38 | 4.89 | 9.25 |
| Pb:Sr | 10.81 | 9.29 | 5.58 | 1.16 | 0.21 |
| Pb:Zn | 10.62 | 10.41 | 7.69 | 9.88 | 6.04 |

However, as more Pb is replaced, the photocurrent begins to decrease and the current drop becomes quite appreciable between the 15Pb:1B′ and 7Pb:1B′ molar ratios for Mg, Mn, Ni, and Sr. The perovskite active layer is even more tolerant of Co, Cu, and Zn whose 3Pb:1B′ devices achieve efficiencies near or exceeding 2%, whereas the other metals have efficiencies at mere fractions of a percent. Although each secondary metal species has its own tolerance limit, as a general rule the perovskite active layer suffers significant decreases in photovoltaic performance for Pb replacement levels exceeding 7Pb:1B′. The transition metal that appears to be the most highly tolerated by the perovskite material is Zn, whose $MA(7Pb{:}1Zn)I_3$ composition achieves an average PCE of 8.8%, which is considerably greater than the average 7.3% achieved by pure Pb devices.

The odd behavior of the Pb:Fe can be partially explained by its photoluminescence emission. As is shown in Figure 6-17, the photoluminescence emission from every film in the Pb:Fe series is two orders of magnitude lower than the pure Pb control sample. In fact, the PL intensity exhibits a 260-fold decrease when only $1/64^{th}$ of the $Pb^{2+}$ content is replaced with $Fe^{2+}$. This suggests that the material has an abundance of traps that promote non-radiative recombination, thereby depleting the amount of photocurrent available for extraction from the devices. It is well-documented that the introduction of Fe into silicon solar cells is very detrimental to performance, as iron atoms have a large capture cross-section, whereby they preferentially trap electrons when the Fe atoms exist as interstitial or substitutional defects in the Si lattice. [146] It is likely that iron behaves similarly in perovskite systems.

The contrary behavior of Pb:Sn mixtures can be largely explained by the film morphology presented in Figure 6-10. The SEM images reveal that the 3Pb:1Sn film has substantially larger grains than samples with lower amounts of Sn. The morphologies between 7Pb:1Sn and 63Pb:1Sn display some of the smallest grains observed from the whole set of mixed-metal materials. It has been demonstrated that perovskite films with larger grains generally exhibit improved photovoltaic performance since there is less chance of non-radiative recombination occurring at trap sites in grain boundaries. Hence, the smaller grain films are more likely to experience lower photocurrents

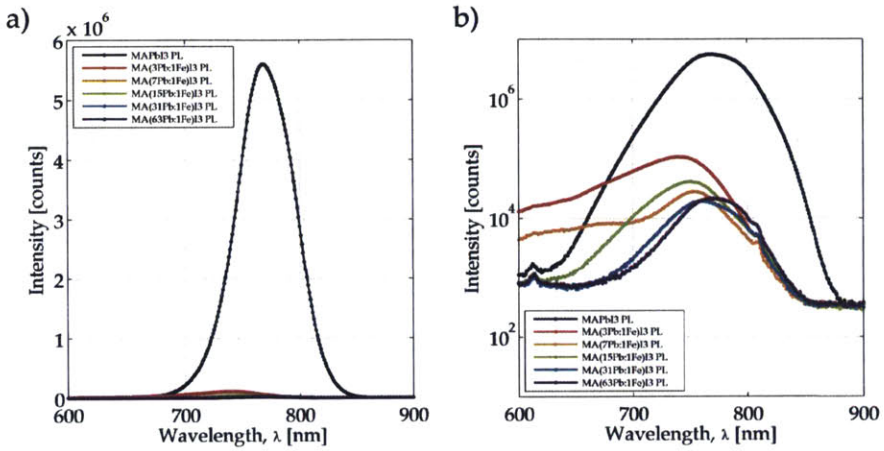


Figure 6-17: The photoluminescence emission spectra for MA(Pb:Fe)$I_3$ perovskite films show substantial emission quenching as illustrated by (a) linear and (b) logarithmic plots of emission intensity.

and lower photovoltages, which is the trend observed for this set of devices. At only 95% purity, $Sn(OAc)_2$ is the least pure acetate precursor salt used in the study. One explanation for the small grain-size might be that one of the impurities in the precursor is capable of disrupting perovskite crystallization in small amounts, but the perovskite lattice is able to exclude it at higher loadings and cause it to separate into a different phase that is more electronically benign. Perhaps the bright white spots seen in the SEM images for the 3Pb:1Sn and 1Pb:1Sn samples (Figure 6-10) correspond to a domain of this impurity, which appear to be charging compared to the large perovskite grains. This explanation is further supported by the observation that the open-circuit voltages and fill-factors were improved in the Pb:Sn samples upon additional light-soaking, which indicates that the films contain high densities of sub-gap trap states that must be first filled with photogenerated carriers before optimum performance can be achieved. In order to be consistent with the other mixed-metal systems, the data reported in Figure 6-16 and Tables 6.3 and 6.4 correspond only to the measurements made after the standard five minutes of light-soaking performed before measuring the JV curves for each device throughout the entire study.

### 6.4.2 Trends in Current-Voltage Characteristics

The current-voltage characteristic for both the forward and reverse sweeps of the champion solar cell for each mixed-metal embodiment is shown in Figure 6-18. As is expected for perovskite solar cells with the inverted architecture, the forward and reverse scans of the pure Pb device are indeed identical. However, hysteresis does arise in many mixed-metal systems and generally becomes more pronounced as more Pb atoms are substituted with a second metal species. For many secondary metal species, the scan from short circuit to forward bias appears normal, but the scan from forward bias to short circuit often noticeably overshoot the current near the maximum power point for 7Pb:1B′ and 15Pb:1B′ samples. These findings suggest that while the photovoltaic behavior of the perovskite lattice is generally quite tolerant to the second metal species, if too many Pb atoms are replaced the additional ions have difficulty securing stable positions within the film and are more likely to become mobile during device operation. The mobile ions can induce the observed hysteresis by adopting a configuration during the forward sweep that is more favorable, such that the reverse scan shows initially excellent performance but then adjusts as these charges relax to their original sites. [169]

The hysteresis is the most dramatic for blends of Ni, Fe, and Co whereas it is minimal in Cu, Mg, Sr, and Zn mixtures.

### 6.4.3 Trends in External Quantum Efficiency

External quantum efficiency (EQE) measurements were performed on multiple solar cells of each mixed-metal composition. The EQE spectra reported for each mixed-metal set in Figure 6-19 were selected from the same device batch to ensure that changes between devices in a given series is a result of changing the metal the Pb:B′ ratio rather than batch to batch variation. Hence, the measurements for the $MAPbI_3$ control devices will vary slightly between each set of blends. Measuring external quantum efficiency yields how efficiently incident photons of a given energy are converted to charges that are collected by the solar cell. As is shown by each of the panels

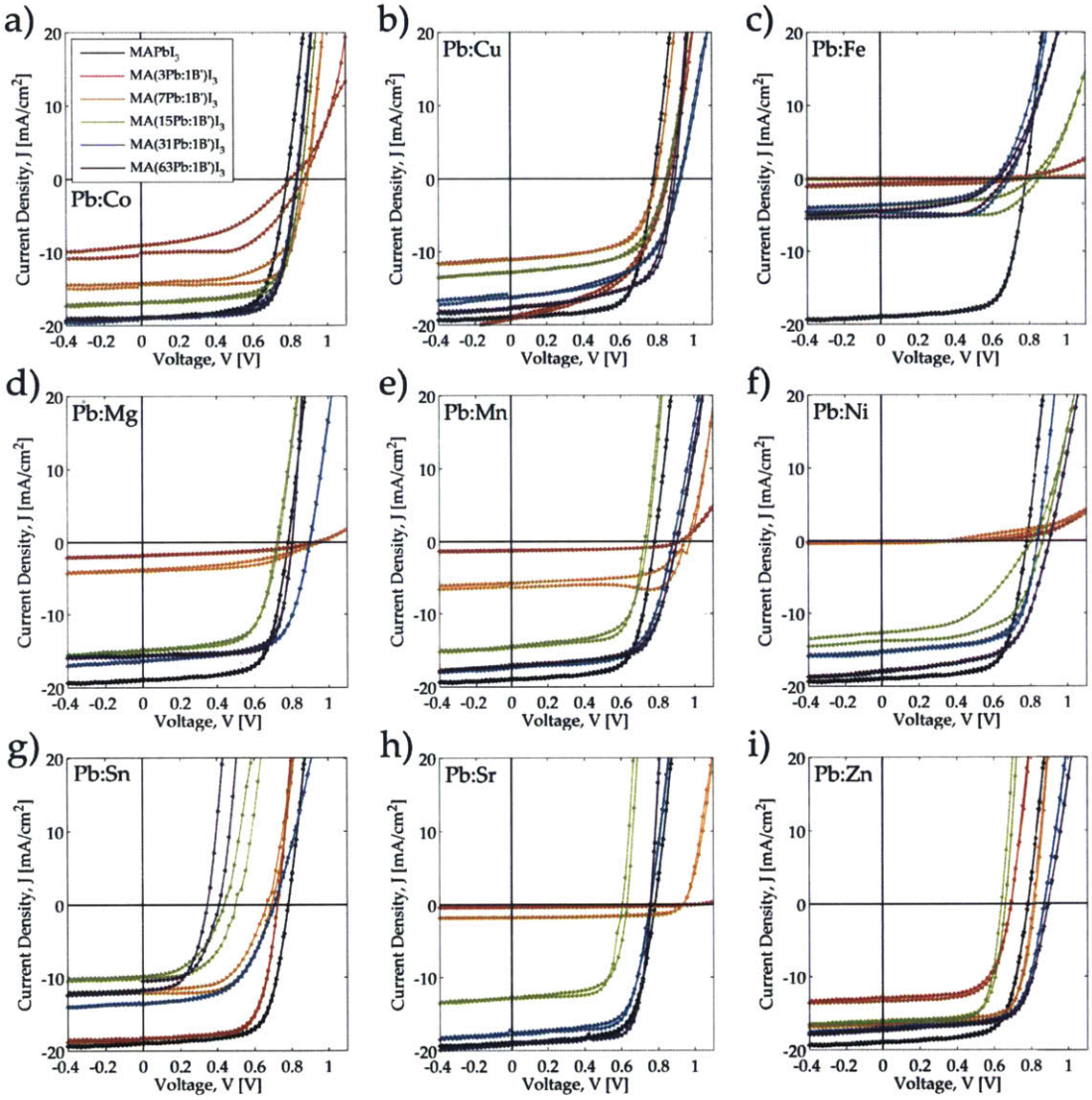


Figure 6-18: Forward and reverse current-voltage ($JV$) characteristic scans measured from the best performing solar cell for each composition in each mixed-metal material set: (a) Pb:Co, (b) Pb:Cu, (c) Pb:Fe, (d) Pb:Mg, (e) Pb:Mn, (f) Pb:Ni, (g) Pb:Sn, (h) Pb:Sr, and (i) Pb:Zn.

in Figure 6-19, the overall shape of the $MAPbI_3$ device remains consistent between device batches. Current starts to be produced near a wavelength of 800 nm and the efficiency quickly rises near the absorption edge and a local maximum occurs around 750 nm. As the photon energies continue to increase there is a small dip in efficiency which is later recovered and the maximum EQE is achieved around 525 nm, which is followed by a stepped drop off in efficiency further into the UV as the solar spectrum

irradiance drops with increasing photon energy.

As expected, the peak efficiency of each composition generally correlates with the trends in the $J_{sc}$ of the solar cells. It does not always correlate with the overall PCE trends because the EQE measurements only consider current and do not capture photovoltage or fill factor. For this reason, some devices that have low photovoltages, such as some of the Pb:Sn have better than expected EQE intensities.

For many mixed-metal material sets, such as Pb:Ni (Figure 6-19f) and Pb:Mg (Figure 6-19d), the shape of the EQE spectra retains the overall character of the pure $MAPbI_3$ plot and the intensity reduces uniformly with increasing B′ content until 7Pb:1B′, at which point the shape changes and the device is relatively more efficient at converting long wavelengths rather than short ones into current. This behavior is clearly demonstrated by the Pb:Mn blends in Figure 6-19e. The 15Pb:1Mn curve is very similar to $MAPbI_3$ and the shape near the absorption edge is maintained in the $MA(7Pb:1Mg)I_3$ spectra, but the efficiency is relatively reduced at shorter wavelengths. The curve becomes even flatter for $MA(3Pb:1Mg)I_3$ where the efficiency at longer wavelengths is also reduced.

Several of the secondary metal species seem to change the shape of the EQE curves in certain wavelength bands. For instance, in Pb:Sr blends (Figure 6-19h), introducing a small amount of Sr preserves the EQE at short wavelengths, as evidenced by the identical spectra of $MA(63Pb:1Sr)I_3$ and $MA(31Pb:1Sr)I_3$ between 350 and 450 nm, but causes the local maximum near the absorption edge to flatten. Similarly, substituting only $1/64^{th}$ of the $Pb^{2+}$ with $Co^{2+}$ causes the EQE to improve in the UV as evidenced by a boost in efficiency between 350 and 400 nm as well as from 600 to 700 nm in Figure 6-19a.

Perhaps the most dramatic improvement in the EQE occurs for the Pb:Zn devices. As shown by Figure 6-19i, the incorporation of Zn causes the EQE spectrum to rise substantially across all wavelengths. Interestingly, as the Zn content increases, only the efficiency between 450 and 800 nm decreases while the efficiency between 300 and 400 nm is maintained with only slight reductions until the Zn content reaches 25%.

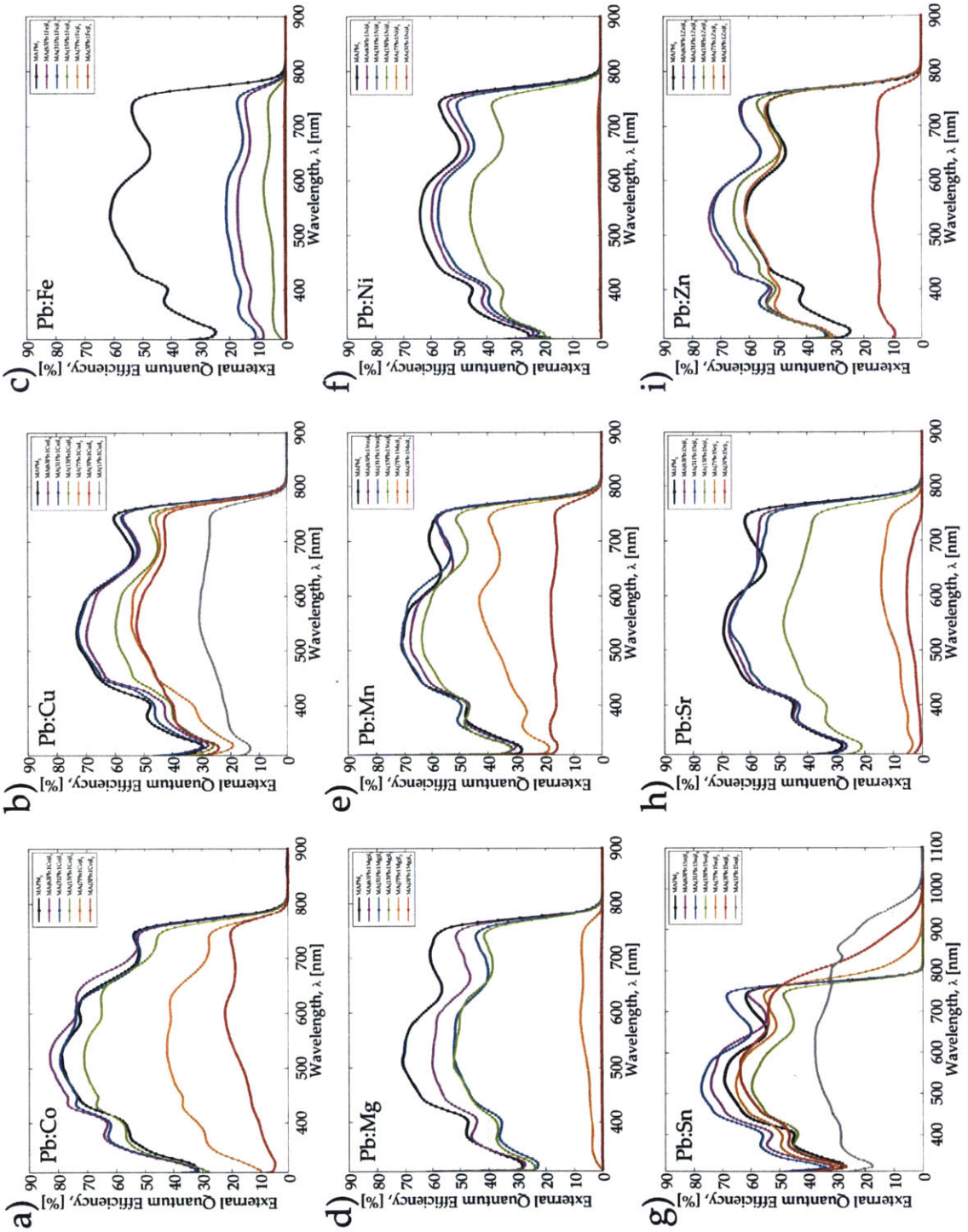


Figure 6-19: Typical external quantum efficiency measurements for each composition in the mixed-metal perovskite sets: (a) Pb:Co, (b) Pb:Cu, (c) Pb:Fe, (d) Pb:Mg, (e) Pb:Mn, (f) Pb:Ni, (g) Pb:Sn, (h) Pb:Sr, and (i) Pb:Zn. Note that the $MAPbI_3$ curve in each plot corresponds to the control device that was fabricated in the same device set as the presented mixed-metal devices.

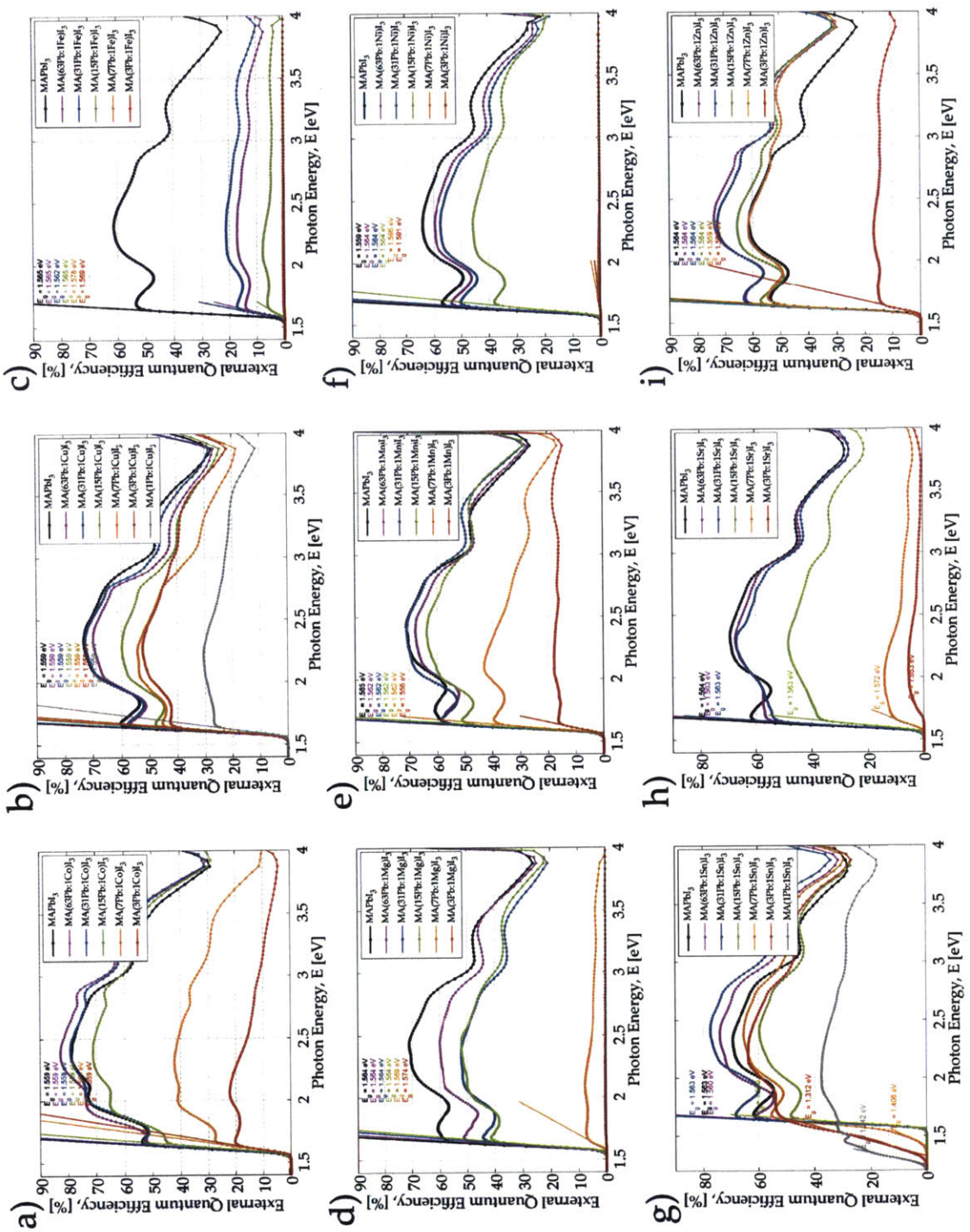


Figure 6-20: The optical band gap, $E_g$, is estimated by fitting a line to the edge of the EQE and extracting the intercept at the $x$-axis for each set of mixed-metal devices: (a) Pb:Co, (b) Pb:Cu, (c) Pb:Fe, (d) Pb:Mg, (e) Pb:Mn, (f) Pb:Ni, (g) Pb:Sn, (h) Pb:Sr, and (i) Pb:Zn. Note that the $MAPbI_3$ curve in each plot corresponds to the control device that was fabricated in the same device set as the presented mixed-metal devices.

Table 6.5: The optical band gap, $E_g$, is estimated by fitting a line to the edge of the EQE and extracting the intercept at the $x$-axis for each set of mixed-metal devices. Note that the $MAPbI_3$ curve in each plot corresponds to the control device that was fabricated in the same device set as the presented mixed-metal devices. The measured value is compared against DFT calculations performed in Chapter 5, if available for the particular composition.

| | Optical Band Gap, $E_g$ [eV] | | | Optical Band Gap, $E_g$ [eV] | |
|---|---|---|---|---|---|
| Material | EQE | DFT | Material | EQE | DFT |
| $MAPbI_3$ | 1.559 | 1.67 | $MAPbI_3$ | 1.559 | 1.67 |
| $MA(63Pb{:}1Co)I_3$ | 1.559 | - | $MA(63Pb{:}1Ni)I_3$ | 1.564 | - |
| $MA(31Pb{:}1Co)I_3$ | 1.559 | - | $MA(31Pb{:}1Ni)I_3$ | 1.564 | - |
| $MA(15Pb{:}1Co)I_3$ | 1.559 | - | $MA(15Pb{:}1Ni)I_3$ | 1.564 | - |
| $MA(7Pb{:}1Co)I_3$ | 1.564 | - | $MA(7Pb{:}1Ni)I_3$ | 1.596 | - |
| $MA(3Pb{:}1Co)I_3$ | 1.559 | 1.77 | $MA(3Pb{:}1Ni)I_3$ | 1.591 | 2.04 |
| $MAPbI_3$ | 1.559 | 1.67 | $MAPbI_3$ | 1.563 | 1.67 |
| $MA(63Pb{:}1Cu)I_3$ | 1.559 | - | $MA(63Pb{:}1Sn)I_3$ | 1.560 | - |
| $MA(31Pb{:}1Cu)I_3$ | 1.559 | - | $MA(31Pb{:}1Sn)I_3$ | 1.563 | - |
| $MA(15Pb{:}1Cu)I_3$ | 1.559 | - | $MA(15Pb{:}1Sn)I_3$ | 1.560 | - |
| $MA(7Pb{:}1Cu)I_3$ | 1.559 | - | $MA(7Pb{:}1Sn)I_3$ | 1.406 | - |
| $MA(3Pb{:}1Cu)I_3$ | 1.559 | - | $MA(3Pb{:}1Sn)I_3$ | 1.312 | 1.34 |
| $MA(1Pb{:}1Cu)I_3$ | 1.559 | - | $MA(1Pb{:}1Sn)I_3$ | 1.242 | 1.06 |
| $MAPbI_3$ | 1.565 | 1.67 | $MAPbI_3$ | 1.564 | 1.67 |
| $MA(63Pb{:}1Fe)I_3$ | 1.565 | - | $MA(63Pb{:}1Sr)I_3$ | 1.563 | - |
| $MA(31Pb{:}1Fe)I_3$ | 1.562 | - | $MA(31Pb{:}1Sr)I_3$ | 1.563 | - |
| $MA(15Pb{:}1Fe)I_3$ | 1.565 | - | $MA(15Pb{:}1Sr)I_3$ | 1.563 | - |
| $MA(7Pb{:}1Fe)I_3$ | 1.578 | - | $MA(7Pb{:}1Sr)I_3$ | 1.572 | - |
| $MA(3Pb{:}1Fe)I_3$ | 1.569 | - | $MA(3Pb{:}1Sr)I_3$ | 1.653 | 2.03 |
| $MAPbI_3$ | 1.564 | 1.67 | $MAPbI_3$ | 1.564 | 1.67 |
| $MA(63Pb{:}1Mg)I_3$ | 1.564 | - | $MA(63Pb{:}1Zn)I_3$ | 1.564 | - |
| $MA(31Pb{:}1Mg)I_3$ | 1.564 | - | $MA(31Pb{:}1Zn)I_3$ | 1.564 | - |
| $MA(15Pb{:}1Mg)I_3$ | 1.564 | - | $MA(15Pb{:}1Zn)I_3$ | 1.564 | - |
| $MA(7Pb{:}1Mg)I_3$ | 1.569 | - | $MA(7Pb{:}1Zn)I_3$ | 1.559 | - |
| $MA(3Pb{:}1Mg)I_3$ | 1.574 | 1.66 | $MA(3Pb{:}1Zn)I_3$ | 1.564 | 2.03 |
| $MAPbI_3$ | 1.565 | 1.67 | $MAPbI_3$ | 1.562 | 1.67 |
| $MA(63Pb{:}1Mn)I_3$ | 1.562 | - | $MA(63Pb{:}1MAI)I_3$ | 1.562 | - |
| $MA(31Pb{:}1Mn)I_3$ | 1.562 | - | $MA(31Pb{:}1MAI)I_3$ | 1.562 | - |
| $MA(15Pb{:}1Mn)I_3$ | 1.562 | - | $MA(15Pb{:}1MAI)I_3$ | 1.567 | - |
| $MA(7Pb{:}1Mn)I_3$ | 1.562 | - | $MA(7Pb{:}1MAI)I_3$ | 1.571 | - |
| $MA(3Pb{:}1Mn)I_3$ | 1.556 | 1.48 | $MA(3Pb{:}1MAI)I_3$ | 1.835 | - |

The EQE spectra also provide information about changes in the optical band gap of the materials. The band gap can be determined by generating Tauc plots where the EQE is plotted against photon energy and a line is fitted to the absorption edge. The optical band gap, $E_g$ is taken as the $x$-intercept of the linear fit. As shown in the Tauc plots of Figure 6-20 and Table 6.5, the majority of the mixed-metal compositions do not show a shift in band gap from $MAPbI_3$. The DFT predictions are also listed in Table 6.5 for convenient reference. As discussed in Chapter 5, the DFT calculations predict that the band gaps of most $MA(3Pb:1B')I_3$ materials will be wider than that of $MAPbI_3$. Mixed-lattices of 3Pb:1Ni, 3Pb:1Sr, and 3Pb:1Zn are expected to increase by 0.37 eV. However, the EQE measurements show that 3Pb:1Zn is identical to $MAPbI_3$ and 3Pb:1Ni only shifts by 0.032 eV. The EQE edge for $MA(3Pb:1Sr)I_3$ produced the largest observed blue-shift with 0.09 eV, which is still substantially less than than predicted.

On the other hand, the DFT calculations predicted that $E_g$ for $MA(3Pb:1Mg)I_3$ would decrease by 0.01 eV, whereas an increase of 0.01 eV was measured. Likewise, only a relatively small increase of 0.1 eV was predicted for $MA(3Pb:1Co)I_3$ whereas no shift was observed.

The two remaining cases of $MA(3Pb:1Mn)I_3$ and $MA(3Pb:1Sn)I_3$ also follow the trend indicated by DFT by demonstrating narrower band gaps. Although the $E_g$ for 3Pb:1Mn was expected to narrow by 0.19 eV, only a 0.009 eV shift was observed. The Pb:Sn devices follow the predicted trends the most closely by demonstrating dramatically narrowed band-gaps for the 3Pb:1Sn and 1Pb:1Sn films.

If a wide-band gap mixed-metal perovskite material such as $MA(3Pb:1Zn)I_3$ (according to DFT predictions) is synthesized and put in contact with the pure $MAPbI_3$ material, any photogenerated charge carriers produced in $MA(3Pb:1Zn)I_3$ would eventually relax down to the lower energy band edges of the $MAPbI_3$ material. Hence, the EQE curve would still show a band gap at 1.57 eV even though both materials are present. However, the presence of the high band gap phase would likely boost the EQE near the absorption edge. Therefore, it is possible that one explanation for the better performance of Pb:Co and Pb:Zn blends at higher wavelengths is that

two phases of perovskites are forming, one of pure $MAPbI_3$ and one that is a true mixed-metal with $Co^{2+}$ or $Zn^{2+}$ occupying some of the B-sites. In this scenario as the content of B′ is decreased, it might be more likely to replace $Pb^{2+}$ at the B-site rather than form a whole new phase, however if only $1/64^{th}$ or $1/32^{nd}$ of the atoms are replaced the regions around the substitution defect might behave like a pocket of $MA(3Pb{:}1B')I_3$ material surrounded by pure $MAPbI_3$.

This scenario also explains why the band gap shifts are obvious for Pb:Sn since the band gap narrows with increasing Sn content. Hence, the photogenerated carriers in a pure $MAPbI_3$ would relax down to the band edges of the $MA(3Pb{:}1Sn)I_3$ lattice and hence the EQE edge would shift accordingly. Thus, the shifting of a mixed-metal material to narrower band gaps would be obvious by a red-shift of the EQE edge, whereas the shifting of a the material to a wider band gap might be obscured.

It is also a possibility that the second metal species never replace the B-site for some of these materials and the EQE edge remains at the expected value for pure $MAPbI_3$ because the only semiconducting crystalline phase in the film is actually $MAPbI_3$ and the second species forms some insulating, benign region that does not contribute to photocurrent generation itself. Yet it could have a role in passivating defects in the crystal, which would allow charges to be more effectively collected throughout the film. One would expect EQE spectra to rise across the whole spectra, but the increase might be larger at short and long wavelengths close to the band edge. The reason is that high energy photons are absorbed closest to the illuminated surface. Hence in our device the photogenerated holes are quickly collected, but the corresponding electrons must traverse through the entire film before being collected at the other side. Likewise, long wavelengths are more likely to penetrate deeper into the perovskite and be absorbed closer to the electron transport layer. In this case, the photogenerated electrons are quickly collected, but the holes must traverse the full film thickness to reach its electrode. This also might explain why Co blends improves efficiencies at either end of the spectrum.

Conversely, if the additional phase is not benign but produces traps, it would cause the whole EQE spectra to drop uniformly, which would explain the behavior observed

at high Pb replacement levels. It is also possible EQE and photocurrent drops are a result of the grains becoming electrically isolated from either one another or the electrodes by insulating material phases or physical gaps, such as those observed form MA(3Pb:1Co)$I_3$ in Figure 6-4.

### 6.4.4 Control Devices

Two sets of control devices were fabricated to investigate how sensitive the device performance is to two other variables in the fabrication conditions: the concentration of the perovskite solution and the molar ratio of MAI:$Pb(OAc)_2$. These conditions are labeled as Pb:DMF and Pb:MAI mixtures in the same manner used for the mixed-metal compositions. These controls are intended to evaluate whether two possible events happen during the fabrication process of the mixed-metal perovskite compositions:

1. **Pb:DMF** is intended to evaluate how a device would perform if the $B'(OAc)_2$ and its corresponding MAI molecules do not become incorporated in the film. Although it is unlikely, one could imagine that the $B'(OAc)_2$ and any excess MAI might evaporate out of the film, should that compound be sufficiently volatile. Hence, the remaining film would be pure $MAPbI_3$ but would be thinned since a lower amount of Pb salt was included in the original perovskite solution. This situation is simulated by diluting the initial 0.8 M $Pb(OAc)_2$ and 2.4 M MAI solution with the appropriate amount of DMF.

2. **Pb:MAI** is intended to evaluate how a device would perform in the event that MAI is unsuccessful at detaching the acetate ions from the $B'^{2+}$ ions. In this situation, the molar ratio between MAI and $Pb(OAc)_2$ would become higher than 3:1. By intentionally changing this ratio, the impact of a stoichiometric mismatch between $MAPbI_3$ precursors on device performance was evaluated.

For each of these conditions several devices were fabricated and tested in the same manner as the devices with mixed-metal compositions. However, instead of using a

solution of 2.4 M MAI and 0.8M $B'(OAc)_2$ in DMF to replace part of the lead content, neat DMF was used for the Pb:DMF cases and 2.4 M MAI in DMF was used for the Pb:MAI cases. The photovoltaic performance statistics, champion $JV$ curves, and the EQE spectra for both of these control sets are shown in Figure 6-21. Likewise, the average and champion performance metrics for both of these controls are tabulated in Table 6.6 and 6.7, respectively.

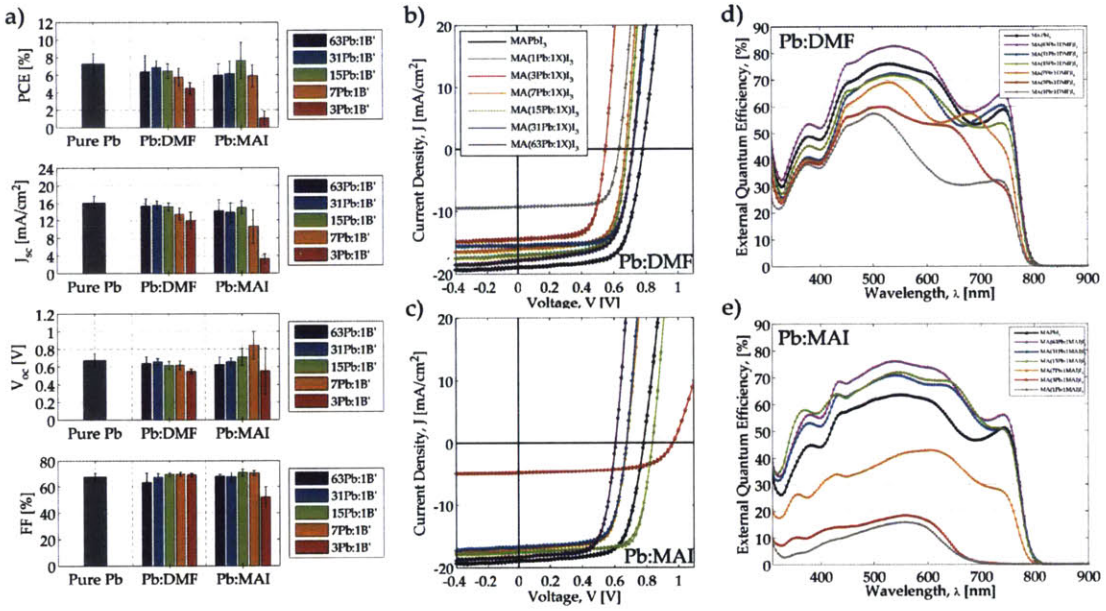


Figure 6-21: The photovoltaic performance of control devices where the $MAPbI_3$ material is diluted with DMF (Pb:DMF) or has an stoichiometric mismatch between the MAI and $Pb(OAc)_2$ precursor materials (Pb:MAI). (a) The compiled average performance metrics of planar mixed-metals for each composition. Error corresponds to the standard deviation. (b-c) Forward and reverse current-voltage ($JV$) characteristic scans measured from the best performing solar cell for each control set. (d-e) Typical external quantum efficiency measurements for each each solar cell control.

For each set of controls, the usual $MAPbI_3$ device performed better on average than any of the control conditions. This demonstrates that both the 3:1 MAI:$Pb(OAc)_2$ molar ratio and the concentration of the perovskite solution have been properly optimized to maximize photovoltaic power conversion efficiency for the pure Pb baseline devices. As expected, the Pb:DMF devices supply lower currents as the perovskite solution becomes increasingly dilute since thinner perovskite films are formed on the

Table 6.6: The compiled average performance metrics for each solar cell control. Error corresponds to the standard deviation.

| Material | Mean Short-Circuit Current Density, $J_{sc}$ [mA/cm$^2$] 63Pb:1B′ | 31Pb:1B′ | 15Pb:1B′ | 7Pb:1B′ | 3Pb:1B′ |
|---|---|---|---|---|---|
| Pb Only | | | 16.02 ± 1.62 | | |
| Pb:DMF | 15.31 ± 1.64 | 15.50 ± 1.04 | 15.10 ± 0.98 | 13.37 ± 1.38 | 11.95 ± 1.87 |
| Pb:MAI | 14.06 ± 2.69 | 13.72 ± 2.31 | 14.92 ± 1.56 | 10.53 ± 3.80 | 3.24 ± 1.11 |

| Material | Mean Open-Circuit Voltage, $V_{oc}$ [V] 63Pb:1B′ | 31Pb:1B′ | 15Pb:1B′ | 7Pb:1B′ | 3Pb:1B′ |
|---|---|---|---|---|---|
| Pb Only | | | 0.67 ± 0.07 | | |
| Pb:DMF | 0.63 ± 0.08 | 0.65 ± 0.04 | 0.62 ± 0.04 | 0.62 ± 0.05 | 0.54 ± 0.03 |
| Pb:MAI | 0.62 ± 0.08 | 0.65 ± 0.04 | 0.71 ± 0.10 | 0.84 ± 0.15 | 0.55 ± 0.26 |

| Material | Mean Fill Factor, FF [%] 63Pb:1B′ | 31Pb:1B′ | 15Pb:1B′ | 7Pb:1B′ | 3Pb:1B′ |
|---|---|---|---|---|---|
| Pb Only | | | 67.53 ± 2.54 | | |
| Pb:DMF | 63.17 ± 7.32 | 67.02 ± 2.99 | 69.11 ± 1.42 | 69.31 ± 1.48 | 68.76 ± 1.41 |
| Pb:MAI | 67.72 ± 1.62 | 67.51 ± 3.68 | 70.68 ± 2.79 | 70.35 ± 2.17 | 51.87 ± 7.90 |

| Material | Mean Power Conversion Efficiency, PCE [%] 63Pb:1B′ | 31Pb:1B′ | 15Pb:1B′ | 7Pb:1B′ | 3Pb:1B′ |
|---|---|---|---|---|---|
| Pb Only | | | 7.27 ± 1.18 | | |
| Pb:DMF | 6.33 ± 1.90 | 6.82 ± 0.81 | 6.45 ± 0.84 | 5.74 ± 1.01 | 4.46 ± 0.67 |
| Pb:MAI | 5.93 ± 1.35 | 6.14 ± 1.43 | 7.63 ± 2.07 | 5.87 ± 1.27 | 1.05 ± 0.80 |

substrate. Thinner films also produce slightly higher fill factors since charge carriers generated in the bulk of the film have a shorter distance to travel to the electrodes and have less grain boundaries to pass through, which results in lower series resistances. The Pb:MAI cases are more interesting because they display similar trends to those observed in the mixed-metal compositions - the voltage generally increases with higher levels of replacement until the 3Pb:1MAI condition, while the current sees a precipitous drop after 7Pb:1MAI. The main difference between this set and the mixed-metal compositions is that the average performance does not improve above the baseline efficiency. However, the 15Pb:1MAI case did once produce an 11% efficient solar cell, which outperforms the champion baseline $MAPbI_3$ device. This finding does suggest that the performance of the solar cell is very sensitive to the stoichiometric ratio of the MAI to acetate precursor materials, which is often difficult to precisely control since both the acetate salts and MAI materials are hygroscopic and the actual water content in the salts when massed is not known. Subsequent

Table 6.7: The best measured performance metric for each solar cell control. $J_{sc}$, $V_{oc}$, and FF do not necessarily correspond to the device with the champion PCE.

| | Best Short-Circuit Current Density, $J_{sc}$ [mA/cm$^2$] | | | | |
|---|---|---|---|---|---|
| Material | 63Pb:1B′ | 31Pb:1B′ | 15Pb:1B′ | 7Pb:1B′ | 3Pb:1B′ |
| Pb Only | | | 18.97 | | |
| DMF | 18.24 | 17.45 | 17.21 | 16.03 | 14.49 |
| MAI | 18.58 | 16.77 | 17.53 | 17.17 | 4.93 |

| | Best Open-Circuit Voltage, $V_{oc}$ [V] | | | | |
|---|---|---|---|---|---|
| Material | 63Pb:1B′ | 31Pb:1B′ | 15Pb:1B′ | 7Pb:1B′ | 3Pb:1B′ |
| Pb Only | | | 0.82 | | |
| DMF | 0.72 | 0.72 | 0.69 | 0.67 | 0.59 |
| MAI | 0.81 | 0.70 | 0.85 | 0.96 | 0.97 |

| | Best Fill Factor FF [%] | | | | |
|---|---|---|---|---|---|
| Material | 63Pb:1B′ | 31Pb:1B′ | 15Pb:1B′ | 7Pb:1B′ | 3Pb:1B′ |
| Pb Only | | | 72.14 | | |
| DMF | 71.45 | 72.41 | 71.85 | 71.59 | 70.94 |
| MAI | 70.30 | 71.58 | 75.17 | 73.47 | 62.75 |

| | Best Power Conversion Efficiency, PCE [%] | | | | |
|---|---|---|---|---|---|
| Material | 63Pb:1B′ | 31Pb:1B′ | 15Pb:1B′ | 7Pb:1B′ | 3Pb:1B′ |
| Pb Only | | | 10.27 | | |
| DMF | 8.62 | 8.12 | 8.20 | 7.62 | 5.61 |
| MAI | 7.76 | 7.98 | 11.00 | 8.23 | 2.90 |

attempts failed to reproduce this 11% performance in four different device batches.

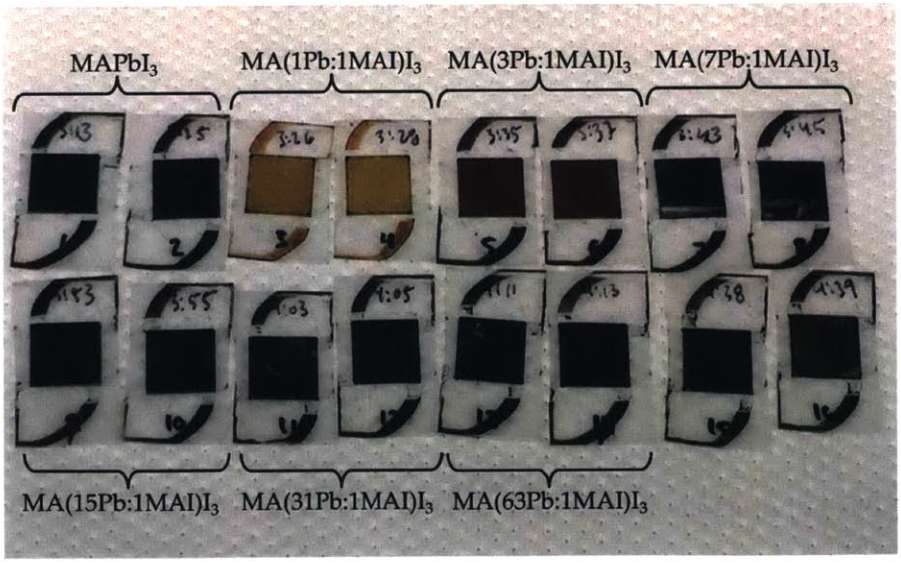


Figure 6-22: The color of the pure Pb perovskite film changes when a significant excess of MAI is added to the precursor solution used to synthesize the active layers of the solar cell.

The other interesting feature of the Pb:MAI control batches is that the color of the film changed from the usual dark brown color to red for 3Pb:1MAI and yellow for 1Pb:1MAI samples as is seen in Figure 6-22. This result is consistent with the EQE trends shown in Figure 6-21e where the MA(1Pb:1MAI)$I_3$ and MA(3Pb:1MAI)$I_3$ compositions produce substantially less current with low energy photons. Although absorption is not efficient between 650 and 800 nm, there is a long absorption tail in this region, which suggests that it might still be the $MAPbI_3$ material but have a number of trap states in the band gap that are detrimental to performance. Alternatively, the excess of MAI might also induce an increased amount of disorder that prevents the material from fully crystallizing. In contrast, Figure 6-21d shows that the Pb:DMF control series maintained the same EQE edge near 800 nm but the efficiency at low photon energies was reduced for thinner samples. This can be explained simply by the fact that thinner films are not able to fully capture these photons and some red and infrared light passes through the films without being absorbed.

## 6.5 High-Performing Mixed-Metal Perovskite Compositions with Reduced Toxicity

The champion current-voltage characteristics presented in Figure 6-18 demonstrate that there are several high-performing devices made from mixed-metal compositions with a high level of lead replacement. The performance parameters for the champion solar cells from each metal fraction is summarized in Table 6.8.

There are two non-toxic metal species that are capable of replacing 25% of the Pb content and achieve high power conversion efficiencies. Specifically, a PCE of 9.3% and 8.3% was measured for champion MA(3Pb:1Sn)$I_3$ and MA(3Pb:1Cu)$I_3$ devices, respectively. Several previous studies have demonstrated that $Sn^{2+}$ can homogeneously replace $Pb^{2+}$ at the B-site of the perovskite lattice, as is evidenced by gradual changes in the lattice parameters and band gap of the mixed material with increasing Sn content. [129, 132, 150] However to our knowledge, the 9.3% MA(3Pb:1Sn)$I_3$3 device is

Table 6.8: Summary of champion solar cells for various levels of Pb replacement by a second metal species

| B′ [%] | Pb [%] | B′ | Device Designation | $J_{sc}$ [mA/cm$^2$] | $V_{oc}$ [V] | FF [%] | PCE [%] |
|---|---|---|---|---|---|---|---|
| 50.00 | 50.00 | Cu | MA(1Pb:1Cu)$I_3$ | 11.3 | 0.70 | 47.5 | 3.4 |
| 50.00 | 50.00 | Sn | MA(1Pb:1Sn)$I_3$ | 8.9 | 0.62 | 39.3 | 2.2 |
| 25.00 | 75.00 | Sn | MA(3Pb:1Sn)$I_3$ | 18.3 | 0.73 | 69.5 | 9.3 |
| 12.50 | 87.50 | Zn | MA(7Pb:1Zn)$I_3$ | 16.6 | 0.82 | 73.1 | 9.9 |
| 6.25 | 93.75 | Co | MA(15Pb:1Co)$I_3$ | 16.9 | 0.86 | 70.3 | 10.2 |
| 3.13 | 96.87 | Co | MA(31Pb:1Co)$I_3$ | 19.1 | 0.83 | 70.0 | 11.1 |
| 1.56 | 98.44 | Co | MA(63Pb:1Co)$I_3$ | 19.0 | 0.84 | 71.5 | 11.4 |
| 0 | 100.00 | - | $MAPbI_3$ | 19.0 | 0.78 | 69.2 | 10.3 |

the highest reported mixed-metal device where 25% of the metal content is composed of tin. In order to further assess the ability of Sn and Cu to replace Pb content, MA(1Pb:B′)$I_3$ devices with 50% Pb replacement were synthesized. The results for the best devices from each set are shown in Table 6.8, although neither of these have surpassed a 4.2% record MA(1Pb:1Sn)$I_3$ device produced by Ogomi *et al.* [129]

### 6.5.1 MA(Pb:Sn)$I_3$ Mixtures

The only mixed-metal system that has been previously characterized in detail uses Sn as the secondary metal species. Therefore, it is prudent to compare the results of our mixed Pb:Sn system with previous findings, especially as this is the first report of using acetate precursors to generate mixed-metal perovskites. The most notable feature of this system is that the band gap of the perovskite material narrows with increasing Sn content. As shown by the Tauc plots for our Pb:Sn devices in Figure 6-20g, the EQE edge is nearly identical to that of pure Pb for samples with low levels of Sn. However, the edge noticeably red-shifts from 1.56 eV to 1.41 eV once the Sn content reaches 1/8$^{th}$ Pb replacement in the MA(7Pb:1Sn)$I_3$ device. As the Sn content increases to 3Pb:1Sn and 1Pb:1Sn molar ratios, the EQE edge continues to red-shift to 1.31 eV and 1.24 eV, respectively. As presented in Table 6.9, these values are nearly identical to the band gaps previously reported for mixed Pb:Sn films. [129] This suggest that the $Sn^{2+}$ ions are indeed replacing $Pb^{2+}$ at the B-site

of the perovskite lattice even when the acetate precursors are utilized.

Table 6.9: Comparison of measured and published band gaps for mixed-metal MA(Pb:Sn)$I_3$ perovskites

| Material | Band Gap, $E_g$ [eV] DFT | EQE Edge | Ref[a] | Experimental % Difference |
|---|---|---|---|---|
| $MAPbI_3$ | 1.67 | 1.56 | 1.57 | 0.6% |
| MA(3Pb:1Sn)$I_3$ | 1.34 | 1.31 | 1.31 | 0.0% |
| MA(1Pb:1Sn)$I_3$ | 1.06 | 1.24 | 1.28 | 3.1% |

[a]Experimental band gaps referenced here are the values reported by Ogomi *et al* in reference [129].

The fact that the band gap gradually transitions with increasing content and that the observed trend matches the DFT predictions, strongly suggests that B-site substitution is occuring for the 7Pb:1Sn and 3Pb:1Sn blends, rather than perovskite phase separation where both pure $MAPbI_3$ and $MASnI_3$ exists side-by-side in the film. In such a situation, one would expect the EQE edge to jump straight to 1.2 eV, the observed value for pure $MASnI_3$. It must be noted however, that it is unclear whether the MA(1Pb:1Sn)$I_3$ is mixed or phase separated since the band gap predicted by DFT in Section 5.5.1 for this case is nearly indistinguishable from the value for $MASnI_3$.

### 6.5.2 MA(Pb:Cu)$I_3$ Mixtures

The identification of Cu as a possible replacement for Pb is a new finding and merits some attention. Although a champion value of 8.3% was obtained for MA(3Pb:1Cu)$I_3$ devices, only one batch of devices was able to attain this level of performance and these devices only achieved high performance during the first current-voltage characteristic measurement. When a second measurement was performed after another five minutes of light soaking, the *JV* curve was unstable as the measured photocurrent was often discontinuous during the reverse voltage sweep from the forward bias towards short-circuit conditions. To explore the possible origins of this strange behavior a set of *JV* sweeps was performed after the solar cell was held at forward bias in the open-circuit configuration for various periods of time. Doing so allows mobile ions and charges to

migrate to a new configuration that might either promote performance or damage it. These tests revealed several interesting observations:

1. The 8.3% solar cell was able to recover from its erratic encore performance after several hours of resting and operate with well-behaved $JV$ curves. However the performance was reduced from 8.3% to 4.3%.

2. As the devices are held at forward bias for longer periods of time, the hysteresis between the forward and reverse sweeps grows until the reverse sweep becomes erratic.

It is unclear exactly why substituting $Cu^{2+}$ produces this behavior, however we speculate it is related to the fact that copper is the only ion out of those investigated that is more stable in a monovalent form. It is possible that sometimes the initial mixed-metal perovskite contains $Cu^{2+}$ ions at the B-site, however during device operation, photogenerated electrons or mobile iodide ions might reduce the $Cu^{2+}$ species to $Cu^{+}$, which would locally disrupt the perovskite crystal and create a set of newly formed mobile ions that would account for the erratic $JV$ behavior. The $Cu^{+}$ ions would then be unable to replace the B-site cation in the perovskite lattice and would form a second phase of CuI in the perovskite film, allowing the device to operate again. It has been reported that CuI is an efficient hole transport material for perovskite devices, [170] and it is possible that it might initially benefit device performance by providing a pathway for hole-transport from the bulk of the lattice. However, CuI can also act as a shunt if it directly contacts the fullerene layer, which would explain why the shunt resistance is noticeably lower for the $JV$ curves of the Pb:Cu blends in Figure 6-18b. A second material phase is clearly observable in the 1Pb:1Cu SEM image presented in Figure 6-5. Furthermore, the XRD spectra for 3Pb:1Cu and 7Pb:1Cu films (Figure 6-2b) display an additional peak at $2\theta = 25.2°$, which is consistent with the (111) planes of CuI. The $JV$ curves for the Pb:Cu devices are also the only ones to demonstrate deviation from diode behavior near reverse bias conditions. This suggests that these films have some intrinsic ferroelectric behavior.

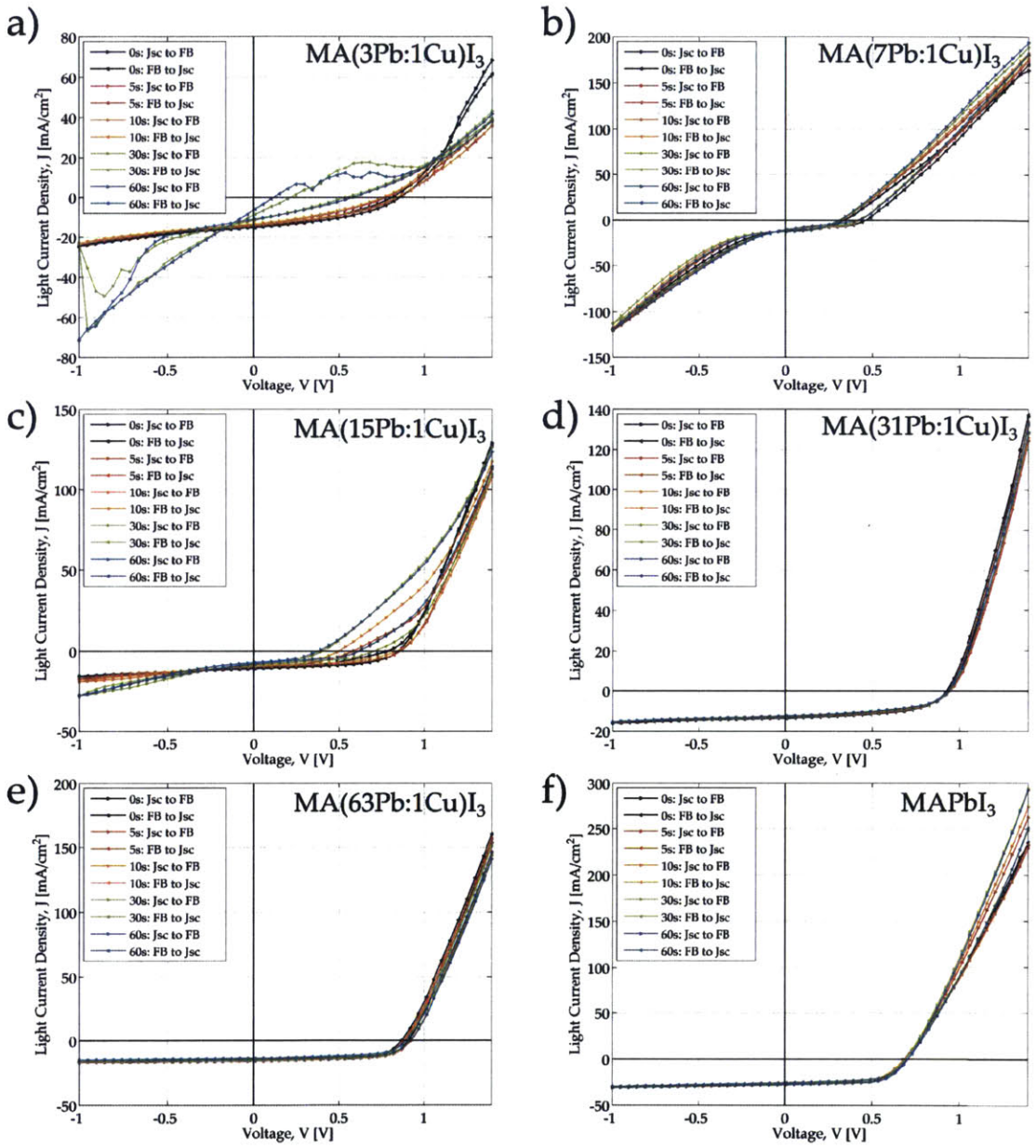


Figure 6-23: The effect of holding each composition of mixed-metal MA(Pb:Cu)$I_3$ solar cells at forward bias (1.4 V) between 0 and 60 s prior to $JV$ curve measurement.

Figure 6-23 presents the results of a study where the MA(Pb:Cu)$I_3$ devices, including the exact device that achieved the 8.3% performance, were first held at forward bias ($V_{bias}$ = 1.4 V) for 0 to 60 seconds prior to measuring the $JV$ curves. For short hold times, the MA(3Pb:1Cu)$I_3$ had minimal hysteresis. However, as the hold times lengthen, the hysteresis between forward and reverse scans increases until eventually the reverse scan completely destabilizes and the $JV$ curve becomes erratic. The devices with lower Cu content demonstrate an increase in hysteresis with increasing hold times, but this instability is not observed. Rather, the MA(7Pb:1Cu)$I_3$ sweeps in Figure 6-23 show substantial deviation from diode behavior near reverse bias, which suggest that the material is somewhat ferroelectric and is able to switch its polarization with applied bias. The only reason the device is not completely poling is that the device structure is asymmetric and charges are unable to be efficiently collected from the device when the applied bias switches polarity. This behavior is also witnessed to a lesser degree in MA(15Pb:1Cu)$I_3$. For devices with even lower Cu content, the $JV$ curves become well-behaved and very little hysteresis or anomalous behavior is observed regardless of bias time.

When the behavior of a device changes substantially with initial biased hold times, some charged particles are responding to the applied electric field through the device and are migrating into a new configuration. Since this behavior is exacerbated with increasing Cu content, it is reasonable to conclude that the Cu content is indeed reponsible for the behavior. It is likely that films with higher Cu content contain more mobile ions or charge carriers that are able to slosh around in response to the electric field and create substantial hysteresis that generate unfavorable conditions for device performance.

## 6.6 Mechanisms for Performance Improvement

By performing both computational and experimental screening studies that evaluate both the theoretical and empirical properties of mixed-metal perovskite films, it is evident that this set of materials is incredibly rich and is displaying many interesting

behaviors that are of both scientific and practical interest. The device performance results clearly reveal that the $MAPbI_3$ is remarkably tolerant to the introduction of many metal species and in several cases the addition of the second metal species has statistically improved device performance over the pure Pb control devices for this particular architecture of perovskite solar cells. The task at hand now is to further investigate the mixed-metal perovskite films in an effort to understand how these secondary species improve performance.

### 6.6.1 Approach

The central challenge is that each of the 45 mixed-metal embodiments studied could be displaying different behavior and analyzing each individually would require substantial time and resources. Since this study is intended to screen through the 45 conditions to identify the situation that maximizes device performance, the embodiment that exhibited the best average performance was chosen for detailed investigation: $MA(31Pb{:}1Co)I_3$. Although there is no guarantee that the mechanism by which $Co^{2+}$ improves performance at this metal fraction is the same as that of other metals, it might be representative of other transition metals and at the very least provide some clues that could allow mixed-metal devices to display even higher performance metrics.

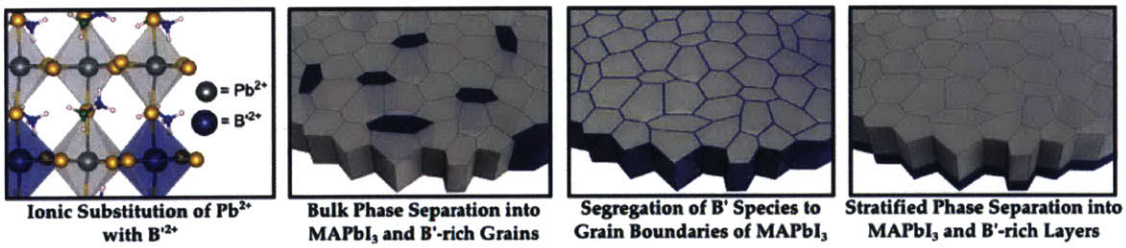


Figure 6-24: There are several possible physical places that the secondary metal species could exist within each mixed-metal perovskite embodiment. a) The $B'^{2+}$ ions could be replacing the $Pb^{2+}$ ions at the B-site of the crystal lattice. b) The B′ species could be forming a separate crystalline or amorphous phase that is homogeneously distributed throughout the film. c) The B′ could be excluded from pure Pb perovskite grains and sit at the grain boundaries. d) The B′ species could be stratifying and preferentially forming a secondary phase at an interface with either the hole or electron transport layer.

The approach taken here is to perform specialized measurements on the mixed-metal MA(31Pb:1Co)$I_3$ material in order to provide additional information that could shed light on the underlying reason why this composition produces the best solar cells with the established fabrication procedure. The main pieces of information that are missing from the previous analyses are:

1. The location of the Co atoms in the perovskite film.
2. How replacing Pb with Co influences the energy of the band edges and Fermi level in the perovskite materials.

As illustrated by Figure 6-24, there are a number of possible options for where the Co atoms could be within the film and establishing their location is paramount to crafting an explanation that correctly interprets the previous device performance and materials characterization data. Likewise, understanding how Co changes the energetics of the perovskite material with respect to the other materials in the inverted architectures could provide important clues about the photovoltaic performance trends.

### 6.6.2 Elemental Identification

Two methods were used to identify the elements present in some of the mixed-metal perovskite films: x-ray photoelectron spectroscopy (XPS) and energy-dispersive x-ray spectroscopy (EDX). XPS measurements were performed on films of MA(31Pb:1Co)$I_3$ and MA(31Pb:1Mg)$I_3$ and in each case Co or Mg was identified in significant quantities in the film. This result confirms that the secondary metal species remains in the perovskite film and do not evaporate out of the film.

Now that the presence of Co has been established, the next step is to determine where the Co atoms are located within the mixed-metal MA(31Pb:1Co)$I_3$ film. To do so, a TEM cross-section was milled from the film with a focused ion beam to allow high-resolution imaging and elemental mapping to be performed over the film cross-section. High-resolution transmission electron microscopy of the cross-section in Figure 6-25a shows both the PEDOT:PSS layer and the perovskite film. Figure 6-25b presents a high-magnification image of the perovskite materials which shows that

allows the material is indeed crystalline, there are local regions where the crystallinity is disrupted and the region is amorphous.

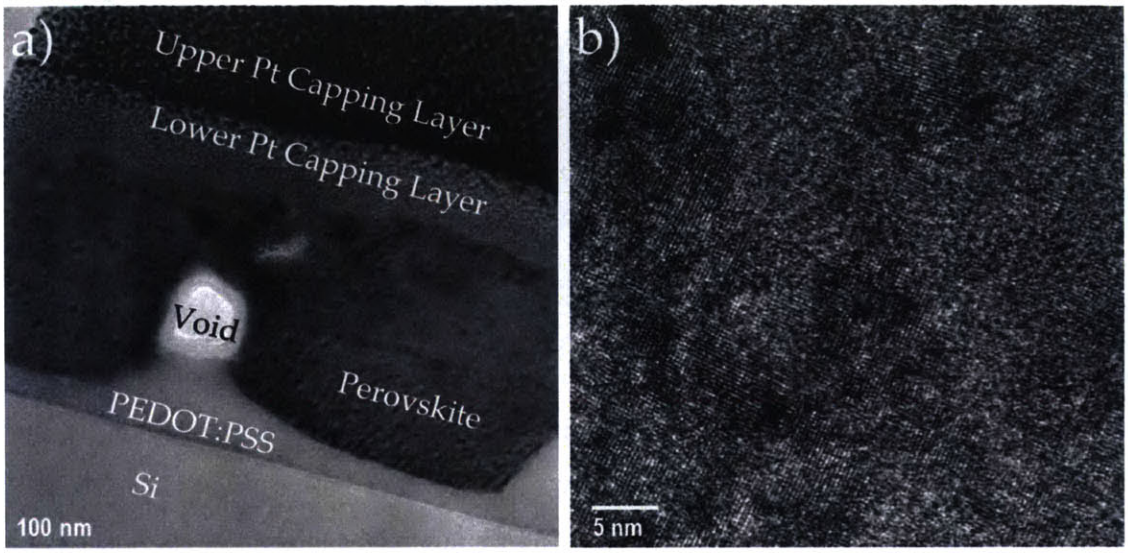


Figure 6-25: a) Low magnification of the film cross-section and b) high-resolution image of the perovskite material for MA(31Pb:1Co)$I_3$.

Elemental mapping was performed on the cross-section shown in Figure 6-26a using energy-dispersive x-ray spectroscopy (EDX) to generate the maps of I, Co, and Pb shown in parts b-d. It is clear from these images that Pb and I are evenly distributed throughout the perovskite layer, although some local variation does exist that suggest that the Pb and I content can vary slightly from grain to grain. In contrast, the Co atoms are dispersed throughout the film but their distribution is not homogeneous. Rather the Co atoms appear to outline regions that are populated by Pb and I, which suggests that the Co atoms are mostly exluded from the perovskite crystal lattice and are relegated to the grain boundaries. The composite image shown in Figure 6-26e helps to identify the different strata of the device cross-section. The EDX energy spectra in Figure 6-26f confirms that Co is indeed present in sufficient quantity to generate a peak above the background noise. By integrating the number of counts of each element over the entire map, an estimate of the relative amounts of each element in the sample can be compared against one another. It is encouraging that Co comprises 3.6% of the total metal content (*i.e.* (Co at.%)/((Co at.%)+(Pb

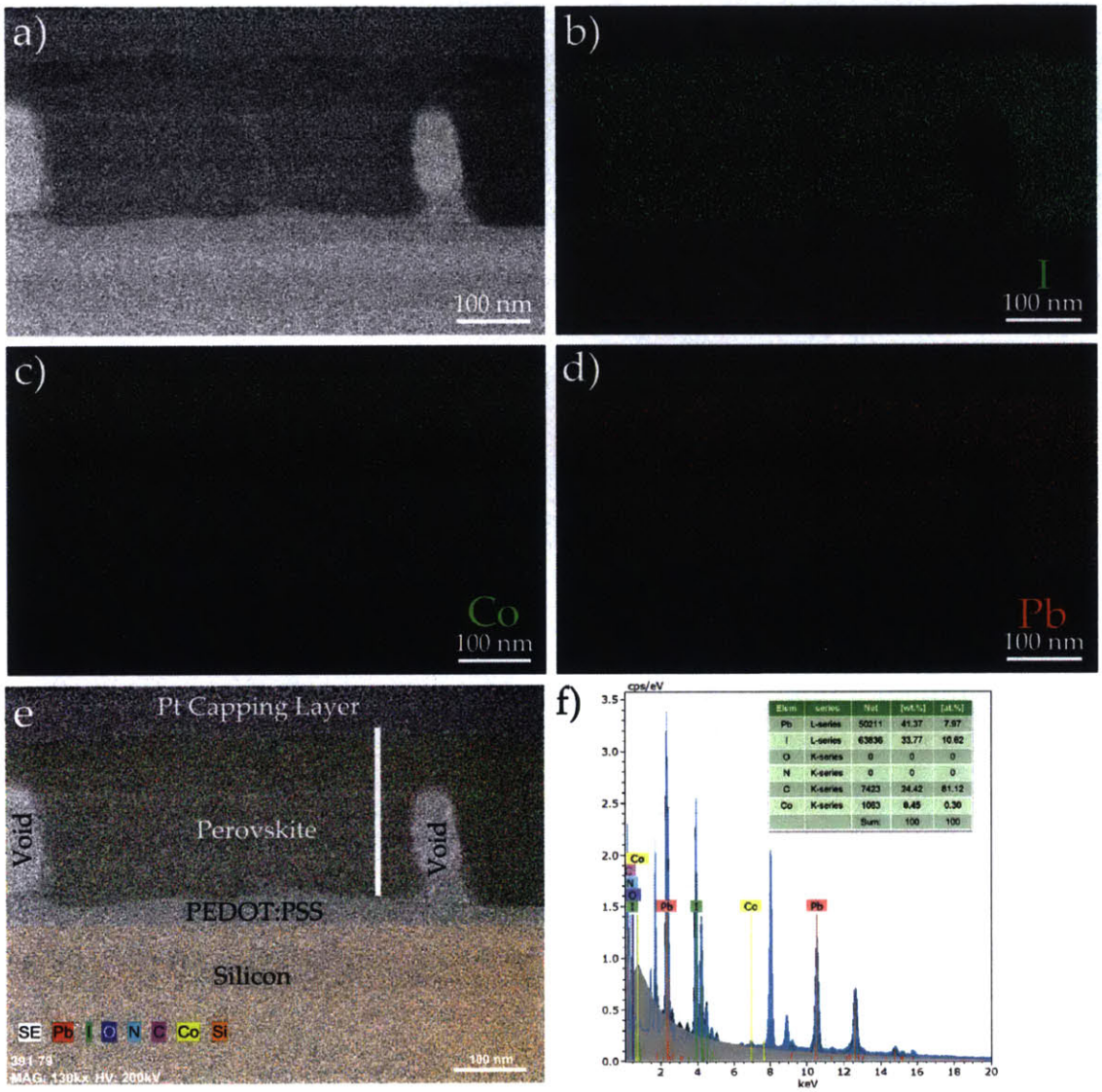


Figure 6-26: a) STEM image of film with elemental mapping of b) I; c) Co; d) Pb; e) Composite image, and f) EDX spectrum

at.%)) = 0.036), which is very close to the expected value of 3.1% based on the stoichiometry of the original acetate-based precursor solution.

### 6.6.3 Band Alignment

Ultraviolet photoelectron spectroscopy (UPS) measurements were performed on PEDOT:PSS, PCBM, and the set of MA(Pb:Co)$I_3$ perovskite compositions in order to establish how the Fermi level and band edge locations shift as a function of Pb:Co mole ratio. These measurements provide the flat band energy levels with respect to vacuum. The CBE is determined by using the measured optical band gap values, which was determined from the Tauc plots of the EQE spectra (Figure 6-20) to be 1.57 eV for all of the perovskite materials in this series. The band gap of PEDOT:PSS and PCBM are taken to be 1.6 eV [171] and 2.35 eV [172], respectively, based on previously reported values. The flat band energies relative to the Fermi level and vacuum level are plotted in Figure 6-27 and tabulated in Table 6.10.

Table 6.10: Experimentally determined flat band energy levels for the solar materials in inverted photovoltaic devices with MA(Pb:Co)$I_3$ active layer compositions.

| Material | Workfunction[a] [eV] | VBE[b] [eV] | CBE [eV] | Band Gap[c] [eV] |
|---|---|---|---|---|
| PEDOT:PSS | 4.76 | 3.54 | 5.14 | 1.60 |
| PCBM | 3.67 | 3.48 | 5.83 | 2.35 |
| $MAPbI_3$ | 5.18 | 4.63 | 6.20 | 1.57 |
| MA(63Pb:1Co)$I_3$ | 4.95 | 4.46 | 6.03 | 1.57 |
| MA(31Pb:1Co)$I_3$ | 4.63 | 4.32 | 5.89 | 1.57 |
| MA(15Pb:1Co)$I_3$ | 4.55 | 4.17 | 5.74 | 1.57 |
| MA(7Pb:1Co)$I_3$ | 4.75 | 4.24 | 5.81 | 1.57 |
| MA(3Pb:1Co)$I_3$ | 4.35 | 4.60 | 6.17 | 1.57 |

[a] As measured with UPS
[b] As measured with UPS
[c] As measured from the EQE edges in the Tauc plots shown in Figure 6-20. Except for PEDOT:PSS and PCBM which are values reported in Reference [171] and [172]

These measurements indicate that replacing some of the Pb content with Co does influence the energy level locations even though the band gap of the perovskite film is the same regardless of Co content. As the Co content is increased from 63Pb:1Co to 15Pb:1Co, all of the energy levels monotonically shift upwards. At 7Pb:1Co, the

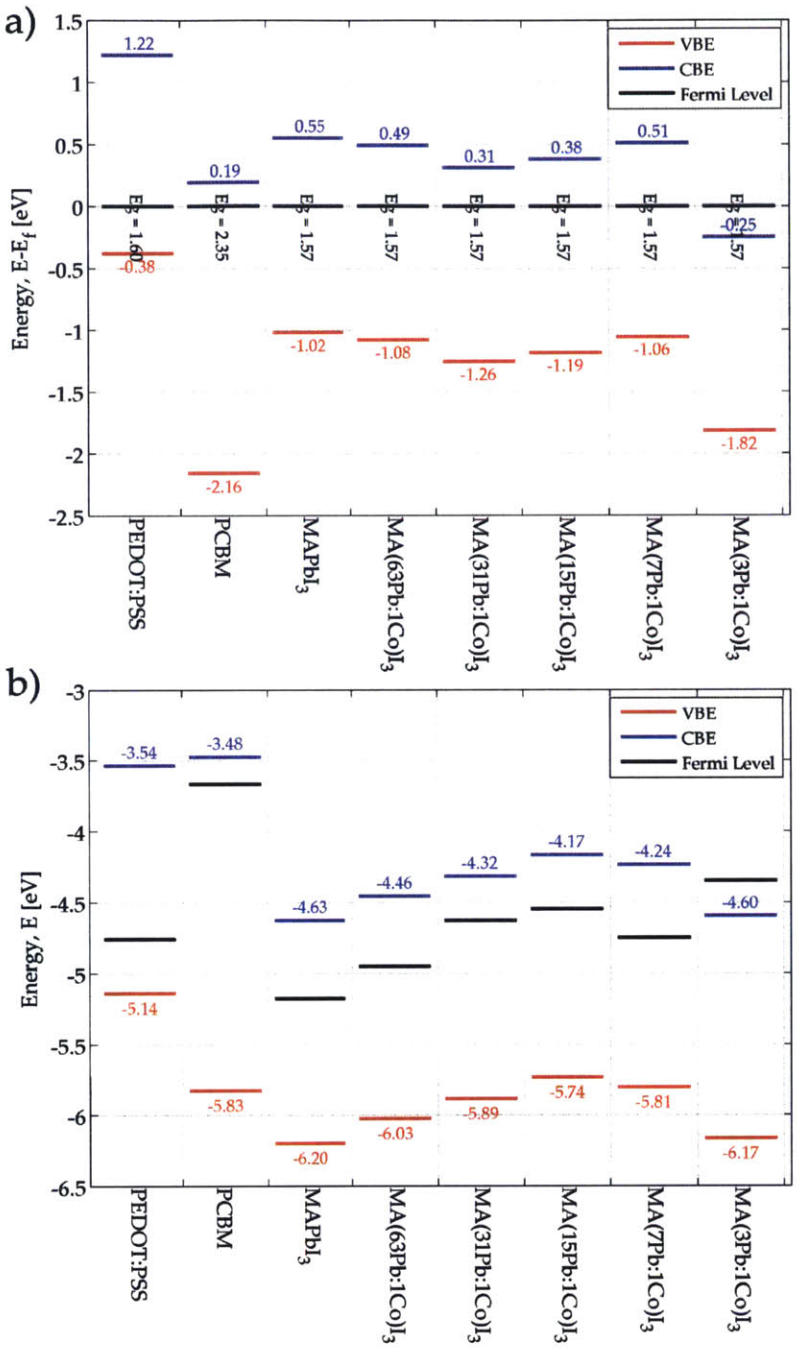


Figure 6-27: The flat band diagrams are constructed for the relevant solar materials in the inverted solar cells fabricated for this experimental screening study: PEDOT:PSS (hole transporter), PCBM (electron transporter), and the MA(Pb:Co)$I_3$ mixed-metal perovskite compositions. The experimentally determined band edges with respect to the (a) Fermi level and (b) vacuum level.

trends is reversed and the VBE position for 3Pb:1Co is identical to $MAPbI_3$, however both the CBE and Fermi level have remained at higher energies. For the 3Pb:1Co composition, if the band gap is still 1.57 eV, then the Fermi level has crossed into the conduction band and the material is supposed to be theoretically metallic. This is in conflict with the observation that solar cells do operate for this perovskite composition and is not fully resolved.

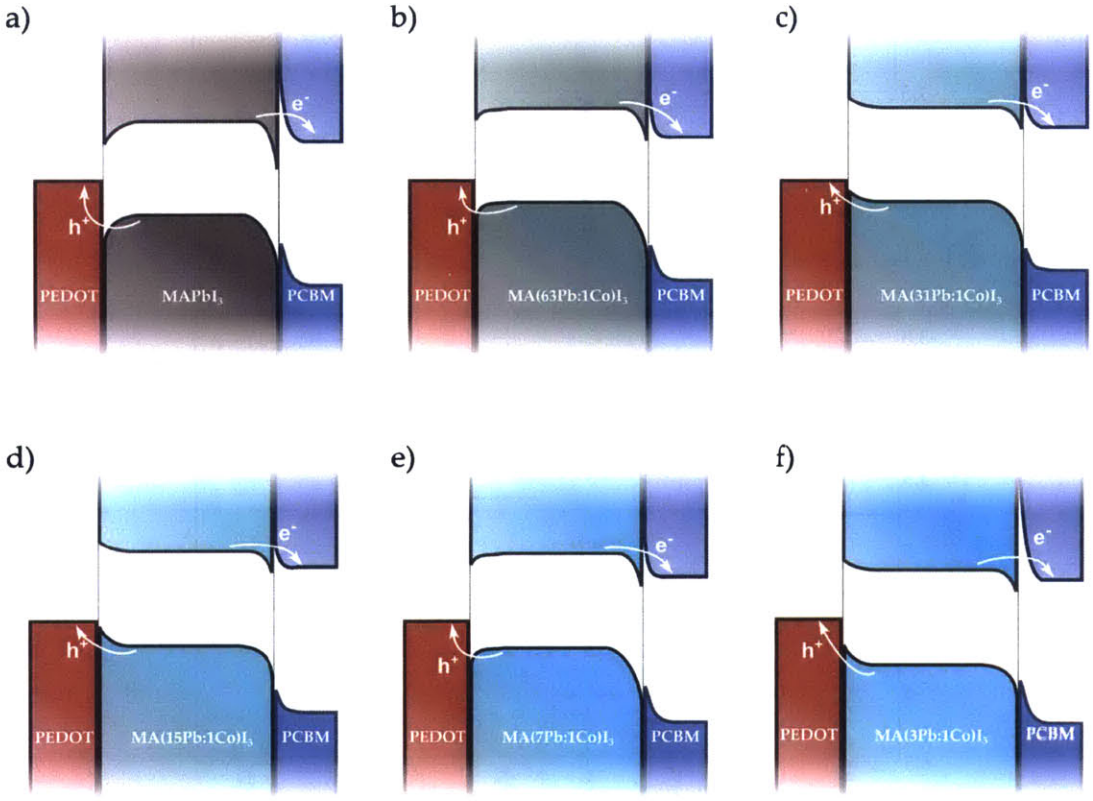


Figure 6-28: The expected band bending behavior for each mixed-metal $MA(Pb:Co)I_3$ perovskite solar cell is drawn schematically. a) The pure $MAPbI_3$ case experiences a barrier at both the PEDOT and PCBM interfaces that must be overcome by thermionic emission or tunneling. b-d) As the Co content increases, the band alignment becomes more favorable and these barriers become smaller and thinner, which is expected to increase both the current and the voltage in the system. e-f) Films with higher Co content begin to experience shifts back towards less favorable band alignments.

To better understand how these shifts in band edges might influence actual device behavior, a band diagram was constructed for each Pb:Co perovskite composition in thermal equilibrium with PEDOT:PSS and PCBM. The $MAPbI_3$ case, shown in Figure 6-28 forms a barrier at both heterojunctions that must either be tunneled though or overcome by thermionic emission. As the content of Co increases, the band alignment is increasingly favorable and the barrier height at both interfaces is reduced. This will allow the holes and electrons to more easily transport across the interfaces into their respective selective contacts, which is expected to produce an increase in the photocurrent. Once the cobalt content reaches a 31Pb:1Co mole ratio, the Fermi level of the perovskite rises above that of PEDOT:PSS, thereby causing the barrier for holes to disappear completely. The band alignment becomes the most favorable at 15Pb:1Co, after which the VBE begins to return to the value for pure Pb.

Although this finding is encouraging, further investigation is required to more rigorously capture the influence of surface dipoles on band bending at the material interfaces through performing additional UPS measurements on thin layers of material stacks or Kelvin Probe-AFM measurements along film cross-sections.

### 6.6.4 Proposed Explanations

In order to explain the observed enhancement of $MA(Pb:Co)I_3$ films, a few potential mechanisms are proposed that attempt to piece together the collected information in ways that explains most of the observed trends. Before doing so, here is a summary of what we know about the Pb:Co mixtures:

1. DFT calculations presented in Section 5.5 predicted that the band gap would widen from 1.67 eV for $MAPbI_3$ to 1.77eV for $MA(3Pb:1Co)I_3$. However, no band gap shifts were observed from either the photoluminescence emission spectra or the EQE edge measurements.

2. The only change in the XRD spectra is that $PbI_2$ peak is present for $MA(31Pb:1Co)I_3$ and samples with lower Co content. Otherwise, each $MA(Pb:Co)I_3$ spectrum

matches that of pure $MAPbI_3$. DFT simulations from Section 5.4.5 suggest that little difference would be observed even in the event of B-site substition of $Pb^{2+}$ with $Co^{2+}$.

3. SEM images reveal film morphology does not substantially change from $MAPbI_3$ with increasing Co content until the $MA(3Pb{:}1Co)I_3$.

4. There is an inverse correlation between PL lifetime and performance. The highest performing devices have the shortest PL lifetimes.

5. The $J_{sc}$ increases initially from $MAPbI_3$ to $MA(63Pb{:}1Co)I_3$, which is followed thereafter by subsequent reductions with increasing Co content.

6. The $V_{oc}$ steadily increases from $MAPbI_3$ to $MA(7Pb{:}1Co)I_3$ with increasing Co content.

7. UPS measurements demonstrate that the band edges and Fermi levels shift closer to the vacuum level with increasing Co from $MAPbI_3$ to $MA(15Pb{:}1Co)I_3$.

The following proposed improvement mechanisms attempt to fit together these clues in order to speculate what is happening inside these Pb:Co mixed composition films.

### Mechanism 1: Competing Effects of Cobalt-Induced Band Shifts and Trap Density Increases

The previous section demonstrates that the band edges of the mixed-metal perovskite film become more favorably aligned with both the electron and hole transport layers with increasing Co content until a composition of $MA(15Pb{:}1Co)I_3$ is reached. In this situation, the photocurrent is expected to increase continuously as more Co content is included in the device until the 15Pb:1Co composition is achieved. The experimental trends shown in Figure 6-16 reveal that the short circuit-current density sees an initial increase with the 63Pb:1Co composition, but gradually and monotonically drops with increasing Co content. Therefore, although the UPS results can explain why we see

some improvement, it is insufficient to fully explain this observed behavior. This suggests that there is at least one other mechanism that is competing against the band alignment improvements to decrease photocurrent. One possible explanation is simply that the the Co ions act as recombination centers that are able to capture charge carriers, which will siphon away current by promoting non-radiative recombination. The EDX elemental mapping (Figure 6-26) reveals that the Co atoms are located fairly evenly throughout the perovskite film and are not localized near a particular material interface. Hence, it is possible that the introduction of Co will promote better band alignment that initially increases current and photovoltage, however the same Co atoms also act as trap sites, which diminish this current increase. In other words, adding Co will decrease the current loss that occurs at the interface between the perovskite and PEDOT:PSS and PCBM, however it will increase the amount of current that is lost in the bulk. This concept is illustrated in Figure 6-29. Initially the collection efficiency increase across the interface outweighs the decrease in transport efficiency in the bulk and the collected current is higher than the baseline $MAPbI_3$ sample. However as more Co is added, the interface becomes more efficient, but the bulk becomes less so. The net result is to slowly diminish the initial photocurrent improvement until eventually enough Co atoms are present to overcome any benefit produced by favorable band edge alignment and the measured current density becomes lower than that generated by $MAPbI_3$.

This could also explain why the measured PL lifetime initially reduces upon introducing Co into the film (Figure 6-15); although more photocurrent is extracted from the perovskite film, there are more trap sites available in the bulk to promote non-radiative recombination before the charges even reach the interface. Since the PL samples were deposited on glass without either PCBM or PEDOT:PSS, any benefits at the interface are not observed and the lifetimes become shorter as more traps are introduced to promote non-radiative recombination in the bulk. Once the Co content is increased to the 3Pb:1Co composition, the addition of Co has slowed down the crystallization of the perovskite film enough to produce larger grains, which are no longer densely packed. As a result, the PL lifetimes rise substantially because

the pure $MAPbI_3$ domains are larger and all of the Co atoms are pushed to the grain boundaries that are now located further away from the center of each grain. However, performance is decreased because the gaps between the grains allows the PCBM layer to directly contact the PEDOT:PSS and create a shunting pathway that reduces the voltage and current.

Normally, introducing defects into the bulk material is expected to reduce the $V_{oc}$ by producing trap states for non-radiative recombination in the band gap. [173] This is in conflict with the measured trends in $V_{oc}$, where we see a steady increase with increasing Co content from $MAPbI_3$ to $MA(7Pb{:}1Co)I_3$. An explanation that resolves this issue is that the $V_{oc}$ improvement happens at the interface between the perovskite and PEDOT:PSS or PCBM. For instance, imagine that the PEDOT:PSS interface with $MAPbI_3$ naturally has many defects, possibly introduced by the presence of residual acetate or iodide ions. A detrimental PEDOT:PSS interface would explain why the baseline $V_{oc}$ is low and why we have observed that treatment with DIO prior to perovskite addition appears to help improve the voltage somewhat. When Co migrates to this interface, it might act to passivate those traps by coordinating with those residual ions to reduce the density of the shallow trap states. Doing so would reduce the surface recombination speed of the carriers at the interfaces and thereby improve the $V_{oc}$. As more Co is added, more of the atoms are likely to arrive at the problematic interface and passivate these existing traps, which might explain the steady $V_{oc}$ rise with increasing Co content.

In this picture, it is not quite clear why the Co atoms are changing the absolute band edge locations of the perovskite film. One possible explanation is that some of the Co ions are migrating to the interfaces with the electron and hole transport layers, which modifies the dipoles at the perovskite surface. It has been previously shown in the DFT calculations of Chapter 5 (see Section 5.8) that the workfunction of an interface depends strongly on the atoms that are terminating the surface and we demonstrated that the absolute band edge locations are expected to change in Pb-based and Sn-based systems upon replacing some of the atoms with other elements at the surface.

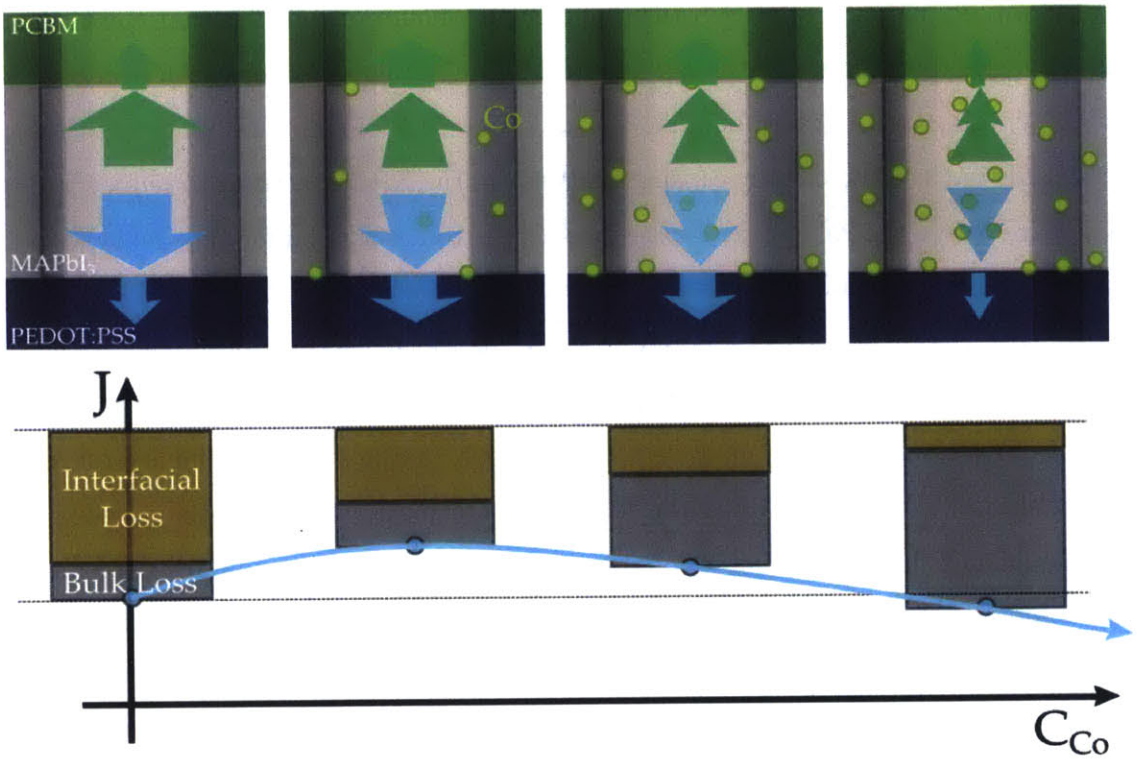


Figure 6-29: The UPS measurements for the MA(Pb:Co)$I_3$ suggest that a barrier exists at both the PCBM and PEDOT:PSS heterojunctions that carriers must overcome through tunneling or thermionic emission. As a result, the $MAPbI_3$ material experiences a substantial current lost at the interfaces and a modest loss due to defects in the bulk material. Introducing cobalt atoms into the material will align the band edges more favorably with PCBM and PEDOT:PSS, causing the interfacial loss to be reduced. However, the presence of Co atoms act as trap sites to promote non-radiative recombination, which increase the loss in the bulk. The net effect, however is to improve the collected current. As the Co content is increased, the interfacial loss continues to decrease while the bulk increases until the net current is reduced compared to the $MAPbI_3$ baseline device.

### Mechanism 2: Cobalt Passivation and Iodide Scavenging

The EDX maps suggest that the cobalt atoms appear to be migrating at least in part to the grain boundaries of the mixed perovskite film. In this scenario, the $Co^{2+}$ atoms are excluded from the perovskite lattice and exist as amorphous material at the grain boundaries. The reason why neither the XRD nor the PL spectra exhibit any changes with increasing Co content is because the only semiconducting material in the film is the pure Pb perovskite, $MAPbI_3$. The reason why both current and

voltage initially increase upon substituting a small amount of cobalt is that the $Co^{2+}$ ions scavenge the excess $I^-$ ions out of the $MAPbI_3$ grains and form electronically benign deposits at the grain boundaries. Any excess $MA^+$ ions would react with the excess $PbI_2$ in the film, thereby causing this peak in the XRD spectrum to reduce and disappear. Hence the role of the cobalt ions here is to act as a buffer that makes the film more tolerant of mismatches in precursor stoichiometries. This might explain in part why the error bars of the device performance metrics are often tighter for mixed-metal series. As more Pb content is replaced with Co, there is an increasing amount of excess iodide that must be scavenged out and less Pb is available to form the perovskite. We observe that the films generate more pinholes with increasing Co content and that the grains become substantially separated at the 3Pb:1Co film morphology. Perhaps as more cobalt material is deposited at the grain boundaries it is more difficult for grains to grow compactly next to one another and physical gaps begin to form between grains, which increasingly isolate them electrically from one another. The PL lifetimes initially decrease because the cobalt material acts as a hole transport that whisks away holes before recombination can occur. This explains the subsequent current rises, as charges are more efficiently carried to the electrodes in the manner of a bulk-heterojunction architecture. As the grains become less connected, the PL lifetimes increase because the carriers persist longer inside their original grains, however the current decreases as it becomes increasingly difficult for charges to find continuous pathways to the electrodes. The device voltages would initially increase with increasing Co content because the Co is cleaning up more of the grains and passivating defects at the grain boundaries, thereby reducing the number of sub-gap traps available to provides states for charges beyond the band edges. However, the voltage drops for the 3Pb:1Co case because the dramatic distance between the grains allows the PCBM electron transport layer to directly contact the PEDOT:PSS hole transport layer and locally circumvent the active material.

If the cobalt phase does indeed help transport charges more efficiently to the electrodes, then charges absorbed deeper in the film would be more likely to become collected at the electrodes. Since lower energy photons are absorbed deepest in the

film, the photogenerated holes need to travel through almost the entire film before being collected at the PEDOT:PSS layer. Hence, the addition of cobalt would help these holes transport out of the device more efficiently. This could explain why there is an increase in the EQE between 600 and 700 nm in Figure 6-19a.

### Mechanism 3: B-site Lattice Replacement

Another explanation for the behavior is that at very low levels of Pb replacement, the perovskite lattice will allow $Co^{2+}$ to fill the vacancy in the B-sites of the perovskite lattice. If only 1 out of every 64 B-sites is occupied by $Co^{2+}$, then the perovskite locally looks like pure $MAPbI_3$ in most places and like $MA(3Pb{:}1Co)I_3$ around the lattice where $Co^{2+}$ substitution occurs. The situation could behave like two separate semiconductors placed in electrical contact as illustrated in Figure 6-30 by a flat band diagram.

In this situation, there are now two effective materials that are able to produce photocurrent and if they each exhibit different band gaps, then the quantum efficiencies will be different at different parts of the solar spectrum. It is expected that the EQE spectra would be increased especially near the band edge of the second material. For instance, the DFT calculations predict that $MA(3Pb{:}1Co)I_3$ would generate a band gap at 1.77 eV, which corresponds exactly to the 700 nm wavelength where the $MA(63Pb{:}1Co)I_3$ becomes more efficient than pure $MAPbI_3$. Additional photocurrent is generated because the EQE is improved at these particular wavelengths. Likewise the photovoltage improves because the photons absorbed near the Co-sites with energies near the $MA(3Pb{:}1Co)I_3$ band edge would initially relax to the local band edge before relaxing down to the $MAPbI_3$ band edges. This might generate a slightly improved voltage, but would cause the PL emission peak to remain at the value for pure $MAPbI_3$. As the Co content is increased, the perovskite lattice might no longer be able to accommodate additional B-site replacement and the excess Co atoms are forced to the grain boundaries. At the grain boundaries, the cobalt material could be generating trap sites that act to promote non-radiative recombination and hence start to siphon away photocurrent. It is also possible that at this point

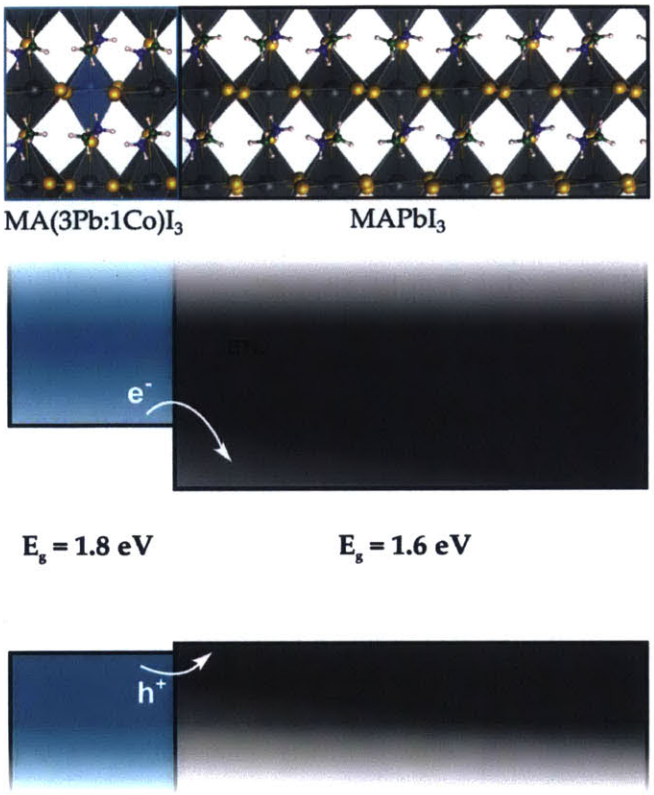


Figure 6-30: If the B-site of a Pb-based perovskite is only sparingly replaced with $Co^{2+}$ ions, the system act locally as if a pure $MAPbI_3$ is placed in electrical contact with a $MAPbI_3$ lattice. According to the DFT calculations, the 3Pb:1Co material will have a wider band gap and any photogenerated charges near the $Co^{2+}$ impurity would relax down to the band edges of the pure $MAPbI_3$ perovskite.

the cobalt phase acts exactly like the proposed manner in the second scenario, which would explain the subsequent increases in PL but decrease in performance. As a result, of it becoming more difficult to remove charges from the interior of the film, the EQE shape of the 63Pb:1Co is largely preserved but the overall efficiencies are reduced everywhere.

Although future investigation is required to fully explain why replacing small amounts of Pb with Co improves the photovoltaic performance of devices fabricated using acetate precursor materials and an inverted device architecture, this work firmly establishes that the device improvement is statistically significant. However, it remains to be seen whether Co substitution would improve the performance of Pb-based perovskite devices that already achieve efficiencies near 20%. It is also uncertain

whether incorporation of Co would occur using other fabrication methods since the most efficient devices are currently fabricated using a two step process where $PbI_2$ films are deposited first and then converted into perovskite with subsequent deposition of the organic cation material. It is likely that with this method a solution of multiple iodide salts would form separate phases, especially since iodide salts adopt a wide array of different crystal lattices, which would make it even more challenging for a mixed-metal perovskite lattice to form afterwards by interdiffusion with a layer of MAI or FAI.

## 6.7 Conclusion

This study fulfills its original goals by successfully fabricating 45 different compositions of mixed-metal solar cells, evaluating how tolerant photovoltaic performance is to the molar ratio of Pb:B′ atoms, and identifying Sn, Cu, and Zn as elements that are capable of generating devices when a substantial portion of the Pb content is replaced. Furthermore, by characterizing the mixed-metal perovskite films with many methods including XRD, XPS, EDS, SEM, TEM, steady-state photoluminescence, TRPL, and UPS a few mechanisms have been speculated that might contribute to the observed performance trends. The specific findings of this exhaustive study are summarized as follows:

1. The performance of $MAPbI_3$ solar cells can be consistently improved by replacing only $1/64^{th}$ of the $Pb^{2+}$ ions in the perovskite precursor solution with $Co^{2+}$, $Cu^{2+}$, $Mg^{2+}$, $Mn^{2+}$, $Ni^{2+}$, $Sr^{2+}$, and $Zn^{2+}$, with the $MA(63Pb{:}1Co)I_3$ embodiment producing a champion efficiency of 11.4%.

2. Introducing iron into the perovskite film quenches the photoluminescence emission and substantially damages photovoltaic performance, even with a metal ratio of 63Pb:1Fe.

3. Generally, the mixed-metal compositions demonstrate performance above or near $MAPbI_3$ when $1/16^{th}$ or less of the $Pb^{2+}$ ions have been replaced. Com-

positions with higher replacement levels usually exhibit a precipitous drop in photocurrent.

4. Champion power conversion efficiencies of 9.3% and 8.3% were achieved for compositions where 25% of the Pb content was replaced with Sn or Cu, respectively. While this performance for the MA(3Pb:1Cu)$I_3$ composition is not sustainable and is difficult to reproduce, high-performing devices can be synthesized more reliably with the MA(3Pb:1Sn)$I_3$ composition, despite the $Sn(OAc)_2$ precursor being only 95% pure.

5. The $MAPbI_3$ films are most tolerant to Zn, which is able to achieve on average an 8.83 $\pm$ 0.94% power conversion efficiency when 12.5% of the Pb content is replaced. This composition also exhibits a desirable film morphology consisting of grains that are both larger and more densely packed together than all other investigated mixed-metal systems.

6. The only mixed-metal perovskite materials to exhibit appreciable changes in band gap was the mixed Pb:Sn series, where the band gap narrowed with increasing Sn content.

7. The presence of Mg and Co in 31Pb:1B′ films was confirmed using x-ray photoelectron spectroscopy (XPS).

8. Elemental mapping with energy dispersive x-ray spectroscopy (EDS) of a TEM cross-section of the MA(31Pb:1Co)$I_3$ reveals that Co atoms are present throughout the film and do not stratify preferentially at a heterojunction. Rather, the maps suggest that some of the Co atoms migrate to the grain boundaries, as evidenced by data points often outlining small domains.

9. Ultraviolet photoelectron spectroscopy measurements reveal that the band edges of the mixed MA(Pb:Co)$I_3$ system will favorably shift with increasing Co content until a composition of 15Pb:1Co is reached, after which the valence band edge shifts closer to the position of $MAPbI_3$. This favorable alignment is ex-

pected to reduce interfacial barriers that arise between the perovskite film and the electron (PCBM) and hole (PEDOT:PSS) transport layers.

It is clear that this study has produced a very rich set of data that has yielded some surprising results. Although only the highest performing composition of $MA(31Pb{:}1Co)I_3$ was investigated in detail, it is likely that many of the other elements considered in the study behave similarly. However, truly understanding the mechanisms that improve or deteriorate photovoltaic performance will require further study of individual cases to confirm this claim.

We have demonstrated that experimental screening is a promising strategy to not only evaluate how compositional changes influence the performance of existing solar materials, but to also discover new ones. This study takes the first step towards producing new non-toxic perovskite materials by attempting to only perturb the Pb-based material through substituting at most 50% of the Pb atoms with a second species. However, future progress in addressing health and safety concerns will require identifying solar materials with even reduced toxicity. Automated screening platforms will likely be a key technology in identifying such materials given that screening studies are quite laborious when rigorously performed manually. Aside from generating new materials, screening approaches will be required to further investigate the underlying mechanisms that limit the performance of current ones by thoroughly exploring the processing parameter space that influence film composition and formation. Such a strategy is also likely to exhaustively determine whether compositional changes can improve the other weakness of perovskite solar materials, long-term stability. As such, we believe that this effort is interesting from both practical and scientific perspectives and it is expected that further investigation into the data set collected here will likely illuminate additional details about the underlying mechanisms that are responsible for the efficient generation of electrical power with perovskite solar materials.

# Chapter 7

# Final Remarks

The overarching goal of this work is to identify new active layer compositions that are capable of improving the performance of solution-processable solar cells by screening through candidate embodiments both theoretically and experimentally. This approach is based on three central concepts:

1. The composition of the active layer of solution-processed solar cells can be easily engineered by simply blending different ingredients into the precursor solutions.

2. The more trials that are attempted either computationally or experimentally to generate new active layer compositions, the more likely that interesting situations will arise that generate favorable results.

3. Computationally assessing the properties of active layer compositions prior to experimentation provides information that not only informs the design of subsequent experimental efforts, but also provides predictions against which empirical data can be compared.

These tenants form the foundation of two different projects aimed at overcoming the classical trade-off between light-harvesting and carrier collection that arises from the inherent degree of disorder exhibited by solution-processed solar materials. The first project explores how various metal nanoparticles could enhance the photocurrent in bulk-heterojunction quantum dot solar cells by evaluating the ability of the solar cell

to absorb light with the finite-difference time-domain (FDTD) method. The second project explores how replacing a fraction of the lead content in $MAPbI_3$ perovskite solar cells with a less-toxic divalent metal species would impact the theoretical electronic properties using density functional theory (DFT). In both instances, the corresponding experimental efforts were able to identify embodiments that significantly improved the photovoltaic performance of actual solar cells.

## 7.1 Summary of Findings

Before discussing the future outlook for the research presented in this dissertation, it is first worthwhile to glance back at the content presented in the preceding chapters and summarize the major findings and key points of interest.

### 7.1.1 Chapter 1

Chapter 1 laid the groundwork for the entire dissertation by explaining the fundamental operating principles of solar cells as well as motivating the need for new photovoltaic technologies capable of reaching price points competitive with conventional energy sources. The central challenge to the widespread adoption of photovoltaic energy technology is primarily cost. At the moment, building a new photovoltaic power plant is roughly two times more expensive than building a new conventional combined-cycle natural gas plant and 1.4 times the cost of a conventional coal plant even with the federal $CO_2$ penalty included in the assessment. Hence, the organic growth of a solar-driven society requires that the cost of solar cell modules be further reduced. Silicon solar cells currently dominate the market, however there is skepticism that the estimated $\$0.40/W_p$ mark required for grid-parity will ever be attainable with silicon since the current low values are artificially deflated by recent overproduction and heavy subsidies from the Chinese Government. This has precipitated a search in academic institutions to develop new solution-processable solar materials that can be manufactured using fundamentally less-expensive methods such as roll-to-roll processing, inkjet printing, slot casting, and spray deposition.

There are five families of solution-processable solar materials of wide-spread research interest: small molecule organic dyes, polymers, chalcogenide inks, quantum dots, and perovskites. Although each of these technologies has surpassed the 10% efficiency mark in the laboratory, these materials must continue to become more efficient in order to first compete with mature photovoltaic technologies such as Si and CdTe before challenging conventional fossil-fuel sources. Unlike current solar technologies, solution-processable solar cells are generally flexible, lightweight, easily processed at low temperatures, and display a wide array of colors and degrees of transparency. These unique attributes open new opportunities to creatively integrate solar cells into previously inaccessible markets, such as electric vehicles, mobile electronics, and multifunctional architecture. However, perhaps the most promising pathway to commercialization is for high-performing solution-processable materials, such as chalcogenides and perovskites, to partner with conventional solar cell manufacturers to produce tandem configurations that can achieve higher performance by simply coating existing panels with a thin film of these materials. Once these solution-processable technologies have reached a sufficient level of maturity, they can split-off from the tandem devices and exist as stand-alone single junction solar modules.

### 7.1.2 Chapter 2

Chapter 2 presented the theoretical background necessary to understand the phenomenon of localized surface plasmon resonance, which arises in noble metal nanoparticles that are embedded in dielectric media. This was accomplished by first presenting the unique optical properties of metals and rigorously analyzing how light scatters from a sub-wavelength metal sphere when illuminated by a plane wave. The analysis reveals that there exists a particular wavelength of light, $\lambda_{LSPR}$, at which the free electrons in the metal nanoparticle collectively resonate to produce an intense secondary electric field in the space directly surrounding the particle. This phenomenon produces two attractive features that can be leveraged in various applications:

1. The resonance wavelength of light is very sensitive to the optical properties of

both the metal nanoparticle and the dielectric function of the media surrounding it. Hence, changes in the local refractive index can be determined by simply monitoring the peak position of the nanoparticle's extinction spectrum.

2. At resonance, the nanoparticle acts to concentrate light in the near-field. This provides a mechanism to overcome the classical diffraction limit and squeeze light into nanoscale features.

Physical pictures were presented to accompany the mathematical framework in order to gain some physical intuition, which is valuable in situations with more complicated nanoparticle geometries where analytical closed-form solutions are no longer available.

The ability of biomolecules such as the M13 bacteriophage to assemble plasmonic complexes was presented and the role of the nanoparticle capping agent in facilitating the assembly process was discussed. It has been found that only metal nanoparticles with weakly adsorbed polar capping agents are able to directly interact with the virus, as the capsid proteins must be able to displace the capping agent to reach the metal surface. Hence, gold nanoparticles capped with citrate and 4-MAP are capable of forming elegant nanoparticle complexes with gold-binding virus variants, while any thiolated capping agent is too hydrophobic and too strongly attached to the metal surface to be removed by the capsid proteins.

Finally, the optics of nanoscale systems was explored using effective medium theory and a model was built to describe the extinction spectra of gold nanoparticles embedded in nanoporous virus and titania films. By matching the measured extinction peak position to the models, the porosity of these systems was determined through simple extinction measurements with a spectrophotometer. Although this discussion focused on the opportunity of plasmonic particles to be utilized as probes for sensing local environments, the theoretical framework forms the foundation for modeling the bulk-heterojunction solar cells presented in Chapter 4.

### 7.1.3 Chapter 3

Chapter 3 presents a new strategy to use the inherent functionality of free-base amino acids to mediate the growth of zincous shells on gold nanoparticles in aqueous solution. By using a visual screening test of colloidal stability, four amino acids were identified out of an initial pool of thirteen candidates as being capable of growing zincous shells on AuNPs and stabilizing the particle surface through electrostatic repulsion. Amorphous zinc oxide shells (a-ZnO) are produced by histidine, tryptophan, and tyrosine, whereas polycrystalline zinc sulfide shells (c-ZnS) are grown using the exact same process but with cysteine. The shell materials were identified and characterized using standard XRD, XPS, EDS, and HRTEM methods. Histidine demonstrates stronger affinity for the a-ZnO material than TRP and TYR, which allows it to enable the controllable growth of uniform and continuous shells with thicknesses between 2 and 25 nm on cores comprised of single AuNPs. Above a $ZnCl_2$ reaction concentration of 2.0 mM, histidine is unable to sufficiently stabilize all of the particles during shell growth and populations emerge with cores comprised of multiple AuNPs.

An anomalous trend was observed in the extinction spectra of the HIS-mediated Au@a-ZnO core-shells where the extinction peak position blue-shifts with increasing shell thickness for samples with coatings greater than 15 nm. By performing generalized Mie theory calculations and comparing the results with the measured extinction spectra of core-shell samples with known shell thickness, it was found that these blue-shifts can arise if the shell material is not purely dielectric, but rather has a small but significant extinction coefficient. From this analysis, it has been inferred that the complex refractive index of the shell material is $1.47 + i0.09$ at wavelengths near 530 nm. This value is lower than previous reports for amorphous zinc oxide films, which suggests that the process of HIS-mediation produces shells with lower density than other methods. Lastly, by virtue of using amino acids to grow and stabilize the core-shells in aqueous solution, it has been shown that biomolecules that express peptides rich in the identified amino acids are able to displace the free molecules capping the particle surface and bind directly to the shell material.

It is anticipated that the thin-shelled Au@a-ZnO particles will be useful in enhancing the light-harvesting ability of solution-processed solar cells by concentrating light through localized surface plasmon resonance. Plasmon-enhanced solar cells require that the metal nanoparticles be coated with thin dielectric shells, which prevent charge trapping and exciton quenching from occurring at the bare metal surface. It is necessary that the shell be as thin as possible, yet continuous, to maximize field-enhancement in the near-field and prevent photocurrent loss. Although these particles are not incorporated into solution-processed solar cells in this dissertation, it is expected that the unprecedented level of control over the shell thickness demonstrated by the HIS-mediated growth process will produce core-shells that successfully enhanced photocurrent production in solution-processable solar cells.

### 7.1.4 Chapter 4

Chapter 4 builds upon the concepts presented in the previous two chapters to theoretically and experimentally evaluate the ability of different metal nanoparticles (AuNPs, AgNPs, and AgNPLs) to enhance the photocurrent of quantum dot bulk-heterojunction solar cells. The optics of the nanostructured solar cells was evaluated by developing material models for the various layers of the solar cells using effective medium theory and numerically solving Maxwell's equations throughout a discretized model of the solar cell with the finite-difference time-domain (FDTD) method. These calculations provided estimates of both the external quantum efficiency (EQE) spectra as well as the expected photocurrent enhancement upon introducing each metal nanoparticle type into the solar cell active layer. Experimental measurements of actual solar cells validated the optical models by reproducing the trends in both the EQE spectra and photocurrent enhancements. It was found that the introduction of AgNPLs yielded the highest theoretical and experimental improvement, which produced a champion device of 3.96% over the 2.93% champion control device. By fitting the experimental $JV$ curves to the standard diode equation with parasitic resistances, it was determined that the 50 mV increase in the observed $V_{oc}$ was a natural result of the increase in photocurrent produced by the plasmonic devices. Furthermore, it

was determined that the near-field penetrated deeper into the blend layer, comprised of both titania and PbS QDs, than a random-packed PbS QD layer. This is useful from a practical standpoint because the larger the extent of the near-field, the greater the chance a PbS QD can experience a higher photon-flux and exist in a defect-free region that can efficiently generate and transport charge carriers.

### 7.1.5 Chapter 5

Chapter 5 presents the theoretical effort to computationally identify new organic-inorganic hybrid perovskite materials with reduced toxicity by systematically replacing a portion of the metal content in the lattice with a second non-toxic metal species. The concept is that replacing only a small fraction of the metal with a different species will only perturb the crystal and electronic structure of the material, thereby preserving the excellent photovoltaic properties of metal triiodide perovskite materials. The crystal and electronic structure of mixed-metal perovskite materials based on Pb, Sn, and Bi were computed using density functional theory (DFT) with the generalized gradient approximation (GGA). These calculations were validated by accurately reproducing the experimental lattice constants reported for $MAPbI_3$, $MASnI_3$, and mixed $MA(Pb:Sn)I_3$ systems and predicting band gaps for these materials that reproduce the experimental trend reported in literature. These benchmarking efforts indicate that we can have good faith in the ability of this computational method to make reasonable predictions of similar yet wholly hypothetical materials that have reduced toxicity or are wholly non-toxic.

The computational screening process revealed that mixed-metal systems provide an opportunity to tune the band gap and band edge locations of the perovskite materials while retaining the overall crystal structure of the pure metal perovskites. The Bi-based candidates generally produced prohibitively large band gaps and effective masses to be of any use as solar materials. However, several Pb-based and Sn-based candidates were identified as promising materials that could potentially perturb the pure perovskite materials into similar or even more favorable solar materials. Thermodynamic stability calculations suggest that it might be difficult to form

mixed-metal Sn-based perovskites when only a quarter of the $Sn^{2+}$ ions are replaced by a second metal species, including $Pb^{2+}$. Likewise, the energy difference between mixed-metal perovskites and phase separated systems is predicted to be less than the ambient thermal energy at room temperature. Therefore, it is difficult to predict with confidence whether the mixed-metal systems are expected to form if attempted experimentally or if the pure $MAPbI_3$ or $MASnI_3$ perovskite material would exclude the second metal species from the lattice and force it to form a separate phase in the film. Therefore, experimental validation is required to investigate the properties of these materials should they form and remain stable under testing conditions. The simulated x-ray diffraction (XRD) spectra are very similar between the perovskite compositions, which indicates that it might be challenging to use XRD measurements to determine if substitution of the second metal species is occurring at the B-site of the perovskite lattice. It is believed that regardless of the accuracy of the absolute values made for the predictions, the observed trends between the samples is valuable and provides useful information about the mechanisms that might be responsible for good solar operation. These values provide a basis against which experimental measurements and trends can be compared to look for indications that secondary metal species are actually taken up into the perovskite lattice and replace $Pb^{2+}$ ions at the B-site.

### 7.1.6 Chapter 6

Chapter 6 presents the corresponding experimental effort to Chapter 5, which systematically evaluates how replacing various amounts of lead with nine different metal species influence material properties and photovoltaic performance. Specifically, we present several embodiments of mixed-metal perovskite devices, where between 1.56% and 25% of the Pb-content has been replaced with a second less-toxic divalent metal species to form methylammonium mixed-metal triiodide compositions, denoted here as $MA(Pb{:}B')I_3$ where $B' = \{Co, Cu, Fe, Mg, Mn, Ni, Sn, Sr, and Zn\}$. This study fulfills its original goals by successfully fabricating 45 different compositions of mixed-metal solar cells, evaluating how tolerant photovoltaic performance is to the molar ratio of Pb:B′ atoms, and identifying Sn, Cu, and Zn as elements that are capa-

ble of generating devices when a substantial portion of the Pb content is replaced. Furthermore, by characterizing the mixed-metal perovskite films with many methods including XRD, XPS, EDS, SEM, TEM, steady-state photoluminescence, TRPL, and UPS, a few mechanisms have been speculated that might contribute to the observed performance trends. The specific findings of this exhaustive study are summarized as follows:

1. The performance of $MAPbI_3$ solar cells can be consistently improved by replacing only $1/64^{th}$ of the $Pb^{2+}$ ions in the perovskite precursor solution with $Co^{2+}$, $Cu^{2+}$, $Mg^{2+}$, $Mn^{2+}$, $Ni^{2+}$, $Sr^{2+}$, and $Zn^{2+}$, with the $MA(63Pb{:}1Co)I_3$ embodiment producing a champion efficiency of 11.4%.

2. Introducing iron into the perovskite film quenches the photoluminescence emission and substantially damages photovoltaic performance, even with a metal ratio of 63Pb:1Fe.

3. Generally, the mixed-metal compositions demonstrate performance above or near $MAPbI_3$ when $1/16^{th}$ or less of the $Pb^{2+}$ ions have been replaced. Compositions with higher replacement levels usually exhibit a precipitous drop in photocurrent.

4. Champion power conversion efficiencies of 9.3% and 8.3% were achieved for compositions where 25% of the Pb content was replaced with Sn or Cu, respectively. While this performance for the $MA(3Pb{:}1Cu)I_3$ composition is not sustainable and is difficult to reproduce, high-performing devices can be synthesized more reliably with the $MA(3Pb{:}1Sn)I_3$ composition, despite the $Sn(OAc)_2$ precursor being only 95% pure.

5. The $MAPbI_3$ films are most tolerant to Zn, which is able to achieve on average an $8.83 \pm 0.94\%$ power conversion efficiency when 12.5% of the Pb content is replaced. This composition also exhibits a desirable film morphology consisting of grains that are both larger and more densely packed together than all other investigated mixed-metal systems.

6. The only mixed-metal perovskite materials to exhibit appreciable changes in band gap was the mixed Pb:Sn series, where the band gap narrowed with increasing Sn content.

7. The presence of Mg and Co in 31Pb:1B′ films was confirmed using x-ray photoelectron spectroscopy (XPS).

8. Elemental mapping with energy dispersive x-ray spectroscopy (EDS) of a TEM cross-section of the MA(31Pb:1Co)$I_3$ reveals that Co atoms are present throughout the film and do not stratify preferentially at a heterojunction. Rather, the maps suggest that some of the Co atoms migrate to the grain boundaries, as evidenced by data points often outlining small domains.

9. Ultraviolet photoelectron spectroscopy measurements reveal that the band edges of the mixed MA(Pb:Co)$I_3$ system will favorably shift with increasing Co content until a composition of 15Pb:1Co is reached, after which the valence band edge shifts closer to the position of $MAPbI_3$. This favorable alignment is expected to reduce interfacial barriers that arise between the perovskite film and the electron (PCBM) and hole (PEDOT:PSS) transport layers.

Although only the highest performing composition of MA(31Pb:1Co)$I_3$ was investigated in detail, it is likely that many of the other elements considered in the study behave similarly. The findings suggest that the addition of Co into the active layer improves the charge transfer efficiency at the interface with PEDOT:PSS and PCBM and passivates trap states, resulting in higher photovoltages and initial increases in photocurrent. While Co improves the interface, it appears to produce trap states in the material bulk that promote non-radiative recombination. Hence, improvement generally occurs for small levels of Pb replacement where the improvement at the interface overcomes any detrimental effects in the bulk. However, the performance reduces with increasing Co content as an increasing trap density in the bulk reduces the number of charges that successfully reach the interfaces for collection.

## 7.2 Looking Forward

It is encouraging that the compositional engineering of both plasmonic and mixed-metal perovskite systems resulted in embodiments with improved photovoltaic performance. This lends credence to the concept that improvements can be easily produced by adjusting the precusor solution of the solution-processable materials. It is expected, however, that introducing plasmonic nanoparticles into the active layer is not a practical way to improve commercial solar cells as the addition of gold and silver into the materials will only increase manufacturing costs. Plasmon-enhancement can help compensate for imperfect light absorption by balancing spectral light-harvesting, however a better approach is to find new materials or processing methods that produce thicker films with less defects. Hence, the second approach of engineering the chemical composition of perovskite materials is expected to be a more fruitful and impactful strategy for improving solar cell performance.

The mixed-metal perovskite study reveals that efficient solar cells can be produced by replacing 25% and 12.5% of the Pb-content with Sn and Zn, respectively, which reveals that the toxicity of the solar cells can be somewhat reduced and still generate relatively high power conversion efficiencies. While this demonstrates that the toxicity of the perovskite can be at least partially addressed, it remains to be seen whether mixed-metal compositions will influence the material's other major weakness: long-term stability. The next steps in evaluating the presented mixed-metal perovskite materials will focus on evaluating the thermal stability of each composition by annealing samples at higher temperatures and noting when the film transitions from the characteristic brown hue to yellow, which indicates phase separation of the $PbI_2$ and MAI materials. It is quite possible that while replacing only $1/64^{th}$ of the Pb content with Co does not appreciably lower the toxicity of the film, it might have a substantial impact on the long-term stability of the perovskite film.

I believe that the approach of computational and experimental screening has the power to optimize the processing conditions of existing solar materials as well as discover new ones. This dissertation demonstrates that this concept has yielded an

incredibly rich data set even when simply trying to perturb existing materials with manual synthesis and measurement methods. The next natural step is to continue spiraling away from $MAPbI_3$ and $MASnI_3$ in search of good photovoltaic materials from increasingly unrelated crystal structures. Exhaustively mapping out new material compositions that span a wide range of organic cations, metal cations, and halide anions will require developing automated processing equipment that is capable of scanning over a large parameter space and evaluating potential solar materials with simple diagnostics, such as photoluminescence and optical microscopy. This pursuit will require the use of traditional mechanical engineering skills such as control theory, mechanical design, and manufacturing in order to identify new solution-processable solar materials that are efficient, stable, and non-toxic. If my vision holds true, perhaps the future realm of solar research might have a place for mechanical engineers after all.

# Bibliography


[1] Jenny Nelson. *The Physics of Solar Cells.* Imperial College Press, London, 2010.

[2] Nathan S. Lewis. Basic Research Needs for Solar Energy Utilization. Technical report, September 2005.

[3] Joel Jean, Patrick R. Brown, Robert L. Jaffe, Tonio Buonassisi, and Vladimir Bulović. Pathways for solar photovoltaics. *Energy & Environmental Science*, 8(4):1200–1219, 2015.

[4] NREL. Best Research-Cell Efficiencies. Technical report, National Renewable Energy Laboratory, http://www.nrel.gov/ncpv/images/efficiency_chart.jpg, June 2015.

[5] Willoughby Smith. Effect of Light on Selenium During the Passage of an Electric Current. *Nature*, 7:303, February 1873.

[6] Charles E. Fritts. On a New Form of Selenium Photocell. *American Journal of Science*, 26:465, 1883.

[7] William Shockley and Hans J. Queisser. Detailed Balance Limit of Efficiency of p-n Junction Solar Cells. *Journal of Applied Physics*, 32(3):510, 1961.

[8] C. W. Tang. Two-Layer Organic Photovoltaic Cell. *Applied Physics Letters*, 48(2):183, 1986.

[9] N. S. Sariciftci, L. Smilowitz, A. J. Heeger, and F. Wudi. Photoinduced Electron Transfer from a Conducting Polymer to Buckminsterfullerene. *Science*, 258(5087):1474–1476, November 1992.

[10] Shigenori Morita, Anvar A. Zakhidoy, and Katsumi Yoshino. Doping Effect of Buckminsterfullerene in Conducting Polymer: Change of Absorption Spectrum and Quenching of Luminescence. *Solid State Communications*, 82(4):249–252, 1992.

[11] Brian O'Regan and Michael Gratzel. A low-cost, high-efficiency solar cell based on dye-sensitized colloidal TiO2 films. *Nature*, 353(6346):737–740, October 1991.

[12] Giles Parkinson. Graph of the Day: The plunging cost of solar PV, March 2013.

[13] First Solar. First Solar Sets Thin-Film Module Efficiency World Record of 17.0 Percent. Technical Report http://investor.firstsolar.com/releasedetail.cfm?ReleaseID=833971, March 2014.

[14] Daniel Simmons. Hard Facts: An Energy Primer. Technical report, Institute for Energy Reseach, March 2015.

[15] SEIA. Solar Energy Facts: 2014 Year in Review. *Solar Energy Industry Association*, December 2014.

[16] Eric Wesoff. Module Costs Dip Below 50 Cents per Watt in JinkoSolar's Strong Q4. *greentechsolar*, 2015.

[17] David Rotman. Can Energy Startups Be Saved? *MIT Technology Review*, April 2012.

[18] Brian Carey, Matt Haskins, Tye Thorson, and Debi Gerstel. Cleantech MoneyTree Report: Q1 2015. Technical report, PricewaterhouseCoopers, May 2015.

[19] Elizabeth Harrington. Report: Solar Energy Subsidies Cost $39 Billion Per Year. *The Washington Free Beacon*, February 2015.

[20] SEIA. Solar Investment Tax Credit (ITC). *Solar Energy Industries Association*, 2014.

[21] Vishal Shah, Jerimiah Booream-Phelps, and Susie Min. Solar 2014 Outlook: Let the Second Gold Rush Begin. Technical report, Deutsche Bank, January 2015.

[22] Dustin Mulvaney. Solar Energy Isn't Always as Green as You Think. *IEEE Spectrum*, August 2014.

[23] Yongye Liang and Luping Yu. A New Class of Semiconducting Polymers for Bulk Heterojunction Solar Cells with Exceptionally High Performance. *Accounts of Chemical Research*, 43(9):1227–1236, September 2010.

[24] Illan J. Kramer and Edward H. Sargent. The Architecture of Colloidal Quantum Dot Solar Cells: Materials to Devices. *Chemical Reviews*, 114(1):863–882, January 2014.

[25] Chia-Hao M. Chuang, Patrick R. Brown, Vladimir Bulović, and Moungi G. Bawendi. Improved performance and stability in quantum dot solar cells through band alignment engineering. *Nature Materials*, 13(8):796–801, May 2014.

[26] Zhijun Ning, Oleksandr Voznyy, Jun Pan, Sjoerd Hoogland, Valerio Adinolfi, Jixian Xu, Min Li, Ahmad R. Kirmani, Jon-Paul Sun, James Minor, Kyle W. Kemp, Haopeng Dong, Lisa Rollny, André Labelle, Graham Carey, Brandon Sutherland, Ian Hill, Aram Amassian, Huan Liu, Jiang Tang, Osman M. Bakr, and Edward H. Sargent. Air-stable n-type colloidal quantum dot solids. *Nature Materials*, 13(8):822–828, June 2014.

[27] Arup K. Rath, Maria Bernechea, Luis Martinez, F. Pelayo Garcia de Arquer, Johann Osmond, and Gerasimos Konstantatos. Solution-processed inorganic bulk nano-heterojunctions and their application to solar cells. *Nature Photonics*, 6(8):529–534, August 2012.

[28] Akihiro Kojima, Kenjiro Teshima, Yasuo Shirai, and Tsutomu Miyasaka. Organometal Halide Perovskites as Visible-Light Sensitizers for Photovoltaic Cells. *Journal of the American Chemical Society*, 131(17):6050–6051, May 2009.

[29] W. S. Yang, J. H. Noh, N. J. Jeon, Y. C. Kim, S. Ryu, J. Seo, and S. I. Seok. High-performance photovoltaic perovskite layers fabricated through intramolecular exchange. *Science*, 348(6240):1234–1237, June 2015.

[30] Julian Burschka, Norman Pellet, Soo-Jin Moon, Robin Humphry-Baker, Peng Gao, Mohammad K. Nazeeruddin, and Michael Grätzel. Sequential deposition as a route to high-performance perovskite-sensitized solar cells. *Nature*, 499(7458):316–319, July 2013.

[31] M. M. Lee, J. Teuscher, T. Miyasaka, T. N. Murakami, and H. J. Snaith. Efficient Hybrid Solar Cells Based on Meso-Superstructured Organometal Halide Perovskites. *Science*, 338(6107):643–647, October 2012.

[32] Giles E. Eperon, Samuel D. Stranks, Christopher Menelaou, Michael B. Johnston, Laura M. Herz, and Henry J. Snaith. Formamidinium lead trihalide: a broadly tunable perovskite for efficient planar heterojunction solar cells. *Energy & Environmental Science*, 7(3):982, 2014.

[33] Michael Graetzel, Rene A. J. Janssen, David B. Mitzi, and Edward H. Sargent. Materials interface engineering for solution-processed photovoltaics. *Nature*, 488(7411):304–312, August 2012.

[34] Michael Grätzel. Recent Advances in Sensitized Mesoscopic Solar Cells. *Accounts of Chemical Research*, 42(11):1788–1798, November 2009.

[35] David Bohm and David Pines. A Collective Description of Electron Interactions: III. Coulomb Interactions in a Degenerate Electron Gas. *Physical Review*, 92(3):609–625, November 1953.

[36] Stefan A. Maier. *Plasmonics: Fundamentals and Applications*. Springer, New York, NY, 2007.

[37] P. B. Johnson and R. W. Christy. Optical Constants of the Noble Metals. *Physical Review B*, 6(12):4370–43479, December 1972.

[38] John D. Jackson. *Classical Electromagnetics*. John Wiley & Sons, Inc, New York, NY, 3rd edition edition, 1999.

[39] Craig F. Bohren and Donald R. Huffman. *Absorption and Scattering of Light by Small Particles*. Wiley-Interscience, New York, NY, 1998.

[40] Jie Zheng, Philip R. Nicovich, and Robert M. Dickson. Highly Fluorescent Noble-Metal Quantum Dots. *Annual Review of Physical Chemistry*, 58(1):409–431, May 2007.

[41] Gustav Mie. Beiträge zur Optik trüber Medien, speziell kolloidaler Metallösungen. *Annalen der Physik*, 330(3):377–445, 1908.

[42] Xiaohua Huang, Ivan H. El-Sayed, Wei Qian, and Mostafa A. El-Sayed. Cancer Cell Imaging and Photothermal Therapy in the Near-Infrared Region by Using Gold Nanorods. *Journal of the American Chemical Society*, 128(6):2115–2120, February 2006.

[43] Prashant K. Jain, Xiaohua Huang, Ivan H. El-Sayed, and Mostafa A. El-Sayed. Review of Some Interesting Surface Plasmon Resonance-enhanced Properties of Noble Metal Nanoparticles and Their Applications to Biosystems. *Plasmonics*, 2(3):107–118, September 2007.

[44] Andy Wijaya, Stefan B. Schaffer, Ivan G. Pallares, and Kimberly Hamad-Schifferli. Selective Release of Multiple DNA Oligonucleotides from Gold Nanorods. *ACS Nano*, 3(1):80–86, January 2009.

[45] Kadir Aslan, Joseph R Lakowicz, and Chris D Geddes. Nanogold-plasmon-resonance-based glucose sensing. *Analytical Biochemistry*, 330(1):145–155, July 2004.

[46] Yu Huang, Chung-Yi Chiang, Soo Kwan Lee, Yan Gao, Evelyn L. Hu, James De Yoreo, and Angela M. Belcher. Programmable Assembly of Nanoarchitectures Using Genetically Engineered Viruses. *Nano Letters*, 5(7):1429–1434, July 2005.

[47] John Turkevich, Peter Cooper Stevenson, and James Hillier. A study of the nucleation and growth processes in the synthesis of colloidal gold. *Discussions of the Faraday Society*, 11:55, 1951.

[48] Valérie J. Gandubert and R. Bruce Lennox. Assessment of 4-(Dimethylamino)pyridine as a Capping Agent for Gold Nanoparticles. *Langmuir*, 21(14):6532–6539, July 2005.

[49] Noémie-Manuelle Dorval Courchesne, Matthew T. Klug, Po-Yen Chen, Steven E. Kooi, Dong Soo Yun, Nina Hong, Nicholas X. Fang, Angela M.

Belcher, and Paula T. Hammond. Assembly of a Bacteriophage-Based Template for the Organization of Materials into Nanoporous Networks. *Advanced Materials*, 26(21):3398–3404, June 2014.

[50] S. Y. Kim. Simultaneous determination of refractive index, extinction coefficient, and void distribution of titanium dioxide thin film by optical methods. *Applied optics*, 35(34):6703–6707, 1996.

[51] S. K. Ghosh and T. Pal. Interparticle coupling effect on the surface plasmon resonance of gold nanoparticles: from theory to applications. *Chemical Reviews-Columbus*, 107(11):4797–4862, 2007.

[52] Xiaogang Han, James Goebl, Zhenda Lu, and Yadong Yin. Role of Salt in the Spontaneous Assembly of Charged Gold Nanoparticles in Ethanol. *Langmuir*, 27(9):5282–5289, May 2011.

[53] Soumen Basu, Sujit Kumar Ghosh, Subrata Kundu, Sudipa Panigrahi, Snigdhamayee Praharaj, Surojit Pande, Subhra Jana, and Tarasankar Pal. Biomolecule induced nanoparticle aggregation: Effect of particle size on interparticle coupling. *Journal of Colloid and Interface Science*, 313(2):724–734, September 2007.

[54] Zhenhua Bai, Rui Chen, Peng Si, Youju Huang, Handong Sun, and Dong-Hwan Kim. Fluorescent pH Sensor Based on Ag@SiO2 Core–Shell Nanoparticle. *ACS Applied Materials & Interfaces*, 5(12):5856–5860, June 2013.

[55] Zhenjiang Zhang, Jing Wang, Xin Nie, Tao Wen, Yinglu Ji, Xiaochun Wu, Yuliang Zhao, and Chunying Chen. Near Infrared Laser-Induced Targeted Cancer Therapy Using Thermoresponsive Polymer Encapsulated Gold Nanorods. *Journal of the American Chemical Society*, 136(20):7317–7326, May 2014.

[56] Yun-Ling Luo, Yi-Syun Shiao, and Yu-Fen Huang. Release of Photoactivatable Drugs from Plasmonic Nanoparticles for Targeted Cancer Therapy. *ACS Nano*, 5(10):7796–7804, October 2011.

[57] Xianguang Ding, Chi Hao Liow, Mengxin Zhang, Renjun Huang, Chunyan Li, He Shen, Mengya Liu, Yu Zou, Nan Gao, Zhijun Zhang, Yonggang Li, Qiangbin Wang, Shuzhou Li, and Jiang Jiang. Surface Plasmon Resonance Enhanced Light Absorption and Photothermal Therapy in the Second Near-Infrared Window. *Journal of the American Chemical Society*, 136(44):15684–15693, November 2014.

[58] Cuiyan Li, Yihua Zhu, Xiaoqing Zhang, Xiaoling Yang, and Chunzhong Li. Metal-enhanced fluorescence of carbon dots adsorbed Ag@SiO2 core-shell nanoparticles. *RSC Advances*, 2(5):1765, 2012.

[59] Nikhil R. Jana, Christopher Earhart, and Jackie Y. Ying. Synthesis of Water-Soluble and Functionalized Nanoparticles by Silica Coating. *Chemistry of Materials*, 19(21):5074–5082, October 2007.

[60] Jifa Qi, Xiangnan Dang, Paula T. Hammond, and Angela M. Belcher. Highly Efficient Plasmon-Enhanced Dye-Sensitized Solar Cells through Metal@Oxide Core–Shell Nanostructure. *ACS Nano*, 5(9):7108–7116, September 2011.

[61] Xiangnan Dang, Jifa Qi, Matthew T. Klug, Po-Yen Chen, Dong Soo Yun, Nicholas X. Fang, Paula T. Hammond, and Angela M. Belcher. Tunable Localized Surface Plasmon-Enabled Broadband Light-Harvesting Enhancement for High-Efficiency Panchromatic Dye-Sensitized Solar Cells. *Nano Letters*, 13(2):637–642, February 2013.

[62] Michael D. Brown, Teeraporn Suteewong, R. Sai Santosh Kumar, Valerio D'Innocenzo, Annamaria Petrozza, Michael M. Lee, Ulrich Wiesner, and Henry J. Snaith. Plasmonic Dye-Sensitized Solar Cells Using Core-Shell Metal-Insulator Nanoparticles. *Nano Letters*, 11(2):438–445, February 2011.

[63] Natalia Kholmicheva, Pavel Moroz, Upendra Rijal, Ebin Bastola, Prakash Uprety, Geethika Liyanage, Anton Razgoniaev, Alexis D. Ostrowski, and Mikhail Zamkov. Plasmonic Nanocrystal Solar Cells Utilizing Strongly Confined Radiation. *ACS Nano*, 8(12):12549–12559, December 2014.

[64] Hyosung Choi, Jung-Pil Lee, Seo-Jin Ko, Jae-Woo Jung, Hyungmin Park, Seungmin Yoo, Okji Park, Jong-Ryul Jeong, Soojin Park, and Jin Young Kim. Multipositional Silica-Coated Silver Nanoparticles for High-Performance Polymer Solar Cells. *Nano Letters*, 13(5):2204–2208, May 2013.

[65] Wei Zhang, Michael Saliba, Samuel D. Stranks, Yao Sun, Xian Shi, Ulrich Wiesner, and Henry J. Snaith. Enhancement of Perovskite-Based Solar Cells Employing Core–Shell Metal Nanoparticles. *Nano Letters*, 13(9):4505–4510, September 2013.

[66] J. Y. Lee and P. Peumans. The origin of enhanced optical absorption in solar cells with metal nanoparticles embedded in the active layer. *Optics Express*, 18(10):10078–10087, 2010.

[67] Seung Uk Son, In Kyu Park, Jongnam Park, and Taeghwan Hyeon. Synthesis of Cu2O coated Cu nanoparticles and their successful applications to Ullmann-type amination coupling reactions of aryl chlorides. *Chemical Communications*, (7):778–779, 2004.

[68] César Clavero. Plasmon-induced hot-electron generation at nanoparticle/metal-oxide interfaces for photovoltaic and photocatalytic devices. *Nature Photonics*, 8(2):95–103, January 2014.

[69] Tsutomu Hirakawa and Prashant V. Kamat. Charge Separation and Catalytic Activity of Ag@$TiO_2$ Core-Shell Composite Clusters under UV-Irradiation. *Journal of the American Chemical Society*, 127(11):3928–3934, March 2005.

[70] Luis M. Liz-Marzán, Michael Giersig, and Paul Mulvaney. Synthesis of Nanosized Gold-Silica Core-Shell Particles. *Langmuir*, 12(18):4329–4335, January 1996.

[71] Yu Lu, Yadong Yin, Zhi-Yuan Li, and Younan Xia. Synthesis and Self-Assembly of Au@$SiO_2$ Core-Shell Colloids. *Nano Letters*, 2(7):785–788, July 2002.

[72] Alan Vanderkooy and Michael A. Brook. Polyvinylpyrrolidone Molecular Weight Controls Silica Shell Thickness on Au Nanoparticles with Diglycerylsilane as Precursor. *ACS Applied Materials & Interfaces*, 4(8):3980–3986, August 2012.

[73] Mathias Schulzendorf, Christian Cavelius, Philip Born, Eoin Murray, and Tobias Kraus. Biphasic Synthesis of Au@$SiO_2$ Core-Shell Particles with Stepwise Ligand Exchange. *Langmuir*, 27(2):727–732, January 2011.

[74] Isabel Pastoriza-Santos, Jorge Pérez-Juste, and Luis M. Liz-Marzán. Silica-Coating and Hydrophobation of CTAB-Stabilized Gold Nanorods. *Chemistry of Materials*, 18(10):2465–2467, May 2006.

[75] Christina Graf, Dirk L. J. Vossen, Arnout Imhof, and Alfons van Blaaderen. A General Method To Coat Colloidal Particles with Silica. *Langmuir*, 19(17):6693–6700, August 2003.

[76] Xiao-Dong Lin, Viviane Uzayisenga, Jian-Feng Li, Ping-Ping Fang, De-Yin Wu, Bin Ren, and Zhong-Qun Tian. Synthesis of ultrathin and compact Au@MnO2 nanoparticles for shell-isolated nanoparticle-enhanced Raman spectroscopy (SHINERS). *Journal of Raman Spectroscopy*, 43(1):40–45, January 2012.

[77] Li Zhang, Douglas A. Blom, and Hui Wang. Au–Cu $_2$ O Core–Shell Nanoparticles: A Hybrid Metal-Semiconductor Heteronanostructure with Geometrically Tunable Optical Properties. *Chemistry of Materials*, 23(20):4587–4598, October 2011.

[78] Li Zhang, Hao Jing, Geoffrey Boisvert, John Z. He, and Hui Wang. Geometry Control and Optical Tunability of Metal–Cuprous Oxide Core–Shell Nanoparticles. *ACS Nano*, 6(4):3514–3527, April 2012.

[79] Chun-Hong Kuo, Tzu-En Hua, and Michael H. Huang. Au Nanocrystal-Directed Growth of Au-$Cu_2O$ Core-Shell Heterostructures with Precise Morphological Control. *Journal of the American Chemical Society*, 131(49):17871–17878, December 2009.

[80] Elena V. Shevchenko, Maryna I. Bodnarchuk, Maksym V. Kovalenko, Dmitri V. Talapin, Rachel K. Smith, Shaul Aloni, Wolfgang Heiss, and A. Paul Alivisatos. Gold/Iron Oxide Core/Hollow-Shell Nanoparticles. *Advanced Materials*, 20(22):4323–4329, November 2008.

[81] Yun Yang, Shuhua Han, Guangju Zhou, Lijie Zhang, Xingliang Li, Chao Zou, and Shaoming Huang. Ascorbic-acid-assisted growth of high quality M@ZnO: a growth mechanism and kinetics study. *Nanoscale*, 5(23):11808, 2013.

[82] Sanjit Manohar Majhi, Prabhakar Rai, and Yeon-Tae Yu. Facile Approach to Synthesize Au@ZnO Core–Shell Nanoparticles and Their Application for Highly Sensitive and Selective Gas Sensors. *ACS Applied Materials & Interfaces*, 7(18):9462–9468, May 2015.

[83] J. Zhang, Y. Tang, K. Lee, and M. Ouyang. Nonepitaxial Growth of Hybrid Core-Shell Nanostructures with Large Lattice Mismatches. *Science*, 327(5973):1634–1638, March 2010.

[84] Wei-Ta Chen, Yin-Kai Lin, Ting-Ting Yang, Ying-Chih Pu, and Yung-Jung Hsu. Au/ZnS core/shell nanocrystals as an efficient anode photocatalyst in direct methanol fuel cells. *Chemical Communications*, 49(76):8486, 2013.

[85] Beau R. Peelle, Eric M. Krauland, K. Dane Wittrup, and Angela M. Belcher. Design Criteria for Engineering Inorganic Material- Specific Peptides. *Langmuir*, 21(15):6929–6933, July 2005.

[86] Christine E. Flynn, Chuanbin Mao, Andrew Hayhurst, Julie L. Williams, George Georgiou, Brent Iverson, and Angela M. Belcher. Synthesis and organization of nanoscale II-VI semiconductor materials using evolved peptide specificity and viral capsid assembly. *Journal of Materials Chemistry*, 13(10):2414–2421, 2003.

[87] John Turkevich, Peter Cooper Stevenson, and James Hillier. A study of the nucleation and growth processes in the synthesis of colloidal gold. *Discussions of the Faraday Society*, 11:55, 1951.

[88] Martin Hoefling, Francesco Iori, Stefano Corni, and Kay-Eberhard Gottschalk. Interaction of Amino Acids with the Au(111) Surface: Adsorption Free Energies from Molecular Dynamics Simulations. *Langmuir*, 26(11):8347–8351, June 2010.

[89] Hannu Häkkinen. The gold–sulfur interface at the nanoscale. *Nature Chemistry*, 4(6):443–455, May 2012.

[90] Suresh K. Bhargava, Jamie M. Booth, Sourabh Agrawal, Peter Coloe, and Gopa Kar. Gold Nanoparticle Formation during Bromoaurate Reduction by Amino Acids. *Langmuir*, 21(13):5949–5956, June 2005.

[91] Joshua Zylstra, Jennifer Amey, Nathaniel J. Miska, Lisa Pang, Corey R. Hine, Julia Langer, Robert P. Doyle, and Mathew M. Maye. A Modular Phase Transfer and Ligand Exchange Protocol for Quantum Dots. *Langmuir*, 27(8):4371–4379, April 2011.

[92] Li Li, Qiaolin Zhang, Yaping Ding, Xiaoyong Cai, Shuqing Gu, and Zhiyuan Cao. Application of l-cysteine capped core–shell CdTe/ZnS nanoparticles as a fluorescence probe for cephalexin. *Analytical Methods*, 6(8):2715, 2014.

[93] Wei-Ta Chen and Yung-Jung Hsu. L-Cysteine-Assisted Growth of Core-Satellite ZnS-Au Nanoassemblies with High Photocatalytic Efficiency. *Langmuir*, 26(8):5918–5925, April 2010.

[94] Corrine K. Thai, Haixia Dai, M. S. R. Sastry, Mehmet Sarikaya, Daniel T. Schwartz, and Francois Baneyx. Identification and characterization of Cu2O- and ZnO-binding polypeptides by Escherichia coli cell surface display: toward an understanding of metal oxide binding. *Biotechnology and Bioengineering*, 87(2):129–137, July 2004.

[95] Si Yun Park, Sunyoung Kim, Jeeyoung Yoo, Keon-Hee Lim, Eungkyu Lee, Kyongjun Kim, Joohee Kim, and Youn Sang Kim. Aqueous zinc ammine complex for solution-processed ZnO semiconductors in thin film transistors. *RSC Advances*, 4(22):11295–11299, 2014.

[96] Joel Jean, Sehoon Chang, Patrick R. Brown, Jayce J. Cheng, Paul H. Rekemeyer, Moungi G. Bawendi, Silvija Gradečak, and Vladimir Bulović. ZnO Nanowire Arrays for Enhanced Photocurrent in PbS Quantum Dot Solar Cells. *Advanced Materials*, 25(20):2790–2796, May 2013.

[97] Qingzhi Wu, Xia Chen, Ping Zhang, Yingchao Han, Xiaoming Chen, Yuhua Yan, and Shipu Li. Amino Acid-Assisted Synthesis of ZnO Hierarchical Architectures and Their Novel Photocatalytic Activities. *Crystal Growth & Design*, 8(8):3010–3018, August 2008.

[98] D. E. Irish, Bruce McCarroll, and T. F. Young. Raman Study of Zinc Chloride Solutions. *The Journal of Chemical Physics*, 39(12):3436–3444, 1963.

[99] Ken-Huang Lin, Shih-Jye Sun, Shin-Pon Ju, Jen-Yu Tsai, Hsin-Tsung Chen, and Jin-Yuan Hsieh. Observation of the amorphous zinc oxide recrystalline process by molecular dynamics simulation. *Journal of Applied Physics*, 113(7):073512, 2013.

[100] J.H. Bruning and Yuen Lo. Multiple scattering of EM waves by spheres part I–Multipole expansion and ray-optical solutions. *Antennas and Propagation, IEEE Transactions on*, 19(3):378–390, May 1971.

[101] Yu-lin Xu. Electromagnetic scattering by an aggregate of spheres. *Applied Optics*, 34(21):4573–4588, July 1995.

[102] Edward D. Palik. *Handbook of Optical Constants of Solids*. Elsevier, 1998.

[103] Jebreel M. Khoshman and Martin E. Kordesch. Optical constants and band edge of amorphous zinc oxide thin films. *Thin Solid Films*, 515(18):7393–7399, June 2007.

[104] John P. Casey, Roberto J. Barbero, Nimrod Heldman, and Angela M. Belcher. Versatile *de Novo* Enzyme Activity in Capsid Proteins from an Engineered M13 Bacteriophage Library. *Journal of the American Chemical Society*, 136(47):16508–16514, November 2014.

[105] Cheng-Hsuan Chou, Wei Lek Kwan, Ziruo Hong, Li-Min Chen, and Yang Yang. A Metal-Oxide Interconnection Layer for Polymer Tandem Solar Cells with an Inverted Architecture. *Advanced Materials*, 23(10):1282–1286, March 2011.

[106] Jun Yang, Rui Zhu, Ziruo Hong, Youjun He, Ankit Kumar, Yongfang Li, and Yang Yang. A Robust Inter-Connecting Layer for Achieving High Performance Tandem Polymer Solar Cells. *Advanced Materials*, 23(30):3465–3470, August 2011.

[107] Jingbi You, Chun-Chao Chen, Ziruo Hong, Ken Yoshimura, Kenichiro Ohya, Run Xu, Shenglin Ye, Jing Gao, Gang Li, and Yang Yang. 10.2% Power Conversion Efficiency Polymer Tandem Solar Cells Consisting of Two Identical Sub-Cells. *Advanced Materials*, 25(29):3973–3978, August 2013.

[108] Rafael Betancur, Pablo Romero-Gomez, Alberto Martinez-Otero, Xavier Elias, Marc Maymó, and Jordi Martorell. Transparent polymer solar cells employing a layered light-trapping architecture. *Nature Photonics*, 7(12):995–1000, October 2013.

[109] Stephen Y. Chou and Wei Ding. Ultrathin, high-efficiency, broad-band, omni-acceptance, organic solar cells enhanced by plasmonic cavity with subwavelength hole array. *Optics Express*, 21(101):A60–A76, 2013.

[110] Noémie-Manuelle Dorval Courchesne, Matthew T. Klug, Kevin J. Huang, Mark C. Weidman, Victor J. Cantú, Po-Yen Chen, Steven E. Kooi, Dong Soo Yun, William A. Tisdale, Nicholas X. Fang, Angela M. Belcher, and Paula T. Hammond. Constructing Multifunctional Virus-Templated Nanoporous Composites for Thin Film Solar Cells: Contributions of Morphology and Optics to Photocurrent Generation. *The Journal of Physical Chemistry C*, pages 13987–14000, June 2015.

[111] Po-Yen Chen, Xiangnan Dang, Matthew T. Klug, Jifa Qi, Noémie-Manuelle Dorval Courchesne, Fred J. Burpo, Nicholas Fang, Paula T. Hammond, and Angela M. Belcher. Versatile Three-Dimensional Virus-Based Template for Dye-Sensitized Solar Cells with Improved Electron Transport and Light Harvesting. *ACS Nano*, 7(8):6563–6574, August 2013.

[112] Xiangnan Dang, Hyunjung Yi, Moon-Ho Ham, Jifa Qi, Dong Soo Yun, Rebecca Ladewski, Michael S. Strano, Paula T. Hammond, and Angela M. Belcher. Virus-templated self-assembled single-walled carbon nanotubes for highly efficient electron collection in photovoltaic devices. *Nature Nanotechnology*, 6(6):377–384, April 2011.

[113] Patrick R. Brown, Donghun Kim, Richard R. Lunt, Ni Zhao, Moungi G. Bawendi, Jeffrey C. Grossman, and Vladimir Bulović. Energy Level Modification in Lead Sulfide Quantum Dot Thin Films through Ligand Exchange. *ACS Nano*, 8(6):5863–5872, June 2014.

[114] Keith W. Johnston, Andras G. Pattantyus-Abraham, Jason P. Clifford, Stefan H. Myrskog, Dean D. MacNeil, Larissa Levina, and Edward H. Sargent. Schottky-quantum dot photovoltaics for efficient infrared power conversion. *Applied Physics Letters*, 92(15):–, 2008.

[115] Lioz Etgar, Thomas Moehl, Stefanie Gabriel, Stephen G. Hickey, Alexander Eychmüller, and Michael Grätzel. Light Energy Conversion by Mesoscopic PbS Quantum Dots/TiO2 Heterojunction Solar Cells. *ACS Nano*, 6(4):3092–3099, 2012.

[116] Xinzheng Lan, Silvia Masala, and Edward H. Sargent. Charge-extraction strategies for colloidal quantum dot photovoltaics. *Nature Materials*, 13(3):233–240, March 2014.

[117] Qiao Zhang, Na Li, James Goebl, Zhenda Lu, and Yadong Yin. A Systematic Study of the Synthesis of Silver Nanoplates: Is Citrate a "Magic" Reagent? *Journal of the American Chemical Society*, 133(46):18931–18939, November 2011.

[118] Iwan Moreels, Detlef Kruschke, Peter Glas, and Jens W. Tomm. The dielectric function of PbS quantum dots in a glass matrix. *Optical Materials Express*, 2(5):496–500, 2012.

[119] Cuong Dang, Joonhee Lee, Craig Breen, Jonathan S. Steckel, Seth Coe-Sullivan, and Arto Nurmikko. Red, green and blue lasing enabled by single-exciton gain in colloidal quantum dot films. *Nature Nanotechnology*, 7(5):335–339, May 2012.

[120] F. A. Dullien and H. Brenner. *Porous Media: Fluid Transport and Pore Structure*. Elsevier Science, 1991.

[121] Gleb M. Akselrod, Ferry Prins, Lisa V. Poulikakos, Elizabeth M. Y. Lee, Mark C. Weidman, A. Jolene Mork, Adam P. Willard, Vladimir Bulović, and William A. Tisdale. Subdiffusive Exciton Transport in Quantum Dot Solids. *Nano Letters*, 14(6):3556–3562, 2014.

[122] Nam Joong Jeon, Jun Hong Noh, Woon Seok Yang, Young Chan Kim, Seungchan Ryu, Jangwon Seo, and Sang Il Seok. Compositional engineering of perovskite materials for high-performance solar cells. *Nature*, 517(7535):476–480, January 2015.

[123] In Chung, Byunghong Lee, Jiaqing He, Robert P. H. Chang, and Mercouri G. Kanatzidis. All-solid-state dye-sensitized solar cells with high efficiency. *Nature*, 485(7399):486–489, May 2012.

[124] Dianyi Liu and Timothy L. Kelly. Perovskite solar cells with a planar heterojunction structure prepared using room-temperature solution processing techniques. *Nature Photonics*, 8(2):133–138, December 2013.

[125] Nam Joong Jeon, Jun Hong Noh, Young Chan Kim, Woon Seok Yang, Seungchan Ryu, and Sang Il Seok. Solvent engineering for high-performance inorganic–organic hybrid perovskite solar cells. *Nature Materials*, 13(9):897–903, July 2014.

[126] Guichuan Xing, Nripan Mathews, Shuangyong Sun, Swee Sien Lim, Yeng Ming Lam, Michael Grätzel, Subodh Mhaisalkar, and Tze Chien Sum. Long-range balanced electron-and hole-transport lengths in organic-inorganic $CH_3NH_3PbI_3$. *Science*, 342(6156):344–347, 2013.

[127] S. D. Stranks, G. E. Eperon, G. Grancini, C. Menelaou, M. J. P. Alcocer, T. Leijtens, L. M. Herz, A. Petrozza, and H. J. Snaith. Electron-Hole Diffusion Lengths Exceeding 1 Micrometer in an Organometal Trihalide Perovskite Absorber. *Science*, 342(6156):341–344, October 2013.

[128] Nakita K. Noel, Samuel D. Stranks, Antonio Abate, Christian Wehrenfennig, Simone Guarnera, Amir-Abbas Haghighirad, Aditya Sadhanala, Giles E. Eperon, Sandeep K. Pathak, Michael B. Johnston, Annamaria Petrozza, Laura M. Herz, and Henry J. Snaith. Lead-free organic–inorganic tin halide perovskites for photovoltaic applications. *Energy & Environmental Science*, 7(9):3061, May 2014.

[129] Yuhei Ogomi, Atsushi Morita, Syota Tsukamoto, Takahiro Saitho, Naotaka Fujikawa, Qing Shen, Taro Toyoda, Kenji Yoshino, Shyam S. Pandey, Tingli Ma, and Shuzi Hayase. $CH_3NH_3Sn_xPb_{(1-x)}I_3$ Perovskite Solar Cells Covering up to 1060 nm. *The Journal of Physical Chemistry Letters*, 5(6):1004–1011, March 2014.

[130] Constantinos C. Stoumpos, Laszlo Frazer, Daniel J. Clark, Yong Soo Kim, Sonny H. Rhim, Arthur J. Freeman, John B. Ketterson, Joon I. Jang, and Mercouri G. Kanatzidis. Hybrid Germanium Iodide Perovskite Semiconductors: Active Lone Pairs, Structural Distortions, Direct and Indirect Energy Gaps, and Strong Nonlinear Optical Properties. *Journal of the American Chemical Society*, 137(21):6804–6819, June 2015.

[131] Edoardo Mosconi, Anna Amat, Md. K. Nazeeruddin, Michael Grätzel, and Filippo De Angelis. First-Principles Modeling of Mixed Halide Organometal Perovskites for Photovoltaic Applications. *The Journal of Physical Chemistry C*, 117(27):13902–13913, July 2013.

[132] Feng Hao, Constantinos C. Stoumpos, Duyen Hanh Cao, Robert P. H. Chang, and Mercouri G. Kanatzidis. Lead-free solid-state organic–inorganic halide perovskite solar cells. *Nature Photonics*, 8(6):489–494, May 2014.

[133] Tom Baikie, Yanan Fang, Jeannette M. Kadro, Martin Schreyer, Fengxia Wei, Subodh G. Mhaisalkar, Michael Graetzel, and Tim J. White. Synthesis and crystal chemistry of the hybrid perovskite ($CH_3NH_3PbI_3$ for solid-state sensitised solar cell applications. *Journal of Materials Chemistry A*, 1(18):5628, 2013.

[134] John P. Perdew, Kieron Burke, and Matthias Ernzerhof. Generalized Gradient Approximation Made Simple. *Physical Review Letters*, 77(18):3865–3868, October 1996.

[135] Paolo Giannozzi, Stefano Baroni, Nicola Bonini, Matteo Calandra, Roberto Car, Carlo Cavazzoni, Davide Ceresoli, Guido L Chiarotti, Matteo Cococcioni, Ismaila Dabo, Andrea Dal Corso, Stefano de Gironcoli, Stefano Fabris, Guido Fratesi, Ralph Gebauer, Uwe Gerstmann, Christos Gougoussis, Anton Kokalj, Michele Lazzeri, Layla Martin-Samos, Nicola Marzari, Francesco Mauri, Riccardo Mazzarello, Stefano Paolini, Alfredo Pasquarello, Lorenzo Paulatto, Carlo Sbraccia, Sandro Scandolo, Gabriele Sclauzero, Ari P Seitsonen, Alexander Smogunov, Paolo Umari, and Renata M Wentzcovitch. QUANTUM ESPRESSO: a modular and open-source software project for quantum simulations of materials. *Journal of Physics: Condensed Matter*, 21(39):395502, September 2009.

[136] Kevin F. Garrity, Joseph W. Bennett, Karin M. Rabe, and David Vanderbilt. Pseudopotentials for high-throughput DFT calculations. *Computational Materials Science*, 81:446–452, January 2014.

[137] Jacky Even, Laurent Pedesseau, Claudine Katan, Mikaël Kepenekian, Jean-Sébastien Lauret, Daniel Sapori, and Emmanuelle Deleporte. Solid-State Physics Perspective on Hybrid Perovskite Semiconductors. *The Journal of Physical Chemistry C*, 119(19):10161–10177, May 2015.

[138] Paolo Umari, Edoardo Mosconi, and Filippo De Angelis. Relativistic GW calculations on $CH_3NH_3PbI_3$ and $CH_3NH_3SnI_3$ Perovskites for Solar Cell Applications. *Scientific Reports*, 4, March 2014.

[139] Valerio D'Innocenzo, Giulia Grancini, Marcelo J. P. Alcocer, Ajay Ram Srimath Kandada, Samuel D. Stranks, Michael M. Lee, Guglielmo Lanzani, Henry J. Snaith, and Annamaria Petrozza. Excitons versus free charges in organo-lead tri-halide perovskites. *Nature Communications*, 5, April 2014.

[140] Constantinos C. Stoumpos, Christos D. Malliakas, and Mercouri G. Kanatzidis. Semiconducting Tin and Lead Iodide Perovskites with Organic Cations: Phase Transitions, High Mobilities, and Near-Infrared Photoluminescent Properties. *Inorganic Chemistry*, 52(15):9019–9038, August 2013.

[141] Yukari Takahashi, Rena Obara, Zheng-Zhong Lin, Yukihiro Takahashi, Toshio Naito, Tamotsu Inabe, Shoji Ishibashi, and Kiyoyuki Terakura. Charge-

transport in tin-iodide perovskite $CH_3NH_3SnI_3$: origin of high conductivity. *Dalton Transactions*, 40(20):5563, 2011.

[142] R. D. Shannon. Revised effective ionic radii and systematic studies of interatomic distances in halides and chalcogenides. *Acta Crystallographica Section A*, 32(5):751–767, September 1976.

[143] Koichi Momma and Fujio Izumi. VESTA 3 for three-dimensional visualization of crystal, volumetric and morphology data. *Journal of Applied Crystallography*, 44(6):1272–1276, 2011.

[144] T. Umebayashi, K. Asai, T. Kondo, and A. Nakao. Electronic structures of lead iodide based low-dimensional crystals. *Physical Review B*, 67(15):155405, April 2003.

[145] Jing Feng and Bing Xiao. Crystal Structures, Optical Properties, and Effective Mass Tensors of $CH_3NH_3PbX_3$ (X = I and Br) Phases Predicted from HSE06. *The Journal of Physical Chemistry Letters*, 5(7):1278–1282, April 2014.

[146] Daniel Macdonald and L. J. Geerligs. Recombination activity of interstitial iron and other transition metal point defects in p- and n-type crystalline silicon. *Applied Physics Letters*, 85(18):4061–4063, 2004.

[147] Feng Wang, Hui Yu, Haihua Xu, and Ni Zhao. $HPbI_3$ : A New Precursor Compound for Highly Efficient Solution-Processed Perovskite Solar Cells. *Advanced Functional Materials*, 25(7):1120–1126, February 2015.

[148] Olga Malinkiewicz, Aswani Yella, Yong Hui Lee, Guillermo Mínguez Espallargas, Michael Graetzel, Mohammad K. Nazeeruddin, and Henk J. Bolink. Perovskite solar cells employing organic charge-transport layers. *Nature Photonics*, 8(2):128–132, December 2013.

[149] Atsuhiko Miyata, Anatolie Mitioglu, Paulina Plochocka, Oliver Portugall, Jacob Tse-Wei Wang, Samuel D. Stranks, Henry J. Snaith, and Robin J. Nicholas. Direct measurement of the exciton binding energy and effective masses for charge carriers in organic-inorganic tri-halide perovskites. *Nature Physics*, 11(7):582–587, July 2015.

[150] Fan Zuo, Spencer T. Williams, Po-Wei Liang, Chu-Chen Chueh, Chien-Yi Liao, and Alex K.-Y. Jen. Binary-Metal Perovskites Toward High-Performance Planar-Heterojunction Hybrid Solar Cells. *Advanced Materials*, 26(37):6454–6460, October 2014.

[151] Xiong Li, Manuel Tschumi, Hongwei Han, Saeed Salem Babkair, Raysah Ali Alzubaydi, Azhar Ahmad Ansari, Sami S. Habib, Mohammad Khaja Nazeeruddin, Shaik M. Zakeeruddin, and Michael Grätzel. Outdoor Performance and Stability under Elevated Temperatures and Long-Term Light Soaking of Triple-Layer Mesoporous Perovskite Photovoltaics. *Energy Technology*, 3(6):551–555, June 2015.

[152] Sneha A. Kulkarni, Tom Baikie, Pablo P. Boix, Natalia Yantara, Nripan Mathews, and Subodh Mhaisalkar. Band-gap tuning of lead halide perovskites using a sequential deposition process. *Journal of Materials Chemistry A*, 2(24):9221–9225, March 2014.

[153] Jun Hong Noh, Sang Hyuk Im, Jin Hyuck Heo, Tarak N. Mandal, and Sang Il Seok. Chemical Management for Colorful, Efficient, and Stable Inorganic–Organic Hybrid Nanostructured Solar Cells. *Nano Letters*, page 130321112645008, March 2013.

[154] Colin D. Bailie, M. Greyson Christoforo, Jonathan P. Mailoa, Andrea R. Bowring, Eva L. Unger, William H. Nguyen, Julian Burschka, Norman Pellet, Jungwoo Z. Lee, Michael Grätzel, Rommel Noufi, Tonio Buonassisi, Alberto Salleo, and Michael D. McGehee. Semi-transparent perovskite solar cells for tandems with silicon and CIGS. *Energy & Environmental Science*, 8(3):956–963, 2015.

[155] Philipp Löper, Soo-Jin Moon, Sílvia Martín de Nicolas, Bjoern Niesen, Martin Ledinsky, Sylvain Nicolay, Julien Bailat, Jun-Ho Yum, Stefaan De Wolf, and Christophe Ballif. Organic–inorganic halide perovskite/crystalline silicon four-terminal tandem solar cells. *Physical Chemistry Chemical Physics*, 17(3):1619–1629, 2015.

[156] Jonathan P. Mailoa, Colin D. Bailie, Eric C. Johlin, Eric T. Hoke, Austin J. Akey, William H. Nguyen, Michael D. McGehee, and Tonio Buonassisi. A 2-terminal perovskite/silicon multijunction solar cell enabled by a silicon tunnel junction. *Applied Physics Letters*, 106(12):121105, March 2015.

[157] Tomas Leijtens, Giles E. Eperon, Sandeep Pathak, Antonio Abate, Michael M. Lee, and Henry J. Snaith. Overcoming ultraviolet light instability of sensitized TiO2 with meso-superstructured organometal tri-halide perovskite solar cells. *Nature Communications*, 4, December 2013.

[158] Anyi Mei, Xiong Li, Linfeng Liu, Zhiliang Ku, Tongfa Liu, Yaoguang Rong, Mi Xu, Min Hu, Jiangzhao Chen, Ying Yang, Michael Grätzel, and Hongwei Han. A hole-conductor–free, fully printable mesoscopic perovskite solar cell with high stability. *Science*, 345(6194):295–298, July 2014.

[159] Feng Hao, Constantinos C. Stoumpos, Robert P. H. Chang, and Mercouri G. Kanatzidis. Anomalous Band Gap Behavior in Mixed Sn and Pb Perovskites Enables Broadening of Absorption Spectrum in Solar Cells. *Journal of the American Chemical Society*, 136(22):8094–8099, June 2014.

[160] Pablo P. Boix, Shweta Agarwala, Teck Ming Koh, Nripan Mathews, and Subodh G. Mhaisalkar. Perovskite Solar Cells: Beyond Methylammonium Lead Iodide. *The Journal of Physical Chemistry Letters*, 6(5):898–907, March 2015.

[161] M. A. Semary, M. F. Mostafa, and M. A. Ahmed. Magnetic susceptibility of (CH3NH3)2FeCl3Br: An example of a canted spin system. *Solid State Communications*, 25(7):443–445, 1978.

[162] H. Zhou, Q. Chen, G. Li, S. Luo, T.-b. Song, H.-S. Duan, Z. Hong, J. You, Y. Liu, and Y. Yang. Interface engineering of highly efficient perovskite solar cells. *Science*, 345(6196):542–546, August 2014.

[163] Henry J. Snaith, Antonio Abate, James M. Ball, Giles E. Eperon, Tomas Leijtens, Nakita K. Noel, Samuel D. Stranks, Jacob Tse-Wei Wang, Konrad Wojciechowski, and Wei Zhang. Anomalous Hysteresis in Perovskite Solar Cells. *The Journal of Physical Chemistry Letters*, 5(9):1511–1515, May 2014.

[164] Yuchuan Shao, Zhengguo Xiao, Cheng Bi, Yongbo Yuan, and Jinsong Huang. Origin and elimination of photocurrent hysteresis by fullerene passivation in $CH_3NH_3PbI_3$ planar heterojunction solar cells. *Nature Communications*, 5:5784, December 2014.

[165] Jin Hyuck Heo, Hye Ji Han, Dasom Kim, Tae Kyu Ahn, and Sang Hyuk Im. Hysteresis-less inverted $CH_3NH_3PbI_3$ planar perovskite hybrid solar cells with 18.1% power conversion efficiency. *Energy & Environmental Science*, 8(5):1602–1608, 2015.

[166] Wei Zhang, Michael Saliba, David T. Moore, Sandeep K. Pathak, Maximilian T. Hörantner, Thomas Stergiopoulos, Samuel D. Stranks, Giles E. Eperon, Jack A. Alexander-Webber, Antonio Abate, Aditya Sadhanala, Shuhua Yao, Yulin Chen, Richard H. Friend, Lara A. Estroff, Ulrich Wiesner, and Henry J. Snaith. Ultrasmooth organic–inorganic perovskite thin-film formation and crystallization for efficient planar heterojunction solar cells. *Nature Communications*, 6:6142, January 2015.

[167] David T. Moore, Hiroaki Sai, Kwan W. Tan, Detlef-M. Smilgies, Wei Zhang, Henry J. Snaith, Ulrich Wiesner, and Lara A. Estroff. Crystallization Kinetics of Organic–Inorganic Trihalide Perovskites and the Role of the Lead Anion in Crystal Growth. *Journal of the American Chemical Society*, 137(6):2350–2358, February 2015.

[168] Dewei Zhao, Michael Sexton, Hye-Yun Park, George Baure, Juan C. Nino, and Franky So. High-Efficiency Solution-Processed Planar Perovskite Solar Cells with a Polymer Hole Transport Layer. *Advanced Energy Materials*, 5(6):n/a–n/a, March 2015.

[169] W. Tress, N. Marinova, T. Moehl, S. M. Zakeeruddin, Mohammad Khaja Nazeeruddin, and M. Grätzel. Understanding the rate-dependent J–V hysteresis, slow time component, and aging in $CH_3NH_3PbI_3$ perovskite solar cells: the role of a compensated electric field. *Energy & Environmental Science*, 8(3):995–1004, 2015.

[170] Jeffrey A. Christians, Raymond C. M. Fung, and Prashant V. Kamat. An Inorganic Hole Conductor for Organo-Lead Halide Perovskite Solar Cells. Improved Hole Conductivity with Copper Iodide. *Journal of the American Chemical Society*, 136(2):758–764, January 2014.

[171] K.A. Nagamatsu, S. Avasthi, J. Jhaveri, and J.C. Sturm. A 12% Efficient Silicon/PEDOT:PSS Heterojunction Solar Cell Fabricated at $< 100$ °C. *Photovoltaics, IEEE Journal of*, 4(1):260–264, January 2014.

[172] Yang Shen, L. Scudiero, and M.C. Gupta. Temperature Dependence of Open-Circuit Voltage and UPS Study for P3HT:PCBM Organic Solar Cells. *Photovoltaics, IEEE Journal of*, 2(4):512–518, October 2012.

[173] Wenchao Yang, Yao Yao, and Chang-Qin Wu. Origin of the high open circuit voltage in planar heterojunction perovskite solar cells: Role of the reduced bimolecular recombination. *Journal of Applied Physics*, 117(9):095502, March 2015.